IHTEC 2017

2nd International Hydrogen Technologies Congress

March 15-18, 2017
Çukurova University,
Adana, Turkey

PROCEEDINGS BOOK

EDITORS
İbrahim DİNÇER
Adnan MİDİLLİ
Mehmet KARAKILÇIK

Adana
2017
ISBN: 978-605-66381-2-1

www.uhtek2017.org

IHTEC 2017

2nd International Hydrogen Technologies Congress

March 15-18, 2017
Çukurova University,
Adana, Turkey

PROCEEDINGS BOOK

ISBN: 978-605-66381-2-1

EDITORS

Prof. Dr. İbrahim DİNÇER
Prof. Dr. Adnan MİDİLLİ
Assoc. Prof. Dr. Mehmet KARAKILÇIK

INDEX

Forewords	4
Committees	7
Scientific Program	8
Keynote Speakers	20
Invited Speakers	27
Oral Proceedings	35
Poster Proceedings	318

FOREWORDS

WELCOMING MESSAGE

to Participants of 2nd International Hydrogen Technologies Congress

15 - 18 March 2017, Adana, Turkey

Fossil fuels (i.e., petroleum, natural gas and coal), which meet most of the world's energy demand today, are being depleted fast. Also, their combustion products are causing the global problems, such as the global warming, climate change, ozone layer depletion, acid rains, oxygen depletion and pollution, which are posing great danger for our environment and eventually for the life in our planet. Many engineers and scientists agree that the solution to these global problems would be replacing the existing fossil fuel system by the Hydrogen Energy System. Hydrogen is the lightest, most efficient and cleanest fuel. Its use will produce no greenhouse gases, no ozone layer depleting chemicals, little or no acid rain ingredients, no oxygen depletion and pollution.

Around the world, there is extensive r&d work on Hydrogen Energy. Internal combustion engines are being modified for hydrogen fuel. Many types of fuel cells - to convert hydrogen efficiently to electricity - are being developed. Vehicle manufacturers have built several experimental cars and buses. Hyundai, Toyota, Honda and Mercedes companies started selling hydrogen fueled cars. Many bus companies are selling hydrogen fueled buses. Siemens Company is selling hydrogen fuel cells powered submarines. Hydrogen fueled appliances based on catalytic combustion have been built. There is research and development work on hydrogen hydride refrigeration and air conditioning systems. Aircraft manufacturers are working on hydrogen fueled subsonic and supersonic transport planes.

Scientists and Engineers from many countries of the world will gather at the IHTEC2017 Conference to present their papers covering the recent advances in hydrogen energy and in hydrogen technologies. All these will no doubt speed up the conversion to hydrogen economy, eliminate global environmental problems, and provide the humankind with higher living standards. I congratulate the organizers of this Congress and wish all the participants a very fruitful meeting and pleasant days in beautiful Adana, Turkey.



T. Nejat Veziroğlu

Honorary Chair, IHTEC2017

President, International Association for Hydrogen Energy

MESSAGE FROM THE PRESIDENT

Organizing the Second International Hydrogen Technologies Congress (initially started as the National Hydrogen Technologies Congress) is another milestone in Turkey's hydrogen energy activities under the leadership of the National Hydrogen Energy Association. Due to the increasing interest in carbon free alternatives hydrogen energy technologies appear to be the central point to formulate energy solutions for all sectors, ranging from industrial to transportation. The past climate change conference in Paris, France a year ago made it clear that the renewable energy based and carbon-free solutions will be critical in addressing both local and global environmental issues and provide clean and sustainable options for implementation.

It is also important to note that the National Hydrogen Energy Association was able to secure one of the next organizations of the 24th World Hydrogen Energy Congress first time in 2022, in Istanbul, Turkey. This is a true achievement of the Association and the efforts of its Board. The Association is now getting ready to be one of the world's most successful societies in the area of hydrogen technologies. This is of course not easy. It requires great efforts from the parties of academia, industry and government agencies, as well as individually from every one of us working in the area of hydrogen and related technologies. It is also equally important for us to primarily focus on coupling renewables and hydrogen energy technologies for implementation.

We are now getting together for our second congress in the area of hydrogen technologies, after organizing the first one in Istanbul, in Cukurova University in Adana, which aims to bring researchers, scientists, engineers and practitioners, who are working in the subject matter area, to provide a forum to exchange ideas, disseminate new research developments and discuss latest advances, new directions and priorities for a carbon-free future with hydrogen. We are happy to have numerous leading researchers here to share the newest ideas and latest technologies and developments. Over 120 technical papers will provide an ample opportunity to learn about a wide range of topics with distinguished presenters from over ten countries. Furthermore, delegates will benefit from the exchange of ideas, problems and solutions with a large number of technical experts.

Many individuals have contributed in significant ways to organize and prepare this conference. As the Association President, I would like to register my sincere appreciation to the Organizing Committee, Executive Organizing Committee, and the honorary chair, Dr. T. N. Veziroglu, the congress chair, Dr. Mehmet Karakilcik and secretary general Dr. Adnan Midilli. Also, I would like to acknowledge the assistance, support and coordination of Bros Congress Team. Last but not least, I warmly thank the congress keynote speakers, authors, session chairs, and all attendees, whose contributions and efforts will make this conference a great success.



Ibrahim Dincer
President
National Hydrogen Energy Association

FOREWORDS

WELCOME FROM THE CONFERENCE CHAIRMAN

I am very happy to serve for "The Second International Hydrogen Technologies Congress" as conference chairman. This congress was initially held in Istanbul in December 2015 as the first one, and we are now ready to start the second one as hosted by Çukurova University in Adana. This conference is organized as an annual event under the National Hydrogen Technologies Association and sponsored by Governor of Adana, the Culture and Tourism Ministry Adana Provincial Directorate of Culture and Tourism Provincial Manager, the Mayor of Adana Metropolitan Municipality, the Mayor of Sarıçam Municipality, Adana Chamber of Industry, Adana Chamber of Commerce, Çukurova TEKNOKENT, Bariş Engineering, Solitek Engineering, UCTEA Chamber of Mechanical Engineers, Adana Branch and Çukurova University Project Development and Coordination Unit (BAP).

This Congress in Çukurova University in Adana focus particularly on "Hydrogen Technologies", and specially on all related systems and applications to cover the entire spectrum to serve for hydrogen economy. It brings together 4 keynote speakers, 2 invited speakers and over 120 participants from 10 countries for a period of four days to discuss, disseminate and network on various aspects of hydrogen production processes ranging from its performance analysis and fuell cells, transportation, distribution, security, strategies and policies and those applications, through the topics, like renewable hydrogen production and technologies, biological hydrogen production and technologies, thermochemical hydrogen production and technologies, electrolytic hydrogen production and technologies, photochemical hydrogen production and technologies, pyrolysis, gasification and plasma hydrogen production, hydrogen production and micro process technologies, hydrogen separation and cleaning technologies, hydrogen storage materials and technologies, hydrogen applications and technologies, hydrogen fuel cells, hydrogen transportation, distribution and security, hydrogen strategies and policies, modeling, energy and exergy analysis. In addition, there is a panel on the last day of the Congress with five distinguished speakers to discuss the clean energy solutions and the role of hydrogen in these solutions

I wish to formally put on record my sincere thanks to numerous key people and organizations that have been instrumental in ensuring the success of IHTEC2017 in Cukurova University in Adana. I would like to thank Prof. Dr. Mustafa Kibar, Rector of Cukurova University and his management for their full support

I would like to register my sincere appreciation to Professor N. T. Veziroğlu, President of International Association for Hydrogen Energy and Founding and Honorary Editor of International Journal of Hydrogen Energy (IJHE) and Professor Ibrahim Dincer, President of National Hydrogen Association and his management along with the Bros Congress Team.

Finally, I would like to thank all keynote speakers, invitied speakers, oral and poster presenters, all participants, all sponsors and the organizing committee members, as well as Bros Congress members for their exemplary contribution and support.



Mehmet Karakilcik

Congress Chair, IHTEC2017

COMMITTEES

Honarary Chairs
Veziroglu, T.N. / USA
Kibar, M. / Rector/CU/Turkey

General Chair
Dincer, I. / Canada/Turkey

Congress Chair
Karakilcik, M. / Turkey

Technical Chair
Midilli, A. / Turkey

Executive Committee
Dincer, I. / HTA/Turkey
Eroglu, I. / HTA/Turkey
Karaosmanoglu, F. / HTA/Turkey
Kargı, F. / HTA/Turkey
Midilli, A. / HTA/Turkey
Solmaz, R. / HTA/Turkey
Tuncer, G. / HTA/Turkey
Yazici, S. / HTA/Turkey

Local Organizing Committee
Akbulut, U. / Turkey
Cilogullari, M. / Turkey
Erden, M. / Turkey
Kalinci, Y. / Turkey
Karakilçik, H. / Turkey
Kilincceker, G. / Turkey
Kucuk, H. / Turkey
Mert, S.O. / Turkey
Oksuz, H.I. / Turkey
San, S. / Turkey

Local Advisory Board
Apak, S. / Turkey
Ata, A. / Turkey
Aydin, K. / Turkey
Basibuyuk, M. / Turkey
Bayrakceken, A. / Turkey
Buyukalaca, O. / Turkey
Colpan, C.O. / Turkey
Devrim, Y. / Turkey
Gumuş, C. / Turkey
Kaval, Y. / Turkey
Kardas, G. / Turkey
Paksoy, H.O. / Turkey
Serin, S. / Turkey
Sahin, A.D. / Turkey
Sahin, B. / Turkey
Şahin, M. / Turkey
Tuncer, G. / Turkey
Yazici, B. / Turkey
Yazici, S. / Turkey
Yilmaz, T. / Turkey

International Scientific Board
Veziroglu, T.N. / USA
Agar, E. / USA
Akansu, S. / Turkey
Ayas, N. / Turkey
Avaca, L.A. / Brazil
Azbar, N. / Turkey
Baykara, S. / Turkey
Bolcich, J.C. / Argentina
Demirci, U. / France
Dewi, E.L. / Indonesia
Dincer, I. / Canada
Dogan, F. / USA
Eljrushi, G.S. / Libya
Eroglu, I. / Turkey
Goltsov, V.A. / Ukraine
Goswami, Y. / USA
Gorgun, H. / Turkey
Guvenc, Z.B. / Turkey
Hamdullahpur, F. / Canada
Hart, D. / Switzerland
Hepbasli, A. / Turkey
İbrahimoglu, B. / Turkey
İlbas, M. / Turkey
Kadirgan, F. / Turkey
Kaplan, Y. / Turkey
Karakoc, H. / Turkey
Karaosmanoglu, F. / Turkey
Kargı, F. / Turkey
Koca, A. / Turkey
Koylu, U.O. / USA
Kumbur, E.C. / USA
Li, X. / Canada
Mao. Z.Q. / China
Marchetti, C. / Italy
Mench, M.M. / U.S.A
Midilli, A. / Turkey
Miranda, P.E. / Brazil
Naterer, G.F. / Canada
Osmanoglu, B. / Turkey
Ozkar, S. / Turkey
Ozkaya, A.R. / Turkey
Ozturk, T. / Turkey
Piskin, S. / Turkey
Pollet, B. / South Africa
Ramenskiy, A.Y. / Russia
Sheffield, J.W. / USA
Solmaz, R. / Turkey
Soo Oh, B. / S. Korea
Srivastava, O.N. / India
Sahin, Ö. / Turkey
Sahin, S. / Turkey
Uchida, H. / Japan
Stolten, D. / Germany
Veziroglu, E.A. / USA
Veziroglu, A. / USA
Yanik, J. / Turkey
Yildiz, İ. / Canada
Yurum, Y. / Turkey

SCIENTIFIC PROGRAM

SCIENTIFIC PROGRAM

March 15, 2017

Mithat Özsan Amphitheater (HALL - A)	
08:00-09:30	Registration
09:30-10:00	**Opening Talks** **Mehmet Karakılçık** *(Congress Chair)* **İbrahim Dincer** *(President, National Hydrogen Energy Association)* **Mustafa Kibar** *(Rector, Cukurova University)*
10:00-10:50	**Overview Talk on Novel Hydrogen Production Technologies** ***Ibrahim Dincer***
10:50-11:00	**Coffee Break**
	Chair: *İnci Eroğlu*
11:00-11:50	**Keynote Speaker** - ***Tayfur Öztürk*** "Development of rare earth free metal hydrides for elecrochemical hydrogen storage"
12:00-13:30	**LUNCH** *(Ç.U. Center Cafeteria)*
13:30-14:00	**Invited Speech - *Halime Paksoy*** "Energy Storage - Key Technology For Sustainable Future"
14:00-15:40	**Session 1** - Biological hydrogen production and technologies **Chair: *Fikret Kargı***
14:00:14:20	[8] Biohydrogen Production with C. intestinale in Lignocellulosic Substrates ***Serpil Özmıhçı, Gülsün Gizem Taylan, Merve Özlem Vurmaz***
14:20-14:40	[18] Biohydrogen Production by Extracted Fermentation from Sugar Beet ***Serkan Eker, Burcu Erkul***
14:40-15:00	[21] Hydrogen gas production from food wastes by electrohydrolysis using a Statical design approach ***Ebru Çokay***
15:00-15:20	[192] Effects of Land Use and Microbial Technology to Obtain Biomass from Salty and Marginal Lands in Turkey ***Ali Khalvati, N. Javani***
15:20-15:40	[54] Effects of Process, Operational and Environmental Variables on Biohydrogen Production Using Palm Oil Mill Effluent (POME) ***Bidattul Syirat Zainal, Shaliza Ibrahim, Ali Akhbar Zinatizadeh, Nuruol Syuhadaa Mohd***
15:40-15:55	**Coffee Break**
15:55-17:35	**Session 4** - Pyrolysis, gasification and plasma hydrogen production **Chair: *Tayfur Öztürk***
15:55-16:15	[2] Performance Investigation of Zirconium Hydrogen Phosphate / Sulphonated Polysulfone Composite Membrane Based DMFCs ***Mustafa Ercelik, Yagmur Ozdemir, Adnan Ozden, Yilser Devrim, Can Ozgur Colpan, Feridun Hamdullahpur***
16:15-16:35	[66] Synthesis of La-Mg-Ni-Co Hydrogen Storage Alloys by Electro-deoxidation ***Alanur Binal Aybar, Mustafa Anik***
16:35-16:55	[87] Co-gasification of Çan Lignite with Kenaf Hydrolysate: Effects of Temperature and Flow rate ***Açelya Seçer, Nilgün Küçet, Arif Hasanoğlu***

16:55-17:15	[88] Comparison of Silica and Alumina Based Catalysts in Hydrogen Production From Biomass ***Birce Pekmezci Karaman, Nurbanu Çakıryılmaz, Hüseyin Arbağ, Nuray Oktar, Gülşen Doğu, Timur Doğu***
17:35-17:50	**Coffee Break**
17:50-18:30	**POSTER Session 1**
18:30-21.30	**COCKTAIL** *(Ç.U. Kayıkhane)*

Mithat Özsan Amphitheater (HALL - B)	
13:30-14:00	**Invited Speech - *Kadir Aydın*** "Future of Hydrogen Usage in Automotive Industry"
14:00-15:40	**Session 2** - Renewable hydrogen production and technologies **Chair: *Adnan Midilli***
14:00:14:20	[90] Investigation of Hydrogen Production Performance of a Reactor Assisted by a Solar Pond by Photoelectrochemical Method ***Mehmet Karakilcik, Mustafa Erden, Muzeyyen Cilogullari, Ibrahim Dincer***
14:20-14:40	[122] Thermodynamic assessment of combined geothermal energy based hydrogen production and liquefaction system ***Yunus Emre Yuksel, Murat Ozturk, Ibrahim Dincer***
14:40-15:00	[132] Hydrogen Production Potential From Solar Energy in Kayseri ***Gamze Genc, Seyfettin Gurel***
15:00-15:20	[146] A Parametric Study on A Run-of-the River Mini Hydropower Plant Integrated Hydrogen Production ***Adnan Midilli, Mert Özsaban***
15:20-15:40	[148] Assessment of a Geothermal Based Integrated System For Power and Hydrogen Production ***Hatice Karakilcik, Mustafa Erden, Mehmet Karakilcik***
15:55-17:35	**Session 5** - Hydrogen fuel cells **Chair: *Hikmet Karakoç***
15:55-16:15	[85] A Rewiew on Novel Flow Field Designs For Pem Fuel Cells and Systematic Comparison of Designs ***Erman Çelik, Irfan Karagöz***
16:15-16:35	[101] Affective Factors Improving Catalyst Layers of PEM Fuel Cell ***Gokce S Avcioglu, Berker Ficicilar, Inci Eroglu***
16:35-16:55	[102] Three-Dimensional Nonisothermal Model Development of High Temprature PEM Fuel Cells ***Berna Sezgin, Dilara Gülçin Çağlayan, Yılser Devrim, Inci Eroğlu***
16:55-17:15	[131] Parametric investigation of 3D geometrical design of pem fuel cells ***Muhammed Mücahit Toprak, Mehmet Utku Badak, Suha Orçun Mert***
17:15-17:35	[133] Electrochemical Property of Nano-Composite Electrolyte for Fuel Cells ***Shalima Shawuti, Ahmet Deniz Benli, Mehmet Ali Gulgun***

SCIENTIFIC PROGRAM

İ. Akif Kansu Congress Hall (HALL - C)	
14:00-15:40	**Session 3** - Hydrogen transportation, distribution, security, strategies and policies **Chair:** ***Özgür C. Çolpan***
14:00:14:20	[10] Cost and Productivity Analysis of Storage and Distribution Processes of a Solar Driven Hydrogen Production Plant ***Murat Emre Demir, İbrahim Dinçer***
14:20-14:40	[80] Numerical modelling of hydrogen-natural gas mixtures flows in looped networks ***Zahreddine Hafsi, Sami Elaoud, Lamjed Hadj Taieb***
14:40-15:00	[126] Optimal Design of a Hydrogen Refueling Station Powered by Wind-PV Hybrid Power System ***Murat Gökçek, Cihangir Kale***
15:00-15:20	[137] Parametric investigation of direct catalytic conversion of synthesis gas to dimethyl ether ***Hatice Merve Can, Zeynep Ilsen Önsan, Ahmet Kerim Avci***
15:20-15:40	[139] Catalytic reforming of glycerol to hydrogen in wall coated microchannels ***Amin Delparish, Ahmet Kerim Avci***
15:55-17:35	**Session 6** - Hydrogen separation and cleaning technologies **Chair:** ***Birgül Yazıcı***
15:55-16:15	[12] Boron based hydrogen storage technologies and synthesis of some metal borohydrides ***Gözde Bayazit, Şadan Özcan, Mükerrem Şahin***
16:15-16:35	[30] Oxygen Production on Asymmetric Terminal Alkynyl Zinc Phthalocyanines and Modified Electrodes Using Click Electrochemical Technique ***Duygu Akyüz, Atıf Koca***
16:35-16:55	[70] Thermodynamic Modeling and Optimization of a Hydrogen Liquefaction System Using Geothermal Energy ***Ceyhun Yılmaz***
16:55-17:15	[96] Synthesis and Characterization of IrxRu1-xO2 Catalysts for the Oxygen Evolution Reactions ***Mehmet Fatih Kaya, Nesrin Demir, Ayşe Bayrakçeken Yurtcan***
17:15-17:35	[161] Optimization of Operation Conditions of Solar Thermal Water Splitting Process ***Ezgi Yavuzyılmaz, Deniz Üner, Serkan Kıncal***

March 16, 2017

Mithat Özsan Amphitheater (HALL - A)	
	Chair: ***Mohamed Hamed***
09:00-09:45	**Keynote Speaker** - ***İnci Eroğlu*** "Development of renewable hydrogen energy systems"
09:45-10:30	**Keynote Speaker - *Fikret Kargı*** "Hydrogen gas production by electrohydrolysis of organic wastes"
10:30-10:45	**Coffee Break**
10:45-12:25	**Session 7** - Biological hydrogen production and technologies **Chair: *Mehmet Suha Yazıcı***
10:45-11:05	[60] Dark fermentative hydrogen gas production from waste peach pulp in a pilot scale reactor ***Hidayet Argun, Siaka Dao***
11:05-11:25	[86] Determining the effect of trace elements on biohydrogen production from fruit and vegetable wastes ***Tugba Keskin Gündoğdu, Kübra Arslan, Haris Nalakath Abubackar, Gozde Duman, Koray Akarsu, Jale Yanık, Nuri Azbar***
11:25-11:45	[144] The Effect of Bacteriologically Generated Carbohydrates on Electrocatalytic Oxidation and Hydrogen Efficiency ***Güray Kılınççeker, Mehmet Karakilcik, Eren Caglar, Mustafa Kemal Sangun***
11:45-12:05	[153]Evaluation of waste paper towel for hydrogen gas production by dark fermentation ***Hidayet Argun, Gülizar Onaran***
12:05-12:25	[123] High Yield Hydrogen Production From Sodium Borohydride By Non-Catalytic Steam Reforming: A Parametric Study ***Meryem Sena Akkuş, Hatice Begüm Murathan, Derya Öncel Özgür, Gülay Özkan, Göksel Özkan***
12:25-13:30	**LUNCH** *(Ç.U. Center Cafeteria)*
	Chair: *Tayfur Öztürk*
13:30-14:15	**Keynote Speaker - *Sema Z. Baykara*** "Hydrogen: Sources and Production"
14:15-15:55	**Session 10** - Hydrogen production and micro process technologies **Chair: *Sema Z. Baykara***
14:15-14:35	[11] Preparation of nickel and bismuth deposited titanium dioxide nano-tubes and investigation of electrochemical hydrogen production performance ***Başak Doğru Mert, Mehmet Erman Mert, Birgül Yazıcı Devrim***
14:35-14:55	[22] Hydrogen Production by Aluminum, Copper Doped Zinc Oxide Semiconductor ***Bulut Hüner, Esra Telli, Murat Farsak***
14:55-15:15	[89] Various Amine Compounds Stabilized Pd(0) Nanoparticles: Synthesis, Identification and Catalytic Use in the Dehydrogenation of Dimethylamine-Borane ***Ebru Köktepe, Sibel Duman***
15:15-15:35	[103] Palladium Based Electrocatalysts for Ethylene Glycol Fuel Cells ***Özlem Gökdoğan Şahin, Hilal Demir Kıvrak***

15:35-15:55	[115] Copper-covered AA6013-T6 Al Anode(Al/Cu) for Al-Air Battery ***Rasiha Nefise Mutlu, Birgül Yazıcı***
15:55-16:10	**Coffee Break**
16:10-17:10	**POSTER Session 2** *(Mithat Özsan Amphitheater Foyer Area)*
18:30-21:00	**GALA DINNER** *(Nezihe Yalvaç Uygulama Oteli)*

Mithat Özsan Amphitheater (HALL - B)	
10:45-12:25	**Session 8** - Thermochemical and photochemical hydrogen production and technologies **Chair:** ***Filiz Karaosmanoğlu***
10:45-11:05	[7] Performance Evaluation of a Photoelectrochemical Hydrogen Production Reactor under Concentrated and Non-Concentrated Light ***Yusuf Biçer, İbrahim Dinçer***
11:05-11:25	[61] Investigation the effect of annealing atmosphere and time on photoelectrochemical (PEC) properties of α-Fe2O3 photoanode ***Selim Demirci, Cevat Sarıoğlu***
11:25-11:45	[149] Transport Limitations of Oxygen Exchange in Solar Thermochemical Hydrogen Production: An Experimental Study on Co3O4 ***Atalay Çalışan, Serkan Kıncal, Deniz Üner***
11:45-12:05	[165] Investigation of Magnetic Field Effect on Hydrogen Production Performance by Aqueous Methanol Electrolysis ***Emrumiye Arli, Zeynep Baz, Hatice Karakilcik, Mehmet Karakilcik, Güray Kılınçeker***
12:25-13:30	**LUNCH** *(Ç.U. Center Cafeteria)*
14:00-16:15	**Session 11** - Hydrogen fuel cells **Chair:** ***Jale Yanık***
14:15-14:35	[3] Investigation of Working Temperature Effect on Micro-Cogeneration Application of Proton Exchange Membrane Fuel Cell ***Yağmur Budak, Yağmur Özdemir, Yılser Devrim***
14:35-14:55	[4] Fabrication of cross-linked Polybenzimidazole membranes for high temperature PEM fuel cells and investigation of the amount of cross-linker used on membrane performance ***Yağmur Özdemir, Necati Özkan, Yılser Devrim***
14:55-15:15	[5] A comparative study on the modelling of flow plates with different channel design in PEM fuel cell / ***Elif Eker Kahveci, İmdat Taymaz***
15:15-15:35	[42] Production of CVD Graphene Electrocatalyst for Oxygen Reduction Reaction ***Mehmet Akif Azder, Ömer Salihoğlu, M. Suha Yazıcı***
15:35-15:55	[43] CVD Graphene Doping for Fuel Cell Electro-catalyst Development: Literature Survey / ***Mehmet Suha Yazici***
15:55-16:15	[109] Hydrogen production from municipal solid wastes by hydrothermal gasification ***Jale Yanik, Gözde Duman, Koray Akarsu, Tugba Keskin Gündoğdu, Kübra Arslan, Nuri Azbar, Haris Nalakth Abubackar***

İ. Akif Kansu Congress Hall (HALL - C)	
10:45-12:25	**Session 9** - Electrolytic hydrogen production and technologies **Chair:** ***Gulfeza Kardas***
10:45-11:05	[99] High-Yield Hydrogen Production Through Aqueous-Phase Reforming of Biomass Hydrolysate Over Carbon Nanotube Supported Pt Catalysts ***Burçak Kaya Özsel, Bahar Meryemoğlu, Berna Niş, Arif Hasanoğlu***
11:05-11:25	[100] Effect of SiC formation on sustainability of H2 production in the presence of Ni core-shell microsphere catalysts ***Gamze Gunduz Meric, Levent Değirmenci***
11:25-11:45	[110] Hydrogen Productionfrom the Methanolysis Ofammonia Borane BY Pd-Co/Al2O3 Coated Monolithic Catalyst ***Hatice Begüm Murathan, Gülay Özkan, Meryem Sena Akkuş, Derya Öncel Özgür, Göksel Özkan***
11:45-12:05	[111] Hydrogen Generation From the Dehydrogenation of Ammonia Borane By Using Amberlyst-15 Supported Catalysts ***Derya Öncel Özgür, Tayyibe Şimşek, Göksel Özkan, Meryem Sena Akkuş, Gülay Özkan***
12:05-12:25	[119] Grain Boundaries Contribution on Ionic Conductivity of Oxide Semiconductors ***Musa Mutlu Can, Shalima Shawuti, Mehmet Ali Gülgün, Ayşe Zehra Aroğuz, Harun Cerit***

SCIENTIFIC PROGRAM

March 17, 2017

Mithat Özsan Amphitheater (HALL - A)	
08:30-10:05	**Session 12** - Hydrogen applications and technologies **Chair:** ***Mustafa Kemal Sangun***
08:30-08:50	[45] Electrochemical preparation and characterization of NiPd deposited Ni-modified carbon felt electrodes and their application for hydrogen evolution reaction in alkaline solution ***Ramazan Solmaz***
08:50-09:05	[113] Two New Bio-inspired Distributed and One Side Inlet Honeycomb Flow Field Designs for PEM Fuel Cells and Performance Investigation of Models via CFD Tools ***Erman Çelik, Irfan Karagöz***
09:05-09:25	[124] Thermodynamic analysis of the carbon dioxide cycles driven by geothermal power system with hydrogen production ***Yunus Emre Yuksel, Murat Ozturk***
09:25-09:45	[143] Investigation of Hydrogen Production by using Silver Covered Platinum Electrode in Base Media ***Guray Kilincceker, Mehmet Karakilcik, Refik Cetin, Mustafa Kemal Sangun***
09:45-10:05	[75] Reduced graphene oxide assembled bimetallic PdM (M = Fe, Ag, Au) alloy nanoparticles as high-performance electrocatalysts for direct borohydride fuel cells ***Önder Metin, Melike Sevim, Marta Martins, Biljana Šljukić, Diogo M.f. Santos***
10:05-10:20	**Coffee Break**
10:20-12:00	**Session 14** - Biological hydrogen production and technologies **Chair:** ***Canan Acar***
10:20-10:40	[44] Preparation of MoPd deposited carbon felt electrodes and investigation of their electrochemical activity for hydrogen ***Derya Dilek Demir, Abdullah Salcı, Ramazan Solmaz***
10:40-11:00	[64] Investigation on part-load performance of a hydrogen-blended gasoline rotary engine at two speeds ***Teng Su, Changwei Ji, Shuofeng Wang, Lei Shi, Jinxin Yang, Xiaoyu Cong***
11:00-11:20	[156] Synthesis of Polymer Supported Ni (II) - Schiff Base Complex and Its Usage as a Catalyst in Hydrogen Generation From NaBH4 Hydrolysis ***Dilek Kilinç, Omer Sahin***
11:20-11:40	[172] Bonding Strength and Fuel Sealing Tests For Crofer®22 APU Solid Oxide Fuel Cell Metallic Interconnects ***Bülent Öztürk, Alparslan Topcu, Sultan Öztürk, Ömer Necati Cora***
11:40-12:00	[177] Study of the electronic properties of titanium oxide thin films for water photolysis and hydrogen production ***Cebrail Gumus, Yuksel Ufuktepe***

SCIENTIFIC PROGRAM

Mithat Özsan Amphitheater (HALL - B)	
08:30-10:05	**Session 13** - Hydrogen transportation, distribution, security, strategies and policies **Chair:** ***Tanay Sıdkı Uyar***
08:30-08:50	[164] Approach to Design of Control Electronic on Energy Storage Systems of Hydrogen Fuel Cell Vehicles ***Yakup Hameş, Kemal Kaya, Ömer Türksoy, Arzu Türksoy***
08:50-09:05	[138] Role of Hydrogen in 100 % Renewable Energy Systems of the Future ***Tanay Sıdkı Uyar***
09:05-09:25	[158] Analysis of Control Strategies for Fuel Saving in the Hydrogen Fuel Cell Vehicles ***Yakup Hameş, Kemal Kaya, Ertuğrul Baltacıoğlu, Arzu Türksoy***
09:25-09:45	[159] Nuclear-based Hydrogen Production Cost Evaluation for Two Possible Nuclear Power Plants ***Fatih Sorgulu, Ibrahim Dincer***
09:45-10:05	[81] Future of the Hydrogen Energy at the light of Transatlantic Trade and Investment Partnership – ''TTIP '' between the USA and EU ***Sudi Apak, Erhan Atay, Duygu Erdoğan, Güngör Tuncer***
10:05-10:20	**Coffee Break**
10:20-12:00	**Session 15** - Hydrogen storage materials and technologies **Chair:** ***Güngör Tuncel***
10:20-10:40	[32] Methods of Hydrogen Storage in Energy Conversion Systems ***Muhittin Bilgili***
10:40-11:00	[41] Comperative analysis of two mobile cooling systems with solar source and energy storage in off-grid areas ***Ümit Deniz Akyavuz, Hasan Özcan***
11:00-11:20	[134] Experimental investigation of Ni-doped multi-walled carbon nanotubes for Hydrogen storage at different temperatures ***Songül Kaskun, Muhammet Kayfeci***
11:20-11:40	[53] Daily Performance Assessment of an Integrated Thermal System on Hydrogen Production ***Ayhan Atiz, Mustafa Erden, Müzeyyen Cilogullari, Mehmet Karakilcik***

12:00-13:30	**LUNCH (Cafeteria)**
14:00-18:00	**TARSUS TAŞKUYU CAVERN ve Eshab-ı Kehf**
18:00-19:00	**DEPARTURE**
19:00-21:00	**DINNER (ATOSEV Restoran)**

SCIENTIFIC PROGRAM

March 18, 2017

Mithat Özsan Amphitheater (HALL - A)	
09:00-11:00	**Session 16** - Modeling, energy and exergy analysis **Chair:** ***Canan Acar***
09:00-09:20	[52] Energetic and Exergetic Investigations of an Innovative Light-based Hydrogen Production Reactor / ***Canan Acar, Ibrahim Dincer***
09:20-09:40	[147] Investigation of the Underground Hydrogen Storage Structures / ***Hatice Karakilcik***
09:40-10:00	[56] Estimation of required hydrogen flow rate for PEMFC by using artificial neural network ***Mehmet Seyhan, Yahya Erkan Akansu, Mustafa Sarioglu***
10:00-10:20	[57] Investigation of Effect of Spark-Plug Plasma Synthetic Jet Actuator on Pem Fuel Cell Performance ***Yahya Erkan Akansu, Mehmet Seyhan, Cihan Yesildag, Vuralcan Hammutoglu***
10:20-10:40	[166] Enhancement of Efficiency on Hydrogen Network via Pinch and Exergy Analysis ***Fatma Alyer, Zehra Özçelik***
10:40-11:00	[171] An investigation on exergetic performance of hydrogen gas flowing through the annular curved duct. / ***Adnan Midilli, Haydar Kucuk, Ugur Akbulut***
11:00-11:15	**Coffee Break**
14:00-16:00	**PANEL (Türkiye'nin Sürdürülebilir Kalkınmasında Temiz Enerji Çözümleri ve Hidrojenin Rolü)**

Mithat Özsan Amphitheater (HALL - B)	
09:00-11:40	**Session 17** - Modeling, energy and exergy analysis **Chair:** ***Ramazan Solmaz***
09:00-09:20	[17] Performance Assessment of Calcium Bromide Thermochemical Cycle for Hydrogen Production / ***Fatih Yilmaz, Reşat Selbaş***
09:20-09:40	[24] Optimization of Particle Number, Substrate Concentration and Temperature of Batch Immobilized Reactor System for Biohydrogen Production by Dark Fermentation ***Pelin Gökfiliz Yıldız, İlgi Karapınar***
09:40-10:00	[181] Modelling of Hydrogen Production From Hydrogen Sulfide in Geothermal Power Plants / ***A. Karapekmez, Ibrahim Dincer***
10:00-10:20	[62] Biohydrogen Production from Acid Hydrolyzed Waste Wheat in a Continuously Operated Packed Bed Reactor / ***Betul Kirli, Ilgi Karapinar***
10:20-10:40	[79] Thermodynamic analysis of OTEC based hydrogen production system ***Murat Öztürk, Fatih Yilmaz, Reşat Selbaş***
10:40-11:00	[188] A Numerical Analysis of an Ejector for Micro Combined Heat and Power Systems Based on 1 kw Solid Oxide Fuel Cell ***Omer Genc, Serkan Toros, Mohammad Ziauddin Chowdhury,***
11:00-11:20	[189] Numerical Investigation of the Effect of Channel Width to Land Ratio on PEM Fuel Cell Performance / ***Mohammad Ziauddin Chowdhury, Omer Genc, Serkan Toros***
11:20-11:40	[151] Parametric Analysis of Hydrogen Storage Taking into Account of Three Different Metal Hydride Materials / ***Ümran Elmas, Fevzi Bedir, Muhammet Kayfeci***
11:40-12:00	[129] Energetic and Economic Analysis of On-board Hydrogen Production System in SI Engine Vehicle ***Habib Gürbüz, Hüsameddin Akçay, Ismail Hakkı Akçay, Selim Demirtürk***

POSTERS / *Chair: Uğur Akbulut*

AbsRef	Abstract Title
0029	Preparation of electrochemically Mo-deposited carbon felt electrodes for alkaline water electrolysis: Optimization of pH, current and metal amount Derya Dilek Demir, Abdullah Salcı, Ramazan Solmaz
0046	Hydrogen production by alkaline water electrolysis at activated Cu/NiCuZn electrodes: Metal ratio, deposition current density and thickness optimizations Ramazan Solmaz, Gülfeza Kardaş
0047	The effect of diameter of three-dimensional silver nanodomes on electrochemical hydrogen production Handan Yüksel, Ayşe Özbay, Mehmet Kahraman, Ramazan Solmaz
0058	Graphene Aerogel supported Platinum catalyst for formic acid electrooxidation Mehmed Selim Çögenli, Ayşe Bayrakçeken Yurtcan
0067	Effect of Temperature on Catalytic Gasification of Biomass for Hydrogen Production Bahar Meryemoğlu, Mehtap Kurtuluş, Ihsan Demirci, Sibel Irmak, Arif Hasanoglu
0068	Low Temperature-Steam Phase Catalytic Gasification of Biomass Hydrolysates Arif Hasanoğlu, Bahar Meryemoğlu, Ihsan Demirci, Sibel Irmak
0074	Catalytic activity of PtRu/C, PtPd/C and PtSn/C bimetalic catalysts toward methanol oxidation reaction Mehmed Selim Çögenli, Ayşe Bayrakçeken Yurtcan
0084	Photoelectrochemical Activity of ZnO Nanorods: Synthesis and characterization Fatih Tezcan, Asad Mahmood, Gülfeza Kardaş
0091	Hydrogen Release from Dehydrogenation of Ammonia Borane by Isolable And Reusable In Situ Generated Oleylamine Stabilized Nickel(0) Nanoparticles Sibel Duman
0094	Bimetallic PdM (M: Au, Fe) Alloy Nanoparticles Assembled on Reduced graphene oxide as Highly Efficient Catalysts for Hydrogen Evolution Reaction Melike Sevim, J.a.s.b Cardoso, D.s.p. Cardoso, D.m.f. Santos, Önder Metin
0097	Synthesis of CoB Nano-Powder as Electrode Material Nilüfer Küçükdeveci, Mustafa Anık
0098	Electrocatalytic Hydrogen Production on GCE/RGO/Au Hybrid Electrode Didem Balun Kayan, Merve Ilhan, Derya Koçak
0105	Noble Metal-Free Oxides for the Oxygen Evolution Reactions Prepared by Adam's Fusion Method Nesrin Demir, Mehmet Fatih Kaya, Mehmed Selim Çögenli
0107	Monodisperse Pd Nanoparticles assembled on rGO-Fe3O4 nanocomposites as a high-performance electrocatalyst for borohydride fuel cells Buse Sündü, Melike Sevim, Marta Martins, Biljana Šljukić, Diogo M.f. Santos, Önder Metin
0116	Development of Tungsten or Ceria Incorporated Mesoporous Alumina Supported Nickel Catalysts for Hydrogen Production through Diesel Steam Reforming Reaction Arzu Arslan Bozdağ, Arife Derya Deniz Kaynar, Naime Aslı Sezgi, Timur Doğu
0117	Sorption Enhanced Steam Reforming of Ethanol with Ceria-SBA-15 Supported Nickel Catalysts Merve Sarıyer, Arzu Arslan Bozdağ, Naime Aslı Sezgi, Timur Doğu
0130	Fabrication, characterization and hydrogen evolution activity of three-dimensional nickel nanodomes Bedia Semra Taşçı, Handan Yüksel, Ramazan Solmaz

SCIENTIFIC PROGRAM

0136	Bimetallic nanoparticles for alcohol oxidation Hilal Demir Kıvrak, Özlem Gökdoğan Şahin
0140	Utilization of N-doped carbon materials obtained from ZIF as catalyst support for PEM fuel cell Niyazi Özçelik, Ayşenur Öztürk, Gamze Bozkurt, Mehmed Selim Çögenli, Ayşe Bayrakçeken Yurtcan
0145	Performance Analysis of a Conceptual Hydrogen Fueled Ramjet Engine: Exergetic Perspective Yasin Şöhret, Selçuk Ekici, T. Hikmet Karakoç
0154	Diamond like carbon (DLC) coated on TiO2-NT-Ag electrode by MW ECR plasma system for hydrogen production Evrim Baran, Zeynep Baz, Ramazan Esen, Birgül Yazıcı
0162	Steam reforming of triolein as a model compound of edible oil for H2 production via thermodynamic analysis Ömer Faruk Gül, Şeyma Özkara Aydınoğlu
0163	Hydrogen Storage Capacity of Palladium Doped Multi Wall Carbon Nanotubes Prepared via Supercritical CO2 Depostion Method Ebru Erünal, Fatma Ulusal, Deniz Kaya, Mustafa Y. Arslan, Bilgehan Güzel, Deniz Üner
0167	Preparation of a Novel Composite Hydrogel Loaded Cobalt and Hydrogen Production from Hydrolysis of NaBH4 Duygu Alpaslan, Tuba Ersen Dudu, Nahit Aktas
0168	The preparation of a composite-catalyst system and Hydrogen Production from Hydrolysis of NaBH4 Tuba Ersen Dudu, Duygu Alpaslan, Nahit Aktas
0169	The Preparation of p(DMAAm-co-APTMACl) Hydrogel and Their Use as Catalyst for Hydrogen Generation from Hydrolysis of NaBH4 Duygu Alpaslan, Tuba Ersen Dudu, Nahit Aktas
0179	Reliability of Numerical SOFC Tools for Computing Spatial Current and Temperature Variations Özgür Aydın, Hironori Nakajima, Tatsumi Kitahara

KEYNOTE SPEAKERS

Hydrogen: Sources and Production

Sema Z. Baykara
Chemical Engineering Department, Yildiz Technical University
e-mail: baykara@yildiz.edu.tr, szbaykara@gmail.com

Abstract
Terms of availability of hydrogen, its properties and possible sources and its production methods, and finally, its relationship with renewable energy utilization, environment and climate are discussed.

Keywords: Hydrogen; sources; production; environment; climate change

1. Introduction

Growth in population and economy in the world are directly proportional to fossil fuel utilization and environment deterioration [1, 2]. The present situation in this relationship is shown in Table 1. At current consumption rates, world's proven coal, oil and natural gas reserves are expected to last for approximately 200, 40 and 60 years. Peak production rates of liquid fuels, and natural gas seem likely to occur in 2005-2015 and in 2030 [3]. Afterwards, the overall resources will be in decline. Sustainability of fossil fuels is a major concern. A "sustainable energy source" would be one that is not substantially depleted by continued use, does not involve significant pollutant emissions or other environmental problems, health hazards or social injustices [4]. Renewable energy forms, especially hydrogen produced from water using solar energy comes very close to this definition.

Various studies are available involving all aspects of hydrogen technology and the rationale for the hydrogen energy system [5] including the present energy system, its depletable fossil fuels and their adverse effects on the environment and climate change [6], the critical role of hydrogen as an energy currency [7], and issues related to climate change and hydrogen energy [1,2].

Table 1. Worldwide fossil fuel consumption and environmental damage 2015 – 2016

Fossil Fuel Consumption [a]	(in 10^{18} J per year)
World coal consumption	112.5
World petroleum consumption	208.6
World natural gas consumption	126.6
World fossil fuel consumption	447.8
Environmental Damage Estimate [b,c]	(in billion $)
Damage due to coal	522.0
Damage due to petroleum	442.8
Damage due to natural gas	252.0
Total damage	1216.8
Demographic and Economic Data	
World population (in billions) [d]	7.4
Damage per capita	$ 164.4
World GWP (in billion $) [e]	$ 74,152.5
GWP per capita	$ 10,020.6
Damage/GWP	0.0164

[a]: BP Statistical Review of World Energy, 2016 (bp.com)
[b]: International Energy Outlook, 2016, DOE/EIA-0484, May 2016 (www.eia.gov)
[c]: Roston E., Climate change may be doubted by some now it's the law, 18 November 2016 (bloomberg.com)
[d]: Population Reference Bureau (www.prb.org)
[e]: Gross Domestic Product, 2015, 1 February 2017 (data.worldbank.org)

2. Hydrogen

Hydrogen is not readily available on Earth in elemental form. However, it can be produced from its compounds found in natural or industrial sources. Hydrogen is the most abundant element in the universe, making up approximately 75% of all matter [8]. In Earth's crust, it is the tenth most abundant element, and it is found in combination with other elements. Hydrogen is not found in Earth's atmosphere since the Earth's gravitational pull is not strong enough (unlike Jupiter and Saturn) to retain the light weight H_2 molecules. Scientist believe that helium and hydrogen, were the first elements formed in the early stages of cosmic evolution.

Hydrogen exists in three isotopes: protium, deuterium and tritium. A standard hydrogen atom (protium) is the simplest of all the elements and consists of one proton and one electron. Molecular hydrogen (H_2) exists in two forms: ortho- and para-hydrogen. Hydrogen is an odorless, colourless gas. With a molecular weight of 2.016, hydrogen is the lightest element. Its density is about 14 times less than air (0.08376 kg/m^3 at standard temperature and pressure). Hydrogen is liquid at temperatures below 20.3 K (at atmospheric pressure). Hydrogen has the highest

energy content per unit mass of all fuels. Its higher heating value is 141.9 MJ/kg, almost three times higher than that of gasoline. Some important properties of hydrogen are compiled in Table 2 [5].

Table 2. Properties of hydrogen [5]

Molecular weight	Amu	2.016
Density	kg/m^3	0.0838
Higher heating value	MJ/kg	141.90
	MJ/ m^3	11.89
Lower heating value	MJ/kg	119.90
	MJ/ m^3	10.05
Boiling temperature	K	20.3
Density as liquid	kg/m^3	70.8
Critical point		
temperature	K	32.94
pressure	Bar	12.84
density	kg/m^3	31.40
Self-ignition temperature	K	858
Ignition limits in air	(vol.%)	4-75
Stoichiometric mixture in air	(vol.%)	29.53
Flame temperature in air	K	2,318
Diffusion coefficient	cm^2/s	0.61
Specific heat (C_p)	kJ(kg.K)	14.89

Except for space programmes, hydrogen is not being used directly as a fuel or energy carrier. It is being used in refineries to upgrade crude oil (hydrotreating and hydrocracking), in the chemical industry to synthesize various chemical compounds (such as ammonia, methanol, etc.), and in metallurgical processes (as a reduction or protection gas). Production of hydrogen as an energy carrier would require an increase in production rates by several orders of magnitude. The energy input for hydrogen production is always greater than the energy output from hydrogen. Consequently, energy, as well as feed stocks, will be required to obtain hydrogen. Considering the levels of energy consumption in the world and the adverse effects of the present fossil based energy sources on the environment, renewable energy sources are ideal for sustainable hydrogen production [9, 10].

On Earth, free hydrogen is scarce. The atmosphere contains trace amounts of it (0.07 per cent), and it is usually found in small amounts mixed with natural gas in crustal reservoirs. A few wells, however, have been found to contain large amounts of hydrogen, such as some wells in Kansas that contain 40 per cent hydrogen, 60 per cent nitrogen and trace amounts of hydrocarbons [11]. The Earth's surface contain about 0.14 per cent hydrogen (tenth most abundant element), most of which resides in chemical combination with oxygen as water.

3. Hydrogen Production Methods

Hydrogen gas has an important role in industrial processes, mostly as feedstocks. Presently, 95% of hydrogen is produced from fossil fuels. Chemical grade hydrogen is possible by water electrolysis. Presently, hydrogen is mostly being produced from fossil fuels (natural gas, oil and coal). Approximately 95% of the hydrogen produced is used captively [8]. Methods involving hydrogen production from hydrocarbons [5, 12-15], coal [5, 12, 16], biomass [17], water [5, 18-37] and compounds like metal hydrides [38] and hydrogen sulphide [39-42] and biological sources [43] are available.

Hydrogen production costs for various technologies are calculated and compared [33]. The results are presented in Table 3. Coal gasification and water electrolysis are commercialized mature technologies, established at higher efficiency and lower product cost ranges. SMR can also be considered in this category. The efficiency of the steam reforming process, expressed as the ratio of the heating value of produced hydrogen and energy input (feedstock, fuel and small amounts of electricity) is about 65 to 75%. The efficiency of partial oxidation is generally lower than for steam reforming, usually about 50%. In the coal gasification process (Koppers-Totzek process), the product is hydrogen at about 2.8 MPa with purity higher than 97.5%. Hydrogen can be obtained from biomass by a pyrolysis/gasification process [17]. The whole system is very much similar to a coal gasification plant. Because of the lower calorific value per unit mass of biomass as compared to coal, the processing facility is larger than that of a comparably sized coal gasification plant. Various methods of hydrogen production from water are available including electrolysis, direct thermal decomposition or thermolysis, thermochemical processes and photolysis. The efficiency levels for water electrolysis may vary from 70 to 90% [18, 19]. Several PV-electrolysis plants are currently operating all over the world [26-30]. Water can be split thermally at temperatures above 2000 K. [31-33].

The degree of dissociation is a function of temperature: only 1% at 2000 K, 8.5% at 2500 K and 34% at 3000 K. Thermochemical production of hydrogen involves the chemical splitting of water at temperatures lower than those needed for thermolysis, through a series of cyclical chemical reactions which ultimately release

hydrogen. Since the mid-1960s, some 2,000 to 3,000 cycles have been invented. After examining their practicability in terms of reaction and process technology, only 20 to 30 remained applicable for large-scale hydrogen production. Some of the more thoroughly investigated thermochemical process cycles are [20, 34, 35]: sulphuric acid - iodine cycle; hybrid sulphuric acid cycle; hybrid sulphuric acid - hydrogen bromide cycle; calcium bromide - iron oxide cycle (UT-3), Iron chlorine cycle (Mark 9). Depending on the temperatures at which these processes are occurring, relatively high efficiencies are achievable (40 to 50%). Photolysis, or direct extraction of hydrogen from water using only sunlight as an energy source, can be accomplished by photobiological systems, photochemical assemblies or photoelectro-chemical cells [36, 37]. Hydrogen production is possible through pyrolysis and hydrolysis of metal hydrides. Lithium and magnesium hydride (LiH, MgH_2), lithium and sodium borohydride ($LiBH_4$, $NaBH_4$), lithium and sodium aluminium hydride ($LiAlH_4$, $NaAlH_4$) are often considered [38].Various techniques are available for hydrogen production by H_2S decomposition [40], which are at different stages of development. Presently these methods can be broadly categorized as the; thermal, thermochemical, electrochemical, photochemical and plasmochemical methods. Biological production of hydrogen (biohydrogen), using (micro) organisms, is a new area of technology for production of usable hydrogen from a variety of renewable resources. Biological systems provide a wide range of approaches to generate hydrogen, that involve direct bio photolysis, indirect biophotolysis, photo-fermentations, and dark fermentations [43].

Table 3. Comparison of manufacturing cost of hydrogen by various solar processes relative to commercial water electrolysis $(cost)_i$ and coal gasification $(cost)_k$

Hydrogen manufacturing process	cost (cost)j	cost (cost)k
a. Solar water electrolysis[1]	1.1	4.4
b. Solar water electrolysis[2]	3.9	15.2
c. Solar water electrolysis[3]	2.6	10.1
d. Solar water thermolysis[4]	3.3	12.5
e. Hybrid solar water thermolysis (a+d)	2.2	8.6
f. Solar[5] coal gasification[6]	0.8	2.9
g. Hybrid solar coal gasification (c+f)	0.7	2.6
h. Solar[5] thermochemical cycle[7]	1.9	7.3
i. Hybrid solar thermochemical cycle[8]	1.6	6.2
j. Commercial water electrolysis	1.0	3.8
k. Commercial coal gasification[6]	0.3	1.0
1. Solar thermal electricity production (parabolic dish & steam turbine). 2. Photovoltaic electricity production (solar cell panels). 3. Solar thermal electricity production (solar tower & steam turbine). 4. Solar process heat production (parabolic dish). 5. Solar process heat production (solar tower). 6. Koppers-Totzek coal gasification process. 7. GA thermochemical cycle. 8. Mark 11 thermochemical cycle.		
Assumptions: Capital charge rate: 15%, Cost of coal: $ 10/ton, Cost of hydropower: $ 0.01/kWh for old power stations, $ 0.1/kWh for new power stations.		

Other relatively new hydrogen production technologies, including the ones using solar energy (PV or thermal) are not as costwise competitive yet, although they are highly pollution-free.
In all cases (natural gas, oil and coal), cost of manufacturing is lower than the “environmental cost” of using the fuel itself. Since that cost is negligible for hydrogen it would be only logical to produce hydrogen from these fuels instead of directly using them.

4. Hydrogen, Environment and Climate Change

Essentially, there are three contending energy systems: (1) the present fossil fuel system, (2) the coal/synthetic fossil fuel system, and (3) the solar hydrogen energy system, which is a special case of the hydrogen energy system. If solar energy, in its direct and/or indirect forms (e.g., hydro, wind, etc.), is used to manufacture hydrogen, then the resulting system is called a “solar hydrogen energy system”. In this system, both the primary and secondary energy sources are renewable and environmentally compatible, resulting in a clean and permanent energy system.
In view of the three energy systems, environmental factors like pollution, vapor generation and environmental damage are at significantly low levels for the solar hydrogen energy system compared to the other energy systems (Table 4).

In Table 4 [7] it can be seen that the coal/synthetic fossil system is the worst from the environmental point of view, while the solar-hydrogen energy system is the best. The solar-hydrogen system will not produce any CO_2, CO, SO_x, hydrocarbons or particulates, except some NO_x. However, the solar-hydrogen-produced NOx is much less than those produced by the other energy systems. This is due to the fact that in the solar hydrogen energy system

only the flame combustion of hydrogen in air will generate NO_x. The other utilization processes (such as direct steam generation, use of hydrogen in fuel cells, hydriding processes, etc.) will not produce any NO_x. There is a notion that the hydrogen energy system would produce more water vapor than the other energy systems, since the fuel is pure hydrogen. When one considers the problem in detail, this is not so [5]. Only the flame combustion of fuels in air or in oxygen will produce water vapor. In the case of hydrogen the other processes will not produce any water vapor. Consequently, and contrary to popular belief, the solar-hydrogen energy system will produce less water vapor than the other systems.

Current utilization of fossil and nuclear fuels has many adverse consequences including air pollution, acid rain, the depletion of natural resources and the dangers of nuclear radiation. Global climate change caused by emissions of greenhouse gases from fossil fuel combustion is the leading problem. The surface temperature of the earth is established at an equilibrium level where the incoming energy from the sun balances the outgoing infrared energy re-radiated from the surface back into space. The Earth's average surface temperature would be-18°C; but its atmosphere includes 'greenhouse gases', principally water vapor, carbon dioxide and methane. Allowing solar radiation to enter but inhibiting the outflow of infrared radiation. The natural 'greenhouse effect' is essential in maintaining the earth's surface temperature at around 15°C a level suitable for life [4].

Table 4. Environment related properties of the main energy systems [7]

Energy System	Pollutants (kg/GJ)						Vapor generation (10^{12} kg/y)			Environmental damage ($/GJ)[c]	Environmental compatibility factor
	CO_2	CO	SO_2	NO_x	HC	PM[a]	Energy System	Global warning	(%)[b]		
Fossil Fuel	72.40	0.80	0.38	0.34	0.20	0.09	8.9	3900	0.782	15.69	0.055
Coal/Synthetic, Fossil Fuel	100.00	0.65	0.50	0.32	0.12	0.14	9.3	3900	0.782	19.45	0.044
Solar-Hydrogen Energy	0.00	0.00	0.00	0.10	0.00	0.00	6.0	0.0	0.001	0.86	1.00

a: Particulate matter
b: With respect to annual vapor generation due to solar heating ($5x10^{17}$ kg/y)
c: in 2005 dollars

Following the industrial revolution, human activities have been adding extra greenhouse gases to the atmosphere. The principal contributor being carbon dioxide from the combustion of fossil fuels (Figure 1 [4]).
Based on carbon dioxide data from 1958 (measured at Mauna Loa, Hawaii) and pre-1958 data (estimated from ice cores), scientists estimate that during the twentieth century these 'anthropogenic' emissions caused a rise in the earth's global mean surface temperature of 0.6°C [44].

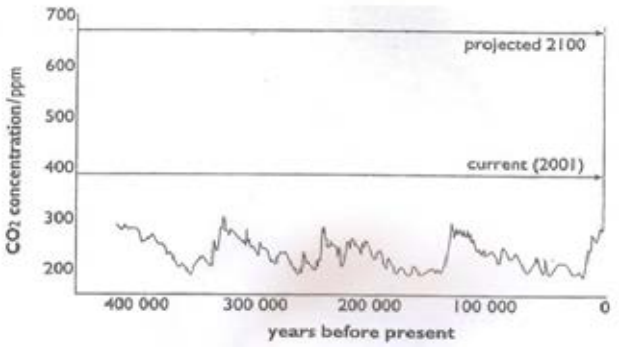


Figure 1. Long-range variation in CO_2 concentration (IPCC data) [4]

For half a million years before the twentieth-century, atmospheric concentrations of CO_2 have varied between about 200 and 300 parts per million by volume (ppmv). But during the twentieth century they rose beyond this range, increasing to 370 ppm by 2001. Projections by the Intergovernmental Panel on Climate Change (IPCC) suggest they could rise to around 700 ppmv by the end of the twenty-first century if no action is taken to limit emissions. The projection shown for 2100 is near the middle of the IPCC range [4]. If emissions are not reduced, the surface temperature is predicted to rise by 1.4 to 5.8°C by the end of the twenty-first century. Leading to increased frequency of climatic extremes, such as floods or droughts, and serious disruption to agriculture and natural ecosystems. Mean sea levels are likely to rise by around 0.5 m. by the end of the century, inundating low lands. And beyond 2100, if major Antarctic ice sheets were to melt much greater sea level rises could occur. The threat of

global climate change caused by carbon dioxide emissions from fossil fuel combustion requires reductions in emissions in the range of 60-80% by the end of the twenty-first century and, ultimately, a switch to low- or zero-carbon energy sources such as renewables and hydrogen produced by renewables.

Activities directed towards reversing the process of climate change have been accelerated since the eighties, and they are becoming more focused on commitment acts from states [45, 46]. Perceived as a scientific and political issue, climate change has been under investigation by scientists for the past hundred years [44-55]. The possibility of changes in climate due to increase in accumulation rate of CO_2 in the atmosphere was first brought up by the Nobel laureate S. Arrhenius in 1879 [47].

In the 1st World Climate Conference which was held in 1979 under the auspices of World Meteorological Organization (WMO), the subject of climate change was brought to public attention, and it was concluded that, long term dependence on fossil fuels and deforestation would result in CO_2 accumulation in the atmosphere which in turn would lead to variations in climate. Through a joint initiative of WMO and United Nations Environmental Program (UNEP), The Intergovernmental Panel on Climate Change (IPCC) was formed and held its 1st meeting in November 1988. First Evaluation Report of IPCC [48] was issued in August 1990. A supplement followed in 1992 [49].

One of the significant initiatives for keeping or reducing the greenhouse gas emissions at a certain level was the UN Framework Convention on Climate Change in June 1992, which was signed by 166 countries and the European Union (EU) within a year and which came into effect on March 21, 1994. Thus, the concept of sustainable growth started maturing.

The Kyoto Protocol involving an agreement for 5% reduction in GHG emissions was concluded hi 1997. The protocol came into effect on February 16, 2005.

Various national initiatives against environmental damage and air pollution were also taken. The Clean Air Act in 1963 and the Clean Air Act Amendments (CAAA) in 1990 of the United States, the Canadian Environmental Protection Act (CEPA) in 1988 [51], and emission control regulations in European Union [52] in 1998 can be mentioned as fundamental examples. Regulations for emission control limit the extent to which plants and vehicles impact air quality. The emission characteristics can be influenced by the level of emission standards, required emission durability, fuel composition and in-use inspection and maintenance [53].

The accord forged in Paris came in force in November 2015; bringing the U.S., China and more than 190 other nations into a UN-sponsored plan to cut the emissions that trap heat in the Earth's atmosphere. The Paris agreement has been hailed as the first universal deal because the previous one, the 1997 Kyoto Protocol, was never ratified by the U.S. and didn't set binding targets for China and India, now among the biggest polluters. This time, nations came forward with voluntary commitments. China has agreed that its emissions will peak in about 2030 and the U.S. pledged to cut greenhouse gases by 26-28 percent in the two decades ending in 2025. The targets aren't legally binding in the same way as Kyoto, though countries must measure and report their progress. Even if all the pledges are met, the globe is expected to warm by as much as 3.4 degrees Celsius this century. That's alarmed the countries most vulnerable to warming, including island states imperiled by rising seas [56].

5. Conclusions

Economic development, energy utilization, environment and climate are interrelated but "securing energy and environment at lowest cost" is becoming increasingly difficult. Although climate change has both natural and anthropogenic components, global warming due to greenhouse gases, especially CO_2, is the main contributor to anthropogenic climate change. According to current estimates, CO_2 content of the atmosphere will approach 400 ppm by 2010, and 600 ppm during the second half of the 21st century.

Even if all the pledges of the Paris agreement in November 2015 are met, the globe is expected to warm by as much as 3.4 degrees Celsius this century. The best alternative would be to sustain the economic growth level by switching to hydrogen economy and using renewable energy sources. Hydrogen produced from water using solar energy will be the most sustainable energy currency in the long term. Timely implementation of educational, financial, legislative, social and technological initiatives are necessary to make this happen.

References

1. Baykara SZ. Ecohealth problems and climate change I: Anthropogenic climate change and ecohealth: worldwide environmental damage. IFSSH World Congress Health Challenges of the Third Millenium. Book of Invited Background Papers, pp 295-313, Istanbul, August 21-26, 2005; Veziroglu TN. Ecohealth problems and climate change II: Permanent solution to environmental problems: hydrogen energy system. IFSSH World Congress Health Challenges of the Third Millenium. Book of Invited Background Papers, pp.315-335, Istanbul, August 21-26, 2005.
2. Veziroglu TN, Gurkan I, Padki MM. Remediation of greenhouse problem through replacement of fossil fuels by hydrogen. Int J Hydrogen Energy 1989; 14(4):257-266.
3. BP Statistical Review of World Energy, (www.bp.com)
4. Boyle G, editor. Renewable energy, power for a sustainable future. Oxford: Oxford University Press, 2004.
5. Veziroglu TN, Barbir F. Hydrogen energy technologies. Vienna: UNIDO, 1998
6. Barbir F, Veziroglu TN, Plass HJ Jr. Environmental damage due to fossil fuel use. Int J Hydrogen Energy 1990; 15(10): 739-750.
7. Baykara SZ. Hydrogen as fuel: a critical technology? Int J Hydrogen Energy 2005; 30(5): 545-553.
8. Chang R. Chemistry. Boston: McGraw Hill, 2002.
9. Twidell J, Weir A. Renewable Energy Resources. London: E & FN Spon, 1986.
10. Sorensen B. Renewable energy: a technical overview. Energy Policy, May 1991.
11. Goebel E., Coveney RM Jr, Angino EE, EJ Zeller EJ, Dreschoff GAM, Geology, Composition, Isotopes of Naturally Occurring H2/N2 Rich

Gas from Wells Near Junction City, Kansas, Oil and Gas Journal, May 1994: 217-222
12. Steinberg M, Cheng HC, Modern and Prospective Technologies for Hydrogen Production from Fossil Fuels, in T.N. Veziroglu,A.N. Protsenko (eds.) Hydrogen Energy Progress, VII, pp.699-740, Pergamon Press, Oxford, 1988.
13. WL Mitchell, Development of a Partial Oxidation Reformer for Liquid Fuels, Proc. Fuel Cells for Transportation TOPTEC: Addressing the Fuel Infrastructure Issue, Alexandria, VA, SAE, Warrendale, PA, 1996.
14. JG Pohleny, NH Scott, Method for Hydrogen Production by Catalytic Decomposition of a Gaseous Hydrocarbon Stream, U.S. Patent 3, 284, 161, 1966.
15. S. Lynum, CO2-Free Hydrogen from Hydrocarbons-The Kvaerner CB&H Process, presentation at 10"1 World Hydrogen Energy Conference, Cocoa Beach, FL, June 1994.
16. Baykara SZ, Bilgen E. Synhesis gas and hi production from solar gasification of Albertan coal. Energy Conversion and Management 1985; 25(4): 391-398.
17. National Hydrogen Association. The Hydrogen Technology Assessment, Phase I, A Report for the NASA, Washington, D.C. 1991.
18. Bonner M, Botts T, McBreen J, Mezzina A, Salzano F, Yang C. Status of Advanced Electrolytic Hydrogen Production in the United States and Abroad, Int J Hydrogen Energy 1984; 9(4): 269-275.
19. Dutta S, Technology Assessment of Advanced Electrolytic Hydrogen Production, Int J Hydrogen Energy 1990; 15(6): 379-386.
20. H Wendt, Water Splitting Methods, in C - J Winter and J. Nitsch (eds.) Hydrogen as an Energy Carrier, Springer-Verlag, Berlin Heidelberg, pp.166-238,1988.
21. Liepa MA,Borhan A. High-Temperature Steam Electrolysis: Technical and Economic Evaluation of Alternative Process Designs, Int J Hydrogen Energy 1986; 11 (7): 435-442.
22. OG Hancock. A Photovoltaic-Powered Water Electrolyzer: Its Performance and Economics in TN Veziroglu and JB Taylor, eds., Hydrogen Energy Progress V, Pergamon Press, New York, pp.335-344, 1984.
23. Carpetis C, An Assessment of Electrolytic Hydrogen Production by Mans of Photovoltaic Energy Conversion, Int J Hydrogen Energy 1984; 9(12): 969-992.
24. Siegel A, SchottT, Optimization of Photovoltaic Hydrogen Production, Int J Hydrogen Energy 1988; 13(11): 659-678.
25. H Steeb, A Brinner, H Bubmann, W Seeger. Operation Experience of a 10 kW PV-Electrolysis System in Different Power Matching Modes, in TN Veziroglu and PK Takahashi, eds., Hydrogen Energy Progress VIII, Vol.2, Pergamon Press, New York, pp.691-700, 1990.
26. H Blank, A Szyszka, Solar Hydrogen Demonstration Plant in Neunburg vorm Wald, in TN Veziroglu, C. Derive, and J. Pettier, eds., Hydrogen Energy Progress IX, Vol.2, pp.677-686, M.C.I., Paris, 1992.
27. Grasse W, Oster F, Aba-Oud H. HYSOLAR: The German-Saudi Arabian Program on Solar Hydrogen-5 Years of Experience, Int J Hydrogen Energy 1992, 17(1): 1-8.
28. Lehman P,Chamberlain CE. Design of a Photovoltaic-Hydrogen-Fuel Cell Energy System, Int J Hydrogen Energy 1991; 16(5): 349-352.
29. Lund PD, Optimization of Stand Alone Photovoltaic System with Hydrogen Storage for Total Energy Self-Sufficiency, Int J Hydrogen Energy 1991; 16(11): 735-740.
30. AG Gaicia-Conde, F Rosa. Solar Hydrogen Production: A Spanish Experience, in TN Veziroglu, C. Derive and J. Pettier, eds., Hydrogen Energy Progress IX, Vol.2, M.C.I., Paris, pp.723-732, 1992.
31. Baykara SZ and Bilgen E. An Overall Assessment of Hydrogen Production by Solar Water Thermolysis, Int. J. Hydrogen Energy 1989; 14(12): 881-889.
32. Baykara SZ. Experimental solar water thermolysis. Int J Hydrogen Energy 2004; 29(14): 1459-1469.
33. Baykara SZ. Hydrogen production by direct solar thermal decomposition of water, possibilities for improvement of process efficiency. Int J Hydrogen Energy 2004; 29(14): 1451-1458.
34. Engels H, et al. Thermochemical Hydrogen Production, Int J Hydrogen Energy 1987; 12(5): 291-29
35. Yalcin S, A Review of Nuclear Hydrogen Production, Int J Hydrogen Energy 1989; 4(5): 551-561.
36. SR. Bull, Hydrogen Production by Photoprocesses, Proc. Int. Renewable Energy Conf., Honolulu, Hawaii, pp.413-426,1988.
37. Willner I, Steinberger-Willner B. Solar Hydrogen Production Through Photo-Biological, Photochemical and Photoelectrochemical Assemblies, Int. J. Hydrogen Energy 1988; 13(10): 593-604.
38. Fakioglu E, Yürüm V, Veziroglu TN. A review of hydrogen storage systems based on boron and its compounds. Int. J Hydrogen Energy 2004; 29(2): 1371-1376.
39. Baykara SZ, Kale A, Veziroglu TN. Possibilities for hydrogen production from H^S in Black Sea. Proc ihec 2005, Istanbul July 13-15, 2005.
40. Zaman J, Chakma A. Production of hydrogen and sulphur from hydrogen sulphide. Fuel Processing Technology 1995;44: 159-198.
41. Cox BG, Clarke PF, Pruden BE. Economics of thermal dissociation of H2S to produce hydrogen. Int J Hydrogen Energy 1998; 23(7): 531-544.
42. Baykara SZ, Figen EH, Kale A, Veziroglu TN. Hydrogen from H2S in the Black Sea. Proc WHEC15, Yokohama, Japan, June 27-July 2, 2004.
43. Levin DB, Pitt L. Love M. Biohydrogen production and limitations to practical application. Int J Hydrogen Energy 2004; 29(2): 173-185.
44. Intergovernmental Panel on Climate Change. Climate change 200: the scientific basis. Cambridge University Press, 2001.
45. Organisation for economic co-operation and development. Action against climate change. The Kyoto Protocol and beyond. OECD. Paris, 1999.
46. Organisation de cooperation et de developpement economiques. Changement clirnatique: les politiques nationales et le Protocole de Kyoto. OECD. Paris, 1999.
47. Türkeş M. From Toronto 1988 to Berlin 1995 Climate Change Accord. Science & Technology, 46-49, June 1995 (in Turkish).
48. Houghton JT, Jenkins GJ, Ephraums JJ, editors. Climate change: The IPCC scientific assessment. Cambridge: Cambridge University Press, 1990.
49. Houghton JT, Callander BA, Varney SK. Climate Change 1992, The supplementary report to the IPCC scientific assessment. Cambridge University Press. Cambridge, 1992.
50. Brown P, Wilson J. US in plan to bypass Kyoto Protocol. Guardian, 28 July 2005.
51. Montgomery CW. Environmental geology. Boston: McGraw-Hill, 2003.
52. Directive on emissions from passenger cars and light-duty commercial vehicles. European Automobile Manufacturers
53. Association (ACEA), Emission 2000, No. 164, Brussels, 7 July 1998.
54. Lenz HP; Cozzarini C. Emissions and air quality. Society of Automotive Engineers Inc. Warrendale PA, 1999.
55. Parry M, Arnell N, Hulme M, Nicholls R, Livermore M. Adapting to the inevitable. Nature 1988; 395: 741.
56. Roston E., Climate change may be doubted by some now it's the law, 18 November 2016 (bloomberg.com)

INVITED SPEAKERS

Future of Hydrogen Usage in Automotive Industry

Kadir Aydın
Çukurova University, Faculty of Engineering and Architecture, Department of Automotive Engineering, 01330, Sarıçam-Adana/Turkey
Email: kdraydin@cu.edu.tr

Abstract
This paper offers an overview of the technologies for hydrogen production with present and future usage in Automotive Industry. Hydrogen is the simplest and the most plentiful element in the Universe. However it is always combined with other elements. Still, the costs of hydrogen production from its combined elements remain high compared to other energy sources; it is extremely difficult to store onboard, the use of natural gas as a feedstock emits CO_2, and there are numerous technical challenges to overcome with these systems. It could take many years of research and development, as well as changes in the energy infrastructure, before hydrogen could have a significant impact on World energy use. In the very long term, electricity and hydrogen are likely to become complementary energy vectors of choice. Hydrogen and the fuel cell are complementary, and each enables the other. Due mainly to its high hydrogen capacity, ammonia has the potential for use as a carrier for hydrogen delivery and distribution. A significant effort would be needed to develop onboard ammonia cracker systems for vehicles.

Keywords: Hydrogen; fuel cell; hydrogen storage; ammonia; hydrogen mobility,

1. Introduction

Hydrogen is already a significant chemical product; about 88% of hydrogen is made from fossil fuels like natural gas, liquid hydrocarbons and coal. This gives rise to quantities of carbon dioxide emissions – each tonne produced gives rise to 11 tonnes of CO_2. Electrolysis is the most common method used to split H_2 from water and currently, about 12% of hydrogen production globally source is presented by electrolyzes. Steam electrolysis uses heat, instead of electricity, to provide some of the energy needed to split water and can make the process more energy efficient.

If oil becomes more expensive, hydrogen may eventually replace it as a transport fuel and in other applications. This development becomes more likely as fuel cells are developed, with hydrogen as the preferred fuel, though portable storage at vehicle scale is a major challenge. Meanwhile hydrogen can be used in internal combustion engines, and it can also be reacted with carbon dioxide at 300-400°C to give methane, using the exothermic Sabatier process. Like electricity, hydrogen for transport use will tend to be produced near where it is to be used. This will have major geo-political implications as industrialized countries become less dependent on oil and gas from distant parts of the world.

Electricity and hydrogen are convertible one to the other as energy carriers. In the short term, hydrogen can be produced economically by electrolysis of water in off-peak periods, enabling much greater utilization of base-load generating plants, including nuclear ones. In future, a major possibility is decomposition of water by direct use of heat from nuclear energy, using a chemical process enabled by high-temperature reactors. The rapidly-growing demand for hydrogen favors technologies with low fuel costs, and the scale of hydrogen demand is appropriate to its production by nuclear reactors. Limited hydrogen pipeline networks already exist, allowing production facilities to be some way from users.

All this points to the fact that while a growing hydrogen economy already exists, linked to the worldwide chemical and refining industry, a much greater one is in sight if storage and handling problems at automotive scale can be overcome. The development of affordable fuel cells will also be vital. With new uses for hydrogen as a fuel, the primary energy demand for its production may approach that for electricity production. Meanwhile, a significant increase in electricity demand is likely due to wider adoption of plug-in hybrid and full electric (PHEV and EV) cars. Charging the batteries of these from mains power will be cheaper than using any internal combustion engines. This demand is becoming significant, and well within the planning horizons for new generating plants.

Nuclear power already produces electricity as a major energy carrier. It is well placed, though beyond the capability of most current plants, to produce hydrogen if this becomes a major energy carrier also. The evolution of nuclear energy's role in hydrogen production over perhaps three decades is seen to be:

- Electrolysis of water, using off-peak capacity,
- Use of nuclear heat to assist steam reforming of natural gas,
- High-temperature electrolysis of steam, using heat and electricity from nuclear reactors, then
- High-temperature thermochemical production using nuclear heat.

Burning hydrogen produces only water vapor, with no carbon dioxide or carbon monoxide. However, it is far from being an energy-dense fuel, and this limits its potential use for motor vehicles. Hydrogen can be burned in a normal internal combustion engine, and some test cars are thus equipped. Trials in aircraft have also been carried out. In the immediate future the internal combustion engine is the only affordable technology available for using hydrogen. For transport, hydrogen's main use will be in fuel cells. A fuel cell is conceptually a refuelable battery, making electricity as a direct product of a chemical reaction. But where the normal battery has all the active ingredients built in at the factory, fuel cells are supplied with fuel from an external source and oxygen from the air. They catalyze the oxidation of hydrogen directly to electricity at relatively low temperatures and the claimed theoretical efficiency of converting chemical to electrical energy to drive the wheels is about 60% (or more). However, in practice about half that has been achieved, except for the higher-temperature solid oxide fuel cells – 46% [1].

Apart from carbon-free production and then distribution to users, on-board storage is the principal problem for hydrogen as an automotive fuel – it is impossible to store it as simply and compactly as gasoline or LNG fuel. The options are to store it at very low temperature (cryogenically), at high pressure, or chemically as hydrides. The last is seen to have considerable potential, though refueling a vehicle is less straightforward. Pressurized storage is the main technology available now and this means that at 345 times atmospheric pressure (34.5 MPa), ten times the volume is required than for an equivalent amount of petrol/gasoline, and the weight penalty of a steel tank was reduced by use of carbon fibre. Earlier, the tank had been about 50 times heavier than the hydrogen it stored, now it is about 20 times as heavy, and the new target is ten times as heavy. One promising hydride storage system utilizes sodium borohydride as the energy carrier, with high energy density. The $NaBH_4$ is catalyzed to yield its hydrogen, leaving a borate ($NaBO_2$) to be reprocessed.

Fuel cells are currently being used in electric forklift trucks, automobiles and buses and this use is expected to increase steadily. They apparently cost about three times as much as batteries but last twice as long (10,000 hours) and have less downtime. Japan had a goal of 5 million fuel cell vehicles on the road by 2020 [2].

The Hydrogen Mobility Europe (H2ME) project announced in 2015 will extend over six years supported by the Fuel Cells and Hydrogen Joint Undertaking (FCH JU) with funding from the EU's Horizon 2020 research program. The initiative is aimed to significantly expand the European hydrogen vehicles fleet and in so doing, to confirm the technical and commercial readiness of vehicles, fueling stations and hydrogen production techniques. Two types of fuel cell electric vehicle will be deployed under H2ME: fuel cell electric cars from Daimler and Hyundai, and fuel cell range-extended vans from Symbio FCell in collaboration with Renault. The fuel cell powertrain is a modular assembly. It is comprised of fuel cell stack, system module, hydrogen tanks, battery and electric motor. Daimler's B-Class F-Cell vehicles are fitted with a 700 bar hydrogen tank in the sandwich floor unit. Its electric motor develops an output of 100 kW, with a torque of 290 Nm, and thus has the power rating of a 2-litre gasoline engine. The zero-emission drive system consumes the equivalent of 3.3 L/100 km of diesel. Hyundai's Tucson ix35 Fuel Cell is the first mass production model of the company's FCEV. The fuel cell system of the ix35 is integrated for high performance and efficiency, and two 700 bar hydrogen tanks provide long distance driving range. Symbio FCell's range-extended fuel cell vehicles are powered by a compact 5 kW fuel cell module coupled with a light 350 bar hydrogen storage unit, a medium-size automotive battery pack and integrated onto the Renault Kangoo ZE platform. The Symbio FCell stack doubles the range of the electric-only Kangoo ZE base vehicle [1].

Current fuel cell design consists of bipolar electrode plates in a frame with electrolyte between, and developer of the most common proton exchange membrane type, a new geometry is required to bring the cost down and make the technology more widely available to a mass market. The normal PEM type operates at about 80°C, using a catalyst which requires a pure hydrogen stream as fuel. Fuel cells are intrinsically not simple and there are no obvious reasons to expect them to become cheap. But at present fuel cells are much more expensive to make than internal combustion engines (burning petrol/gasoline or natural gas). In the early 2000s, PEM units cost over $1000 per kilowatt, compared with $100/kW for conventional internal combustion engine. The target cost for a PEM fuel cell stack is below €100/kW, which will require reducing the amount of palladium catalyst. In mid-2016 hydrogen was being supplied in the UK at GBP 10/kg (€12/kg) which works out at 25p/kWh (€0.30/kWh). The direct methanol fuel cell (DMFC) technology is practical for portable electronic uses but not favored for automotive use at present. Other fuel cell technologies include the high-temperature PEMFC operating up to 200°C which is less vulnerable to catalyst poisoning by CO, phosphoric acid fuel cell (PAFC) – well developed but high-temperature and used only for stationary power generation, the solid oxide fuel cell (SOFC) – operating over 800°C, hence mainly used for stationary power generation, and the molten carbonate fuel cell (MCFC) – high-temperature (about 650°C) and accepting a variety of fuels, for stationary power generation [1].

Hydrogen and fuel cell technologies promise considerable benefits in terms of energy security and CO_2 emission, but they require significant technical breakthroughs, cost reduction and appropriate policies to enter the

energy market. Fuel cell and hydrogen energy is highly fragmented. The initial use of hydrogen for transport is likely to be municipal bus and truck fleets, and prototypes have already been on the road in many parts of the world. These are centrally-fueled, so avoid the need for a retail network, and on-board storage of hydrogen is less of a problem than in cars. Hydrogen is likely to conquer a significant market share only if effective policies for CO_2 mitigation and energy security are in place and with considerable reductions of hydrogen and fuel cell cost.

2. Motor Vehicle Production

World population has reached to almost 7.5 billion and world motor vehicle production has increased continuously with the population increase and reached to 95 million in 2016 (Table 1). 72 million automobiles and 23 million commercial vehicles have been manufactured in 2016 the world total motor vehicle production of 95 million (Table 2). The private automobile is the primary mode of transportation for developed countries. In developed countries, more than 80% of households have a personal vehicle. This level of private automobile ownership and use has had profound impacts on the economy and people's lifestyles. But the scale of automobile use in around the world has also come at a cost. Energy is needed to power an automobile, and most of this energy comes from the burning of fossil fuels in the vehicle's engine. This burning or "combustion" process produces emissions that pollute the air and contribute to climate change. In fact, transportation is a major source of these emissions. To make substantial reductions in emissions, we need to reduce their overall transportation energy use. One way this can be accomplished is by minimizing the amount of fuel that an engine needs to burn while being operated – or, in other words, increasing vehicle fuel efficiency. Other alternative is to use zero emissions vehicles. Hydrogen is the one of the economic alternative fuel sources for zero emissions vehicles.

Table 1. World motor vehicle productions [3]

Year	Production	Change
1997	54,434,000	
1998	52,987,000	-2.7%
1999	56,258,892	6.2%
2000	58,374,162	3.8%
2001	56,304,925	-3.5%
2002	58,994,318	4.8%
2003	60,663,225	2.8%
2004	64,496,220	6.3%
2005	66,482,439	3.1%
2006	69,222,975	4.1%
2007	73,266,061	5.8%
2008	70,520,493	-3.7%
2009	61,791,868	-12.4%
2010	77,857,705	26.0%
2011	79,989,155	3.1%
2012	84,141,209	5.3%
2013	87,300,115	3.7%
2014	89,747,430	2.6%
2015	90,086,346	0.4%
2016	**94,976,569**	**4.5%**

Table 2. Cars and commercial vehicle productions in 2016 [3]

Country	Cars (2016)	Commercial Vehicles (2016)	Total (2016)	Change
Total	**72,105,435**	**22,871,134**	**94,976,569**	**4.5%**
China	24,420,744	3,698,050	28,118,794	14.5%
USA	3,934,357	8,263,780	12,198,137	0.8%
Japan	7,873,886	1,330,704	9,204,590	-0.8%
Germany	5,746,808	315,754	6,062,562	0.5%
India	3,677,605	811,360	4,488,965	7.9%
South Korea	3,859,991	368,518	4,228,509	-7.2%
Mexico	1,993,168	1,604,294	3,597,462	0.9%
Spain	2,354,117	531,805	2,885,922	5.6%
Canada	802,057	1,568,214	2,370,271	3.8%
Brazil	1,778,464	377,892	2,156,356	-11.2%
France	1,626,000	456,000	2,082,000	5.6%
Thailand	805,033	1,139,384	1,944,417	1.8%
UK	1,722,698	93,924	1,816,622	8.0%
Turkey	**950,888**	**535,039**	**1,485,927**	**9.4%**
Czech Rep.	1,344,182	5,714	1,349,896	8.3%
Russia	1,124,774	179,215	1,303,989	-5.4%
Indonesia	968,101	209,288	1,177,389	7.2%
Iran	1,074,000	90,710	1,164,710	18.6%
Italy	713,182	390,334	1,103,516	8.8%
Slovakia	1,040,000	0	1,040,000	0.1%

3. Hydrogen Production

Many scenarios have been developed for economic hydrogen production in the world. Today hydrogen is produced economically from fossil fuel sources. Figure 1 shows alternative production methods for sustainable hydrogen production using both fossil fuels and renewable energy sources.



Figure 1. Sustainable hydrogen production [4]

The key is to develop processes that produce significantly more hydrogen gas than the energy used to extract the hydrogen. Hydrogen production is an estimated $100 billion industry but the cost factor and the fact that 95% of it is from a non-renewable energy source; i.e.; the natural gas found in petroleum oil wells, probably negates the benefits of its production.

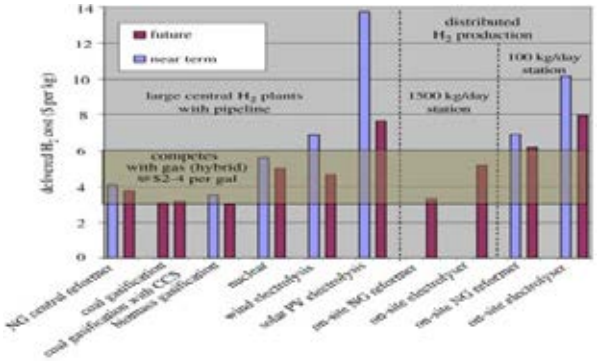


Figure 2. Hydrogen supply pathway [5]

Figure 2 compares the projected delivered cost of hydrogen transportation fuel produced via different pathways for 'near term' (scaled-up infrastructure with current technology) and 'future' systems (full-scale infrastructure with advanced technologies beyond 2015). Costs are likely to come down as technology advances, and that production from hydrocarbons generally costs less than electrolytic hydrogen production. All centralized generation alternatives assume that hydrogen is deployed at a massive scale. On-site generation alternatives assume that in the long term stations deliver either 1500 kg of H_2 per day, which would supply about as many cars per day as do current gasoline stations, or 100 kg of H_2 per day, which would be typical of near-term demonstration H_2 stations serving a relatively small number of early HFCVs. These small stations are estimated to have significantly higher hydrogen cost because they would not benefit from economies of scale.

Figure 2 also shows the range for hydrogen fuel costs to compete with gasoline on a dollar-fuel-cost-per-mile basis, based on a gasoline hybrid vehicle competing with an HFCV. If H_2 costs $3–6 per kg, the fuel cost per mile for an HFCV would be about the same as for an efficient gasoline hybrid using gasoline at $2–4 per gallon, given an assumed HFCV fuel economy that is 1.5 times higher than a comparable gasoline hybrid vehicle. As figure 4 shows, most hydrogen production systems are estimated to deliver hydrogen for less than $6 per kg in the long run. The cost of H_2 would thus be competitive with gasoline (in hybrid vehicles) on a fuel-cost-per-mile basis in the

USA, Europe and Japan [6]. $2-4 per gallon hydrogen production cost can competes the fossil fuel use in Automotive Industry.

4. Hydrogen Vehicle

A hydrogen vehicle (Figure 3) is a vehicle, such as an automobile, aircraft, or any other kind of vehicle that uses hydrogen as its primary source of power for locomotion. These vehicles generally use the hydrogen in one of two methods: electrochemical conversion in a fuel-cell or combustion:

- In combustion, the hydrogen is burned in engines in fundamentally the same method as traditional gasoline cars.
- In fuel-cell conversion, the hydrogen is reacted with oxygen to produce water and electricity, the latter of which is used to power electric motors.

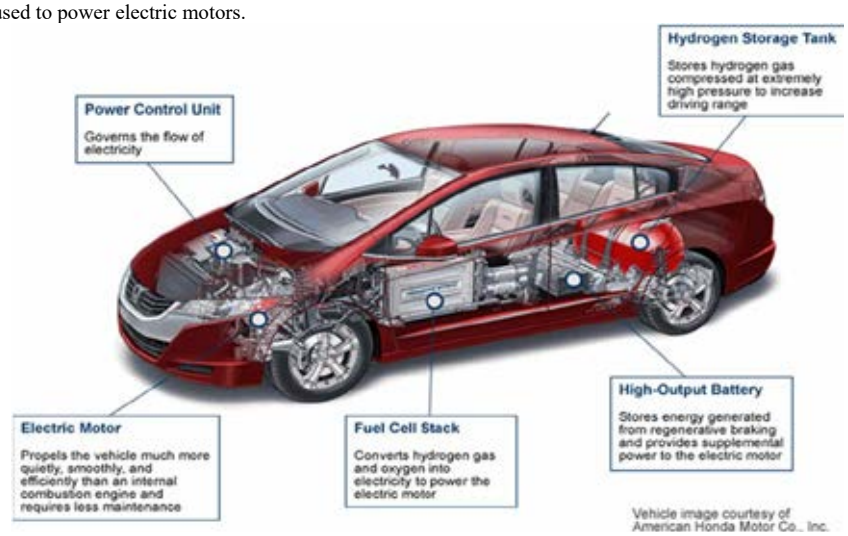


Figure 3. A hydrogen car

The molecular hydrogen needed as an on-board fuel for hydrogen vehicles can be obtained through various thermochemical methods utilizing natural gas, coal (by a process known as coal gasification), liquefied petroleum gas, biomass (biomass gasification), by a process called thermolysis, or as a microbial waste product called biohydrogen or biological hydrogen production. Hydrogen can also be produced from water by electrolysis. If the electricity used for the electrolysis is produced using renewable energy or nuclear power, the production of the hydrogen would (in principle) result in no net carbon dioxide emissions.

Hydrogen is an energy carrier, not an energy source, so the energy the car uses would ultimately need to be provided by a conventional power plant. A suggested benefit of large-scale deployment of hydrogen vehicles is that it could lead to decreased emissions of greenhouse gases and ozone precursors. The pollution generated at the point of use in the vehicle would be greatly reduced compared to conventional automobile engines.

5. Hydroxy Gas (HHO)

Hydroxy Gas (HHO) is a trademark and comes from the separation of water molecules H-OH with electrolysis that contains (theoretically) 67% H_2 and 33% O_2. It has high calorific value than fossil fuels and it could be an alternative hydrogen carrier for Automotive Industry. Using the experimental set-up shown in Figure 4, ddifferent electrolytes ($KOH_{(aq)}$, $NaOH_{(aq)}$, $NaCl_{(aq)}$) with different reactor designs (plate reactor, cylindrical reactor, wire reactor) (Figure 5) are tested to produce more hydroxy gas with same given energy. It is found from the experiments that plate type reactor with NaOH produced more HHO gas with the same amount of catalyst and electric energy. When the engine speed decreases under the critical value (2500 rpm for SI and 1750 rpm for CI engines in this experiment), flow rate has to be decreased to prevent HHO occupy too much volume due to the long opening time of intake valve at low speeds. Otherwise reduction in volumetric efficiency is inevitable unless hydroxy electronic unit (HECU) is serial connected to the HHO system (constant voltage, current and HHO flow rate), due to minimum ignition energy of HHO which is a strongly decreasing function of equivalence ratio, pre-ignition and knock occurrence is probable strongly. Also, low lean flammability limit of HHO results advantages only under dilute

(lean) conditions. All experimental results from Gasoline and Diesel Engines show that performance and exhaust

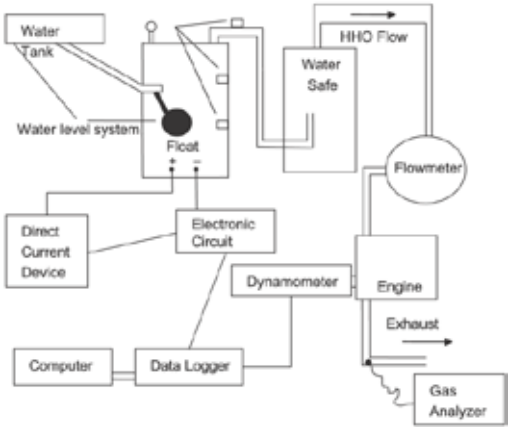


Figure 4. General view of HHO experimental set-up

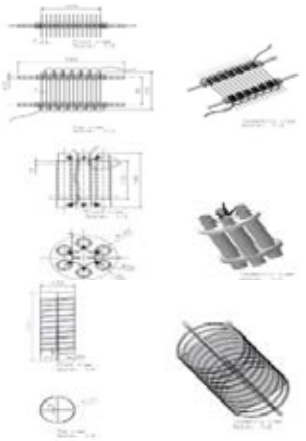


Figure 5. Types of tested reactors

emission values have improved with hydroxy gas addition to the fossil fuels except NO_x exhaust emissions [7].

6. Conclusions

Hydrogen and fuel cell technologies promise considerable benefits in terms of energy security and CO_2 emission, but they require significant technical breakthroughs, cost reduction and appropriate policies to enter the energy market. Fuel cell and hydrogen energy is highly fragmented. The initial use of hydrogen for transport is likely to be municipal bus and truck fleets, and prototypes have already been on the road in many parts of the world. These are centrally-fuelled, so avoid the need for a retail network, and on-board storage of hydrogen is less of a problem than in cars. Hydrogen is likely to conquer a significant market share only if effective policies for CO_2 mitigation and energy security are in place and with considerable reductions of hydrogen and fuel cell cost.

Hydroxy Gas (HHO) could be an alternative hydrogen carrier for Automotive Industry in the short term. Plate type reactor with NaOH produced more HHO gas with the same amount of catalyst and electric energy. Performance and exhaust emission values of both gasoline and diesel engines have improved with hydroxy gas addition to the fossil fuels except NO_x exhaust emissions. In the very long term, electricity and hydrogen are likely to become complementary energy vectors of choice. Hydrogen and the fuel cell are complementary, and each enables the other. Recent research suggests that ammonia could also be used as a high-density, low-pressure means of storing hydrogen, with a compact on-board conversion device producing hydrogen for fuel cell vehicles with low, or possibly no, nitrogen oxide (NO_x) emissions.

References

1. Transport and Hydrogen Economy, Available from: http://www.world-nuclear.org/information-library/non-power-nuclear-applications/transport/transport-and-the-hydrogen-economy. aspx
2. Japan Gambles on Toyota's Hydrogen Powered Car, Available from: https://www.ft.com/content/328df346-10cb-11e7-a88c-50ba212dce4d
3. 2016 Production Statistics, Available from: http://www.oica.net/category/production-statistics/
4. Hydrogen Production In The Coming Hydrogen Economy, Available from: https://newenergytreasure.com/2014/06/28/hydrogen-production-in-the-new-hydrogen-economy/
5. Delucchi MA, Yang C, Burke AF, Ogden JM, Kurani K, Kessler J, Sperling D. An assessment of electric vehicles: technology, infrastructure requirements, greenhouse-gas emissions, petroleum use, material use, lifetime cost, consumer acceptance and policy initiatives. Philosophical Transacrions of the Royal Society A. 2014;372(2006):20120325.
6. Li X, Ogden JM. Understanding the design and economics of distributed tri-generation systems for home and neighborhood refueling. I. Single family residence case studies. J. Power Sources 2011;196:2098–2108.

7. Yilmaz AC, Uludamar E, Aydin K. Effect of hydroxy (HHO) gas addition on performance and exhaust emissions in compression ignition engines. International Journal of Hydrogen Energy 2010;35:11366–11372.
8. Is Ammonia the Secret to Better Hydrogen Cars? Available from: http://www.autoblog.com/2014/06/30/ammonia-secret-to-better-hydrogen-cars/

ORAL PROCEEDINGS

ORAL PROCEEDINGS

Performance Investigation of Zirconium Hydrogen Phosphate / Sulphonated Polysulfone Composite Membrane Based DMFCs

Mustafa Ercelik[1], Yagmur Ozdemir[2], Adnan Ozden[3], Yilser Devrim[4], C. Ozgur Colpan[1,5], Feridun Hamdullahpur[3]
[1] Dokuz Eylul University, The Graduate School of Natural and Applied Sciences, Mechanical Engineering Department, Tinaztepe Campus, 35397, Buca, Izmir, Turkey
[2] Middle East Technical University, The Graduate School of Natural and Applied Sciences, Department of Polymer Science and Technology, 06800, Ankara, Turkey
[3] Department of Mechanical and Mechatronics Engineering, University of Waterloo, 200 University Avenue West, Waterloo, ON N2L 3G1, Canada
[4] Atılım University, Department of Energy System Engineering, 06836 Incek, Ankara, Turkey
[5] Dokuz Eylul University, Faculty of Engineering, Mechanical Engineering Department, Tinaztepe, Buca, Izmir, 35397, Turkey
Email: mustafaercelik13@gmail.com

Abstract
Performance of direct methanol fuel cells (DMFCs) highly depends on the type of electrolyte employed as well as the electrolyte's performance-determining characteristics (e.g., methanol suppression capability, proton conductivity, water uptake capacity, and thermal and oxidative stability). In the context of this study, as potential alternatives to commonly used Nafion® membranes, zirconium hydrogen phosphate/sulfonated polysulfone (ZrP/sPS) hybrid membranes were prepared so as to alleviate the negative consequences of undesirable methanol permeation from the anode to cathode as well as phenomena triggered mainly by methanol crossover (e.g., Pt poisoning at the cathode). The prepared hybrid membranes were characterized through Electrochemical Impedance Spectroscopy (EIS) and water uptake measurement. Electrochemical performance analyses of the hybrid membranes were conducted in a single cell under various methanol concentrations at a constant cell temperature. As the result of the conducted analyses, in particular, ZrP/sPS hybrid membranes with the sulfonation levels of 35% and 42% were found to be promising as because their unique characteristics, such as advanced proton conductivity and methanol suppression capability.

Keywords: Direct methanol fuel cells; Organic/Inorganic hybrid membranes; Zirconium Hydrogen Phosphate; Single cell performance testing.

1. Introduction

Direct methanol fuel cells (DMFCs) have received increasing attention and considered to be a potential candidate for portable applications because of their characteristics, including the ability to operate with liquid methanol, which is easy to store, handle, and has a high energy density [1-4]. However, there are still technical limitations (e.g., methanol crossover, poisoning of precious catalyst, high manufacturing costs, and low durability and stability) remaining unsolved, which inevitably inhibits the large-scale commercialization of DMFCs [5,6]. Therefore, particularly during the last decades or so, fuel-cell researchers have mainly focused on the development of innovative materials as well as fabrication techniques to find sustainable solutions to aforementioned technical limitations.

As one of the performance-limiting components of DMFCs, proton-exchange membrane (PEM), which not only serves a bridge in the proton conduction but also separate fuel from oxidant, has been widely studied to achieve an ideal membrane characteristics. Hence, conventional PEMs (e.g., Nafion® 115) provide the desirable membrane properties, including high proton conductivity, high chemical, mechanical and thermal stability, in a limited operating-condition range (up to ~80°C) [7]. Furthermore, since Nafion® 115 was not designed specifically for DMFC applications, its use also generates additional constraints: high manufacturing costs (since methanol crossover can only be alleviated using high catalyst loadings) and high fabrication costs (because of the inherently high price of the materials that Nafion® membranes are being made of).

In an effort to develop alternative proton-conducting mediums as well as circumvent the restrictions related to the use of Nafion® membranes, zirconium hydrogen phosphate/sulfonated polysulfone (ZrP/sPS) hybrid membranes with different sulfonation degrees (ZrP/sPS 20 (20%), ZrP/sPS 35 (35%), and ZrP/sPS 42 (42%)) and a

constant concentration of ZrP (2.5%) were synthesized. For this purpose, first, sulfonated polysulfone (sPS) was manufactured via the post-sulfonation technique using trimethylsilyl chlorosulfonate. Second, Chlorotrimethylsilane and chlorosulfonic acid were used to produce trimethylsilyl chlorosulfonate. Next, as casting solvent and inorganic filler, N,N-dimethylacetamide (DMAC) and ZrP were used, respectively. The characteristics of the synthesized ZrP/sPS 20 (20%), ZrP/sPS (35%), and ZrP/sPS 42 (42%) membranes and commercial Nafion® 115 were also investigated by Electrochemical Impedance Spectroscopy (EIS) and water uptake measurement. Single cell performance tests were performed for the DMFCs based on ZrP/sPS 20, ZrP/sPS 35, and ZrP/sPS 42 hybrid membranes as well as for that based on Nafion® 115 under various methanol concentrations (0.50 M, 1.00 M, and 2.00 M) at 75°C.

2. Experimental Study

sPS polymers were synthesized according to the procedure previously reported in Ref. [8]. ZrP/sPS hybrid membranes were prepared with the solution casting method. sPS polymer solutions with a concentration of 10 wt.% were dissolved in DMAc at 60°C. After then, proper amounts of the ZrP (2.5 wt.%) were dispersed by a sonicator in the sPS polymer solution. Next, the prepared solution was cast in a tray and heated at 80°C for 30 min.

Water uptake capabilities of the membrane were calculated with the weight difference of wet and dry samples of a membrane (as defined in Eq. (1)). To this end, the membranes were first dried in a vacuum oven at 100°C temperature for 6 h and then immediately weighed. The membrane samples were immersed in distilled water for 24 h.

$$\text{Water Uptake} = \left[\frac{(W_{wet} - W_{dry})}{W_{dry}}\right] \times 100 \quad (1)$$

where W_{wet} and W_{dry} are the weights of the water-swollen and dry membrane sample, respectively.

Proton conductivities were measured via a ZIVESP2 Electrochemical Workstation by simply following the four probe technique in a frequency range of 65 mHz to 65 MHz. The measurements were performed under three different temperatures, which are: 140°C, 165°C, and 180°C. The specific conductivity [σ, (S cm^{-1})] was calculated utilizing the measured resistance, as evident in Eq. (2) [9];

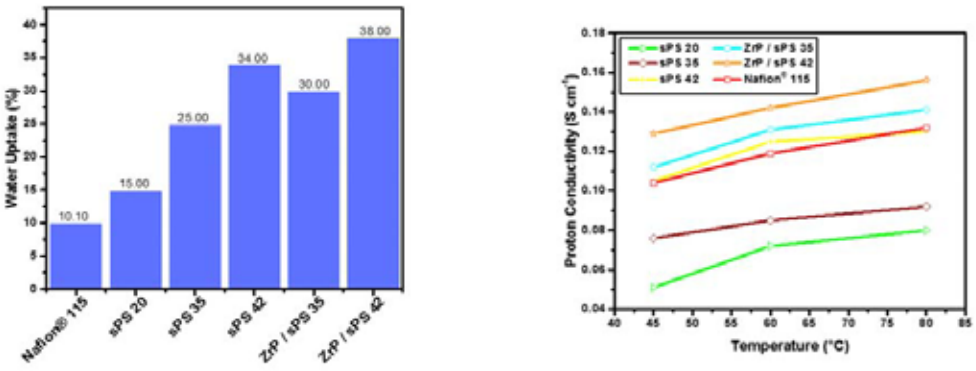
$$\sigma = (1/R) \times (l/A) \quad (2)$$

where, l is the distance between the two electrodes (cm), R is the measured membrane resistance (Ω), and A is the effective cross-sectional area of the membrane sample (cm^2).

For single cell experiments, the Nafion® 115 membrane was boiled in each of the following solutions respectively: 3 wt.% hydrogen peroxide (H_2O_2), deionized (DI) water, 5 wt.% sulphuric acid (H_2SO_4), and deionized (DI) water for 1 h at 80°C. Another activation procedure, involves the steps of boiling the membranes in a 0.50 M H_2SO_4 solution for 1 h and washing them with deionized (DI) water, was employed for the synthesized hybrid membranes. For the aim of preparation of the membrane electrode assemblies (MEAs), the catalyst ink for the cathode was prepared mixing Pt/C, deionized (DI) water, 15 wt.% Nafion® solution, and alcohol to a glass vial, consecutively. In this process, the DI water and Pt/C catalyst were mixed by a shaker (IKA® MS 3 Basic) for 30 s. Then, the final solution, which includes Pt/C catalyst, DI water, 15 wt.% Nafion® solution, and alcohol, was mixed by a sonicator (Misonix Sonicator 3000) under a pulse mode (0.50 s ON and 0.50 s OFF) for 2 min [10]. Likewise, the anode catalyst ink was prepared with the same procedure but PtRu/C catalyst was used. The anode and cathode electrodes with active areas of 25 cm^2 were prepared by coating the catalyst inks on carbon cloth and carbon paper with an automatic film applicator (TQC-AB3120). The catalyst coated electrodes were dried under room temperature overnight. The Nafion® 115 and ZrP/sPS membranes were placed between the coated anode and cathode backing layers and hot-pressed. The manufactured MEAs were placed and tested under the reported procedure in our previous study in Ref. [11]. During the experiments, cell temperature was set at 75°C. The flow rates of the humidified oxygen and methanol solution were set to 600 ml/min and 2.00 ml/min, respectively.

3. Results and Discussion

The water uptake and proton conductivity values of ZrP/sPS hybrid, commercial Nafion® 115, and sPS membranes as the function of temperature and membrane specification are shown in Fig. 1 (a) and (b), respectively. Since the elevated temperature promotes the dissociation of hydrogen, all the membranes exhibited an obvious increase in their proton conductivities with the rise in the temperature [11]. In addition, as can be seen from Fig. 1 (b), the incorporation of ZrP inorganic particles into the polymeric matrix noticeably increased the proton conductivities of the membranes.



(a) **(b)**

Fig. 1. (a) Water uptake and (b) proton conductivity values of sPS, ZrP/sPS hybrid membranes, and commercial Nafion® 115.

The methanol concentration is a key parameter that possesses a significant effect on the DMFC performance. If the methanol solution with the optimum concentration is supplied to DMFC, it could be possible to achieve an improved DMFC performance. Fig.2 displays the change in the peak power densities of the DMFCs based on ZrP/sPS 42, ZrP/sPS 35, ZrP/sPS 20, and Nafion® 115 with the changing methanol concentration (from 0.50 M to 2.00 M). Because the concentration of the methanol affects both the rate of methanol transport to the electrochemical reaction region and methanol crossover, it influences the peak power densities than can be obtained from the cell as well. When methanol is supplied to the cell at low concentrations, the measured OCVs for all the DMFCs were found to be significantly high compared with those of recorded at elevated concentrations (as evident in Tab. 1). In other words, the OCVs demonstrated decreasing trend with increasing concentration of supplied methanol, which could be mainly attributed to a performance limiting phenomenon, primarily referred to as mixed potential and is a common cause of voltage and performance losses. However, for the increase of methanol concentration (from 0.50 M to 2.00 M), the decays in the OCVs of the DMFCs based specifically on ZrP/sPS 35 and ZrP/sPS 42 hybrid membranes were distinguishably lower as compared to that of the DMFC based on Nafion® 115 membrane, which further confirms their methanol-blocking properties, even though the thicknesses of the ZrP/sPS 35 and ZrP/sPS 42 hybrid membranes were distinguishable smaller than that of the commercial Nafion® 115.

Table 1. Open circuit voltage (OCV) values of the ZrP/sPS 20, ZrP/sPS 35, ZrP/sPS 42, and Nafion® 115 membrane with 0.50 M, 1.00 M, and 2.00 M methanol concentrations at 75°C.

	Open Circuit Voltage Values (V)			
Methanol Concentration (M)	ZrP/sPS 20	ZrP/sPS 35	ZrP/sPS 42	Nafion® 115
0.50	0.69	0.71	0.72	0.73
1.00	0.72	0.73	0.75	0.76
2.00	0.65	0.67	0.79	0.71

Similarly, the peak power densities of the DMFCs increased with changing methanol concentration (from 0.50 M to 1.00 M). The peak power densities of the DMFCs based on ZrP/sPS 20, ZrP/sPS 35, ZrP/sPS 42, and Nafion® 115 were found to sharply increase from 73 to 108 mW cm^{-2}, 81 to 114 mW cm^{-2}, 85 to119 mW cm^{-2}, and 72 to 105 mW cm^{-2} (at 75°C cell temperature). In contrast, for further increase (from 1.00 M to 2.00 M), the peak power densities were observed to decrease from 108 to 65 mW cm^{-2}, 114 to 68 mW cm^{-2}, 119 to 70 mW cm^{-2}, and 105 to 65 mW cm^{-2} for the DMFCs constructed with ZrP/sPS 20, ZrP/sPS 35, ZrP/sPS 42, and Nafion® 115 membranes, respectively (at 75°C cell temperature). Namely, all the DMFCs exhibited performance deteriorations with increased methanol concentration from 1.00 M to 2.00 M (e.g., a peak power decrease of ~40% for ZrP/sPS 20, ~41% for ZrP/sPS 35, ~42 for ZrP/sPS 42, and ~38% for Nafion® 115, all relative to the 2.00 M case and the data obtained at the cell temperature of 75°C). These performance deteriorations were observed due to the undesired methanol crossover phenomenon at highest methanol concentration [11].

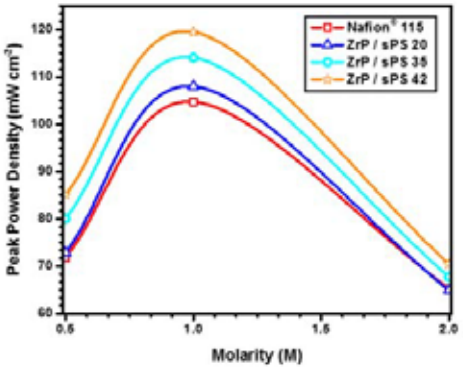


Fig. 2. Comparison of the peak power densities of the DMFCs based on ZrP/sPS 42, ZrP/sPS 35, ZrP/sPS 20, and Nafion® 115 with the methanol concentrations of 0.50 M, 1.00 M, and 2.00 M at 75°C.

Fig. 3 presents the comparison of potential versus current density as well as power density versus current density curves of the ZrP/sPS 20, ZrP/sPS 35, and ZrP/sPS 42 with that of Nafion® 115 in single cell DMFC under the same operating conditions. As seen from Fig. 3, the highest cell performance (based on peak power densities) was observed for the DMFC based on ZrP/sPS 42 with a power density of 119 mW cm^{-2} (at 1.00 M and 75°C).

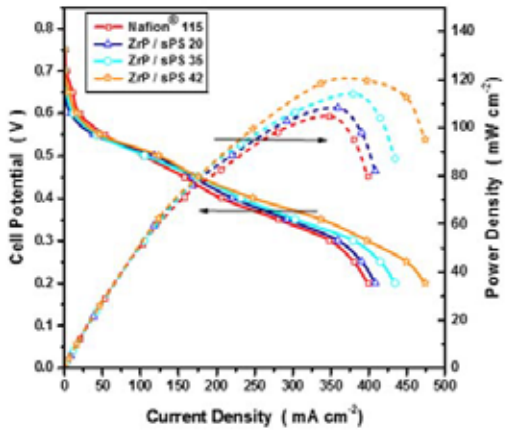


Fig. 3. Power and polarization curves for the DMFCs based on ZrP/sPS 42, ZrP/sPS 35, ZrP/sPS 20, and Nafion® 115 at 1.00 M and 75°C.

4. Conclusions

In this study, DMFCs based on hybrid membranes with different sulfonation degree (20%, 35%, and 42%) and a constant ZrP (2.5%) and a commercial Nafion® 115 membrane were investigated experimentally. Performance studies were conducted by varying the methanol concentration between 0.50 M and 2.00 M at 75°C. The main conclusions of this study are summarized by:

- The highest performance was obtained with the DMFC based on ZrP/sPS 42 as 119 mW cm^{-2} at 1.00 M methanol concentration.
- The DMFCs based on ZrP/sPS 20, ZrP/sPS 35, and Nafion® 115 membrane shows 108 mW cm^{-2}, 114 mW cm^{-2}, and 105 mW cm^{-2} peak power densities at 1.00 M methanol concentration, respectively.
- For all the studied methanol concentrations (0.50 M, 1.00 M, and 2.00 M), all the DMFCs in this study provided their maximum power density values at 1.00 M methanol concentration.
- The DMFCs based on ZrP/sPS 42 seems to be more promising in term of performance and as compared to DMFCs based on ZrP/sPS 20, ZrP/sPS 35, and Nafion® 115.

References

1. Wang C, Li H, Zhao J, Zhu Y, Yuan WZ, Zhang Y. Graphene Nanoribbons As A Novel Support Material for High Performance Fuel Cell Electrocatalysts. International Journal of Hydrogen Energy. 2013;38(30):13230-13237.
2. Ercelik M, Ozden A, Devrim Y, Colpan CO. Investigation of Nafion Based Composite Membranes on The Performance of DMFCs. International Journal of Hydrogen Energy. 2017;42(4): 2658-2668.
3. Zhang J, Yin G, Wang Z, Shao Y. Effects of MEA Preparation on The Performance of a Direct Methanol Fuel Cell. Journal of Power Sources. 2006;160(2):1035-1040.
4. Hogarth WH, Da Costa JD, Lu GM. Solid Acid Membranes for High Temperature (>140°C) Proton Exchange Membrane Fuel Cells. Journal of Power Sources. 2005;142(1):223-237.
5. Wu QX, Zhao TS, Chen R, Yang WW. Effects of Anode Microporous Layers Made of Carbon Powder and Nanotubes on Water Transport in Direct Methanol Fuel Cells. Journal of Power Sources. 2009;191(2):304-311.
6. Colpan CO, Fung A, Hamdullahpur F. 2D Modeling of a Flowing-Electrolyte Direct Methanol Fuel Cell. Journal of Power Sources. 2012;209:301-311.
7. Devrim Y. Preparation and Testing of Nafion/Titanium Dioxide Nanocomposite Membrane Electrode Assembly by Ultrasonic Coating Technique. Journal of Applied Polymer Science. 2014;131(15).
8. Devrim Y. Fabrication and Performance Evaluation of Hybrid Membrane Based on a Sulfonated Polyphenyl Sulfone/Phosphotungstic Acid/Silica for Proton Exchange Membrane Fuel Cell at Low Humidity Conditions. Electrochimica Acta. 2014;146:741–51.
9. Özdemir Y, Üregen N, Devrim Y. Polybenzimidazole Based Nanocomposite Membranes With Enhanced Proton Conductivity for High Temperature PEM Fuel Cells. International Journal of Hydrogen Energy. 2017;42(4):2648-2657.
10. Colpan CO, Ouellette D, Glüsen A, Müller M, Stolten D. Reduction of Methanol Crossover in a Flowing Electrolyte-Direct Methanol Fuel Cell. International Journal of Hydrogen Energy. 2017. In press, doi: 10.1016/j.ijhydene.2017.01.004.
11. Ozden A, Ercelik M, Ozdemir Y, Devrim Y, Colpan CO. Enhancement of Direct Methanol Fuel Cell Performance Through The Inclusion of Zirconium Phosphate. International Journal of Hydrogen Energy. 2017. In press, doi: 10.1016/j.ijhydene.2017.01.188.

ORAL PROCEEDINGS

Investigation of Working Temperature Effect on Micro-Cogeneration Application of Proton Exchange Membrane Fuel Cell

Yağmur Budak[1], Yağmur Özdemir[2], Yılser Devrim[1]
[1]Atılım University Energy System Engineering Department, Incek Ankara Turkey
[2]Middle East Technical University, Polymer Science and Engineering Department, Cankaya Ankara Turkey
Email: yagmurbudak13@gmail.com , e167187@metu.edu.tr , yilser@gmail.com

Abstract
In this study, it was aimed to increase the productivity of proton exchange membrane fuel cell (PEMFC) by micro-cogeneration application and compare the fuel cells which have different operation temperature. The 1.2 kW PEMFC operating temperature at 65 ºC was compared with the 1.2 kW PEMFC operating temperature at 165 ºC. First of all, 1.2 kW PEMFCs which have two different working temperature were designed by using experimentally determined current density values. Then the cooling method is chosen for heat transfer to the city water which used for house hot water demand. Same cooling systems have been used in the designed micro- cogeneration systems due to the observe difference of the released heat values from the PEMFC according to the working temperatures. As a result of the design calculations, PEMFC with micro-cogeneration applications simple payback times were determined.

Keywords: High temperature PEMFC; low temperature PEMFC; micro-cogeneration; cost analysis.

1. Introduction

Fuel cell is an electrochemical device which converts the chemical energy to electricity. PEMFC gain the highest interest because of their high power densities, modular structures and negligible emission rates [1]. This type of fuel cells has a different usage area; such as residential use, transportation system, military applications and defending systems. According to working temperature, PEMFCs are separate two types. Low temperature (LT) PEMFC operates temperature range of 60-80ºC, high temperature (HT) PEMFC operates temperature over than 100ºC [2]. HT-PEMFC advantages are improved tolerance to impurities such as CO, easier heat rejection, enhanced electrode kinetics, easier water management and no need humidification [3]. LT-PEMFC advantages are economic, low working temperature and higher gas sealing [4].

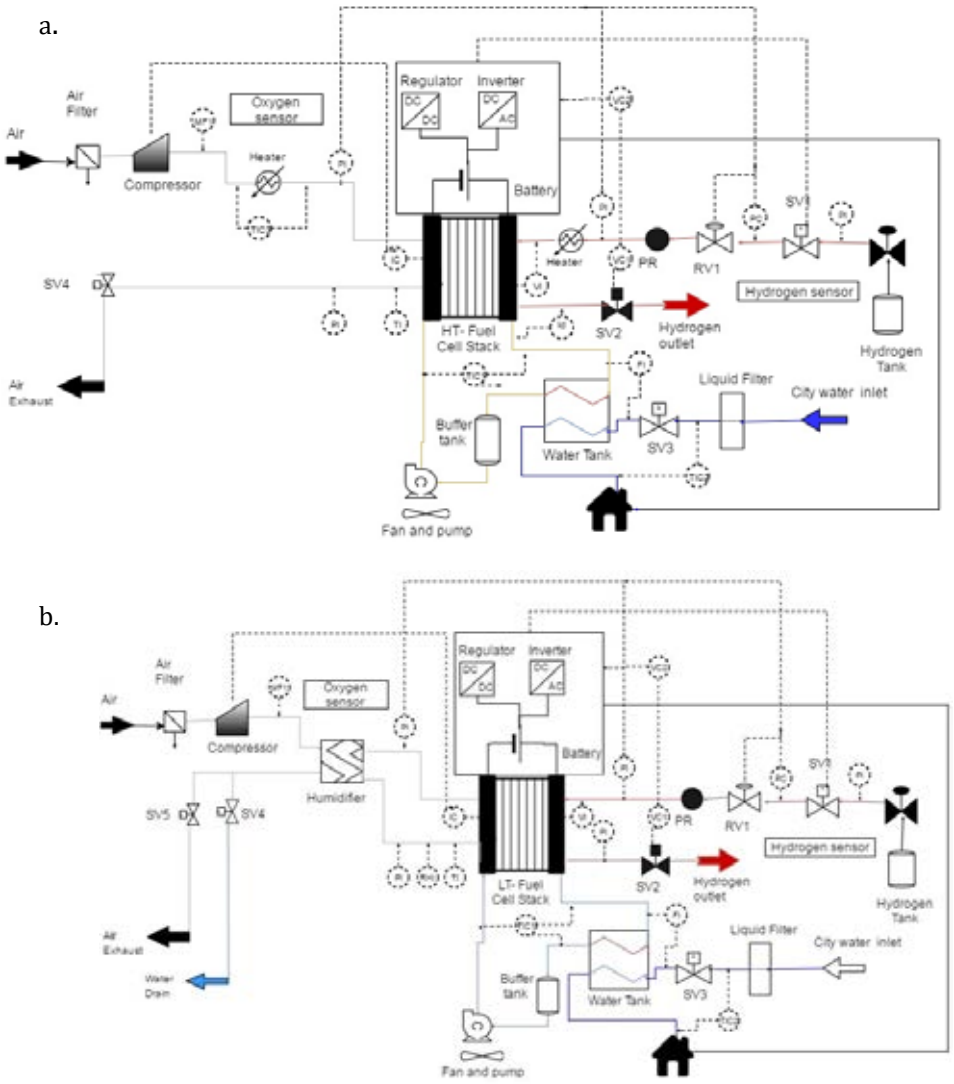
Cooling of the stack is one of the important design considerations when developing a stack for an application. Stack is cooled to stabilized operation temperature and heat transmission to other application. There are two main types of cooling infrastructure that are used within the stack; air cooling system and liquid cooling system. The air cooling systems are separated three types; cathode air, cooling plate and heat spreader [5]. Air cooling principle behind the air cooling system is that air used to remove the heat generated by the stack. This is often the cheaper method of cooling the stack as the only balance of plant required is an air pump to pass air though the cell [6]. Air cooling systems for HT-PEMFC have some disadvantages such as decreased the heat flux and increased the size of heat exchanger [5]. On the other hand, the liquid cooling system works by the introduction of cooling plates in the stack [7]. Liquid cooling systems are separated three types; water, oil and evaporative cooling. Evaporative cooling for HT-PEMFC caused membranes phosphoric acid loss [5]. A liquid is pumped through these channels and heat is removed from the stack by this heat exchanger effect in liquid cooling system. This type of cooling is suitable for large scale stacks as scaling up this liquid cooling system does not increase the power demands of the balance of plant significantly [8]. After cooling process, the waste heat can be used micro-cogeneration systems.

Micro-cogeneration is utilization of both power and heat simultaneously [2]. Besides the primary electrical output of the system, hot water also can be used for heating applications or hot water reservoir. For high power capacity micro-cogeneration application, usually solid oxide fuel cells (SOFC) are being used. But lately, for low power household applications, PEMFC are found to be useful. Micro cogeneration applications increase the overall system efficiency. With this increase, economic gain is achieved in a long term.

Economy is one of the important issues for PEMFC. Simple payback time is a basic method which can be used to evaluate feasibility of residential fuel cell. Simple payback time shown, how soon the investment will pay back, but this system ignored the interest lost or spent during that period, inflation, or changes in electricity and natural gas prices [2]. Micro cogeneration system's economic gain can be shown with this method.

In this study, 1.2 kW LT- PEMFC micro cogeneration supplication was compared with the 1.2 kW HT-PEMFC micro-cogeneration application. Fuel cells designed for different membrane type. Then the PEMFCs were

cooled with heat transfer oil 32 [9]. The waste heat satisfies a house hot water need. Finally, PEMFC with and without micro-cogeneration application's simple payback times were determined.



FI: Flow indicator, IC: Stackcurrent controller, MF1: Mass air flow sensor,PC: Pressure controller, PI:Pressure indicator, RHI: Relative humidity indicator,PR: Pressure regulator,RV1:Relief valve, SV2: Purgesolenoid valve, SV1-SV3-SV4-SV5: solenoid valve for hydrogen inlet, TI: Temperature indicator,TIC: Temperature indicator and controller, VC1-VC2: Voltage controller

Fig. 1.a) HT-PEMFC and b) LT-PEMFC micro-cogeneration application flow diagram

In Fig.1, schematics of the PEMFC micro-cogeneration application can be seen. In Fig. 1-a, air passed through the filter and send to the pre-heater with the help of compressor. Hydrogen taken from storage tank and send to the pre-heater. Then the gases feed to the HT-PEMFC, which supplies the electrical demand of house. In Fig 1-b, air passed through the filter and send to the humidifier with the help of compressor. Hydrogen taken from storage tank, then the gases feed to the HT-PEMFC, which supplies the electrical demand of house. Main specifications of the

PEMFCs are summarized in Table 1. The excess heats are used to supply hot water of the house. For the micro-cogeneration application, heat transfer oil 32 is used to remove heat from PEMFC are directed to water tank which is used for heating city water heating purposes for the house. After water tank, ethylene glycol circulated in buffer tank by help of fan pump. Flows are controlled by valves, indicators and controllers.

Table1. Properties of the LT and HT- PEMFC stacks

PEM Fuel Cell Type	Design Parameters	Value
HT-PEMFC	Current density(at 0.6 V)	0.4 A/cm^2
	Membrane	PBI/H_3PO_4
	Cell area	165 cm^2
	Cell number	30
	Maximum power	1200 W
LT-PEMFC	Current density(at 0.6 V)	1 A/cm^2
	Membrane	Nafion 212
	Cell area	165 cm^2
	Cell number	12
	Maximum power	1200 W

2. Experimental Study

Assumptions used in the calculations are:

- The PEMFC micro-cogeneration systems operate in steady state conditions.
- The ideal gas principles are applied to gases.
- Flows are assumed one dimensional.
- Kinetic and potential energies are negligible.
- LT-PEMFC stack consist of Nafion® 212 membrane. HT-PEMFC stack consist of polybenzimidazole and phosphoric acid membrane (Celtec® P1000).
- Working temperatures of LT-PEMFC stack is 65ºC and HT-PEMFC stack is 165 ºC.
- PEMFC outlets include only water vapor.

PEMFC calculations

H_2 is feed into the PEMFCs at the anode side. N_{H2} is hydrogen concentration and depends on the stoichiometric ratio S_{H2} current density I (A/cm^2), cell area A (cm^2) and number of cell N_{cell}. F is the Faraday constant. The H_2 concentration at the anode gas inlet of the PEMFCs can be defined as follows:

$$N_{H_2} = S_{H_2}.\frac{I.A}{2.F}.N_{cell} \quad (1)$$

Air is feed into PEMFCs at the cathode side. Air included 21% oxygen. N_{O2} is hydrogen concentration and depends on the stoichiometric ratio S_{O2}, current density I (A/cm^2), cell area A (cm^2) and number of cell N_{cell}. r_{o2} is oxygen volume in air. The O_2 and air concentration at the anode gas inlet of the PEMFCs can be defined as follows:

$$N_{O_2} = S_{O_2}.\frac{I.A}{4.F}.N_{cell} \quad (2)$$

$$N_{air} = \frac{S_{O_2}}{r_{O_2}}.\frac{I.A}{4.F}.N_{cell} \quad (3)$$

Energy balance for PEMFC defined as follow:

$$\sum \dot{E}_{mass,in} - \sum \dot{E}_{mass,out} + \dot{Q} - \dot{W}_{net} = 0 \quad (4)$$

where $\Sigma \dot{E}_{mass,in}$ is total enthalpy of inlet gases, $\Sigma \dot{E}_{mass,out}$ is total enthalphy of outlet gases and water. Air is humidified in LT-PEMFC so inlet gases have water vapor in this type of PEMFC. Q is heat dissipation from the PEMFC stacks to ambient and/or water. W_{net} is net power production by PEMFC.

Heat dissipation calculation
Maximum heat dissipation from PEMFCs stack by natural convection and radiation defined as follow:

$$Q_{dis} = \frac{T_s - T_o}{R_{th}} \quad (5)$$

where Q_{dis} is the heat dissipation, T_s is stack surface temperature, T_o is the temperature of surrounding walls, R_{th} is thermal resistance. Heat dissipation from LT-PEMFC stack can be ignored but heat dissipation from HT-PEMFC is high value. HT-PEMFC is insulated with fiber glass. Insulated material thickness defined as follow:

$$\Delta x = \frac{k.\Delta T.A}{Q_{dis}} \quad (6)$$

where k is thermal conductivity, ΔT is temperature difference between T_s and T_o, A is heat transfer area of HT-PEMFC stack.

Micro-cogeneration system calculation
Energy balance in the water tank can be defined as follow;

$$\dot{m}_{hto}.c_{p,hto}.\Delta T_{hto} = \dot{m}_{cw}.c_{p,cw}.\Delta T_{cw} \quad (7)$$

where $\dot{m}_{hto}$ and $\dot{m}_{cw}$ are mass flow rates of PEMFC heat transfer oil and city water which used house water requirement respectively. $c_{p,hto}$ *and* $c_{p,cw}$ are specific heats of PEMFC heat transfer oil and city water which used house water requirement respectively. ΔT_{hto} and ΔT_{cw} are heat transfer oil and city water temperature change respectively.

Simple payback time calculation
Simple payback time in PEMFC defined as follow;

$$SPT = \frac{C_{fc}}{8760.CF.\left[C_{el} - \frac{C_{h_2}}{\overline{\eta_{fc}}}\right]} \quad (8)$$

Where C_{fc} specific cost of fuel cell power system per kW of nominal power, 8760 is the number of hours in a year, CF is the capacity factor previously, C_{el} is cost of electricity [10], C_{h2} is cost of hydrogen [11] and $\overline{\eta_{fc}}$ is average annual efficiency of the fuel cell system. Simple payback time for PEMFC micro-cogeneration application defined as follow;

$$SPT_{chp} = \frac{C_{fc}.P_{fc}}{AEP.\left[C_{el}\frac{C_{h_2}}{\eta_{el}} + \left(\frac{\eta_{tot}}{\eta_{el}} - 1\right).f_{hu}.\frac{C_{fuel}}{\eta_{heat}}\right]} \quad (9)$$

Where AEP is amount of electricity annually produced, P_{fc} is fuel cell power system nominal power, η_{tot} is total fuel cell efficiency, f_{hu} is heat utilization factor and η_{heat} is efficiency of convectional heat generation. Heat utilization factor defined as follow;

$$f_{hu} = \frac{AHP}{AEP.\left(\frac{\eta_{tot}}{\eta_{el}} - 1\right)} \quad (10)$$

Where AHP is amount of heat used per year.

3. Results and Discussion

PEMFC results:

PEMFC system results for different working temperature can be seen in Table 2. As seen from Table 2, released heat is increased with humidification. Also its show that working temperature not effect to H_2 and Air consumption.

Table 2. PEMFC design results for different working temperature

	H_2 consumption(g/s)	**Air consumption (g/s)**	**Air humidty(g/s)**	**Heat release (W)**
LT-PEMFC	0.025	1.78	0.22	1368
HT-PEMFC	0.025	1.78	0	1308

Micro-cogeneration application results:

Micro- cogeneration system results for different working temperature can be found Table 3. HT-PEMFC is insulated with fiber glass which has 1 cm thickness. As seen from Table 3, temperature difference between inlet and outlet temperature heat transfer oil and city water with increasing working temperature. The results of Table 3, experimentally tried and tested.

Table 3. PEMFCs micro cogeneration application results

	Q_{dis} (W)	**$C_{p,hto}$ (Kj/kg.°C)**	**ΔT_{hto} (°C)**	**$\dot{m}_{hto}$ (kg/s)**	**Q_{hto} (W)**	**$\dot{m}_{cw}$ (kg/s)**	**ΔT_{cw} (°C)**
LT-PEMFC	63.6	2.4	13	0.071	2215	0.02	26
HT-PEMFC	498	2.4	25	0.071	4260	0.02	50

Simple payback time results:

Simple payback time and simple payback time with micro-cogeneration application can be found in Table 4. Values which used for calculation also can see in Table 4. As seen from Table 4 payback time of the LT-PEMFC is lower than HT-PEMFC. It is related to the cost of the material and component of the systems.

Table 4. Simple Payback Time calculation values and results

	C_{fc} $/ kW	**CF**	**Cel** $/ kW	**C_{h2}** $ / kW	**ñfc**	**η_{tot}**	**C_{fuel}**	**η_{heat}**	**fhu**	**SPT (year)**	**SPT_{chp} (year)**
LT- PEMFC	346.27	0.88	0.16	0.042	0.3	0.70	0.068	0.9	2.68	2.22	0.39
HT-PEMFC	740.52	0.88	0.16	0.042	0.3	0.69	0.068	0.9	3.02	4.75	0.833

4. Conclusions

In this study, we have investigated the working temperature effect on micro-cogeneration application of proton exchange membrane fuel cell. LT-PEMFC and HT-PEMFC are designed and energy balances were conducted. LTPEM fuel cell produced more heat than HT-PEMFC. Since heat dissipated from HT-PEMFC non-ignorable, insulation is designed for HT-PEMFC system to reduce heat loss by convection and radiation. Liquid coolants are increased efficiency of micro-cogeneration systems. Heat transfer oil 32 was chosen for heat transfer from PEMFC stacks thanks to the high thermal stability, long life, not deposited properties. The micro- cogeneration results show that temperature difference higher in HT-PEMFC even both systems used same flow rate of coolant and city water. Both systems efficiency increase with micro-cogeneration application.HT-PEMFC efficiency increase 30% to 69% and LT-PEMFC efficiency increase 30% to 70% efficiency. LT-PEMFC efficiency increase more than HT-PEMFC because of the thermal outputs. Cost analyses are conducted for both systems and results showed that PEMFC systems are more cost efficient when used with micro cogeneration application and LT-PEMFC are more economic than HT-PEMFC. The results obtained in the study show that the use of the heat generated from PEMFC improves the system efficiency and more efficient micro-cogeneration system can be achieved by using high working temperature of PEMFC.

Acknowledgement

This study was supported by The Scientific and Technological Research Council of Turkey (TUBITAK) 1001 (Grant number: 214M301) Project. The author gratefully acknowledge to TEKSIS (METU-Technopolis, TURKEY).

Nomenclature

A	Cell area (cm^2)
C_p	Specific heats
C_{fc}	Specific cost of fuel cell power system per kW of nominal power
CF	Capacity factor previously
C_{el}	Cost of electricity
C_{h2}	Cost of hydrogen
C_{fuel}	Cost of fuel used for heating
$\dot{E}$	Enthalpy
f_{hu}	Heat utilization factor
F	Faraday constant (96485 A.s/mole)
I	Current density (A/cm^2)
$\dot{m}$	Mass flow rate (g/s)
N	Rates of consumed and generated gases (mole/s)
N_{cell}	Number of cell
Q	Heat dissipation
P_{fc}	Fuel cell power system nominal power
r_{o2}	Oxygen volume in air
R_{th}	Thermal resistance
S_{H2}	Stoichiometric ratio
T	Temperature (°C or K)
W_{net}	Net power
$\overline{\eta_{fc}}$	Average annual efficiency
η_{tot}	Total fuel cell efficiency
η_{heat}	Efficiency of convectional heat generation.

Acronyms

AEP	amount of electricity annually produced
AHP	amount of heat used per year
HT	High temperature
LT	Low temperature
PEMFC	Proton exchange membrane fuel cell
SPT	Simple payback time

References

1. Devrim, Y., Erkan, S., Baç, N., & Eroglu, I. (2012). Improvement of PEMFC performance with Nafion/inorganic nanocomposite membrane electrode assembly prepared by ultrasonic coating technique. international journal of hydrogen energy, 37(21), 16748-16758.
2. Barbir, F. (2012). PEM fuel cells: theory and practice. Academic Press.
3. Araya, S. S., Zhou, F., Liso, V., Sahlin, S. L., Vang, J. R., Thomas, S., ... & Kær, S. K. (2016). A Comprehensive Review of Pbi-Based High Temperature Pem Fuel Cells. International Journal Of Hydrogen Energy, 41(46), 21310-21344.
4. A Stack Cost Comparison of 100 kW Combined Heat and Power Fuel Cell Systems. Website: http://lma.berkeley.edu/
5. Song T., Yi J., Kim J., Choi K. Challenges and Opportunities of Thermal Management for High –Temperature Proton Exchange Membrane Fuel Cells,2010.
6. A. A. C. B. A.J. del Real, “Journal of Power Sources,” pp. 310-324, 2007.
7. A. C. E. C. O.J. Murphy, “Electrochimica Acta,” pp. 3829-3840, 1998.
8. X. W. J. Clement, “Applied Thermal Engineering,” pp. 268-274, 2013
9. Petrol ofisi; Heat transfer Oil 32
10. Elektrik Fiyatları. (n.d.). Retrieved April 29, 2017, from http://www.enerjiatlasi.com/elektrik-fiyatlari/
11. Çalışan A., Sarıalp G., Bayar İ., Gerçeker D, Oğulgönen C.G., Kılıç O. Residental Fueling with Hydrogen. METU,201

Fabrication of Cross-linked Polybenzimidazole Membranes for High Temperature PEM Fuel Cells and Investigation of the Amount of Cross-linker Used on Membrane Performance

Yağmur Özdemir[1], Necati Özkan[2], Yılser Devrim[3]
[1]Middle East Technical University, Graduate School of Natural and Applied Sciences, Polymer Science and Technology, 06800 Ankara
[2]Central Laboratory, Middle East Technical University, 06800 Ankara
[3]Atılım University, Faculty of Engineering, Energy Systems Engineering, 06836 Ankara
Email: e167187@metu.edu.tr, nozkan@metu.edu.tr, yilser.devrim@atilim.edu.tr

Abstract
Today, a lot of research on development of alternative low cost, high temperature membranes for proton exchange membrane (PEM) fuel cells is being conducted due to the limitations of industry standard perfluoro-sulfonic acid (PFSA) membranes. These limitations, such as the decrease in performance at temperatures above 80 ºC and high cost, restrains the commercialization of PEM fuel cells. Polybenzimidazole (PBI) based membranes are being investigated as an alternative to Nafion® membranes. Fuel cells with PBI/Phosphoric Acid (PA) were found to be successful due to their high thermochemical stability between 120˚C–180˚C with high conductivities. However, acid leaching is a major concern in the presence of liquid water which leads to a drop of conductivity of many orders of magnitude during fuel cell operation. Cross-linking the membranes is an alternative way to prevent acid being leached from the membranes. In this study, Bisphenol A diglycidyl ether (BADGE) was used as cross-linker for PBI membranes. Aim of this study was to prepare cross-linked PBI membranes for HT-PEMFCs and to investigate the effect of cross-linker amount on the performance of the membranes. Cross-linked membranes prepared with 2.5 wt. %, 5 wt. % and 7.5 wt. % of BADGE (PBI/BADGE 2.5 %, PBI/BADGE 5 %, PBI/BADGE 7.5 %), were characterized and compared with pristine PBI membrane. TGA and FTIR analyses, proton conductivity measurements, acid leaching and chemical stability tests were conducted within the scope of this study. Membrane Electrode Assemblies (MEAs) with 5cm^2 active area were prepared for HT-PEMFC tests. Then, MEAs were tested at 160ºC, using hydrogen and air as reactants. Results showed that cross-linked membranes performed better in HT-PEMFC tests compared to pristine PBI membrane.

Keywords: Cross-linked PBI membrane; High Temperature PEM Fuel Cell; Hydrogen Energy.

1. Introduction

Energy consumption/production relying solely on combustion of fossil fuels is predicted to cause severe future impact on world economics and ecology. Electrochemical energy systems are one of the best alternatives for fossil fuels and they are being studied intensively. Fuel cells are electrochemical systems that produce electrical energy from chemical energy by using hydrogen as the fuel and an oxidizer. They can provide energy as long as reactant gases are fed to the system. There are many different types of fuel cells operating under different temperatures and using different electrolytes. PEMFCs have attracted much attention due to their high energy density and modular structure. Recent studies showed that HT-PEMFCs operates at temperatures higher than 100°C may be commercially more viable because of their higher CO tolerance, high fuel efficiency, mobility and compatibility to reforming units. PBI type membranes are preferred for HT-PEMFC applications as polymer electrolyte. PBI is a thermoplastic polymer which has high thermal stability. However, PBI is not a proton conducting polymer, thus PBI membranes are doped with PA before usage. Doped acid quantity determines the proton conductivity of the PBI membranes. When the acid doped PBI membranes are in direct contact with water or water vapor, free acid starts to leach from the membrane, which results in poor conductivity. In order to reduce the acid leached from the membranes during operation, cross-linking can be a novel method.

Studies focus on three types of cross-linking mechanism for PBI based membranes: 1) ionic cross-linking 2) covalent cross-linking and 3) organic-inorganic PBI hybrid membranes. Covalent cross-linking refers to a process in which cross-linking of PBI can be done by thermal treatment [1] or an amide type [2] linkage between imidazole groups of the polymer. In this type of cross-linking reaction, functional group(s) cross-linkers react with the imidazole groups to form covalently cross-linked structures. In the literature, there are studies on dicloromethyl phosphoric acid[3], diglycidil ether bisphenol-A[4], 1,3-bis(2,3-epoxypropoxy)-2,2-dimethylpropane [5].

In this study, BADGE cross-linker is used as cross-linking agent for PBI membranes in different amounts, 2.5%, 5%, 7.5%. It is pointed out that there is a few of literature covering the comparison of the above mentioned cross-linked membranes in terms of investigating acid leaching from the membranes and its effects on HT-PEMFC

performance. In this study, pristine PBI, PBI/BADGE %2.5, PBI/BADGE %5, and PBI/BADGE %7.5 membranes were characterized according to acid leaching, proton conductivity, FTIR, TGA and their HT-PEMFC test results.

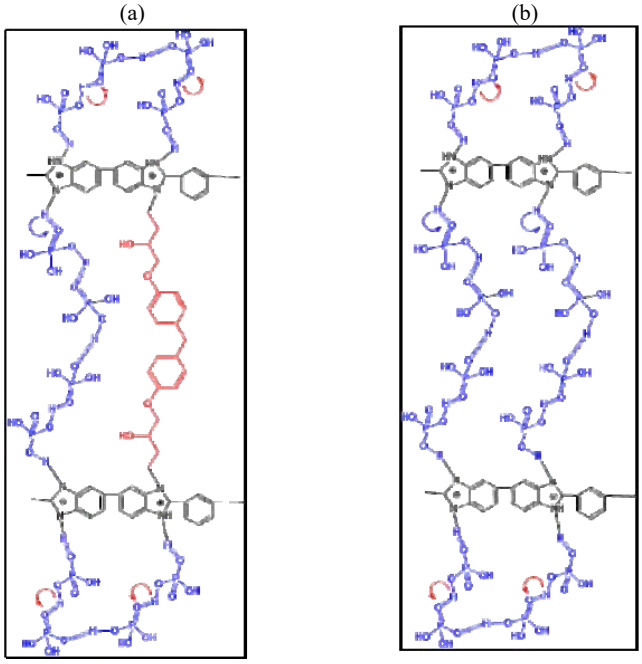
2. Experimental Study

2.1. Materials

PBI polymer used was obtained from Danish Power Systems. PA (%85) was obtained from Sigma-Aldrich (USA) and N-N Dimethylacetamide (DMAc, Merck) was used as received. Cross-linker BADGE was purchased from Sigma-Aldrich (USA). De-ionized water was purchased from Sigma-Aldrich (USA) and used as received. All solvents used were high-grade reagents.

2.2. Membrane Preparation and Characterization

In this study, for membrane preparation, 2.5 wt. % PBI polymer was dissolved in 10 mL solvent (DMAc), at 80°C temperature. Pristine PBI membrane was prepared by pouring the solution into petri dish and drying at 80°C to evaporate the remaining solvent. The membrane was dried at 80°C for 24 hours and stripped from the petri dish. In order to remove the remaining solvent in the membranes, PBI based membranes were washed in boiling water. Cross-linked membranes were prepared by adding BADGE cross-linker to the PBI solution. BADGE was mixed with 1 mL DMAc and then they were mixed with PBI solution. The mixture was later poured onto a petri dish and dried at 80°C for 24 hours. In order to complete the cross-linking reaction, the membranes were further heat treated. The duration and temperature of the heat treatment process was determined according to previous literature reports on BADGE. For PBI/BADGE membranes, thermal treatment was at 135ºC for an hour. The chemical structure of the cross-linked membranes is given in Scheme 1 [4]. As can be seen in the Scheme 1, cross-linking reactions occurred between the epoxy groups of the cross-linkers and the -NH groups of PBI. The membranes were subsequently immersed in 85 % PA for one week. PA doping was undertaken at room temperature.



Scheme 1. Structures of the acid doped PBI based membranes (a) PBI/BADGE, (b) Pristine PBI

Thermal Gravimetric Analyzer (Perkin Elmer Pyris 1 TGA) was used for thermal analyses of the membranes. The temperature range employed was 25°C - 800°C at a heating rate of 10°C min^{-1} under a nitrogen atmosphere. The PBI matrix needs to incorporate a large quantity of PA to achieve high proton conductivity values. The pristine PBI and cross-linked PBI membranes were doped using PA solution. The weight gain due to both acid and water was

estimated by comparing the weight before and after acid doping. The acid doping level of the membrane is expressed as the number of PA moles per PBI repeat unit. In order to determine the acid retention capability of the prepared membranes, acid leaching tests were conducted. The procedure from the literature was used to determine the effect of cross-linker used on the acid leaching [6]. The stability of the membranes was tested by extraction in DMAc, as described previously by Heinz et al [7]. The proton conductivity of the membranes was determined using a ZIVE SP2 Electrochemical Workstation (WonATech, Korea). All measurements were performed in longitudinal direction with 4 probe EIS as a function of temperature. AC impedance was measured between 65 MHz and 65 mHz for all membranes. Measurements were done at three different temperatures, 140, 165 and 180°C and under dry conditions. Membrane electrode assemblies (MEAs) with PBI and cross-linked PBI membranes were fabricated by an Ultrasonic Coating Technique as described previously [8]. The performance of the fabricated MEAs was evaluated after conditioning for 5 h at 0.6 V. The current and voltage of the cell were monitored and logged throughout the operation of the cell by the fuel cell test software (TECHSYS-HYGO). Once the steady state was achieved, starting with the OCV value, the current–voltage data was collected by changing the voltage values from the load. The reactant gas stoichiometry was 1.5 and 2.5 for hydrogen and air, respectively. The polarization curves were recorded at atmospheric pressure using dry air and hydrogen at 165°C. HT-PEMFC test durations for the membranes were approximately 40 hours for each.

3. Results and Discussion

Thermal gravimetric analysis results of the membranes are given in Figure 1. It is seen that all the membranes retain more than 95% of their weight up to temperature of about 180°C. Pristine PBI membrane was stable up to 400°C which indicates the good thermal stability of the polymer. Degradation of cross-linked structure was observed at around 180°C for all of the cross-linked membranes. The third weight loss at about 400°C is attributed to the degradation of the polymer main chain. From these results, it is concluded that the PBI/BADGE cross-linked membranes are thermally stable enough for HT-PEMFC applications.

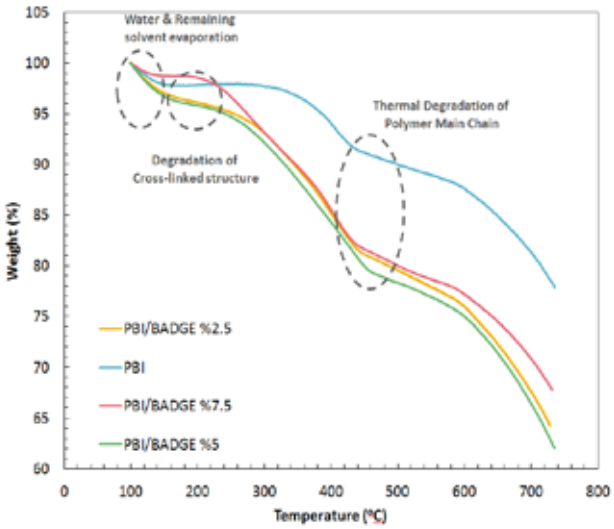


Figure 1. TGA analysis for pristine PBI and PBI/BADGE membranes

Figure 2 shows the FTIR spectra of pristine PBI and cross-linked PBI/BADGE %5 membrane. It is found that two absorption peaks, i.e., ~1230 cm $^{-1}$ due to C-O-C asymmetric stretching and ~2900 cm $^{-1}$ due to C-H stretching [4] which are different from IR spectra of pristine PBI, indicating that the blending of the epoxy in the PBI. However, the 776 cm^{-1} and 834 cm^{-1} due to the epoxide ring asymmetric stretching vibration, which are observed in the IR spectrum of epoxy in literature, do not appear in the IR spectrum of the PBI/BADGE crosslinked membranes, suggesting the opening of the epoxide ring in the PBI/BADGE blend [4].

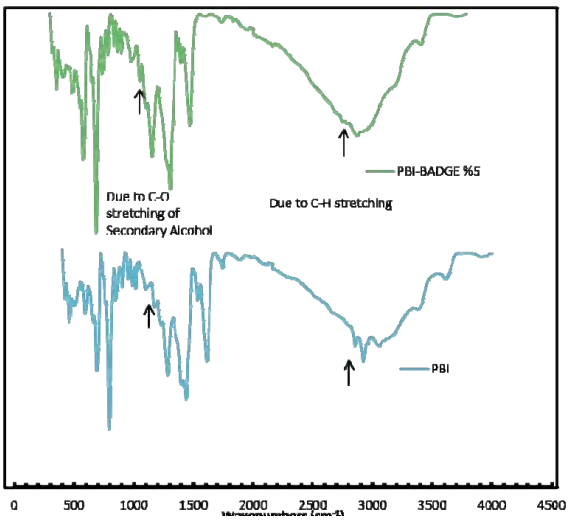


Figure 2. The FTIR spectra of PBI/BADGE %5 membrane (top) and pristine PBI membrane (bottom). Upward arrows indicating; ~1230 cm $^{-1}$ due to C-O-C asymmetric stretching and ~2900 cm $^{-1}$ due to C-H stretching.

Table 1 shows the results obtained from proton conductivity, acid leaching, acid doping and extraction in DMAc tests. It can be seen that proton conductivity values of all membranes increased at elevated temperatures. Lowest acid leaching value was observed with PBI/BADGE %5 membrane whilst it has the highest proton conductivity values among the cross-linked membranes. Extraction ratios of the membranes give information about degree of cross-linking occurred. These results indicate that the most efficient cross-linker ratio was 5 wt.% for BADGE epoxy resin. Acid loss percentage results suggest that as the cross-linking is an effective way to decrease acid loss from the PA doped PBI based membranes. Lower diffusivity of PA into the cross-linked structure leads to a decrease in acid loss percentage. It arguably results in slightly lower proton conductivities as can be seen from Table 1, however it does not pose a significant problem since the proton conduction mechanism is Grotthus mechanism to a large extent and long range mobility of the acid molecules is not crucial in this regard [9].

Table 1. The results of proton conductivity, acid retention, acid doping and extraction in DMAc tests.

Membrane	**Proton Conductivity**			**Acid Loss Percentage (%)**	**Acid Doping Level**	**Extract Ratio (%)**
	140ºC	**165ºC**	**180ºC**			
PBI/BADGE 2.5 %	0.0487	0.0721	0.0970	77.7	14.3	83
PBI/BADGE 5 %	0.0716	0.1146	0.1227	73.4	12.3	90
PBI/BADGE 7.5 %	0.0448	0.0561	0.0686	85.0	10.7	88
PBI	0.0794	0.1030	0.1439	85.2	13.7	0

Figure 3 shows the results of HT-PEMFC tests. Highest HT-PEMFC result was obtained with PBI/BADGE %5 membrane. Second best performing membrane was found as pristine PBI membrane. PBI/BADGE %7.5 membrane performed poorly compared to the other membranes. It showed maximum power density of 0.019 W cm $^{-2}$. The highest maximum power density reached was 0.121 W cm $^{-2}$ with PBI/BADGE %5 membrane. OCV values were

between 0.85-1 V for all the membranes except PBI/BADGE %2.5. Low OCV value by this membrane can be associated with high H_2 crossover rate from the membrane or difficulties with MEA preparation such as pin-hole formation, non-compatibility between the ionomer used and polymer membrane, etc.

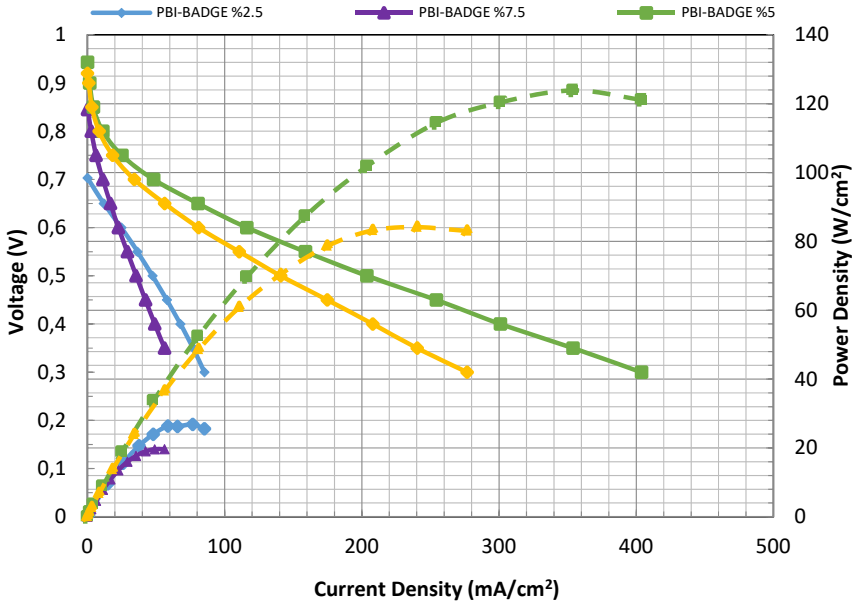


Figure 3. HT-PEMFC test results of pristine PBI and PBI/BADGE cross-linked membranes.

These results suggest that acid leaching has adverse effects on HT-PEMFC performance of PBI based membranes. PBI/BADGE %7.5 membrane was found to be the worst performing membrane in terms of acid leaching and proton conductivity. The influences of low proton conductivity and high acid loss percentage can be observed in these HT-PEMFC test results. Also, highest performance was achieved with PBI/BADGE %5 membrane which also had the lowest acid loss and second highest proton conductivity. The interesting result here is that pristine PBI membrane which showed the highest proton conductivity performed worse than PBI/BADGE %5 membrane which proves the importance of acid leaching from the membranes. In the literature, Lin et al. obtained 0.172 W.cm-2 power density with a PBI/BADGE membrane with higher cross-linker amount [4]. According to the HT-PEMFC tests, it can be concluded that although the power density is not explicitly high, the overall performance of PBI/BADGE %5 membrane was found to be higher than a pristine PBI membrane which gives indications for suitability for medium to high temperature PEMFC applications.

4. Conclusion

In this study, cross-linked PBI membranes were prepared and characterized by TGA, FTIR, proton conductivity, acid leaching, acid doping and extraction in DMAc tests. The objective of this study was to increase HT-PEMFC test performances of PBI membranes by blending BADGE cross-linker. TGA analysis proved that all the membranes have enough thermal stability for the operating temperatures of HT-PEMFCs. FTIR spectra showed the successful introduction of BADGE cross-linker to the PBI matrix. Proton conductivity values of cross-linked membranes were found to be lower than pristine PBI membrane due to the lower diffusivity of PA into the cross-linked structure of the membranes. As for the HT-PEMFC tests, PBI/BADGE %5 membrane was the best performing cross-linked membrane with maximum power density of 0.121 W cm $^{-2}$. Thus, the results of HT-PEMFC tests suggest PBI/BADGE %5 membrane can be suitable for HT-PEMFC applications.

Acknowledgement

This study is supported by The Scientific and Technological Research Council of Turkey (TÜBİTAK), under the research project 1001-214M301.

References

1. Gillham JK. Polymer Structure: Cross-Linking of a Polybenzimidazole. Science (80-) 1963;139.
2. Han M, Zhang G, Liu Z, Wang S, Li M, Zhu J, et al. Cross-linked polybenzimidazole with enhanced stability for high temperature proton exchange membrane fuel cells. J Mater Chem 2011;21:2187. doi:10.1039/c0jm02443k.
3. Noyé P, Li Q, Pan C, Bjerrum NJ. Cross-linked polybenzimidazole membranes for high temperature proton exchange membrane fuel cells with dichloromethyl phosphinic acid as a cross-linker. Polym Adv Technol 2008;19:1270–5. doi:10.1002/pat.1123.
4. Lin H-L, Chou Y-C, Yu TL, Lai S-W. Poly(benzimidazole)-epoxide crosslink membranes for high temperature proton exchange membrane fuel cells. Int J Hydrogen Energy 2012;37:383–92. doi:10.1016/j.ijhydene.2011.09.049.
5. Wang S, Zhang G, Han M, Li H, Zhang Y, Ni J, et al. Novel epoxy-based cross-linked polybenzimidazole for high temperature proton exchange membrane fuel cells. Int J Hydrogen Energy 2011;36:8412–21. doi:10.1016/j.ijhydene.2011.03.147.
6. Maity S, Singha S, Jana T. Low acid leaching PEM for fuel cell based on polybenzimidazole nanocomposites with protic ionic liquid modified silica. Polym (United Kingdom) 2015;66:76–85. doi:10.1016/j.polymer.2015.03.040.
7. Heinzl C, Ossiander T, Gleich S, Scheu C. Transmission electron microscopy study of silica reinforced polybenzimidazole membranes. J Memb Sci 2015;478:65–74. doi:10.1016/j.memsci.2014.12.051.
8. Devrim Y, Devrim H, Eroglu I. Polybenzimidazole/SiO2 hybrid membranes for high temperature proton exchange membrane fuel cells. Int J Hydrogen Energy 2016;41:10044–52. doi:10.1016/j.ijhydene.2016.02.043.
9. Søndergaard T, Cleemann LN, Becker H, Aili D, Steenberg T, Hjuler HA, et al. Long-term durability of HT-PEM fuel cells based on thermally cross-linked polybenzimidazole. J Power Sources 2017;342:570–8. doi:10.1016/j.jpowsour.2016.12.075.

Performance Evaluation of a Photoelectrochemical Hydrogen Production Reactor under Concentrated and Non-Concentrated Light

Yusuf Bicer, Ibrahim Dincer
Clean Energy Research Laboratory, Faculty of Engineering and Applied Science, University of Ontario Institute of Technology, 2000 Simcoe Street North, Oshawa, Ontario L1H 7K4, Canada
Email: yusuf.bicer@uoit.ca, ibrahim.dincer@uoit.ca

Abstract
This work presents the performance analyses of a newly developed photoelectrochemical (PEC) reactor for the production of hydrogen under no-light and concentrated solar radiation. With a newly developed experimental system, the solar light is concentrated about ten times and the spectrum is divided using cold mirrors for better light utilization. The photoelectrochemical reactor is examined at different applied potentials and the hydrogen production quantities are measured. Copper oxide, which is used as a light-sensitive material, is electrochemically coated on the cathode metal plate to increase the rate of hydrogen evolution under illumination. The experiments are conducted to investigate the variation of reactor performance with intensified light conditions and the results obtained are compared with the dark conditions. The present results reveal that the hydrogen evolution rate was 41.34 mg/h for concentrated light measurement and 34.73 mg/h for no-light measurements at 2.5 V applied potential. The corresponding photocurrent generated under concentrated light at 2.5 V is found to be 0.63 mA/cm^2. Under concentrated light, the hydrogen production rates increase considerably showing the positive effect of photocurrent contribution.

Keywords: Hydrogen production; photoelectrochemical process; solar energy; concentrated light; performance.

1. Introduction

As a renewable and abundant supply, solar energy is a prospective sustainable solution to the growing energy demand of the world with an addition of a storage technique. Solar energy is intermittent source with day/night cycles. Therefore, solar energy is desired to be stored in a different form of energy in order to deliver an uninterrupted supply. As a chemical fuel, hydrogen is an encouraging storage medium. Photoelectrochemical hydrogen production is considered a major category under renewable energy based hydrogen production options. Increasing the solar utilization has the capability to enhance the overall efficiency of solar-to-hydrogen. Photochemical water reduction requires the flat-band potential of the semiconductor exceeding the oxidation potential of water of 1.23 V at pH = 0 or 0.82 V at pH = 7. A single band gap device requires, at a minimum, a semiconductor with a 1.6 to 1.7 eV band gap in order to produce the open circuit potential required to split water. When other voltage loss issues are also taken into account, a band gap above 2 eV is usually essential [1]. The utilization of two semiconductor materials stays as an attractive choice for capturing a large share of the solar spectrum, with the two band gaps tuned to absorb corresponding sections of the solar spectrum [1]. Alternatively, using spectrum splitters, the multi-product generation can be increased leading higher overall efficiencies.

Lopes et al. [2] studied a PEC cell for testing different photoelectrodes configurations, appropriate for continuous operation and for easily collect the produced gases. Photocurrent–voltage characteristics were obtained for all samples characterized under three different conditions namely no membrane separating the anode and the cathode evolution; using a Teflon® diaphragm and using a Nafion®212 membrane. The proposed Teflon diaphragm was successfully implemented in the new PEC cell, with around 47% photocurrent density enhancement when transparent WO_3 photoelectrode was used. Minggu et al. [3] expressed in their study that the main requirement for the photocell or photoreactor is to allow maximum light to reach the photoelectrode. They studied an overview of the photoelectrode configurations and the possible photocell and photoreactor design for hydrogen production by PEC water splitting. The ideal design of the photocell and photoreactor is such that the photoelectrode has a maximum exposure to light. Ismail et al. [4] indicated in their review that hydrogen generation from water splitting by UV and visible light-driven photocatalysis has made new advances. A number of synthetic amendment methods for adapting the electronic structure to improve the charge separation in the photocatalyst materials were discussed in that study. The studies concerning the development of new co-catalysts can provide supplementary breakthroughs in obtaining highly efficient photocatalysts. The quantum efficiency of photocatalyst materials upon visible and UV illumination were also reviewed. Acar et al. [5,6] conducted energy, exergy and cost analyses studies for a continuous type hybrid photoelectrochemical hydrogen production system which generates Cl_2 and NaOH as useful commodities in addition to hydrogen. The efficiency of the integrated system is calculated as 4% with annual production of 2.8 kg of hydrogen per square meter of heliostat. The proposed system brings low hydrogen

production cost and zero GHG emissions during operation in addition, the hybrid system has a potential to further lower production costs and rise energy and exergy efficiencies as photoelectrochemical cell technologies develop. Acar et al. [6] also analyzed a continuous type hybrid system thermodynamically for hydrogen manufacture which photoelectrochemically splits water and realizes chloralkali electrolysis. Throughout the night time, the scheme can function fully with electricity and on cloudy days when solar irradiation is not satisfactory, electricity can be applied to help the photoelectrochemical process.

In this study, a photoelectrochemical hydrogen production reactor is built having a large membrane surface area (930 cm^2). The membrane electrode assembly is formed using stainless steel electrodes and Nafion membrane. The cathode plate is deposited with copper oxide (Cu_2O) to form photocathode. An experimental setup consisting of Fresnel lens, cold mirrors, photovoltaics and photoelectrochemical reactor is constructed to test the performance of the reactor under concentrated light. The applied potential is varied from 1.5 V to 2.5 V for no-light and concentrated light measurements.

2. Experimental Study

Photoelectrochemical hydrogen production system consists of mainly a photoelectrochemical reactor, light source, power source and optical tools. The developed PEC reactor shown in Fig. 1 is tested both under actual sun light outside using solar concentrator and optical filters. The utilized pyranometer is silicon-cell pyranometer which is only sensitive to a part of the solar spectrum, approximately 350-1100 nm. This range of spectrum represents around 80% of total shortwave radiation. But, silicon-cell pyranometers are calibrated to estimate total shortwave radiation across the entire solar spectrum. A cold mirror is an optical device that reflects certain part of the electromagnetic spectrum and lets other part go through it. The cold mirrors used in the experiments are positioned at 45º to be able to reflect 95% of the spectrum with a wavelength of 400 to 690 nm and transmit 90% of the spectrum with a wavelength of 700 to 1150 nm [7]. In total, six cold mirrors are utilized forming a rectangular area of 769.62 cm^2 in order to increase the illuminated area on the PEC cell as depicted in Fig. 1.



Fig. 1. The photoelectrochemical reactor, cold mirrors and Fresnel lens in the experimental setup

The Nafion membrane is used where the anode surface is iridium ruthenium oxide and the cathode is platinum black (PtB). Both catalysts have a density of 3 mg/cm^2. Iridium-ruthenium oxide ($IrRuO_x$) is the anode electro-catalyst of the membrane which is known for fast kinetics and the electro-catalyst loading. A membrane electrode assembly is built with stainless steel anode and cathode plates. The cathode plate is electrochemically deposited with copper oxide photosensitive material enhancing the hydrogen evolution as photocathode. Photoelectrochemical (PEC) hydrogen generation system in this study comprises of primarily a photoelectrochemical cell with a membrane electrode assembly, light source (concentrated), electricity supply and optical tools such as Fresnel lens and spectrum splitting mirrors as illustrated in Fig. 1. After the Fresnel lens, the light is split using spectrum splitting cold mirrors. The higher wavelength spectrum is used for photovoltaics and lower wavelength spectrum is used for PEC cell to increase the solar energy utilization.

3. Results and Discussion

The solar light intensity hitting on the PEC cell is one of the critical parameters affecting the overall performance. Hence, the irradiance values are recorded for each test. The ambient irradiance is between 960 to 990 W/m^2 during the applied potentials of 1.5 V to 2.5 V. The reported irradiances are the average values. Based on the illuminated areas, the total energy rates on the PEC cell were calculated which ranged between 168 W and 228 W. The total

current through the PEC cell and generated hydrogen mass flow rates at 1.5 V applied voltage are comparatively shown in Fig. 2.

Table 1. Irradiance measurements on the PEC cell and ambient during EIS experiments

Parameter	**Irradiance (W/m^2)**				
Applied Voltage	***1.5 V***	***1.7 V***	***1.9 V***	***2 V***	***2.5 V***
Ambient	989	979	980	981	961
PEC Reactor (Concentrated area: 351 cm^2)	5628	4681	5656	5829	5684
PEC Reactor (Non-concentrated area:1054 cm^2)	210	203	205	220	210
Solar Power on PEC Reactor (W)	220	186	220	228	222

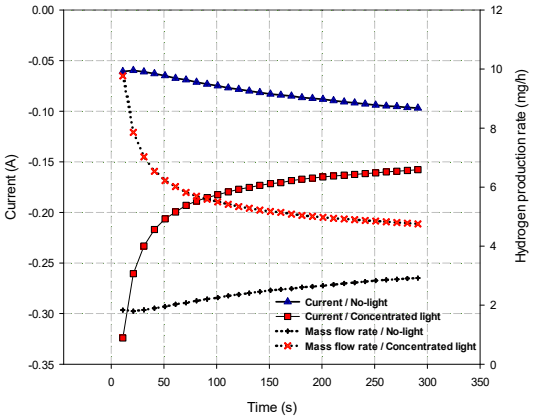


Fig. 2. Comparison of hydrogen production rate and current in the PEC reactor at 1.5 V applied potential under concentrated light and no-light

It is seen that there is significant photocurrent generation. Since there is photocathode for hydrogen production, negative potential is applied yielding a negative sign in the current. The average photocurrent during the experiment is calculated as 0.31 mA/cm^2. The average hydrogen production rate is 2.44 mg/h and 5.77 mg/h for no-light and concentrated light measurements, respectively. The hydrogen production rate increases more than 100% under concentrated light. The total current through the PEC cell and generated hydrogen mass flow rates at 1.7 V applied voltage are comparatively shown in Fig. 3. The hydrogen production rate for the concentrated light is about 7.75 mg/h whereas it is about 4.47 mg/h at no-light on average. The average photocurrent generated under concentrated light increases to 0.31 mA/cm^2. Although the average photocurrent is almost constant for 1.7 V applied voltage, the hydrogen production rate is higher because of externally supplied current.

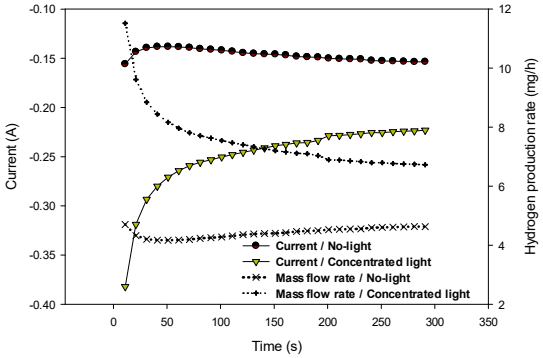


Fig. 3. Comparison of hydrogen production rate and current in the PEC reactor at 1.7 V applied potential under concentrated light and no-light

The generated hydrogen mass flow rates and total current through the PEC cell at 1.9 V applied voltage are comparatively shown in Fig. 4. Higher applied voltage yields higher total current and hydrogen production rates. On average, the hydrogen evolution rate is 10.95 mg/h for concentrated light measurement and 9.1 mg/h for no-light measurement. The average photocurrent generated under concentrated light at 1.9 V is found to be 0.18 mA/cm^2. However, the effect of photocurrent decreased in this case although the total hydrogen evolution rate increased. The total current through the PEC cell and generated hydrogen mass flow rates at 2 V applied voltage are comparatively shown in Fig. 5.

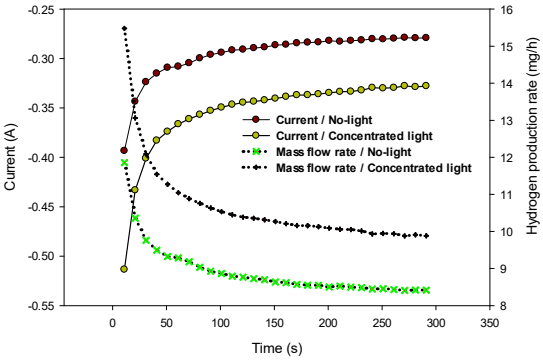


Fig. 4. Comparison of hydrogen production rate and current in the PEC reactor at 1.9 V applied potential under concentrated light and no-light

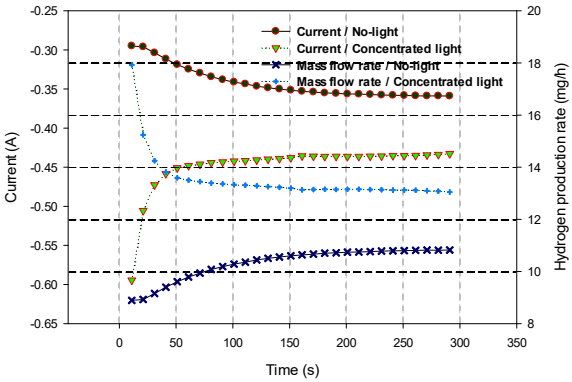


Fig. 5. Comparison of hydrogen production rate and current in the PEC reactor at 2 V applied potential under concentrated light and no-light

On average, the hydrogen evolution rate is 13.88 mg/h for concentrated light measurement and 10.4 mg/h for no-light measurement. The average photocurrent generated under concentrated light at 2 V is found to be 0.33 mA/cm^2. The total current through the PEC cell and generated hydrogen mass flow rates at 2.5 V applied voltage are comparatively shown in Fig. 6. On average, the hydrogen evolution rate is 41.34 mg/h for concentrated light measurement and 34.73 mg/h for no-light measurement. The contribution of photocurrent to the hydrogen production is about 6.5 mg/h. The average photocurrent generated under concentrated light at 2.5 V is found to be 0.63 mA/cm^2. It is important to note that although there are higher photocurrents during the test, the values reported here represent the average.

The photoelectrochemical cell having Cu_2O coated cathode plate is tested for photoelectrochemical characterization for hydrogen production at 1.7 V to 2.5 V applied potentials as shown in Fig. 7. The hydrogen evolution rate improves by rising voltage however in general the effect of photocurrent decreases except some cases. There are some variations in the photocurrent generations caused by the non-stability of the solar light.

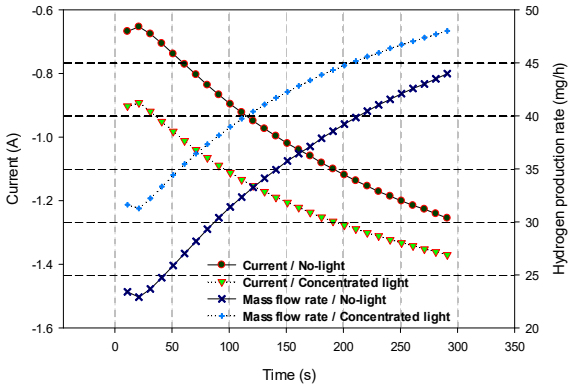


Fig. 6. Comparison of hydrogen production rate and current in the PEC reactor at 2.5 V applied potential under concentrated light and no-light

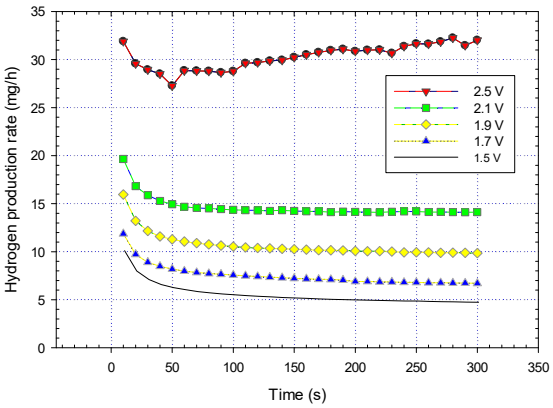


Fig. 7. The comparison of hydrogen evolution rates at different applied potentials under concentrated light in the integrated system

In addition, the change of sun position during the experiments cannot be compensated since the setup is manually tracking the sun light. The accumulated charges during the hydrogen production experiment at 1.7 V are calculated to be 89.9 C and 108.1 C, respectively for concentrated light and non-concentrated light. Overall, under concentrated light, the hydrogen production rates increase considerably showing the effect of photocurrent contribution. Further studies for the tandem-semiconductors to increase the photo-absorption are under investigation.

4. Conclusions

In this study, a photoelectrochemical hydrogen production reactor is built and tested under concentrated and split spectrum at different applied potentials to investigate the contribution of photogenerated current. Maximum utilization of solar energy plays an important role in the photo-conversion processes. The spectrum of solar light can be concentrated and separated for various applications to improve the overall system performance for solar energy conversion processes. In this way, multiple products such as electricity, fuels, heating and cooling can be produced within the same system. The generated photocurrent at 1. 7 V is measured as 0.31 mA/cm^2 corresponding to a total hydrogen production rate of 7.75 mg/h under concentrated illumination. The activation resistance declines as the applied voltage increases. This is explained as the reaction necessities a definite amount of energy to drive it. Hence, in low voltages, if small amount of electrons is present, a larger resistance is available for driving the reaction. The concentrated irradiance levels range between 4681 W/m^2 to 5829 W/m^2 although the spectrum is divided and only lower wavelengths (<700 nm) are directed to photoelectrochemical reactor.

Acknowledgement

The authors acknowledge the support provided by the Natural Sciences and Engineering Research Council of Canada.

Nomenclature

e	Charge of an electron (1.60217657 × 10^{19} C)
I	Irradiance (W/m^2)
J	Current density (mA/cm^2)
$\dot{m}$	Mass flow rate (mg/h)
R	Reflectance
$\mathcal{T}$	Transmittance
T	Temperature (°C or K)

Greek Letters

η	Efficiency
λ	Wavelength

Acronyms

CPV Concentrated photovoltaic
GHG Greenhouse gas emission
IPCE Incident photon to charge carrier efficiency
NOCT Nominal operating cell temperature
PEC Photoelectrochemical
PV Photovoltaic
RHE Reversible hydrogen electrode
STH Solar-to-hydrogen
UV Ultraviolet

References

1. Weber MF, Dignam MJ. Efficiency of Splitting Water with Semiconducting Photoelectrodes. J Electrochem Soc. 1984;131(6):1258–65.
2. Lopes T, Dias P, Andrade L, Mendes A. An innovative photoelectrochemical lab device for solar water splitting. Sol Energy Mater Sol Cells. 2014;128:399–410.
3. Minggu LJ, Wan Daud WR, Kassim MB. An overview of photocells and photoreactors for photoelectrochemical water splitting. Int J Hydrogen Energy. 2010;35(11):5233–44.
4. Ismail AA, Bahnemann DW. Photochemical splitting of water for hydrogen production by photocatalysis: A review. Sol Energy Mater Sol Cells. 2014;128:85–101.
5. Acar C, Dincer I. Experimental investigation and analysis of a hybrid photoelectrochemical hydrogen production system. Int J Hydrogen Energy. 2017;42(4):2504–11.
6. Acar C, Ghosh S, Dincer I, Zamfirescu C. Evaluation of a new continuous type hybrid photo-electrochemical system. Int J Hydrogen Energy. 2015;40(34):11112–24.
7. High Performance Cold Mirrors - Edmund Optics Inc. [cited 2017 Jan 16]. Available from: http://www.edmundoptics.com/optics/optical-mirrors/hot-cold-mirrors/high-performance-cold-mirrors/3149/

ORAL PROCEEDINGS

Cost Analysis of Storage and Distribution Processes of Hydrogen Delivery Scenarios

Murat Emre Demir[1] and Ibrahim Dincer[1,2]
[1]Clean Energy Research Laboratory, Faculty of Engineering and Applied Science, University of Ontario Institute of Technology, 2000 Simcoe Street North, Oshawa, Ontario L1H 7K4, Canada
[2]Faculty of Mechanical Engineering, Yildiz Technical University, Besiktas, Istanbul, Turkey
Emails: murat.demir@uoit.ca, ibrahim.dincer@uoit.ca

Abstract
In this study, performance and cost assessment studies, including the stages of hydrogen storage and distribution, of three different hydrogen delivery scenarios are undertaken comparatively. The produced hydrogen is stored under different temperatures and pressures and then transported to the nearby cities for distribution. Three different scenarios are examined for the process of transport of the produced hydrogen to the distribution centers. Transportation for hydrogen by the pressurized tanks, cryogenic liquid hydrogen tanker and the gas pipelines are selected for the studies under the considered scenarios. Moreover, the transmission options from the distribution center to the target consumer are also examined for three different conditions. As a result, the hydrogen production capacity, the levelized cost of energy distribution (in $/kg), the infrastructure costs (truck, tanker number, gas line costs, etc.) for the selected transmission scenario are calculated. Additionally, the environmental impact (greenhouse gas (GHG) emissions) and the design parameters of the proposed system (e.g., number of hydrogen fuel stations and the distance between these stations, the length of the distribution lines, etc.) are determined The highest levelized cost of delivery is obtained as 8.02 $/kg H_2 for the first scenario whereas the lowest cost is obtained as 2.73 $/kg H_2 for third scenario.

Keywords: Hydrogen production; hydrogen storage systems; hydrogen distribution systems; cost analysis.

1. Introduction

Hydrogen is treated as one of the cleanest energy carriers and potentially chemical feedstock for sectoral, including industrial, applications. Nonexistence of the carbon emission throughout the energy production processes in contrast of the conventional fossil fuels makes them viable and environmentally friendly choice. Hydrogen is the lightest element in the periodic table with a very low density per unit volume. It has nearly 14 times less density than the air. Hydrogen is a colorless, unscented, tasteless, and nontoxic gas, under most conditions and changes its phase from gas to liquid state at -252.9^{o}C under 1 atm pressure. Furthermore, hydrogen is highly diffusive in the surrounding air where it diffuses in the atmosphere rapidly and is able to leak through tiny gaps. All these properties of hydrogen lead storage and transmission problem [1].

Regarding to hydrogen usage in fuel cells, the delivery process of hydrogen can be classified under two main categories, depending on transportation processes which includes transmission and distribution of hydrogen from through designated places; or it could categorized regarding the fueling operations, involving the transfer of H_2 into the final unloading device as an liquid onsite storage tank or compressed gas hydrogen storage tubes. Hydrogen delivery processes from a centralized H_2 production plant requires both transportation and fueling processes. Three main transportation options are illustrated in Figure 1a-c. In those methods, hydrogen is transported in combinations of transmission by liquid tanker, which carries liquefied hydrogen under cryogenic conditions, compressed hydrogen gas transmission by tube trailers or distribution by pipelines. Also, a novel approach to the H_2 delivery is illustratively presented in Figure 1d, which proposes to the transportation of the H_2 after employing a chemical reaction or physical adsorption with a material. This kind of transportation pathway option is still in research and development [2].

Optimizing the transportation process of H_2 regarding the parameters as cost effectiveness, environmentally benign and easy to operate is very important for the stakeholders. Thus, there have been many past studies which have focused on transportation storage of H_2 by several researchers [3–12]. Yang and Ogden [7] developed models in order to obtain delivery distances and to predict transport costs, possible emissions and usage of energy from several sections of the delivery chain. Simbeck and Chang [11] developed an infrastructure cost modules for producing, handling, distributing, and dispensing hydrogen from a centralized production facility and fueling station on-site facility for fuel cell automobile applications. Also, cost estimation of novel technologies on hydrogen storage and delivery are attracting the attention of the researchers. Moroz et al. [8], investigated the potential applications of the metal hydride based H_2 storage-delivery systems and made their technical and economic comparison to conventional compressed gas H_2 storage and delivery.

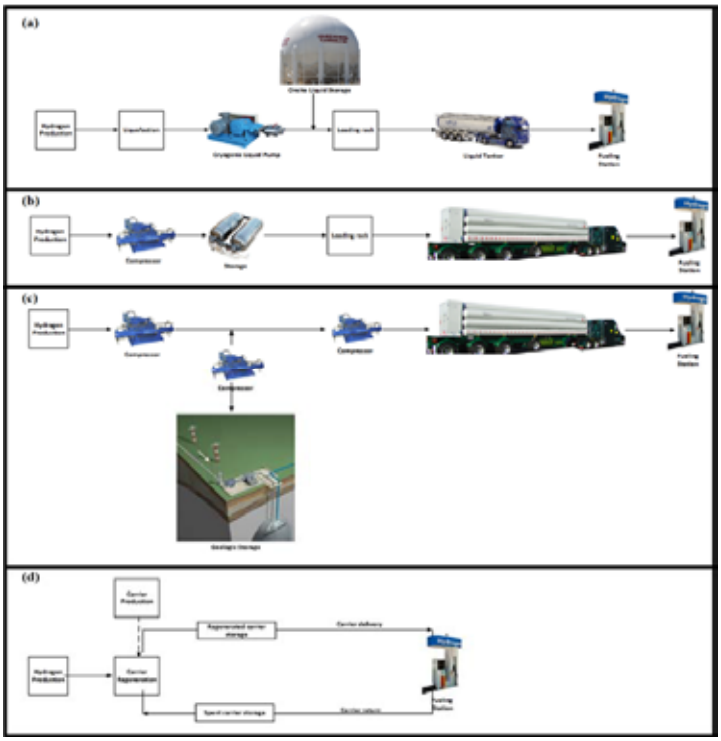


Figure 1. The main Hydrogen delivery pathways

2. System Description

In this study, an economic analysis of three different hydrogen delivery scenarios is performed with H2A Delivery Components Model [13] which is developed by the U.S. DOE Hydrogen and Fuel Cells Program. All pathways of the three scenarios are illustrated in Figure 2, Figure 3 and Figure 4. In the first scenario, hydrogen is produced in the production plant located in a rural region, and then it is compressed until it reaches to pipeline pressure and fed into a transmission pipeline. The pipeline delivers liquefied hydrogen to a liquefier where the hydrogen changes its phase from gaseous to the liquid state. Liquefied hydrogen is stored in transshipment point (onsite liquid hydrogen storage) which is placed close to the city gate. Hydrogen is loaded from the liquid depot to cryogenic liquid hydrogen tanker trucks and distributed to fueling stations all over the city.

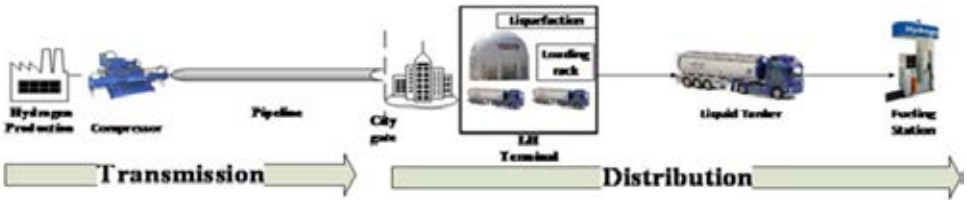


Figure 2. Hydrogen delivery pathways of Scenario 1

In the second scenario, hydrogen is compressed into a cavern, which supplies geologic storage for the possible plant outages. Then, the same compressor extracts H_2 from the geologic storage and push it into the pipeline, which delivers H_2 to the gaseous hydrogen terminal, which is located adjacent to the hydrogen production facility. Pressurized tube-trailer trucks take the hydrogen from the terminal and distribute to fuel stations. Transmission process of the third scenario is quite similar to the first scenario.

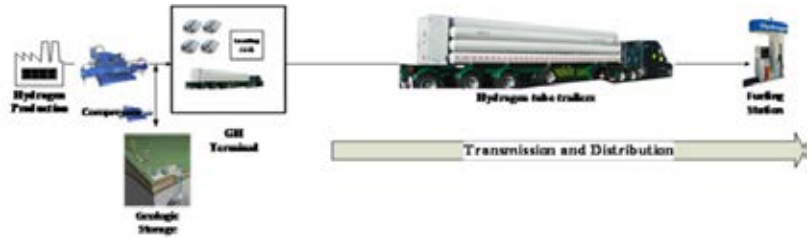


Figure 3. Hydrogen delivery pathways of Scenario 2

In the third scenario, different from the second scenario, transmission pipeline feeds the distribution pipeline system. Average terminal demand of hydrogen is set 4,372 kg/day for the first 2 scenarios and 80,000 for the last scenario to compare large scale and small-scale systems.

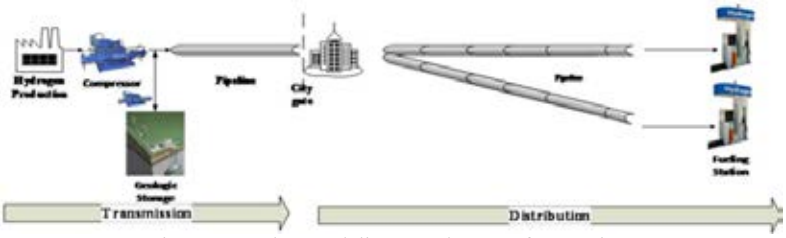


Figure 4. Hydrogen delivery pathways of Scenario 3

Scenario 1

The main design parameters of the first scenario is tabulated in Table 1. Majority of design parameters and economic assumptions of all scenarios are based on the default data in the H2A Delivery Component Model Program [13].

Table 1. Design Parameters of Scenario 1

Transmission pipeline		**Delivery Liquid Trucks**	
Design Parameters	**Value**	**Design Parameters**	**Value**
Average Hydrogen Flowrate Out (kg/day)	4,518	Tank Water Volume (m3)	65.0
Transmission Pipeline Inlet Pressure (kPa)	6.895	Tanker Useable Delivery Capacity (%)	95%
Desired Transmission Pipeline Outlet Pressure (kPa)	4.826	Round-Trip Distance (km)	100
Transmission Pipeline Temperature (°C)	25	Average Truck Gas Mileage (km/L)	2.6
Transmission Pipeline Length (km)	100	Number of Stations Served	4
Terminal		Total Time to Load Truck (hours)	3.0
Design Parameters	**Value**	Total Time to Unload Truck at each Station (hours)	3.5
Average Terminal Demand (kg/day)	4.372	Average Truck Speed (km/hour)	58.0
Liquid Pump Isentropic Efficiency (%)	75	**Refueling Station**	
Hydrogen Loss During Liquefaction (%)	0.5	Average Daily Capacity of Hydrogen Refueling Station (kg/day)	1093
Useable Percent of Liquid Storage Unit (%)	90	Mechanism of Dispensing from Liquid Hydrogen	Dispense as gas
Liquid Hydrogen Truck Loading Losses (%)	0.5	Liquid Hydrogen Delivery Pressure (atm)	2
Boil-off (%/day)	0.25	Recovery Compressor Outlet Pressure (atm)	442
Surge: % Above the System Average Demand	10	Compressed Gas Storage Temperature (°C)	25
Number of Days of Surge	120	Storage Tank Useable Capacity (%)	95%
Number of Days of Winter Demand Lag	120	Cryogenic Pump Boil-Off (% average daily demand)	2%

All scenario analyses start after the first compression of hydrogen at the exit of hydrogen production plant. First compressors are assumed in a part of the production plant and are not included in scenarios. In scenario 1, 4,518 kg hydrogen is supplied from the production plant at 6.9 MPa pressure to the to the transmission pipeline daily. The plant is located 100 km away from the city gate. A small portion of the

hydrogen is lost during the transmission process at the rate of 1.252 (kg/km year) which is assumed based on the losses from U.S. natural gas pipeline infrastructure. An onsite liquid hydrogen storage facility is placed near to the provincial border of the city which consists, a liquefaction system, cryogenic liquid hydrogen pumps and liquid hydrogen storage system to compensate possible hydrogen production plant outages and peak loads. During the storage of liquid hydrogen, a small portion of it will boil off and be expelled through a valve and some of the liquid hydrogen is lost during the loading process to the trailers. The liquefier is sized to compensate those losses corresponded in Table 1. Yearly hydrogen demand is not stable. Surge percentage above the system average presents the maximum demand of the hydrogen. In this scenario, peak demand is assumed to be 10% higher than the system average. The number of days of surge indicates the maximum number of days of the peak surge in a year. The storage is used during this period [14]. After the liquefaction, hydrogen is loaded onto trucks and distributed the designated refueling stations. The liquid hydrogen is pumped to the delivery pressure at the refueling station, and vaporized before being stored here. In this scenario, it is assumed that a truck serves four stations per day with a round trip route by 100 km.

The economic assumptions of the first scenario is given in Table 2. It is assumed that Scenario 1 starts up in 2017 and analysis is carried over for 20 years. All the particular components of the system endure for 5 to 20 years without needing a replacement. The model utilizes the Modified Accelerated Cost Recovery System (MACRS) to calculate the system components depreciation [15].

Table 2. Economic Assumptions of Scenario 1

Economic Assumptions	**Value**
Assumed start-up year	2017
Analysis period (years)	20
Liquefier, LH_2 Pump, LH_2 Storage, Pipeline, Terminal, MACRS Depreciation Schedule Length (years)	15
Refueling station MACRS Depreciation Schedule (years)	7
Tractor and Tank Trailer MACRS Depreciation Schedule Length (years)	5
Liquefier, LH_2 Pump, LH_2 Storage, Terminal, Refuel Station (except dispensers), Tank trailers Lifetime (years)	20
Pipeline Lifetime (years)	15
Dispenser Lifetime (years)	10
Tractor Lifetime (years)	5
Analysis period (years)	20
Inflation Rate (%)	1.9%
Total Tax Rate (%)	38.9%
Unit installed cost of piping, LH_2 ($/m)	1650

Table 3. Design Parameters of Scenario 2

Geologic Terminal			
Design Parameters		**Value**	
Average Terminal Demand (kg/day)		4372	
Cavern Maximum Pressure (atm)		125	
Cavern Minimum Pressure (atm)		20	
Cavern Temperature (°C)		10	
Pressure of Hydrogen Delivered to Terminal (atm)		20	
Tube Maximum Operating Pressure (atm)		480	
Surge: % Above the System Average Demand		10	
Number of Days of Surge		120	
Number of Days of Winter Demand Lag		120	
Tube Trailer Delivery		**Refueling Station**	
Design Parameters	**Value**	**Design Parameters**	**Value**
Tube Maximum Operating Pressure (atm)	480	Vehicle Maximum Pressure (bar)	350
Tube Minimum Pressure (atm)	15	Dispensing Components	Booster Compressor
Number of Tubes	10	Average Daily Capacity of Hydrogen Refueling Station (kg/day)	1093
Tube Water Volume (m3)	2.99	Number of fueling stations	4
Round-Trip Distance (km)	100	Number of Dispensers for Per Station	6
Average Station Hydrogen Demand (kg/day)	1,093	Hydrogen Temperature at the Station (°C)	25
Average Truck Speed (km/hour)	58	Number of Installed Compressors	3

Scenario 2

The main design parameters of the second scenario are presented in Table 3. Yearly overall hydrogen delivery of the first and second scenarios are kept constant to see the influence of the liquefaction of the hydrogen on delivery process. A geologic storage facility (cavern) is collocated with the hydrogen production plant in this scenario. As the geological storage is set as the underground cavern, the temperature of it is below ambient conditions. In the model, the pressure of the H_2 delivered to the Terminal is selected as 20 atm, which is also the outlet pressure of the hydrogen production plant. Hydrogen is compressed after the terminal, and its pressure reaches up to 480 atm at the H_2 tube. Three compressors are installed for loading process of H_2 to the trailers. Throughout all compression processes in the system, 0.5% of the H_2 is lost.

In order to maximize the usage of the tractor, it is assumed that a single truck can visit multiple refueling stations as the trailers are assumed to be left at a forecourt station and used as onsite storage. A single truck will be carrying several trailers around to the stations that it will serve [14]. In this scenario, it is assumed that each tractor is moving with 10 tubes when it leaves the terminal and serving four stations per day. The economic assumptions of the second scenario is similar with the first one. Majority of the system components have 20 year lifetime. The financial analysis assumptions of the second scenario are listed in Table 4.

Table 4. Economic Assumptions of Scenario 2

Economic Assumptions	**Value**
Assumed start-up year	2017
Compressor, Cavern.GH_2 Storage, Terminal MACRS Depreciation Schedule Length (years)	15
Refueling station dispenser MACRS Depreciation Schedule (years)	7
Tractor and Tank Trailer MACRS Depreciation Schedule Length (years)	5
Remainder of Terminal MACRS Depreciation Schedule (years)	15
Terminal Compressor, Cavern, GH_2 Storage, Truck Trailer Lifetime (years)	20
Tractor Lifetime (years)	5
Trailer Lifetime (years)	20
Analysis period (years)	20
Inflation Rate (%)	1.9%
Total Tax Rate (%)	38.9%

Scenario 3

Design parameters of the third scenario are tabulated in Table 5. Scenario 3 assumed to be the delivery pathway for a large-scale hydrogen production facility. The second and the third scenarios have the similar transmission period, but the infrastructure of the third scenarios transmission pipeline is designed to deliver hydrogen almost 20 times higher than the second scenario. The pipeline network is containing the main transmission pipe with two branches of the trunk pipeline. The trunk pipelines are located at the city gate and also are divided into many branches called distribution pipelines to supply the hydrogen to the forecourt stations. In this scenario, 60 distribution pipelines are installed to serve 80 refueling stations.

The same approach is applied for the assumptions of the financial analysis. All scenarios starts in 2017 and analysis lasts for 20 years. Tax rates and MACRS depreciation schedule lengths are kept identical for all scenarios. The economic assumptions of Scenario 3 are listed in Table 6.

Beside the design inputs listed above, Land and operation and maintenance costs are also taken into account in this study. All the terminals are installed in a suburban area, hence cost analysis is conducted based on city gate land costs. Produced CO_2 emissions throughout the pathways are also taken into account in the scope of study. The model utilizes the physical property of feedstocks and environmental data from Greenhouse Gas, Regulated Emissions and Energy Use in Transportation (GREET) model, developed by Argonne National Laboratory [16].

Table 5. Design Parameters of Scenario 3

Pure Pipeline Geologic Storage System Design Inputs		**Transmission, Trunk and Distribution Pipelines**	
Design Input	**Value**	**Design Input**	**Value**
Average Terminal Demand (kg/day)	80,000	Transmission Pipeline Inlet Pressure (psia)	1,000
Cavern Maximum Pressure (atm)	125	Pipeline Temperature (°C)	25
Cavern Minimum Pressure (atm)	20	Transmission Pipeline Length (km)	100
Cavern Temperature (°C)	10	Trunk Pipeline Inlet Pressure (psia)	600
Pipeline Pressure (atm)	65	Number of Trunk Pipelines	2
Hydrogen Temperature at Terminal (°C)	25	Length of Single Trunk Pipeline (km)	112.6
Refueling Station		Transmission Pipeline Inlet Pressure (psia)	1,000
Design Input	**Value**	Trunk Pipeline Inlet Pressure (psia)	600
Average Daily Capacity of Hydrogen Refueling Station (kg/day)	1000	Distribution Pipeline Location	In City
Number of Refueling Station	80	Distribution Pipeline Inlet Pressure (psia)	400
Pressure of Hydrogen Delivered to Refueling Station (atm)	20	Number of Distribution Pipelines	60
Number of Dispensers per Station	2	Trunk Pipeline Inlet Pressure (psia)	600
Maximum Low Pressure Storage Pressure (atm)	172		
Minimum Low Pressure Storage Pressure (atm)	15		

Table 6. Economic Assumptions of Scenario 3

Economic Assumptions	**Value**
Assumed start-up year	2017
Real After-tax Internal Rate of Return (%)	10.0%
Terminal, Cavern, Pipeline MACRS Depreciation Schedule Length (years)	15
Refueling station MACRS Depreciation Schedule (except compressors) (years)	7
RS compressors MACRS Depreciation Schedule (except compressors) (years)	5
Terminal Compressors, Cavern, Pipeline Lifetime (years)	20
Dispenser, and RS compressor Lifetime (years)	10
Remainder of Refueling station (years)	20
Analysis period (years)	20
Inflation Rate (%)	1.9%
Total Tax Rate (%)	38.9%

3. Results and Discussions

The analyses are conducted using H2A Delivery Components Model Version 2.0 in order to determine the infrastructural characteristics of the scenarios. Delivered hydrogen per year, levelized cost of the system components and their overall contribution to the delivered cost of hydrogen, operation and maintenance cost of the scenarios, the CO_2 emission by the components and their contribution to the overall emissions, the required land for the installation and lastly, the capital investment costs are obtained as the main results.

The model extrapolates the technology and costs based on the values in 2005. Yearly overall hydrogen deliveries by the pathway options are presented in Figure 5. As expected, Scenario 3 has the highest amount of delivery as it fed by a large plant. Annually, 29,200 tons hydrogen is carried by the pipelines in the third scenario, and it is followed by the first and second scenarios with 1,596 tons/kg delivery. However, Scenario 3 has the largest leakage ratio among the scenarios. Over 84 tons hydrogen is lost through the pipeline network per year.

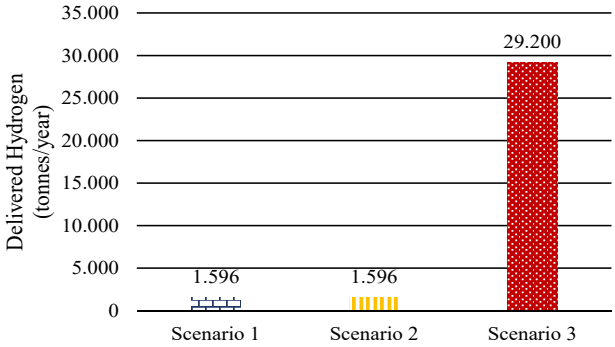


Figure 5. Annual hydrogen deliveries of the scenarios.

The land required for the construction of the systems elements and their shares over the overall terrain need is demonstrated in Figure 6. In this comparison, the third scenario is not included since the model does not provide the required land calculations for the terminal of the entire pipeline delivery pathways. Even though both scenarios take almost same space regarding their terminals, refueling stations distinguish their required lands slightly. For both scenarios, terminals have the largest portion of the land requirement. In Scenario 1, liquefier; and In Scenario 2 the truck loading compressors covers an area of 8,167 and 10,000 m^2 respectively, which results in relatively higher land necessity by the terminals.

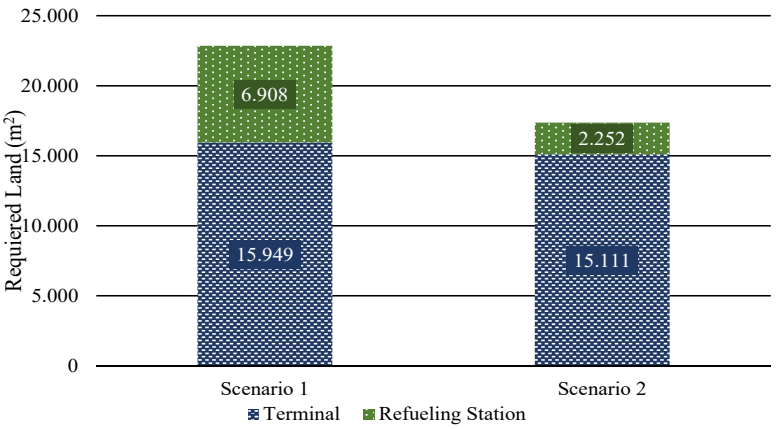


Figure 6. Land requirements of the scenarios.

The overall operation and maintenance (O&M) costs of the scenarios and the contribution of the delivery system elements are individually presented in Figure 7. Since Scenario 3 has considerably higher hydrogen delivery rate than the Scenario 1 and Scenario 2, it also possesses the largest expenses during the operation of the system. 80 forecourt station of the third scenario consists the primary expense item for the delivery pathway. Overall electricity cost has the highest share of the O&M costs of the third scenario`s refueling stations. Compressors are the primary energy consumer for these stations. Considering the first scenario, the terminal contributes the O&M expenses most. Liquefiers causes around 50% of the terminal`s O&M expenditures due to large electric consumption of these devices. Permits, licensing, insurance and taxes also have a significant importance on annual operation and maintenance costs. Overall $9M is paid annually for these costs in Scenario 3. Overhead and General and Administrative (G&A) expenses are also taken into account for the operation and maintenance costs calculations. General and Administrative expenses refer to expenditures related to the daily operations of the facilities. These costs are calculated based on total labor cost. Also the expenses due to rental places like forecourt stations are considered during the calculations of O&M costs

In order to determine the environmental effects of the scenarios, onsite and upstream CO_2 emissions are also determined in this study. All the emission results are obtained by using GREET data and presented in Figure 8. Figure 8 indicates the generated CO_2 emission through the delivery process by the system per energy released from utilization of H_2. High energy requirement with low efficiency causes significantly large CO_2 emissions by the liquefier. Since, only the third delivery pathway include the liquefier, it produces the highest amount of CO_2 per delivered hydrogen energy. Compressors and the trucks are the other main sources of the emissions. Pure pipeline transmission appears to be the most environmentally friendly transmission option among all the pathways. It only emits 28 g CO_2 per MJ hydrogen energy that is 382 and 26 times less than the first and second delivery pathways.

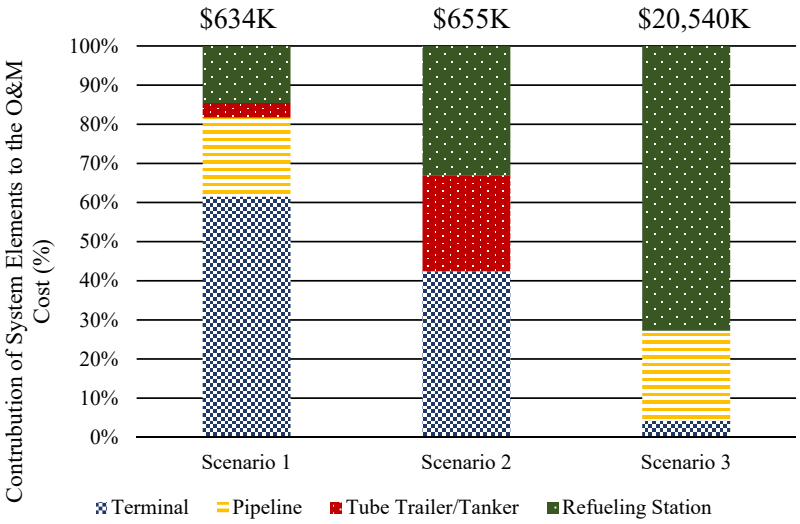


Figure 7. Operation and maintenance costs of the scenarios.

The present value of scenario component`s capital investment and their contribution to the overall system values are shown in Figure 9. The largest capital investment is needed by the third scenario, as it consists 80 refueling stations where the first two scenarios serve only four stations. Almost $200M present value of capital investment is required for only the refueling stations, which is around $2.5M per station. Lands of refueling station are assumed to be rented. Otherwise, capital investment cost of the third scenario would have been increased significantly. Also it can be implemented from the Figure 9 that, infrastructure of the pipeline system requires the higher investment money compare to the tube trailer and tanker delivery. When the equivalent systems regarding the hydrogen delivery capacity (Scenario 1 and Scenario 2) are compared, it can be seen that, the model with pipeline structure has higher investment costs. Over $20M investment is needed to build transmission pipes of the first scenario where this value is 7 times less for the second scenarios for both transmission and delivery processes ($2.98M). In Scenario 1 the terminal costs slightly more than half of the overall capital cost. The main reason of this situation is the high prices of liquefaction systems. $29.5M terminal capital cost consists of $22M of the liquefaction expenses. On the other hand, terminal cost of the second scenario is the least among all scenarios. The compressors of the cavern cost $1.6 M, which is quiet inexpensive compared to the liquefier.

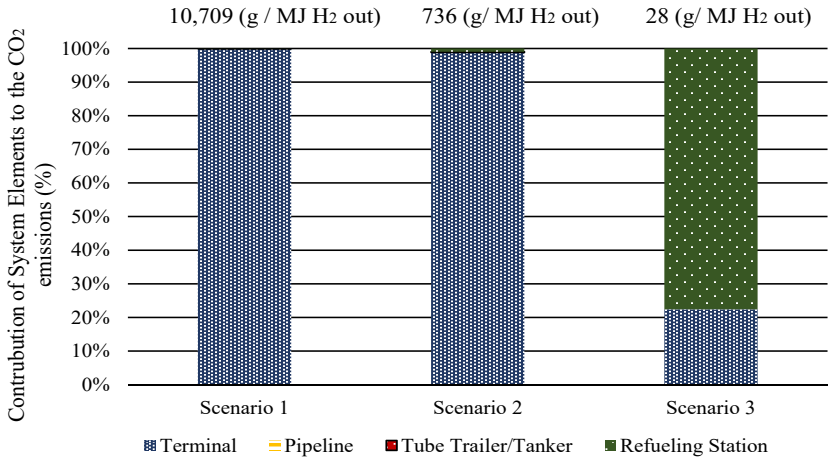


Figure 8. Produced CO_2 emissions of the scenarios.

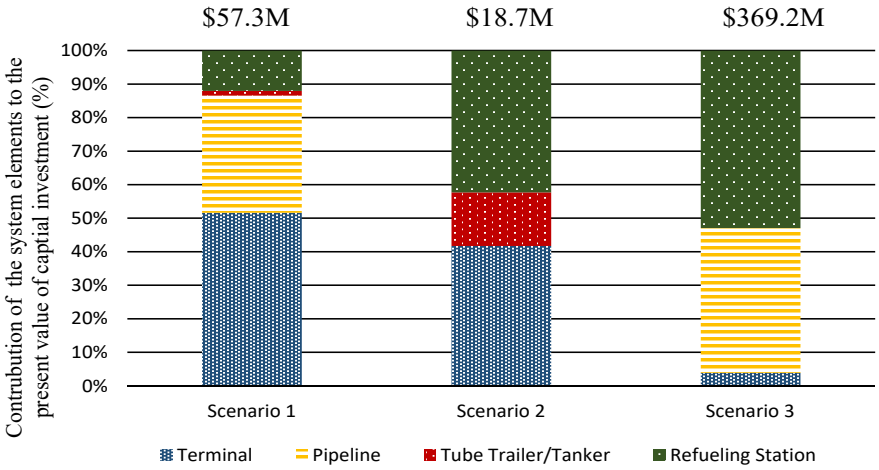


Figure 9. The present value of the systems' capital investment.

Finally, the levelized delivered hydrogen costs in \$/kg H_2 of the system components and their contribution to the overall costs are presented in Figure 10. The first scenario has the highest levelized costs with 8.02 \$/kg H_2, and it is followed by the second and third scenarios with a levelized delivered hydrogen costs of 2.86 \$/kg H_2 and 2.73 \$/kg H_2 respectively. In Figure 10, it appears that hydrogen delivery in liquid state is not economical with the current technology due to high liquefaction costs. Also for the small-scale delivery pathways, pipeline delivery is an expensive option as it is compared to the truck delivery. High construction costs of pipeline infrastructure is not convenient for hydrogen production from a small plant. In contrast, pure pipeline delivery pathways appears to be a decent economical way for carrying hydrogen. As the capacity of the hydrogen delivery increases, the share of pipeline costs decreases as well. Even though Scenario 1 only uses the pipeline delivery from the outside of the city to the city gate (transmission process), it has more cost share over the levelized hydrogen cost of the pipeline system in Scenario 3 (In Scenario 3 pipeline network includes both transmission and delivery processes). As the second scenario delivers the hydrogen without changing its phase and only with uses the trucks for both delivery and transmission processes it also has reasonable delivery costs.

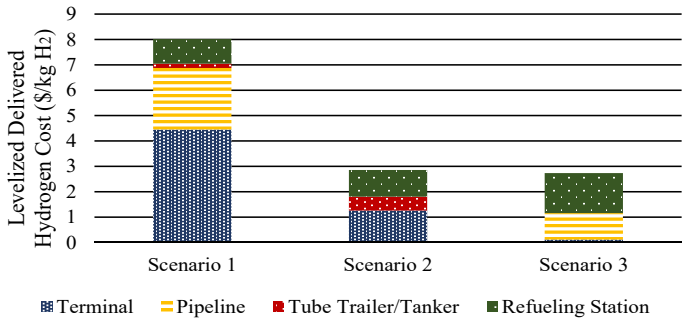


Figure 9. Levelized delivered hydrogen costs

Conclusions

In this study, we conduct both cost and environmental impact analysis including the stages of hydrogen storage, transmission and distribution of a hydrogen delivery infrastructure. The produced hydrogen is stored and transported to the nearby cities for distribution. Three different scenarios are examined for the process of transportation of the produced hydrogen to the distribution centers. The concluding remarks from this study can be stated as follows:

- Considering the large scale power plants H_2 delivery with pipeline network is a suitable option by $2.73 cost per kg delivered H_2
- Considering the small scale power plants H_2 delivery with tube trailers without liquefying is a suitable option by $2.86 cost per kg delivered H_2
- Liquefying the hydrogen increases the capital investment cost considerable.
- High amount of CO_2 is produced due to high electric consumption with lower efficiency at liquefier.
- Large scale pipeline delivery is obtained as the most environmentally friendly transportation option of the H_2 among the scenarios
- Operation and maintenance costs are highly dependent on the number of refueling stations serving.
- Novel storage and delivery technologies, such as metal hydrides and alienates can be investigated for further studies.

Nomenclature

CO_2	Carbon dioxide
H_2	Hydrogen
G&A	General and administrative
GH_2	Gaseous hydrogen
GHG	Greenhouse gas
GREET	Greenhouse gas, regulated emissions and energy use in transportation
LH_2	Liquid hydrogen
MACRS	Modified accelerated cost recovery system
O&M	Overall operation and maintenance (O&M)
US DOE	United States Department of Energy

References

1. Dinçer I, Joshi AS. 2013. *Solar based hydrogen production systems*. *Springer briefs in energy*.
2. U.S. Department of Energy. 2015. *Fuel Cell Technologies; Office Multi-Year Research, Development and Demonstration Plant*. *Fuel Cell Technol. Off. Multi-Year Res. Dev. Demonstr. Plant*.
3. Haeseldonckx D, D'haeseleer W. 2007. The use of the natural-gas pipeline infrastructure for hydrogen transport in a changing market structure. *Int. J. Hydrogen Energy*. 32:1381–1386.
4. Seymour EH, Murray L, Fernandes R. 2008. Key Challenges to the introduction of hydrogen—European stakeholder views. *Int. J. Hydrogen Energy*. 33:3015–3020.
5. Gerboni R. 2016. 11 – Introduction to hydrogen transportation. *Compend. Hydrog. Energy*., pp 283–299.
6. Stetson NT, McWhorter S, Ahn CC. 2015. *Compendium of Hydrogen Energy - Vol. 2, Hydrogen Storage, Distribution and Infrastructure*. 2.
7. Yang C, Ogden J. 2007. Determining the lowest-cost hydrogen delivery mode. *Int. J. Hydrogen Energy*. 32:268–286.

8. Moroz S, Tan XF, Pierce J, Greaves M, Duguid A, Dumur K, Ng J. 2013. Systems based on hypo-eutectic Mg-Mg2Ni alloys for medium to large scale hydrogen storage and delivery. *J. Alloys Compd.* 580:S329–S332.
9. Tsuda K, Kimura S, Takaki T, Toyofuku Y, Adaniya K, Shinto K, Miyoshi K, Hirata K, Christiani L, Takada M, Kobayashi N, Baba S, Nagamatsu Y, Takata M. 2014. Design proposal for hydrogen refueling infrastructure deployment in the Northeastern United States. *Int. J. Hydrogen Energy*. 39:7449–7459.
10. Ogden JM, Mintz M, Ringer M. 2004. H2A scenarios for delivering hydrogen from a central production plant to light-duty vehicles. *15th Annu. NHA Hydrog. Conf.* Los Angeles.
11. Simbeck DR, Chang E. 2002. Hydrogen Supply: Cost Estimate for Hydrogen Pathways – Scoping Analysis *Natl. Renew. Energy Lab.*:71.
12. Amos W a. 1999. Costs of Storing and Transporting Hydrogen. *Other Inf. PBD 27 Jan 1999; PBD 27 Jan 1999; PBD 27 Jan 1999.*:Medium: ED; Size: vp.
13. DOE Hydrogen and Fuel Cells Program: DOE H2A Delivery Analysis. [cited 4 March 2017]. Available from https://www.hydrogen.energy.gov/h2a_delivery.html.
14. DOE. 2006. H2A Delivery Components Model Version 1 . 1 : Users Guide. *U.S Dep. Energy*.
15. Publication 946 (2016), How To Depreciate Property. [cited 6 March 2017]. Available from https://www.irs.gov/publications/p946/.
16. Argonne National Laboratory. GREET model. 2016. http://greet.es.anl.gov.

Preparation of nickel and bismuth deposited titanium dioxide nano-tubes and investigation of electrochemical hydrogen production performance

Başak Doğru Mert, Mehmet Erman Mert, Birgül Yazıcı
Çukurova University, Science and Letters Faculty, Chemistry Department, 01330 Balcalı, Adana/ Turkey
Email: bdogru@cu.edu.tr, erman_mert@hotmail.com, byazici@cu.edu.tr

Abstract
In this study, titanium dioxide nano-tubes were produced and doped with Ni and Bi particles with the help of electrochemical process, to put forth the catalytic efficiency of electrodes on hydrogen evolution reaction (HER) in 1 M KOH, electrochemical impedance spectroscopy and polarization measurements were obtained. The characterization was achieved by cyclic voltammetry, scanning electron microscopy and energy dispersive X-ray analysis. The water wettability characteristics of electrode surfaces were investigated by measurement of contact angle. Due to produce nano-tubes, 17.5 V anodizing potential applied to Ti anode and Pt cathode during 30 min. in 0.1 M HF solution. The electrodeposition of nickel and bismuth was performed by galvanostatically in 30,00% $NiSO_4.7H_2O$, 1,00% $NiCl_2.6H_2O$, 1,25% H_3BO_3 (pH: 3.5) and 1 M HNO_3 + 0,1 M $Bi(NO_3)_3.5H_2O$ + 0,1 M $C_4H_6O_6$ (pH: 1.7-2.0). The $[Ni^{2+}]$:$[Bi^{3+}]$ ratio was 99.5:0.5 in deposition bath. Titanium dioxide nano-tubes were used as working electrode, nickel as counter electrode and Ag/AgCl (3 M KCl) electrode was used as the reference electrode. Results showed that, Ni and Bi deposited titanium dioxide nano-tubes decrease the hydrogen over potential and increase HER efficiency.

Keywords: Electrocatalysis; Hydrogen; TiO_2 nano-tube.

1. Introduction

The produce energy without polluting environment is a social responsibility for every human. We should consider future generations and nature. Therefore, development of new methods and improvement of conventional technology has crucial importance. For this purpose hydrogen is convenient alternative energy source. The electrolytic production of hydrogen, is getting in a center of scientific researches, as a part of the renewable energy cycle for truly sustainable systems [1-5]. The fundamental focus of the research in electrocatalysis is; discover electrode materials that exhibit desirable electrochemical stability and to show improved electroactivity toward typical electrochemical reactions [6-9]. Another important point is; these materials should not be expensive and should be abundantly available. Therefore, electrocatalytic hydrogen evolution on various electrode materials and from various electrolyte solutions is one of the most frequently studied phenomena [10-14]. Results show that, convenient electrodes are usually made of Ni, Co, V, Mo, etc. composite coatings or alloys and especially the trace amount of metal additives in Ni coating, improves the properties of coating [15-21]. These metal coatings can be succeeded by several methods: depositing Ni together with an active metal like such as Zn then etched it in a concentrated alkaline solution [20,22] and deposition of electrocatalytic metals with the help of electrodeposition [13-21], or thermal spray technique, etc. In this study we focused on nickel-bismuth binary coating on titanium dioxide nano-tubes and we investigate the electrocatalytic effect of electrodes on hydrogen evolution reaction (HER) in alkaline solution.

2. Experimental

2.1. Preparation of titanium oxide nano-tubes and electrodeposition of metal particles

Titanium oxide nano-tubes were prepared by anodizing technique. The two electrode system was used: Ti was anode and Pt was cathode, for anodizing Matrix power supply (MPS-3003L-3) instrument was used at 298K. The procedure was summarized as:

a) a cylindrical titanium with 0.785 cm^2 of the surface area used as working electrode. The surface of electrode was abraded by emery paper down to 1200 grade. Then, it was cleaned by acetone/ethanol mixture and pure water.
b) a platinum sheet (with 2 cm2 surface area) was used as counter electrode. The 17.5 V anodizing potential applied during 30 min. in 0.1 M HF solution.

The electrodeposition of nickel and molybdenum was performed by galvanostatically using Iviumstat Electrochemical Interface (with serial number AO6063) with a three-electrode configuration. In this system, TiO_2 (titanium oxide nano-tubes) was used as working electrode, nickel as counter electrode and an Ag/AgCl (3 M KCl) electrode was used as the reference electrode.

(a) The nickel deposition bath composition was 30% $NiSO_4.7H_2O$, 1% $NiCl_2.6H_2O$, 1.25% H_3BO_3.

(b) The 0.1 M $Bi(NO_3)_3.5H_2O$ and 0.1 M tartaric acid ($C_4H_6O_6$) containing1 M HNO_3 (pH: 1,7-2,0) The molar ratio of Ni^{2+}/Bi^{3+} in the NiBi plating bath was 99.5:0.5.

The constant current density of 5 mA cm^{-2} was applied and 100 µg metal (Ni and Bi) was deposited per cm^{-2} of Ti/TiO_2 electrode surface, operation time was calculated via Faraday's laws. The total charge was taken into account the current efficiency is 100%, and the pore volume was neglected.

2.2. Electrochemical measurements

The electrochemical measurements were carried using by CHI 660D A.C. electrochemical analyzer at room temperature, open to atmosphere. A platinum sheet (with 2 cm^2 surface area) was used as the counter electrode and Ag/AgCl (3 M KCl) electrode was used as the reference electrode for electrochemical analysis such as cathodic polarization curves, cyclic voltammetry and impedance measurements. The electrolyte in all measurements was 1 M KOH aqueous solution.

The cyclic voltammetry measurements were obtained in the potential ranges between −1.4 V and 0.8 V (vs. Ag/AgCl) with a scan rate of 0.1 V s^{-1}. The polarization curves were obtained with a scan rate of 0.001 V s^{-1}. The EIS experiments were conducted at -1.5 V (vs. Ag/AgCl) in the frequency range with high limit of 100 kHz and low limit of 0.01 Hz. The amplitude was 0.005 V. The EIS study was performed using a ZView software was used to analyze the data.

2.3. Surface characteristics

The surface morphologies of electrodes were examined by SEM. The SEM images were taken using a Carl Zeiss Evo 40 SEM instrument at high vacuum and 10 kV EHT. The chemical composition of electrodes surfaces were investigated by energy dispersive X-ray spectrometer (EDX), a part of SEM device. The contact angles of bi-distilled water on electrode surfaces were determined by Biolin Scientific Attension Theta Lite Optical Tensiometer. For this purpose Young-Laplace equation was used [21].

3. Results and discussion

3.1. Electrochemical measurements

The cathodic polarization curves of electrodes were presented in Fig.1. For Ti/TiO_2, in the initial cathodic scan which was seen at potential range from -1.0 to -1.3 V, diffusion controlled oxygen reduction was detected and then current density increased with H_2 evolution reaction (HER) but values were very low. The higher current density was detected for Ni and NiBi deposited electrodes. It is known that alloying the left-hand side transition metals (e.g., Fe, Co, Ni, etc.) with the right-half transition metals (e.g., Pt, Ag, Bi, etc.) results in apparent changes in bonding strength, stability and activity which is called synergism and gives maximal activity in the HER [21].

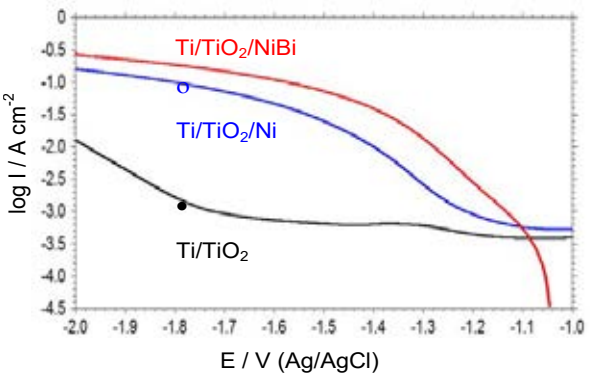


Figure 1. The cathodic polarization curves of Ti/TiO_2 (•), $Ti/TiO_2/Ni$ (o), $Ti/TiO_2/NiBi$ (-) in 1 M KOH solution.

The cyclic voltammograms of electrodes were seen in Fig.2. For $Ti/TiO_2/Ni$, the peak at -0.72 V, was imputed Ni/Ni^{2+} oxidation, the transformation of α-$Ni(OH)_2$ to β-$Ni(OH)_2$ was seen between the potential ranges of −0.6 to 0.4 V (vs Ag/AgCl) [17]. The peak centered at 0.45 V was assigned to the Ni^{2+}/Ni^{3+} transition and the cathodic peak at almost 0.5 V, was assigned to the Ni^{3+}/Ni^{2+} reduction. In Fig. 2 $Ti/TiO_2/Ni$ has higher catalytic effect than Ti/TiO_2. But the maximum cathodic current density was detected for $Ti/TiO_2/NiBi$ and further, the initial potential of cathodic current was lower for $Ti/TiO_2/NiBi$.

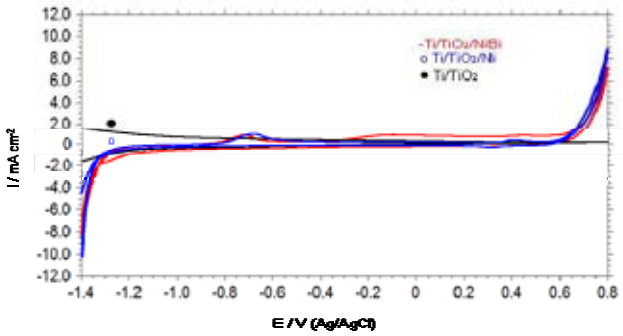


Figure 2. The cyclic voltammogram of Ti/TiO_2 (•), $Ti/TiO_2/Ni$ (o), $Ti/TiO_2/NiBi$ (-) in 1 M KOH solution.

The EIS results were given in Fig. 3. Ti/TiO_2 exhibited higher resistance than $Ti/TiO_2/Ni$ and $Ti/TiO_2/NiBi$. In Fig. 3, the semi-circular shape in the Nyquist plots of $Ti/TiO_2/Ni$ and $Ti/TiO_2/NiBi$ is noticed that [22] the hydrogen evolution reaction is mainly controlled by a charge transfer process. 2.52 and 1.93 Ω cm^2 were observed in the Nyquist plot of $Ti/TiO_2/Ni$ and $Ti/TiO_2/NiBi$, respectively.

3.2. Surface characteristics

The SEM and EDX results were presented in Fig. 4. The nanotubes are seen in Fig. 4a and the spherical structures on TiO_2 nanotubes are seen in Fig. 4b. The pore lengths were between 198.85 and 217.84 nm, pore diameters were between 5 and 10 nm. The Ni and Bi particles were seen in EDX spectra (Fig. 4c).

The contact angles of initial water droplets on electrode surfaces were presented in Fig. 5. Kim et al. [17] declared the results of the water contact angle measurements of TiO_2 films on Ti foils as almost 84°, in this study for Ti/TiO_2 electrode contact angle was almost 79°. Further 54° and 61° were detected for $Ti/TiO_2/Ni$ and $Ti/TiO_2/NiBi$, respectively. which were lower than Ti/TiO_2 due to high roughness of these electrodes. As seen from results in Fig. 5, all contact angles are lower than 90° and consequently surfaces are hydrophilic.

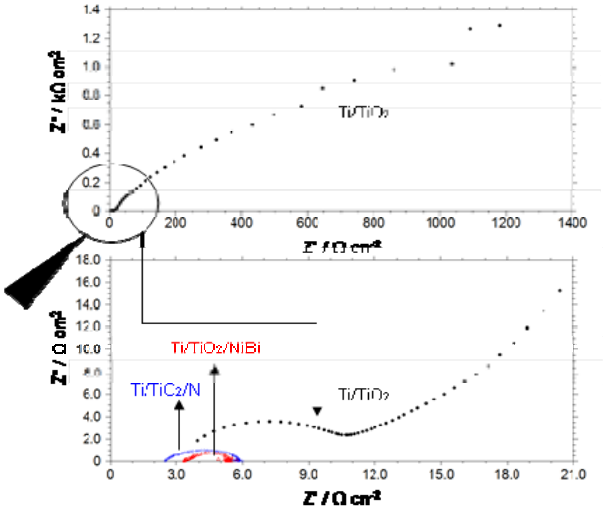


Figure 3. The Nyquist plots of Ti/TiO_2 (•), $Ti/TiO_2/Ni$ (o), $Ti/TiO_2/NiBi$ (Δ) in 1 M KOH solution.

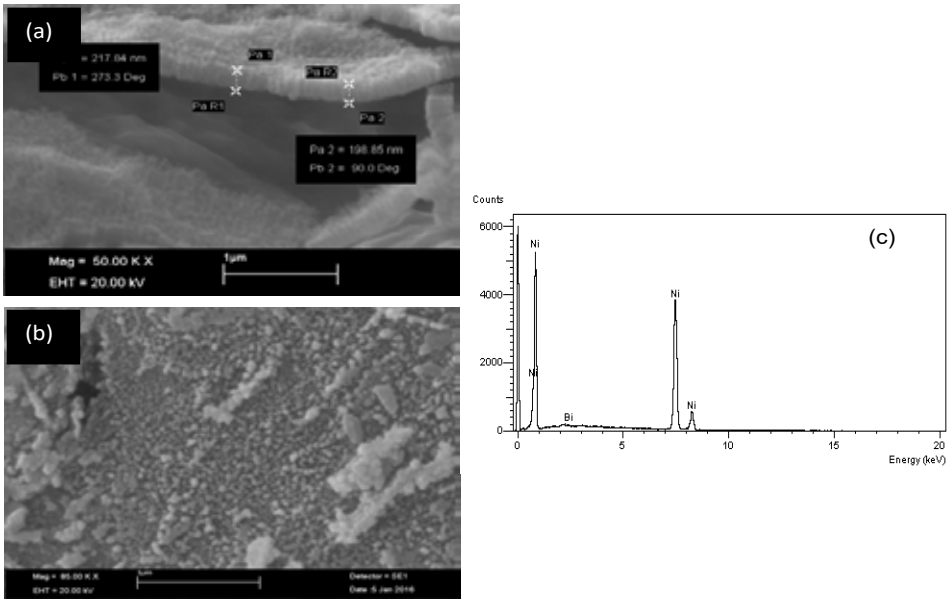


Figure 4. The cross-section SEM micrograph of Ti/TiO_2 (a) SEM micrograph of Ti/TiO_2/NiBi (b) and EDX spectra of Ti/TiO_2/NiBi (c).

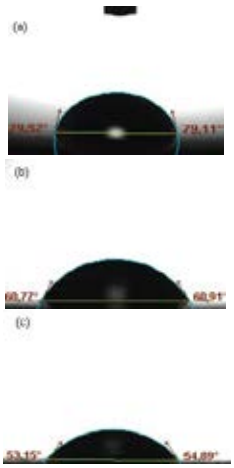


Figure 5. The contact angle for water droplet on Ti/TiO_2 (a), Ti/TiO_2/Ni (b), Ti/TiO_2/NiBi (c)

4. Conclusions

The electrocatalytic activity of the bare Ti electrode for HER was enhanced by two-step procedure. Initially anodizing was obtained and titanium oxide nanotubes (Ti/TiO_2) were produced and then Ni and Bi particles were electrochemically deposited on nano-tubes (Ti/TiO_2/NiBi). Results showed that; the Ti/TiO_2/NiBi has a compact and porous structure, Ni and Bi particles were dispersed homogenously on electrode surface. Ti/TiO_2/NiBi has hydrophilic character and higher HER activity.

Acknowledgements

The authors are greatly thankful to Çukurova University Research Fund for financial support (FBA-2016-6498).

References

1. Gan J, Bangalore R, Wu Z, Penley D, Zheng Y., (2016). Hydrogen-reduced bismuth oxyiodide nanoflake arrays with plasmonic enhancements for efficient photoelectrochemical water reduction. Electrochim. Acta 219: 20–27.
2. Kumar KM, Bhavani K, Srinivas B, Kumar SN, Sudhakar, NG, Venugopal A., (2016). Nano structured bismuth and nitrogen co-doped TiO_2 as an efficientlight harvesting photocatalyst under natural sunlight for theproduction of H_2 by H_2O splitting. Applied Catalysis A: General 515: 91–100.
3. Bai Y, Chen T, Wang P, Wang L, Ye L., (2016). Bismuth-rich $Bi_4O_5X_2$ (X = Br, and I) nanosheets with dominant {101} facets exposure for photocatalytic H_2 evolution. Chemical Engineering Journal 304: 454–460.
4. Shen TFR, Lai MH, Yang TCK, Fu IP, Liang NY, Chen WT., (2012). Photocatalytic production of hydrogen by vanadium oxides under visible light irradiation. Journal of the Taiwan Institute of Chemical Engineers 43:95-101.
5. Zheng H, Mathe M., (2011). Hydrogen evolution reaction on single crystal WO_3/C nanoparticles supported on carbon in acid and alkaline solution. Int J Hydrogen Energy 36:1960-1964.
6. Shibli SMA, Dilimon VS., (2007). Effect of phosphorous content and TiO_2-reinforcement on Ni–P electroless plates for hydrogen evolution reaction. Int J Hydrogen Energy 32:1697-1700.
7. Song LJ, Meng HM., (2010). Effect of carbon content on Ni-Fe-C electrodes for hydrogen evolution reaction in seawater. Int J Hydrogen Energy 35:10060-10066.
8. Solmaz R, Döner, A, Kardaş G., (2009). The stability of hydrogen evolution activity and corrosion behavior of NiCu coatings with long-term electrolysis in alkaline solution. Int J Hydrogen Energy 34:2089-2094.
9. Petrov Y, Schosger JP, Stoynov Z, Bruijn F., (2011). Hydrogen evolution on nickel electrode in synthetic tap water-alkaline solution. Int J Hydrogen Energy 36 :12715-12724
10. Rosalbino F, Maccio D, Saccone A, Angelini E, Delfino S., (2011). Fe-Mo-R (R=rare earth metal) crystalline alloys as a cathode material for hydrogen evolution reaction in alkaline solution. Int J Hydrogen Energy 36 :1965-1973.
11. Dong H, Lei T, He Y, Xu N, Huang B, Liu CT., (2011) Electrochemical performance of porous Ni_3Al electrodes for hydrogen evolution reaction. Int J Hydrogen Energy 36:12112-12120.
12. Im JS, Kwon O, Kim YH, Park SJ, Lee YS., (2008). The effect of embedded vanadium catalyst on activated electrospun CFs for hydrogen storage. Microporous Mesoporous Mater 115:514-521.
13. Abouatallah RM, Kirk DW, Thorpe SJ, Graydon JW., (2001). Reactivation of nickel cathodes by dissolved vanadium species during hydrogen evolution in alkaline media. Electrochim Acta 47:613-621.
14. Shibli SMA, Dilimon VS., (2008). Development of TiO_2-supported nano-RuO_2-incorporated catalytic nickel coating for hydrogen evolution reaction. Int J Hydrogen Energy 33:1104-1111.
15. Solmaz R, Döner A, Kardaş G., (2008). Electrochemical deposition and characterization of NiCu coatings as cathode materials for hydrogen evolution reaction. Electrochem Commun 10:1909-1911.
16. Zhang Y, Ozaki T, Komaki M, Nishimura C., (2002). Hydrogen permeation characteristics of vanadium–aluminium alloys. Scripta Materialia 47:601-606.
17. Kim K, Tai SW, Kim DY, Sang-Jin C, Bae I., (2009). Change in Water Contact Angle of Carbon Contaminated TiO_2 Surfaces by High-energy Electron Beam. Bull. Korean Chem. Soc. 30: 1067-1070.
18. Herraiz-Cardona I, Ortega E, Vazquez-Gomez L, Perez-Herranz V., (2011). Electrochemical characterization of a NiCo/Zn cathode for hydrogen generation. Int J Hydrogen Energy 36:11578-11587
19. Herraiz-Cardona I, Ortega E, Garcia-Anton J, Perez-Herranz V., (2011). Assessment of the roughness factor effect and the intrinsic catalytic activity for hydrogen evolution reaction on Ni-based electrodeposits. Int J Hydrogen 36:9428-9438.
20. Solmaz R, Kardaş G., (2007). Hydrogen evolution and corrosion performance of NiZn coatings. Energy Convers Manage 48:583-591.
21. Mert ME, Kardaş G., (2011). Electrocatalytic behaviour of NiBi coatings for hydrogen evolution reaction in alkaline medium. J Alloys Compd 509:9190-9194.
22. Solmaz R, Döner A, Kardaş G., (2010). Preparation, characterization and application of alkaline leached CuNiZn ternary coatings for long-term electrolysis in alkaline solution. Int J Hydrogen 35:10045-10049.

Performance Assessment of Calcium Bromine Thermochemical Cycle for Hydrogen Production

Fatih YILMAZ[1], Reşat SELBAŞ[2]
[1]Department of Electrical and Energy, Vocational School of Technical Sciences, Aksaray University, 68100, Aksaray, Turkey
[2]Department of Energy System Engineering, Faculty of Technology, Suleyman Demirel University 32100, Isparta, Turkey
Email: fatiyilmaz7@gmail.com, resatselbas@sdu.edu.tr

Abstract:
In this study, performance assessment of calcium bromine (Ca-Br) thermochemical/ hybrid cycle for hydrogen production. The performance of each step of the cycle is evaluated according to energy and exergy analyses at different reference ambient temperatures. The overall energy and exergy efficiency of the cycle are calculated as 46.64%, 59.04%, respectively, at 25 ºC reference ambient temperature.

Keywords: Energy; exergy; hydrogen, $Ca\text{-}Br_2$

1. Introduction

Currently, the greenhouse gas emission and environmental problems continues increases from usage of fossil fuels. Thus, the average temperature increases will be inevitable in the world [1]. At the same time, the fossil fuel resources limited and to prevent the environment problems trends towards is very important of renewable and sustainable energy. The renewable energy sources have many advantages such as the countries were independent of the other countries. Renewable energy sources are consist of solar, wind, geothermal and hydrogen (H_2) etc.

Presently, almost 96% hydrogen produced from fossil fuels. Therefore, the gas emission into atmosphere is continuing [2]. Nevertheless, it is expected that renewable based on hydrogen production with water electrolysis from solar and wind or thermochemical cycles to a competitive in the world. These methods are more environmentally friendly. Hydrogen is an energy carrier and the most common element in the sun. As well as hydrogen is unscented and colorless under ambient temperature and pressure. When it is combined with water, producing water. It does not exist on earth in its atomic form, it is only found combined with other elements [3]. Moreover, hydrogen is considered the fuel of the future. For a more environmentally friendly hydrogen production, fossil sources based on hydrogen production methods must be left and renewable energy assisted electrolysis or thermochemical methods must be introduced. Thermochemical and hybrid cycles are used only heat/heat and electric and with input water molecules decomposition into oxygen and hydrogen by chemical reactions. This process is to produce low cost hydrogen through thermally decomposing the water as a result of a number of chemical reactions, lower than 2500-3000 ° C temperatures required for thermolysis. The schematic diagram is shown that thermochemical and hybrid cycle in Fig.1

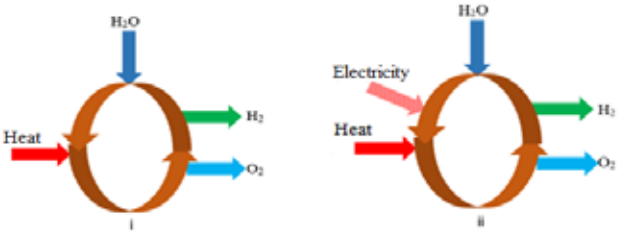


Fig. 1. The schematic diagram of thermochemical and hybrid cycle

When the literature is examined, it can be seen that there are many different studies about to thermochemical cycles. However, there have been study only a part in terms of application, efficiency and economy. There are some studies in literature for hydrogen production with thermochemical cycles [5-10]. Ozcan et al. investigated that energy and exergy analyses of solar-based Mg-Cl thermochemical cycle for hydrogen and power production [11]. The energy and exergy analyzes of the whole system were found to be 18.8% and 19.9%, respectively. Balta et al. performance assessment of various clorin family thermochemical cycles for hydrogen production [12]. In this study, they have been studies Cu-Cl, Mg-Cl, Fe-Cl, and V-Cl thermochemical cycles and it has been suggested that the performance of V-Cl thermochemical cycle is good. As a result of, when the literature is

investigated for hydrogen production via thermochemical and hybrid cycles it is understand that many studies about to Cu-Cl, Mg-Cl cycles.

In this paper, energy and exergy performance assessment of Calcium bromide (Ca-Br) thermochemical cycle for hydrogen production is discussed in detail. We also have been investigated efficiencies changing of each steps and overall cycle according to reference environment temperature. For these calculations, was used the engineering equation solver (EES) a namely packet program.

2. Ca-Br Cycle

The Ca-Br cycle is a hybrid cycle using both heat and electricity for hydrogen generation and consists of three steps. The maximum temperature required for this cycle is shown in the first (step I) at 730 ºC. The chemical reactions and temperatures occurs in the cycle is given in Table 1.

Table 1. The chemical reactions and temperatures.

Reactions	Temperature (ºC)
$CaBr_2+H_2O=CaO+2HBr$	730 ºC (Step I)
$CaO+Br_2=CaBr2+½O_2$	550 ºC (Step II)
$2HBr=H_2+Br_2$	80 ºC (Step III)

In the step I, $CaBr_2$ and H_20 enters with reaction to form CaO and HBr. This step takes place chemical reaction at about 730 ºC. A chemical reaction takes place in the step II at 500 ºC, in which calcium oxide (CaO) and bromine (Br_2) enter as reactants and calcium bromide ($CaBr_2$) and oxygen are produced. This step can be named oxygen production step. In the last step of the cycle, is an electrochemical reaction occurs, HBr is decomposition by an electrochemical cell at about 70-80 ºC for hydrogen generation. This hybrid cycle take place two chemical reactions and one electrochemical reaction. As a result of, the Ca-Br_2 cycle using only heat and electricity to decomposition water for hydrogen generation.

3. Analyses

The law of conservation of energy, which is based on the first law of thermodynamics, is the basic method to investigation a system. Furthermore, as well as the energy conversation law the second law of thermodynamic to assessment of the efficiency of a system will give results that are more realistic. To better understand the energy flows in system, we need to use the exergy methods besides energy methods.

The mass balance for steady-state process can be expressed by;

$$\sum \dot{m}_{in} - \sum \dot{m}_{out} = 0 \quad (1)$$

where ṁ is the mass flow rate, and the subscript in stands for inlet and out for outlet. The general energy balance can be illustrated in the rate form below;

$$\sum \dot{E}_g - \sum \dot{E}_ç = \Delta \dot{E}_{sistem} \quad (2)$$

For the chemical processes [13] can write general energy balance;

$$Q - W = \sum n_R \left(\overline{h}_f^o + \overline{h} - \overline{h}^o\right)_R - \sum n_P \left(\overline{h}_f^o + \overline{h} - \overline{h}^o\right)_P \quad (3)$$

where $\overline{h}$, is represent sepecific enthalpy, $\overline{h}^0$ is defination specific enthalpy of reference point and $\overline{h}_f^0$ is is express specific entahlp of formation, n stands for number of moles. Also R and P are symbolized reactants and production, recpevtively.

The exergy efficiecny can be used to analyzed and imporoved of any thermal processes. There are widely used methods todays. The general exergy equations of a processes can be expressed as [13];

$$\sum \dot{E}x_{in} - \sum \dot{E}x_{out} - \sum \dot{E}x_{dest} = \Delta \dot{E}_{system} \quad (4)$$

Where, $\dot{E}x_{in}$ is inlet exergy by maas, heat and work and $\dot{E}x_{out}$ is outle exery rate by heat, mass and work. For asteady-state system, $\Delta \dot{E}_{system}$ is zero and so Eq.(4) can be wriiten as Eq. (5), in Eq.(5), $\dot{E}x_{dest}$ is represented as exergy destruction.

$$\sum \dot{E}x_{in} - \sum \dot{E}x_{out} = \sum \dot{E}x_{dest} \quad (5)$$

The exergy associated with a process at a specified state is the sum of two contributions: physical and chemical [13];

$$ex = ex^{ph} + ex^{ch} \quad (6)$$

By ignoring the specific kinetic and potential exergy of the compounds, specific exergy term can be written as:

$$ex = (h - h_0) - T_0(s - s_0) + ex^{ch} \quad (7)$$

$$\dot{E}x = \dot{m}.ex \quad (8)$$

To calculte inlet and outlet enthalpy and entropy of the system for chemical proceses using shomate equations;

$$\bar{h} - \bar{h}_0 = A*T + B*\frac{T^2}{2} + C*\frac{T^3}{3} + D*\frac{T^4}{4} - E*\frac{1}{T} + F - H \quad (9)$$

$$\bar{s} = A*\ln(T) + B*T + C*\frac{T^2}{2} + D*\frac{T^3}{3} - E*\frac{1}{2T^2} + G \quad (10)$$

where T is 1/1000 of the specified temperature (in K) of compound and A, B, C, D, E, F,G and H are constants, as given in Table 1 for reactants and products [14]. The chemical exergy based on a typical exergy reference environment exhibiting standard values are given Table 2. The values of the standard chemical exergies for the reactants and products are taken from the literature [15].

The last step of Ca-Br cycle includes electrochemical reactions. The amount of electricity energy demand is calculated using Nernst equation depend on the change in Gibbs free energyΔG, as shown by [16]

$$\Delta G = -nFE \quad (11)$$

$$W_{el} = -\Delta G \quad (12)$$

where F denotes Faraday's constant, which is taken as 96485 C/mol, E is the cell potential of the cells and n is the number of moles of electrons exchanged in an electrochemical reaction.

Finally, the overall energy and exergy efficiency of the cycle calculated by equations (13) and (14);

$$\eta_{cycle} = \frac{LHV_{H2}}{\sum \dot{Q} + W_{el}} \quad (13)$$

$$\psi_{cycle} = \frac{Ex_{H2}}{\sum \dot{E}x_Q + W_{el}} \quad (14)$$

where $\dot{Q}$ the required total heat rate of cycle, LHV_{H2} lower heating values of hydrogen that is taken 239.92 kJ/mol, W_{el} is reqiured total work rate, Ex_{H2} is chemical exergy rate of hydrogen.

3. Results and discussion

In proposed paper, we performance assessment of Ca-Br thermochemical cycle for hydrogen production. Also, the theoretical studies, we investigated the energy and exergy efficiency of each steps in cycle according to various parameters, including reference temperature, reaction temperature. In this cycle, the calculations are depend on one mol hydrogen production. We make the assumptions to calculations given below;

- ✓ The reference temperature and pressure are taken as 25 °C and 1 atm,respectively.
- ✓ All reactions, the inlet and outlet reactans and products occurs at specific reaction temperature and 1 atm reactipn pressure
- ✓ All procesed are considered the stady-state and steady-flow.
- ✓ The kincetic and potential energies are disregarded.

The formation aentlapy, referencen entropy and Shomate constans for Ca-Br thermochamical cycle as given Table 2. The constants are used to calculate Ca-Br coumponds enthalpy at reaction point of temperature. Also, the standard chemical exergy values are given in Table 3.

Table 2. Enthalpy of formation, reference entropy and Shomate constants for reactants of Ca- Br cycle

Compounds	$\bar{h}_f^0$ (kJ/mol)	$\bar{s}_0^0$ (kJ/mol*K)	A	B	C	D	E	F	G	H
CaBr2	-683.25	129.64	103.140	-71.94	75.73542	-17.10511	-1.15240	-715.31760	266.21290	-683.24
H_2O	-241.83	188.84	30.092	6.83	6.7934	-2.5345	0.0821	-250.8810	223.3967	-241.82
CaO	-557.33	62.31	49.954	4.88	-0.3521	0.0462	-0.8251	-652.9718	92.5610	-635.08
HBr	-36.44	198.7	31.714	-13.69	23.35567	-9.008529	-0.028758	-45.57464	240.0428	-36.443
Br2	30.91	245.38	38.527	-1.976	1.52610	-0.19839	-0.18581	18.87620	391.48630	30.901
O_2	0	205.15	30.032	8.772	-3.98813	0.78831	-0.74159	-11.32468	236.16630	0
H_2	0	130.68	33.0661	-11.36	11.432816	-2.772874	-0.158558	-9.980797	172.707974	0

Table 3. Standard chemical exergy of the Ca-Br compounds

Compounds	$\overline{ex}^{ch}$ (kJ/mol)
$CaBr_2$	150
H_2O	9.34
CaO	128.94
HBr	115.02
Br_2	103.88
O_2	3.97
H_2	236.1

The changing exergy efficiency of step I with various reference temperatures and reaction temperatures displayed in Fig. 3. As can see from this figure, the exergy efficiency of step I is computed as 85.50%, at reaction and reference temperature are constant as 700 ºC and 30 ºC. While the reaction temperature increase, the exergy efficiency of step I decrease. However, the reference temperature increases at constant reaction temperature with the exergy efficiency of step I increases.

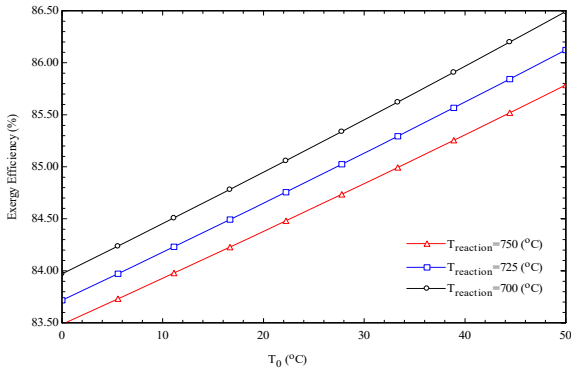


Fig. 3. The changing of exergy efficiency with various reference and reaction temperatures for step I.

Fig. 4. shows the variance of exergy efficiency in the step II with various reference and environment temperatures. As seen from this figure, when the reaction temperature increasing from 500 ºC to 600 ºC at fixed reference temperature, the exergy efficiency of step II increases. On the other hand, the exergy efficiency of step II decreases with the reference temperature increase. The exergy efficiency of step II calculated as 87.50% at reference and reaction temperatures, 25 ºC and 550 ºC, respectively.

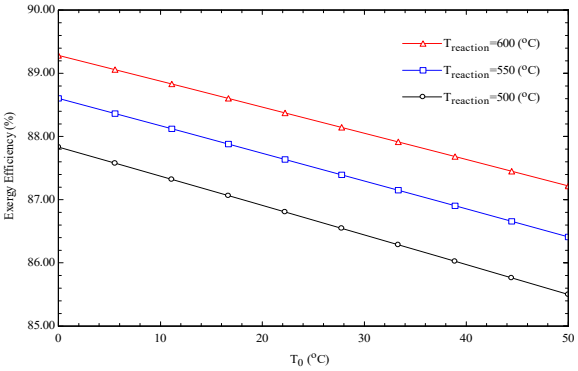


Fig.4. The changing of exergy efficiency with various reference and reaction temperatures for step II.

The last step of Ca-Br thermochemical cycle, which is namely hydrogen production step, takes place electrochemical reaction about 80 ºC. The effect of reference temperature of step III on the exergy efficiency at

different reaction temperatures illustrated in Fig.5. The exergy efficiency of step III increase with reference temperature increasing from 0 ºC to 50 ºC at constant reaction temperature.

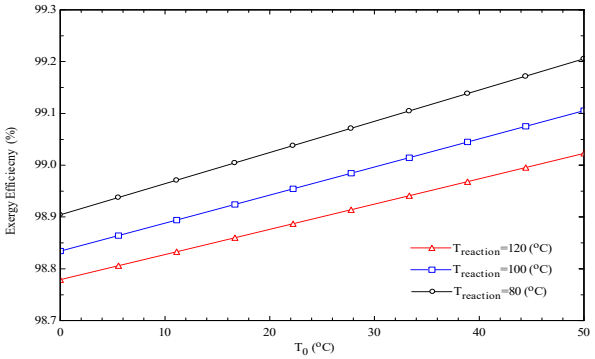


Fig. 5. The changing of exergy efficiency with various reference and reaction temperatures for step III

In Fig.6, was displayed that the effect of reference temperature on the energy, exergy efficiency and total exergy destruction of Ca-Br cycle. As can be seen from this figure, if the reference temperature increases, the exergy efficiency of cycle increases and total exergy destruction decrease. The energy efficiency of this cycle is remain constant 46% with reference temperature increases.

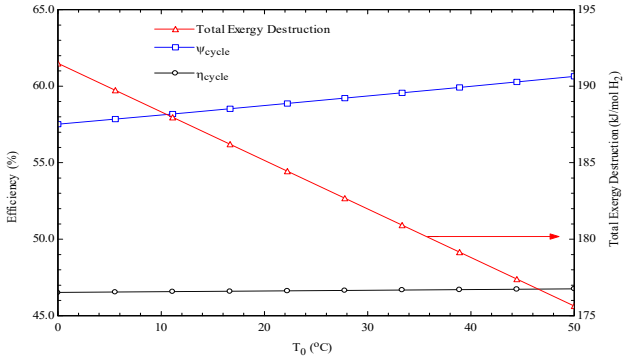


Fig. 6. The effect of reference temperature on energy, exergy efficiencies and total exergy destruction Ca-Br cycle

4. Conclusion

In this proposed the paper, the energy and exergy efficiency each steps of Ca-Br cycle and overall cycle are calculated and presented according to various parameters. The maximum heat demand of cycle is shown step I with 730 ºC temperature. Finally, some of the result remarks can be drawn from this study follow as;

- The energy and exergy efficiency of Ca-Br cycle are calculated as 46.68 % and 59.04%, respectively.
- The electric energy demand in the last step, which takes places electrochemical reaction, is calculated as 112 kJ/mol H_2.
- The total heat requirement of Ca-Br cycle found as 409 kJ/ mol H_2.
- The thermochemical cycles promising technology and environmentally kindly methods for hydrogen production.
- The energy efficiency about remains constant while the reference temperature increases.

Thermochemical cycles will be very effective methods for sustainable hydrogen production with environment impact coming years.

Nomenclature

E	energy
Ex	exergy
Ex	specific exergy
ex^{ch}	chemical exergy
ex^{ph}	physical exergy
$\bar{h}$	specific enthalpy
$\bar{h}^0$	specific enthalpy at reference state
$\bar{h}_f^0$	specific enthalpy of formation
LHV_{H2}	lower heating value of hydrogen
$\bar{m}$	molar flow rate
N	mol number
$\bar{s}$	specific molar entropy
Q	heat
T	temperature
W	work

References:

1. Ültanır, M.Ö., 1995.Hidrojen Enerjisi ve Türkiye'de Hidrojene Geçiş Sorunları". Türkiye 6. Enerji Kongresi Teknik Oturum Bildirileri-1. s.549-563. Dünya Enerji Konseyi Türk Millî komitesi. İzmir.
2. Ewan, B.C.R. and Allen, R.W.K., 2005. A Figure of Merit Assessment of the Routes to Hydrogen". International Journal of Hydrogen Energy. 30. 809-819.
3. 3. Temiz enerji Yayınları. Hidrojen Enerjisi E.T: 13.01.2017. http://habitatdernegi.org/tr/dl/yayin/TemizEnerjiYayinlari/Y_O_Hidrojen.pdf
4. Balta, M.T., 2010. Jeotermal Esaslı Hidrojen Üretim Sistemlerinin Ekserji ve Eksergoekonomik Analizi. Ege Üniversitesi Fen Bilimleri Enstitüsü. Doktora Tezi. İzmir.148s.
5. Carty, R.H. Mazumder, M.M. Schreider, J.D. and Pangborn, J.B., 1981. Thermochemical Hydrogen Production. Chicago. IL: Gas Research Institute for the Institute of Gas Technology 1-4: GRI-80/0023.
6. Beghi, G.E., 1986. A Decade of Research on Thermochemical Hydrogen at the Joint Research Centre. ISPRA. International Journal Hydrogen Energy. 11(12), 761–771.
7. Yalcin, S., 1989. A Review of Nuclear Hydrogen Production. International Journal of Hydrogen Energy. 4(8), 551-561.
8. Fletcher, E.A., 2001. Solar Thermal Processing: A Review. J. Solar Energy Eng., 123, 63–74.
9. Funk, J.E., 2001. Thermochemical Hydrogen Production: Past and Present. International Journal of Hydrogen Energy. 34, 4256-4267.
10. Mc Quillan, B.W. Brown, L.C. Besenbruch, G.E. Tolman, R. Cramer, T. and Russ, B.E., 2005. High Efficiency Generation of Hydrogen Fuels Using Solar Thermo-Chemical Splitting of Water. Annual report GA-A24972 San Diego. CA.
11. Ozcan, H. Dincer, İ., 2014. Energy and Exergy Analyses of A Solar Driven Mg-Cl Hybrid Thermochemical Cycle For Co-Production Of Power And Hydrogen. International Journal of Hydrogen Energy. 39. 15330 - 15341.
12. Balta, M.T. Dincer, İ. Hepbasli, İ., 2016. Comparative Assessment of Various Chlorine Family Thermochemical Cycles for Hydrogen Production. International Journal of Hydrogen Energy. 41. 7802 - 7813.
13. Cengel, Y.A. and Boles, M.A., 2008. Thermodynamics: An Engineering Approach. 6th edition. McGraw-Hill. NY.
14. National Institute of Standards and Technology (NIST), 2016. http://webbook.nist.gov/chemistry/
15. Exergoecology Portal (EP), 2016. http://www.exergoecology.com/excalc/
16. Barbir F., 2005. PEM fuel cells theory and practice. Oxford: Elsevier;

Biohydrogen Production by Extracted Fermentation from Sugar Beet

Serkan Eker, Burcu Erkul
Department of Environmental Engineering, Dokuz Eylul University, Izmir, Turkey
Email: serkan.eker@deu.edu.tr

Abstract
In this study, sugar beet was used as substrate for formation of biohydrogen gas by extracted dark fermentation at different size of sugar beet particles. It is possible to increase the production efficiency for biohydrogen gas production by extracted fermentation. While microorganisms consume the readily soluble sucrose from sugar beet in the liquid, they also consume insoluble sucrose in the sugar beet.

Therefore, surface area of substrate, substrate and biomass concentrations are of important parameters that affecting hydrogen gas production. For this purpose, sugar beet was prepared as cubes particles to investigate effects of surface area of substrate. The surface area was changed 0.06 cm^2, 0.54 cm^2, 1.5 cm^2, 2,94 cm^2, and 6 cm^2 for single cube. Microorganism concentration (1 g/L) and sugar beet concentration (60 g/L) were kept constant in all the bottles according to previous study results. Cumulative biohydrogen gas volume increased depending on time and reached the highest level at the end of 168 hours. The highest biohydrogen gas production efficiency was obtained from 0.06 cm^2 sugar beets (146.25 ml). The lowest cumulative biohydrogen gas production was obtained from 6 cm^2 sugar beet containing bottle (73.75 ml). Biohydrogen gas production was not observed in the control bottle. Gompertz constants were calculated by Statistica software for different surface area of sugar beet. Cumulative biohydrogen fproduction data were correlated and the highest biohydrogen gas production potential values were calculated at 0.06 cm^2 (143.61 mL/h) and 0.54 cm^2 (94.46 mL/h) of surface area.

Keywords: Biohydrogen production; dark fermentation; extracted fermentation, sugar beet

1. Introduction

The world's energy consumption provided from fossil fuel, nuclear fuel and renewable resources increased with increasing global population. Different types of fossil fuels are widely used to provide energy. The combustion of fossil fuels has serious negative effects on the environment because of the greenhouse gas emissions. Recently, there has been a large increase in international agreements to use of renewable energy source such as hydrogen. Hydrogen is one of promising energy source. It is considered as alternative fuel of the future because of clean oxidation products generation after burning and its high-energy contents [1-3]. But many challenges are known to shift from fossil fuels to hydrogen energy. High cost of production and storage are important factor that caused delaying in considering hydrogen as an alternative energy source.

Many technologies can be used for production of hydrogen today [1, 4]. But, high cost of production and storage are important factor that caused delaying in considering hydrogen as an alternative energy source. Therefore, cheap and environment-friendly hydrogen production methods should be developed. Biological method has several advantages as compared to the other methods such as chemical or electrochemical methods. Biological process requires low energy and low operational cost. Biohydrogen can be produced at ambient temperature and pressure and produced from different substrate sources. Researchers have been working on the production of biohydrogen with various agricultural products or agricultural wastes. It's reported that the dark fermentation is the most promising way to biohydrogen production [1, 5]. It's regarded as favorable method because of simplicity of process, high hydrogen production rates, variable feed material utilization especially wastes. All of these advantages make dark fermentation more favorable among other biological methods.

Various kinds of microorganism are available for biological production of hydrogen. Anaerobic or facultative anaerobic bacteria achieve biohydrogen production by dark fermentation under anaerobic conditions [1]. The most commonly used microorganisms are Clostridium, Enterobacter, Bacillus, thermophilic bacteria species and treatment sludge taken from acetogenic phase of treatment plant [2, 6-9]. But mixed microorganism culture is preferable. Pure culture can be contaminated by some hydrogen consuming bacteria species [1, 7-12]

Extracted fermentation (Ex-Ferm) technique is a process that extraction and fermentation of sucrose processes were carried out simultaneously in a substrate - water suspension. Ethanol production from sugar cane by using the Ex-Ferm technique was studied [13]. According to results of experiments, the concept of Ex-Ferm for ethanol fermentation is technically feasible [13-18]. According to results of analysis, sugar consumption was above 98% depending on the yeast strain and Ex-Ferm cycles. It's reported that the concept of EX-FERM ethanol fermentation is technically feasible [19, 20].

There are a lot of studies about biohydrogen production by dark fermentation with agricultural products, and its processing waste or wastewater in the literature [1, 6, 21-25]. But the difference of this study from the literature is extracted fermentation method to improve formation of biohydrogen gas.

2. Experimental Study

Batch experiments were carried out 250 ml serum bottles. (Isolab-Germany Boro 3.3). Silicone rubber stoppers and screw were used to avoid gas leakage. L-cysteine-HCl.H_2O (0.1g/L) was added to obtain anaerobic conditions and argon gas was passed through the bottles before incubation [3].

There are three important parameters that affecting biohydrogen gas production. These are surface area of beet, substrate and biomass concentration. According to results of the previous studies, the highest biohydrogen gas production was obtained at 60 g/L of sugar beet and 1 g/L of biomass. The effect of surface area on biohydrogen formation experiments were conducted at five different particles size between 0.06 cm^2 and 6 cm^2, which was given for surface of one beet particle. Sugar beets, dried at room temperature, were prepared as cubic particles to obtain different size. Pore surface of sugar beet was neglected for calculation of real surface area. The highest surface area in the total was provided with the smallest cubic particles.

The anaerobic sludge was obtained from the acidogenic phase of the anaerobic treatment plant of the Pakmaya Baker's Yeast Company in Izmir, Turkey. In order to eliminate methanogenic bacteria, the anaerobic sludge was heated for 2 h at100 ºC and pH=5.9. The nutrient media was prepared to provide optimum C/N/P ratio of 100/2/0.5 for microorganisms [3]. ORP values varied between −200 and −300 mV and pH was adjusted between 6.5 and 7.5 by manual pH control, using 5 M NaOH solution during the experiments.

Total gas production, percentage hydrogen in total gas, initial and final total sugar concentrations were monitored throughout the experiments. Samples were centrifuged at 8000 rpm for 15 minutes to remove solids. Acid-phenol spectrophotometric method was used to determined total sugar content [26].

Biomass concentration in the inoculum was determined by filtering 5 ml sample through a 0.45 µm milipore filter, drying at 105 ºC and determining the constant dry weight according to the Standard Methods [27]. Water displacement method was used for total gas volume measurements by using a solution containing sulfuric acid (2%) and NaCl (10%). Samples were taken from head space of the bottles by using gas tight glass syringes. The measurements were carried out via gas chromatograph (HP Agilent 6890) everyday. The column was Alltech, Hayesep D 80/100 6" × 1/8" × 085". The carrier was nitrogen gas (30 ml/min) for these measurements and the head pressure was 22 psi. Oven temperature was 35 ºC and temperatures of injection, detector, and filament were 120ºC, 120ºC, 140ºC respectively. The following equation were used for calculation of cumulative hydrogen gas volume.

$$V_{H2,\,i} = V_{H2,\,i-1} + V_W\, C_{H2,i} + V_{G,i}\, C_{H2,i} - V_{G,i-1}\, C_{H2,\,i-1} \quad (1)$$

where $V_{H2,i}$ and $V_{H2,\,i-1}$ are the volumes of cumulative hydrogen (ml) calculated after the i^{th} and the previous measurement; V_W is the total gas volume measured by the water displacement method (ml); $C_{H2,i}$ is the concentration of H_2 gas in the total gas measured by the water displacement method (%); $V_{G,i}$ and $V_{G,i-1}$ are the volumes of the gas in the head space of the bottle for the i^{th} and the previous measurement (ml); $C_{H2,i}$ and $C_{H2,\,i-1}$ are the percent H_2 in the head space of the bottle for the i^{th} and the previous measurement.

The cumulative hydrogen volume versus time data were correlated with Gompertz Equation. Constants were determined by regression analysis via Statistica software. Gompertz Equation is shown below [28].

$$H_{(t)} = P \exp\left\{-\exp\left[\left(\frac{R_m \times e}{P}\right)(\lambda - t) + 1\right]\right\} \quad (2)$$

where, H(t) is cumulative hydrogen gas volume (ml) at any time t, P is the maximum potential hydrogen formation (ml), R_m is the maximum rate of hydrogen formation (ml/h), λ is duration of the lag phase (h), e is 2.718 and t is time (h).

3. Results and Discussion

Surface area of substrate is one of important parameters that affecting hydrogen gas production. Surface area affects the sugar amount that dissolving in liquid. For this aim, six bottles, including a control bottle without microorganism, were prepared to investigate effects of surface area on cumulative hydrogen gas production. Fig. 1 depicts variation of cumulative hydrogen formation with time for different surface area of single sugar beet. The surface area for single sugar beet was varied between 0.06 and 6 cm^2 while sugar concentration was kept constant at 60 g/L and biomass concentration was kept constant at 1 gr/L. Cumulative hydrogen gas production reached the highest level at the end of 120 h of incubation time for all bottles. The highest hydrogen formation was obtained at small sugar beet particle. Cumulative biohydrogen formation was 146.25 ml when the surface area of sugar beet particle was 0.06 cm^2. The lowest cumulative hydrogen formation was obtained at large sugar beet particle. The lowest biohydrogen gas formation (73.75 ml) was obtained with surface area of sugar beet of 6 cm^2. Biohydrogen gas formation was not observed in the control bottle. The results show that biohydrogen gas formation increased with decreasing particles size of sugar beet.

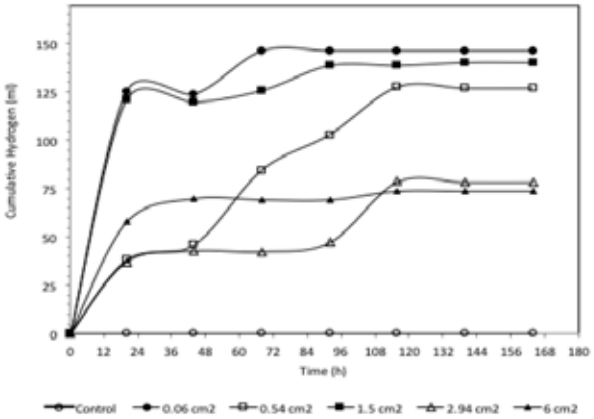


Fig. 1. Variation of cumulative hydrogen formation with time for different surface area of sugar beet.

Fig. 2 shows the variation of total sugar concentration in the liquid phase with time at different surface area for single sugar beet particle. Ex-Ferm method is a process that extraction and fermentation processes of sugar were carried out simultaneously in a substrate - water suspension. Some of the sugar is easily dissolved in water and the rest remains in the sugar beet. While microorganisms are consuming the soluble sugar in the liquid, it also consumes insoluble sugar in the sugar beet. Soluble sugar was dissolved at the beginning and sugar concentration increased with increasing surface area of single sugar beet particle. But, sugar consumption by microorganisms was increased with time.

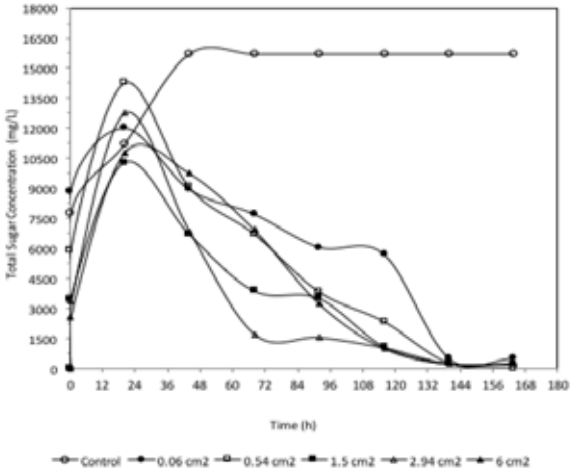


Fig. 2. Variation of total sugar concentration in liquid with time at different surface area for single sugar beet particle.

Cumulative hydrogen formation data presented in Fig. 1 were correlated with Gompertz equation. Equation was solved by using Statistica software and constants were presented in Table 1. The highest hydrogen production potential values were calculated at 0.06 cm^2 and 0.54 cm^2 of surface area. The highest cumulative hydrogen gas was predicted as 139 ml at 0.06 cm^2 of surface area for single sugar beet. The results of potential hydrogen formation, obtained at 0.06 cm^2 and 0.54 cm^2 of sugar beet surface area, were almost same. Maximum hydrogen formation rate was predicted as 144 mL/h at 0.06 cm^2 of surface area for single sugar beet. The results show that microorganisms could readily reach sugar in the liquid and insoluble sugar into the sugar beet. The

small particles provide high mass transfer. Therefore, high biohydrogen formation can be obtained at smaller particles or high total surface area in total.

Table 1. Gompertz equation constants for various sugar beet surface areas.

Sugar Beet Surface Area (cm^2)	P(mL)	R_m (mL/h)	λ (h)	R^2
0.06	139.85	143.61	2.62	0.99
0.54	139.85	94.46	8.80	0.99
1.5	133.84	9.65	3.89	0.99
2.94	57.68	67.71	2.63	0.83
6	69.42	66.97	0.96	0.98

4. Conclusions

Ex-Ferm was used in the experiments to improve biohydrogen gas formation. Ex-Ferm is a process that extraction and fermentation process were carried out simultaneously in a substrate - water suspension. The effect of surface area of sugar beet was investigated by changing size of single cubic sugar beet. Surface area for single cubic particle were varied between 0.06 cm^2 and 6 cm^2. Sugar beet concentration was kept constant at 60 g/L and microorganism concentration was kept constant at 1 g/L during the experiments. The highest biohydrogen formation was obtained at high surface area, which was provided by small cubic particle of sugar beet. The highest hydrogen production efficiency was obtained as 146.25 ml with 0.06 cm^2 of sugar beet. Soluble sugar can be transfer to liquid depends on surface area of cubic particle. Mass transfer limitation for extraction and dissolving of sugar can be avoid by providing high surface area with small particles. Some of the sugar is easily dissolved in water and the rest remains in the sugar beet. While microorganisms are consuming the soluble sugar in the liquid, it also consumes insoluble sugar in the sugar beet.

Gompertz constants were calculated by Statistica software. The highest hydrogen production potential values were calculated at 0.06 cm^2 and 0.54 cm^2 of surface area. The maximum hydrogen formation rate was obtained from 0.06 cm^2 sized sugar beet. The results show that microorganisms could reach to sugar readily into the beet. The lowest lag phase was calculated as 0.96 h at 6 cm^2 of sugar beet. Lag phase decrease with increasing sugar beet size except 0.06 cm^2.

Acknowledgement

This study was supported by Dokuz Eylul University, Scientific Research Projects.

References

1. Kapdan IK, Kargi F. Bio-hydrogen production from waste materials. Enzyme Microb Tech. 2006;38:569-82.
2. Argun H, Kargi F. Bio-hydrogen production by different operational modes of dark and photo-fermentation: An overview. Int J Hydrogen Energ. 2011;36:7443-59.
3. Eker S, Sarp M. Hydrogen gas production from waste paper by dark fermentation: Effects of initial substrate and biomass concentrations. Int J Hydrogen Energ. 2017;42:2562-8.
4. Hallenbeck PC. Fermentative hydrogen production: Principles, progress, and prognosis. Int J Hydrogen Energ. 2009;34:7379-89.
5. Hallenbeck PC, Benemann JR. Biological hydrogen production; fundamentals and limiting processes. Int J Hydrogen Energ. 2002;27:1185-93.
6. Argun H, Kargi F. Effects of sludge pre-treatment method on bio-hydrogen production by dark fermentation of waste ground wheat. Int J Hydrogen Energ. 2009;34:8543-8.
7. Chen SD, Lee KS, Lo YC, Chen WM, Wu JF, Lin CY, et al. Batch and continuous biohydrogen production from starch hydrolysate by Clostridium species. Int J Hydrogen Energ. 2008;33:1803-12.
8. Qian CX, Chen LY, Rong H, Yuan XM. Hydrogen production by mixed culture of several facultative bacteria and anaerobic bacteria. Prog Nat Sci. 2011;21:506-11.
9. Lin CY, Lee CY, Tseng IC, Shiao IZ. Biohydrogen production from sucrose using base-enriched anaerobic mixed microflora. Process Biochem. 2006;41:915-9.
10. Lin CY, Hung WC. Enhancement of fermentative hydrogen/ethanol production from cellulose using mixed anaerobic cultures. Int J Hydrogen Energ. 2008;33:3660-7.
11. Zhang C, Xing XH. Quantification of a specific bacterial strain in an anaerobic mixed culture for biohydrogen production by the aerobic fluorescence recovery (AFR) technique. Biochem Eng J. 2008;39:581-5.
12. Argun H, Kargi F, Kapdan IK. Microbial culture selection for bio-hydrogen production from waste ground

wheat by dark fermentation. Int J Hydrogen Energ. 2009;34:2195-200.
13. Rolz C, Decabrera S. Ethanol from Sugar-Cane - Flask Experiments Using the Ex-Ferm Technique. Appl Environ Microb. 1980;40:466-71.
14. Rolz C, Decabrera S, Dearriola MC. Effects of Sugarcane Chip Sizes on Their Conversion to Ethanol Using the Ex-Ferm Process. Chem Eng Commun. 1986;45:111-8.
15. Decabrera S, Dearriola MC, Morales E, Demicheo F, Rolz C. Ex-Ferm Ethanol-Production in Packed-Bed Fermenters - a 3 Cycle Operation Employing Chipped Sugarcane. Biotechnol Lett. 1981;3:497-502.
16. Decabrera S, Dearriola MC, Morales E, Demicheo F, Rolz C. Ex-Ferm Ethanol-Production Using Chipped Sugarcane in Packed-Bed Fermenters. Eur J Appl Microbiol. 1982;14:21-8.
17. Decabrera S, Dearriola MD, Morales E, Demicheo F, Rolz C. Ex-Ferm Ethanol-Production Using Peeled Ground Sugarcane in Packed-Bed Fermenters. J Ferment Technol. 1982;60:77-86.
18. Decabrera S, Dearriola MD, Rolz C. Effects of Sugarcane Chip Pretreatments on Their Conversion to Ethanol Using the Ex-Ferm Process - Particle-Size, Storage, Drying or Ensilage. Enzyme Microb Tech. 1986;8:491-7.
19. Rolz C. A New Technology to Ferment Sugar-Cane Directly-the Ex-Ferm Process. Process Biochem. 1980;15:2-+.
20. Rolz C. New Technology to Ferment Sugar-Cane Directly the Ex-Ferm Process. Int Sugar J. 1980;82:47-51.
21. Keskin T, Hallenbeck PC. Hydrogen production from sugar industry wastes using single-stage photofermentation. Bioresource Technol. 2012;112:131-6.
22. Panagiotopoulos IA, Karaoglanoglou LS, Koullas DP, Bakker RR, Claassen PAM, Koukios EG. Technical suitability mapping of feedstocks for biological hydrogen production. J Clean Prod. 2015;102:521-8.
23. Ozkan L, Erguder TH, Demirer GN. Effects of pretreatment methods on solubilization of beet-pulp and bio-hydrogen production yield. Int J Hydrogen Energ. 2011;36:382-9.
24. Ozgur E, Mars AE, Peksel B, Louwerse A, Yucel M, Gunduz U, et al. Biohydrogen production from beet molasses by sequential dark and photofermentation. Int J Hydrogen Energ. 2010;35:511-7.
25. Zhu GF, Liu CX, Xu GH, Li JZ, Gao YL, Chen LJ, et al. Simultaneous Biohydrogen Production and Wastewater Treatment in Continuous Stirred Tank Reactor (CSTR) Using Beet Sugar Wastewater. Iceet: 2009 International Conference on Energy and Environment Technology, Vol 2, Proceedings. 2009:737-+.
26. Dubois M, Gilles KA, Hamilton JK, Rebers PA, Smith F. Colorimetric method for determination of sugars and related substances. Anal Chem. 1956;8:350-66.
27. Greenberg AE, Clesceri LS, Eaton AD, editors. Standard methods for the examination of water and wastewate. 21st edn American Public Health Association (APHA). Washington DC, USA. 2005.
28. Han SK, Shin HS. Biohydrogen production by anaerobic fermentation of food waste. Int J Hydrogen Energ. 2004;29:569-77.

Hydrogen gas production from food wastes by electrohydrolysis using a Statical design approach

Ebru Çokay
Department of Environmental Engineering, Dokuz Eylul University, Buca, Izmir, Turkey
Email:ebru.cokay@deu.edu.tr

Abstract
Food waste was subjected to different DC voltages for hydrogen gas production by using aluminum electrodes and a DC power supply. Effects of applied DC voltage on the rate and extent of hydrogen gas production were investigated. Effects of the applied DC Voltage, reaction time and initial water content (%) on percent hydrogen gas production, cumulative hydrogen production and percent TOC removals from food wastes by electrohydrolysis were investigated. Box-Behnken statistical experiment design was used for optimizing these reaction conditions. The optimal DC voltage/reaction time/water content ratio resulting in the maximum hydrogen gas production (100%), the highest cumulative hydrogen production (7000 mL), and TOC removal (33%) was found to be 5/75/80. Electrohydrolysis of food waste was proven to be an effective method for hydrogen gas production.

Keywords: Hydrogen gas; TOC removal; DC voltage; electrohydrolysis; food wastes, Box-Behnken

1. Introductıon

Search for clean and high energy fuels has gained significant attention over the last fifty years due to recent energy shortages and air pollution caused by the utilization of fossil fuels. Among the other alternative clean fuels, hydrogen gas stands out due to relatively high energy content (122 kJ g^{-1}) as compared to fossil fuels. [1].

Hydrogen gas is identified as one of the major clean energy sources of the future due to its high energy content and reduced green house gas emissions as compared to fossil fuels. Hydrogen gas is not readily available in nature and is produced by costly processes such as steam reforming of natural gas or electrolysis of water requiring high energy inputs. [2-3]. Hydrogen gas production by fermentation of carbohydrate rich renewable raw materials such as biomass has been considered as a viable approach due to operation under mild conditions. Major obstacles in bio-hydrogen production by fermentation are low hydrogen yields and formation rates due to slow bacterial metabolisms. [4-7]. In order to replace photo-fermentation by a more effective hydrogen production method, external DC voltage was applied to dark fermentation effluent to yield much faster and more efficient hydrogen gas production as compared to photo-fermentation [8]. For that reason, hydrogen gas production by electrohydrolysis of organic compounds present in waste materials is a rather new approach.

In our previous studies on H_2 gas production from electrohydrolysis of waste organic compounds, anaerobic sludge, olive mill wastewater (OMW) and leaachate wastewater were used as raw materials for effective H_2 gas production [5, 6]. Our approach for hydrogen gas production by electrohydrolysis of food waste is entirely novel and different from the reported studies in terms of hydrogen gas formation mechanism. For that reason food wastes was used as the raw material for hydrogen gas production in this study.

Design of experiments

Statistical design of experiments reduces the number of experiments to be performed, considers interactions among the variables and can be used for optimization of the operating parameters in multivariable systems. A modified central composite experimental design known as the Box-Behnken design, is an independent, rotatable quadratic design with no embedded factorial or fractional factorial points where the variable combinations are at the midpoints of the edges of the variable space and at the center [8]. By careful design and analysis of experiments, Box-Behnken design allows calculations of the response function at intermediate levels which were not experimentally studied and shows the direction if one wishes to change the input levels in order to decrease or increase the response [9].

The major objective of this study is to investigate the effects of the applied DC Voltage, reaction time and initial water content (%) on percent hydrogen gas production, cumulative hydrogen production and percent TOC removals from food wastes by electrohydrolysis. Box-Behnken statistical experiment design was used for optimizing these reaction conditions.

2. Materıals And Methods

A schematic diagram of the experimental set up is depicted in Figure 1. The experimental set-up consisted of a DC power supplier, two aluminum electrodes and 1 L serum bottles. The food waste (300 ml) was placed inside serum bottles. Aluminum electrodes were immersed inside the bottles containing the food wastes and connected to the DC power supply by wires.

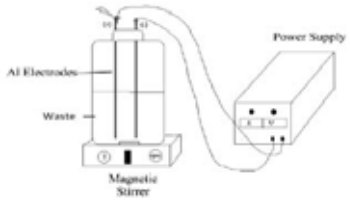


Fig. 1. A schematic diagram of the experimental set-up

The applied DC voltages (V) and the amperes (A) were monitored during the course of experiments. The applied voltage was kept constant throughout every experiment. Hydrogen gas was sampled from the head space of the bottles by using gas-tight glass syringes and hydrogen concentration was determined by using a gas chromatograph. The cumulative hydrogen gas produduction was determined by adding the hydrogen volume determined by the water displacement method to the hydrogen gas in the head space of the bottles as desribed in our previous studies [5-6]. Food wastes samples were removed from the bottles everyday and total organic carbon (TOC) analyses was using A Shimadzu TOC Analyzer.

3. Results and Discussion

Box-Behnken statistical experiment design and response surface methodology (RSM) were used for this purpose by considering the reaction time (X_1), DC voltages (X_2), water content (X_3) and) as the independent and percent hydrogen gas production (Y_1), cumulative hydrogen production (Y_2) and percent TOC removals (Y_3) as the dependent variables. The Box-Behnken statistical experiment design and the RSM were reported to be useful in optimization of the three variable response functions, predicting the response of the fitted model and checking the adequacy of the model by the ANOVA tests. The low, center and high levels of each variable are designated as -1, 0, and +1 respectively as shown in Table 1.

Table 1. The levels of variables in Box-Behnken statistical experiment design

Variable	Symbol	Low (-1)	Center (0)	High (+1)
Reaction Time (H)	X_1	25	50	75
DC Voltage, (V)	X_2	1	3	5
Water Content, (%)	X_3	60	75	90

The dependent variables (or objective functions) were percent hydrogen gas production (Y_1), cumulative hydrogen gas production (Y_2), and percent TOC removal (Y_3). The experimental conditions and observed results as removal percentages using Box-Behnken design for hydrogen gas production are also presented in Table 2.

Table 2. Results of the Box-Behnken experiments at the pre-determined experimental points
HGP: Hydrogen Gas production, CHGV: Cumulative Hydrogen Gas Volume

Run No	Actual and coded levels of variables			Experimental results		
	X_1, Reaction Time (h)	X_2, DC Voltage, (V)	X_3, Water Content, (%)	Y_1, HGP (%)	Y_2, CHGV (ml)	Y_3, TOC Removal (%)
1	50	1	60	26.00	63.20	3.83
2	**75**	**5**	**75**	**100.00**	**6411.00**	**32.80**
3	75	1	75	32.80	218.00	8.63
4	50	5	60	94.10	1302.00	7.89
5	**75**	**3**	**90**	**100.00**	**4250.00**	**22.25**
6	75	3	60	100.00	1792.00	11.20
7	**50**	**5**	**90**	**100.00**	**4255.00**	**16.45**
8	25	3	90	75.80	985.00	7.80
9	25	1	75	14.00	34.00	0.90
10	50	1	90	16.40	76.00	1.80
11	25	5	75	79.40	1032.00	2.32
12	25	3	60	55.70	446.00	5.58
13	50	3	75	90.80	2204.00	7.72
14	50	3	75	90.00	1873.00	7.72
15	50	3	75	92.00	2203.00	7.10

3.1. Hydrogen gas evolution

Figure 2 depicts variation of hydrogen gas production (%) with time for different applied DC voltages betwen 1 V and 5 V. Hydrogen gas production increased up to 4V and then slightly decrased with increasing voltages above 4V at 75 hour reaction time. The highest cumulative hydrogen gas (6410 ml) was obtained with 5V. Percent hydrogen gas in the gas phase reached to pure H_2 gas (100 % H_2) at 4V and 5 V. Pure hydrogen gas formation in the gas phase is a significant development since the produced hydrogen gas can directly be used in fuel cells.

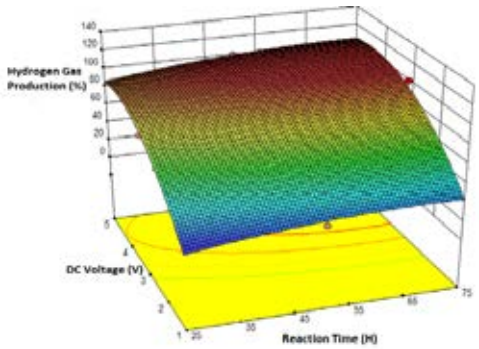


Fig. 2. Variation of percent hydrogen gas with different reaction times at different DC voltages by electrohydrolysis method.

4. Conclusion

The Box-Behnken statistical experiment design was used to generate statistically reliable results for hydrogen gas production by electrohydrolysis and to determine the optimum reaction time, DC voltage and water content maximizing the hydrogen gas production, cumulative hydrogen gas volume and TOC removal. Reaction time and DC voltage played important roles for hydrogen gas production using electrohydrolysis.

Reaction time and DC voltage played important roles for hydrogen gas production using electrohydrolysis. According to experiments and ANOVA results, water content of waste is not important parameter for the production of hydrogen gas, also organic matter removal in waste.

The optimal DC voltage/reaction time/water content ratio resulting in the maximum hydrogen gas production (100%), the highest cumulative hydrogen gas production (7000 mL) and TOC removal (33%) was found to be 5/75/80. Electrohydrolysis of food waste was proven to be an effective method for hydrogen gas production and TOC removal.

References

1. Winter CJ. Into the hydrogen energy economy-milestones. Int J Hydrogen Energy 2005;30:681e5.
2. Kapdan IK, Kargi F. Biohydrogen production from waste materials. Enzyme Microb Technol 2006;38:569-82.
3. Das D, Veziroglu TN., Hydrogen production by biological processes: survey of literature. Int J Hydrogen Energy 2001;26:13-28.
4. Call D, Logan BE. Hydrogen production in a single chamber microbial electrolysis cell lacking a membrane. Environ Sci Technol 2008;42:3401-6.
5. Kargi F, Catalkaya Ebru C, Uzuncar S., Hydrogen gas production from waste anaerobic sludge by
6. electrohydrolysis: effects of applied DC voltage. Int J Hydrogen Energy 2011;36:2049-56.
7. Kargi F, Catalkaya EC. Hydrogen gas production from olive mill wastewater by electrohydrolysis with simultaneous COD removal. Int J Hydrogen Energy 2011;36:3457-64.
8. Sastry SV, Khan MA., Aqueous based polymeric dispersion: Plackett–Burman design for screening of formulation variables of atenolol gastrointestinal therapeutic system, Pharm. Acta Helv. 73 (1998) 105-112.
9. Hamed E, Sakr A., Application of multiple response optimization technique to extended release formulations design, J. Control. Rel. 73 (2001) 329-338.

ORAL PROCEEDINGS

Optimization of Particle Number, Substrate Concentration and Temperature of Batch Immobilized Reactor System for Biohydrogen Production by Dark Fermentation

Pelin Gokfiliz Yildiz[1], Ilgi Karapinar[2]
[1]Dokuz Eylul University, The Graduate School of Natural and Applied Sciences, Biotechnology Department, Izmir, Turkey
[2]Dokuz Eylul University, Department of Environmental Engineering, Izmir, Turkey
Email: pelingokfiliz@hotmail.com, ilgi.karapinar@deu.edu.tr

Abstract
Using immobilized growth cultures for biohydrogen production by dark fermentation is superior to suspended cultures since higher hydrogen production yields, volumes and rates can be obtained by immobilized cultures. One of the important factors in immobilized bioprocesses is the type of support material used for immobilization of microorganisms. Hydrogen productivity of the bioprocess can be enhanced by using porous support materials which provide high biomass holding capacity and help better gas retrieve in the process. By considering these facts, biohydrogen production by dark fermentation in an immobilized batch process was studied and fermentation conditions which maximize hydrogen yield and production rate was optimized by using Box-Wilson statistical experimental design method in this study. Support particle used for immobilization purpose was polyester fiber with bead diameter Dp= 0.5 cm. Acid hydrolyzed wheat starch syrup, which was obtained by hydrolysis of waste wheat powder by sulfuric acid at pH=2 and T= 90 ºC for 15 min, was used as substrate. Heat and acid pretreated anaerobic sludge was used as inoculum. The independent variables were X_1; particle number (PN=120-240), X_2; initial total sugar concentration (TS_0=10-30 g/l) and X_3; fermentation temperature (T=35-55ºC). Quadratic response equations for both independent variables were developed, coefficients of response equations were determined. The optimum conditions for the maximum hydrogen yield (Y_{H2} = 3.21 mol H_2/mol glucose) and production rate (HPR= 73.3 ml H_2/h) were predicted as PN= 240, TS_0 = 10 g/l and T= 44.9 ºC..

Keywords: Biohydrogen; Box–Wilson design; dark fermentation; immobilization; optimization.

1. Introduction

Hydrogen production by dark fermentation is a cost effective and environmentally friendly method which provides utilization of organic wastes and hence waste management with energy generation [1]. The challenge in the biohydrogen production by dark fermentation is to obtain high yields and rates of hydrogen formation to make the process capable of compete with the other existing or developing physical and chemical production technologies [2]. Therefore, one of the research interests on this field is to develop bioprocesses to obtain higher hydrogen yields. Recently, the attentions have been devoted to immobilized bioprocess technologies considering the benefits of high biomass holding capacity, relatively feasible operation conditions and also better process performance. Also, it was shown that immobilized systems are superior over suspended ones in terms of hydrogen production performance [3,4].

There are numbers of factors like fermentation environment, substrate and nutrients concentrations, microorganism type that affect process performance of fermentation and it may be difficult to determine the optimal operating conditions for maximum hydrogen yield. Response surface methodology (RSM) such as Box-Wilson, Central Composite Design and Box-Behnken statistical designs are the most preferred ones for optimization of conditions / bioprocesses due to their advantages like obtaining a large amount of information from a small number of experiments and analyzing the interaction effects of independent variables on the response [5,6]. Even though RSM methods have been recently applied for H_2 production by suspended cultures [7-9], there are limited numbers of research studies considering optimization of immobilized process for hydrogen production. One of them is optimization of immobilized hydrogen production process using mycelia obtained from *Aspergillus niger* Y3 fermentation as a carrier material for the factors such as mycelia pellet dosage, mycelia pellet size, and culturing time [10]. Detailed RSM studies are required for hydrogen production in an immobilized system to gain more knowledge about the effects of the factors in this system. By considering these facts, this study was designed to determine the optimum particle number, initial substrate concentration and temperature to maximize hydrogen yield (Y_{H2}, mol H_2/mol glucose) and hydrogen production rate (HPR, ml H_2/h) by dark fermentation in the batch immobilized hydrogen production process. Box–Wilson statistical experiment design method was applied to evaluate the effects of these factors on the yield and the rate of production.

2. Experimental Study

The mixed microbial culture was obtained from the acidogenic phase of anaerobic wastewater treatment plant of PAK MAYA Baker's Yeast Company in Izmir, Turkey. Anaerobic sludge was diluted with pure water (1:1 ratio). To inhibit methanogens and to select spore forming hydrogen producing bacteria in the sludge, it was boiled at 100 ºC for an hour and pH of the sludge was adjusted to 5.9 during heat pretreatment.

Acid hydrolyzed waste wheat powder (AHWWP), which was obtained from Soke Flour Company in Soke, Aydın, Turkey, was used as substrate. The wheat was first ground and then sieved down to 70 mm size. In order to hydrolyze wheat starch to maltose and glucose units, the ground wheat was mixed with H_2SO_4 solution (pH = 2) and autoclaved at T = 90 ºC for t = 15 min.[11] The solid phase of hydrolyzed wheat powder solution was separated by centrifugation at 8000 rpm for 20 min. Supernatant sugar solution was neutralized to pH = 7 by addition of 10% NaOH. Oxidation reduction potential was adjusted to ORP < -150 mV by adding Na-thioglycolate (200 mg/L) to the feed in the beginning of the experiments. $(NH_4)_2SO_4$, KH_2PO_4 and $FeSO_4$ were added to the fermentation medium at the optimal ratio of N/P/Fe/C = 2/0.8/1.5/100 as nitrogen, phosphorus and iron source, respectively, to overcome nutrient limitations [7].

Polyester fiber was used as support material for immobilization. Particles were prepared in round shape with particle diameter approximately Dp=0.5 cm and they were surrounded with stainless steel metal wire to prevent particles from dispersing. Batch fermentation experiments were conducted in 610 ml serum bottles with 200 ml fermentation volume. Bottles containing support particles and fermentation medium were inoculated with heat treated sludge culture. Particle number, initial substrate concentration and fermentation temperature were varied according to the Box-Wilson experimental conditions given in Table 1. Initial pH of fermentation medium was adjusted to 5.5-6.0. ORP was controlled under -100 and -300 mV. The bottles were closed with silicone rubber stoppers and screw caps. Argon gas was passed through the cultivation media to maintain anaerobic conditions.

Box–Wilson statistical experiment design method was used to determine the effects of particle number, initial substrate concentration and fermentation temperature on Y_{H2}, (mol H_2/mol glucose) and HPR (ml H_2/h). Particle number (X_1), initial substrate concentration (X_2) and temperature (X_3) were independent variables while the Y_{H2} and the HPR were the objective functions. Particle number (X_1) was varied between PN=120 and 240, initial substrate concentration (X_2) was between TS_0= 10 and 30 g/l and temperature (X_3) range was T=35-55 ºC. The experiments consisted of six axial (A), eight factorial (F) and centre (C) points. The centre point was repeated three times. The experimental conditions determined by the Box–Wilson statistical design method were given in Table 1.

Table 1. Experimental conditions of the Box-Wilson statistical design.

Experimental point	*X1*		*X2*		*X3*	
	Coded value	Actual value	Coded value	Actual value	Coded value	Actual value
A_1	+1.73	215	0	20	0	45
A_2	-1.73	145	0	20	0	45
A_3	0	180	+1.73	26	0	45
A_4	0	180	-1.73	14	0	45
A_5	0	180	0	20	+1.73	51
A_6	0	180	0	20	-1.73	39
F_1	+1	240	+1	30	+1	55
F_2	+1	240	+1	30	-1	35
F_3	+1	240	-1	10	+1	55
F_4	+1	240	-1	10	-1	35
F_5	-1	120	+1	30	+1	55
F_6	-1	120	+1	30	-1	35
F_7	-1	120	-1	10	+1	55
F_8	-1	120	-1	10	-1	35
C_1	0	180	0	20	0	45
C_2	0	180	0	20	0	45
C_3	0	180	0	20	0	45

X1; Particle number, X2; Initial substrate concentration (g/l), X3;Temperature (ºC)

The following quadratic function is used for correlation of the responses with independent three variables as X_1, X_2 and X_3.

$$Y = \beta_0 + \beta_1 X_1 + \beta_2 X_2 + \beta_3 X_3 + \beta_{12} X_1 X_2 + \beta_{13} X_1 X_3 + \beta_{23} X_2 X_3 + \beta_{11} X_1^2 + \beta_{22} X_2^2 + \beta_{33} X_3^2 \quad (1)$$

where Y is the predicted response for Y_{H2} and HPR; β_0 is model constant; β_1, β_2 and β_3 are the linear coefficients; β_{12}, β_{13} and β_{23} are the coefficients of two level interactions of variables; β_{11}, β_{22} and β_{33} are the quadratic coefficients. The experimental results obtained from the experiments presented in Table 1 were used for determination of the coefficients in Eq. 1 using a Design Expert 7.0 software (trial version) by regression analysis.

Samples removed from the fermentation medium were centrifuged at 8000 rpm. The clear supernatants were used for total sugar analysis. Total sugar concentrations were determined by the acid-phenol spectrometric method [12]. The total gas volume produced was determined everyday by water displacement method by using sulfuric acid (2%) and NaCl (10%) containing solution. Hydrogen gas was sampled from the head space of the bottles by using gas-tight glass syringes. Hydrogen gas concentration in the gas phase and in the head space of the bottle after argon gas was passed through was measured by using a gas chromatograph (HP Agilent 6890). The column was Alltech, Hayesep D 80/100 6" × 1/8" × 085". Nitrogen gas was used as carrier with a flow rate of 30 ml min^{-1} and the head pressure was 22 psi. Temperatures of the oven, injection, detector, and filament were 35 ºC, 120 ºC, 120 ºC, 140 ºC, respectively. pH and ORP of the fermentation medium were monitored everyday by using a pH meter and ORP meter with relevant probes (WTW Sci., Germany). pH was maintained between 5.5 and 6 by manual pH control, using 5 M NaOH solution. ORP values varied between −100 and −300 mV, in general.

In batch fermentations, cumulative hydrogen gas volume (CHV) versus time data were correlated with the Gompertz equation (Eq. 2) to determine the constants by regression analysis with Statistica 5. The Gompertz equation has the following form:

$$H_{(t)} = P\ exp\left\{-exp\left[\frac{R_m e}{P}(\lambda - t) + 1\right]\right\} \quad (2)$$

where $H_{(t)}$; CHV (ml) at any time t, P; the maximum potential hydrogen formation (ml), R_m; the maximum rate of hydrogen formation, HPR (ml/h), λ; duration of the lag phase (h), e; 2.718, t; time (h)

3. Results and Discussion

Variations of Y_{H2} and HPR with particle number, initial substrate concentration and temperature were investigated by using Box-Wilson statistical experiment design approach. The linear, two factor interaction and quadratic coefficients of the response functions for Y_{H2} and HPR were determined by regression analysis. The response equation for yield and rate with coefficients were given in Eq. 3 and Eq. 4, respectively. Predicted responses at the experimental points were calculated by using developed response equations.

$$Y_{yield} = -11.1 - 0.0883X_1 + 0.154X_2 + 0.821X_3 - 0.000656X_1X_2 - 0.000206X_1X_3 - 0.000413X_2X_3 + 0.000310X_1^2 - 0.000391X_2^2 - 0.00831X_3^2 \quad (3)$$

$$Y_{rate} = -663 - 0.734X_1 - 9.30X_2 + 37.1X_3 - 0.0120X_1X_2 - 0.000192X_1X_3 + 0.0307X_2X_3 + 0.00296X_1^2 + 0.2491X_2^2 - 0.415X_3^2 \quad (4)$$

The results of the Box-Wilson design experiments are presented in Table 2 along with the predicted values from the response function. The predictions for Y_{H2} (R^2=0.89) and HPR (R^2=0.94) were in good agreement with the experimental results (Table 2)

The statistical significance of the fitting model for Y_{H2} and HPR, as well as linear, two level interactions and the quadratic terms in the fitting model were evaluated through variance analysis (ANOVA). The results of ANOVA for yield and rate were given in Table 3. "Prob > F" values of the model terms which are less than 0.05 were evaluated as significant. As indicated in Table 3, model term (β_0) for Y_{H2} and HPR were significant. Statistical analysis also showed that temperature, the interaction between particle number and TS_0, quadratic effect of particle number were significant for Y_{H2}. Besides, the interaction between particle number and TS_0, quadratic effect of TS_0 and temperature affected HPR significantly.

3.1 Optimization of hydrogen production in immobilized batch process

The optimum operating conditions of dark fermentation were determined by using Design Expert 7.0 software (trial version). By using response function coefficients, within the range of factors in Box-Wilson experimental design, values of independent variables that maximize Y_{H2} and HPR were determined. Optimization tool of the software was

run to determine the conditions that maximize both yield and rate. It was found that hydrogen yield of Y_{H2} = 3.21 mol H_2/mol glucose and hydrogen production rate of HPR= 73.3 ml H_2/h could be obtained when particle number is PN = 240; initial substrate concentration is TS_0 = 10 g/l and temperature is T = 44.9 ºC with desiriblity level of D=0.988 (Fig. 1).

Table 2. Observed and predicted values of responses at experimental points

Experimental point	Hydrogen yield (Y_{H2}) (mol H_2/mol glucose)		Hydrogen production rate (HPR) (ml H_2/h)	
	Observed	Predicted	Observed	Predicted
A_1	2.18	2.11	33.97	30.83
A_2	2.01	2.04	24.21	25.01
A_3	1.50	1.69	29.99	32.55
A_4	1.90	1.68	38.75	33.98
A_5	1.48	1.57	10.5	10.9
A_6	1.35	1.23	10.39	7.78
F_1	1.90	1.74	22.39	20.47
F_2	1.39	1.50	7.76	9.36
F_3	2.44	2.59	28.92	31.16
F_4	2.25	2.18	32.69	32.32
F_5	2.59	2.66	24.61	25.18
F_6	2.07	1.93	15.65	13.61
F_7	2.04	1.93	8.36	6.96
F_8	0.87	1.03	5.54	7.66
C_1	1.91	1.70	25.19	24.29
C_2	1.42	1.70	22.39	24.29
C_3	1.68	1.70	19.32	24.29
R^2	0.89		0.94	

Table 3. ANOVA for hydrogen yield (Y_{H2}, mol H_2/mol glucose) and hydrogen production rate (HPR, ml H_2/h)

Source	Sum of Squares		Degree of freedom		Mean Square		F Value		p-value (Prob > F)	
	Y_{H2}	HPR	Y_{H2}	HPR	Y_{H2}	HPR	Y_{H2}	HPR	Y_{H2}	HPR
Model	2.80	1537.5	9	9	0.311	171	5.96	12.2	0.0140	0.00168
X_1	0.0299	216	1	1	0.0299	216	0.572	15.4	0.474	0.00575
X_2	0.00139	12.3	1	1	0.00139	12.3	0.0266	0.875	0.875	0.381
X_3	0.699	59.1	1	1	0.699	59.1	13.4	4.21	0.00808	0.0794
X_1X_2	1.24	418	1	1	1.24	418	23.8	29.7	0.00180	0.000952
X_1X_3	0.123	0.106	1	1	0.123	0.106	2.35	0.00753	0.169	0.933
X_2X_3	0.0136	75.3	1	1	0.0136	75.3	0.261	5.36	0.625	0.0538
X_1^2	0.446	40.7	1	1	0.446	40.7	8.55	2.90	0.0222	0.133
X_2^2	0.000576	234	1	1	0.000576	234	0.0110	16.7	0.919	0.00469
X_3^2	0.260	650	1	1	0.260	650	4.98	46.3	0.0608	0.000253
Residual	0.365	98.3	7	7	0.0522	14.0				
Lack of Fit	0.245	*81.1*	5	5	0.0490	*16.2*	0.815	*1.88*	0.631	*0.382*
Pure Error	0.120	*17.2*	2	2	0.0601	*8.62*				
Cor Total	3.17	1635.8	16	16						

X1; Particle number, X2; Initial substrate concentration (g/l), X3; Temperature (ºC)

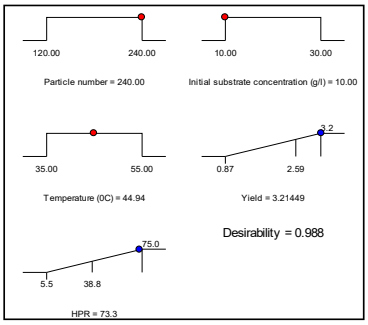


Fig. 1. Optimum dark fermentation conditions resulting for the maximum hydrogen yield (Y_{H2}, mol H_2/mol glucose) and hydrogen production rate (HPR, ml H_2/h).

3.2 The effect of independent variables on hydrogen yield and hydrogen production rate

Quadratic response equations were used to predict the hydrogen yields and hydrogen production rates at the conditions within the ranges of factors and then three-dimensional response surface plots were obtained. One of the independent variables was set at its optimum value given in Fig. 1 and effects of other variables on the response were investigated within the experimental range.

Fig. 2a depicts the variation of Y_{H2} with fermentation temperature and particle number at initial total sugar concentration of TS_0= 10 g/l. Although the particle numbers were changed in the reactor, optimum temperature range did not vary and it was observed between T=40-50 ºC. This may have caused due to moderate thermophiles were dominant in the microbial culture. Kumar et al. [13] demonstrated the relationship between optimum fermentation temperature and dominant bacterial species in the inoculums. They analyzed optimum substrate concentration, pH and temperature by using RSM for hydrogen production from de-oiled jatropha waste inoculated with heat pretreated sewage sludge. Optimum temperature was determined as 55.1 ºC and PCR-DGGE results demonstrated that *Clostridium* sp. such as *C. thermopalmarium*, *C. thermobutyricum*, as well as *Bacillus* sp. were the predominant organisms in the sludge. Fig. 2b shows variation of Y_{H2} with particle number and initial substrate concentration at constant fermentation temperature of T=45 ºC. The yield increased from 2.40 to 3.12 mol H_2/mol glucose with increasing substrate concentration from 10 g/l to 30 g/l at low particle number as PN=120. However, for the high particle numbers such as at PN=240, the yield decreased from 3.21 to 2.45 mol H_2/ mol glucose with increasing substrate concentration. The effect of temperature and initial substrate concentration on the yield of formation was evaluated at particle number PN= 240 in Fig. 2c. Optimum temperature, which gave the highest hydrogen yields at all substrate concentrations, was around 45 ºC. On the other hand, increasing the initial substrate concentration from 10 g/l to 30 g/l resulted in a substantial decrease in the yield for the studied range of fermentation temperature.

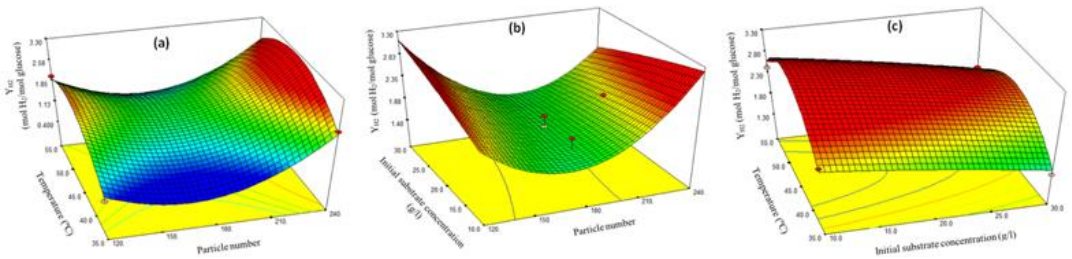


Fig. 2. The three-dimensional response surface plots showing the effects of (a) temperature and particle number (TS_0= 10 g/l), (b) initial substrate concentration and particle number (T= 45 ºC), (c) temperature and initial substrate concentration (PN=240) on hydrogen yield (Y_{H2}, mol H_2/mol glucose).

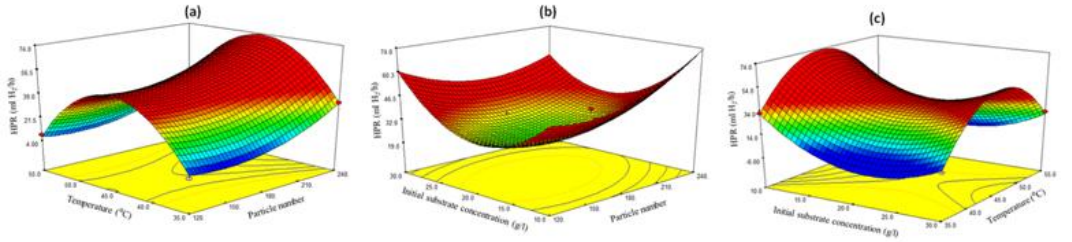


Fig. 3. The three-dimensional response surface plots showing the effects of (a) temperature and particle number (TS_0=10 g/l), (b) initial substrate concentration and particle number (T= 45 ºC), (c) initial substrate concentration and temperature (PN=240) on hydrogen production rate (HPR, ml H_2/h).

Hydrogen production rate was calculated by using Gompertz equation. The results depicted that fermentation temperature had a substantial effect on the production rate. The highest production rates were obtained between 45 ºC and 50 ºC for any particle number at 10 g/l substrate concentration (Fig. 3a). Similar to hydrogen yield, the maximum rate was observed at PN=240. Fig. 3b shows the variation of HPR with initial substrate

concentration and particle number at T= 45 ºC. When both TS_0 and PN increased, HPR decreased gradually and reached to its minimum value at TS_0 of 20 g/l and PN of 180. The maximum rate was predicted as 74 ml/h at PN=240 and TS_0= 10 g/l. When particle number was set to PN=240, optimum temperature was around 45 ºC at each substrate concentration (Fig. 3c). Lower rates were observed at substrate concentrations above 20 g/l in comparison to the rate at low substrate concentrations around 10 g/l.

4. Conclusions

One of the research challenges in hydrogen production by a biological process is to obtain maximum production rate and yield close to the theoretical one as much as possible. Operating conditions such as particle number (PN), initial substrate concentration (TS_0) and temperature (T) in the immobilized batch fermentation affected the process performance. The optimum conditions resulting in the maximum hydrogen yield of Y_{H2} = 3.21 mol H_2/mol glucose, and production rate of HPR = 73.3 ml H_2/h were predicted as PN= 240, TS_0= 10 g/l and T= 44.9 ºC. A substantial improvement in the productivity was achieved by optimizing fermentation conditions.

Acknowledgements

This study was supported by Dokuz Eylul University with grant number 2011.KB.FEN.028.

References

1. Kapdan IK, Kargi, F.Bio-hydrogen production from waste materials. Enzyme Microb Tech. 2006;38:569-82.
2. Singh L, Wahid ZA. Methods for enhancing bio-hydrogen production from biological process: A review. J Ind Eng Chem. 2015;21:70-80.
3. Keskin T, Giusti L, Azbar N. Continuous biohydrogen production in immobilized biofilm system versus suspended cell culture. Int J Hydrogen Energ. 2012;37:1418-24.
4. Gokfiliz P, Karapinar I. The effect of support particle type on thermophilic hydrogen production by immobilized batch dark fermentation. Int J Hydrogen Energ. 2017;42:2553–61.
5. Bas D, Boyaci IH. Modeling and optimization I: Usability of response surface methodology. J Food Eng. 2007;78:836-45.
6. Montgomery DG. Design and analysis of experiments. fifth ed, John Wiley & Sons, the United States of America, 2001.
7. Oztekin R, Kapdan IK, Kargi F, Argun H. Optimization of media composition for hydrogen gas production from hydrolyzed wheat starch by dark fermentation. Int J Hydrogen Energ. 2008;33:4083-90.
8. Mangayil R, Aho T, Karp M, Santala V. Improved bioconversion of crude glycerol to hydrogen by statistical optimization of media components. Renew Energ. 2015;75:583-89.
9. Mishra P, Das D. Biohydrogen production from *Enterobacter cloacae* IIT-BT 08 using distillery effluent. Int J Hydrogen Energ. 2014; 39:7496-507.
10. Zhao L, Cao GL, Yao J, Ren HY, Ma F, Ren NQ, et al. Optimization of immobilization parameters of *Thermoanaerobacterium thermosaccharolyticum* W16 on a new carrier for enhanced hydrogen production. RSC Advances. 2012;2:7391-5.
11. Kapdan IK, Kargi F, Oztekin R. Effects of operating parameters on acid hydrolysis of ground wheat starch: maximization of the sugar yield by statistical experiment design. Starch-Starke. 2011;63:311-8.
12. Dubois M, Gilles K, Hamilton J, Rebers P, Smith F. Colorimetric method for determination of sugars and related substances. Anal Chem. 1956;28:350-6.
13. Kumar G, Bakonyi P, Sivagurunathan P, Nemestóthy N, Bélafi-Bakó K, Lin CY. Improved microbial conversion of de-oiled Jatropha waste into biohydrogen via inoculum pretreatment: Process optimization by experimental design approach. Biofuel Res J. 2015;5:209-14.

Methods of Hydrogen Storage in Energy Conversion Systems

Muhittin Bilgili
Gazi University, Faculty of Engineering, Mechanical Engineering Department,
Maltepe 06570 Ankara, Turkey.
E-mail: bilgili@gazi.edu.tr

Abstract
Alternative systems that meet today's energy needs are an important research topic. The required energy can be provided in different ways instead of the conventional systems. Fuel cells operating by hydrogen can be used to provide this energy conversion. An effective and safe storage method is required for fuel cells to provide the necessary hydrogen during operation. In this study, the current hydrogen storage methods and new developments in these methods will be investigated. For example, in a fuel cell application where the power source is portable, a storage tank that carries hydrogen is needed. During the design of this reservoir, both volume and weight must be considered. In fixed applications, storage may not be so critical, as solutions can be found by connecting fuel cells to a hydrogen-to-natural gas pipeline. However, when a portable application is considered, a tank that stores high-density hydrogen is needed, even if the stack of fuel cells is optimally placed at a very small location. This can cause the total system to be too large to be accepted. Similarly, in automobile applications, a tank that stores hydrogen is needed. The hydrogen tank feeding the system must be at the capacity to pass the total distance covered by the fuel tanks in vehicles using fossil fuels. It is also expected that the energy densities in terms of volume and weight will be at least comparable to those of fossil fuel tanks. In this respect, it can be seen that it is difficult to store hydrogen in volumetric and weight as high energy density. This work will focus on the comparison of hydrogen storage methods developed today and the emerging innovations.

Key Words: Hydrogen; hydrogen storage; compressed hydrogen; liquid hydrogen; metal hydrides

1. Introduction

The need for clean and inexhaustible energy resources is increasing day by day due to the depletion of fossil fuels and harmful effects on the environment. The researches that scientists have done to meet this need in different ways has gained importance. In addition to renewable energy sources, in recent years there have been studies on the use and storage of hydrogen. Hydrogen can be used as fuel in the internal combustion engines. In addition to this, as a result of the electrochemical reaction in the fuel cell with the use of hydrogen, direct current can be generated. Particularly the PEM fuel cell is an alternative electrochemical energy converter device that provides clean energy in transportation and personal electronic applications where low system weight and portability are important [1].

It has been revealed that the widespread use of hydrogen in energy conversion systems will depend on technological developments that reduce cost in hydrogen production. However, the excess electric energy can be used to produce and store hydrogen and this is an alternative for today. The widespread availability of energy stored in this way depends on the development of fuel cell based automotive technologies [2].

Storability is perhaps the most important feature of hydrogen. Nowadays, the fact that there is still no suitable method for storing energy in large quantities increases the importance of hydrogen. If an example is given; If it were possible to store the energy from hydroelectric power plants today, the energy problem would have been solved greatly. Countries such as Canada and New Zealand, where hydroelectric power is abundant, are also known to have launched programs in this direction. This approach is based on continuous operation of hydroelectric power plants at a certain density, while excess energy is evaluated this will be used in the production of hydrogen by electrolysis of water and energy is stored in this way [2].

2. Hydrogen Storage Methods

As the technology that uses hydrogen increases, it needs to develop in the infrastructure that provides hydrogen. At this point, it is critical to store the hydrogen efficiently, efficiently and safely. Hydrogen can be stored in different methods today. Hydrogen can be stored as compressed gas, as liquid hydrogen, as hydride (chemical hydride, metal hydride) and carbon nanotubes. Research on the use of hydrogen as fuel in vehicles contributes to the development of traditional physical storage methods (liquefied hydrogen or pressurized gas containing tanks). However, it is investigated to store hydrogen smaller volumes for portable applications [1].

An automobile application case:

How much hydrogen is required for an automobile application can be calculated from the gasoline tank of a regular gasoline vehicle. An average car is estimated to be 15 gallons (56.7 liters) of storage and multiplied by the density of octane (C_8H_{18}) (917 kg / m^3), it is found to have 52 kg fuel. When the combustion heat of octane is

calculated from chemical reaction reactions, 48.35 [MJ/kg] is calculated. From this, the combustion heat is multiplied by the total fuel amount and the typical gasoline fuel storage capacity is 2.51 × 103 MJ [1].

Table 1. Selected Thermodynamics Properties of Fuels [1]

Property / Fuel	Hydrogen (H_2)	Gasoline* (C_8H_{18})	Ethanol (C_2H_5OH)	Methanol (CH_3OH)
Boiling Point (K)	20	398	352	338
Heat of combustion based on LHV (MJ/kg)	120.97	44.43	28.87	19.94
Density (at STP) (kg/m^3)	0,09	703	789	792
Flammability limits in air (%)	4 - 75	1 – 6.5	3.3 - 19	6 - 36

*the thermodynamics properties of gasoline are determined with octane.

If we assume that the average fuel cell efficiency is 2 times that of a gasoline powered internal engine, we will need half of that value. Therefore, an energy of 1.25x10^3 MJ will be enough. The heat of combustion of hydrogen is 120.97 MJ/kg as shown in Table 1. Thus the amount of hydrogen we need is calculated as 10.4 kg. This amount seems to be quite advantageous when compared with gasoline. The amount needed for gasoline was 52 kg. However, when it is taken into account the density difference, the problem of hydrogen storage will be seen. At the room temperature and pressure, the density of hydrogen is 0.08988 kg/m^3. This value is about 8000 times less than the density of gasoline. If the average driving distance is assumed to be about 550 km with the gasoline tank, the 15 gallon hydrogen tank will have a room temperature and pressure range of only about 0.08 km (80 m). Clearly, there must be a method that is not too large or too heavy to store enough hydrogen.

From this automobile case, it is necessary to store approximately 5-10 kg H_2 depending on the fuel cell efficiency, in order for hydrogen to be able to replace conventional gasoline-powered automobile applications. Similar calculations can be made in portable electronic applications. The hydrogen required for these different applications can technically be stored in a variety of ways [1].

2.1. Compressed Gas

The most common and mature hydrogen storage technology is to store as compressed gas in the pressurised tanks. Those can have the form of vessels or bottles, and are so far manufactured in sizes between 100 kWh to 10 MWh of hydrogen capacity [9]. Hydrogen gas is compressed inside high-pressure tanks. To realize this process that needs energy and the volume occupied by hydrogen gas is generally large. This causes hydrogen to have a lower energy density than conventional gasoline tanks.

Hydrogen is currently stored at pressures of 200-250 bar in 50-liter cylindrical vessels. In addition to this, the storage pressure can reach up to 600-700 bar. Even in 50-liter tanks, the volumetric energy density of hydrogen is very low. On the other hand, storage tanks are heavy due to high pressure [3].

Hydrogen exhibits ideal gas properties at very high pressures and very low temperatures, so the number of molecules and mass at a given pressure and temperature can be calculated from the ideal gas equation (Eq.1 and Eq.2). In these equations, n is the number of moles of hydrogen, M is the Molecular weight and R is ideal gas constant. $\left(R = \frac{R_u}{M}\right)$ The energy that can be obtained from hydrogen is shown in Eq.3.

$$n = \frac{PV}{R_u T} \quad (1) \qquad m = n\,M \quad (2) \qquad E = m\Delta H \quad (3)$$

The ΔH in the Eq.3 indicates the heat of combustion of the hydrogen gas. This value is 120.97 MJ / kg for hydrogen. The volumetric energy density of the hydrogen is calculated by the Eq. 4

$$W_{volumetric} = \frac{E}{V} = \frac{m\Delta H}{V} = \frac{\left(\frac{PV}{RT}\right)\Delta H}{V} = \frac{P\Delta H}{RT} \quad (4)$$

As it can be seen from this correlation, the energy density increases with pressure. However, the increase in pressure is limited by the strength of the storage tank material. For example, MAN's hydrogen-powered trial bus consists of 9 tanks with a capacity of 172 liters and a pressure of 250 bar. This system can store 30 kg hydrogen gas. An energy of 46 GJ is obtained from this gas, but 40 MJ energy is required to compress the gas to 250 bar [3].

Table 2. Properties of Composite Compressed Hydrogen Vessels of 200, 400 and 700 bars [1].

Property	200 bar	400 bar	700 bar
Internal volume (L)	50	50	50
Vessel diameter (m)	0,3	0,3	0,3
Vessel length (m)	1	1	1
Vessel weight (kg)	25	45	85
Stored energy (kWh)	24	43	66
Stored H_2 (kg)	0,7	1,3	2,0
Vessel-to-hydrogen weight ratio	35,7	34,7	42,5
Weight specific energy storage (kWh/kg)	0,96	0,96	0,78
Volume specific storage (kWh/L)	0,48	0,86	1,32

Compressed gas storage tanks are widely used in different sectors daily life (medical oxygen, helium, welding equipment, etc.). The storage pressures of these tanks are normally below 17 MPa (170 bar). According to the International Energy Agency, underground storage is stored at 2 MPa to 18 MPa, during transport from 35 MPa to 50 MPa, and in electric vehicles at pressures up to 70 MPa in in-car storage [10]. Today, in the vast majority of hydrogen fueled vehicles on the road, fiber composite wound tanks operating at 35 MPa service pressure are used for hydrogen storage. In these systems, there is usually an increase in volumetric hydrogen capacity and cost with pressure increase [9].

However, while the technology and safety of these storage tanks are being developed, hydrogen is needed at high pressures up to 71 MPa (700 bar) in vehicle applications [1]. With the 71 MPa pressure tank, mass storage density of 1.3 kWh/kg and storage capacity of 0.8 kWh/L were achieved [5]. It is seen that the US Department of Energy needs to make further progress when the 2010 hydrogen storage targets are compared to 2.0 kWh/kg 1.5 kWh/L. Compared to other competing technologies, however, compressed gas storage has been well developed. Figure 1 shows an improved tank for storing compressed hydrogen at high pressure. Modern high-pressure gas-phase storage tanks are fabricated by embedding plastic or metallic thin inner liner into composite matrix material, high tensile load bearing fiber weave. These tanks, called composite tanks, are considerably lighter and more durable than their predecessor metallic ones [1].

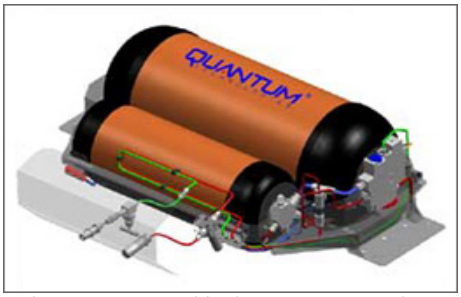


Fig. 1. Compressed hydrogen storage tank [4]

2.2. Liquid Hydrogen

When hydrogen is cooled to 20 K, it will be transformed into the liquid phase and as long as it is kept at 20 K or lower, it will stay in the liquid form. To store hydrogen as a liquid it must first be cooled to the required temperature. This can be achieved by compressing and cooling the hydrogen. Energy is needed for this process and 30 percent of energy stored by the liquid hydrogen is used in the storage process. To preserve the storage tanks from temperature changes the tanks are insulated and to be able to store hydrogen under pressure the tanks are strengthened [3].

The limits regarding liquid hydrogen storage are a function of continuing the tank safety and maintaining the storage temperature that the liquid hydrogen requires. The energy required to bring hydrogen to the liquid phase, the pressure and temperature required to maintain the storage tank makes this method much more expensive than the other methods. The studies focusing on liquid hydrogen storage are focused on composite tank materials and advanced methods to bring hydrogen to the liquid state. The density of liquid hydrogen is 71 kg/m^3; this is also the density of compressed hydrogen gas at 900 bar. Storing hydrogen in the liquid form is a lot safer than compressing the gas because it can be done in drastically lower pressure than compressed gas. Keeping hydrogen at such low temperatures requires good heat insulation of storage depots. In

addition to this, the cooling down process of hydrogen takes a significant amount of time. To liquidize hydrogen 11 kWh/kg energy is needed. This energy also translates to 28% percent of the fuel energy.

In a liquid hydrogen tank several insulation techniques are applied. These are vacuum isolation, vapor cooled radiation shield and several layered heat insulation. These insulation layers are shown in Figure 2 [3].

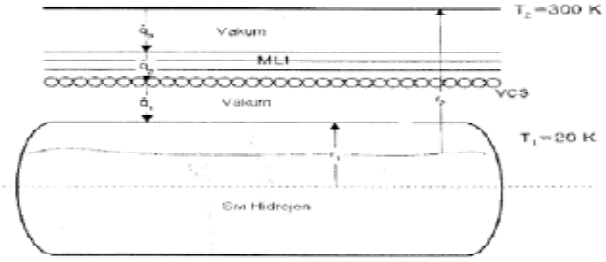


Fig. 2. A cross-section of a liquid hydrogen tank

2.3. Storage in the form of Hydrides

Metals and chemical hydrides offer a potential solution to the hydrogen storage problem. In this method hydrogen is stored as a component of the solid matrix parts and is released by a chemical reaction or heat addition. Storing hydrogen using this method is safer and can be controlled easier. There are two general ways to store hydrogen with this method. These are using chemical hydrides or metal hydrides to store hydrogen.

The main difference between chemical and metal hydrides is the reversibility of the process. Processes using metal hydrides can be reversible if the right temperature and pressure conditions are met whereas processes using chemical hydrides are not. For metal hydride systems the performance of the system depends on the properties of the metal hydride selected for the system. Desired properties of these systems are high specific power output, compact design, long life and low performance degradation in addition to being economic [8].

Both of these ways have the potential to solve the hydrogen storage problem but the method has to reach a high mass storage density and have a lower cost in comparison to other storage methods. Another thing to watch out for in this method is availability rate and the desorption rate of the hydrogen. In contrast to the compressed hydrogen storage method, the release rate of hydrogen from the hydride storage and the matching of the hydrogen that the fuel cell needs is another important issue. To achieve this, suitable heat transfer methods and flow systems should be applied.

As seen in the figure showing the hydrogen stored per unit volume the advantage that metal hydrides offer in comparison to other methods is the higher volumetric energy density of metal hydrides (Figure 3).

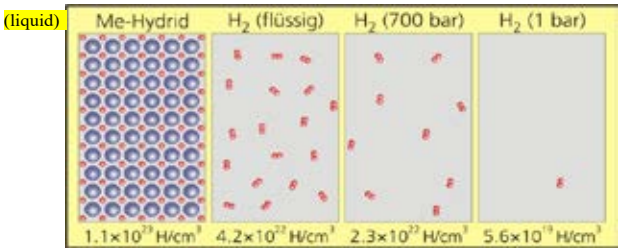


Fig. 3. Comparison of volumetric hydrogen storage densities [6].

During my graduate studies, I have modelled the absorption of $LaNi_5$ in metal hydride beds by using numerical models. In addition to this, experimental studies have been concluded to find out the absorption and desorption rates of $LaNi_5$ [3,7]. The absorption/desorption curves regarding $LaNi_5$ in room temperature has been obtained experimentally and given in Figure 4.

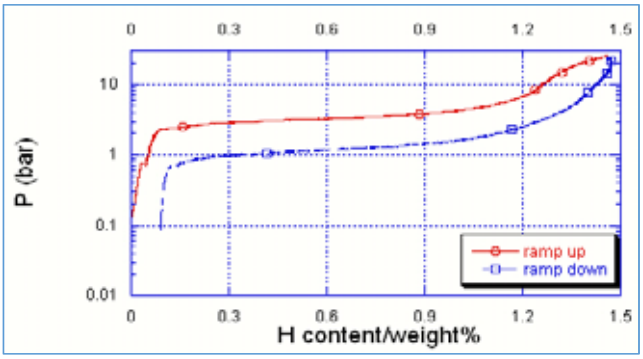


Fig. 4. Absorption/Desorption curves regarding $LaNi_5$ at the room temperature [7].

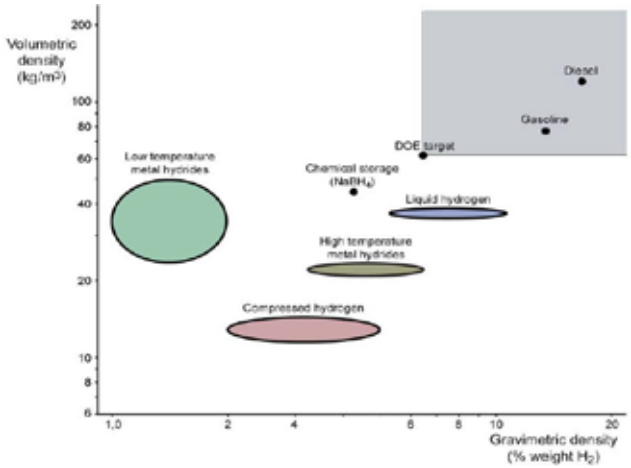


Fig. 5. Comparison of hydrogen storage technologies in regards to specific energy density [6].

3. Conclusion

In this study various hydrogen storage methods and the advantages/disadvantages of these methods has been explained. The comparison of the hydrogen storage technologies in regards to the specific energy density has been given in Figure 5. As it can be seen from this figure to achieve the target storage zone there should be improvements in the current methods in regards to both the volumetric and gravimetric energy densities of these methods. The widespread use of hydrogen in the future depends on the safety and efficiency of hydrogen storage methods.

Acknowledgment

I would like to thank Uğur İnanç İnci and Çağatay Erdem for my postgraduates who supported my work.

Nomenclature

E	energy
ΔH	the heat of combustion
m	mass
M	the molecular weight
n	the number of moles
P	pressure
R	ideal gas constant
T	temperature
V	volume

W Volumetric energy density

References

1. Mench M. Matthew, "Fuel Cell Engines", pp.426-438, John Wiley & Sons, (2008).
2. Wikipedia.org, "Hydrogen storage", Mayıs, 2012.
3. Bilgili M., "Numerical Analysis of Hydrogen Absorbtion in Metal Hydride Beds", Master of Science Thesis, Gazi University, Institute of Science and Technology, Ankara, 14-23 (2003).
4. U.S. Department of Energy, Energy Efficency & Renewable Energy, web page, May 2012. http://www1.eere.energy.gov/hydrogenandfuelcells/storage/hydrogen_storage.html
5. Dubno W. and Geving B., "Low Cost, High Efficiency, High Pressure Hydrogen Storage", DOE 2006 Annual Progress Report, Part IV. E Hydrogen Storage/Compressed/Liquid Tanks, Department of Energy, Washington, DC, 2006, pp.521-524.
6. http://www.nanotechnologies.qc.ca/projects/hydrogen/hydrogen_storage , web sayfası, 2012.
7. Muhittin Bilgili**,** Paola Gislon, and Pier Paolo Prosini, "A Flexible PcT System to Study H_2 Storage in Metal Hydrides", International Hydrogen Energy Congress & Exhibition (IHEC-2005), 13-15 July 2005, Istanbul-TURKEY. (Poster Presentation)
8. Shahin Shafiee , Mary Helen McCay "Different reactor and heat exchanger configurations for metal hydride storage systems- A review", International Journal of Hydrogen Energy 41 (2016), p.9462-9470
9. Technology roadmap hydrogen and fuel cells, Technical Annex, Alexander Körner, 29 Jun 2015. (http://www.sciencedirect.com/science/refhub/S0360-3199(16)32328-X/sref53)
10. Scott McWhorter and Grace Ordaz, "Onboard Type IV Compressed Hydrogen Storage Systems – Current Performance and Cost", DOE Fuel Cell Technologies Office Record, July 17, 2013.

CVD graphene as catalyst support for acid electrolytes

M. Suha Yazici, M. Akif Azder, Omer Salihoglu
Energy Institute, Marmara Research Centre, TUBITAK
P.K. 21, Gebze, 41470 Turkey
Email: suha.yazici@tubitak.gov.tr

Abstract
Graphene was produced from CVD process and successfully transferred as electrode materials. Raman spectroscopy results confirmed multi-layer structure formation. Oxygen reduction capabilities of various substrates were evaluated in 0,1M $HClO_4$ electrolyte. CVD grown graphene was utilized as support material for its oxygen kinetics behavior. Multi-layer graphene has provided μA level current, but still far from practical usage. Number of layers has to be reduced and doped to reach practical oxygen reduction currents (mA to A per area).

Keywords: Graphene; catalyst; fuel cell; CVD.

1. Introduction

Oxygen reduction in electrochemical processes is the largest contributor of losses and efforts continuing for improved kinetics through material innovation. Platinum (Pt) is considered as best catalyst for oxygen reduction reaction and commonly used [1-5]. Efforts continue to replace Pt with non-precious metals/alloys to enhance commercial viability of electrochemical processes [6-9]. Graphene has been utilized for this purpose, but commonly processed with chemical approaches through layer separation from graphite powder. Graphene produced by CVD process requires alternative approaches to obtain suitable materials for heterogeneous nature of gas-liquid catalytic activities. Electrocatalyst that are used in heterogeneous electrochemical systems, i.e. fuel cells, require 3-phase contact with gas and liquid present. If graphene can be produced in 3D form, it will help achieving fast charge transfer and high gas/liquid permeability leading to high catalyst conversion. Polymer electrolyte membrane fuel cells are potential target in need of stable and low cost catalyst. Graphene has been utilized for this purpose, but commonly processed with chemical approach through graphite layer separation. CVD process is not user friendly to produce graphene for heterogeneous electrocatalytic applications.

2. Experimental Study

CVD process was utilized to grow graphene on metal structures that were processed at 850-1035 °C. Ar, N_2, H_2, CH_4 were used as carrier gases at varying flow rates. The following temperature-time schedule was applied for the graphene growth (Fig. 1).

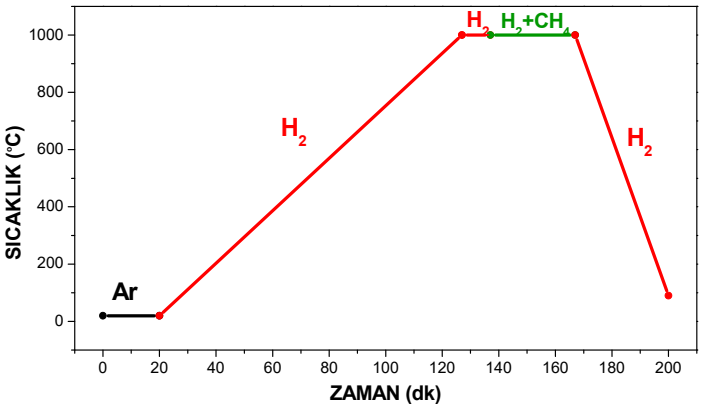


Fig. 1. Typical temperature-time schedule for grapheme growth

Following growth of graphene, base metal support was etched away. Graphene structures were transferred onto suitable electrode substrates and tested in three-cell configuration in 0,1M $HClO_4$ electrolyte to simulate acidic

conditions. Working electrode was either glassy carbon electrode (GCE) with 0,196 cm^2 area (RDE) or flat surface supported by expanded graphite sheet (EGS).Pt wire was used as counter electrode while saturated calomel electrode (SCE) was utilized as reference electrode.

3. Results and Discussion

Figure 2 shows SEM images for graphene grown on 20 micron copper foil for 1 hour. Due to extended growth time, grapheme flake formation was clearly seen at 200 micron magnification. Compare to clean copper surface, presence of 1.6% C was confirmed after graphene growth.

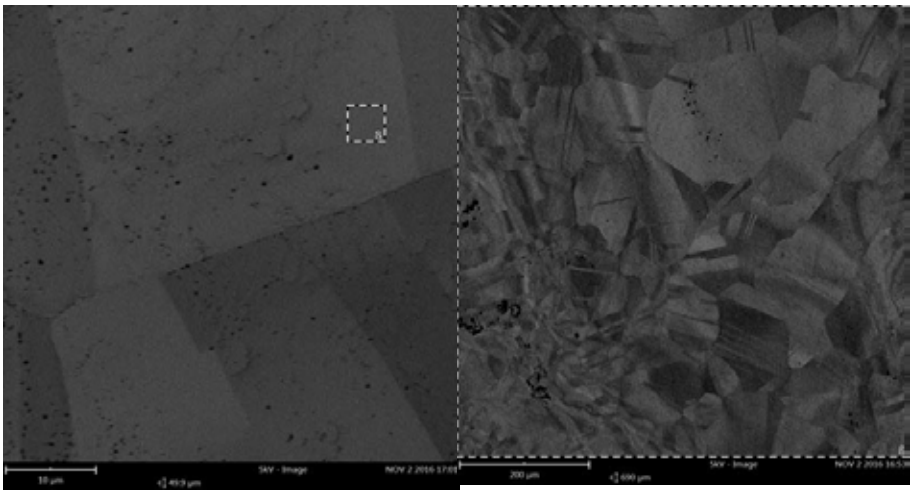


Fig 2. SEM pictures of CVD grown grapheme surface on copper foil at 10 and 200 micron magnification

Raman Spectroscopy in Fig. 3 shows G peak at 1571 cm^{-1} significantly higher than 2D peak at2700 cm^{-1} (G/2D >>1) confirming formation of multilayer graphene. Raman spectroscopy response also showed very defective graphene structure which might be due to presence of impurities in the furnace.

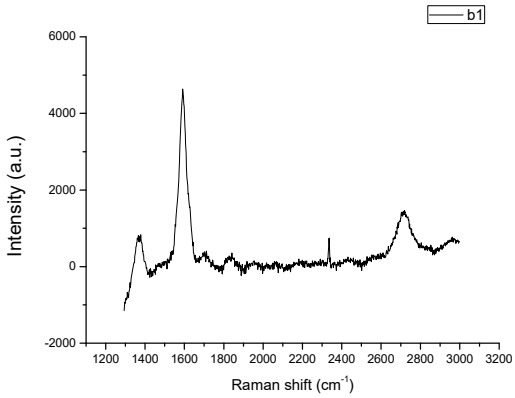


Fig. 3. Raman spectroscopy for graphene grown on copper foil

Before testing graphene samples in acid electrolyte, background current was measured by testing GC and EGS electrodes without coating. Electrochemical response of RDE measurements with (RDE400-P-G7) and without

(RDE400-GC) graphene in 0,1M $HClO_4$ electrolyte is presented in Fig. 4. Graphene was contributing catalytic activity by itself indicated, not only by shift in open circuit potential (OCP), but also by increasing current.

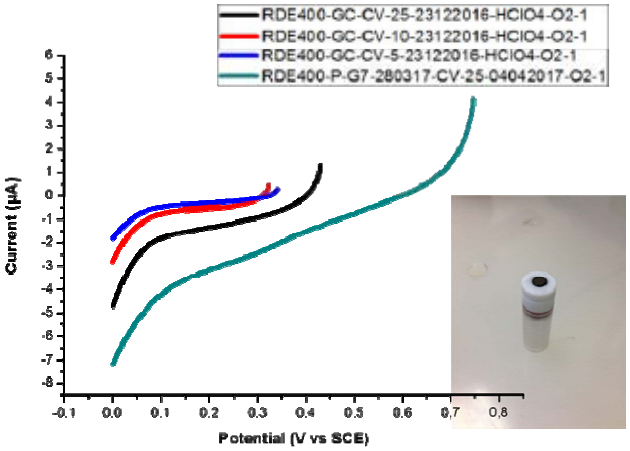


Fig. 4. Oxygen reduction polarizations for Glassy Carbon (GC) electrode on RDE (400 rpm) measurement with and without graphene in 0,1M $HClO_4$ electrolyte

When there was no catalyst or graphene on GC, current was able to reach 1-2 µA current. When graphene was introduced on GC, current value was around 3-4 µA without any catalyst or doping. It is expected to increase current value by reducing the number of layers formed on graphene.

Similar tests were carried out by using 0.31 mm thick and 0.5 mm wide flexible graphite sheet (FGS). These electrodes with approximately 0.25 cm^2 active area were immersed 1 cm into the electrolyte and tested. FGS samples also do not show significant catalytic activity (30-40 µA), but higher than GC due to porous structure (Fig. 5).

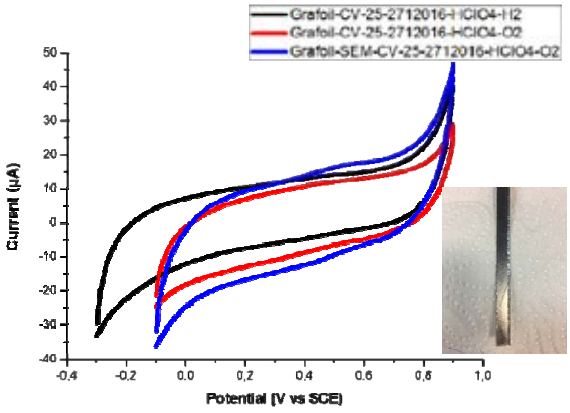


Fig. 5. CV response of flexible graphite sheet for oxygen reduction activity in 0,1M HClO4 electrolyte.

When graphene was produced and transferred onto silicon (Si) substrate, µA level of current was produced (Fig. 6). When there is no graphene present on the Si, current was nano-amper (nA) levels. As soon as a few layers of graphene was transferred onto Si, µA level of current was produced.

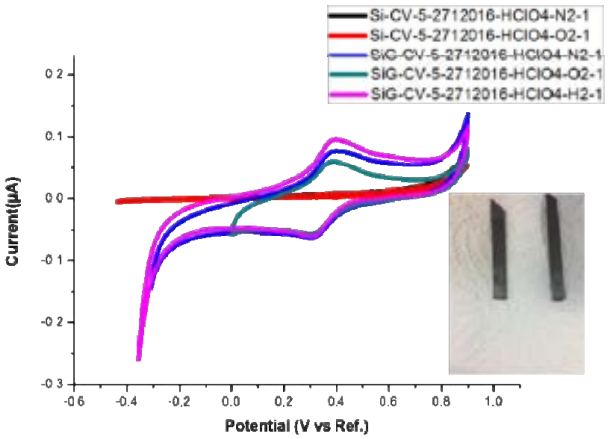


Fig. 6. Polarization of silicon plates without (Si) and with graphene (SiG) in 0,1M $HClO_4$ electrolyte.

Measurement and electrode system was also tested with commercially available catalysts so that newly developed graphene electrode could be compared. Commercially available 20%Pt on carbon was utilized to prepare 0.26 mg Pt on GC electrode. Fig. 7 shows results of polarization and CV measurements utilizing RDE at 400, 900 and 1600 rpm. Oxygen reduction reaction has started around 0.7 V (vs SCE) and increased with rotation rate. Similarly, hydrogen oxidation response was very clear (Fig.7-a)

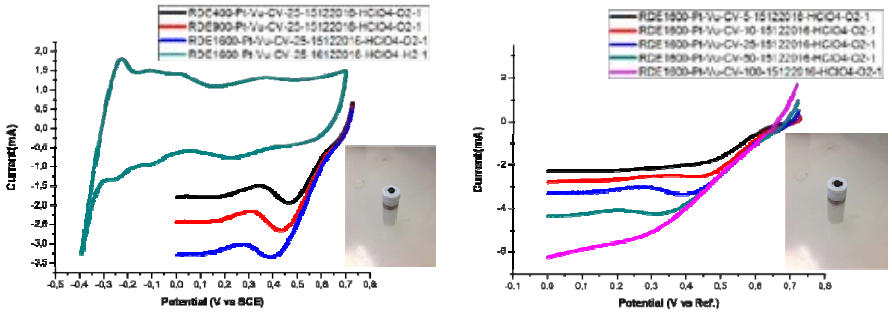


Fig. 7. CV and polarization response of Pt catalyst in RDE measurements at different rotation rate (a) and scan rate (b).

4. Conclusions

It was concluded that transfer of CVD grown graphene was successful and catalyst loading process could start for further tests on carbon cloth and paper. CV response of graphene structures were similar to multi-layer graphite. It is concluded that direct catalytic benefit of graphene can be obtained if number of layers are reduced. In order to achieve this, growth time has to be reduced below 1 minute so that number of layers can be limited to a few layers. Graphene grown on copper was not suitable for fuel cell applications. New approach to grow porous graphene will be developed and tested with doping.

Acknowledgement

Financial support provided by the TUBITAK-ARDEB through 1003 program under contract # 215M302 is greatly acknowledged.

References

1. Kinoshita, K, Carbon: Electrochemical and Physicochemical Properties, 1988.
2. Seselj et.al., Graphene-supported platinum catalysts for fuel cells, Sci. Bull. (2015) 60(9):864–876
3. Banham et.al., A review of the stability and durability of non-precious metal catalysts for the oxygen reduction reaction in proton exchange membrane fuel cells / Journal of Power Sources 285 (2015) 334e348
4. Candelaria et.al., Nanostructured carbon for energy storage and conversion, Nano Energy(2012) 1, 195–220
5. Jaeyoung Lee et.al., Oxygen electrocatalysis in chemical energy conversion and storage technologies, Current Applied Physics 13 (2013) 309-321]
6. Kim, et.al., Important roles of graphene edges in carbon-based energy storage devices, Journal of Energy Chemistry 22(2013)183–194
7. Park et.al., Optimization of catalyst layer composition for PEMFC using graphene based oxygen reduction reaction catalysts with different compositions of nafion, Journal of Power Sources 286 (2015) 166e174.
8. Surbhi Sharma et.al., Support materials for PEMFC and DMFC electrocatalysts—A review, Journal of Power Sources 208 (2012) 96–119,
9. Yaldagard et.al., Carbonaceous Nanostructured Support Materials for Low Temperature Fuel Cell Electrocatalysts—A Review, World Journal of Nano Science and Engineering, Vol.3 No.4(2013)

ORAL PROCEEDINGS

Energetic and Exergetic Investigations of an Innovative Light-Based Hydrogen Production Reactor

Canan Acar [1] and Ibrahim Dincer [1]
[1]Faculty of Engineering and Natural Sciences, Bahcesehir University
Çırağan Caddesi No: 4–6 34353 Beşiktaş, Istanbul, Turkey
[2]Faculty of Engineering and Applied Science, University of Ontario Institute of Technology
2000 Simcoe Street North, Oshawa, Ontario, L1H 7K4, Canada
Email: Canan.Acar@eng.bau.edu.tr

Abstract
Hydrogen is a highly versatile energy carrier that may become one of the key pillars to support the future CO_2-free energy infrastructure. When used in fuel cells, H_2 is converted to water and it gives little or zero exhaust of greenhouse gases. For H_2 economy to succeed, it needs to be produced in a clean, sustainable, reliable, and feasible way. The main objective of this study is to thermodynamically analyze and experimentally investigate a continuous type hybrid photoelectrochemical H_2 generation reactor. This system enhances solar spectrum use by employing photocatalysis and PV/T. Additionally, by replacing electron donors with electrodes to drive the photocatalysis, the potential of pollutant emissions are minimized. In this study, the present reactor is tested under electrolysis operation during which the present reactor is investigated under three different inlet mass flow rates (0.25, 0.50, and 0.75 g/s). The results are compared to the thermodynamic model outputs. Parametric studies are run by varying the inlet mass flow rate between 0–1 g/s. The present experimental results show that the highest hydrogen production rate is observed at 0.75 g/s, which is 2.43 mg/h. The highest energy and exergy efficiencies are calculated at 0.25 g/s, which are 36% and 32%, respectively. In addition, thermodynamic model results are confirmed to have a good agreement with the experimental results.
Keywords: Energy; exergy; efficiency; hydrogen; photoelectrochemical; sustainability; solar

1. Introduction

With the continuous worldwide increase in population and standards of living, meeting the ever-increasing global energy demand in an affordable, clean, reliable, and sustainable manner has become one of the most challenging tasks of the twenty first century [1]. As a consequence of their restricted supply and non-homogeneous resource distribution, fossil fuels are not anticipated to keep pace with the growing energy needs [2]. Along with that, while fossil fuel resources are becoming harder to extract while the easily accessible reserves are exhausted, the fossil fuel prices continue rising [3]. In conjunction with financial matters, GHG (mainly CO_2) emissions as a consequence of fossil fuel consumption, and their influence on global warming, have been causing significant worries [4, 5].

The underlying motivation of this work is the potential for taking advantage of water electrolysis in a hybrid photoelectrochemical reactor to improve the solar spectrum utilization and hydrogen production yield. For this purpose, a system consisting of a photoactive ion selective membrane is developed as a medium for solar fuel generation.

In this regard, a novel hybrid photoelectrochemical reactor is tested during electrolysis process under three different inlet mass flow rates (0.25, 0.50, and 0.75 g/s). Current generation, hydrogen production, energy and exergy efficiencies, and exergy destruction is calculated at each inlet mass flow rate. Thermodynamic model outputs are compared to the experimental results and in the end, the optimum inlet mass flow rate is calculated for highest possible hydrogen production rate, energy and exergy efficiencies, and lowest possible exergy destruction rate.

2. System Description

The present experimental setup has eight main components, namely (I) reactor; (II) electrolyte feed tanks; (III) electrolyte dump tanks; (IV) peristaltic pumps; (V) water displacement cylinder; (VI) heaters; (VII) potentiostat; and (VIII) solar simulator and (a) and (b) terms specify the anolyte and catholyte, respectively. During present study, anolyte and catholyte feed and dump only include H_2O. H_2 gas leaves the catholyte dump tank (III.b) and O_2 gas leaves the anolyte tank (III.a) The process flows as the anolyte and catholyte feeds are prepared in (II.a and II.b) before entering to the reactor (I), for instance, during operations at higher temperatures, these tanks are heated via (VI.a and IV.b). The feed flow rates are monitored and controlled by peristaltic pumps (IV.a and IV.b). Anolyte and catholyte outlet streams, called dump, are sent to dump tanks (III.a and III.b). H_2 gas leaving (III.b) is collected and measured by volumetric water displacement technique. The gas product from (III.a), O_2, is not measured and released towards the vent.

In the last years, the electrodeposition procedure has appealed particular attention for the Cu_2O thin film processing. Electrodeposition has two most important benefits, specifically its uncomplicatedness and the low operating temperature requirements. These advantages lead to more affordable processes and applicability to a wide range of industrialized applications. Deposition parameters can easily be adjusted during electrodeposition process,

which allows the control of reaction stoichiometry, film thickness, and Cu_2O microstructure much easily. Cu_2O films are electrodeposited in a three-electrode arrangement in galvanostatic method based on the procedure described in [6]. In the electrodeposition setup, working electrode is the MEA described above, counter electrode is a Pt wire wrapped around graphene, and reference electrode is Ag/AgCl. Cu_2O is electrodeposited by reduction of an alkaline solution of cupric lactate. The electrolytic solution contains 0.4 M copper (II) sulfate and 3 M lactic acid as chelating agent to stabilize Cu^{2+} ions by complexing. The electrolytic solution temperature is set to room temperature (about 20°C). The pH of the bath is adjusted to 11 by adding KOH solution. The electrodeposition process is shown in Figure 1.

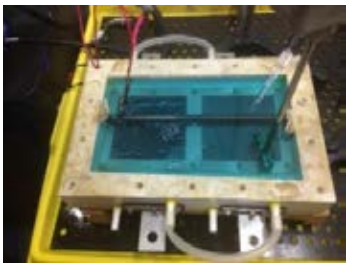


Figure 1. Present experimental setup during electrodeposition process.

3. System Analysis

Thermodynamic performance of the hybrid reactor is examined by conducting quantitative energy and exergy analyses. Here, the assumptions, basic concepts, procedure, and equations utilized to assess system performance are expressed and discussed in detail. Throughout this analysis, the subsequent assumptions are made:

- The environmental temperature (T_0) and pressure (P_0) are 20°C and 1 atm, respectively.
- All streams and components are at operating temperature and pressure at all times.
- All processes take place in steady-state and steady-flow.
- All processes carry on to completion.
- The changes in potential and kinetic energies are negligible.
- The change in the control volumes (reactor and integrated system units) is disregarded.
- Both H_2 and O_2 gases are presumed to be ideal.
- The heat losses to environment are neglected.
- The auxiliary components are assumed to be well insulated and capable of conducting electricity with no loss.

Overall mass, energy, entropy and exergy balance equations are listed and modified based on the assumptions and operating conditions of the hybrid reactor. The heat and/or work input and output, entropy generation, and exergy destruction rates, and energetic and exergetic effectiveness are evaluated from the aforementioned balance equations.

4. Results and Discussion

The average values of the current measurement results at selected inlet mass flow rates of 0.25, 0.50, and 0.75 g/s during the electrolysis experiments are presented in Figure 2 where the average standard deviation in current measurements is 0.002 A. Figure 2 shows that the current measurements increase with increasing inlet mass flow rates. The primary reason of this tendency is that with increasing mass flow rates, depleted ions are replaced more frequently and this prevents negative or positive ion accumulation. Positive or negative ion accumulation slows the redox reactions down and reduces the corresponding current generation due to ion replacement. Therefore, preventing and/or minimizing positive or negative ion replacement increases the current generation.

The experimental and model H_2 production outputs at different inlet mass flow rates are presented in Figure 3. Each experimental run is repeated three times at each inlet mass flow rate resulting an average standard deviation of 0.1 g/h. Figure 3 shows that the effect of the inlet mass flow rate on the H_2 production is similar to the current measurement results presented in Figure 2.

In addition, Figure 3 indicates that the model outputs are in a good agreement with the experimental results. On average, the model predicts about 0.3 g/h higher H_2 production resulting an average difference of 24.9%. This difference could potentially be caused from the assumptions of steady-state steady-flow, negligible kinetic and potential energy changes, heat losses to the environment; and conductivity losses.

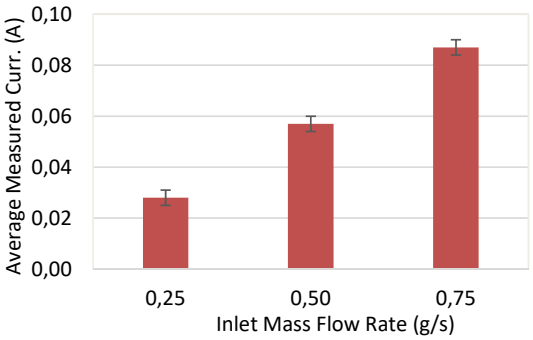


Figure 2. Effect of inlet mass flow rate on current measurement results.

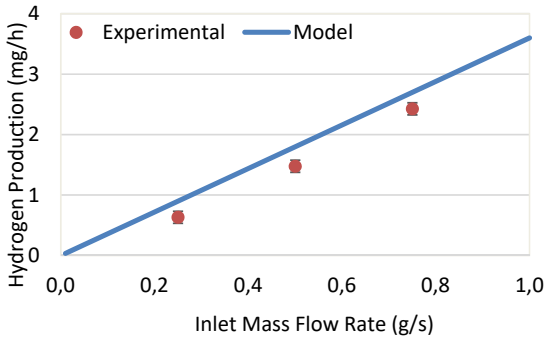


Figure 3. Effect of inlet mass flow rate on H_2 production with comparison of experimental and model outputs.

The effect of the inlet mass flow rate on the energy efficiency is presented in Figure 4. The experimental results show that when the inlet mass flow rate is increased from 0.25 to 0.75 g/s, the energy efficiency decreases from about 36% to 31%. The reason of this decrease is the increase in pump load and voltage requirements with increasing inlet mass flow rates. Each experimental run is repeated three times at each inlet mass flow rate resulting an average standard deviation of around 4%.

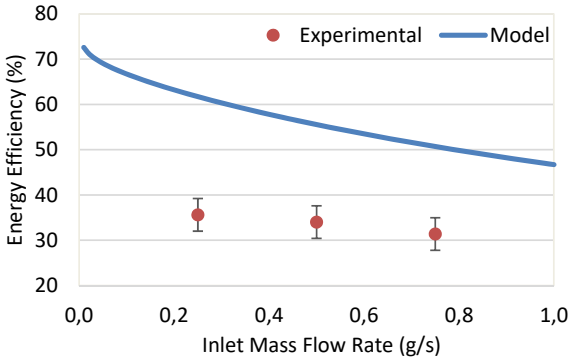


Figure 4. Effect of inlet mass flow rate on energy efficiency with comparison of experimental and model outputs.

From Figure 4, it can be seen that the energy efficiency results of the experimental runs and model outputs have similar tendencies, which can be considered as an acceptable level of agreement. Within the selected inlet mass flow rate interval of 0.25 to 0.75 g/s, on average, the model predicts about 22% higher energy efficiency. The primary reason for this difference is the assumptions used when developing the thermodynamic and electrochemical models, as discussed earlier in this section.

Figure 5 shows the effect of the inlet mass flow rate on the exergy efficiency. The experimental results show that when the inlet mass flow rate is increased from 0.25 to 0.75 g/s, the exergy efficiency decreases from about 32% to 27%. Similar to the energy efficiency results, increasing pump input and voltage requirements lowers the exergy efficiency at increasing inlet mass flow rates. Each experimental run is repeated three times at each inlet mass flow rate resulting an average standard deviation of around 3%.

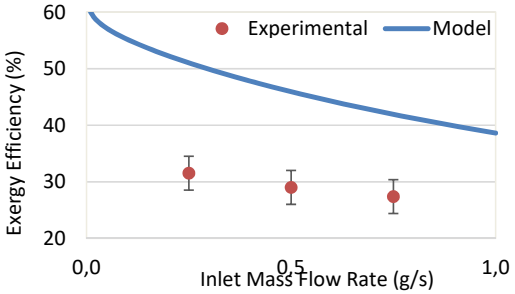


Figure 5. Effect of inlet mass flow rate on exergy efficiency with comparison of experimental and model outputs.

The experimental runs take place at 0.25, 0.50, and 0.75 g/s inlet mass flow rates and within the selected inlet mass flow rate interval, the experimental results and model outputs have similar behaviors. Within the selected inlet mass flow rate interval, on average, the model predicts about 17% higher exergy efficiency (Figure 5). The main cause of this variance is the assumptions taken into account when developing the thermodynamic and electrochemical models, which are discussed earlier in this section.

The effect of the inlet mass flow rate on the exergy destruction is presented in Figure 6. When evaluating the exergy destructions, the experimental results and the electrochemical and thermodynamic models are used together to evaluate the effect of the inlet mass flow rate on exergy destruction. Figure 6 shows that the lowest exergy destruction rate is observed at 0.1 g/s, which is about 0.003 W. With increasing inlet mass flow rates, the rate of exergy destruction increases due to increasing pump input and voltage requirements.

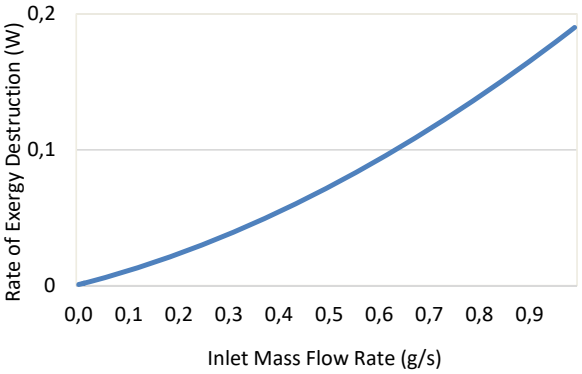


Figure 6. Effect of inlet mass flow rate on exergy destruction–model outputs.

In order to find the optimum inlet mass flow rate, the thermodynamic model results are normalized and ranked based on the following equations:

- For criteria that are preferred to be maximized (e.g., energy and exergy efficiencies and H_2 production rate):

$$rank = \frac{i-minimum}{maximum-minimum} \times 10 \quad (1)$$

- For criteria that are desired to be minimized (e.g., exergy destruction rate):

$$rank = \frac{maximum-i}{maximum-minimum} \times 10 \quad (2)$$

Here i denotes the individual data point at a specific inlet mass flow rate and *maximum* and *minimum* correspond to the maximum and minimum values of a specific criteria (i.e., energy and exergy efficiencies, H_2 production rate, and exergy destruction rate) within the selected inlet mass flow rate interval between 0 and 1 g/s. Normalized rankings

of H_2 production, energy and exergy efficiencies, and exergy destruction rates within based on the thermodynamic model results are given in Figure 7 along with their average rankings.

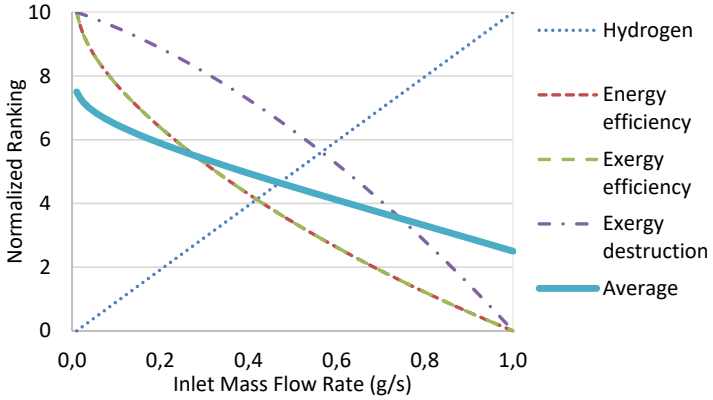


Figure 7. Normalized rankings of H_2 production, efficiencies, and exergy destruction at different inlet mass flow rates.

Figure 7 shows that except the H_2 production rate, all other performance criteria have decreasing rankings with increasing inlet mass flow rate. As a result, the average ranking is decreasing with increasing inlet mass flow rate, too. However, selecting 0 g/s inlet mass flow rate would mean zero H_2 production, and the aim is to produce H_2; therefore, 0.25 g/s is selected as the inlet mass flow rate which gives an average ranking of 6.5/10, which is high enough and acceptable within the given inlet mass flow rate interval.

5. Conclusions

The aim of this study is to experimentally and thermodynamically investigate a hybrid photoelectrochemical system to convert solar energy to hydrogen energy which can potentially become an energy carrier that is as affordable and convenient as the current fossil fuel resources, less harmful to the environment, and practically safe when in use. The effect of the inlet mass flow rate on H_2 production rate and energy and exergy efficiencies are investigated experimentally. The experimental results are compared to the thermodynamic model outputs. Also, the thermodynamic model calculations are carried out using the EES software to investigate the effect of the inlet mass flow rate on H_2 production, energy and exergy efficiencies, and exergy destruction. The following are the summary of findings from the present experimental studies:

- The highest hydrogen production rate is observed at 0.75 g/s, which is 2.43 mg/h.
- The highest energy and exergy efficiencies are calculated at 0.25 g/s, which are 36% and 32%, respectively.
- Thermodynamic model results are in good agreement with the experimental results
- 0.25 g/s is the selected optimum inlet mass flow rate which gives the highest possible hydrogen production rate, energy and exergy efficiencies, and lowest possible exergy destruction within the selected inlet mass flow rate interval of 0 to 1 g/s.

References

1. Acar, C. (2016). Experimental investigation and analyses of continuous type hybrid photoelectrochemical hydrogen production systems (Doctoral dissertation, University of Ontario Institute of Technology).
2. Acar, C., Dincer, I., Naterer, G. F. (2016). Review of photocatalytic water-splitting methods for sustainable hydrogen production. International Journal of Energy Research, 40(11), 1449-1473.
3. Acar, C., Dincer, I. (2013). Comparative environmental impact evaluation of hydrogen production methods from renewable and nonrenewable sources. In Causes, Impacts and Solutions to Global Warming (pp. 493-514). Springer NY.
4. Acar, C., Dincer, I. (2016). Experimental investigation and analysis of a hybrid photoelectrochemical hydrogen production system. International Journal of Hydrogen Energy.
5. Dincer, I., Rosen, M. A. (2013). Exergy. Elsevier: Oxford.
6. Wang, P., Wu, H., Tang, Y., Amal, R., Ng, Y. H. (2015). Electrodeposited Cu_2O as photoelectrodes with controllable conductivity type for solar energy conversion. The Journal of Physical Chemistry C, 119(47), 26275–26282.

Daily Performance Assessment of an Integrated Thermal System on Hydrogen Production

Ayhan Atiz[1], Mustafa Erden[2], Müzeyyen Cilogullari[2], Mehmet Karakilcik[2],
[1]Faculty of Education, Mathematics and Science Education, Alanya Alaaddin Keykubat University, Antalya, Turkey
[2]Department of Physics, Faculty of Sciences and Letters, University of Cukurova, 01330 Adana, Turkey.

Abstract
In this study, hydrogen production performance of an integrated thermal system is investigated. The system is consisting of solar pond, evacuated tube solar collectors, Organic Rankine Cycle (ORC) and water electrolysis system. In the integrated system, the output water at higher temperature can be obtained from the evacuated tube solar collector supported by the solar pond in a short time for a day. The higher temperature of input water plays a key role on the power efficiency of the ORC and also on the rate of the hydrogen production by the electrolysis of water. For this purpose, thermodynamic analysis is carried out to better understand the effects of the performance of the system components on the rate of the hydrogen generation by using the Engineering Equation Solver (EES) program. As a result, significant amounts of hydrogen can be produced in a short time.

Key words: Solar pond; evacuated tube solar collector; hydrogen production; energy; exergy.

1. Introduction

The solar energy is one of the best sources of renewable alternative energy. Increasing energy demand is necessarily produced from renewable energy. Non-renewable energy sources both damage the environment and are exhausted. So the solar energy is one of the best alternatives to non-renewable energy sources. There are many systems that generate heat or electricity by utilizing solar energy. Solar ponds and solar collectors produce thermal energy while photovoltaic (PV) generate electricity. Hydrogen can be produced by utilizing heat energy. So in this system, we used evacuated solar collector and solar pond [1]. Solar ponds are one of the good heat storage systems. The temperature of each layer of the inner zones solar pond depends on the incident radiation, zone thicknesses, shading areas of the zones and overall heat loss. The modification of the zone thicknesses increases pond performance and stability of the pond [2]. Evacuated tube solar water heaters has good thermal efficiency and high water temperature able to be accomplished as compared to the flat-plate solar water heaters [3]. A study consisting of solar collectors integrated into the solar pond has been done. In this system, it has been seen that the thermal performance of the heat reservoir of the solar pond can be significantly increased by using the solar collector. Using these systems together with electrolysis, chemical or photoelectric systems hydrogen can be produced. [4]. Investigated a study the hydrogen generating performance of a Proton Exchange Membrane (PEM) electrolyzes powered by a Photovoltaic and Thermal System (PV/T) with a surface area of 1.28 m^2 at a constant temperature with a panel cooling system through a heat exchanger by removing the heat from the PV cells. The model simulation was done with the Engineering Equation Solver (EES) [5]. An integrated system consists of a solar pond, evacuated collectors and an Organic Rankine Cycle (ORC) was designed. EES simulation was used for this model. In the above work we have seen it is possible to produce hydrogen using solar energy. Sufficient amount of hot water is required for hydrogen production in ORC. Evacuated tube collectors and solar pond have been used to provide hot water.

2. System Description

The present system, as seen schematically in Fig. 1, includes a salinity gradient solar pond, in-pond heat exchangers, evacuated solar collectors, cooling tower, an ORC which contains isobutene as a working fluid to produce electricity and electrolysis system to generate hydrogen gas. The inlet water to the ORC that was preheated by passing through the heat exchanger in the solar pond can be easily raised to higher temperatures by the help of the evacuated solar collectors in a short time. The thermal energy generated in this way is used to run the ORC and the hydrogen gas is produced by using the electrical energy generated by the ORC. Also the waste heat comes from the ORC is given into the cooling tower by the help of the condenser.

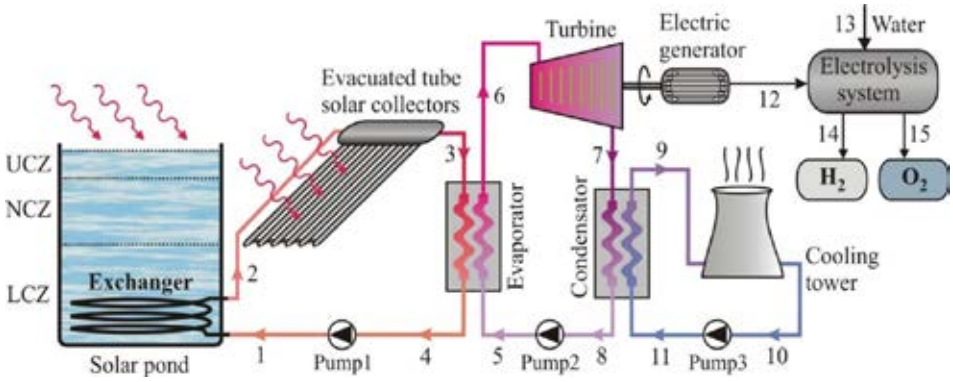


Fig. 1. Schematic of the integrated system

2.1. Solar pond

Solar energy is collected and stored in the solar pond as heat which can be surely used as a source of heat for industrial processes and the generation of electricity. A solar pond consists of three layers of water, which are upper convective zone (UCZ), non-convective zone (NCZ) and heat storage zone (HSZ). The HSZ absorbs and stores an important amount of solar energy as heat. So this zone has the highest temperature of solar pond and heat has been extracted from the HSZ [6].

The general energy balance for the HSZ can be written as:

$$Q_{HSZ,stored} = Q_{HSZ,in} - Q_{bottom} - Q_{up} - Q_{HSZ,side} - Q_{ext} \quad (1)$$

where $Q_{HSZ,stored}$ is the heat stored in the HSZ, $Q_{HSZ,in}$ is the amount of the solar radiation entering the HSZ, Q_{bottom} is the heat loss to the bottom wall from the HSZ, Q_{up} is the heat loss to the NCZ from the HSZ and $Q_{LCZ,side}$ is the heat loss to the side wall from the HSZ and Q_{ext} is the heat loss by extraction.

2.2. Heat exchanger

Heat exchangers are devices that make easy the exchange of heat between two fluids at different temperatures that are separated by a solid wall [7].

The rate of heat transfer in a heat exchanger can be expressed as:

$$\dot{Q} = UA_s\Delta T_{lm} \quad (2)$$

where, U is the overall heat transfer coefficient that accounts for the contribution of the effects on heat transfer such as convection and conduction, A_s is the heat transfer area, ΔT_{lm} is the logarithmic mean temperature difference which is given as:

$$\Delta T_{lm} = \frac{\Delta T_1 - \Delta T_2}{\ln\left(\frac{\Delta T_1}{\Delta T_2}\right)} \quad (3)$$

where $\Delta T_1 = T_{HSZ} - T_{exc,out}$ and $\Delta T_2 = T_{HSZ} - T_{exc,in}$

Here T_{HSZ} stands for the temperature of the HSZ of the pond, $T_{exc,out}$ stands for the temperature of the outlet water from the exchanger and $T_{exc,in}$ stands for the temperature of the inlet water to the exchanger as shown in Fig. 1.

2.3. Evacuated solar collectors

The evacuated tubular solar evacuated tube solar water heater typically consists of 15–40 flooded single ended tubes in direct connection to a horizontal tank. The solar absorber tube consists of two concentric glass tubes sealed at one

end with an annular vacuum space and a selective surface absorber on the outer surface (vacuum side) of the inner tube [8]. The useful energy gain of collector surface area is given by [9]:

$$\dot{Q}_U = \eta \dot{E}_{net} \quad (4)$$

Where η the efficiency for the evacuated solar collectors, $\dot{E}_{net}$ is the total energy of solar radiation reaching surface of collectors or solar pond: [10].

$$\dot{E}x_{solar} = \dot{E}_{net}\left[1 - \frac{4}{3}\left(\frac{T_0+273}{T_s}\right) + \frac{1}{3}\left(\frac{T_0+273}{T_s}\right)^4\right] \quad (5)$$

where $\dot{E}x_{solar}$ is the exergy of solar radiation coming on the surface of the solar systems can be get as follows $T_s = 6000$ K the surface temperature of the sun $T_0 = 28$ °C is the reference temperature.

2.4. Organic Rankine Cycle (ORC)

The Organic Rankine Cycle that it is based on the vaporization of a high pressure liquid which is in turn expanded to a lower pressure thus releasing mechanical work. The cycle is closed by condensing the low pressure vapor and pumping it back to the high pressure. Therefore, the Organic Rankine Cycle involves the same components as a conventional steam power plant (a boiler, a work producing expansion device, a condenser and a pump). However, the working fluid is an organic compound characterized by a lower ebullition temperature than water and allowing power generation from low heat source temperatures [11]. Energy efficiency of the integrated system is expressed as:

$$\eta_{int,sys} = \frac{\dot{W}_{net}}{\dot{Q}_{ev}} \quad (6)$$

where $\dot{Q}_{ev}$ is the input heat to the ORC and the $\dot{W}_{net}$ net power output of the ORC.

Table 1. Thermodynamics parameters of the integrated system

No	Fluid	Temperature (°C)	Pressure (kPa)	Mass flow rate kg/s)	Enthalpy (kJ/kg)	Entropy (kJ/kg°C)	Exergy (kW)
0	Air	28	101.3	-	117,4	0,408	-
1	H_2O	37	200	0.5	155,1	0,532	0,61
2	H_2O	55	200	0.5	230,4	0,768	4,88
3	H_2O	110	200	0.5	461,3	1,419	40,01
6	Isobutane	100	2000	0.2	466,6	1,814	73,68
7	Isobutane	80	1750	0.2	405,4	1,647	84,64
8	Isobutane	40	1750	0.2	297,5	1,323	95,07
5	Isobutane	39	2000	0.2	295	1,314	94,78

3. Results and discussions

Temperature, pressure, mass flow rate, enthalpy, entropy and exergy are found in Table 1. These values are used for the calculations to make the thermodynamic analysis. The temperature of the storage zone of the solar pond that has a surface area 241 m^2 is proposed to be 65 °C. The inlet and outlet water temperatures to the heat exchanger are assumed to be 40 °C and 60 °C, respectively. The temperature of the outlet water from the exchanger is upgraded to 110 °C by using the evacuated tube collector that has a surface area 300 m^2.

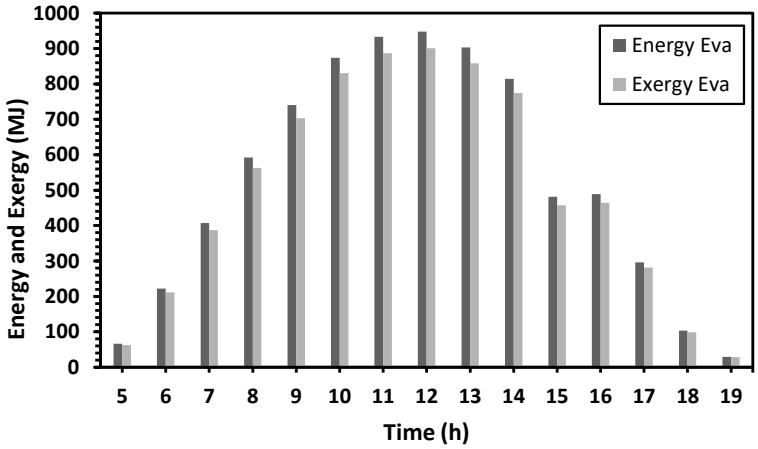


Fig. 2. Daily energy and exergy distributions of the solar radiation for evacuated tube collectors for selected day in July

Fig. 2 shows that the solar radiation is reached at 5 o'clock in the morning until 19 in the evening and the maximum energy and exergy was get values at 12 o'clock at a day in day. Accordingly, the maximum value of solar energy and exergy for evacuated solar collectors were 947 MJ and 900 MJ at noon. Total solar energy and exergy reaching the surface of the collectors for 300 m^2 are 7899MJ and 7507MJ.

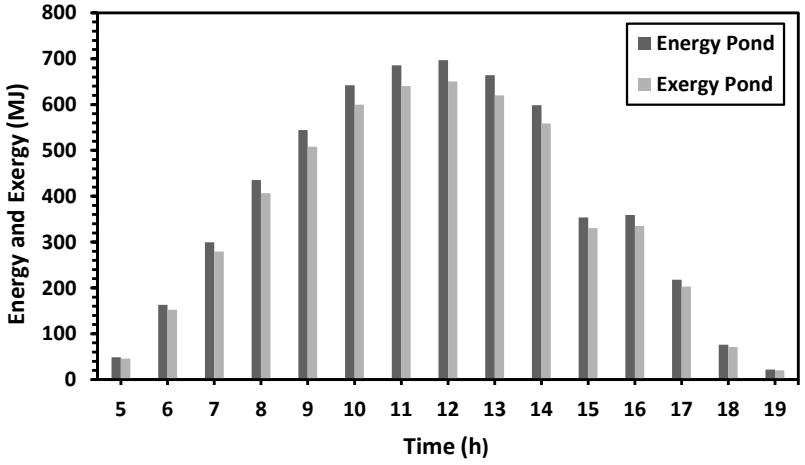


Fig. 3. Daily energy and exergy distributions of the solar radiation for solar pond for selected day in July

As seen Fig. 3, accordingly, the maximum value of solar energy for the solar pond were 696 MJ and 650 MJ. Total solar energy and exergy reaching the surface of the solar pond for 217 m^2 are 5806 MJ and 5518 MJ. The surface area of the collector is larger than the surface area of the solar pond.

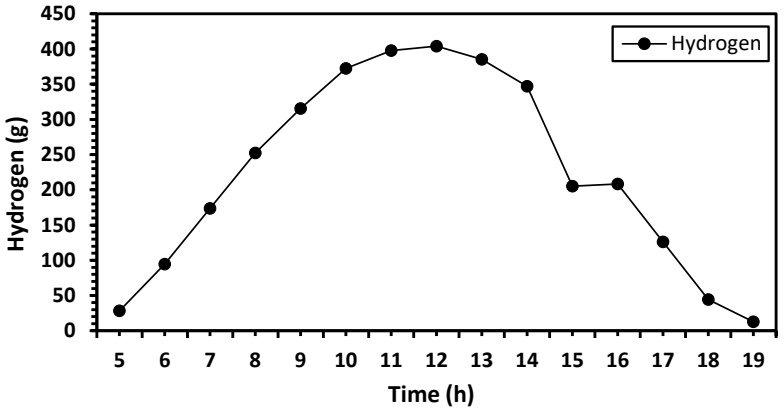


Fig. 4. Hydrogen production during hours for a day in July

As seen here in the Fig. 4, the hydrogen production connected to electricity generation that started to produce from the morning. It reached maximum value 404 g at 12 o'clock in the afternoon. Then it declined and reached a minimum value through the evening 12.6 g. The total of hydrogen 3368 g were produced throughout the day in water electrolyzes.

4. Conclusions

In this study, hydrogen production performance of an integrated thermal system that consists of a solar pond, evacuated tube solar collectors and an ORC was investigated. Consequently, the solar pond has preheated the water inlet the system which sent it to the vacuum tube collectors. Then the collector further the water temperature was increased to upgrade the thermal performance of the ORC. It was observed that a significant amount of electrical power can be generated in the ORC system by increasing the temperature of the water and mass fluid in ORC within a short time. The generated power in the model system was used to produce hydrogen gas by electrolysis system. Significant quantities of hydrogen gas were produced as the final output of the system. In the future it is concluded that renewable energy systems may have an important place in hydrogen production.

References

1. Karakilcik M, Dincer I, Rosen M. Performance investigation of a solar pond. Applied Thermal Engineering. 2006;26:727-735.
2. Shafii MB, Mamouri SJ, Lotfi MM, Mosleh HJ. A modified solar desalination system using evacuated tube collector. Desalination. 2016;396:30-38.
3. Atiz A, Bozkurt I, Karakilcik M, Dincer I., Investigation of Effect of Using Evacuated Tube Solar Collector on Solar Pond Performance. Springer International Publishing Switzerland, Progress in Clean Energy. 2015;2:261-273.
4. Cilogluları M, Erden M, Karakilcik M, Dincer I., Investigation of hydrogen production performance of a Photovoltaic and Thermal System. Int. J Hydrogen Energy. 2017;42:2547-2552.
5. Erden M, Karakilcik M, Dincer I, Performance investigation of hydrogen production by the flat-plate collectors assisted by a solar pond. Int. J Hydrogen Energy. 2017;42:2522-2529.
6. Bozkurt I, Karakilcik M. The daily performance of a solar pond integrated with solar collectors. Solar Energy. 2012;86:1611-1620.
7. Cengel YA. Heat and Mass Transfer, Third Edition, Mc Graw Hill, 2006.
8. Budihardjo I, Morrison GL. Performance of water-in-glass evacuated tube solar water heaters. Solar Energy. 2009;83:49–56.
9. Duffie JA, Beckman WA. Solar engineering of thermal process, 2nd Ed. New York: Wiley Interscience. 1991.
10. Petala R. Exergy of undiluted thermal radiations. Solar Energy. 2003;74:469-488.
11. Quoilin S, Van Den Broek V, Declaye S, Dewallef P, Lemort V. Techno-economic survey of Organic Rankine Cycle (ORC) systems. Renewable and Sustainable Energy Reviews. 2013;22:168–186.

Effects of Process, Operational and Environmental Variables on Biohydrogen Production Using Palm Oil Mill Effluent (POME)

[1]Bidattul Syirat Z., [2]Shaliza I., [2]Ali Akhbar Z., [1]Nuruol Syuhadaa M.
[1]Department of Civil Engineering, University of Malaya, 50603, Kuala Lumpur, MALAYSIA.
[2]Department of Applied Chemistry, Faculty of Chemistry, Razi University, Kermanshah, IRAN.
E-mail: bid_syirat@yahoo.com, shaliza@um.edu.my

Abstract
In this study, raw palm oil mill effluent (POME) and POME sludge collected from Jugra Palm Oil Mill, Banting, Selangor were used as a substrate and inoculum, for biohydrogen production. This study aims to produce biohydrogen with the highest hydrogen yield and COD removal efficiency (%) with optimum process, operation and environmental variables. Prior to its use, POME sludge was heat-treated at 100°C for 1 hour to promote Hydrogen Producing Bacteria (HPB). Experiments were conducted in 156ml serum bottles with different reaction temperature (30°C, 40°C and 50°C) and different inoculum size to substrate ratio (I:S) with lowest range: 10:90, middle range: 20:80 and highest range: 40:60 of inoculum:substrate (v/v). Experiments were designed using Response Surface Methodology (RSM) and were conducted for 8 hr, 16 hr and 24 hr of reaction time. Optimum condition of biohydrogen production was achieved with COD removal efficiency of 31.38% with hydrogen yield of 17.76 ml H_2 g^{-1} COD removed. The inoculum substrate ratio was 0.66, with- 40:60 (I:S) (i.e <20 g L^{-1} CODin) with reaction temperature of 49.16°C and reaction time of 16 hours.

Keywords: Palm Oil Mill Effluent (POME); biohydrogen; COD removal; response surface methodology (RSM).

1. Introduction

Hydrogen (H_2) is one of the potential biofuel that has a lot of benefits as it possesses a clean energy and environmental-friendly characteristics. Therefore, vast researches on the potential of H_2 as a renewable biofuel resources have been conducted in order to enhance hydrogen production using different kind of sources and technologies [1,2].

One of the plausible resources for the biohydrogen production in Malaysia is from the treatment of palm oil-based industry's wastewater. Malaysian palm oil industry is a highly-regulated industry and is one of the world's largest palm oil exporter. Currently it accounts for 39% of world palm oil production and 44% of world exports [3]. Despite its many beneficial qualities, there are some negative aspects associated with the production of palm oil. Large amounts of wastewater, known as palm oil mill effluent (POME) released from palm oil mills (POMs) can jeopardize the environment and biogas released from POME during anaerobic treatment is a serious challenge resulted from the current production processes [4, 5]. Some other methods have been proposed for POME treatment, including evaporation ponds, thermal treatment, physicochemical, and biological treatments. For the wastewater to be treated by biological means, its BOD/COD ratio need to be greater than 0.5, [6] and with reference to the published values of BOD and COD [7], aerobic and anaerobic treatment is clearly suitable for POME as the BOD/COD ratio is greater than 0.5. Moreover, biological treatment is also preferable due to its cost effectiveness as compared to chemical treatment.

In dark fermentation process, substrate that contains carbohydrate is converted to organic acids, hydrogen and CO_2 by mesophilic or thermophilic bacteria. In the second stage, the effluent of dark fermentation containing organic acids such as acetate and lactate, or volatile fatty acids (VFAs) are utilized in photo-fermentation by photosynthetic bacteria for further hydrogen production [8]. Dark fermentation process produces high production rate of hydrogen, but with low hydrogen yield [9] and [10]. Dark fermentation is a process at which organic pollutants are converted into hydrogen by dark fermentative bacteria, thus yield organic acids (acetate and butyrate) and alcohols as by-products, in the absence of oxygen. Guo et al., [11] in their study, produced hydrogen and methane using high concentration of corn stalk (60 g L^{-1}) as substrate. They reported a higher maximal hydrogen yield of 79.8 ml H_2 g^{-1} substrate and 2.56 mol H_2 mol^{-1} hexose, in comparison to Chu et al., [12] that obtained 67 ml H_2 g^{-1} substrate with 60 g L^{-1} wheat stalk as a substrate. On the other hand, Kim et al., [13] reported 2.11 ml H_2 g^{-1} substrate was produced when 56.1 g COD L^{-1} of mixture of food waste and sewage sludge is used as a substrate. The most recent batch study done by Norfadilah et al., [14] used high concentration of raw POME as a substrate (influent COD concentrations were 32,000 mg L^{-1} to 86,400 mg L^{-1}), and they reported a maximum hydrogen production yield of 5.98 L H_2 L^{-1} -med at 10% POME sludge. Additionally, study done by Mohammadi et al. [15] using pre-

settled POME as substrate reported that the maximum hydrogen yield obtained was 124.5 mmol H_2 g^{-1} COD removed. However, the study was done at low COD influent of 3 g L^{-1} COD – 10 g L^{-1} COD.

Based on the presented studies, most of them were done at high substrate concentration (>20 g L^{-1} COD) and the hydrogen generation as well as additional methane production were done through a single hydrogen fermentation or two-stage process combining hydrogen fermentation and anaerobic digestion. However, batch experiment study using POME sludge as inoculum and pre-settled POME as a substrate, both at higher and lower substrate concentration, is still lacking and need more information on operational and process optimization. Therefore, further study is necessary in order to fully assess the potential benefit of using low concentration and high concentration of pre-settled POME as a substrate for biohydrogen production in a single stage.

2. Materials and methods

2.1 Seed sludge (Inoculum) Preparation

The raw feed sludge was the sludge collected after acidification process and was obtained from Jugra Palm Oil Mill, Banting, Selangor, Malaysia and stored in a cold room at 4 °C prior to its use as inoculum. The inoculum was prepared at 5.4 g MLVSS L^{-1}. Prior to its use, the sludge was heat-treated at 100 °C for an hour to enrich hydrogen-producing bacteria (HPB) and to inactivate the hydrogentrophic methanogens. The characteristics of the seed sludge were presented in Table 1.

Table 1. Characteristics of the seed sludge (inoculum) and raw POME (substrate).

Parameter	Unit	Heat-treated POME sludge (Inoculum)	Raw POME (substrate)	Pre-settled POME (substrate)
Total Suspended Solid (TSS)	mg TSS/l	27,611 ± 2,149	-	-
Volatile Suspended Solid (VSS)	mg VSS/l	19,167 ± 2,357	-	-
Total COD	mg COD/l	-	52,122 ± 96	28,122 ± 419
Soluble COD	mg COD/l	-	25,666 ± 943	26,466 ± 2,963
pH	-	7.42	4.99	4.99

2.2 Raw POME (substrate) Preparation

The substrate was the POME collected from Jugra Palm Oil Mill, Banting, Selangor, Malaysia after acidification process. Prior to its use, raw POME was allowed to settle before the supernatant was extracted and used as a substrate. The supernatant was called pre-settled POME. The characteristics of the substrate were presented in Table 1.

2.3 Batch fermentation Experiment

Batch tests were conducted with 156 ml serum bottles with a working volume of 100 ml. The reaction starts right after the substrate was mixed with inoculum with initial COD of 32,320 mg L^{-1} for 0.11 (inoculum:substrate (v/v)), initial COD of 28,720 mg L^{-1} for 0.39 (inoculum:substrate (v/v)) and initial COD of 16,720 mg L^{-1} for 0.67 (inoculum:substrate (v/v)), without any pH adjustment. Then, the pH of the mixture was adjusted to pH 5.5±0.2 with 1N HCL or 1N NaOH. Prior to the test, the serum bottles were purged with nitrogen gas for 10 mins at 10 ml min^{-1} in order to create anaerobic conditions. All batch tests were conducted based on the RSM data using Design Expert® Software (Stat-Ease Inc., version 7.0.0). The total biogas composition was monitored by gas chromatography. The liquid samples were analysed for effluent COD at 8, 16 and 24 hours' intervals.

2.4 Analytical Methods

Total suspended solids (TSS), volatile suspended solids (VSS), and chemical oxygen demand (COD) were analysed at 8 hours intervals and the tests were conducted in accordance to APHA Standard Methods 2540 D, 2540 G, and 5220 D, respectively.

The biogas composition was analysed by a gas chromatograph (Perkin Elmer, AutoSystem Gas Chromatograph, 600 Series LINK) equipped with a thermal conductivity detector (TCD) and a pack GC column Supelco, with 40/80 carboxen 1000, MR2924D, 10' x 1/8'. Argon was used as a carrier gas at a flowrate of 30 ml min^{-1}. The temperatures of the oven, injector and detector were 100°C, 150°C and 200°C respectively. The gas sample used for injection was 0.5 ml using gas tight syringe 2500 µl Hamilton, USA.

2.5 Kinetic Study

The statistical method of factorial using design of experiment (DOE) will eliminate systematic errors as well as minimize the number of experiments. In this batch mode study, H_2 production from POME was analysed and optimized by employing a central composite design (CCD) of response surface methodology (RSM). The effects of inoculum:substrate (I:S), reaction temperature and fermentation time on the process responses were then explained. Each factor was evaluated at high, central and low levels to estimate the experimental variability, experimental design, as well as the corresponding experimental results. A total of twenty experimental sets were prepared, with the application of 6 replicates at the centre point. To visualize the effects of the studied variables, a three-dimensional (3D) plots were used. The simultaneous interactions of the variables on the responses were also studied from those plots. The coefficients of the polynomial model were obtained using Eq. (1);

$$Y = \beta_0 + \beta_i X_i + \beta_j X_j + \beta_{ii} X_i^2 + \beta_{jj} X_j^2 + \beta_{ij} X_i X_j + \ldots \quad (1)$$

where β is the regression coefficient, i is the linear coefficient and j is quadratic coefficient. Based on P value at 95% confidence level, the terms of the model will be selected or rejected. Then, the results were analysed by using ANOVA (Design Expert® software). With respect to the 3D plots and their respective contour plots, the effects of simultaneous interaction of the variables on the responses were investigated. The ANOVA values for RSM are shown in Table 2.

3. Results and Discussion

3.1 COD removal efficiency

From Table 2, Model F-value of 22.32 implied that the model is significant. Values of Prob > F less than 0.05 indicated that the model terms are significant. In this case, A and C^2 are both significant model terms. Some of the insignificant model terms were eliminated to simplify the model. The regression equation of the reduced quadratic model for the response is as follows:

$$\text{COD rem. eff.} = 40.24 - 9.87A - 1.42B + 1.11C + 2.07AB + 0.89AC - 7.08C^2 \quad (2)$$

Table 2. ANOVA for response surface models applied.

1. Response: COD removal efficiency.						
Source	**Sum of Squares**	**df**	**Mean Square**	**F Value**	**Prob > F**	
Model	1297.78	6	216.30	22.32	< 0.0001	significant
A-I:S	974.13	1	974.13	100.51	< 0.0001	significant
B-Temperature	20.10	1	20.10	2.07	0.1735	
C-Reaction time	12.35	1	12.35	1.27	0.2793	
AB	34.26	1	34.26	3.53	0.0827	
AC	6.29	1	6.29	0.65	0.4351	
C^2	250.65	1	250.65	25.86	0.0002	significant
R-Squared	0.91					
Adj R-Squared	0.87					
2. Response : H_2 Yield (ml H_2/g COD removed)						
Source	**Sum of Squares**	**df**	**Mean Square**	**F Value**	**Prob > F**	
Model	743.99	6	124.00	14.77	< 0.0001	significant
A-I:S	402.50	1	402.50	47.95	< 0.0001	significant
B-Temperature	26.86	1	26.86	3.20	0.0969	
C-Reaction time	125.08	1	125.08	14.90	0.0020	significant
AC	77.78	1	77.78	9.27	0.0094	significant
B^2	72.67	1	72.67	8.66	0.0114	significant
C^2	0.013	1	0.013	1.500E-003	0.9697	
R-Squared	0.87					
Adj R-Squared	0.81					

From the 3D response surface plots (Figure 1A), it can be seen that COD removal efficiency increased as the inoculum substrate ratio increased under mesophilic condition for 8 hours' reaction time. However, COD removal efficiency slowly decreased as reaction temperature increased from mesophilic to thermophilic condition. This trend can be seen for reaction time of 8 hours, 16 hours and 24 hours (Figure 1). These interactions implied that inoculum substrate ratio (A) and reaction time (C) were not significantly affecting COD removal efficiency. The highest COD removal efficiency of 49.50% reported to be at 30°C for 8 hour reaction time at the initial COD concentration of 32,320 mg L^{-1} with 0.11 inoculum substrate ratio.

3.2 Hydrogen Yield

From Table 2, hydrogen yield regression model was significant as the model F value is equal to 14.77. Values of Prob > F less than 0.0500 indicated that model terms are significant. In this case A, C, AC, and B^2 are significant model terms. The R-squared (R^2) value of the model was 0.87. After reduced some of the quadratic model, the regression equation for the response is as follows:

$$H_2 \text{ Yield} = 6.23 + 6.34A + 1.64B - 3.54C - 3.12AC + 4.77B^2 - 0.063C^2 \quad (3)$$

Figure 2 showed 3D surface plots of the model for hydrogen yield, as a function of I:S (A) and reaction time (C) at different reaction temperature, namely 30°C, 40°C and 50°C. From the response surface plots (Figure 2A, 2B, 2C), the increment of hydrogen yield has been observed as the I:S decreased from 32,320 mg L^{-1} to 16,720 mg L^{-1} CODin at the initial reaction time of 8hr. However, hydrogen yield decreased as the reaction time increased to 24 hr. These interactions implied that inoculum substrate ratio (I:S) and reaction time may significantly affect the hydrogen yield.

Additionally, the designed test was monitored for a fermentation time of 24 h in order to understand the variation during the fermentation period in producing maximum hydrogen yield without shifting the process towards methanogenesis. During this batch experiment, no methane gas detected during the course of all experiments. Thus, the results suggested that heat treatment had successfully inhibit methanogenic bacteria in the mixed bacterial consortium. Other than that, this study also showed that the reaction (fermentation) time have significant effects on the hydrogen yield. Based on Figure 2, the maximum amount of hydrogen yield of 28.47 ml H_2 g^{-1} COD removed was obtained at inoculum substrate ratio (I:S) of 0.67 (initial COD concentration of 16,720 mg L^{-1}) at 8 hr reaction time and 50°C of reaction temperature (Figure 2C). Subsequently, the highest hydrogen yield of 15.8447 ml H_2 g^{-1} COD removed was detected at reaction temperature of 50°C for 0.40 inoculum substrate ratio with reaction time of 8 hours.

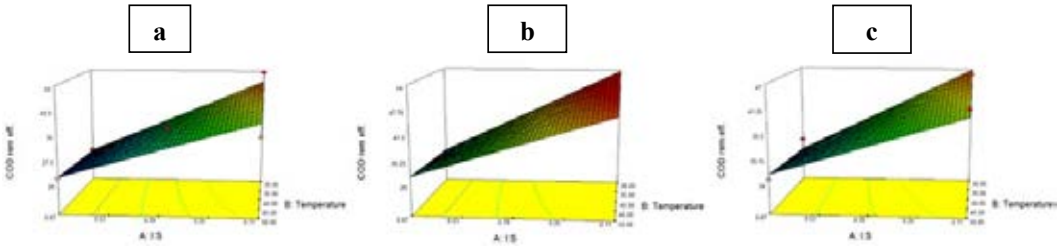


Figure 1. 3D image of effects of inoculum:substrate and reaction temperature (h) on COD removal efficiency (%) at (a); 8 hrs reaction time; (b) 16 hrs reaction time; (c) 24 hrs reaction time.

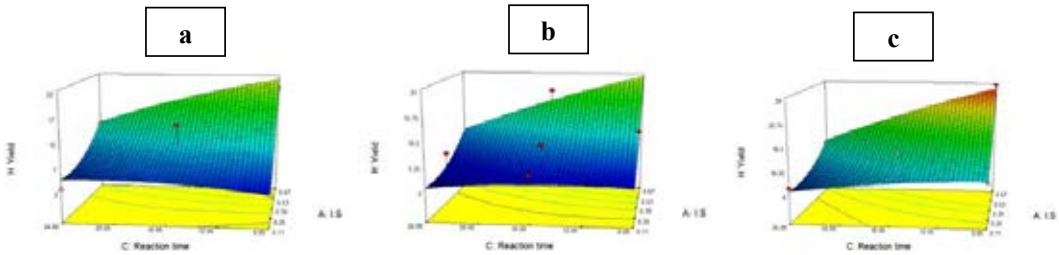


Figure 2. 3D image of effects of inoculum:substrate and reaction (fermentation) time (h) on Hydrogen Yield (ml H2/g COD removed) at reaction temperature of (a) 30°C; (b) 40°C; (c) 50°C.

4. Conclusions

The effects of three most important variables namely inoculum:substrate (I:S), reaction temperature and fermentation time of the granulated sludge in hydrogen production was evaluated using batch mode. Central composite design (CCD) of response surface methodology (RSM) was used to find interactions between selected variables. COD removal efficiency and hydrogen yield (YH_2) were studied as responses. The highest COD removal efficiency was achieved at 49.50% with 0.11 I:S (>20 g L^{-1} CODin), 30°C reaction temperature and 8 hour fermentation time. The highest hydrogen yield of 28.47 ml H_2 g^{-1} COD removed was obtained at I:S of 0.66 (<20 g L^{-1} CODin), reaction temperature of 50°C and 8 hour fermentation time. Based on the optimization process using RSM, it can be concluded that lower substrate concentration (not more than 20 g/L) for biohydrogen production using pre-settled POME as a substrate was achieved, with optimum reaction time of 16 hours under thermophilic condition (40-50 °C). However, there are several factors that has be considered for biogas production in a larger scale.

Acknowledgements
A big thank to University of Malaya for the financial support under Industrial Prototype Grant (grant number RU019D-2014A).

References

1. Antonopoulou, G., et al., Biofuels generation from sweet sorghum: fermentative hydrogen production and anaerobic digestion of the remaining biomass. Bioresour Technol, 2008. 99(1): p. 110-9.
2. Das, D. and T. Veziroglu, Advances in biological hydrogen production processes. International Journal of Hydrogen Energy, 2008. 33(21): p. 6046-6057.
3. Malaysian Palm Oil Council (MPOC). 2016.
4. Hosseini, S.E. and M. Abdul Wahid, Pollutant in palm oil production process. Journal of the Air & Waste Management Association, 2015. 65(7): p. 773-781.
5. Yacob, S., et al., Baseline study of methane emission from anaerobic ponds of palm oil mill effluent treatment. Sci Total Environ, 2006. 366(1): p. 187-96.
6. Metcalf and Eddy, Wastewater Engineering Treatment and Reuse. 4th ed. 2003: McGraw Hill.
7. DATA FOR ENGINEERS: POME. 2004, Palm Oil Engineering Bulletin. p. 34-35.
8. Afsar, N., et al., Hydrogen productivity of photosynthetic bacteria on dark fermenter effluent of potato steam peels hydrolysate. International Journal of Hydrogen Energy, 2011. 36(1): p. 432-438.
9. Li, C. and H.H. Fang, Fermentative hydrogen production from wastewater and solid wastes by mixed cultures. Critical Reviews in Environmental Science and Technology, 2007. 37(1): p. 1-39.
10. Saraphirom, P. and A. Reungsang, Enhancement of biohydrogen production from sweet sorghum syrup by anaerobic seed sludge in an anaerobic sequencing batch reactor by nutrient and vitamin supplementations. Environ Technol, 2013. 34(17-20): p. 2503-11.
11. Guo, Y.-C., et al., Co-producing hydrogen and methane from higher-concentration of corn stalk by combining hydrogen fermentation and anaerobic digestion. International Journal of Hydrogen Energy, 2014. 39(26): p. 14204-14211.

Dark fermentative hydrogen gas production from waste peach pulp in a pilot scale reactor

Hidayet Argun, Siaka Dao
Environmental Engineering Department, Faculty of Engineering, Pamukkale University, Kınıklı Campus- 20070, Denizli-Turkey
Email: hargun@pau.edu.tr, siakadao90@yahoo.fr

Abstract
Hydrogen gas production from waste peach pulp using dark fermentation was studied in a pilot scale reactor. In this context the reactor was operated with and without inoculation at 45 g TS/L initial waste peach pulp concentration. Hydrogen gas production was faster when no inoculum was used. The hydrogen production rates and yields with and without inoculum addition were 6.05 L H_2/h, 735.66 mL H_2/g TOC and 12.62 L H_2/h, 855.66 mL H_2/g TOC, respectively. The hydrogen percentage in the biogas was about 50% in both set of experiments. Glucose in the waste was completely consumed and the TOC percentage was about 25% at the end of experiments. Experimental results were correlated with the Gompertz equation to compare the hydrogen production performance of the experiments. It was concluded that hydrogen could be more effective produced from waste peach pulp without any microbial inoculation.

Keywords: Waste peach pulp; pilot scale reactor; dark fermentation; bio-hydrogen.

1. Introduction

The rapidly increase in the global energy demand led to the fast consumption of finite fossil fuel reserves [1]. Besides fossil fuel combustion for energy production results in greenhouse gas emissions which are significant contributors for global warming [2]. Therefore countries are searching for alternative sustainable and clean energy fuels such as hydrogen gas (H_2) which is accepted as the energy carrier of the future [3]. H_2 is the most abundant element in the universe but H_2 gas is not available for direct use [4]. Therefore H_2 is produced with intensive energy dependent technologies such as steam reforming of natural gas, water electrolysis and the pyrolysis of biomass [5]. H_2 production from waste biomass by dark fermentation (DF) is an alternative technology. However, it is still in research stage and has not found application at large scale [6–8]. During DF, the substrate can be converted into volatile fatty acids, H_2 and CO_2 by microorganisms such as strict anaerobic spore forming *Clostridia* sp [9]. The theoretical maximum H_2 yield in DF is 524.5 mL H_2/ g COD when glucose is used as the sole carbon source (35 ºC, 1 atm) [10]. However, reported yields are lower than the theoretical value due to microbial limitations [11]. Most of the studies on DF are reported in small laboratory scale experiments [12–16] and there is lack of information for the experience of large scale operation [7]. In this context we investigated H_2 production from waste peach pulp (WPP) in a 140 L pilot scale reactor. The reactor was operated with and without inoculum addition for H_2 production and the results were compared accordingly.

2. Experimental Study

2.1 Inoculum

Heat treated anaerobic sludge (ANS) was used as inoculum. The ANS was obtained from an anaerobic waste water treatment plant of Pakmaya Baker's Yeast Company and boiled for one hour at pH: 5.5 to eliminate any methanogenic activity. ANS was grown on molasses growth media for one day at 37 ºC that contained 20 gCOD, 1.9 g $(NH_4)_2SO_4$, 0.44 g KH_2PO_4, 0.1 g $FeSO_4.7H_2O$, 0.2 g $MgSO_4$ and 0.1 g L.cysteine-HCl per liter. The reactor was inoculated with one litre sludge.

2.2 Substrate

Waste peach pulp (WPP) was used in DF experiments as substrate. WPP was obtained from a local fruit juice concentrates and purees factory and stored at -18 º C for further use. The WPP used in this study had the same composition as the WPP used in our previous study. The working volume of the reactor was 70 L and the C/N/Fe/Ni ratio of the media was adjusted to 100/2.09/3.89/0.047/0.043 using $(NH_4)_2SO_4$, KH_2PO_4, $FeSO_4.7H_2O$ and $NiCl_2.6H_2O$. The head space of the reactor was flushed with argon gas and the experiments took place at 37 ºC for 90 days. The initial TOC and TS concentrations were 38 and 45 g/L, respectively.

2.3 Reactor setup and experimental procedure

Experiments were done in a 140 L reactor and the working volume was 70 L. The pH was monitored and controlled with an automatic pH dosage pump (Tekna evo cod.TPR 603NHH0000). A centrifugal pump was used to stir the

fermentation media periodically (model BK 50 316 H 11-1 m Q 20-100L /min). The total gas was measured using a drum type gas meter (TG0.5/5 RİTTER) and the resulting gas was collected in a gas bag.

2. 4 Analytical Methods

Hydrogen percentage in the biogas was determined with a gas chromatograph (GC agilent 7820A). The oven, back inlet and back detector (TCD) temperatures of the GC were 110°C, 230°C, 250°C, respectively. Liquid samples were subjected to biomass, TOC, TKN, TP, glucose and volatile fatty acid (VFA) analyses. Biomass and glucose concentrations were determined according to the standard methods [17]and phenol-acid method [18], respectively. All other analyses were done as described in our previous study[19]. The hydrogen yield is this study stands for the amount of cumulative hydrogen volume per consumed amount of TOC. Gompertz [20] (Eq. 1) equation coefficients were determined using the regression analysis tool of the software Statistica (trial version):

$$H(t) = P \exp\left\{-\exp\left[\frac{R_m e}{P}(\lambda - t)\right] + 1\right\} \quad (1)$$

where P is the maximum hydrogen production potential in (mL), R is the hydrogen production rate in (mL H_2/h) and λ is the lag phase (h).

3. Results and Discussion

The variation of gas and liquid phase parameters with time during DF without inoculation is presented in Fig.1. Cumulative H_2 volume and TVFA concentration increased while TOC and glucose concentration decreased. H_2 production started after 20 hour adaptation period and reached its maximum (300 L) in about 70 h. The lag phase for H_2 production was related with the available glucose concentration. As can be seen in Fig.1, the sharp increase in the cumulative H_2 volume was observed during the fast consumption of glucose. Glucose concentration decreased from 23.5 to 0.8 g/L indicating effective consumption for microbial activity. The TOC removal efficiency and final TOC concentration were 22% and 12.81 g/L, respectively. TOC consumption was not as effective as glucose utilization (Fig. 1) since microorganisms preferred to consume readily available sugars instead hardly degradable carbon sources stacked within WPP. TVFA was another product observed during DF. TVFA concentration increased from 1 to 9.85 g/L with a TVFA conversion yield of 0.38 gTVFA/g glucose. The final TOC percentage in the dried residue at the end of the experiment and the maximum H_2 percentage in the biogas were 28.1 and 58.2, respectively. The hydrogen production rate and yield without inoculum addition were 12.62 L H_2/h and 855.66 mL H_2/g TOC, respectively. The Gompertz equation coefficients were determined as P: 299.75 L H_2, Rm: 12.62 L H_2/h, λ: 15.55 h (R^2: 0.99) which were in accordance with the cumulative H_2 formation curve in Fig.1.

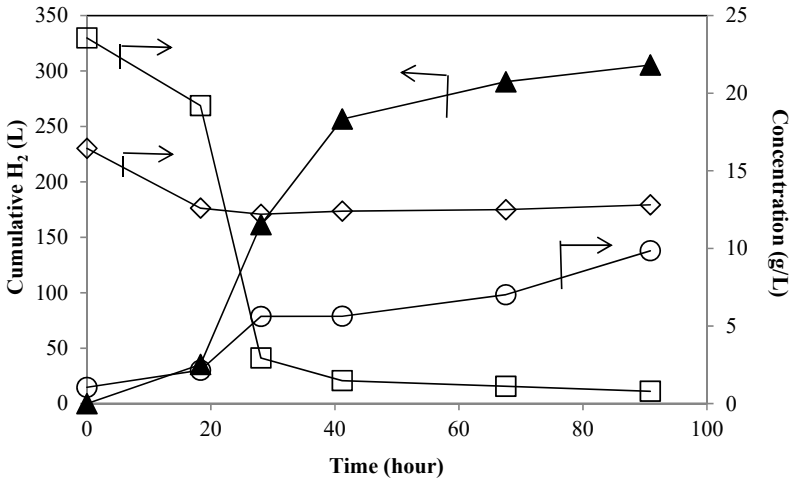


Fig. 1. Variation of cumulative H_2 volume (▲), glucose (□), TOC (◊) and TVFA (o) concentrations with time for the experiment without microbial inoculation.

Experimental results for H_2 production with inoculum addition are presented in Fig. 2. The trend for the fermentation parameters with time in Fig.1 was similar with the experiment without inoculum addition (Fig. 2). However, there were differences in H_2 production performance. H_2 formation started after a longer adaptation period (25 h) than the experiment without inoculum addition. The maximum cumulative H_2 volume (250 L) on the other hand was 50 L less than the maximum cumulative H_2 formation in Fig.1. Glucose consumption was slower and took longer time when compared with Fig.1. H_2 production was parallel with glucose consumption in Fig.1. However, H_2 formation in Fig.2 started after half of the glucose was consumed. TVFA formation was half of the TVFA formation in Fig.1. The VFA formation yield for the experiment with inoculation was 0.244 gTVFA/g glucose. The TOC removal efficiency, final TOC percentage in the dried effluent and maximum H_2 percentage in the biogas were 31%, 31.02%and 56.17%, respectively. Gompertz equation coefficients for the inoculated H_2 production experiment were P: 268.04 L H_2, Rm: 6.05 L H_2/h, λ: 21.27 h (R^2: 0.99). H_2 formation yield and rate were 6.05 L H_2/h, 735.66 mL H_2/g TOC, respectively.

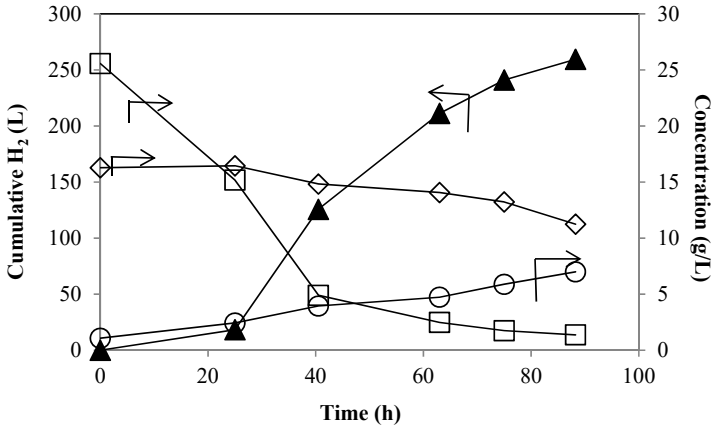


Fig. 2. Variation of cumulative H_2 volume (▲), glucose (□), TOC (◊) and TVFA (o) concentrations with time for the experiment with microbial inoculation.

4. Conclusions

Hydrogen production from waste peach pulp with and without microbial inoculation was studied in a pilot plant reactor. H_2 production performance was more efficient when the substrate was not inoculated with heat treated anaerobic sludge. The H_2 formation yields for both systems was comparable around 800 mL H_2/g TOC, but H_2 formation rate was twice as fast when no inoculum was used. Moreover glucose consumption and TVFA formation were more efficient in the system without inoculation as well. The natural microflora within waste peach pulp was more capable to adapt to the substrate and to produce fast hydrogen. It was expected that external inoculation would contribute well to hydrogen formation. However, the inoculation haltered hydrogen formation and substrate consumption probably due to the presence of microorganisms shifting the pathway towards other product formation. Hydrogen production from waste peach pulp in a pilot scale reactor without inoculation was found to be an effective method.

Acknowledgement:

This study was supported by TUBİTAK with a grant number 113M994. Also the full conference attendance was financially supported by Pamukkale University Scientific Research Projects Coordination Unit (PAÜ-BAP) with a grant number 2017KRM002 PAÜ-ADEP. The authors are thankful for TUBİTAK and PAÜ-BAP for their support.

Nomenclature

H_2 Hydrogen gas

Acronyms

ANS	Anaerobic Sludge
COD	Chemical Oxygen Demand
GC	Gas Chromatograph
DF	Dark Fermentation
TKN	Total Kjeldahl Nitrogen
TP	Total Phosphorous
TOC	Total Organic Carbon
TS	Total Solids
VFA	Volatile Fatty Acids
TVFA	Total Volatile Fatty Acids
WPP	Waste Peach Pulp

References

1. Sinha P, Pandey A. An evaluative report and challenges for fermentative biohydrogen production. Int J Hydrogen Energy 2011;36:7460–78.
2. Liu C-M, Chu C-Y, Lee W-Y, Li Y-C, Wu S-Y, Chou Y-P. Biohydrogen production evaluation from rice straw hydrolysate by concentrated acid pre-treatment in both batch and continuous systems. Int J Hydrogen Energy 2013;38:15823–9.
3. Hallenbeck PC, Abo-Hashesh M, Ghosh D. Strategies for improving biological hydrogen production. Bioresour Technol 2012;110:1–9.
4. Das D, Veziroğlu TN. Hydrogen production by biological processes: a survey of literature. Int J Hydrogen Energy 2001;26:13–28.
5. Dincer I, Acar C. Review and evaluation of hydrogen production methods for better sustainability. Int J Hydrogen Energy 2014;40:11094–111.
6. Azbar N, Levin DB. State of the art and progress in production of biohydrogen. Bentham Science Publishers; 2012.
7. Tapia-Venegas E, Ramirez-Morales JE, Silva-Illanes F, Toledo-Alarcón J, Paillet F, Escudie R, et al. Biohydrogen production by dark fermentation: scaling-up and technologies integration for a sustainable system. Rev Environ Sci Biotechnol 2015;14:761–85.
8. Kumar G, Bakonyi P, Periyasamy S, Kim SH, Nemestóthy N, Bélafi-Bakó K. Lignocellulose biohydrogen: Practical challenges and recent progress. Renew Sustain Energy Rev 2015;44:728–37.
9. Levin DB, Pitt L, Love M. Biohydrogen production: Prospects and limitations to practical application. Int J Hydrogen Energy 2004;29:173–85.
10. Singh R. Fermentative Biohydrogen Production Using Microbial Consortia. In: Gupta VK, Tuohy MG, editors. Biofuel Technol. Recent Dev., Heidelberg: Springer; 2013, p. 273–99.
11. Argun H, Pelin G, Kapdan IK. Biohydrogen Production Potential of Different Biomass Sources. In: Singh A, Rathore D, editors. Biohydrogen Prod. Sustain. Curr. Technol. Futur. Perspect., New Delhi: Springer India; 2017, p. 11–48.
12. Shah AT, Favaro L, Alibardi L, Cagnin L, Sandon A, Cossu R, et al. Bacillus sp . strains to produce bio-hydrogen from the organic fraction of municipal solid waste. Appl Energy 2016;176:116–24.
13. Soltan M, Elsamadony M, Tawfik A. Biological hydrogen promotion via integrated fermentation of complex agro-industrial wastes. Appl Energy 2017;185:929–38.
14. Xia A, Cheng J, Ding L, Lin R, Song W, Su H, et al. Substrate consumption and hydrogen production via co-fermentation of monomers derived from carbohydrates and proteins in biomass wastes. Appl Energy 2015;139:9–16.
15. Zhang Y, Zhang F, Chen M, Chu P, Ding J, Zeng RJ. Hydrogen supersaturation in extreme-thermophilic (70 ° C) mixed culture fermentation. Appl Energy 2013;109:213–9.
16. Singh A, Rathore D, editors. Biohydrogen Production: Sustainability of Current Technology and Future Perspective. Springer India; 2017.
17. Eugene W. Rice, Rodger B. Baird, Andrew D. Eaton LSC. Standard Methods for the Examination of Water and Wastewater. Am Water Work Assoc Public Work Assoc Environ Fed 2012:1469.
18. DuBois M, Gilles KA, Hamilton JK, Rebers P a., Smith F. Colorimetric Method for Determination of Sugars and Related Substances. Anal Chem 1956;28:350–6.
19. Argun H, Dao S. Hydrogen gas production from waste peach pulp by dark fermentation and electrohydrolysis. Int J Hydrogen Energy 2016;41:11568–76.
20. Lee KS, Hsu YF, Lo YC, Lin PJ, Lin CY, Chang JS. Exploring optimal environmental factors for fermentative hydrogen production from starch using mixed anaerobic microflora. Int J Hydrogen Energy 2008;33:1565–72.

ORAL PROCEEDINGS

Investigation the effect of annealing atmosphere and time on photoelectrochemical (PEC) properties of α-Fe_2O_3 photoanode

Selim Demirci[1,2], Cevat Sarıoğlu[1]
[1]Marmara University, Department of Metallurgical and Materials Engineering, Kadiköy, 34722, Istanbul, Turkey
[2]Marmara University, Institute of Pure and Applied Sciences, Kadiköy, 34722 Istanbul, Turkey
Email: selim.demirci@marmara.edu.tr, cevat.sarioglu@marmara.edu.tr

Abstract
Photoelectrochemical (PEC) cells offer the ability to convert electromagnetic energy from our largest renewable source, the Sun, to stored chemical energy through the splitting of water. The aim of this study is the fabrication of α-Fe_2O_3 (hematite) photoanodes and application them for hydrogen production. In this study, hematite photoanodes were successfully fabricated by thermal oxidation of the commercial cold-rolled steel at 500 °C in pure water vapor and air atmosphere for various time. PEC performance of the as-produced α-Fe_2O_3 photoanodes were investigated. The crystal phase structure and surface morphologies of the α-Fe_2O_3 photoanodes were characterized using an X-ray diffractometer (XRD) and field emission scanning electron microscopy (FESEM), respectively. PEC studies of the α-Fe_2O_3 photoanodes were assessed in the 0.1 M NaOH electrolyte solution. The results showed that hematite photoanodes had high crystalline phase and the annealing atmosphere influenced the morphology of the α-Fe_2O_3 photoanodes. The PEC findings exhibited that the α-Fe_2O_3 photoanode annealed 15-min in water vapor had best PEC performance achieving photocurrent density 0.228 mA/cm^2 at 1.57 V vs. V_{RHE} and highest carrier density value (N_D=1.15×10^{21} cm^{-3}). Furthermore, the photoanodes annealed in water vapor atmosphere revealed at least seven times higher PEC performance than that of photoanodes annealed in air. Thermal oxidation method in water vapor is an efficient methods for enhancement of PEC performance of α-Fe_2O_3 photoanodes.

Keywords: Hematite; Thermal oxidation; Water vapor; Photoelectrochemical (PEC)

1. Introduction
α-Fe_2O_3 has attracted considerable attention as an intrinsic n-type semiconductor oxide which has different technological application fields such as gas-sensor, magnetic devices, pigments, photocatalytic fields, photoanodes, rechargeable lithium-ion batteries and optoelectronic [1], [2], [3], [4]. One of the important fields of the hematite is application in the for PEC water splitting as a photoanode. α-Fe_2O_3 is currently considered to be a promising candidate for solar hydrogen production owing to its low toxicity, wide abundance, low cost, low band gap (~ 2.1 eV) and chemical stability. α-Fe_2O_3 theoretical solar-to-hydrogen efficiency can be as large as 16.8% under solar irradiation (AM 1.5 G illumination, 100 mW/cm^2) at 1.23 V vs RHE, generating a photocurrent density of 12.6 $mAcm^{-2}$ [5], [6]. In spite of the great traits of the hematite semiconductor, it have some disadvantages properties which affect the PEC performance. α-Fe_2O_3 possesses a very short state lifetime (10 ps), a low absorption coefficient, poor electrical conductivity and short hole diffusion length which restricts the utilization of hematite in PEC [7], [8]. In order to overcome the above-mentioned limitations of α-Fe_2O_3 and improve the efficiency, researches have been focus on nanostructures (1D structures) to satisfy the requirement of short hole diffusion distance beside doping of photo electrodes and surface modification of photo-electrodes with catalysis [5], [9, 10]. Up to now, several diversity techniques have been used in order to synthesize hematite nanostructure. Among the production techniques, the thermal oxidation method is very single-step, simple and cost efficient process. This technique does not require specific and expensive equipment. A lot of researchers have focused on growth and fabrication of the hematite nanowire and nanorod nanostructures by means of thermal oxidation method so far in the literature. When the Fe or steel is oxidized at high temperature, the oxide consists of multilayer scales in the sequence of Fe/FeO/Fe_3O_4/Fe_2O_3 based on at which temperature iron or steel are oxidized. Below 570 °C, the phase FeO does not form according to the iron–oxygen system [11, 12]. Herein, for the first time we tried to show PEC properties of α-Fe_2O_3 photoanodes synthesized in pure water vapor atmosphere at different annealing time. Also, hematite photoanodes were synthesized in air atmosphere to in order to gain insight into effect of the different atmosphere treatment and time on the morphological, optical and PEC properties of the α-Fe_2O_3 nanostructure

2. Experimental Section
Commercial cold-rolled steel sheet (DIN EN 10130) was used in the experiment as a substrate. The composition of the steel was given in Table 1. The cold-rolled steel were mechanically polished with different SiC emery papers (with the following grades: 320, 800 and 1000), then ultrasonically rinsed in a bath of acetone, ethanol and deionized (DI) water for each 15 min, respectively. Thermal oxidation process was carried out in a tube furnace (Protherm) for various oxidation time under water vapor (wv) and air atmosphere at 500 °C. A steam cleaner machine (Karcher SC 1) was employed to provide water vapor (wv) which was injected to the furnace. The pressure of water vapor was 0.3 MPa. The water vapor rate was 35 g/min in the continuous steaming mode

of the machine. The surface morphologies of all samples were characterized by field emission scanning electron microscopy (FEI Sirion XL30 FEG SEM). Phase identification and crystal structures of the samples were performed by X-ray diffractometer (XRD, Bruker AXS D2 Phaser). The PEC measurements were conducted in a conventional three electrode system by means of potentiostat (Reference 600 Potentiostat/ Gamry) under AM 1.5G solar light irradiation (100 $mWcm^{-2}$, Asahi Spectra/HAL-320 Solar Simulator).

Table 1. The chemical composition (in wt. (%)) of the Cold-Rolled Steel (DIN EN 10130).

Material	C %	P %	S %	Mn %
Cold-Rolled Steel (DIN EN 10130)	0.07-0.12	0.02-0.045	0.02-0.045	0.3-0.6

3. Result and Discussion

The sharp and intense peaks in spectra are indication of the presence of highly crystalline hematite nanostructure. The crystallinities of the photoanodes increased with the annealing time due to increasing of mobility of surface layer and surface diffusion of Fe ions [13]. High crystalline phase has positive effect on PEC properties. Moreover, it can be seen from Fig. 1 that α-Fe_2O_3 phase is not only structure which was obtained because of the substrate material. Magnetite and pure iron phases have also been observed. The main diffraction peaks at 35.46 (110) coincide with the JCPDS values (PDF Card No: 00-033-0664) which correspond to crystal structure of hematite phases [14]. There are two main peaks for α-Fe_2O_3, which generally appear at 33.3° and 35. 66°, respectively.

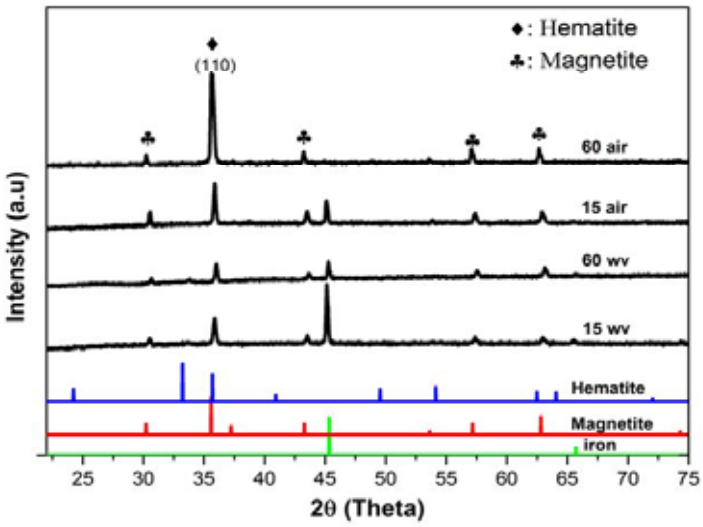


Fig. 1. XRD spectra of the α-Fe_2O_3 photoanodes annealed in water vapor and air atmosphere

Fig. 2 displays the images of morphology of the prepared α-Fe_2O_3 photoanodes annealed in water vapor and air atmosphere, respectively. It can be concluded from the images that all samples have a uniform nanostructure. As can be seen from Fig. 2(a), the nanorod shaped structures dominated on the substrate for water vapor annealed α-Fe_2O_3 photoanodes. However, the diameter and width of the nanorods gradually increased with rising annealing time under water vapor atmosphere. Therefore, the nanorod structure was not observed for 60-min annealed α-Fe_2O_3 photoanode in Fig. 2(b). As for α-Fe_2O_3 photoanodes annealed under air atmosphere, it can be seen in Fig. 2(c) and (d), nanowhisker shaped structure was observed for α-Fe_2O_3 photoanode annealed in air atmosphere. The nanowhisker morphology transformed to nanoplate structures by increasing annealing time. Nanostructure with high aspect ratio up to certain extent is the best morphology for enhanced the PEC performances because of eliminating of drawbacks of α-Fe_2O_3 photoanodes in terms of short hole diffusion and recombination rates [15].

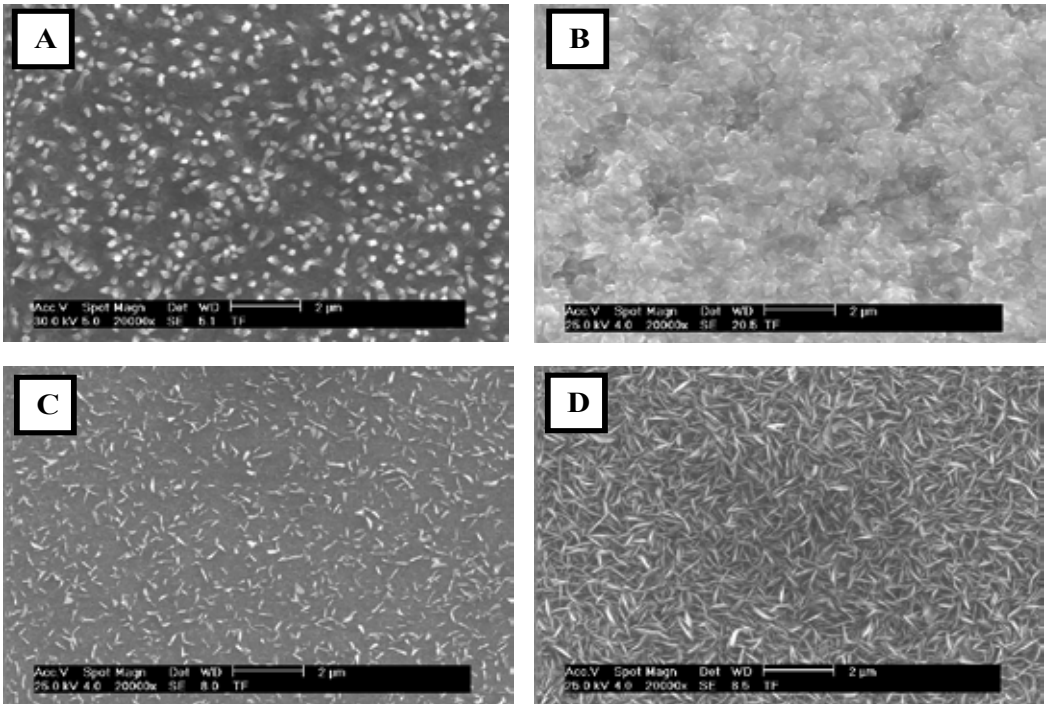


Fig. 2. FESEM images of α-Fe_2O_3 photoanodes (a) 15-min annealed in water vapor, (b) 60-min annealed in water vapor, (c) 15-min annealed in air and (d) 60-min annealed in air.

Fig. 3 demonstrates PEC performances of the α-Fe_2O_3 photoanodes, measured in 0.1 M NaOH solution. It can be observed from Fig. 3 that among the various annealing time conditions, the 15 min-annealed α-Fe_2O_3 photoanode in water vapor atmosphere exhibits the highest photocurrent density value throughout the measured potential range. The photocurrent density of 15 min-annealed α-Fe_2O_3 photoanode reached to 0.021 mA/cm^2 at 1.23 V vs. RHE and a maximum photocurrent of 0.228 mA/cm^2 at 1.57 V vs. RHE is also obtained. Moreover, the photoanodes annealed under water vapor atmosphere possess at least seven times higher photocurrent density than that of photoanodes annealed under air atmosphere when they were exposed to same annealing time. The photocurrent densities of the α-Fe_2O_3 photoanodes at 1.23 and 1.57 V_{RHE} were summarized in the Table 2.

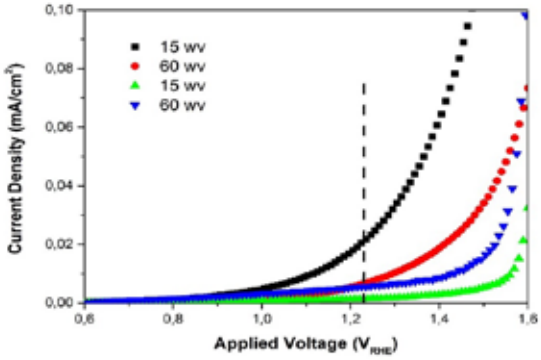


Fig. 3. Current density versus potential plots for α-Fe_2O_3 photoanodes annealed at different time and atmosphere.

Table 2. Photocurrent density values at 1.23 and 1.57 V_{RHE}, flat band potential (V_{FB}) and surface carrier density (N_D) of the hematite photoanodes subjected to the various thermal treatment time at 500 °C in water vapor and air atmosphere.

Materials	J at 1.23 V_{RHE} (mA/cm^2)	J at 1.57 V_{RHE} (mA/cm^2)	V_{FB}	N_D (cm^{-3})
15 wv	0.021	0.228	0.305	1.15×10^{21}
60 wv	0.0048	0.072	0.59	7.55×10^{19}
15 air	0.0015	0.032	0.535	2.77×10^{20}
60 air	0.0055	0.11	0.602	4.52×10^{20}

Mott–Schottky analysis was employed in order to determine both carrier density and flat band potential of the α-Fe_2O_3 photoanodes at the semiconductor/electrolyte interface using the equation (1) [16] in 0.1 M NaOH in the dark conditions.

$$\frac{1}{C^2} = \left(\frac{2}{q\varepsilon\varepsilon_o N_D}\right)\left(V - V_{FB} - \frac{kT}{q}\right) \quad (1)$$

where q is the electron charge (1.602 × 10^{-19} C), N_D is charge carrier density, C is the capacitance of the depletion region, V_{FB} is the flat band potential, V is the potential difference across the semiconductor space charge region, ε_o is the electric permittivity of vacuum (8.85×, 10^{-14} Fcm^{-1}), ε is the semiconductor dielectric constant (α-Fe_2O_3 = 80) [17] and k is Boltzmann constant, T is the absolute temperature. Fig. 4 demonstrates the Mott-Schottky plots of the α-Fe_2O_3 photoanodes. The x axis and y axis of Mott-Schottky curve represent capacitance and potential. As can be seen from Fig. 4 that all photoanodes have a positive slopes, which indicates that all of them are n-type semiconductors with electrons as the majority. The flat potential can be also estimated using linear fitting of the Mott–Schottky curves. The intercept of the linear fitting of the Mott-Schottky curve at the x-axis gives the flat band potential (V_{FB}) when $1/C^2$ is extrapolated to zero point. Furthermore, the smaller slope means having a higher carrier density for the α-Fe_2O_3 photoanodes. Also, carrier density values of the hematite photoanodes were calculated using the following equation (5) [18].

$$N_D = \frac{2}{q\varepsilon\varepsilon_o A^2 slope} \quad (2)$$

According to the equation (2), the α-Fe_2O_3 photoanode annealed, which showed the best PEC properties, for 15 min-annealed possessed the highest N_D value. These result are in good agreement with the PEC performance. The determined values of V_{FB} and N_D for all hematite electrodes are summarized in the Table 2.

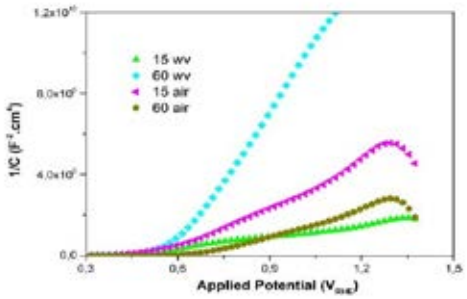


Fig. 4. Mott–Schottky plots of the α-Fe_2O_3 photoanodes.

4. Conclusion

In this present study, α-Fe_2O_3 photoanodes were synthesized under water vapor and air atmosphere at 500 °C for different annealing time in order to evaluate photochemical properties. It is a single-step, simple and environment method. XRD measurements revealed that crystalline hematite phase was obtained. It can be mentioned that the atmosphere condition influenced the morphology of the α-Fe_2O_3 photoanodes based on the FESEM results. It was observed that morphology structure depends on the annealing atmosphere. The nanorods were generally formed under water vapor atmosphere, whilst nanowhisker and nanoplate structures were fabricated on the substrate materials. Moreover, one can be said that the hematite photoanodes annealed under water vapor atmosphere showed at least seven times higher PEC properties that that of photoanodes annealed

under air for same annealing time. The maximum photocurrent densities were obtained 0.021 $mAcm^{-2}$ at 1.23 V vs. RHE and 0.228 $mAcm^{-2}$ at 1.57 V vs. RHE, respectively for 15-min annealed α-Fe_2O_3 photoanode under water vapor. This is in good agreement with the Mott–Schottky plots that indicate that this photoanode possesses the highest carrier density, which increases its conductivity.

Acknowledgements
This work is supported by the Marmara University (Bapko project no: FEN-A-131216-0544).

References

1. Xu D, Rui Y, Mbah VT, Li Y, Zhang Q, Wang H. Binary nickel and iron oxide modified Ti-doped hematite photoanode for enhanced photoelectrochemical water splitting. International Journal of Hydrogen Energy. 2016;41:873-81.
2. Zhang Z, Hossain MF, Takahashi T. Self-assembled hematite (α-Fe2O3) nanotube arrays for photoelectrocatalytic degradation of azo dye under simulated solar light irradiation. Applied Catalysis B: Environmental. 2010;95:423-9.
3. Hao HY, Sun DD, Xu YY, Liu P, Zhang GY, Sun YQ, et al. Hematite nanoplates: Controllable synthesis, gas sensing, photocatalytic and magnetic properties. J Colloid Interface Sci. 2016;462:315-24.
4. Wang X, Zhang M, Liu E, He F, Shi C, He C, et al. Three-dimensional core-shell Fe2O3@carbon/carbon cloth as binder-free anode for the high-performance lithium-ion batteries. App. Surface Science. 2016;390:350-6.
5. Sivula K, Le Formal F, Grätzel M. Solar Water Splitting: Progress Using Hematite (α-Fe2O3) Photoelectrodes. ChemSusChem. 2011;4:432-49.
6. Andebet Gedamu Tamirat, John Rick, Amare Aregahegn Dubale, Sub W-N, Hwang B-J. Using hematite for photoelectrochemical water splitting: a review of current progress and challenges. Nanoscale Horizons. 2016;1:243-67.
7. Lee MH, Park JH, Han HS, Song HJ, Cho IS, Noh JH, et al. Nanostructured Ti-doped hematite (α-Fe2O3) photoanodes for efficient photoelectrochemical water oxidation. International Journal of Hydrogen Energy. 2014;39:17501-7.
8. Zhang YC, Zhang HN, Ji HW, Ma WH, Chen CC, Zhao JC. Pivotal Role and Regulation of Proton Transfer in Water Oxidation on Hematite Photoanodes. Journal of the American Chemical Society. 2016;138:2705-11.
9. Wang M, Wang H, Wu Q, Zhang C, Xue S. Morphology regulation and surface modification of hematite nanorods by aging in phosphate solutions for efficient PEC water splitting. International Journal of Hydrogen Energy. 2016;41:6211-9.
10. Jang JT, Ryu H, Lee WJ. The growth of hematite by electrochemical deposition for PEC applications. Journal of Alloys and Compounds. 2015;638:387-92.
11. Chen RY, Yeun WYD. Review of the High-Temperature Oxidation of Iron and Carbon Steels in Air or Oxygen. Oxidation of Metals. 2003;59:433-68.
12. Budiman F, Bashirom N, Tan WK, Razak KA, Matsuda A, Lockman Z. Rapid nanosheets and nanowires formation by thermal oxidation of iron in water vapour and their applications as Cr(VI) adsorbent. Applied Surface Science. 2016;380:172-7.
13. Hiralal P, Unalan HE, Wijayantha KGU, Kursumovic A, Jefferson D, MacManus-Driscoll JL, et al. Growth and process conditions of aligned and patternable films of iron(III) oxide nanowires by thermal oxidation of iron. Nanotechnology. 2008;19:455608.
14. Lian XJ, Yang X, Liu SJ, Xu Y, Jiang CP, Chen JW, et al. Enhanced photoelectrochemical performance of Ti-doped hematite thin films prepared by the sol-gel method. Applied Surface Science. 2012;258:2307-11.
15. Fu YM, Dong CL, Zhou ZH, Lee WY, Chen J, Guo PH, et al. Solution growth of Ta-doped hematite nanorods for efficient photoelectrochemical water splitting: a tradeoff between electronic structure and nanostructure evolution. Physical Chemistry Chemical Physics. 2016;18:3846-53.
16. Hahn NT, Mullins CB. Photoelectrochemical Performance of Nanostructured Ti- and Sn-Doped α-Fe2O3 Photoanodes. Chemistry of Materials. 2010;22:6474-82.
17. Le Formal F, Tetreault N, Cornuz M, Moehl T, Gratzel M, Sivula K. Passivating surface states on water splitting hematite photoanodes with alumina overlayers. Chemical Science. 2011;2:737-43.
18. Kronawitter CX, Vayssieres L, Shen SH, Guo LJ, Wheeler DA, Zhang JZ, et al. A perspective on solar-driven water splitting with all-oxide hetero-nanostructures. Energy & Environmental Science. 2011;4:3889-99.

Biohydrogen Production from Acid Hydrolyzed Waste Wheat in a Continuously Operated Packed Bed Reactor

Betül Kirli[1], Ilgi Karapinar[2]
[1]Dokuz Eylul University, Graduate School of Natural and Applied Sciences, Department of Biotechnology, Tinaztepe Campus, Buca, Izmir, Turkey
[2]Dokuz Eylul University, Department of Environmental Engineering, Tinaztepe Campus, Buca, Izmir, Turkey
E-mail: ilgi.karapinar@deu.edu.tr

Abstract
The effect of hydraulic retention time on biohydrogen production from acid hydrolyzed waste wheat by dark fermentation in a continuously operation up flow packed bed reactor containing metal mesh covered plastic scouring sponge pad was investigated . The substrate was waste wheat which was sieved down to 70 µm size (less than 200 mesh) first and then, hydrolyzed by using H_2SO_4 at pH=2 and 90 °C in an autoclave for 15 min. The sugar solution obtained from hydrolysis of waste wheat was used as carbon source after neutralization and nutrient addition. Particle number in the reactor was 85 with dimensions of L=1, W=1, D=0.5 cm**.** The reactor was operated at hydraulic retention times (HRTs) between 2 and 13 h at constant initial total sugar concentration of TS_0=5 g/L. The highest volumetric hydrogen production rate and yield were obtained as VHP= 1.75 L H_2 / L d and Y_{H2}=1.6 mol/mol TS, respectively at HRT= 2 h. Metal mesh covered plastic scouring sponge pad was an effective support particle to obtain high hydrogen yield and rate at short HRT. The results depicted that metal mesh covered scouring sponge pad particles can be used as microorganism immobilization material for efficient biohydrogen production by dark fermentation.

Keywords: Biohydrogen; dark fermentation; hydraulic retention time; packed bed, waste wheat.

1. Introduction

Hydrogen is a renewable and a clean gas with high energy value. It is considered as an alternative energy source. However, the technology for hydrogen gas production must be improved to make hydrogen competitive with other renewable energy sources. Biological methods, recently, received a significant attention among the other available physical and chemical methods. Biohydrogen gas production from carbohydrate rich waste materials is one of the major concerns. Dark and photofermentation are two biohydrogen production methods. Dark fermentation is preferred due to high hydrogen production rates and yields, requirement of simple operation conditions and controls. Wide varieties of studies have been conducted about the effect of substrate, microbial culture type and environmental condition on hydrogen gas production by batch dark fermentation [1-8]. The recent studies have been devoted to investigation of different immobilized or suspended growth bioprocess technologies with continuous operation [9-11]. Type of bioprocess used for continuous fermentative biyohydrogen production are continuous stirred tank reactor (CSTR), membrane bioreactor (MBR) [4], packed bed bioreactor [5,12], fluidized bed bioreactor [6,12], up-flow anaerobic sludge bed bioreactor (UASB) [13] and trickling filter bioreactor (trickling BIOFILTER) [8]. The main parameters that have been studied so far are comparison of immobilized and suspended culture systems, selection of particle type for immobilized systems and also determination of best operation conditions such as hydraulic retention time (HRT) and organic loading rate (OLR).The studies indicated that immobilized systems are superior over suspended growth systems for hydrogen production [14]. Immobilized systems have certain advantages over suspended culture system such as higher biomass holding capacity, operating the system at low retention times without washout of organisms, longer biomass retention times, resistance to high organic loading rates, the high rate of substrate conversion to product [15]. However, improper mixing, mass transfer limitations, efficient gas retrieving and biomass accumulation are the shortcomings of immobilized systems to be solved [15,16]. Hydrodynamic assay after a long term operation in packed bed reactor conducted by Peixoto et al. (2011) showed about 3 times HRT less than the initial HRT due to biomass accumulation [5]. The immobilization techniques used has substantial effect on the hydrogen productivity of the systems. Entrapment into a gel matrix, for instant, has been widely used. Although biomass loss is minimum by this method, the long term stability of the matrix and substrate diffusion limitations were the problems. Immobilization on a solid surface, especially on porous support particle, relatively eliminates these problems [17]. Support particle characteristics substantially affect the operation conditions as organic loading rate, HRT and gas retrieving. It was observed that porous support particles could be more advantageous than non-porous ones regarding to gas retrieving, biomass holding capacity. Si et al. (2015) suggested that although hydrogen gas is almost insoluble in water and would escape from aqueous medium, insufficient liquid-to-gaseous phase component transport may take place packed bed reactor [18].

Some of the particle types used in packed bed reactor for hydrogen production purposes are coir [19], polyethylene pellets [20], polyurethane foam [13], polyethylene rings [18], ceramic ring [21], ceramic beads

[22], clay beads [23] and some porous support particles as plastic scouring sponge pad, plastic nylon sponge, black porous sponge, plastic scouring sponge pad with metal mesh, plastic nylon sponge with metal mesh [2] and pumice stone [21]. Some of the problems observed in packed bed reactor are performance losses in the short term because of the negative effects of operational factors, such as biomass accumulation and inadequate pH conditions [15]. pH proved to be a key factor for obtaining continuous hydrogen production, and the optimal results were observed in a pH range from 5,1 to 5,2. Long term operation of the reactor resulted in slight decline in hydrogen production. This result was explained as, most likely, biomass aging, which was characterized by the proliferation of non-hydrogen producing bacteria. Moreover, it was stated that the low porosity of particle caused by the random arrangement of support media in packed-bed reactors hinders the removal by bottom discharge of interstitial acidogenic biomass that accumulates in the bed, which could affect the biomass retention. So, selection of support material type and determination of optimum operating conditions are some of the main research subjects about hydrogen production in immobilized growth systems. Hydraulic retention time (HRT) is one of the parameters in continuously operated system. However, its effect on hydrogen production yield has not been clearly stated yet. High hydrogen yields were obtained at low HRTs in some studies and relatively longer HRTs in other ones [14]. The relationship between support particle characteristic and HRT is one of the reasons of this variation. Therefore, the conditions in continuously operated immobilized systems must be determined specific to the support particle type. Our previous study resulted in that metal mesh covered plastic scouring sponge pad was the best support particle with 2,1 mol/ mol glucose production yield among the others namely plastic scouring sponge pad, plastic nylon sponge, black porous sponge, plastic nylon sponge with metal mesh by repeated batch operation [2]. As a second part of this study, the effect of HRT on biohydrogen production in continuously operated up-flow packed bed reactor with this particle was investigated. It was aimed to determine the best HRT which results in the highest hydrogen yield and production rate with this particle.

2. Materials and Methods

Microorganism: The mixed microbial culture was obtained from the acidogenic phase of anaerobic wastewater treatment plant of PAKMAYA Baker's Yeast Company in Izmir, Turkey. In order to select hydrogen producing, spore forming acidogenic bacteria and to eliminate hydrogen consuming methanogens, sludge was boiled for 5 h at 100 °C and pH=5.9. Heat pretreated anaerobic sludge was cooled and used as inoculum.

Preparation of Substrate: Acid hydrolyzed waste wheat powder (AHWP) was used as substrate. Waste wheat was obtained from SOKE wheat flour producing company in Aydın, Turkey. Waste wheat was ground and sieved down to 70 µm size (less than 200 mesh). The ground wheat was then hydrolyzed under acidic condition by sulfuric acid at pH=2, T=90 °C for 15 min in an autoclave [24]. The solid phase of hydrolyzed wheat powder solution was separated by centrifugation at 8000 rpm for 20 minutes. Supernatant sugar solution was neutralized to pH=7 by addition of 10% NaOH. Oxidation reduction potential was adjusted to ORP<-150 mV by adding Na-thioglycolate (200 mg/L) to the feed in the beginning of the experiments. The nitrogen and phosphorous content of powdered wheat (PW) was not sufficient for fermentation. PW contained nearly 97% (w/w) starch, 3,4 mg N/ g PW, 1,72 mg P/g PW, 1,25 mg Fe/g PW. The total nitrogen, phosphorus, iron and TOC contents of 15 g/L total sugar solution of AHWP were approximately N= 53±1 mg/L, P= 12.1 ± 0.5 mg/L, Fe(II)= 19.7±0.3 mg/L and TOC= 6000 mg/L resulting in N/P/Fe/C ratio of 0.9/0.2/0.32/100. Therefore, external urea (CON_2H_4), KH_2PO_4 and $FeSO_4$ addition was required as nitrogen, phosphorus and iron source, respectively, at the optimal ratio of N/ P/ Fe/ C = 2/ 0.8/ 1.5/100 to overcome nutrient limitation [25].

Continuous Operation of Up-flow Packed Bed Reactor: Plastic scouring sponge covered with metal mesh particle was used as support material in continuously operation packed bed reactor. Particle number in the reactor was 85 with dimensions of L=1, W=1, D=0,5 cm**.** Packed bed reactor was made up of stainless steel in dimensions of L=57 cm, D=8 cm with liquid volume of 2100 ml. The gas was collected from the top and given to the gas collection unit trough gas tight tubing. The system was fed from the bottom during continuous operation and the effluent was collected from the 4th sampling port from the bottom. The temperature was controlled at 37^{0}C with a heating jacket around the reactor. During start up and for the immobilization purpose, reactor was fed with 5 g/l total sugar obtained from hydrolysis of ground wheat for at least two weeks. Then, system was operated continuously at different hydraulic retentions of HRT=2 h, 4h, 6h, 10h and 13 h. Total sugar concentration was kept constant at 5 g/L in continuous operation. Feeding tank which contained hydrolyzed ground wheat was preserved at 4^{0}C against to contamination. Total gas volume, % hydrogen in total gas, total sugar concentration in the effluent, pH, temperature and ORP were monitored daily. pH was controlled at pH=6 when required.

Analytical Methods: Samples removed from the liquid phase everyday were centrifuged at 8000g and the clear supernatant was used for analysis of total sugar (TS) based on acid-phenol spectrometric method (Dubois et al.

1956). The amount of total gas produced was determined by water displacement method everyday using sulfuric acid (2%) and NaCl (10%) containing solution. The hydrogen gas volume was calculated by multiplying the total gas volume by the hydrogen concentration. Hydrogen gas was sampled from the gas collection port of the reactor by using gas-tight glass syringes. Hydrogen gas concentration in the gas phase was determined by using a gas chromatograph (HP Agilent 6890). The column was Alltech, Hayesep D 80/100 6" x 1/8" x 085". Nitrogen gas was used as carrier with a flow rate of 30 ml min^{-1} and the head pressure was 22 psi. Temperatures of the oven, injection, detector, and filament were 35°C, 120°C, 120°C, 140°C, respectively.

3. Results and Discussions

Transition behavior of the system for hydrogen production at different HRTs was depicted in Figure 1. The reactor was at dynamic state up to t=96 hours of operation and it reached to steady state with the hydrogen production volume of V_{H2}=1600 ml at HRT= 13 h. Hydrogen production in the first seventy-two hours was around V_{H2}=1325 ml at HRT=10 h. Volume steadily increased to 2700 ml up to t=96 hours of operation and remained almost at this value for the rest of operation. A substantial increase in volume of production was observed with the decrease in HRT from 13 h to 10 h. Daily hydrogen production volume was V_{H2}=1250 ml for the first 48 h operation at HRT=6 h and the steady state volume was V_{H2}=3100 ml. Hydrogen gas volume produced after the first 24 hours of continues operation was around V_{H2}=1200 ml at HRT=4 h. The gas production increased to V_{H2}=3082 ml after 8 days of operation and then daily hydrogen production volume remained almost constant at this value. The final HRT examined in the study was HRT=2 h. Daily production was 1500 ml at the beginning of operation (t=24). It reached to V=2400 ml for the periods between t=48 h and t=96 h. Then a steady increase in the volume to 3680 ml was observed up to t=168 h. Finally, it remained constant there until t=192 h. The volume produced at this HRT was the highest one among the obtained volume at other HRTs.

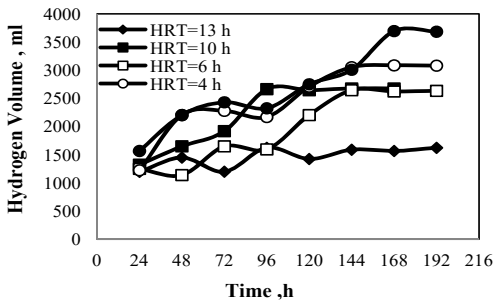


Fig.1. Variation of hydrogen volume with time at different HRT

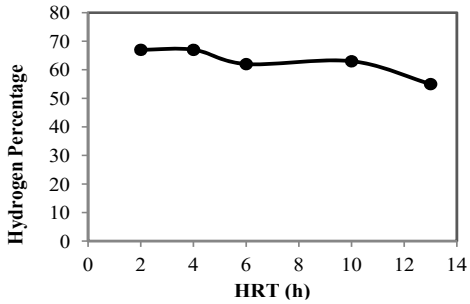


Fig.2. Variation of hydrogen percentage in total gas with HRT

The percentage of hydrogen in the total gas slightly increased from 55% to 67% as HRT was decreased from HRT=13 h to HRT=2 h (Figure 2). The variation of hydrogen content of the produced gas with HRT has been investigated in some studies In general the percentages of hydrogen in packed bed systems by dark fermentation has been reported as in range of 27%- 50% [12, 27-30]. A relationship between hydrogen percentage and HRT has not been defined, yet. A decrease in hydrogen content from 37% to 30 % in the gas mixture was reported when HRT was reduced from 2 h to 0.5 h [27].On the other hand, hydrogen percentage reached to maximum value of 50% when HRT was reduced from 24 h to 2 h [31]. However, H_2 percentage was around 38% for the studied HRT between 4h and 8h [12]. Hydrogen content obtained in this study is relatively higher compared to reported studies. The particle type could be one of the reasons for higher hydrogen percentage. Porous structure of the particle could ease the release of produced gas from the biofilm to the liquid phase and also gas retrieve from liquid phase to head space. Volumetric hydrogen production rate is a one of the parameters to compare the hydrogen production potentials of different bioprocesses, substrate and particle types. The VHP for long HRTs (HRT=13 h) was only 0.75 L H_2 /L d as given in Figure 3. Decreasing hydraulic retention time to HRT=2 h substantially improved volumetric hydrogen production rate and it reached to VHP=1.75 L H_2/L d at HRT=2 h.

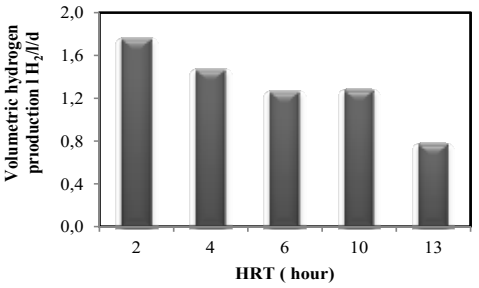


Fig.3. Variation of volumetric hydrogen production rate (l H_2/l/d) with HRT

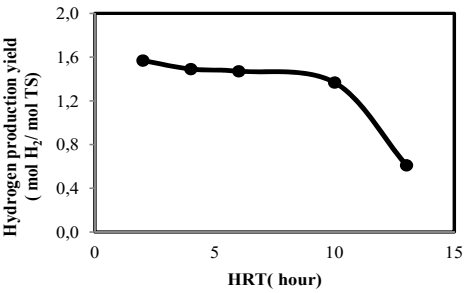


Fig.3. Effect of HRT on hydrogen production yield (mol H_2/mol TS)

Similarly, the yield of production reached to maximum level as Y_{H2}=1.6 mol H_2/mol TS at HRT=2 h (Figure 4). There are several possible reasons for higher hydrogen yield and rate at short HRT. One of them is efficient gas retrieve with increasing in linear liquid velocity in the bioreactor at short HRT. This result was also supported by the findings of Si et al. [18]. The increased hydrogen yield mainly was attributed to improved mass transfer and enhanced contact of microbe and bulk solution. It was also stated that with the decrease of HRT suggested the low HRT might enhance the release of hydrogen gas, and avoid further conversion of produced hydrogen through methanogenesis and homoacetogenesis. In otherwords, no hydrogen consuming microorganisms like homoacetogens were generated at HRTs up to 4 h. Another reason could be decreasing in exposure time to produced volatile fatty acids which could be inhibitory to hydrogen production. The common result observed in the packed bed system for the effect of HRT on hydrogen production is that rate increases but the yield decreases when HRT shortened. The result has been explained as inhibition of production due to accumulation of hydrogen gas in the liquid phase with the increase in organic loading rates as HRT decreased [27]. It has been also concluded that soluble product profile could change from butyric acid to non-hydrogen producing or hydrogen consuming organic acid as lactic acid or propionic acid, respectively [30-31], finally, a shift in the microbial population from hydrogen producers to non-hydrogen producers could occur with the decrease in HRT [27.33]. Similar result was observed by Si et al. that low HRT (2 h) would decrease the relative abundance of the hydrogen producer *Clostridiaceae* and accelerate the proliferation of non-hydrogen-producing microorganism, primarily attributed to the families *Ruminococcaceae* and *Leuconostocaceae* [18].

Biohydrogen production in continuously operated packed bed reactors revealed that there is a strong relationship between particle type, immobilization type, hydraulic retention time and hydrogen productivity. It has been concluded that mass transfer limitation is more significant in entrapped cells than surface attachment, self-flocculation or in suspended cultures [30]. Therefore, substantial difference in the effect of HRT on H_2 production can be observed depending on the immobilization type or particle type used in the process. Chang et al., (2002) studied on the effect of hydrogen production by using three different packed bed materials as gourd fiber, expanded clay, activated carbon in a continuoesly operated packed bed reactor [27]. HRT was varied between 0.5h and 5 h. The reactor was operated at mesophilic conditions (35 °C) with carbon source of sucrose (20 g COD /L). Biomass holding capacities of the immobilization materials were compared. It was observed that pumpkin fiber (0.94 g VSS/L) and expended clay (VSS = 1.85 g/L) were not as good as activated carbon (5,53 g VSS/L) in terms of biomass holding capacity. The maximum hydrogen production rates with expended clay and activated carbon were obtained as 0.415 L / hr / L at HRT = 2 and 1.32 L/h L at HRT=1 h, respectively. Lower HRTs resulted in cessation of hydrogen production with elevated percentage of CO_2 in the gas phase because of inactivation of hydrogen producers and substrate inhibition effect. Chojnacka et al. (2011) operated immobilized reactors one with granites stone as support particle and immobilization technique and the other one with granite stone and granular sludge together to investigate the performance of both adhesion and self-granulation for hydrogen production [33]. HRT was varied between 10-18 h. Reactor with only granite stone generated 35.7 % hydrogen while the other reactor produced about 48.6 % with the production yield of 5.48 molH_2/mol sucrose. It was concluded that granite with granular sludge is a better reactor media for hydrogen generation. Keskin et al. (2011) used porous immobilization materials namely ceramic ferrule and pumice stone in a packed bed system [21]. Process was operated at HRT=1,5-24 h. Hydrogen production rates were reported as 2.98 L H_2/L d at HRT= 1.5 h with ceramic ring, 2.28 L H_2/L d for pumice stone at HRT = 3 h. Jo et al, (2008) used non porous polyurethane foam as the support material in packed bed bioreactor at HRT=1-24 h [31]. Hydrogen production rate increased when HRT was decreased from 24 hours to 2 hours. Maximum H_2 production rate was obtained as

7.2 L H_2/L d at HRT = 2 hr. Lignocellulosic materials like rice straw, bagasse and coir was used as support material for biohydrogen production purpose by dark fermentation [34]. The results indicated that hydrogen production rate increased with increasing dilution rate to D= 0.9 h^{-1} (HRT=1 h) for all matrixes and the maximum rate was obtained as 62 mmol/ h L with coir. Recirculation of effluent enhanced the production rate resulting in 75.6 mmol/L h with 9.4 h^{-1} dilution rate. Si et al (2015) obtained increase in the yield from 1.31 mol/ mol glucose to 1.62 mol / mol glucose by shortening the HRT from 24 h to 4 h and suggested that the HRT not only enhanced the mass transfer, but also affected the microbial consortia. However, accumulation of nonhydrogen producing lactic acid was observed at HRT=2 h. The effect of organic loading rate on hydrogen production in an up-flow anaerobic reactor containing low density polyethylene pellets was investigated by Ferraz Júnior et al. [20]. Maximum yield was obtained as 2.0 mol-H_2 /mol-glucose at OLR of 25.7 g COD/L d. Roy et al. obtained maximum H_2 production rate of 1.7 L/L h was observed at a dilution rate and recycle ratio of 0.8 h^{-1} and 0.6 [19].

Conclusions

Hydrogen production volume and yield increased with decreasing HRT. Yields and rates at HRT=2 were almost two times of that at HRT=13 h. The maximum daily hydrogen production volume reached up to 3500 ml, volumetric production rate raised to 1.7 L H_2 /l d and yield was maximum (1.6 mol H_2 / mol TS) at HRT=2 h. Hydrogen purity in total gas reached up to 67% with decreasing HRT. Dark fermentative hydrogen production is a promoting technology for biological renewable gas generation. Immobilized systems should be the first choice to get high volume of production. However, process needs further improvements for higher productions in order to make it compete with the other chemical or physical ones.

Acknowledgment

This study was supported by Dokuz Eylul University with the grant number 2011.KB.FEN.028.

References

1. Kapdan IK, Kargi F. Bio-hydrogen production from waste materials. Enzyme and Microbial Technology 2006;38:569-582
2. Kirli B, Kapdan IK. Selection of microorganism immobilization particle for dark fermentative biohydrogen production by repeated batch operation. Renewable Energy 2016; 87:697-702.
3. Ding J, Wang XF, Ren NQ, Guo WQ CFD. Optimization of continuous stirred-tank (CSTR) reactor for biohydrogen production. Bioresource Technol 2010; 101: 7005-13.
4. Oh SE, Iyer P, Bruns MA, Logan BE. Biological hydrogen production using a membrane bioreactor. Bioechnol and Bioeng 2004;87:119-27
5. Peixoto G, Saavedra NK, Varesche MBA, Zaiat M. Hydrogen production from soft-drink wastewater in an upflow anaerobic packed-bed reactor. Int J Hydrogen Eng, 2011;36:8953-66.
6. Barros AR, Amorim ELC, Reis CM, Shida GM, Silva, EL. Biohydrogen production in anaerobic fluidized bed reactors: Effect of support material and hydraulic retention time. Int J Hydrogen Eng 2010; 35:3379–88
7. Chang FY, Lin CY. Biohydrogen production using an up-flow anaerobic sludge blanket reactor. Int J Hydrogen Eng 2004;29: 33-39.
8. Arriaga S, Rosas I, Alatriste-Mondrago´n F, Razo-Flores E. Continuous production of hydrogen from oat straw hydrolysate in a biotrickling filter. Int J Hydrogen Eng 2011;36: 3442-49.
9. Han W, Liu DN, Shi YW, Tang JH, Li YF, Ren NQ. Biohydrogen production from food waste hydrolysate using continuous mixed immobilized sludge reactors. Bioresource Technol 2015;180: 54–58.
10. Wongthanate J, Polprasert C. Immobilized biofilm in thermophilic biohydrogen production using synthetic versus biological materials Braz. Arch. Biol. Techn 2015; 58:124-130
11. Chu CY, Wu SY, Shen YC. Biohydrogen production performance in a draft tube bioreactor with immobilized cell. Int. J. Hydrogen Energ 2012; 37: 15658–15665.
12. Wu KJ, Chang CF, Chang JS. Simultaneous production of biohydrogen and bioethanol with fluidized-bed and packed-bed bioreactors containing immobilized anaerobic sludge. Process Biochemistry 2007a; 42;7:1165-1171.
13. Reyes JC, Carmona MC, Ruiz CDB, Flores ER Cell wash-out enrichment increases the stability and performance of biohydrogen producing packed-bed reactors and the community transition along the operation time. Renewable Energy 2016;97:266-273.
14. Azbar N, Kapdan IK. Use of Immobilized Cell Systems in Biohydrogen Production. State of the Art and Progress in Production of Biohydrogen, Editors; Azbar N, Levin D. Bentham Science Publishers. ISBN: 978-1-60805-411-4,2012

15. Fuess LT, Kiyuna LSM, Garcia ML, Zaiat M Operational strategies for long-term biohydrogen production from sugarcane stillage in a continuous acidogenic packed-bed reactor Int J Hydrogen Energy 2016;41: 8132-8145.
16. Othong S, Prasertsan P, Karakashev D, Angelidaki I High-rate continuous hydrogen production by *Thermoanaerobacterium thermosaccharolyticum* PSU-2 immobilized on heat-pretreated methanogenic granules. Int J Hydrogen Energy 2008;33:6498–508.
17. Ivanova G, Rákhely G, Kovács KL. Hydrogen production from biopolymers by *Caldicellulosiruptor saccharolyticus* and stabilization of the system by immobilization. Int J Hydrogen Energy 2008; 33(23): 6953-61.
18. Si B, Li J, Li B, Zhu Z, Shen R, Zhang Y, Liu Z. The role of hydraulic retention time on controlling methanogenesis and homoacetogenesis in biohydrogen production using upflow anaerobic sludge blanket (UASB) reactor and packed bed reactor (PBR) Int J of Hydrogen Energy 2015; 40: 11414-11421.
19. Roy S, Vishnuvardhan M, Das D Continuous thermophilic biohydrogen production in packed bed reactor. Applied Energy 2014;136:51–58.
20. Ferraz-Júnior ADN, Zaiat M, Gupta M, Elbeshbishy E, Hafez H, Nakhla G Impact of organic loading rate on biohydrogen production in an up-flow anaerobic packed bed reactor (UAnPBR). Bioresource Technol 2014:164; 371–379.
21. Keskin T, Aksöyek E, Azbar N Comparative analysis of thermophilic immobilized biohydrogen production using packed materials of ceramic ring and pumice stone. Int J of Hydrogen Energy 2011;36: 15160-15167.
22. Athanasios S. Dounavis, Ioanna Ntaikou, Gerasimos Lyberatos, Production of biohydrogen from crude glycerol in an upflow column Bioreactor. Bioresource Technol 198 (2015) 701–708
23. Leite JAC, Fernandes BS, Pozzi E, Barboza M, Zaiat M Application of an anaerobic packed-bed bioreactor for the production of hydrogen and organic acids Int J of Hydrogen Energy 2008;33:579 – 586
24. Kapdan IK, Kargi, F, Oztekin R. Effects of operating parameters on acid hydrolysis of ground wheat starch: Maximization of the sugar yield by statistical experiment design Starch/Sta¨ rke 2011;63: 311–318.
25. Oztekin R, Kapdan IK, Kargi F, Argun H. Optimization of media composition for hydrogen gas production from hydrolyzed wheat starch by dark fermentation. Int J Hydrogen Eng 2008;33: 4083-90.
26. Dubois, M., Gilles, K.A., Hamilton, J.K., Rebers, P.A. & Smith, F. Colorimetric method for determination of sugars and related substances. Analitic Chemistry 1956; 8, 350–366.
27. Chang JS, Lee KS, Lin PJ. Biohydrogen production with fixed-bed bioreactors. Int J of Hydrogen Energy 2002; 7;11-12:1167-1174.
28. Wu SY, Lin CN, Chang JS Chang JS. Biohydrogen production with anaerobic sludge immobilized by ethylene-vinyl acetate copolymer. Int J of Hydrogen Energy 2005; 30; 13-14:1375-1381.
29. Fritsch M, Hartmeier W, Chang JS. Enhancing hydrogen production of *Clostridium butyricum* using a column reactor with square-structured ceramic fittings. Int J of Hydrogen Energy 2008; 33; 22: 6549-6557.
30. Wu KJ, Chang JS. Batch and continuous fermentative production of hydrogen with anaerobic sludge entrapped in a composite polymeric matrix. Process Biochemistry, 2007; 42;2:279-284.
31. Jo JH, Lee DS, Park D, Park JM. Biological hydrogen production by immobilized cells of *Clostridium tyrobutyricum* JM1 isolated from a food waste treatment process. Bioresource Technol 2008;99;14:6666-6672.
32. Basile MA, Dipasquale L, Gambacorta A. The effect of the surface charge of hydrogel supports on thermophilic biohydrogen production. Bioresource Technol 2010; 101(12): 4386-94.
33. Chojnacka A, Błaszczyk MK, Szczęsny P, Nowak K, Sumińska M, Tomczyk-Żak K, Zielenkiewicz U, Sikora A Comparative analysis of hydrogen-producing bacterial biofilms and granular sludge formed in continuous cultures of fermentative bacteria Bioresource Technol 2011;102 (21):10057–10064.
34. Kumar N, Das D. Continuous hydrogen production by immobilized *Enterobacter cloacae* IIT-BT 08 using lignocellulosic materials as solid matrices. Enzyme Microb Tech 2001; 29(4-5): 280-287.

ORAL PROCEEDINGS

Thermodynamic analysis of OTEC based hydrogen production system

Fatih Yilmaz[1], Murat Öztürk[2] Reşat Selbaş[3],
[1]Department of Electrical and Energy, Vocational School of Technical Sciences, Aksaray University, 68100. Turkey
[2]Department of Mechatronic Engineering, Faculty of Technology, Suleyman Demirel University 32100, Isparta, Turkey
[3]Department of Energy System Engineering, Faculty of Technology, Suleyman Demirel University 32100, Isparta, Turkey
Email: fatiyilmaz7@gmail.com

Abstract
In this study, the thermodynamic assessment of an ocean thermal energy conversion (OTEC) based hydrogen production plant is performed using the energy and exergy analysis. This integrated system is consisted of the heat exchangers, turbine, condenser, pumps, solar collector system, hot storage tank, cold storage tank and proton exchange membrane (PEM) electrolyzer. The exergy destruction rate, exergy destruction ratio and exergy efficiency of OTEC based hydrogen production system components and whole system are analyzed by using the balance equations, such as mass, energy, entropy and exergy, and also energy and exergy efficiency equations. In addition to that, the impacts of different design indicators and reference ambient parameters on the exergy destruction rate and exergy efficiency of OTEC based hydrogen production system are analyzed.

Keywords: OTEC; integrated system,; hydrogen energy.

1. Introduction

Today, energy production methods are not sustainable and environmentally as generally derived from fossil-based fuels. In this context, there also give rise to considerable environmental deterioration, global warming, ozone depletion, acid rain, health problem, and security issues for the community. In addition, due to the limited reserves and non-environmental of fossil-based fuels, their use will become more limited next years.

Recently, various possible solution to these problems associated with harmful pollutant emission from fossil-based fuels have evolved. Hydrogen energy systems appear to be one of the most effective solutions, and can play a significant role in providing better environment and sustainability [1, 2]. However, today hydrogen production methods are generally based on fossil fuels resources [3, 5]. Thus, the environmentally problems also continue increasing.

Many studies have been presented in the literature on the clean hydrogen production methods. Khalid et al. [6], presented a comparative assessment of two integrated systems for hydrogen production using electrolyzed and fuel calls. The hydrogen production by electrolysis is used turbine to produce power in system 1, and is used proton exchange membrane fuel cell in other system, which is system 2. The overall energy and exergy efficiency of system1 and system 2 calculated as 20.7%, 21.0%, and 24.7%, 18.9%, respectively. Hassoun and Dicer [7], studied an energy and exergy analyses of renewable energy based integrated system for a net zero house energy. Rabbani et al. [8], have proposed a novel multigenerational hydrogen production system in terms of performance assessment. They have studied that energy and exergy efficiency of solar-based multigeneration system. Ratlamwala and Dincer [9], was developed a novel multigeneration system for producing hot water, heating, cooling, hydrogen and electricity. In addition, various researchers have analyzed and presented relate to multigeneration systems for hydrogen and energy production [10-12].

In this study, the thermodynamic assessment of an ocean thermal energy conversion (OTEC) based hydrogen production plant is performed using the energy and exergy analysis. This integrated system is consisted of the heat exchangers, turbine, condenser, pumps, solar collector system, hot storage tank, cold storage tank and proton exchange membrane (PEM) electrolyzer.

2. System description

The OTEC based integrated system for hydrogen production is illustrated in Fig. 1. As seen from this figure, this integrated system is consisted of three sub-system, such as i-) Solar collector process, ii-) Hydrogen production system, and iii-) OTEC process. In the OTEC process, the warm sea water is used for useful heat generation and deep sea water is utilized for decrease the entropy level of condenser.

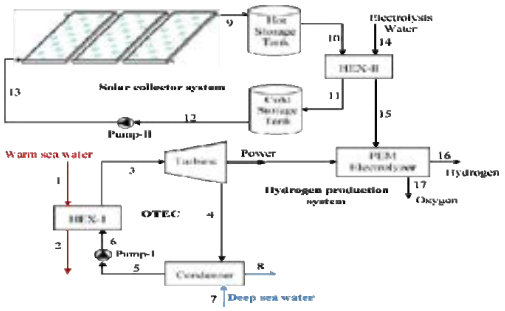


Figure 1. OTEC based hydrogen production system

3. General Analysis and Performance Assessment

Thermodynamic analysis is generally based on four balance equations, such as i-) mass balance equation, ii-) energy balance equation, iii-) entropy balance equation, and iv-) exergy balance equation [13]. In the steady state conditions, the mass balance equation can be written as follows;

$$\sum \dot{m}_i = \sum \dot{m}_e \quad (1)$$

In the steady state conditions, the energy balance equation can be given as follows;

$$\sum \dot{m}_i h_i + \sum \dot{Q}_i + \sum \dot{W}_i = \sum \dot{m}_e h_e + \sum \dot{Q}_e + \sum \dot{W}_e \quad (2)$$

In the steady state conditions, the entropy balance equation can be written as follows:

$$\sum \dot{m}_i s_i + \sum \left(\frac{\dot{Q}}{T}\right)_i + \dot{S}_{gen} = \sum \dot{m}_e s_e + \sum \left(\frac{\dot{Q}}{T}\right)_e \quad (3)$$

The exergy balance equation can be defined as follows;

$$\sum \dot{m}_i ex_i + \sum \dot{E}x_i^Q + \sum \dot{E}x_i^W = \sum \dot{m}_e ex_e + \sum \dot{E}x_e^Q + \sum \dot{E}x_e^W + \dot{E}x_D \quad (4)$$

where ex is the specific exergy, $\dot{E}x^Q$ is the exergy rate of heat energy transfer, $\dot{E}x_W$ is the exergy rate associated with shaft work and $\dot{E}x_D$ is the exergy destruction rate. The specific exergy can be defined as follows;

$$ex = ex_{ph} + ex_{ch} + ex_{pt} + ex_{kn} \quad (5)$$

where ex_{ph}, ex_{ch}, ex_{pt} and ex_{kn} are the physical, chemical, potential and kinetic exergy, respectively. For this paper, ex_{pt} and ex_{kn} are accepted as negligible, because the exergy exchange rates of these physical quantity are very small. In geothermal power plants, the physical (or flow exergy) and chemical exergy rates must be written, because the working fluid comes from underground has different dissolved solid salts or minerals. These exergy values can be written as follows;

$$ex_{ph} = h - h_o - T_o(s - s_o) \quad (6)$$

$$ex_{ch} = \sum n_i(u_i^0 - u_i^{00}) \quad (7)$$

where u_i^0 is chemical potential of i^{th} component in thermomechanical equilibrium and u_i^{00} is the chemical potential of i^{th} component in chemical equilibrium [14]. The exergy rates associated with heat transfer and work across the boundary of a control volume can be defined as follows, respectively;

$$\dot{E}x_Q = \left(1 - \frac{T_o}{T}\right)\dot{Q} \quad (8)$$

$$\dot{E}x_W = \dot{W} \quad (9)$$

Also, the exergy destruction rate can be calculated as

$$\dot{E}x_D = T_0 \dot{S}_{gen} \quad (10)$$

HEX-I; The mass, energy, entropy and exergy balance equations for HEX-I can be written under the steady state and steady flow conditions as

Mass: $\dot{m}_1 = \dot{m}_2; \dot{m}_3 = \dot{m}_6$ (11)

Energy: $\dot{m}_1 h_1 + \dot{m}_6 h_6 + \dot{Q}_{HEX-I} = \dot{m}_2 h_2 + \dot{m}_3 h_3$ (12)

Entropy: $\dot{m}_1 s_1 + \dot{m}_6 s_6 + \dot{Q}_{HEX-I}/T_{HEX-I} + \dot{S}_{gen,HEX-I} = \dot{m}_2 s_2 + \dot{m}_3 s_3$ (13)

Exergy: $\dot{m}_1 ex_1 + \dot{m}_6 ex_6 + \dot{E}x_{HEX-I}^Q = \dot{m}_2 ex_2 + \dot{m}_3 ex_3 + \dot{E}x_{D,HEX-I}$ (14)

Turbine; Under the steady state and steady flows conditions, the mass, energy, entropy and exergy balance equations for turbine can be defined as

Mass: $\dot{m}_3 = \dot{m}_4$ (15)

Energy: $\dot{m}_3 h_3 = \dot{m}_4 h_4 + \dot{W}_{tur}$ (16)

Entropy: $\dot{m}_3 s_3 + \dot{S}_{gen,tur} = \dot{m}_4 s_4$ (17)

Exergy: $\dot{m}_3 ex_3 = \dot{m}_4 ex_4 + \dot{W}_{tur} + \dot{E}x_{D,tur}$ (18)

Condenser; The mass, energy, entropy and exergy balance equations are given for condenser under the steady state and steady flow conditions.

Mass: $\dot{m}_4 = \dot{m}_5; \dot{m}_7 = \dot{m}_8$ (19)

Energy: $\dot{m}_4 h_4 + \dot{m}_7 h_7 = \dot{m}_5 h_5 + \dot{m}_8 h_8$ 20)

Entropy: $\dot{m}_4 s_4 + \dot{m}_7 s_7 + \dot{S}_{gen,con} = \dot{m}_5 s_5 + \dot{m}_8 s_8$ 21)

Exergy: $\dot{m}_4 ex_4 + \dot{m}_7 ex_7 = \dot{m}_5 ex_5 + \dot{m}_8 ex_8 + \dot{E}x_{D,con}$ 22)

Pump; The mass, energy, entropy and exergy balance equations for pump can be defined under the steady state and steady flow conditions as follows:

Mass: $\dot{m}_5 = \dot{m}_6$ (23)

Energy: $\dot{m}_5 h_5 + \dot{W}_p = \dot{m}_6 h_6$ (24)

Entropy: $\dot{m}_5 s_5 + \dot{S}_{gen,p} = \dot{m}_6 s_6$ (25)

Exergy: $\dot{m}_5 ex_5 + \dot{W}_p = \dot{m}_6 ex_6 + \dot{E}x_{D,p}$ (26)

Hot Storage Tank; Under the steady state and steady flow conditions, the mass, energy, entropy and exergy balance equations for hot storage tank is defined as follows;

Mass: $\dot{m}_9 = \dot{m}_{10}$ (27)

Energy: $\dot{m}_9 h_9 + \dot{Q}_{HST} = \dot{m}_{10} h_{10}$ (28)

Entropy: $\dot{m}_9 s_9 + \dot{Q}_{HST}/T_{HST} + \dot{S}_{gen,HST} = \dot{m}_{10} s_{10}$ 29)

Exergy: $\dot{m}_9 ex_9 + \dot{E}x^{Q}_{HST} = \dot{m}_{10} ex_{10} + \dot{E}x_{D,HST}$ (30)

Cold Storage Tank; Under the steady state and steady flow conditions, the mass, energy, entropy and exergy balance equations for cold storage tank is defined as follows;

Mass: $\dot{m}_{11} = \dot{m}_{12}$ (31)

Energy: $\dot{m}_{11} h_{11} + \dot{Q}_{CST} = \dot{m}_{12} h_{12}$ (32)

Entropy: $\dot{m}_{11} s_{11} + \dot{Q}_{CST}/T_{CST} + \dot{S}_{gen,CST} = \dot{m}_{12} s_{12}$ (33)

Exergy: $\dot{m}_{11} ex_{11} + \dot{E}x^{Q}_{CST} = \dot{m}_{12} ex_{12} + \dot{E}x_{D,CST}$ (34)

Flat-plate solar collector; Under the steady state and steady flow conditions, the mass, energy, entropy and exergy balance equations for flat-plate solar collector is defined as follows;

Mass: $\dot{m}_9 = \dot{m}_{13}$ 35)

Energy: $\dot{m}_9 h_9 + \dot{Q}_{FPSC} = \dot{m}_{13} h_{13}$ (36)

Entropy: $\dot{m}_9 s_9 + \dot{Q}_{FPSC}/T_{FPSC} + \dot{S}_{gen,FPSC} = \dot{m}_{13} s_{13}$ (37)

Exergy: $\dot{m}_9 ex_9 + \dot{E}x^{Q}_{FPSC} = \dot{m}_{13} ex_{13} + \dot{E}x_{D,FPSC}$ (38)

The actual useful energy gain from flat-plate solar collector can be defined as follows;

$\dot{Q}_{FPSC} = F_R A[I_s(\tau\alpha)A - U_L(T_{FPSC} - T_o)]$ (39)

where F_R is the heat removal factor, A is the surface area is the collector, I_s is the solar radiation, τ is the transmission coefficient, α is the absorption coefficient of plate, U_L is the collector overall heat loss coefficient, T_{FPSC} and T_o are the collector and reference temperature, respectively.

3.1 Energy and Exergy Efficiencies

The definitions of energy and exergy efficiencies are a significant opinion in decision making regarding energy source usage [15]. For any energy production or utilization process, the non-dimensional ratio of quantities is frequently utilized to define the energy and exergy efficiencies. The energy and exergy efficiencies of OTEC plant, and its components are evaluated in order to investigate the performances of investigated geothermal power processes. The energy efficiency (η) and exergy efficiency (ψ) equations for steady state conditions can be defined as follows, respectively;

$$\eta = \frac{energy\ in\ product\ outputs}{total\ energy\ inputs} \quad (40)$$

$$\psi = \frac{exergy\ in\ product\ outputs}{total\ exergy\ inputs} \quad (41)$$

The energy and exergy efficiency equations of OTEC system components are given in Table 1.

Table 1. Energy and exergy efficiencies of OTEC system components

System components	Energy efficiency	Exergy efficiency
Solar collector	$\eta_{rpsc} = \frac{\dot{m}_{10}(h_{10} - h_{11})}{Q_{rpsc} + W_{p-a}}$	$\psi_{rpsc} = \frac{\dot{m}_{10}(ex_{10} \quad ex_{11})}{Ex^{Q}_{rpsc} + W_{p-a}}$
Hydrogen production	$\eta_{HP} = \frac{\dot{m}_{14}LHV_{hydrogen}}{\dot{m}_{13}h_{13} + W_{otec}}$	$\psi_{HP} = \frac{\dot{m}_{14}ex_{H_2}}{\dot{m}_{13}ex_{13} + W_{otec}}$
OTEC	$\eta_{otec} = \frac{W_T}{\dot{m}_1(h_1 - h_2) + W_{p-f}}$	$\psi_{otec} = \frac{W_T}{\dot{m}_1(ex_1 - ex_2) + W_{p-f}}$

4. Results and discussion

In the modelling of OTEC based integrated process, the Engineering Equation Solver (EES) software program is used for efficiently system design. Table 2 gives the thermodynamic parameters for modelling of ocean thermal based organic Rankine cycle system for hydrogen production.

Table 2. Thermodynamic properties of OTEC based integrated process

State	Temperature (°C)	Pressure (kPa)	Mass flow rate (kg/s)	Enthalpy (kJ/kg)	Entropy (kJ/kg-K)	Exergy (kW)
1	38.58	508.7	86.99	162	0.5531	942.4
2	13.81	302.9	86.99	56.14	0.1996	132.1
3	36.46	1563	28.52	586.8	2.142	5144
4	11.89	1220	28.52	404.5	1.718	2674
5	7.89	1220	28.52	213.9	1.05	2445
6	7.9	1563	28.52	214	1.048	2459
7	1.2	277.8	103.4	5.309	0.01837	19.4
8	13.75	179.1	103.4	57.86	0.206	158.2
9	86	130	9.649	360.2	1.146	454
10	82	125.4	9.649	343.4	1.099	415.9
11	76	125.4	9.649	318.7	1.027	361.4
12	42.8	102	9.649	179.3	0.6095	122.7
13	42.82	132.2	9.649	179.4	0.6097	123.1
14	5	101.3	0.7343	21.12	0.07625	0.1397
15	84	101.3	0.2367	351.8	1.123	10.66
16	80	101.3	0.01649	4723	16.81	304.7
17	80	101.3	0.2102	50.8	0.1564	103.9

Fig. 2, illustrates the exergy destruction rate of sub-components and whole system. The highest exergy destruction rate is seen in OTEC while the lowest exergy destruction rate seen in solar collector system. The total exergy destruction rate is calculated as 4934 kW. Fig.3, introduces that, energy and exergy efficiency of the sub-systems and whole system. As seen from Fig.3, the highest energy and exergy efficiency are found as 51.67% and 42.84, in hydrogen production system. Also, the lowest energy and exergy efficiency found as 26.85% and 18.28% in OTEC.

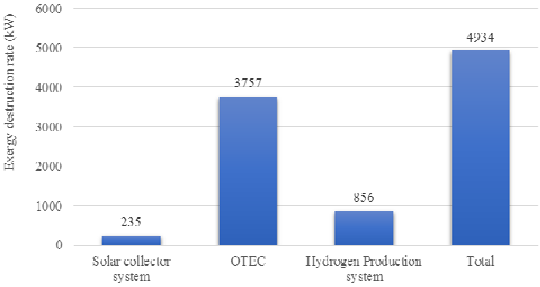


Fig. 2. Exergy destruction rates of the system sub-components and whole system

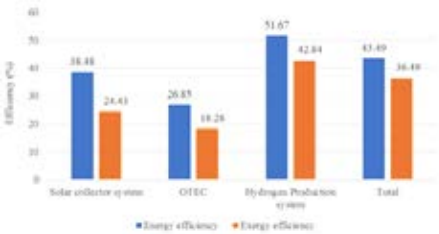


Fig. 3. Energy and exergy efficiency of the sub-systems and whole system

Fig.4, and 5 show that, the effects of solar intensity on exergy destruction rate and exergy efficiency of sub-systems and whole system. While solar intensity increasing from 400 ºC to 1100 ºC, exergy destruction rate of sub-systems and whole system increases except OTEC. But, the highest increase in aspect exergy efficiency is shown in the solar collector sub-system, as seen in Fig.5

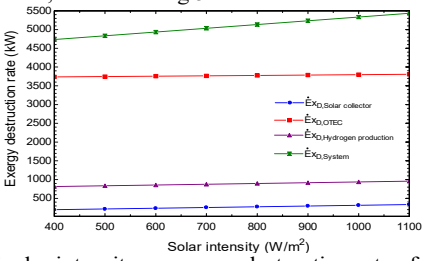


Fig. 4. The effects of solar intensity on exergy destruction rate of sub-systems and whole system

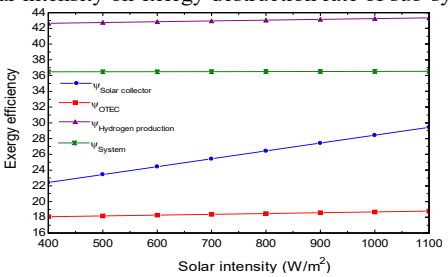


Fig. 5. The effects of solar intensity on exergy efficiency of sub-systems and whole system

The effects of reference temperature on exergy efficiency of sub-systems and whole system given in Fig.6. According to that Fig. as the reference temperatures increase in from 10 ºC to 40 ºC, efficiency of sub-systems and whole system increases.

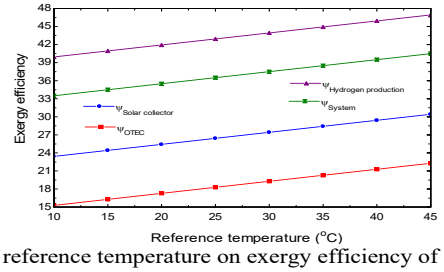


Fig. 6. The effects of reference temperature on exergy efficiency of sub-systems and whole system

Fig.7 displays that the exergy destruction rate of hydrogen production system increases from about 815 kW to 865 kW, as the increase of PEM electrolyzer temperature. As can be seen from Fig, as the increase of PEM electrolyzer temperature, exergy efficiency of hydrogen production system also increase.

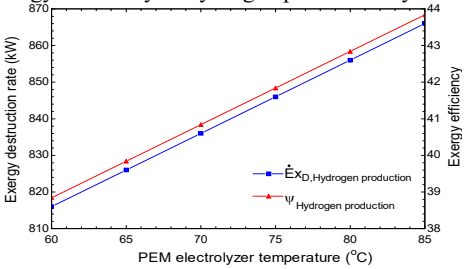


Fig. 7. The effects of PEM electrolyzer temperature on exergy destruction rate and exergy efficiency of hydrogen production system

5. Conclusions

In this study, the thermodynamic assessments outputs of integrated process driven by the ocean thermal energy are detailed presented. Because an energy analysis cannot provide adequate information for the energy loss rates, an exergy analysis is performed to investigate actual performances and exergy destruction rates of whole process and its components. In addition, the parametric studies are conducted to understand how solar intensity, warm sea water temperature, reference temperature and PEM electrolyzer inlet temperature influence the exergy efficiency and exergy destruction rate of investigated system for a more efficient process design. Based on the thermodynamic assessment, the integrated process for hydrogen production present positive environmentally effect. Finally, we have drawn the following concluding remarks from the results of the present paper;

- Increasing solar radiation intensity causes an increase in the exergy efficiency of the sub-systems and whole system.
- Increasing ambient temperature causes an increase in the exergy efficiency of the all sub-systems and whole process.
- Increasing warm sea water temperature causes an increase in the exergy efficiency of the all sub-systems and whole process.
- Exergy efficiencies of the solar collector system, OTEC process, hydrogen production system and integrated system are found as 24.43%, 18.28%, 42.84% and 36.49%, respectively.

Nomenclature

$\dot{E}_D$	Exergy destruction rate (kW)
$\dot{E}_x$	Exergy flow rate (kW)
$\dot{m}$	Mass flow rate (kg/s)
$\dot{Q}$	Heat transfer rate (kW)
A	Surface area (m^2)
Con	Condenser
CST	Cold Storage Tank
ex	Specific exergy (kJ/kg)
FPSC	Flat-plate solar collector
h	Specific enthalpy (kJ/kg)
Hex	heat exchanger
HST	Hot Storage Tank
I	Irradiance (W/m^2)
OTEC	Ocean thermal energy conversion
P	pump
PEM	Proton exchange membrane
s	Specific entropy (kJ/kg K)
T	Temperature (°C or K)

Greek Letters

η	Energy efficiency
ψ	Exergy efficiency

Acronyms

e	exit
in	input

References

1. Dincer I. Technical, environmental and exergetic aspects of hydrogen energy systems. International Journal of Hydrogen Energy, 2002;27:265-85.
2. Dincer I. Environmental and sustainability aspects of hydrogen and fuel cell system. International Journal of Energy Research, 2007;31:29-55.
3. Kothari R, Buddhi D, Sawhney RL. Comparison of environmental and economic aspects of various hydrogen production methods. Renew Sustain Energy Rev, 2008;12:553-63.
4. Barreto L, Makihira A, Riahi K. The hydrogen economy in the 21st century: a sustainable develop.
5. Yilmaz F., Balta, MT, Energy and exergy analyses of hydrogen production step in boron based thermochemical cycle for hydrogen production, International Journal of Hydrogen Energy, 42 (2017) 2485-2491
6. Khalid F, AydinM, Dincer, I, Rosen,MA., Comparative assessment of two integrated hydrogen energy systems using electrolyzers and fuel cells, International Journal of Hydrogen Energy, 41(2016), 19836-19846.
7.Hassoun A, Dincer I. Analysis and performance assessment of multigeneration system powered by organic Rankine cycle for a net zero energy house. Appl Therm Eng, 2015;76:25-36.
8. H. Rabbani, H., Dincer, I., Rahnamayan, S., A novel multigenerational hydrogen production system: Performance evaluation, International journal of hydrogen energy, 2017 (in press)
9. Ratlamwala T, Dincer I. Development of a geothermal based integrated system for building multigenerational needs. Energy Build 2013;62:496–506.
10. Al-Sulaiman FA, Dincer I, Hamdullahpur F. Exergy modeling of a new solar driven trigeneration system. Sol Energy, 2011;85:2228–43.
11. Khalid F, Dincer I, Rosen MA. Energy and exergy analyses of a solar-biomass integrated cycle. Sol Energy, 2015;112:290–9.
12. Ziapour B, Palideh V, Mohammednia A. Study of an improved integrated collector-storage solar water heater combined with the photovoltaic cells. Energy Convers Manage, 2014;86:587–94.
13. Dincer, I., Rosen, M. A. "Exergy: energy, environment and sustainable development", Second Ed., Newnes, 2012.
14. Kotas, T. "The exergy method of thermal plant analysis", Krieger Publishing Company, 1985.
15. Bejan, A., Tsatsaronis, G., Moran, M. "Thermal Design and Optimization", New York: Wiley Interscience, 1996.

ORAL PROCEEDINGS

Transatlantic Trade and Investment Partnership between the USA and EU - The Future of Hydrogen In Consideration of TTIP

Sudi Apak[1], Erhan Atay[2], Duygu Yücel[3], Güngör Tuncer[4]
[1]Faculty of Economics and Administrative Sciences, Esenyurt University, İncirtepe Mahallesi, Doğan Araslı Blv. No:79, 34510 Beylikdüzü Osb/Esenyurt/İstanbulTurkey
[2]Economy Department, Trakya University, Turkey
[3]Edirne Social Sciences of Vocational School, Trakya University, Turkey
[4]Management Department, Kavram University, Turkey
Email: sudiapak@gmail.com

Abstract
Nowadays, every scientist accepts that hydrogen energy system is the most advanced technology for satisfying the ever increasing necessity for energy sustainably without polluting the environment. Sustainable development has come into prominence aside from regulating subjects in the 12th round of TTIP – Transatlantic Trade and Investment Partnership which has been continuing since 2013 between the USA and the EU. In this regard, the already clean energy type hydrogen energy draws attention to the non-sustainability of current fossil based fuels in the future. When the cooperation possibilities about regulative subjects are taken into account, the EU and the USA authorities guarantee that under no circumstances there will be decrease in the applied high standards about protecting the environment. Again, the implementations towards the aim of familiarizing the standards and regulations, which are being implemented between USA and EU that are going to be relevant for hydrogen energy, are still in process. According to the researches, hydrogen is approximately three times more expensive than the other fuels in the current conditions and it relies on cost decreasing technological developments for producing hydrogen to use it as a common energy source. In addition to this, storing the unnecessary electric energy, generated in daily or seasonal periods, as hydrogen can be evaluated as a valid alternative for the present. Being able to use this kind of stored energy commonly relies upon developing automotive technologies based on fuel cells for public transport. In the upcoming periods, covering many subjects like energy and financial services will be in question and this will absolutely have an impact on the future of the renewable hydrogen energy based on TTIP nations.

Keywords: TTIP; USA; EU; hydro energy; environment.

1. Introduction

When we consider the currently ambiguous attitudes about reluctance of the newly elected president of the USA Donald Trump, there is no publically declared date for concluding the TTIP negotiations. This ambiguous situation about TTIP was present along with the criticisms of different parties from the start.

In the negotiations thus far, 97% of the customs tariff line has been dealt with, even the secondary official suggestions about these tariffs has been presented. It has been foreseen that most of these tariff lines will be removed along with the TTIP's coming into force. Developments about determining the period which the tariff lines, that are impossible to remove immediately, will be gradually decreased has started.

Negotiations about the 3% percent remainder part of tariffs of products specified as critical are being planned for realizing in the upcoming stages. It is being estimated that these products are consisting of agriculture, textile and automotive sectors even though there is no detailed explanation about this subject [1].

Hydrogen draws attention as a very important alternative fuel for both economic and environmental aspects. Besides, hydrogen energy is a renewable energy type and in comparison with the current underground riches it displays the characteristics of availability for producing and usage for everyone. Economic vehicle manufacturing, energy and transport sectors can be influenced in a positive way by the hydrogen energy produced by renewable energy sources.

Hydrogen energy is making clean, silent and affordable flight a possibility. For example, a team that does study in Germany has tested a plane which leaves nothing but water vapors in the atmosphere. 2 military test pilot and 2 puppet passengers has participated in the flight that took 10 minutes. "HY4" named 4-seated plane, which carried out its first flight in Stuttgart Airport in September, produces electric energy by using hydrogen and oxygen. The only output of the system that transfers the produced electricity to the motor by fuel cells is water vapor. Shortly, the plane flies with hydrogen.

2. TTIP and the Economic Relations between the EU and the USA

While the USA and the EU create the most important market for themselves, it is known that the trade relation between them constitutes the highest dual trade relation network in the world and this provides employment opportunity for a total of 15 million individuals in that economy [2].

The most important dual relation in the world is the one between the EU and the USA. Both of the actors are economic superpowers and the relation between them constitutes 54% of the global economic production and more than one fourth of the global product trade. They spend 75% of the world's defense expenses. Even though the Western Europe governments criticize the USA policies behind closed doors, they usually present an agreeing image in front of the public opinion with the consciousness of importance of the Atlantic Treaty [3].

One of the most important subjects, which will be discussed with the EU membership of England coming to an end (Brexit), will be the attitude and policy of the USA towards the EU. USA that improved its relations with the EU by its historical and strategic partner England can be a more difficult partner for the EU from now on. It is possible for the relations about both political and economic issues to weaken. In this manner, the most important effect in the recent period can be felt within the scope of TTIP. The future of the partnership, which is being strived to be performed with a series of hardship and delay, can become more difficult when the groups that support this partnership in the absence of England weaken [4].

Table 1. Estimated macroeconomic effects of EU – USA partnership

	Assertive scenario (Full deregulation) Long term	***Humble scenario (Partial deregulation) Long term***
Real income (billion Euro)	40,8	18,3
USA EU	121,5	53,6
Increase in Real income (%)	0,28	0,13
USA EU	0,72	0,32
Real wage rise (unskilled labor)	0,35	0,16
USA EU	0,82	0,36
Real wage rise (skilled labor)	0,38	0,17
USA EU	0,78	0,34
Export rise (%)	6,06	2,68
USA EU	2,07	0,91

Source: [5]

In other respects, the rough opposition executed towards the compromises like agricultural products, consumer health and environment safety that will be given by the EU Ministry of Agriculture, points out to the resistance that can be encountered in the approval period of the possible letter of agreement by the Europe Commission and Parliament. Actually, the two basic objectives aimed for achieving with this agreement is to stop the rise of China as a global actor and limit the powers of the nations for paving the way for multinational companies. The comprising of a technology supported intensive competition environment will become inevitable because the limiting means for importation, like product standards with FTA (Free Trade Agreement) between the EU and the USA, will lose their effectiveness. It is possible that the regulations on food health and environment safety will be decreased instead of increasing, like how it happened in EU, in the free trade area to be created [6].

According to the TÜSİAD (Turkish Industrialists' and Businessmen's Association) *Görüş* journal, the FTA that is going to be carried out between the EU and the USA will provide 119 billion Euro to the economy of the European Union annually; 95 billion Euro to the economy of the USA annually. Besides, it is being expected that a 6 percent increase in exportation for the European Union and 8 percent increase in exportation for the USA. This way, it has been mentioned that as a conclusion of the calculations, a growth in the rates of 0.5% and 1.0% will be provided [7].

3. The Future of Hydrogen Energy According to the TTIP Agreement Between the USA and the EU

Still with ongoing negotiations, Free Trade Agreement (FTA) that aims for the trade and investment partnership between the EU and the USA appears to be an important means to mobilize the global dynamics that are going to accelerate the foreign trade between the parties. The subject process, aside from removing commercial limitations between the globally biggest two economic blocks in case of being concluded positively, it has the quality of creating results that can surpass the both sides of Atlantic [6].

It is known that vehicles that can operate with hydrogen fuel in the projects performed by the cooperation of the USA and the EU is getting more common and their mass production has started. For this reason, hydrogen motors are being used and the necessary hydrogen for these motors can be provided from hydrogen stations. Energy organizations of the USA and the EU foresee that the hydrogen energy will replace fossil resources like petrol and natural gas (depleting) [8].

World Energy Council (WEC) makes some predictions about the energy consumption amounts and energy production technologies in the future. In these predictions by WEC, it has been stated that the world population will be 10.2 billion in 2050. Again, with these predictions it has been estimated that globalization will increase the energy necessity in the world and economic development. Aside from that, the increasing of annual carbon dioxide emission will rise from 6.4Gt to 9-15Gt after the depleted fuels being used. Based upon this information, investing on alternative energy sources is investing on the futures of the nations [9].

Hydrogen being able to be stored thanks to its boron components, points out in the not too distant future the transportation vehicles equipped with hydrogen fuel cells will spread all over the world. This kind of development shows that there will be a "blast" in the hydrogen production across the world. A concrete example for this is the researches of an organization named Britain Royal Automobile Club (RAC) about the years of 2050. They emphasize in their researches about the futuristic automobiles that an average Europe automobile in 2050 will have the same volume and weight as the vehicles of present day but they will absolutely use suppressed hydrogen as fuel [10].

Sustainability of hydrogen depends on using renewable energy sources in the long term. Especially in the second half of the 21st century, there are pretty strong estimations about hydrogen being an important energy source for transportation and industry sectors [9].

Another parameter for hydrogen energy is about the carbon dioxide in the atmosphere. It is estimated that the carbon dioxide rate in the atmosphere will reach 520 ppm in 2050. By using hydrogen, it is estimated that these amounts can be decreased [11].

4. Conclusion

The most important characteristics of hydrogen energy is that it does not leave any residual or mark that can affect nature and human life when used, it only leaves water behind. The world changes its energy system. This change will come from hydrogen based systems, namely fuel cells that can convert hydrogen to electricity. Hydrogen based systems, namely fuel cells that can convert hydrogen to electricity are being researched. Many automotive firms have commenced the necessary works for marketing and manufactured hybrid prototypes like hydrogen gasoline internal combustion engine or hydrogen fuel.

Aside from that, alongside with conventional fuels like petrol or coal affecting the ecological balance, these fuels will deplete in a near future, the entire humanity's one of the most prominent problem is finding new, clean and renewable energy sources and developing new and productive technologies about these resources. Also it is being observed that the developed countries show important increases in R&D and actualize new projects in the recent years.

As a conclusion about TTIP, by taking into consideration the intense continuation of the works about familiarizing the regulations and the standards relevant to hydrogen energy being implemented between the USA and the EU; it will be possible to see clearly if we will share a fate such as the Trans Pacific Partnership (TPP) losing its popularity with the new USA under the leadership of D. Trump. For this reason, the future of trade relationship between the USA and the EU must be evaluated according to the developing perspective of a clean type of energy; hydrogen energy and economy.

References

1. McKeon M. TTIP Negotiations: A Summary of Round 11, Bertelsmann Foundation, 2015.
2. Akman MS. AB-ABD Transatlantik Ticaret ve Yatırım Ortaklığı (TTIP) ve Türkiye [The EU-USA Transatlantic Trade and Investment Partnership (TTIP) and Turkey], Tepav Report: R20135, İstanbul. 2013:3.

3. Mc Cormick J. Avrupa Birliği Siyaseti [European Union Politics], Trans. Doğancan Özsel, Liberte Pub., Ankara, 2015:508.
4. Simon L. Britain, the EU and the future of Europe: A geostrategic perspective, The Rusi Journal. 2015;160(5):16-23.
5. Ecorys. [cited 2009 May 18]. Available from: www.ecorys.com.
6. Güllü İ. AB-ABD Serbest Ticaret Anlaşması sürecine Türkiye-AB Gümrük Birliği Anlaşması özelinde bir bakış [An Evaluation of the EU-USA Free Trade Agreement process from the perspective of Turkey-EU Customs Union Agreement], Bilge Strateji. 2014;6(11):89–106.
7. Yılmaz M. Türkiye Transatlantik Ekonomik Ortaklıkta Yer Almalı [Turkey should be a part of the Transatlantic Economic Partnership], TÜSİAD Görüş, İstanbul. 2013;78:2.
8. Bakkalcı C, Öz E. Borun Önemi ve Türkiye'de Bor [Boron's Importance and Boron in Turkey], TİSK Akademi. 2007;2(4): 266.
9. Bayar H, Onat, N. Sürdürülebilir Kalkınma ve Hidrojen [Sustainable Development and Hydrogen], IV. Ulusal Hidrojen Enerjisi Kongresi ve Sergisi Bildiriler Kitabı [Proceedings of the IV. National Hydrogen Energy Congress and Exhibition, Kocaeli. 2009:215, 217.
10. Calestous J, Cheong LY. Innovation: Applying Knowledge in Development, UN Millennium Project, NY. 2005: 76.
11. Erdener H et al. Sürdürülebilir Enerji ve Hidrojen [Sustainable Energy and Hydrogen], ODTÜ Toplum ve Bilim Merkezi Pub., Ankara. 2007.

Determining the Effect of Trace Elements on Biohydrogen Production from Fruit and Vegetable Wastes

Tugba Keskin Gündoğdu[1], Kubra Arslan[1,3], Haris Nalakth Abubackar[1], [4]Gozde Duman[2], Koray Akarsu[2,3], JaleYanık[2,3], Nuri Azbar[1,3*]

[1]Ege University, Engineering Faculty, Bioengineering Department, 35100, Izmir, Türkiye
[2]Ege University, Faculty of Science, Chemistry Department, 35100, Izmir, Türkiye
[3]Ege University, Center for Environmental Studies, 35100, Izmir, Türkiye
[4]UniversityLa Coruña,Faculty of Sciences and Center for Advanced Scientific Research(CICA),LaCoruña, Spain

E-mail address: nuriazbar@gmail.com, keskin.tugba@gmail.com

Abstract
Dark fermentative hydrogen production from fruit and vegetable wastes (FVW) is a very effective, energy efficient and environmentally friendly method. However many factors can influence the production yields such as organic loading rate, hydraulic retention times, pH and temperature etc. Trace elements are one of the important parameters for dark fermentative hydrogen production because they work as cofactors in hydrogen formation biochemistry. Lack or excess of trace element concentrations in the basal medium could be an important reason for the low yield of hydrogen production. In this study, the effects of 11 factors (Fe, Ni, Zn, Co, Cu, Mn, Al, B,Se, Mo, W) was tested at two levels in terms of biohydrogen production from FVW. Each of the experimental set-ups was conducted as duplicates in 100-ml serum bottles at initial pH of 7 (under thermophilic conditions (55 ± 1°C). Flocculated biomass obtained from an industrial-scale anaerobic thermophilic bioreactor was used as an initial inoculum. The wastes (FVW) were collected from the main hall of Izmir Municipality. The trace elements were added to reactors according to statistical design. The cumulative biohydrogen values were changed between 30-75 mL and the hydrogen content was changed between 15-30%. The positive effects of trace element addition observed clearly in comparison to BHP reactors without its addition. An enhancement of 1.2 to 2.5 times of biohydrogen production was determined. The most effective trace elements were found as Zn and Ni during biohydrogen production. The digestate were sent to be treated by supercritical water gasification.

Keywords: Biochemical Hydrogen Potential; Biohydrogen production; Trace elements.

1. Introduction

Environmental pollution caused by use of fossil fuels as well as the risk of depletion of its reserves urges to find clean, renewable and environmentally friendly energy sources. Hydrogen is one of the best alternatives-fuel because after combustion as a fuel or conversion to electricity it produces only water as a byproduct [1]. Worldwide economic development and population growth cause a huge amount of waste generation and the uncontrolled discharge of municipal solid wastes is the main source of several environmental problems in many countries. All around the world especially developing countries are facing environmental and socio-economic problems because of uncontrolled discharging of municipal solid wastes. This situation is reducing the quality and sustainability of life conditions. After a careful eliminating process, Fruit and Vegetable Wastes can be converted into useful renewable energies [2]. Among various hydrogen production technologies, biohydrogen production is very feasible and efficient energy production method with the advantage of converting organic wastes into H_2at ambient temperature and pressure [3].

Hydrogen, carbondioxide, volatile fatty acids are produced during the acidogenesis phase of degradation of organic wastes by anaerobic fermentative bacteria. Mixed culture, which is a combination of anaerobic microorganisms have the ability to ferment organic wastes and generate clean energy, H_2 [3]. Most of the studies on dark fermentative hydrogen production focused on the effects of temperature, substrate type, and concentration. Recently, the importance of metallic ions on hydrogen production was understood and studies were performed for optimizing different trace elements. The higher amounts of trace elements may also inhibit hydrogen production yields [4].

Trace elements have a specific function on metabolic pathway of anaerobic microorganisms for hydrogen production. Ni^{+2} and Fe^{+2} are the most important trace elements since they are the components of the active site of hydrogenases. The hydrogenases may be classified as [Fe]-only, [Ni–Fe], and [Ni–Fe–Se] hydrogenases. Since Mg^{+2}can act as transporter molecule of adenosine triphosphate (ATP) in the cell, it is the other active site component of many enzymes. Zn^{+2} and Mn^{+2} have several functions on the biochemistry of hydrogen production because they are essential for the growth and survival of the cells [5]. There is no common decision on the concentrations of the

trace metals in literature becauseof concentrations of these components strongly dependent on the inoculum and the substrate type. So optimization processes become very important for different fermentation processes. There are a lot of techniques that can be used for optimization such as classical methods, statistical and mathematical approaches. Every technique has its own advantages and disadvantages but classical methods are known to be time consuming and expensive. Statistical methods are effective, efficient, economical and robust [6].

Experimental design methods can be applied by selecting certain factors in a controlled manner to obtain the effects by analyzing the results followed by ANOVA tests. These methods are very important for biohydrogen fermentation because of its complexity and may be influenced by many factors such as substrate type, temperature, pH, inoculum type, trace element concentrations, etc.

In this study, the effect of 11 factors (Fe, Ni, Zn, Co, Cu, Mn, Al, B, Se, Mo, W) was tested at two levels in terms of biohydrogen production from FVW. Each of the experimental set-ups was conducted in duplicates in 100-ml serum bottles at an initi l pH of 7 under thermophilic conditions (55 ± 1°C). Flocculated biomass obtained from an industrial scale anaerobic thermophilic bioreactor was used as an initial inoculum. The wastes were collected from main hall of Izmir Municipality. The trace elements were added to reactors according to statistical design.

Experimental Study

1.1. Inoculum and Substrate

The fruit and vegetable wastes were collected from the main hall of Izmir Municipality during winter season. The composition of the waste is: Zucchini (5%), parsley (3%), dill (3%), cucumber (6%), portulaca (5%), lettuce (5%), green beans (6%), potato (10%), eggplant (6%), tomato (6%), water cress (3%), lemon (7%), red pepper (5%), green pepper (5%), cabbage (5%), cauliflower (10%). The flocculated inoculum was taken from the full scale thermophilic anaerobic reactor of a distillery company. The inoculum used without any pre-treatment.

1.2. Biochemical Hydrogen Potential (BHP) tests

Biochemical Hydrogen Potential (BHP) tests were conducted at 100 mL dark serum bottles. Inoculum used was 10%and the dry matter content of the substrate at each bottle were 5%. Macro elements ($NaHCO_3$, NH_4Cl, KH_2PO_4 and K_2HPO_4) were added separately. The microelements were added according to the Table 1 which designed by the statistical program. All experiments were run in duplicates. After addition of the trace elements, the bottles were closed with rubber septa and sealed with aluminum rings. The headspace was flushed with argon to provide anaerobic conditions for the microorganisms. The BHP reactors were kept in a incubator at 55±2°C.

1.3. Trace Elements and Statistical Analysis

The trace elements and its concentrations were decided according to the literature. The max and min levels of the trace elements are; Fe (4-140 mg/L); Co (2-20 mg/L); Cu (0.5-50 mg/L); Mn (0.5-50 mg/L), Mo (0.3-30 mg/L), Ni (0.3-30 mg/L), Se(0.5-50 mg/L),W (0.4-40 mg/L), Zn (0.8-80mg/L), B (0.2-20 mg/L) and Al (0.8-80 mg/L), respectively. These minimum and maximum values of trace elements were used in Plackett-Burman Statistical Design by Design Expert 7.0. The suggested combinations of concentrations for fractional factorial design are listed in Table 1. The BHP tests were then conducted according to Table 1 and the results were analyzed by Design Expert 7.0.

For biohydrogen production all the components of the process do not contribute to the production yields with the same importance, therefore, the main effects parameters should be selected and the non-contributing parameters should be eliminated. Plackett and Burman published a work on 1946 and suggested a type called fractional factorial design to detect the major factors of a process with n number of experiments (n; 2,4,12…). The Placket-Burman is a 2 level design for economically detecting the main effects with ignoring the interactions of the parameters. Each level in Plackett-Burman design is presented in 2 levels (maximum and minimum), each horizontal row represents the factors and a vertical row presents the levels of the factors. The Plackett-Burman design results can be analyzed by statistical programs with further ANOVA analysis [7].

1.4. Analytical Methods

Chemical oxygen demand (COD) and suspended solid content was measured according to the standard methods [8]. The initial and final pHs of reactors were measured with pH meter (Sartorius). Total biogas production was measured by glass syringe.H_2 content of total biogas was determined by a GC (6890N Agilent) equipped with a thermal conductivity detector and HayesepD 80/100 packed column [9].Organic acids were analyzed using a GC (6890N Agilent) equipped with a flame ionization detector and DB-FFAP 30 m × 0.32 mm × 0.25 mm capillary column (J&W Scientific).The trace element analysis was conducted by ICP-OES by IZSU.

Table1. Trace element concentrations of BHP reactors

Reactor	Macronutrient (mL)	FVWare (g)	Inoculum (mL)	Fe (mg/L)	Co (mg/L)	Cu (mg/L)	Mn (mg/L)	Ni (mg/L)	Se (mg/L)	W (mg/L)	Zn (mg/L)	B (mg/L)	Al (mg/L)
BHP1	1	15	7	4	2	0,5	20	0,5	10	20	0,4	60	20	5,0
BHP2	1	15	7	4	20	20	0,5	20	10	20	0,4	0,0	0,2	5,0
BHP3	1	15	7	4	2	0,5	0,5	0,5	0,5	0,5	0,4	0,0	0,2	0,005
BHP4	1	15	7	100	2	0,5	0,5	20	0,5	20	0,4	60	0,0	20	5,0
BHP5	1	15	7	100	20	0,5	0,5	0,5	10	0,5	0,4	60	60	0,2	5,0
BHP6	1	15	7	4	2	20	0,5	20	10	0,5	0,4	60	60	20	0,005
BHP7	1	15	7	100	2	20	20	20	0,5	0,5	0,4	60	60	0,2	5,0
BHP8	1	15	7	100	20	20	0,5	0,5	0,5	20	0,4	60	60	20	0,005
BHP9	1	15	7	100	2	20	20	0,5	10	20	0,4	60	0,0	0,2	0,005
BHP10	1	15	7	100	2	0,5	20	20	10	0,5	0,4	0,0	0,0	20	0,005
BHP11	1	15	7	4	2	20	20	0,5	0,5	0,5	0,4	60	0,0	20	5,0
BHP12	1	15	7	4	20	0,5	20	20	0,5	20	0,4	60	60	0,2	0,005
Control	1	15	7	0	0	0	0	0	0	0	0	0	0	0	0
Waste	1	15	7	0	0	0	0	0	0	0	0	0	0	0	0
Waste+Inoculum	1	15	7	0	0	0	0	0	0	0	0	0	0	0	0

2. Results and Discussion

2.1. Characterization of wastes

The characterization results of FVWare presented in Table 2. The pH of the wastes has an acidic character because of the dominant fruits of the winter season. The organic content shows that these wastes are highly biodegradable. The trace element concentrations are very low except Na and Al which shows that there is a need of addition of trace elements to waste medium for a successful hydrogen production.

Table2. Characterization results of fruit and vegetable wastes (FVW)

Parameter	Unit	Average Value (Std Deviation)
pH	-	4.63±0.14
VSS	%	8±1.35
COD	g/L	84.13±19.98
NH_4^+-N	g/L	100±84.85
Total N	g/L	3.31±0.4
Fe	mg/L	17.05±6.1
Co	mg/L	0.05±0.04
Cu	mg/L	1.19±0.62
Mn	mg/L	1.93±0.88
Ni	mg/L	0.19±0.05
Se	mg/L	0.009±0.004
Zn	mg/L	2.40±0.55
B*	mg/L	1.78±0.39
Na	mg/L	193.37±50.64
Al	mg/L	9.39±4.53

Biochemical Hydrogen Potential Test Results

BHP tests were conducted according to the Table 1. Trace element concentrations varied with different BHP reactors. A control reactor including only biomass and water and another control reactor (waste+inoculum) without a trace element were also-tested for 300 hours.

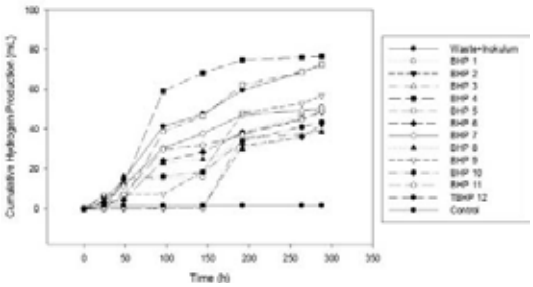


Figure 1. Cumulative hydrogen production

Figure 1 illustrates the effect of trace elements on cumulative hydrogen production in batch tests with different concentrations of trace elements. The results showed that most of the production ceased within 150 h. At first 100 h of H_2production, the slopes of the curves had a trend to increase. BHP 6, BHP 7, BHP 8and BHP 9 showed another increasing trend of H_2 production. The lag phase of all reactors lasted about 20 h. A maximum 80 mL of biohydrogen production were observed with BHP 5. Lowest hydrogen production was observed for thewaste+inoculum reactor.

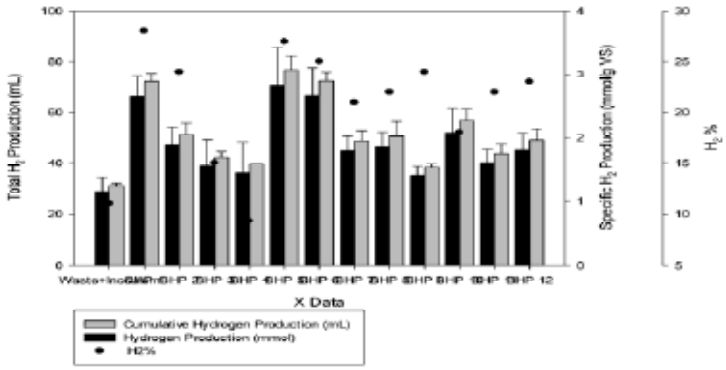


Figure 2. Total H_2 production, Specific H_2 Production and Hydrogen Percentages

Figure 2 represents the values of total H_2 production, specific H_2 production and H_2 percent of all reactors. Specific hydrogen production values changed between 1 to 3 mmol/g VS. Minimum specific hydrogen production values were obtained by waste+inoculum while a maximum value was observed at BHP 5. The gas content analysis showed that the biogas produced from the anaerobic fermentation consist ofonly H_2 and CO_2 without methane. Hydrogen content of the total gas produced changed between 15-27%.

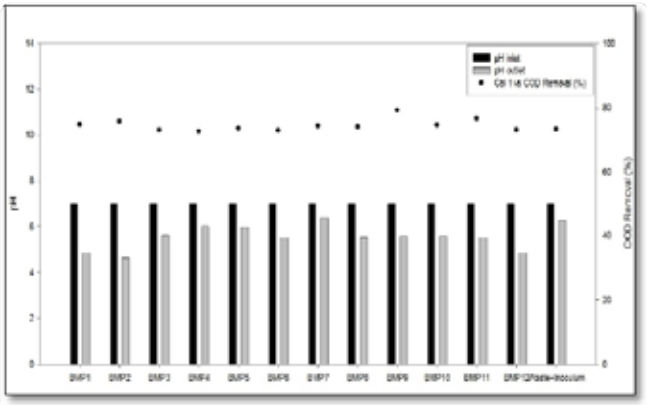


Figure 3. COD removal and pH values

The initial pH of all the reactors was adjusted to pH 7 because of the acidic character of the substrate. The pH values at the end of the process were measured between 4 and 5.5. The decrease of the pH values can be caused by volatile fatty acid production during anaerobic fermentation. The COD removal values changed between 70-78 % which shows the high degradation of the organic content of the wastes (Figure 3).

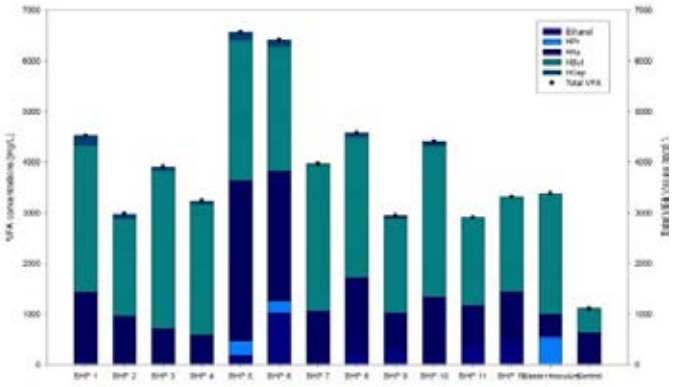


Figure 4. Soluble metabolite concentrations

The major soluble metabolites produced by anaerobic inoculum in this study were acetic and butyric acid. The propionic acid production was very low which is a good advantage for biohydrogen production. The low values of hydrogen percentages are directly related to higher amounts of butyric acid production. The volatile fatty acid production is directly proportional to the total biohydrogen production values (Figure 4).

The most important result of this study is the positive effect of trace element addition on biohydrogen production from fruit and vegetable wastes. Figure 5 shows the effect of different concentrations briefly. The hydrogen production potentials were enhanced by 2 to 3 times with trace element addition in comparison to the BHP reactor without trace elements.

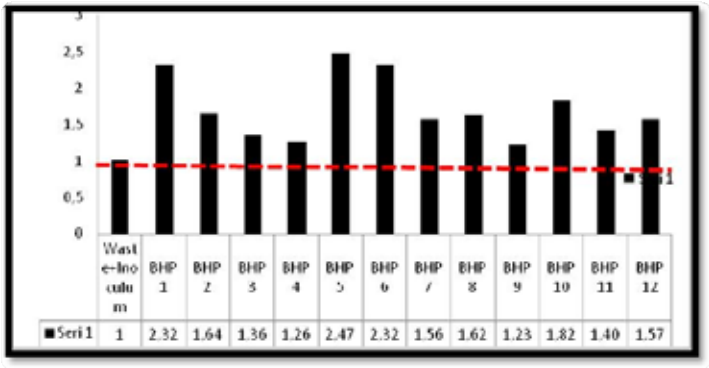


Figure 5. Biohydrogen production enhancement

2.2. Results of Statistical Analysis

The Plackett-Burman design was used to detect the major elements for biohydrogen production. The results presented above were analyzed by Design Expert 7.0. The model was significant with $p=0.0033<0.005$ and $R2=0.9933$. The main effective parameters were; Fe ($p=0.0027<0.005$), Zn ($p=0.0014<0.005$) and Ni ($p=0.0007<0.005$) which is in accordance with literature values. The pareto chart shows all the trace elements and effect ranking for biohydrogen production from fruit and vegetable wastes (Figure 6).

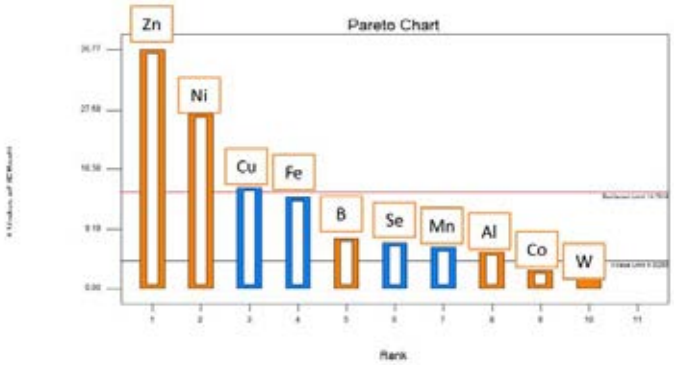


Figure 6. Pareto Chart for Plackett-Burman Design

3. Conclusions

The fruit and vegetable waste disposal is a serious environmental problem and biohydrogen production from these waste by dark fermentation can be an efficient, sustainable and environmentally friendly approach. Trace element concentration optimization is essential for increasing the hydrogen production yields because biohydrogen production can directly be affected bythe high or low concentrations of trace elements. The trace element needs for biohydrogen process depends on substrate or inoculum type. The major trace elements of biohydrogen production process from fruit and vegetable wastes are Fe, Zn, Cu and Ni. The addition of trace elements enhanced the hydrogen production values 2 to 3 times.

Acknowledgement

We wish to thank TUBITAK-MAG-215 M 314 for the financial support of this study. We also thank IZSU for their kind supports. HNA thanks the Xunta de Galicia (Spain) for his postdoctoral fellowship (ED 481B-2016/195-0)

Nomenclature

FVW	Fruit and Vegetable Wastes
BHP	Biochemical Hydrogen Potential
GC	Gas Chromatography
COD	Chemical Oxygen Demand
ATP	Adenosine Tri Phosphate

References

1. Tenca A, Schievano A, Perazzolo F, Adani F ,Oberti R.Biohydrogen From Thermophilic Co-Fermentation Of Swine Manure With Fruit And Vegetable Waste: Maximizing Stable Production Without pH Control. Bioresource Technology. 2011;102: 8582–8588
2. Shin H.S., Youn J.H. Conversion of Food Waste into Hydrogen by Thermophilic Acidogenesis. Biodegradation. 2005; 16: 33–44.
3. Wang J and Wan W. Factors Influencing Fermentative Hydrogen Production: A Review.International Journal of Hydrogen Energy. 2009; 34: 799–811.
4. Yang HJ, Shen JQ. Effect of Ferrous Iron Concentration on Anaerobic Bio-Hydrogen Production From Soluble Starch. Int J Hydrogen Energy. 2006; 31:2137–46.
5. Mohan V and Srikanth S.Regulatory Function Of Divalent Cations in Controlling the Acidogenic Biohydrogen Production Process.RSC Advances.2012; 2: 6576–6589
6. Singh V, Haque S, Niwas R, Srivastava A, Pasupuleti M and Tripathi CKM.Strategies for Fermentation Medium Optimization: An In-Depth Review. Front. Microbiol. 2017; 7: 2080-2087.
7. Wang J and Wan W. Experimental Design Methods for Fermentative Hydrogen Production: A Review International Journal Of Hydrogen Energy. 2009; 34: 235–244.
8. American Public Health Association, 1998. Standard Methods for the Examination of Water and Wastewater, 20th ed., Washington DC, USA
9. Azbar N, Çetinkaya Dokgöz FT,Peker Z.Optimization of Basal Medium for Fermentative Hydrogen Production from Cheese Whey Wastewater, International Journal of Green Energy, 2009; 6(4): 371-380.

Co-gasification of Çan Lignite with Kenaf Hydrolysate: Effects of Temperature and Feed Flow Rate

Açelya Seçer, Nilgün Küçet, Arif Hasanoğlu
Chemistry Department, Faculty of Arts and Science, Çukurova University, Adana
Email: acsecer@cu.edu.tr, ahesenov@cu.edu.tr

Abstract
In this study it was aimed to develop a technology in which the lignocellulosic biomass (kenaf) which solubilized in water via a thermal process will be subjected to a continuous catalytic gasification process with Çan coal under atmospheric pressure and at 700-900°C temperatures for the production of high yields of hydrogen. In the process of co-gasification of Çan lignite with kenaf hydrolysate the water was directly vaporized in the gasification reactor instead of producing steam with a steam generator. Co-gasification of biomass hydrolysate and coal occurred in the absence of a catalyst. The effect of feed (kenaf hydrolysate) flow rate (0.3-2.0 ml/min) and temperature (700-900°C) on hydrogen production and gasification yields were investigated. The optimum feed flow rate for maximum gas (1695.8±18.5 ml) and hydrogen production (% 74.3±1.1) was observed when the feed flow rate was 0.5 ml/min. The results showed that further increase in feed flow rate resulted less gas and hydrogen yield. Effects of temperature on gasification and hydrogen yield were investigated. Total gas volume increased approximately two times when increasing the gasification temperature from 700 to 900°C. Coal and hydrolysate were gasified separately in the absence of a catalyst as a baseline. Synergism effects were observed for co-gasifying of Çan coal and kenaf hydrolysate. The total gas volume (3060 ml) obtained from the co-gasifying of Çan coal and kenaf hydrolysate were higher (486 ml) than the arithmetical average value of the yields from individual coal and hydrolysate gasifying proses.

Keywords: Hydrogen; biomass hydrolysate; coal; gasification; co-gasification.

1. Introduction

The increasing need for energy in line with the decline in energy resources necessitates the development of new energy sources or the retrofitting of traditional energy sources that create some disturbances in their use in environmental terms. The current reserves of the fossil fuels, production costs, usage amounts and the extrapolation of the these statistics to future indicates that the the fossil fuels will be major for providing world's energy requirements in the future. Furthermore, coal, probably, will be the most dominant energy source in the first half of 22 th century [1]. Therefore, researches on coal and coal derivatives are getting more important for improving the alternative usage of coal, such as production of hydrogen from coal. Coal gasification (CG) offers one of the most versatile and clean ways to convert coal into electricity, hydrogen, and other valuable energy products. Rather than burning coal directly, gasification breaks down coal into its basic chemical constituents [2]. Hydrogen and other coal gasses can also be used to fuel power-generating turbines and for a wide range of commercial products. In the recent studies, some advantages of gasification of biomass and coal together instead of gasifying coal or biomass alone have been found in the literature [3]. In the process of co-gasification (COG) of coal and biomass, coal is used in a more environmentally friendly manner while biomass is available on a commercial scale. Gasification of coals with high sulfur and ash contents with various sources of biomass having low sulfur and ash contents is a promising technology; Biomass and wastes cause harmful gasses such as CO_2, NOx, and SOx to decrease [4, 5]. The high reactivity of the biomass improves the gasification process .The most effective catalysts in the carbon gasification process are the alkali metal salts (especially potassium). However, these salts are very expensive and most of the potassium salts pass into the gaseous phase during gasification, which is carried out at high temperatures. Alkaline salts (especially potassium) in the upper part of the herbaceous, especially in the biomass and co-gasification, are inexpensive catalysts [6,7]. Lignocellulosic biomass is a promising material to become a substitute for fossil sources because of its abundance in nature, low price and utilization area which does not compete with the food and lignocellulosic biomass can be converted into fuels or chemicals. The complex structural and chemical mechanisms of lignocellulosic biomass cause resistance to deconstruction which cause pretreatment requirements [8]. One of these pretreatments to is subcritical water hydrolysis process in which water is used in reaction medium so it makes the process totally environmentally friendly. The maximum solubility yields of biomass materials were found to be between 70-75% that was achieved at 250°C in subcritical water medium [9]. Co-gasification of hydrolyzed biomass may lead to higher gasification yields in order to the increase in gasifible contents of biomass by hydrolysis and still have the inorganic salts acting like catalyst at the same time in the hydrolysis solution. Steam is used as gasification agent in traditional methods of production of hydrogen from coal and the process temperatures are over 1000 °C. Also, a steam generator is used to produce steam, and carrier gasses are used in these traditional methods. In this

study, a modified method, which will be called as atmospheric pressure vapor phase reforming (AVPR), in which water is directly vaporized in the gasification reactor instead of producing steam with steam generator, was used to produce hydrogen from coal.

In this study, Çan lignite was co-gasified with kenaf (Hibiscus cannabinus L.) hydrolysate with AVPR method at different flow rates (0.3-2.0 ml/min) and temperatures (700-900°C). Effects of flow rate and temperature on hydrogen production and gasification yields were investigated.

2.Experimental Study

In this work, Turkish coal and a kenaf biomass were selected for gasification and co-gasification experiments. The relevant analytical data regarding the Çan coal and kenaf biomass are given in Table 1. The coals were ground to pass 60 mesh, sealed under nitrogen, and kept at -20°C until they were used in the gasification experiment.

Table 1. Analytical Data of Çan Coal and kenaf biomass.

	Kenaf	Çan Lignite
C (wt %, daf)[a]	48,6	49,2
H (wt %, daf)	5,7	4,6
N (wt %, daf)	0,1	1,1
S (wt %, daf)	-	4,7
O (wt %, daf)[b]	41,3	40,4
Moisture (wt %)	10,4	5,1
Ash (wt %, dry)	3,1	21,3

[a]daf = dry and ash free. [b]Calculated from difference.

The experimental study consists of two parts: Hydrolysis and gasification. In the first part, hydrolysis of Kenaf biomass is performed at sub-critical conditions. The hydrolysis of kenaf biomass was performed in a 500 ml PARR 4575 model HP/HT reactor equipped with a magne-drive mixing system. A pre-determined amount of ground kenaf (10 g, dry basis) and 350 ml water were placed in the reactor. The reactor was sealed and air was swept out by successive pressurizing and depressurizing with carbon dioxide. The mixture was heated at the rate of 4.7°C/min up to 250°C. After heating to 250°C, the reactor was pressurized with CO_2 using ISCO 260D pump (Isco Inc., Lincoln, Nebraska) at 4060 psi. The temperature used for hydrolysis experiments was 250°C. Following mixing (1000 rpm) the reactor contents for 2 hours continuously via the magne-drive, the reactor was taken out of the heating system and quenched in an ice-cold water bath. The hydrolysate solution was collected and filtered. The solid residue was dried in a vacuum oven and used for calculation of percent hydrolysis. The hydrolysate solution was filtered through 0.2 mm nylon filter and the clear solution was analyzed for total organic content (TOC). The percent hydrolysis of sorghum was found to be 72.7% in this procedure.

AVPR of kenaf hydrolysate and coal were performed in a continuous flow fixed bed reactor (Figure 1). The Çan coal (1g) was loaded into a stainless steel tubular reactor (inner and outer diameter of 0.56 and 1.4 inches, respectively). The tubular reactor (50 cm in length) was placed in an oven with the programmable temperature controller. The reactor was then heated with a rate of 30°C/min up to desired temperatures (700-900°C). Then 20 ml of kenaf hydrolysate (The carbon content of 2000 mg/l) was introduced into the tubular reactor at a feed flow rate of 0.3-2.0 ml/min (using an HPLC pump. Coal and kenaf hydrolysate were reacted separately in the absence of a catalyst as a baseline. The products formed in AVPR runs were cooled to 20°C C by using PolyScience digital temperature controller cryostat. Liquid and gaseous products were separated in the gas liquid separator unit after gasification. The gaseous products were bubbled through a cadmium acetate solution, so that H_2S precipitated quantitatively as CdS. Gravimetric determination of precipitated CdS gave the H_2S yield by back calculation. Other gaseous products were analyzed by a gas chromatograph. Gaseous products were collected into gas buret that was filled with water and the volume of the gas mixture measured by water displacement. Gas products were characterized using a Thermo Finnigan Trace Gas Chromatography equipped with a TCD detector. GC column was Supelco Carboxen 1010 plot fused silica capillary (30 m x 0.32 mm i.d.).

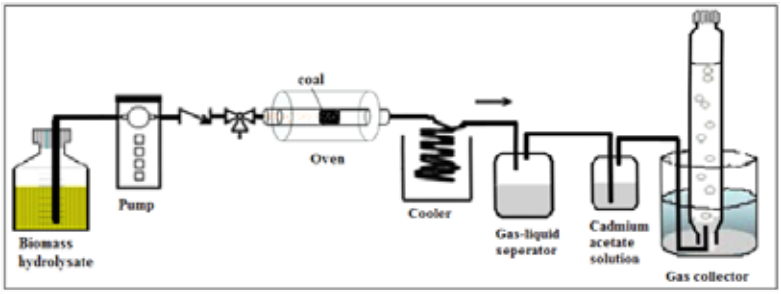


Figure 1. The gasification system

2. Results and Discussion

The composition of gaseous products obtained from co-gasification of coal and kenaf hydrolysate at 700°C were given in Table 2. In this set of experiments, 20 ml of sorghum hydrolysate (2000 mg/l C content) was introduced into the tubular reactor at a feed flow rate of 0.3, 0.5, 1.0. 1.5 and 2.0 ml/min. The gas formed from the co-gasification of coal with kenaf hydrolysate was found to be composed of mainly H_2, CO_2, CO, CH_4 and H_2S (precipitated quantitatively as CdS). However, the main gas product obtained from coal liquefactions was H_2.

Table 2. Comparison of different feed flow rate on co-gasification process (process conditions: 700°C constant temperature, 2000 mg/l carbon content of the feed)

Flow Rate (ml/min)	Total gas volume (ml)	H_2 (%)	CO_2 (%)	CO (%)	CH_4 (%)
0.3	1128,9±23,6	70.6±0,8	13.06±0.6	11.1±0,2	4.7±0,1
0.5	1695,8±38,9	73,6±2,8	7,8±0,8	13,6±0,1	5,1±0,1
1.0	1149,1±35,5	67,6±0,8	15,9±,0.1	11,3±2,8	5,6±0,3
1.5	824,6±31,8	65,7±5,3	16,9±2,0	11,3±1,4	6,6±0,1
2.0	687,6±16,3	62,9±0,5	13,2±0,2	14,2±0,5	9,7±0,6

The increase of feed flow rate from 0.3 to 0.5 resulted in higher hydrogen and total gas volume. Further increase of feed flow rate resulted in lower hydrogen and total gas yield. As seen from the Table 2, the highest total gas yield was observed at 0.5 ml/min (1695,8±38,9 ml) feed flow rate, while the lowest total gas was observed at 2.0 ml/min (687,6±16,3 ml) feed flow rate. The higher feed flow rate means shorter residence and contact time of biomass feed hydrolysate with coal resulting in less dehydrogenation and water-gas shift reaction possibilities and hence low hydrogen yield. So, in the conditions of lower feed flow rate the gasification agent (hydrolysate) passes through coal, there will be more interactions and gasification yield will be higher. The main subject of this study is to evaluate the hydrogen producing ability of the co-gasification process so that, the total gas mixture is analyzed in terms of hydrogen percent. The maximum percentage of hydrogen was obtained in the case of 0.5 ml/min feed flow rate. It was again seen that, as the flow rate increased there would be a decrease in the amount of hydrogen existing in the gas mixture. The results show that the CH_4 and CO yields were increased as a result of increasing the feed flow rate.

Effects of temperature on gasification and hydrogen yield were investigated. Coal samples are gasified at 0.5 ml/min feed flow rate at temperatures of 700, 800 and 900°C. Temperature is one of the most significant parameter that effects gasification yields and proportions of the gaseous mixture because of the thermodynamic behaviors of the reactions and the balance between exothermic and endothermic reactions [10, 11, 12]. Some studies showed that higher carbon conversions due to increasing temperatures tend to higher gasification yields [13, 14, 15]. The results related with the effect of temperature on co-gasification of coal and kenaf hydrolysate are given in Table 3.

Table 3. Effect of temperature on co-gasification of coal and kenaf hydrolysate (process conditions: 0.5 ml feed flow rate, 2000 mg/l carbon content of the feed)

Temperature (°C)	Total gas vol. (ml)	H_2 (%)	CO_2 (%)	CO (%)	CH_4 (%)
700	1695±38,9	73,6±2,8	7,8±0,8	13,6±0,1	5,1±0,1
800	2460±23,6	70,1±0,9	15,9±1,2	9,8±0,1	4,2±0,1
900	3060±46,2	70,3±1,1	16,3±1,8	10,6±0,2	2,8±0,1

Total gas volume increased approximately two times high when increasing the gasification temperature from 700 to 900°C. This result may come from the fact that the thermodynamic behavior of the system at 900°C that favors the gasification reactions that gives a higher gasification yield as described above. The main component of the gas mixture is hydrogen (more than 70 %), but it also contains CO_2, CO and CH_4 in different proportions. The two most effective reactions on hydrogen production, water gas reaction and methane reforming, are endothermic and are favored at elevated temperatures resulting in a higher hydrogen yield due to the increases in process temperatures [3, 16, 17]. It has been reported that in case of COG, more CO_2 production can be expected because of the higher oxygen contents of biomass. But in case of an increase in temperature, the consumption of CO_2 increases during the reactions of dry reforming of CH_4/light hydrocarbons/tar as well as the influence of Boudard reactions [3, 18, 19]. But in presence of H_2O vapor, the secondary water gas reaction takes places. This reaction is also endothermic and has a lower ΔH value (90.2 kj/mol) than that of Boudard reaction (172 kj/mol) and dry reforming reactions of methane (242 kj/mol) [3]. An Increase in CO_2 proportions has been observed from 700°C to 800°C due to the increasing carbon conversions by increasing temperatures. There is not a significant difference between these proportions at the temperatures of 800°C and 900°C. The increase in reaction temperatures also favors the two endothermic reactions, dry reforming and steam reforming of CH_4, so that a decrease in CH_4 proportions have been observed with increasing temperatures. The CO proportion is also decreased as the temperature increased from 700 to 800°C. The total amount of CO in the gas mixture in terms of milliliters is increased when the temperature is increased from 800 to 900°C. The CO forming reactions, steam reforming of methane and the primary water gas reactions are endothermic again, and are favored by increasing temperatures resulting an increase in CO amounts in final gaseous products at the end of gasification processes at elevated temperatures [3].The results indicate that 0.5 ml/min hydrolysate flow rate and 900°C temperature are the optimum reaction conditions for a high gasification and high hydrogen yield.

Coal and hydrolysate were gasified separately in the absence of a catalyst as a baseline. The comparisons of the total gas volume and the product distribution between individual gasification of coal and kenaf hydrolysate are shown in Table 4. Synergism effects were observed for co-gasifying of Çan coal and kenaf hydrolysate. The total gas volume (3060 ml) obtained from the co-gasifying of Çan coal and kenaf hydrolysate were higher than the arithmetical average value of the yields from individual coal and hydrolysate gasifying proses.

Table 4. Total gas volume and gas compositions formed from the individual gasification of Çan coal and kenaf hydrolysate and co-gasification of coal with kenaf hydrolysate in the absence of a catalyst (process conditions: 900°C constant temperature, 0.5 ml feed flow rate, 2000 mg/l carbon content of the feed)

	Total gas vol. (ml)	H_2 (%)	CO_2	CO	CH_4
Çan Lignite	2324±70,7	67,1±0,4	17,5±0,4	12,6±0,2	2,9±0,3
Hydrolysate	256±16,4	77,1±0,8	11,5±0,2	8,8±0,1	1,8±0,1
Co-gasification	3060±27,6	70,3±0,3	14,3±0,2	11,6±0,1	2,8±0,1

It has been observed that by gasification of kenaf hydrolysate and Çan lignite together, the volume of the final gas is 486 ml higher than the cumulative sum of gas quantities obtained when Çan lignite and Kenaf hydrolysate are gasified alone indicating a synergetic effect on gasification yield. The hydrogen yield of COG is also higher. The mineral matter of Çan lignite which can be caused catalytic effect on hydrogen production. It was also observed that the CO_2 proportions of the final product were lowered by COG processes.

Conclusions

In this study, co-gasification of kenaf hydrolysate with Çan lignite is performed at different feed flow rates and temperatures to evaluate gasification performances and hydrogen yields and effects of performing COG instead of CG and BM. It has been observed that high feed flow rate negatively affected total gas volume and hydrogen yield

due to the lower interactions. Temperature was one of the most effective parameter on co-gasification reactions, showed that at higher temperatures endothermic carbon conversion reactions and hydrogen production reactions are favored so that, gasification yields and hydrogen amounts in final gas mixtures can be increased by increasing process temperature to 900°C. Synergism effects were observed for co-gasifying of coal and kenaf hydrolysate. The total gas volume (3060 ml) obtained from the co-gasifying of Çan coal and kenaf hydrolysate were 486 ml higher than the arithmetical average value of the yields from individual coal and hydrolysate gasifying proses.

Acknowledgement
This study was funded by Çukurova University Research Grant. (Project number: FDK-2016-5653)

Acronyms
AVPR Aqueous Vapour Phase Reforming
BM Biomass Gasification
CG Coal Gasification
COG Co-gasification

References
1. WorldEnergyOutlook, 2016. Available from: https://www.iea.org/media/publications/weo/WEO2016Chapter1.pdf
2. Minchener JA.Coal gasification for advanced power generation. Fuel.2005;17,2222-2235.
3. Taba LE, Irfan MF, Daud W, Chakrabarti, MH. The effect of temperature on various parameters in coal, biomass and CO-gasification: A review.Renewable and Sustainable Energy Reviews.2012:16, 5584–5596.
4. Fermoso J,Arias B, Plaza MG, Pevida C, Rubiera F, Pis JJ. High-pressure CO-gasification of coal with biomass and petroleum coke. FuelProcessingTechnology.2009; 90, 926–958.
5. Hernandez JJ, Aranda-Almansa G, Serrano C. CO-gasification of biomasswastesandcoal–cokeblends in an entrainedflowgasifier: an experimentalstudy. EnergyFuel 2010;24, 2479–2567.
6. Zhu W, Song W, Lin W. Catalytic gasification of char from CO-pyrolysis of coal and biomass. Fuel Processing Technology. 2008; 89, 890-896.
7. Brown RC, Liu Q, Norton, G.. Catalytic effects observed during the CO-gasification of coal and switchgrass. Biomass and Bioenergy. 2000; 18, 499–506.
8. Kumar P, Barett DM, Delwiche MJ, Stroeve P. Methods for pretreatment of lignosellulosic biomass for efficient hydrolysis and biofuel production. Industrial&Engineering Chemistry Research. 2009; 48(8), 3713-3729.
9. Meryemoğlu,B ,Hesenov A, Irmak S, Atanur O, Erbatur O. Aqueous phase reforming of biomass using various types of supported precious metal and raney-nickel catalysts for hydrogen production. International Journal of Hydrogen Energy. 2010;35,12580-12587.
10. Fermoso J, Arias B, Plaza MG, Pevida C, Rubiera F, Pis JJ, et al. High-pressure CO-gasification of coal with biomass and petroleum coke. Fuel Processing Technology 2009;90:926–32.
11. Pinto F, Franco C, Andre´ RN, Tavares C, Dias M, Gulyurtlu I, et al. Effect of experimental conditions on CO gasification of coal, biomass and plastics wastes with air/steam mixtures in a fluidized bed system. Fuel 2003;82:1967–76
12. Xiao X, Meng X, Le DD, Takarada T. Two-stage steam gasification of waste biomass in fluidized bed at low temperature: Parametric investigations and performance optimization. Bioresource Technology 2011;102:1975–81.
13. Seo MW, Goo JH, Kim SD, Lee SH, Choi YC. Gasification characteristics of coal/biomass blend in a dual circulating fluidized bed reactor. Energy Fuel 2010;24:3108–18.
14. Franco C, Pinto F, Gulyurtlu I, Cabrita I. The study of reactions influencing the biomass steam gasification process. Fuel 2003;82:835–42.
15. Nikoo MB, Mahinpey N. Simulation of biomass gasification in fluidized bed reactor using ASPEN PLUS. Biomass Bioenergy 2008;32:1245–54.
16. Kim YJ, Lee JM, Kim SD. Coal gasification characteristics in an internally circulating fluidized bed with draught tube. Fuel 1997;76:1067–73.
17. Huang J, Yitian F, Chen H, Wang Y. Coal gasification characteristic in a pressurized fluidized bed. Energy Fuel 2003;17:1474–9.
18. Pohorely´ M, Vosecky´ M, Hejdova´ P, Puncocha´ r M, Skoblja S, Staf M, et al. Gasification of coal and PET in fluidized bed reactor. Fuel 2006;85:2458–68.

ORAL PROCEEDINGS

Investigation of Hydrogen Production Performance of a Reactor Assisted by a Solar Pond by Photoelectrochemical Method

Mehmet Karakilcik[1,*], Mustafa Erden[1], Müzeyyen Cilogulları[1], Ibrahim Dincer[2]
[1]Department of Physics, Faculty of Sciences and Letters, University of Cukurova, Adana 01330, Turkey
[2]Faculty of Engineering and Applied Science, University of Ontario Institute of Technology (UOIT), 2000 Simcoe Street, North Oshawa, Ontario, L1H 7K4, Canada

Abstract
In this study, the hydrogen production performance of a reactor assisted by a solar pond by photoelectrochemical method is examined conceptually. The main components of the new integrated system are a solar pond, a photovoltaic panel (PV) and a hybrid chlor-alkali reactor which consists of a semiconductor anot, photocathode and cation exchange membrane. The proposed system produces hydrogen via water splitting reaction and also yields the by products namely chlorine and sodium hydroxide while consumes saturated NaCl solution and pure water. In order to increase the effciency of the reactor, the saturated hot NaCl solution at the heat storage zone (HSZ) of the solar pond is transferred to the anot section and the heated pure water by heat exchanger in the HSZ is transfered to cathode section. The electrodes are used as electron donors for photochemical hydrogen production with diminishing the power requirement from the PV panel that is used to provide the necessary electrical energy for the electrolysis. The results confirm that the thermal performance of the solar pond plays a key role on the hydrogen production efficiency of the reactor.

Keywords: Hydrogen production; photoelectrochemical process; solar energy; solar pond; exergy efficiency.

1. Introduction

Hydrogen is a clean energy carrier that can be produced from renewable sources. Solar based hydrogen production methods have been extensively investigated in recent years. Among these methods, photoelectrochemical water decomposition is considered as a promising method for hydrogen production [1-4]. Bicer and Dincer [5] investigated the effects of different light intensities on the efficiencies both of the photovoltaic (PV) cell and photoelectrochemical (PEC) hydrogen production experimentally. They used Fresnel lens and dielectric mirror to concentrate solar light and divide into two to be utilized by PV and by PEC. Casallas et al. [6] constructed and tested a novel photoelectrochemical cell for hydrogen production by using a polymeric membrane photocathode that is produced by electro-deposition of CuO/CuO_2 semiconductor photocatalysts on the cathode surface. Test results show that using this photocathode enhances the rate of hydrogen production by increasing the current density and lowering the bias voltage. Acar and Dincer [7] investigated a hybrid chlor alkali-photoelectrochemical system that produces hydrogen, chlorine and sodium hydroxide experimentally. This hybrid system maximizes the solar energy utilization by combining photochemical and electrochemical processes. Rabbani et al. [8] developed and analyzed a new photoelectrochemical reactor to produce hydrogen, chlorine and sodium hydroxide. They investigated the effect of applied voltage, amount of catalyst (zinc sulfide) and light intensity on the production rate. Karakilcik et al. [9] investigated the performance of a solar pond by theoretically and experimentally. For the experimental purpose of this study, they built an insulated solar pond with a surface area of 4 m^2 and a depth of 1.5 m at Cukurova University in Adana, Turkey. The highest thermal efficiency was obtained for August as to be 4.5% for the upper convective zone, 13.8% for the non-convective zone and 28.1% for the heat storage zone, respectively.

In the open literature, there have been no studies on the coupling photoelectrochemical chlor alkali cell with a solar pond. The goal of this study is to combine a photoelectrochemical chlor alkali cell with a solar pond to use the heat storage property of the pond. This study also aims to conceptually analyze the performance of the integrated system.

2. System description

In this study, hydrogen production performance of a reactor assisted by a solar pond with photoelectrochemical method is examined conceptually. The main components of the new integrated system are a solar pond, a photovoltaic panel (PV) and a hybrid chlor-alkali reactor that consists of a semiconductor anot, photocathode and cation exchange membrane, and NaCl and NaOH solutions as anolyte and catholyte, respectively. The integrated system increases solar energy utilization by taking advantage of the solar energy harvesting properties of solar pond, photocathode and PV panels. In the presence of sunlight, the reactor takes advantage of both photoelectrolysis and photocatalysis to produce H_2, Cl_2 gases and NaOH.

Fig.1 shows the schematic of the integrated system, along with inlet and outlet streams. The streams 4 and 5 are in gas phase and the remaining streams are in liquid phase. The saturated hot NaCl solution at the HSZ of the solar pond is transferred to the anot section and the heated pure water by heat exchanger in the HSZ is transferred to the cathode section. After passing through the reactor, the depleted aqueous solution of sodium

chloride is enriched by the salt reservoir. The membrane is used to separate the product gases namely H_2 and Cl_2 and to neutralize the OH^- ions in the cathode section by selectively permitting the transfer of Na^+ ions from the anode to the cathode section. The reactor has optically transparent walls to allow the illumination of the photocathode during photoelectrochemical production processes.

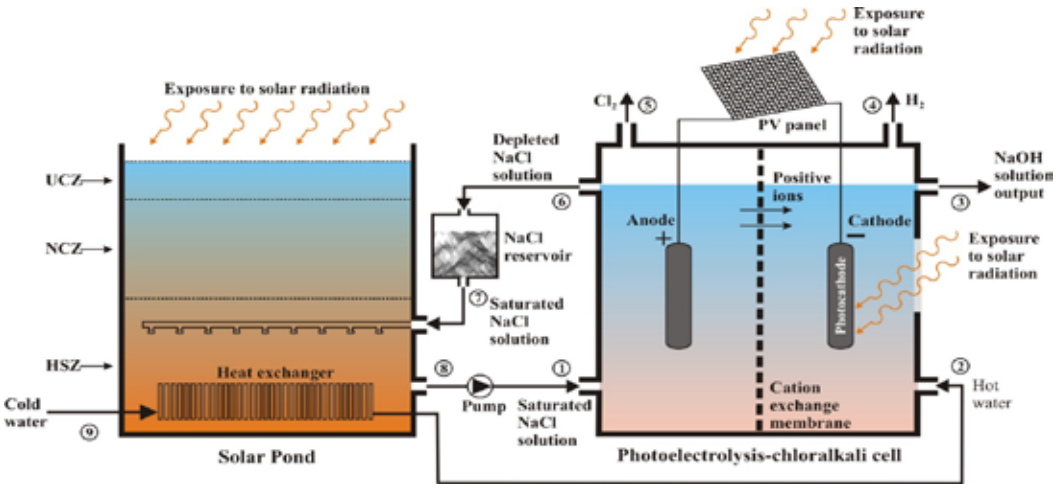


Fig. 1. Schematic of the integrated system.

Note that the cell reduces water at the photo-cathode according to the half reaction:

$$2H_2O_{(l)} + 2e^- \rightarrow H_{2(g)} + 2OH^-_{(aq)} \qquad E^0 = -0.8277\ V \qquad (1)$$

At the anode, chlorine is formed from saturated NaCl aqueous solution as follows:

$$2Cl^-_{(aq)} \rightarrow Cl_{2(g)} + 2e^- \qquad E^0 = 1.36\ V \qquad (2)$$

According to equations 1 and 2, the total cell voltage (E^0) is 2.1877 V which is higher than 1.23 V for water electrolysis.

The sodium ions form in the anolyte by NaCl dissociation and migrate from the anolyte to the catholyte through the cation exchange membrane. The caustic soda forms in the catholyte can be written as follows:

$$Na^+_{(aq)} + OH^-_{(aq)} \rightarrow NaOH_{(aq)} \qquad (3)$$

3. Analysis

During the course of this study, the following assumptions are made for the analysis:

- The ambient temperature (T_0) and pressure (P_0) are 25 °C and 1 atm, respectively.
- The reactants and products are at reaction temperature and pressure in all chemical reactions.
- All processes occur at steady state.
- The changes in potential and kinetic energies, heat losses are neglected.
- The evaporation from the surface of the pond and water lost from the HSZ are neglected.
- Both hydrogen and chlorine gases are assumed to be ideal gases.

The steady state mass balance equation (MBE) for the solar pond can be written as:

$$\dot{m}_7 + \dot{m}_9 = \dot{m}_8 + \dot{m}_2 \qquad (4)$$

where $\dot{m}_7$ and $\dot{m}_9$ signify the mass flow rates in (kg/s) of enriched brine and the pure water that entering the solar pond while $\dot{m}_8$ and $\dot{m}_2$ denote the mass flow rates in (kg/s) of hot saturated brine and pure water that leaving the solar pond, respectively.

The related balance equations for the reactor are as follows [10]:

The steady state MBE for the reactor can be written as:

$$\dot{m}_1 + \dot{m}_2 = \dot{m}_3 + \dot{m}_4 + \dot{m}_5 + \dot{m}_6 \quad (5)$$

where $\dot{m}_1$ and $\dot{m}_2$ represent the mass flow rates in (kg/s) of hot saturated brine and hot pure water that entering the reactor while $\dot{m}_3$, $\dot{m}_4$, $\dot{m}_5$ and $\dot{m}_6$ denote the mass flow rates in (kg/s) of sodium hydroxide (NaOH) solution, hydrogen gas, chlorine gas, and depleted brine that leaving the reactor, respectively.

The mass flow rate of salt (NaCl) entering the anode section can be written as:

$$\dot{m}_{s1} = \dot{m}_1 x_{s1} \quad (6)$$

where x_{s1} signifies the mass fraction of NaCl entering the reactor in stream 1.

The mass flow rate of water ($\dot{m}_{w1}$) entering the anode section can be written as:

$$\dot{m}_{w1} = \dot{m}_1 - \dot{m}_1 x_{s1} \quad (7)$$

The mass flow rate of NaCl leaving the anode section can be written as:

$$\dot{m}_{s6} = \dot{m}_6 x_{s6} \quad (8)$$

where x_{s6} denotes the mass fraction of NaCl leaving the reactor in stream 6.

The mass flow rate of water leaving the anode section can be written as:

$$\dot{m}_{w6} = \dot{m}_6 - \dot{m}_6 x_{s6} \quad (9)$$

Thus the rate of NaCl consumption ($\dot{m}_{sc}$) in the anode section can be written as:

$$\dot{m}_{sc} = \dot{m}_{s1} - \dot{m}_{s6} \quad (10)$$

Thus, the mass flow rate of chlorine gas leaving the anode section in stream 3 can be written as:

$$\dot{m}_5 = \frac{\dot{m}_{s1} - \dot{m}_{s6}}{1.64} \quad (11)$$

The mass flow rate of hydrogen gas leaving the anode section in stream 4 can be written as:

$$\dot{m}_4 = 0.02 \frac{x_{s1} - x_{s6}}{1 - x_{s6}} \dot{m}_1 \quad (12)$$

The energy balance equation (EnBE) for the reactor can be written as:

$$\dot{m}_1 h_1 + \dot{m}_2 h_2 + \dot{W}_{in} + \dot{Q}_{in} = \dot{m}_3 h_3 + \dot{m}_4 h_4 + \dot{m}_5 h_5 + \dot{m}_6 h_6 \quad (13)$$

where h_{1-6} signifies the specific entalpies of the associated streams, $\dot{W}_{in}$ represents the the total work input to the system, $\dot{Q}_{in}$ denotes the heat input to the system.

During electrolysis, the work input is electricity and it can be written as:

$$\dot{W}_{in} = Vi \quad (14)$$

where V is applied voltage in volts and i is current in ampers.

On the other hand, during photoelectrolysis and photoelectrochemical processes, the work input is solar energy.

Photoelectrolysis processes: $\dot{W}_{in} = \eta_{pv} I A_{pv}$ (15)

Photoelectrochemical processes: $\dot{W}_{in} = \eta_{pv}(1 - \alpha) I A_{pv} + \alpha I A_{pc}$ (16)

where η_{pv} and A_{pv} are the efficiency and area of PV panel, respectively. I is the light intensity in (W/m^2), α is the portion of the solar light spectrum used by photocathode for photocatalytic hydrogen production and A_{pc} is the area of photocathode.

Consequently, the energy efficiency equation can be written as:

$$\eta_{en} = \frac{\dot{m}_6(HHV_{H_2}) + \dot{m}_3 h_3 + \dot{m}_5 h_5}{W_{in} + \dot{m}_1 h_1 + \dot{m}_2 h_2} \quad (17)$$

where HHV_{H_2} is the higher heating value of hydrogen (142 MJ/kg).

The entropy balance equation for the reactor can be written as:

$$\dot{m}_1 s_1 + \dot{m}_2 s_2 + \frac{\dot{Q}_{in}}{T_0} + \dot{s}_{gen} = \dot{m}_3 s_3 + \dot{m}_4 s_4 + \dot{m}_5 s_5 + \dot{m}_6 s_6 \quad (18)$$

where s_{1-6} signify the spesific entropies of the associated streams. $\dot{s}_{gen}$ is the rate of entropy generation of the reactor.

The exergy balance equation (ExBE) for the reactor can be written as:

$$\dot{m}_1 ex_1 + \dot{m}_2 ex_2 + \dot{W}_{in} + \dot{Q}_{in}\left(1 - \frac{T_0}{T}\right) = \dot{m}_3 ex_3 + \dot{m}_4 ex_4 + \dot{m}_5 ex_5 + \dot{m}_6 ex_6 + EX_d \quad (19)$$

where ex_{1-6} signifies the specific exergies of the associated streams and EX_d represents the rate of exergy destruction within the system. T is the system temperature.

Since the exergy efficiency of a system is the ratio of the useful exergy to the total exergy input, the exergy efficiency of the system can be written as:

$$\eta_{ex} = \frac{\dot{m}_3 ex_3 + \dot{m}_4 ex_4 + \dot{m}_5 ex_5}{\dot{W}_{in} + \dot{m}_1 ex_1 + \dot{m}_2 ex_2} \quad (20)$$

4. Results and discussion

For the parametric studies, light intensity is kept constant at 600 W/m^2 and the operating temperature is being varied. Thus the system is tested at four different temperatures (30, 40, 50 and 60 °C) and the mass balance equations are used to investigate the relationship between the inlet (NaCl and pure water) and outlet (NaOH, chlorine and hydrogen gases) mass flow rates. Furthermore, the relationships between the applied power and rate of chlorine and hydrogen generation are also investigated.

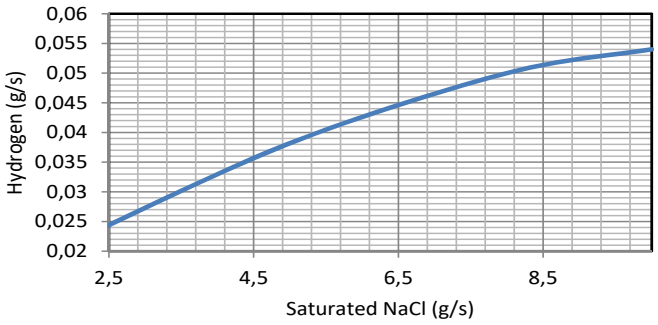


Fig. 2. Effect of saturated NaCl inlet flow rate on hydrogen production rate.

Figs. 2 and 3 show the effect of saturated brine inlet flow rate on the rates of H_2 and Cl_2 generation. The operating temperature and ligth intensity are kept constant 30 °C and 600 W/m^2, respectively. It is clear that the H_2 and Cl_2 generation rates increase as the flow rate of NaCl is increased. The maximum H_2 and Cl_2 generation rates are around 0.05359 g/s and 1.635 g/s, respectively while saturated NaCl and fresh water inlet rates to provide these production rates is 10 g/s.

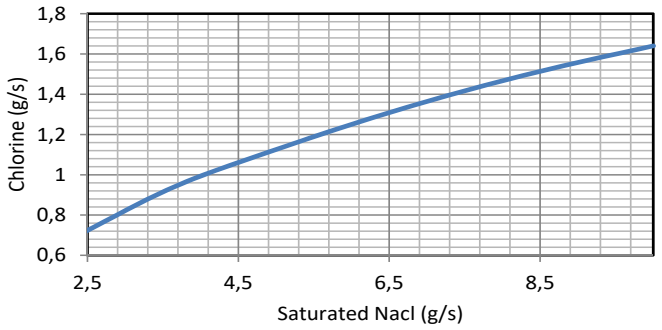


Fig. 3. Effect of saturated NaCl inlet flow rate on chlorine production rate.

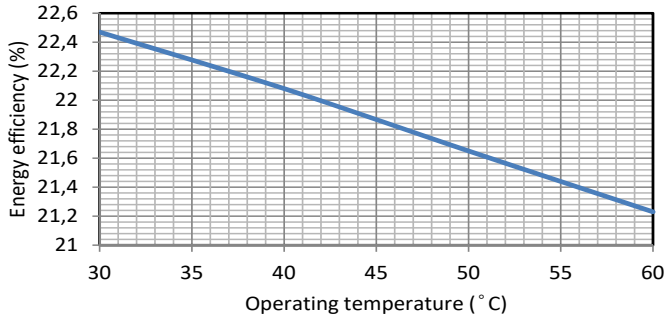


Fig. 4. Effect of operating temperature on the energy efficiency of the system.

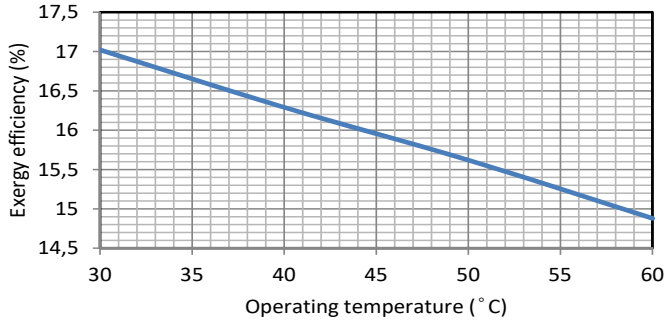


Fig. 5. Effect of operating temperature on the exergy efficiency of the system.

Figs. 4 and 5 show decreasing energy and exergy efficiency with increasing temperatures from 30 °C to 60 °C while the light intensity are kept constant at 600 W/m^2. Thus the results show that there is a inverse relation between high product gas yields and high energy and exergy efficiencies within given temperature range and light intensity.

5. Conclusions

In this study, hydrogen production performance of a reactor assisted by a solar pond by photoelectrochemical method is examined conceptually. The proposed system produces hydrogen, chlorine and sodium hydroxide. The results show that hydrogen production increased while energy and exergy efficiency decrease with increasing temperature due to thermal loss of the system.

References

1. Acar C, Dincer I. Analysis and assessment of a continuous-type hybrid photoelectrochemical system for hydrogen production. Int J Hydrogen Energy. 2014;39:15362-15372.
2. Xing Z, Zong X, Pan J, Wang L. On the engineering part of solar hydrogen production from water splitting:nphotoreactor design. Chem Eng Sci. 2013;104:125-146.
3. Ahmad H, Kamarudin SK, Minggu LJ, Kassim M. Hydrogen from photo-catalytic water splitting process: a review. Renew Sustain Energy Rev. 2015;43:599-610.
4. Liao CH, Huang CW, Wu JCS. Novel dual-layer photoelectrode prepared by RF magnetron sputtering for photocatalytic water splitting. Int J Hydrogen Energy. 2012;37:11632-11639.
5. Bicer Y, Dincer I. Experimental investigation of a PV-Coupled photoelectrochemical hydrogen production system. Int J Hydrogen Energy. 2017;42:2512-2521.
6. Casallas C, Dincer I, Zamfirescu C. Experimental investigation and analysis of a novel photo-Electrochemical hydrogen production cell with polymeric membrane photocathode. Int J Hydrogen Energy. 2016;41:7968-7975.
7. Acar C, Dincer I. Experimental investigation and anlysis of a hybrid photoelectrochemical hydrogen production system. Int J Hydrogen Energy. 2017;42:2504-2511.
8. Rabbani M, Dincer I, Naterer GF. Experimental investigation of hydrogen production in a photo-electrochemical chloralkali process. Int J Hydrogen Energy. 2016;41:7766-7781.
9. Karakilcik M, Dincer I, Rosen M.A. Performance investigation of a solar pond. Int J Hydrogen Energy. 2006;26:727-735.
10. Ghost S, Dincer I. Development and analysis of a new light-based hydrogen production system. Int J Hydrogen Energy. 2016;41:7976-7986.

Effective Factors Improving Catalyst Layers of PEM Fuel Cell

Gokce S. Avcioglu[1,*], Berker Ficicilar[2], Inci Eroglu[1]
[1]Department of Chemical Engineering, Middle East Technical University, 06800 Ankara, Turkey
[2]Department of Chemical Engineering, Ondokuz Mayıs University, 55139 Samsun, Turkey
e-mail: gokce.avcioglu@metu.edu.tr, berker.ficicilar@omu.edu.tr, ieroglu@metu.edu.tr

Abstract
Water management is one of the major challenges of low-temperature hydrogen/air proton exchange membrane (PEM) fuel cells. Water produced on the active sites of the cathode catalyst layer (cCL) condenses while it moves along the pores of the electrode. Accumulation of liquid water in the pores prevents oxidant gas from reaching active sites. Mass transport limitation occurring in the porous structure causes lower performance. The effect of Pt percentage in catalyst on performance has been investigated by comparing the performances of membrane electrode assemblies prepared with 20% and 70% Pt/C catalysts using ultrasonic coating technique. The power density obtained at 0.45 V increased by the increase in the Pt weight percentage on Pt/C catalyst, from 0.28 to 0.64 W/cm^2 for H_2/air. SEM images prove that the thickness of the catalyst layer increases by increasing Pt load, which causes cracks in the catalyst layer. Thinner electrodes have lower charge transfer resistance according to electrochemical impedance spectroscopy (EIS) results. The inclusion of 30 wt. % Polytetrafluoroethylene (PTFE) nanoparticles in catalyst ink enhanced the cell performance for those electrodes manufactured with 20 % Pt/C at higher current densities by providing two-phase flow. However, increasing hydrophobic catalyst layers did not significantly affect the performance of the fuel cell using the commercial catalyst having 70% Pt/C. Electrochemical active surface area (ESA) of these electrodes were by calculated from cyclic voltammograms. The addition of PTFE nanoparticles, increased the electrochemical surface area (ESA) of the electrodes prepared with 20 % Pt/C, however, reverse effect was observed for the 70% Pt/C.

Keywords; Proton exchange membrane; fuel cell performance; electrocatalyst; catalyst layer; hydrophobic nanoparticle; water management

1. Introduction

Water management is one of the key challenges for low-temperature fuel cells. Water is generated as a byproduct of oxygen reduction reaction at the triple phase boundaries in the cathode catalyst layer. Besides, water vapor enters the cell with humidified reactant gasses. The presence of liquid water in the cell is essential because of providing proton conduction through the ionomer. However, the excess amount of water causes pore-blocking. This leads to mass transport limitations causing decrease in reaction kinetics. Hydrophobic treatment of components of electrodes on the route of the liquid water enhances the water removal.

In the literature, various studies were performed on hydrophobic treatment of gas diffusion layers (GDLs) and microporous layers (MPLs) to facilitate water removal. The addition of hydrophobic agents into the catalyst layers has some disadvantages. They may cover Pt particles which cause decline in activity due to discontinuity in the ionic and electronic network. However, with a two-step preparation of catalyst ink prevents decline in activity [1]–[3]. Friedmann and Nguyen [2, 3] achieved to enhance performance with hydrophobized cathode catalyst layer prepared with 45 wt. % Pt on carbon support with respect to conventional catalyst layers. In our previous study, we achieved improved performance with hydrophobic catalyst layers with respect to conventional catalyst layers prepared with 20 wt. % Pt on Vulcan XC72R [4]. In our latter studies, we used PTFE and fluorinated ethylene propylene (FEP) as hydrophobic agents [5, 6]. In those studies, the commercial catalyst included 70 wt. % Pt on carbon black. Performance enhancement was observed for conventional catalyst layers and hydrophobic catalyst layers with respect to the catalyst layers prepared with commercial catalyst consist of lower amount of Pt.

The aim of this paper was to investigate the influence of Pt percentage in commercial catalyst on the performance of conventional and hydrophobic catalyst layers. The influence of Pt loading and composition of catalyst on the performance of electrodes was investigated.

2. Materials and Methods

Catalyst ink preparation: The commercial catalysts consist of 70 wt. % Pt and 20 wt. % Pt on carbon support. Two different catalyst inks were prepared. Conventional catalyst layers were manufactured by catalyst inks including water, Nafion solution (15 wt. % 1100 EW, Ion Power, Inc., USA) and isopropyl alcohol (Sigma-Aldrich Co. LLC., USA). Hydrophobic catalyst layers were manufactured via two-step ink preparation method [1]. In the first step, catalyst was impregnated with half amount of Nafion solution. After mixing for 24 h step, ink was dried in an oven (Binder GmbH, Germany). In the second step, the dried catalyst ink was impregnated with remained Nafion solution. Finally, PTFE dispersion (10 wt. %), and isopropyl alcohol (IPA) were added to the ink, respectively. Prepared ink was mixed for 24 h in a water bath with a magnetic stirrer at room

temperature. Nafion and PTFE amount on dry basis in the catalyst inks was fixed at 30 wt. %. Electrochemical and physical characterizations were carried out with dried catalyst ink in an oven under atmospheric pressure at 40 °C for 96 h.

Performance testing: Electrodes were manufactured with ultrasonic coating technique (ExactaCoat DMC-2100, Sono-Tek Corporation, USA). The operating frequency of the instrument was 48 kHz. Coating ink was sprayed onto 34 BC gas diffusion layers (SGL Technologies GmbH, Germany) with a flow rate of the 0.3 ml/min. Gas diffusion layers were 315 µm thick and were hydrophobized with 5 wt. % PTFE with standard Microporous Layer (MPL) on one side. Two different Pt loading were studied which are 0.4 mg Pt/cm^2 and 1.2 mg Pt/cm^2. Nafion 212 membrane (Ion Power, Inc., USA) were used as proton conductor. A single cell with an active area of 5 cm^2 (Model: FC05-01 SP REF, Electro-CChem Inc., USA) was used for performance testing. Silicon gaskets (0.18 mm) were used as sealer. Graphite plates provide mixed serpentine flow of reactant gases. Single cell was tightened on each bolt with a torque of 1.7 Nm. The Test Station (Henatech, Turkey) includes external humidification system for both reactant gasses. Temperatures of bubblers were adjusted to 70 °C; while fuel cell temperature was adjusted to 70.2°C. Back pressure (3 psi) was applied to both anode and cathode exhaust. Fuel cell was operated at H_2/Air gas feeding modes. Volumetric flow rates for hydrogen and air were adjusted to 0.1slpm and 0.6slpm, respectively. Before recording the V-I data, for the purpose of conditioning, the cell was operated 1 h at 0.3V, and then 3.5h at 0.5V. At the end of every hour MEA was kept at OCV for 5 min, and then at 0.1 V for 5 min. Data for polarization curve were taken for three times using a visual basic program. Cell voltage varied with a step size of 0.05 V from 1 to 0.3 V.

Conventional catalyst layers did not have PTFE. On the other hand, 30PTFE-AC represents the MEA that has 30 wt. % PTFE on both anode and cathode catalyst layers; while without-PTFE represents the MEA that had no PTFE in catalyst layers.

SEM measurements: High-resolution scanning electron microscope system (FEI QUANTA 400F Field Emission, FEI Company, USA) included secondary electrons (SE)SEM images of membrane electrode assemblies (MEAs) were used to determine the cross-section image of MEAs. MEAs were broken into two pieces with liquid nitrogen. Samples were coated with ultrathin (5 nm) gold/palladium alloy coating to provide conductivity.

Electrochemical impedance spectroscopy analysis: A frequency response analyzer (FCI4/Series G, Gamry Instruments, USA) was used to collect the impedance data. FRA was connected to an electronic load (RBL 488, TDI-Dynaload, TDI Power, USA). A homemade voltage follower circuit was used to isolate grounds and unwanted current flow between FRA and load. The amplitude of the AC current was kept at 10% of the DC current. The impedance data was collected at galvanostatic mode between 2.5 kHz and 0,1 Hz with 10 points/decade. Real and imaginary part of frequency response was measured at fast mode to minimize fluctuations in responses. After collecting data of polarization curve, the cell was held at 0.5 V until the system is stabilized, then real and imaginary part of frequency responses of Nyquist plot were measured at 0.5 V.

3. Results and Discussion

Performance testing: Performance increase with increase of Pt percentage in the commercial catalyst was determined with performance testing. Figure 1 shows the polarization and V-I curves of conventional and hydrophobic catalyst layers prepared with 20 % and 70 % Pt/C. Performance of conventional catalyst layers (CLs) at 0.45V increased from 0.28W/cm^2 to 0.64W/cm^{2}for MEA's having 0.4 mg/cm^2 Pt loading. High Pt content in commercial catalyst resulted in increase in performance more than 2-fold, because the ratio of Pt to total dry mass of components ($X_{Pt/TM}$) increased more than 3-fold (Table 1). When CLs were manufactured with 70 % Pt/C, thickness of the CLs decreases. This is figured out from the ratio of Pt amount to total dry mass of components ($X_{Pt/TM}$) in the catalyst ink (Table 1). As the ratio of Pt amount decreases with respect to total dry mass of components in the catalyst ink, allowed to manufacture thinner electrodes. This leads to enhanced mass, ionic and electronic transport. Significant increase was observed in open circuit voltage (OCV) (from 0.94V to 1.01V). Total Pt amount in both CLs is the same for both samples, however, number of Pt particles in the unit area increases for thinner CLs. This leads to enhanced electrochemical connectivity between Pt particles. Consequently, kinetic activity increased. Therefore, increase in open circuit voltage could attribute to increased kinetic activity. Conventional CLs prepared with 20 % Pt/C showed a steeper slope in the ohmic region compared to conventional CLs prepared with 70 % Pt/C. In the mass transport region of conventional CLs prepared with 70 % Pt/C, performance decreases with increasing current density. That is up to high water concentration in the porous and ionic structure. Increase in kinetic activity leads to increase in water generation rate. While generated water provides high water saturation in the ionic structure, it causes pore blocking due to excess amount. This resulted in enhanced ionic conduction, but decreased rate of reactant transport. Therefore, ohmic resistance decreased; while mass transport resistance increased compared to conventional CLs prepared with 20 % Pt/C.

When Pt loading on the electrode increased three-fold to 1.2mg/cm^2, thickness of the catalyst layers increased two-fold (Figure 2). Performance of high Pt loaded CLs was 0.60 W/cm^2 at 0.45V; while it was 0,64 W/cm^2 at 0.45V. Open circuit voltage of high Pt load CLs (OCV=0,99V) was slightly lower than low Pt load CLs (OCV=1.01V) prepared with the same catalyst. However, in the low current density region (≤ 0,7 A/cm^2), despite the increased thickness, high Pt load CLs (1.2 mg/cm^2) have higher cell voltage than low Pt load CLs (0,4 mg/cm^2). This is interpreted as high Pt loaded CLs showed higher activity when rate of water production was low. In the ohmic region (between 0.1 and 1.0 A/cm^2), high Pt load CLs have steeper slope with respect to low Pt load CLs. Therefore, in the mass transport region (between 1.0 and 1.6 A/cm^2), performance of high Pt load CLs was lower than low Pt loaded CLs. Decrease in performance is attributed to increasing in charge transfer resistance (Figure 3) which is the main reason of decrease in ohmic resistance.

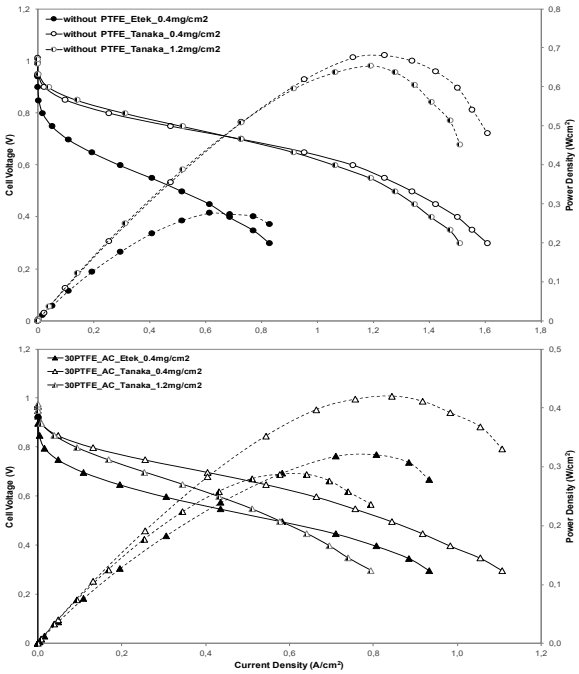


Figure 1. Effects of increase in Pt percentage in commercial catalyst and Pt loading on the performance of conventional and hydrophobic catalyst layers at H_2/Air feed.

Performance of hydrophobic catalyst layers (hCLs) with 0.4 mg/cm^2 Pt load increased from 0.32 to 0.41 W/cm^2 at 0.45V with the increase in Pt content in the commercial catalyst. Hydrophobic CLs prepared with 20 % Pt/C ($X_{Pt/TM}$=0.08) was thicker than hCLs prepared with 70 % Pt/C ($X_{Pt/TM}$=0.27). Reduced thickness of CLs provided enhanced mass, ionic and electronic conduction even in the case of hydrophobic catalyst layers. This led to increase in performance with respect to thicker hCLs. Open circuit voltage of hydrophobic catalyst layers (hCLs) prepared with 70 % Pt/C (OCV=0.97V) was higher than the catalyst layers prepared with 20 % Pt/C (OCV=0.93V). Open circuit voltage of hCLs consists of 1.2 mg/cm^2 load was also 0.97 V. High Pt content in the commercial catalyst provided higher kinetic activity. In the ohmic region, slopes of two samples with 0.4 mg/cm^2 Pt loading were very similar. This means that ohmic resistances are very similar, although both CLs have different thicknesses. On the other hand, hydrophobic catalyst layer consists of 1.2 mg/cm^2 Pt load, have a steeper slope in the ohmic region with respect to other hydrophobic CLs. This indicated that increase in thickness in the case of highly active CLs decreases ionic conduction. Generated water causes pore flooding but the road to exhaust is too long. Therefore, the film thickness surrounding agglomerates increases which led to increase in charge transfer resistance (Figure 3). For all samples, in the mass transport region, rate of performance with increasing current density was similar and lower compared to conventional CLs. This is attributed to PTFE in the CLs, which enhanced water management by alleviating pore flooding.

However, performance of hCLs prepared with 70 % Pt/C for both samples was lower than conventional CLs prepared with 70% Pt/C. Performance of low Pt load hydrophobic CLs (0.41 W/cm^2) was lower with respect to low Pt load conventional CLs prepared with 70 % Pt/C (0,64 W/cm^2). On the other hand, performance of high Pt load hydrophobic CLs (0.29 W/cm^2) was lower with respect to low Pt load conventional CLs prepared with 70 % Pt/C (0.60 W/cm^2). However, in the case of CLs prepared with 20 % Pt/C, performance of hydrophobic catalyst layers (0.32 W/cm^2) was higher than conventional CLs (0.28 W/cm^2). Nafion addition followed by PTFE addition resulted in pore blocking. Nafion and PTFE addition to 20 % Pt/C caused 90 % of the pores to be blocked, while it is 98% of the pores for 70 % Pt/C (Table 1). Reaction (primary pores) and transport volumes (secondary pores) decreased due to pore blocking. This leads to further decrease in performance for CLs prepared with 70 % Pt/C compared to 20% Pt/C. The ratio of carbon amount to total dry mass of components ($X_{C/TM}$) is 0.8 for 20 % Pt/C; while it is 0.3 for 70 %Pt/C. This means that 20 %Pt/C have higher amount of free spaces on carbon. In other words, there are free pores in carbon particles of 20 % Pt/C, which does not contain ant Pt particles. Free pores in carbon particles of 70 %Pt/C were almost 40 % lower than 20 % Pt/C. This means that most of the pores occupied by Pt particles. Therefore, when PTFE was added to both catalysts, volume of open primary and secondary pores was higher in the 30PTFE_Etek (0.006 cm^3/g and 0.03 cm^3/g) than 30PTFE_Tanaka (0.001 cm^3/g and 0.013 cm^3/g). This allows improved performance for hCLs prepared with 20 % Pt/C.

Figure 2 showed the cross-section images of MEAs with conventional catalyst layers. The image on the right shows the MEA prepared with low Pt load with CLs (0.4 mg/cm^2); while image on the left shows MEA prepared with high Pt load with CLs (1.2 mg/cm^2). Low Pt load CLs is straight from the end to end as high Pt load CLs. The thicknesses of the CLs were measured with ImageJ software. It is found out that the thickness of the CLs is changing along the whole length of CLs. However, the average thickness of low Pt load CLs is measured as 4 µm; while it is 8 µm for high Pt load CLs. There is any deformation in membrane and CLs observed for low Pt loaded electrodes. However, cracks (shown with red arrows) are seen in the lengthwise of CLs for high Pt loaded electrodes. This means that when the thickness of the CLs increases, this causes cracks in CLs. However, membrane occupied the spaces between disconnected CLs, this may prevent complete discontinuity of CLs.

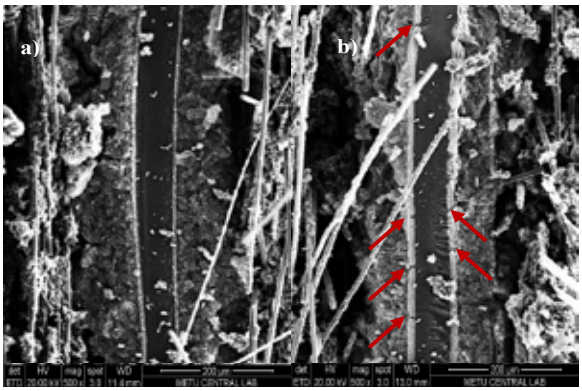


Figure 2. Effect of Pt loading on the thickness of conventional catalyst layers: a) MEA with low Pt load CLs, b) MEA with high Pt load CLs.

Figure 3 shows Nyquist plots of conventional catalyst layers with low and high Pt loading. Impedance spectrum for both samples shows a high frequency arc. The intercept of the high-frequency impedance arc on the real axis represents the total ohmic resistance of the cell (R_{HF}), while high-frequency arc represents charge transfer resistance (R_{ct}). To determine R_{HF} and R_{ct} an equivalent circuit modeling was used. The equivalent circuit model representing reaction steps were explained in detail in our previous studies [5, 6].

Modeling results reveal that high-frequency resistance of conventional CLs with low Pt loading (0.4 mg/cm^2) is 0.051 Ω, whereas charge transfer resistance of anode is 0.030 Ω and cathode is 0.385 Ω. On the other hand, high-frequency resistance of conventional CLs with high Pt loading (1.2 mg/cm^2) is 0.052 Ω, while charge transfer resistance of anode is 0.022 Ω and cathode is 0.519 Ω. The thickness of the high Pt loaded CL (8 µm) is 2-fold of the thickness of the low Pt loaded CL (4 µm). High-frequency resistances of both samples are similar. This is interpreted as increase in thickness of CLs does not negatively affect membrane humidification. However, charge transfer resistance of cathode side was increased with the increase in the thickness of the CL. This is up to increased transport limitations in addition to disruption in ionic and electronic network (Figure 2).

When the thickness of the CL increases, it is difficult to remove water from the pores. While some of the pores are completely closed to reactant transport, some of them are partly filled with liquid water. Therefore, reactants at cathode side cannot freely move through the partly and completely blocked pores. This causes decrease in consumption rate of reactants at the triple phase boundaries. As the thickness of the CL increases, electrons travel a longer path length. This may cause to decrease in reaction rate due to decrease in the number of arriving electrons in unit time to the reaction boundaries.

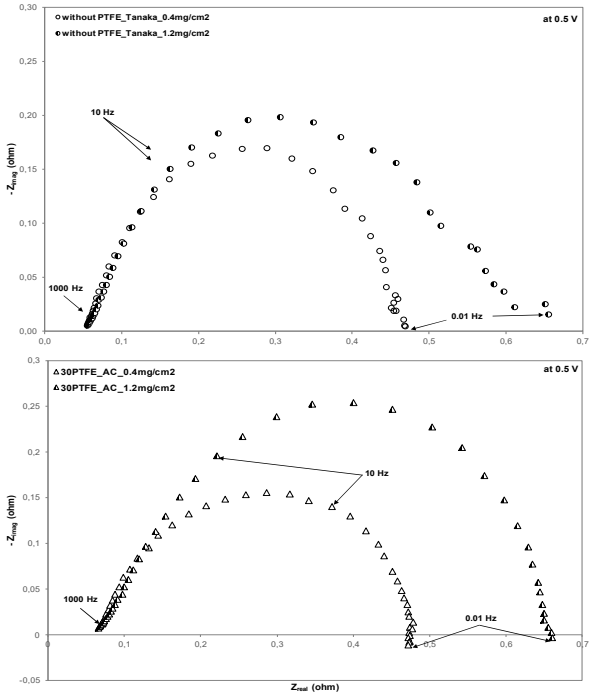


Figure 3. Effect of Pt load of the conventional and hydrophobic CLs on charge transfer resistance.

Equivalent circuit modeling of Nyquist plots reveals that high-frequency resistance of hydrophobic CLs with low Pt loading (0.4 mg/cm^2) is 0.068 Ω, whereas charge transfer resistance of anode and cathode is 0.153 Ω and 0.255 Ω, respectively. On the other hand, high-frequency resistance of conventional catalyst layers with high Pt loading (1.2 mg/cm^2) is 0.061 Ω, while charge transfer resistance of anode and cathode is 0.107 Ω and 0.492 Ω, respectively. High-frequency resistances of both samples are similar. Charge transfer resistance of cathode side for hydrophobic CLs with low Pt load is lower than high Pt loading hydrophobic CLs. This means that increase in thickness of CLs increases charge transfer resistance. However, PTFE addition to CLs increases high-frequency resistance and charge transfer resistance of anode side according to conventional CLs. This is interpreted as when PTFE is added to CLs this decrease the water saturation in the pores. This resulted in decrease in the water amount transported by electroosmotic drag and back diffusion which is either generated by chemical reaction at cathode or enter the cell with reactant gasses. This may cause the decrease in the level of membrane humidification. On the other hand, charge transfer resistance of anode in the case of hydrophobic CLs is 5 times higher than the charge transfer resistance of anode of conventional CLs. This may up to decreased electrochemical surface area due to unemployed active surfaces stuck in closed pores by PTFE. This may also up to decreased water saturation in the anode CL, which limits ionic conduction. The increase in charge transfer resistance of cathode side for hydrophobic catalyst layers with respect to conventional catalyst layers may also up to decreased electrochemical surface area (Table 1).

Table 1 summarizes the characteristic of Pt/C, Nafion impregnated Pt/C and hydrophobic catalyst layers. XRD results revealed that the diameter of Pt particles of 20 % Pt/C (2.7 nm) was smaller than 70% Pt/C (3,5 nm). As Pt/C was impregnated with Nafion, the diameter of Pt particles increased to 3.9nm for 20 % Pt/C and to 3.7nm for 70 % Pt/C. This reveals that Nafion impregnation caused Pt agglomeration. Addition of PTFE to Nafion impregnated catalyst reduced Pt particle size due to ink preparation. Hydrophobic catalysts were

prepared with 2-step ink preparation method. This led to homogenous distribution of agglomerated Pt particles for 20 % Pt/C and 70 % Pt/C, the diameters were 3.5 nm and 3.4 nm, respectively. While Nafion was impregnated to 20 % Pt/C, 75 % of cumulative pore volume were blocked. Further addition of PTFE caused further decrease (60 %) in opened pores. In the case of 70 % Pt/C, 88 % of total pores were blocked with Nafion addition, while 88 % of remained pores were blocked by PTFE addition. Primary pore volume remained in hydrophobic catalyst prepared with 20 % Pt/C was 0.006 cm^3/g and secondary pore volume was 0.03 cm^3/g. In the case of 70 % Pt/C, primary and secondary pore volume of hydrophobic catalyst were 0.001 and 0.013 cm^3/g, respectively. Electrochemical surface area of commercial catalyst decrease to 70 and 62 m^2/g when Nafion was added. PTFE addition to Nafion impregnated catalyst resulted in further decrease in electrochemical surface area, because, in each component addition, more pores were occupied. This caused decrease in electrochemical surface area. The ratio of Pt amount to total dry mass of components ($X_{Pt/TM}$) allows us to compare the thickness of CLs. As $X_{Pt/TM}$ increases, thickness of CLs decreases. Therefore, thinnest CLs were manufactured for 70 % Pt/C; while the thickest CLs were manufactured for without PTFE_Etek. The ratio of carbon amount to total dry mass of components ($X_{C/TM}$) allows us to compare the free spaces in CLs that can be occupied by Nafion and PTFE. As $X_{C/TM}$ increases, free spaces increase in the CLs. This could prevent pore blocking of Nafion and PTFE. Therefore, decrease in electrochemical surface area could be alleviated. Free space present in the 20 % Pt/C was higher than 70 % Pt/C, this allows higher ESA for the first sample.

Table 1. Characteristics of Pt/C, Nafion impregnated Pt/C and hydrophobic catalysts.

Catalyst	*d_{Pt} (nm)*	*Cum. Pore Volume (cm^3/g)*	*Pri. Pore Volume (cm^3/g)*	*Sec. Pore Volume (cm^3/g)*	*ESA (m^2/g)*	*$X_{Pt/TM}$*	*$X_{C/TM}$*
20 % Pt/C	2.7	0.27	0.059	0.136	77	0.20	0.8
without PTFE_Etek	3.9	0.10	0.015	0.083	70	0.14	0.6
30PTFE_Etek	3.5	0.04	0.006	0.030	45	0.08	0.3
70 % Pt/C	3.5	0.34	0.082	0.190	65	0.70	0.3
without PTFE_Tanaka	3.7	0.11	0.010	0.091	62	0.48	0.2
30PTFE_Tanaka	3.4	0.02	0.001	0.013	50	0.27	0.1

4. Conclusions

According to these results, conclusions can be drawn as below;

- High Pt content in the commercial catalyst decreases thickness of the CLs.
- Thin CLs allows enhanced mass, ionic and electronic properties. Therefore, cell performance increase with conventional and hydrophobic CLs prepared with 70 % Pt/C.
- High Pt loading (1.2 mg/cm^2) increases the thickness of conventional and hydrophobic CLs.
- Increased thickness of the catalyst layers causes increased charge transfer resistance. This led to performance decrease.
- Carbon amount in the commercial catalyst is as important as Pt amount for hydrophobic CLs. Low carbon amount in the commercial catalyst resulted in the blockage of most of the pores by Nafion and PTFE. Therefore, lower performance was obtained with hydrophobic catalyst layers compared to conventional catalyst layers which were prepared with 70 % Pt/C.

References

1. Nguyen TV, Natarajan D, Jain R., "Optimized Catalyst Layer Structure for PEM Fuel Cells," ECS Trans., vol. 1, no. 6, pp. 501–508, 2006.
2. Friedmann R, Nguyen TV., "Optimization of the Cathode Catalyst Layer Composition using a Novel 2-step Preparation Method," ECS Trans., vol. 16, no. 2, pp. 2021–2029, 2008.
3. Friedmann R, Nguyen TV., "Optimization of the Microstructure of the Cathode Catalyst Layer of a PEMFC for Two-Phase Flow," J. Electrochem. Soc., vol. 157, no. 2, pp. B260–B265, 2010.
4. Avcioglu GS, Ficicilar B, Bayrakceken A, Eroglu I, "High performance PEM fuel cell catalyst layers with hydrophobic channels," Int. J. Hydrogen Energy, vol. 40, no. 24, pp. 7720–7731, 2015.
5. Avcioglu GS, Ficicilar B, Eroglu I, "Effect of PTFE nanoparticles in catalyst layer with high Pt loading on PEM fuel cell performance," Int. J. Hydrogen Energy, pp. 1–11, 2016.
6. Avcioglu GS, Ficicilar B, Eroglu I, "Influence of FEP nanoparticles in catalyst layer on water management and performance of PEM fuel cell with high Pt loading," Int. J. Hydrogen Energy, 2016.

ORAL PROCEEDINGS

Three-Dimensional Non-Isothermal Model Development of High Temperature PEM Fuel Cells

Dilara Gulcin Caglayan[1*], Berna Sezgin[1], Yilser Devrim[2] and Inci Eroglu[1]
[1]Chemical Engineering Department, Middle East Technical University, Ankara, TURKEY
[2]Energy Systems Engineering Department, Atılım University, Ankara, TURKEY
Email: e173875@metu.edu.tr, berna.sezgin@metu.edu.tr, yilser.devrim@atilim.edu.tr, ieroglu@metu.edu.tr

Abstract
In this study three-dimensional two mathematical models of a High Temperature PEM Fuel Cell are developed by using Comsol Multiphysics for isothermal and non-isothermal operation conditions. The active area of the cell having phosphoric acid doped PBI membrane as an electrolyte is 25 cm2. The flow channels have triple mixed serpentine geometry. Inlet temperatures of anode and cathode reactants are taken as 438 K. The model results include concentration, pressure, velocity profiles of anode and cathode compartments as well as the temperature profile within the fuel cell. Conservation of mass, momentum and charge are used with the appropriate assumptions and boundary conditions. For the non-isothermal model energy balance is included in order to take into account the temperature variation within the system. The non-isothermal model is simulated for two different operation voltages, which are 0.45 V and 0.60 V. According to the non-isothermal model results, the temperature gradients are determined as 0.31 K and 0.18 K for operation voltages of 0.45 V and 0.60 V, respectively. Based on Faraday's law, consumed amount of hydrogen and oxygen are dependent on the current density, which is inversely proportional to the operation voltage in the activation and ohmic regions. The current density is directly related to the source term in the conservation of energy. As the current density increases, the heat evolving due to the reaction increases. Since the temperature variation within the cell is not significant, it is concluded that isothermal operation assumption can be taken as a good approximation.

Keywords: High Temperature PEM Fuel Cell; Three-dimensional modeling; Non-isothermal.

1. Introduction

Modeling of fuel cells has been important, since it elucidates the conservation of mass, momentum and energy taking place within the system boundaries. It has been a useful tool in order to explain the fundamentals of the transport phenomena taking place within the system especially in the cases where it is not possible to determine them by means of experiments. The system can be designed and optimized with fewer experiments with the help of a validated model. In addition, the response of the system to the changing operation conditions can be predicted by altering the model input parameters.

In the Table 1, some of the mathematical models developed for HT-PEMFC are illustrated with respect to their chronological order. Most of the models are developed for steady-state operation, since the influence of model parameters on the performance is aimed to be examined. On the other hand, there exist dynamic models in order to investigate the system behavior at start-up. 1D model only considers the changes occurring across MEA, but on the MEA surface or along the flow channels. For instance, they are unable to take into account the change in the pressure or the concentration of the species along the flow channels. There exist 2D and 3D models in recent years. However, 2D models are not able to predict all the phenomena occurring within the system such as change in the concentration of reactants along flow channels. Although 3D models require more time to compile due to their complexity, an appropriate and validated model could elucidate the system behavior in all aspects. The 3D models existing in literature either considers the system as a single channel or half-cell. When the model domain is taken as single channel, the model fails to predict the system behavior along the flow channels. For instance, the change in the oxygen concentration from cathode inlet to outlet is not taken into consideration in a single channel model. However, it is important to consider the pressure and the concentration variation along the flow channels, since they influence the performance of the fuel cell. Besides the single cell models, there exist half-cell models which evaluate the entire active area of the cell. In the half-cell models the anode overpotential is taken as constant or neglected. This current study involves the 3D model of a single cell taken into account entire active area and flow channels.

In the previous paper, Caglayan et al. [1] investigated influence of the operation temperature on the performance of a HT-PEMFC by assuming isothermal operation, and changing the operation temperature of the cell. It has been concluded that operation temperature is a key parameter on the performance of the fuel cell. However, the validity of isothermal operation assumption has not been discussed yet. In this study, a non-isothermal mathematical model is developed for HT-PEMFC in order to observe the change in the temperature within the single cell having an active area of 25 cm^2. The results of non-isothermal model are compared with the previous ones [1].

Table 1. Solution technique of mathematical models for HT- PEMFC in literature

Authors	Year	Model Dimension	Model Domain	Solution Technique	I/NI
Cheddie & Munroe [2,3]	2006	1D	Single cell	Runge-Kutta Method	NI
Cheddie & Munroe [4]	2006	3D	Single channel	FEMLAB 3.1i	NI
Hu et al. [5]	2006	2D	Half cell yz-plane	FEMLAB	I
Peng & Lee [6]	2006	3D	Single channel	FLUENT 6.1	NI
Cheddie & Munroe [7]	2007	2D	Single cell xz-plane	FEMLAB 3.1i	NI
Scott et al. [8]	2007	1D	Single cell	Comsol Multiphysics	I
Ubong et al. [9]	2009	3D	Single channel	Comsol Multiphysics	I
Lobato et al. [10]	2010	3D	Single half-cell	Comsol Multiphysics	I
Siegel et al. [11]	2011	3D	Single cell	Comsol Multiphysics	NI
Reddy & Jayanti [12]	2012	3D	Single channel	ANSYS-Fluent	NI
Kvesić et al. [13,14]	2012	3D	Single cell+cooling	ANSYS-Fluent	NI
Su et al. [15]	2012	2D	Single cell yz-plane	Comsol Multiphysics	NI
Chippar & Ju [16]	2013	3D	Single channel	FLUENT	NI
Bezmalinović et al. [17]	2014	2D	Single cell xz-plane	Comsol Multiphysics	I
Lang et al. [18,19]	2015	2D	Single cell xz-plane	Finite Element Method	NI
Elden et al. [20]	2016	2D	Single cell yz-plane	Comsol Multiphysics	NI
Sezgin et. al [21]	2016	3D	Single channel	Comsol Multiphysics	I
Caglayan et. Al [1,22]	2016	3D	Single cell	Comsol Multiphysics	I

2. Model Development

The non-isothermal model is developed for the HT-PEMFC with triple mixed serpentine flow channel geometry. In addition to the equations used in isothermal model, conservation of energy is applied for the system. Fig. 1 shows the domain used in Comsol Multiphysics. The physical properties of the fuel cell are available in the previous study conducted by Caglayan et al. [1] In addition; the thermal properties used in the non-isothermal model are given in Table 2.

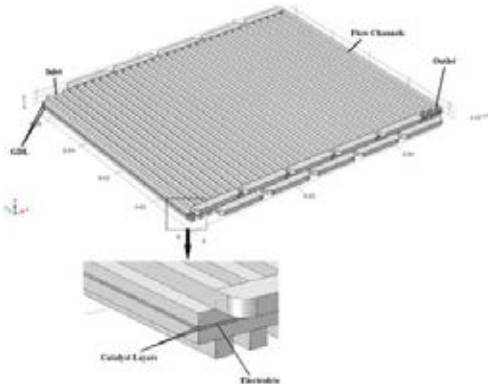


Fig. 1. The domain used in Comsol Multiphysics with triple mixed serpentine flow channel geometry

Table 2. Thermal properties of components used in non-isothermal model

Description	Value	Unit
Thermal conductivity of GDL [20]	1.15	W m^{-1} K^{-1}
Thermal conductivity of membrane [16]	0.95	W m^{-1} K^{-1}
Thermal conductivity of hydrogen [23]	0.204	W m^{-1} K^{-1}
Thermal conductivity of air [23]	0.03	W m^{-1} K^{-1}
Specific heat capacity of hydrogen [23]	14400	J kg^{-1} K^{-1}
Specific heat capacity of air [23]	1010	J kg^{-1} K^{-1}
Specific heat capacity of GDL [23]	1050	J kg^{-1} K^{-1}
Specific heat capacity of membrane [16]	1650	J kg^{-1} K^{-1}

Assumptions

- Steady state
- Laminar flow
- All reactants and products are in gaseous phase
- All gases and water obey the ideal gas law
- No crossover of gases and water through the membrane
- The physical properties of the components are constant
- GDL is composed of isotropic and homogeneous porous materials.

Governing Equations

Conservation of mass, momentum and charge balances around the components of the system are defined in the previous article Caglayan et al. [1]. In the non-isothermal model, conservation of energy is considered as well as the conservation of mass, momentum and charge equations used in the isothermal model. The general form of conservation of energy is given in Eq. 2.1:

$$\nabla.\left(\rho C_p u T\right) = \nabla(k^{eff}\nabla T) + S_T \quad (2.1)$$

$$\rho C_p = \varepsilon\left(\rho C_p\right)_f + (1-\varepsilon).\left(\rho C_p\right)_s \quad (2.2)$$

where T is temperature (K), C_p is the specific heat (J kg^{-1} K^{-1}), k^{eff} is the effective thermal conductivity (W m^{-1} K^{-1}) and S_T is the source term in the energy balance varying for each component within the model domain. For the fluid phase and solid matrix subscripts f and s are used, respectively. There is no source term in the flow channels and GDL. The source term for the catalyst layers is given below;

$$S_T = i_c\left(\eta + T\frac{dU_o}{dT}\right) + \frac{I^2}{\kappa^{eff}} \quad (2.3)$$

Source term for the membrane is given below;

$$S_T = \frac{I^2}{\kappa^{eff}} \quad (2.4)$$

$$\eta = \emptyset_s - \emptyset_e - U_o \quad (2.5)$$

Where η is the overpotential (V), U_o is the thermodynamic equilibrium potential (V) which depends on temperature as given below;

For anode; $U_o = 0$ (2.6)

For cathode; $U_o = 1.23 - 9.10^{-4}(T - 298.15)$ (2.7)

Boundary Conditions

- Continuity at all boundaries
- No slip for all channel walls
- Suppress backpressure
- Constrain outer edges set to zero for both inlet and outlet
- Thermal insulation for all walls
- Bipolar plates on the both side of the cell set to electric ground and cell operation potential

3. Results and Discussion

Fig. 2 shows the temperature variation within the single cell having the inlet feed temperature of 165 ºC according to the model results. The temperature difference at 0.6 V and 0.45 V of operation voltage is calculated to be 0.18 and 0.31 ºC, respectively. The average current density at the operation voltage of 0.6 V is determined as 0.224 A cm^{-2}, whereas that value increases to 0.313 A cm^{-2} when the operation temperature is taken as 0.45 V. In the study published by Samsun et al. [24], the fuel cell attains 160 ºC, when the anode and cathode feed temperatures are taken as 151 ºC and 160 ºC, respectively. According to the model developed by Kvesic et al. [14], the temperature gradient within a cell having an active area of 200 cm^2 does not exceed 10 ºC. At an average current density of 0.3 A cm^{-2} the temperature difference is approximately 2 ºC; on the other hand, this value increases to 5 ºC at 0.6 A cm^{-2}. In their study Lüke et al. [25], for a 200 cm^2 HT-PEMFC modeled with cooling the temperature gradient determined as 3 ºC at 0.4 A cm^{-2}. Considering the active area being 25 cm^2, and heat evolving within the system due to the exothermic reaction, the results agree well with the findings available in the literature.

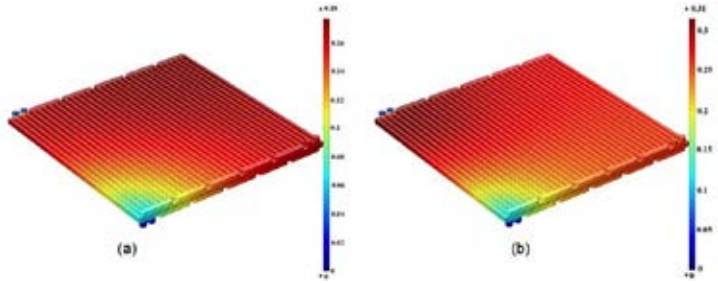


Fig. 2. Temperature distribution with inlet feed temperature of 165 ºC and (a) 0.6 V and (b) 0.45 V

According to Fig. 3, which represents temperature isocontours at 0.6 V and 0.45 V, the maximum value of the temperature is attained around outlets. As it is expected, temperature gradient is proportional to the current density. The difference in the temperature increases with increasing average current density. It is caused by the generation term in the conservation of energy, since the reaction taking place in the cell is exothermic. The temperature increase around the inlets of anode and cathode compartments can be observed by having a look at Fig. 3. The increase in the temperature around cathode inlet is more dominant compared to anode inlet. This may be caused by the reaction kinetics being highly dependent on the concentration of oxygen rather than hydrogen. Since concentration of oxygen is highest at the inlet and it decreases along the channel, the reaction is fastest around the cathode inlet. Because of the reaction is being the fastest around cathode inlet, the temperature increase around that part is higher due to the exothermic reaction.

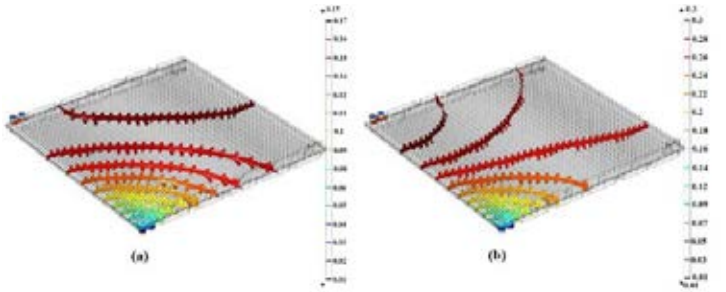


Fig. 3. Temperature isocontours at different operation voltages (a) 0.6 V (b) 0.45 V at 165 ºC

4. Conclusions

A non-isothermal mathematical model of HT-PEMFC is developed in order to check the validity of isothermal operation assumption. The non-isothermal model is simulated for the operation voltages of 0.6 V and 0.45 V, that have average current density as 0.224 A cm^{-2} and 0.313 A cm^{-2}, respectively. The isothermal model results give a better performance compared to the non-isothermal case. According to the model results the temperature increase within the cell is found to be less than 1 ^{o}C, which is reasonable taking into account the single cell having an approximate power output of 5 W at the operation voltage of 0.6 V. The change in the temperature is determined as 0.18 ^{o}C and 0.31 ^{o}C at 0.6 V and 0.45 V, respectively. Basing on these results, it can be said that isothermal operation assumption valid for this cell.

Acknowledgement

This study is supported by The Scientific and Technological Research Council of Turkey (TUBITAK) 1001 (Grant number: 214M301) Project. We acknowledge Assoc. Prof. Dr. Serkan KINCAL for his contribution on Comsol Multiphysics, and also Huseyin DEVRIM, Tek-Sis, and Danish Power Systems for the design parameters.

Nomenclature

Cp	Specific heat (J kg^{-1} K^{-1})
I	Current (A)
i	Transfer current density (A m^{-2})
k	Thermal conductivity (W m^{-1} K^{-1})
S_T	Source term (J m^{-2} s^{-1})
T	Temperature (K)
u	Velocity (m s^{-1})
U_o	Thermodynamic equilibrium potential (V)

Subscripts and superscripts

a	Anode
c	Cathode
e	Electrolyte phase
eff	Effective
f	Fluid phase
s	Solid phase

Greek Letters

ε	Porosity
Ø	Phase potential (V)
μ	Dynamic viscosity (kg m^{-1} s^{-1})
η	Overpotential (V)
ρ	Fluid density(kg m^{-3})

Acronyms

1D	One-dimensional
2D	Two-dimensional
3D	Three-dimensional
GDL	Gas diffusion layer
HT-PEMFC	High Temperature PEM fuel cell
I	Isothermal
MEA	Membrane electrode assembly
NI	Non-isothermal
PBI	Polybenzimidazole
PEMFC	Polymer electrolyte membrane fuel cell

References

1. Caglayan DG, Sezgin B, Devrim Y, Eroglu I. Three-dimensional modeling of a high temperature polymer electrolyte membrane fuel cell at different operation temperatures. Int J Hydrogen Energy 2016;41:10060–70.

2. Cheddie D, Munroe N. Mathematical model of a PEMFC using a PBI membrane. Energy Convers Manag 2006;47:1490–504.
3. Cheddie D, Munroe N. Parametric model of an intermediate temperature PEMFC. J Power Sources 2006;156:414–23.
4. Cheddie DF, Munroe NDH. Three dimensional modeling of high temperature PEM fuel cells. J Power Sources 2006;160:215–23.
5. Hu J, Zhang H, Hu J, Zhai Y, Yi B. Two dimensional modeling study of PBI/H3PO4 high temperature PEMFCs based on electrochemical methods. J Power Sources 2006;160:1026–34.
6. Peng J, Lee SJ. Numerical simulation of proton exchange membrane fuel cells at high operating temperature. J Power Sources 2006;162:1182–91.
7. Cheddie DF, Munroe NDH. A two-phase model of an intermediate temperature PEM fuel cell. Int J Hydrogen Energy 2007;32:832–41.
8. Scott K, Pilditch S, Mamlouk M. Modelling and experimental validation of a high temperature polymer electrolyte fuel cell. J Appl Electrochem 2007;37:1245–59.
9. Ubong EU, Shi Z, Wang X. Three-Dimensional Modeling and Experimental Study of a High Temperature PBI-Based PEM Fuel Cell. J Electrochem Soc 2009;156:B1276.
10. Lobato J, Cañizares P, Rodrigo MA, Pinar FJ, Mena E, Úbeda D. Three-dimensional model of a 50 cm2 high temperature PEM fuel cell. Study of the flow channel geometry influence. Int J Hydrogen Energy 2010;35:5510–20.
11. Siegel C, Bandlamudi G, Heinzel A. Systematic characterization of a PBI/H3PO4 sol-gel membrane - Modeling and simulation. J Power Sources 2011;196:2735–49.
12. Harikishan Reddy E, Jayanti S. Thermal management strategies for a 1 kWe stack of a high temperature proton exchange membrane fuel cell. Appl Therm Eng 2012;48:465–75.
13. Kvesić M, Reimer U, Froning D, Lüke L, Lehnert W, Stolten D. 3D modeling of a 200 cm2 HT-PEFC short stack. Int J Hydrogen Energy 2012;37:2430–9.
14. Kvesić M, Reimer U, Froning D, Lüke L, Lehnert W, Stolten D. 3D modeling of an HT-PEFC stack using reformate gas. Int J Hydrogen Energy 2012;37:12438–50.
15. Su a., Ferng YM, Hou J, Yu TL. Experimental and numerical investigations of the effects of PBI loading and operating temperature on a high-temperature PEMFC. Int J Hydrogen Energy 2012;37:7710–8.
16. Chippar P, Ju H. Numerical modeling and investigation of gas crossover effects in high temperature proton exchange membrane (PEM) fuel cells. Int J Hydrogen Energy 2013;38:7704–14.
17. Bezmalinović D, Strahl S, Roda V, Husar A. Water transport study in a high temperature proton exchange membrane fuel cell stack. Int J Hydrogen Energy 2014;39:10627–40.
18. Lang S, Kazdal TJ, Kühl F, Hampe MJ. Experimental investigation and numerical simulation of the electrolyte loss in a HT-PEM fuel cell. Int J Hydrogen Energy 2015;40:1163–72.
19. Kazdal TJ, Lang S, Kühl F, Hampe MJ. Modelling of the vapour-liquid equilibrium of water and the in-situ concentration of H3PO4 in a high temperature proton exchange membrane fuel cell. J Power Sources 2014;249:446–56.
20. Elden G, Çelik M, Genç G, Yapıcı H. The effects of temperature on transport phenomena in phosphoric acid doped polybenzimidazole polymer electrolyte membrane fuel cell. Energy 2016;103:772–83.
21. Sezgin B, Caglayan DG, Devrim Y, Steenberg T, Eroglu I. Modeling and sensitivity analysis of high temperature PEM fuel cells by using Comsol Multiphysics. Int J Hydrogen Energy 2016;41:10001–9.
22. Caglayan, DG. (2016). Investigation of temperature profile in high temperature PEM fuel cell (Master's Thesis). Middle East Technical University, Ankara, Turkey.
23. Wu H, Berg P, Li X. Non-isothermal transient modeling of water transport in PEM fuel cells. J Power Sources 2007;165:232–43.
24. Samsun RC, Pasel J, Janßen H, Lehnert W, Peters R, Stolten D. Design and test of a 5 kWe high-temperature polymer electrolyte fuel cell system operated with diesel and kerosene. Appl Energy 2014;114:238–49.
25. Lüke L, Janßen H, Kvesić M, Lehnert W, Stolten D. Performance analysis of HT-PEFC stacks. Int J Hydrogen Energy 2012;37:9171–81.

ORAL PROCEEDINGS

Palladium Based Electrocatalysts for Ethylene Glycol Fuel Cells

Ozlem Gokdogan Sahin, Hilal Demir Kıvrak
Department of Chemical Engineering, Faculty of Engineering, Selcuk University, Konya, Turkey
Department of Chemical Engineering, Faculty of Engineering, Yüzüncü Yıl University, Van, Turkey
Email: ozlem@selcuk.edu.tr, hilalkivrak@gmail.com

Abstract
Carbon nanotubes (CNTs) supported palladium based core-shell and alloy catalysts were synthesized by $NaBH_4$ reduction method. The resulting catalysts exhibited high electrical catalytic activity for ethylene glycol (EG) electro-oxidation in alkaline solution. The electrocatalytic activity of the palladium-based core-shell and alloy bimetallic catalysts toward the EG electro-oxidation reaction has been investigated by cyclic voltammetry (CV), chronoamperometry (CA) and electrochemical impedance spectroscopy (EIS) techniques. The results show that Mn-Pd/CNTs core-shell catalyst has better electrocatalytic properties for EG electro-oxidation reaction compared to Zn-Pd/CNTs core–shell, Mn-Pd/CNTs alloy and Zn-Pd/CNTs alloy catalysts. Moreover, the electro-oxidation of EG on Mn-Pd/CNTs (core–shell) was observed at lower onset and peak potentials, higher current and faster kinetics (lower impedance) than at the other three catalysts. Moreover, Mn-Pd/CNTs (core–shell) increases the electrocatalytic activity and stability of the electrode.

Keywords: Palladium based electrocatalysts; ethylene glycol electro-oxidation; fuel cells.

1. Introduction

Direct alcohol fuel cells (DAFCs) have been widely investigated due to their high potential in green energy technologies [1]. DAFCs are suitable fuel cell systems that use a wide range of liquid fuels such as methanol, ethanol, and ethylene glycol (EG) [2]. Among the alcohols used in DAFCs, EG is noticeable due to its many advantages such as lower toxicity, higher energy density and reaction activity [3]. EG is obtained from oxidation of ethylene, thus it can be produced in renewable and environmentally friendly ways [4]. Pt is the most active catalyst for alcohol oxidation. However, easy poisoning by intermediate products and high cost of Pt would restrict its application in DAFCs. Palladium is considered as a suitable electrocatalyst with remarkable electrocatalytic activity toward some small organic molecules. The use of alkaline medium also eliminates the problem of the catalysts poisoning by carbon monoxide (CO) and improves the alcohol electro-oxidation. The Pd catalytic activity may be increased by the addition of metal or metal oxides. Thus, Pd-based catalysts seem to be promising catalysts in DAFCs [5]. In order to improve the catalytic activity, the core-shell structures of catalysts could be synthesized [6]. Core-shell nanoparticles with thin noble metal shells are of great importance in chemical catalysis [7]. Moreover, the catalyst support material also plays a great role on the catalyst performance. Carbon materials with high surface area and good crystallinity provide a high dispersion of catalyst particles and facilitate electron transfer, resulting in better device performance. Studies have shown that carbon nanotubes increase the electrocatalytic properties of several metal catalysts.

In this study, carbon-supported Mn-Pd/CNTs and Zn-Pd/CNTs core-shell and alloy bimetallic catalysts were synthesized by $NaBH_4$ reduction method. Both the structural and electrochemical characterization of the catalysts has been examined. Electrooxidation of ethylene glycol in alkaline media has been performed by cyclic voltammetry, chronoamperometry and impedance spectroscopy.

2. Experimental Study

All reagents used were of analytical grade provided by Merck and used without further purification. For each experiment, a freshly prepared electrode and solution was used. Catalysts were synthesized by $NaBH_4$ reduction method. Carbon supported palladium based core-shell and alloy catalysts were synthesized by using $NaBH_4$ as reducing agent. Necessary amount of palladium, manganese and zinc precursor were dispersed in water and stirred for 30 min. A freshly prepared solution of 20 mg $NaBH_4$ in 5.00 mL water was added dropwise into the above solution under vigorous stirring. After 30 min, 20 mg MWCNTs was added into the above solution. After stirring for an additional for 8 h, the black solid was separated by centrifuging at a speed of 3600 rpm, washed with deionized water for several cycles, and then dried overnight in an oven at 70 °C. For comparison, catalysts were also obtained directly by co-reducing the H_2PdCl_4 and $MnCl_2$ or $ZnCl_2$ as precursors in a carbon nanotube suspension using the dropwise addition of $NaBH_4$ at room temperature with stirring.

Before modification, the electrode surfaces were polished with 0.3 and 0.05 mm alumina slurry and then rinsed thoroughly with water. Then, the polished electrode was ultrasonicated in ultrapure water and ethanol for 5 min, respectively. For the electrode preparation, 5 mg of catalyst was added into 1 mL of 0.5% Nafion solution to obtain catalyst mixture. Then, 3 mL of the mixture was dripped onto the cleaned glassy carbon electrode. Finally, the prepared electrode was dried at room temperature to remove the solvent. Electrochemical measurements were carried out by CHI model 6043d electrochemical analyzer (CH Instruments) in a conventional three-electrode cell. A saturated Ag/AgCl electrode was used as the reference and a Pt wire as the counter electrode. Electrochemical experiments were performed in 1.0 M KOH electrolyte. Electrolytes were deaerated by high-purity nitrogen. All electrochemical experiments were performed at room temperature.

3. Results and Discussion

The electrocatalytic performance of the palladium based core-shell and alloy catalysts towards ethylene glycol (EG) oxidation were investigated by cyclic voltammetry in 1.0 M KOH + 1.0 M EG solution. As shown in Fig. 1, two well-defined anodic peaks appeared in the forward scan and the backward scan, relating to the electrooxidation of EG and the intermediate carbonaceous species, respectively. It could be seen that Mn-Pd/CNTs core-shell catalyst offered the highest peak current in the forward scan (217.7 μA) compared with Zn-Pd/CNTs core-shell catalyst (114.7 μA), Mn-Pd/CNTs alloy catalyst (66.7 μA), and Zn-Pd/CNTs (61.9 μA) alloy catalyst, revealing Mn-Pd/CNTs core-shell catalyst had the highest mass activity. Moreover, the onset potential with Mn-Pd/CNTs core-shell catalyst was more negative than the other three catalysts, indicating ethylene glycol was more easily oxidized on the Mn-Pd/CNTs core-shell catalyst. Meanwhile, the ratio of the forward anodic peak current (I_f) to the backward anodic peak current (I_b) can be used to evaluate the catalyst tolerance to the intermediate carbonaceous species accumulated on the catalyst surface. The I_f /I_b ratio of the Mn-Pd/CNTs core-shell catalyst was 8.54, higher than that of Zn-Pd/CNTs core-shell catalyst (5.52), Mn-Pd/CNTs alloy catalyst (5.23) and Zn-Pd/CNTs alloy catalyst (5.14), suggesting a much better poison tolerance to carbonaceous intermediates of the Mn-Pd/CNTs core-shell catalyst and thus EG could be oxidized more efficiently (Table 1).

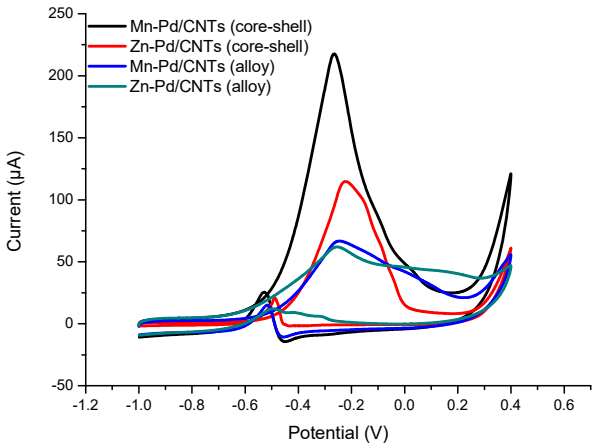


Fig. 1. CVs of Mn-Pd/CNTs (core-shell) and Zn-Pd/CNTs (core-shell), Mn-Pd/CNTs (alloy) and Zn-Pd/CNTs (alloy) modified GCE in 1.0 M KOH+1.0 M EG (50 mV s-1)

Table 1. Comparative electrocatalytic properties of the MPd nanocatalysts towards ethylene glycol oxidation reaction in 1.0 M EG/1.0 M KOH.

Electrocatalyst	E_{onset} (V)	E_p (V)	I_f/I_b
Mn-Pd/CNTs (core-shell)	-0.6	-0.265	8.54
Zn-Pd/CNTs (core-shell)	-0.4	-0.221	5.52
Mn-Pd/CNTs (alloy)	-0.5	-0.225	5.23
Zn-Pd/CNTs (alloy)	-055	-0.254	5.14

The stability of the catalysts towards ethylene glycol electro-oxidation was also studied by chronoamperometry at -0.35 V in 1.0 M KOH + 1.0 M EG (Fig.2). The chronoamperometric curves exhibit a sharp decrease at the initial period due to the accumulation of intermediate species at the surface of catalysts. However, Mn-Pd/CNTs catalyst shows a higher initial current and a higher current at the longer time. This confirms that Mn-Pd/CNTs core-shell catalyst has higher electrocatalytic activity, higher resistance to CO, and better long term stability compared to the other three catalysts. Thus, EIS has been used to examine the electrochemical behavior of the catalysts for further investigation.

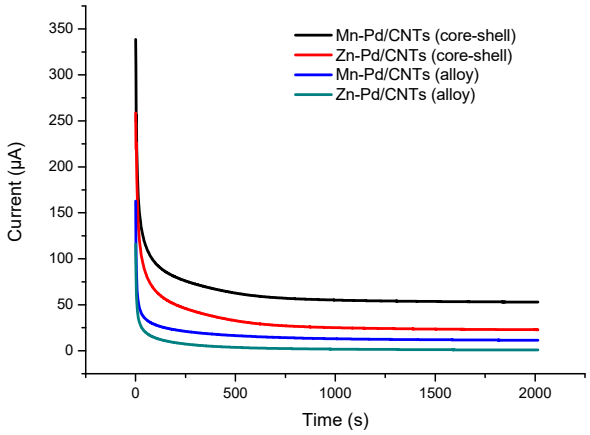


Fig. 2. Chronoamperometric curves at -0.35 V of EG electro-oxidation in 1.0 M KOH + 1.0 M EG on Mn-Pd/CNTs (core-shell) and Zn-Pd/CNTs (core-shell), Mn-Pd/CNTs (alloy) and Zn-Pd/CNTs (alloy) modified GCE

Fig. 3. displays the Nyquist plots of EIS for Mn-Pd/CNTs (core-shell) and Zn-Pd/CNTs (core-shell), Mn-Pd/CNTs (alloy) and Zn-Pd/CNTs (alloy), respectively. All electrodes exhibit semicircle that has been considered as a measure of electron transfer resistance. The semicircle diameter of Mn-Pd/CNTs (core-shell) is much smaller than Zn-Pd/CNTs (core-shell), Mn-Pd/CNTs (alloy) and Zn-Pd/CNTs (alloy) catalysts, indicating that Mn-Pd/CNTs (core-shell) has lower charge transfer resistance and faster reaction rate for ethylene glycol electro-oxidation reaction.

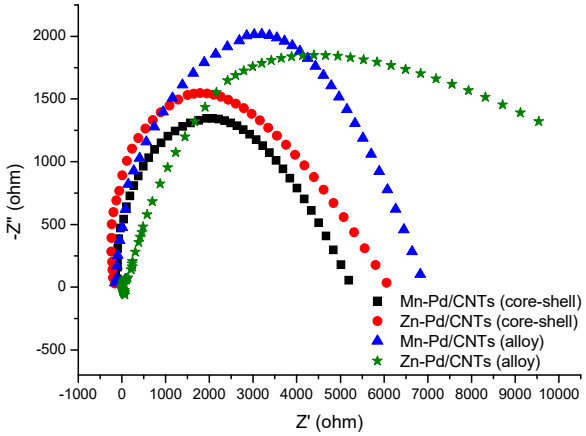


Fig. 3. Nyquist plots of GCE-modified Mn-Pd/CNTs (core-shell) and Zn-Pd/CNTs (core-shell), Mn-Pd/CNTs (alloy) and Zn-Pd/CNTs (alloy) at -0.35 V measured in 1.0 M KOH + 1.0 M EG.

Electrochemical results indicated that the catalytic activity of the catalyst followed the order Mn-Pd/CNTs (core-shell) > Zn@Pd/CNTs (core-shell) > MnPd/CNTs (alloy) > ZnPd/CNTs (alloy). These results, combined with the cyclic voltammetry (CV) tests above, confirmed the high electrocatalytic stability and activity of Mn-Pd/CNTs for electro-oxidation of EG. These results also indicated that the core shell structure provides OH_{ads}, which sped up the oxidation of the adsorbed alcohols.

4. Conclusions

In this study, different carbon supported Pd-based catalysts for ethylene glycol electro-oxidation were synthesized. The electrochemical evaluation via CV, CA and EIS showed that Mn-Pd/CNT core-shell catalyst has higher catalytic activity towards ethylene glycol electro-oxidation in alkaline media with higher current and lower onset potential in comparison with the other three synthesized catalysts.

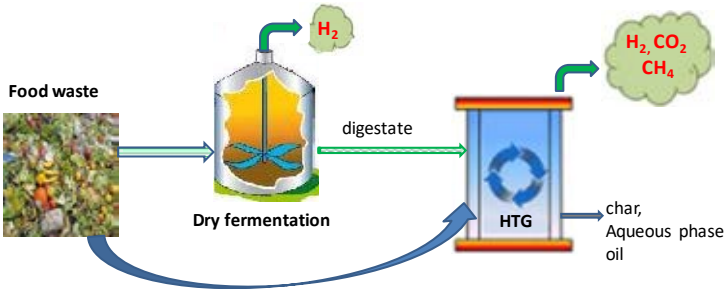
References

1. Nacef, M., Affoune A.M. (2011). Comparison between direct small molecular weight alcohols fuel cells and hydrogen fuel cell's parameters at low and high temperature, thermodynamic study. Int J Hydrogen Energy;36, pp. 4208-4219.
2. Antolini, E., Gonzalez, E.R. (2010). Alkaline direct alcohol fuel cells. J Power Sources, 195, pp. 3431-3450.
3. Matsuoka, K., Inaba, M., Iriyama, Y., Abe, T., Ogumi, Z., Matsuoka, M. (2002). Anodic Oxidation of Polyhydric Alcohols on a Pt Electrode in Alkaline Solution Fuel Cells, 2, pp.35–39.
4. Serov A. and Kwak C. (2010). Recent achievements in direct ethylene glycol fuel cells (DEGFC), Appl. Catal. B Environ., 97, pp. 1–12.
5. Bianchini, C.; Shen, P.K. (2009). Palladium-based electrocatalysts for alcohol oxidation in half cells and in direct alcohol fuel cells. Chem. Rev., 109, pp.4183–4206.
6. Long, N.V., Duy Hien, T., Asaka, T., Ohtaki, M., Nogami, M., (2011). Synthesis and characterization of Pt–Pd alloy and core-shell bimetallic nanoparticles for direct methanol fuel cells (DMFCs): Enhanced electrocatalytic properties of wellshaped core-shell morphologies and nanostructures. Int. J. Hydrogen Energy, 36, pp. 8478–8491.
7. Zhou W, Lee JY. (2007). Highly active core-shell Au@Pd catalyst for formic acid electrooxidation. Electrochem Commun; 9: pp.1725–9.

Hydrogen production from municipal solid wastes by hydrothermal gasification

Gözde Duman[1], Jale Yanık [1,2*], Koray Akarsu[2], Tugba Keskin Gündoğdu[3], Kübra Arslan[2], Haris Nalakth Abubackar[4], Nuri Azbar[2,3]
[1]Ege University, Faculty of Science, Chemistry Department, 35100, İzmir, Türkiye
[2]Ege University, Center for Environmental Studies, 35100, İzmir, Türkiye
[3]Ege University, Engineering Faculty, Bioengineering Department, 35100, İzmir, Türkiye
[4] University La Coruña, Faculty of Sciences and Center for Advanced Scientific Research (CICA), La Coruña, Spain
Email: jale.yanik@ege.edu.tr

Abstract
Hydrogen is an important energy carrier that will have an important place today and in the future. The importance of hydrogen production increases when it is produced by the processes with low energy requirements or from renewable energy sources, such as biomass. Hydrogen production from biomass is carried out by thermo-chemical and biochemical routes. One of the thermo-chemical methods is the gasification of biomass in supercritical water. For wet biomass containing large amounts of water up to 90%, hydrothermal gasification (HTG) appears as a useful technology, besides anaerobic digestion. HTG produces the H_2 and CO_2 at temperatures of 400 °C or higher. Because of the high water excess, up to half of the H_2 formed originates from water, the conversion of CO with water into H_2 and CO_2. In this study, HTG of fruit and vegetable wastes and of digestate from dry anaerobic digestion of fruit and vegetable wastes was carried out at different temperatures. The effect of temperature and catalyst on efficiency of hydrogen production was investigated. H_2 yields were increased extremely by increasing of temperature and using catalyst. In addition, the temperature led to also increase in CH_4 production. For food wastes, the H_2 yields were 62 mmol/L waste and 146 mmol/L waste for 400 and 450 °C, respectively. For digestate, the H_2 yields were found to be 289 mmol/L in absence catalyst. The use of all catalysts tested (trona, seaweed ash, K_2CO_3) significantly increased H_2 production for both food waste and digestate. K_2CO_3 exhibited the highest catalytic activity, yielding 415 mmol H_2/L for food waste and 595 mmol H_2/L for digestate. The results showed that HTG is a promising process for production of hydrogen from biomass in a biorefinery concept.



Kewwords: Hydrothermal gasification; hydrogen production; biomass.

1. Introduction

In recent years, renewable energy sources have gained increasing attention due to social, economical and environmental concerns such as increasing world energy demand, climate change via increased greenhouse gas (GHG) emissions, overwhelming usage of fossil fuels and uncertain energy security [1]. Hydrogen, which is a very versatile energy carrier, can be one of the most profound solutions for these problems. Most of hydrogen is currently used in chemical processes such as ammonia and methanol manufacturing, removing sulfur from gasoline, hydrocracking of heavy hydrocarbons into gasoline. The demand for hydrogen is expected to increase over the next ten years, for both traditional usage and new areas mainly Fisher Tropsch industry and fuel cell application [2]. Even though hydrogen mainly produces from fossil fuels, biomass is an alternative source for green hydrogen production.

Biomass can be converted to hydrogen by biochemical and thermochemical processes. Among thermochemical processes applied for biomass conversion, hydrothermal gasification (HTG) is an attractive process and is a research subject of high interest [3]. Different from conventional gasification processes for H_2 production, the energy-intensive drying of wet biomass can be avoided as water is needed in HTG. Hydrothermal gasification is one of important conversion techniques, which can enhance the transformation of biomass to gas products at supercritical

conditions. Above the critical point, i.e. at temperature and pressure above 374.1 °C and 22.1 MPa, water exhibited unique properties such as low viscosity, high diffusivity and low dielectric constant. Due to lower the dielectric constant and the number of hydrogen bonds than those of ambient water, supercritical water acts as organic solvent which is effective in dissolving many organic compounds and gases and thus providing the homogeneity in reaction media [4]. Moreover, water does not only behave like solvent, it is also a reactant producing H_2 in HTG conditions. Although HTG of biomass is a complex process, a simple reaction can represent the overall chemical conversion;

$$CH_xO_y + (2\text{-}y)H_2O \rightarrow CO_2 + (2\text{-}y+x/2)H_2$$

In recent years, profound investigations have been conducted on HTG of biomass under supercritical conditions. In these studies, different types of biomass such as wood sawdust, agricultural residue, animal, waste, food industry waste, sewage sludge, micro and macro algae, wastewater, paper waste sludge have been investigated [5]. There are two approaches for HTG of biomass in terms of operating temperature; low temperature HTG (between 374 °C -550 °C) and high temperature HTG (between 550°C -700°C) [6]. Due to high activation energy of gasification reactions producing H_2, catalysis is necessary for future development of low temperature HTG technology [7]. In recent years, various catalysts have been evaluated to increase H_2 yield with high gasification efficiency. Both homogenous alkali catalysts such as K_2CO_3, NaOH, KOH, $CaCO_3$, Na_2CO_3, $KHCO_3$ and heterogeneous transition metal catalysts mainly as Ni, Pd, Co, Mo and Zn [8]. The use of alkali salts as catalyst provides high H_2 yields from water gas shift reaction and increases gasification efficiency. Moreover, in presence of alkali catalysts, tar/char formation is suppressed by producing simpler intermediates which could be easily converted to H_2 [9]. The mechanism of water-gas shift reaction during HTG by using K_2CO_3 was also purposed by Sinag et al. [10].

The objective of this work is to examine hydrothermal gasification of fruit and vegetable wastes (food waste) and its digestate from dry anaerobic digestion process with and without catalyst. To the best knowledge, no work has been reported on comparison of HTG results of the waste and its digestate.

2. Experimental Study

In this study, hydrothermal gasification of fruit and vegetable wastes (food waste) and its digestate which produces from dry anaerobic digestion process was carried out at different temperatures (400 °C and 450 °C). The food wastes were collected from main hall of Izmir Municipality. The properties of food waste and its digestate were given in Table 1. In order to increase H_2 content in product gas, trona ($Na_2CO_3.NaCO_3.2H_2O$), K_2CO_3 and seaweed ash were used as catalyst. Seaweed was collected from Sinop coast on the Blacksea, Turkey (June, 2010), it was a mixture of different algae species. The seaweed contains mainly Ca (15.6%), Mg (9.2%), Na (7.8%) and K (7.1%). Seaweed ash were obtained by burning seaweed at 800 °C for 4 hours. Trona, which is a natural mineral, was supplied by Eti Soda Inc., Turkey.

Table 1. Properties of food waste and digestate

	Solid content, % wt.	Properties of Solid		
		Volatile matter, % wt.	Ash , % wt.	HHV, MJ/kg
Food waste	11.4	61.1	5.8	19.0
Digestate	12.4	67.0	16.6	17.9

Hydrothermal gasification experiments were carried out in autoclave reactor (Buchi Glassuster Limbo model). The reactor had a volume capacity of 450 mL designed to a maximum temperature and pressure of 500 °C (internal temperature) and 600 MPa, respectively. Buchu btc model PID controller was used to ensure accurate temperatures and efficient heating cooling of the reactor and jacket. The reactor was equipped with a pressure release valve, safety valve, pressure gauge and an external magnetic stirrer. Figure 1 shows the experimental set up of hydrothermal gasification.

After loading 150 g of the food waste/digestate, the reactor was sealed by using torque. In case of catalytic studies, adequate amount of catalyst was added and mixed in the reactor. N_2 line was connected to the reactor and flushed with nitrogen to remove the air inside the reactor. Then, reactor was pressurized with N_2 to 10 bar as initial pressure. The reactor was heated to 350 °C with a heating rate 10° C/min, then heated to desired temperature at a rate of 5 °C/min. The reactor was held at this temperature for 1 hour.



Figure 1. Hydrothermal gasification set-up

During the reaction, the pressure was observed between 400-320 bar and 460-490 bar at temperatures of 400 °C and 450 ° C, respectively. Once the reaction time was completed, the reactor was rapidly cooled to room temperature by integrated water cooling system with maximum capacity. Gas product was collected from the vent line using a Tedlar bag and measured by using water replacement method. The solid residue (char) was separated from reactor contents by filtration under vacuum; dried at 105 °C and then weighted. The liquid product consisted of two phases (aqueous and oil phases). The aqueous phase and oil were separately weighted and then stored at 4 °C in sealed bottles for further analysis. The oil and char yields were calculated based on solid content of food waste and digestate.

The product gas analysis was carried out by Agilent 7890A gas chromatograph which has five valves and three detectors. The hydrocarbon gases were analyzed in FID (Flame ionization dedector) channel. The first TCD (Thermal conductivity dedector) channel was configured to detect permanent gases, which include CO_2, CO and N_2. The second TCD Channel was dedicated to analyze hydrogen only.

3. Results and Discussion

3.1 Hydrothermal gasification of food waste

In order to investigate the effect of temperature on the yield of gas products, HTG of food waste was conducted at 400 °C and 450 °C in presence and absence of trona. In case of catalytic run, trona was added to 1 wt. % of solid content of food waste.

The gas products composed of hydrogen, carbon dioxide and methane as major components and C_2-C_5 hydrocarbons such as ethane, propane and butane as minors (Fig.2). Almost no CO formation was observed in gas products. In absence of catalyst, the amounts of H_2, CH_4 and hydrocarbon gases produced at 400 °C were lower than that at 450 °C while CO_2 amount was nearly same. H_2 amount was increased by 133% (from 62 mmol/L to 146 mmol/L) by the increasing of the temperature from 400 °C to 450 °C. As well known, the reaction temperature is the most important parameter affecting HTG. High temperature facilitates the formation of low molecular weight compounds by breaking the ring by facilitating free radical reactions which increase the gas yield [11]. For both temperatures, a remarkable increase in H_2 production was observed by using trona. It should be also noted that in experiments at 400 °C H_2 amount was higher than that of CH_4, while HTG at 450 °C produced more CH_4 than H_2. It is clearly seen that both temperature and catalyst were effective for H_2 gas production. In this group experiments, no oily product was obtained whereas char formation was observed. The char amounts obtained at 400 °C decreased from 32.2 % to 24.9% by using trona, whereas the char amounts from HTG at 450 °C were similar in presence and absence of catalyst.

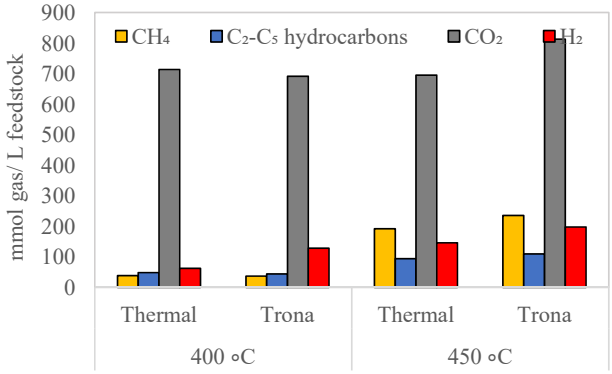


Figure 2. Effect of temperature on gas composition from HTG of food waste

In order to investigate the effect of catalyst amount on gas composition, HTG of food waste was conducted at 450 °C by using of different amount of trona (Fig. 3). The catalyst amount was calculated based on solid content of food waste. The high catalyst loading yielded more production of CO_2, H_2, CH_4 and C_2-C_5 hydrocarbons. As the amount of catalyst increased from 1% to 5 %, H_2 yield increased gradually, while further increase has slightly effect on both H_2 and total gas yield. The highest H_2 amount was found to be 360 mmol/L in presence of 10 % catalyst; which was only %10 more than H_2 amount obtained by adding 5% catalyst. Although, no oily phase was obtained both thermal run and in presence of 1% trona, higher trona loading than 1% led to formation of oily product. On the other hand, high trona loading decreased the formation of char. The char yields were 5.3 %, 1.6% and 0.6 while oil yields were in the 14.0%, 16.0% and 18.8% for the trona amounts of 2.5%, 5% and 10%, respectively.

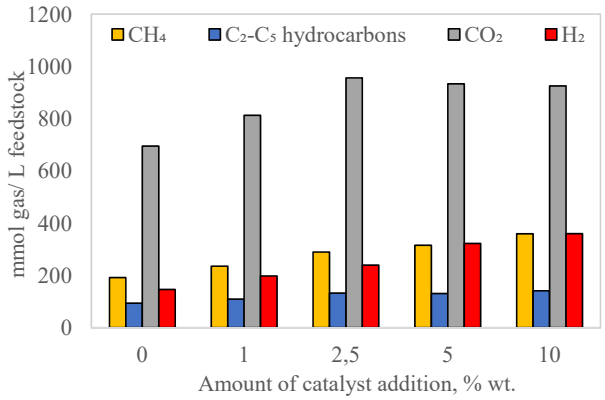


Figure 3. Effect of catalyst amount on gas composition from HTG of food waste

Due to its low cost and its high catalytic activity, alkali salts is considered as a promising catalyst for HTG. For this purpose, different types of catalysts which exhibits alkali properties was used as catalyst. HTG experiments were performed at 450 °C with the addition of 5% catalyst.

The effect of catalyst type on gas composition from HTG of food waste can be seen in Fig. 4. Comparing with thermal HTG, all catalyst used was increased both H_2 and overall gas yield. Among the catalysts, K_2CO_3 gave the highest yield of H_2 (415 mmol/L). Seaweed ash and trona showed similar activity in terms of H_2 production (308 and 322 mmol/L, respectively). The highest CO_2 was observed in presence of trona. The reason might be due to the decomposition of carbonate species in trona to form CO_2. The oil yields were 15.6 % for K_2CO_3 and 21.2 % for seaweed ash.

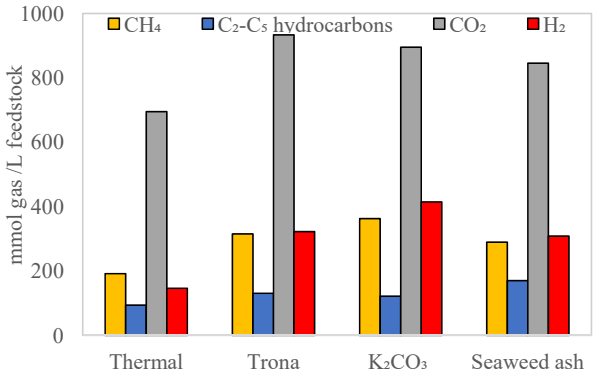


Figure 4. Effect of catalyst type on gas composition from HTG of food waste

3.2 Hydrothermal gasification of digestate

Digestate from anaerobic fermentation of food waste was also gasified under HTG conditions with the addition of 5% catalyst (trona, seaweed ash and K_2CO_3) and in absence of catalyst at 450 °C. Similar to HTG of food waste, the use of catalyst increased H_2 production from HTG of digestate (Table 5). The catalysts used had no marked effect in the formation of C_2-C_5 hydrocarbons. The highest H_2 yield (595 mmol/L) was observed in presence of K_2CO_3. Trona had also good catalytic activity in terms of H_2 production as in the case of food waste. However, compared to thermal run, the rise in H_2 amount was only 20% by using seaweed ash while the amount of other gases did not significantly change. The use of catalyst also decreased the coke formation. Thermal gasification yielded a 16.1% char without oil formation while small amounts of char (1.8-3.3%) were obtained from catalytic gasification. The oil yields for trona, K_2CO_3 and seaweed ash were 13.2%, 12.1% and 13.8%, respectively. The oil yield obtained from digestate was lower than that from food waste at same HTG conditions. Amount of all individual gases obtained from digestate was found to be higher than that from food waste. A possible reason can be explained as follows; macro structural components in food waste are hydrolyzed into smaller compounds during dry fermentation and these small molecules can be easily converted into gas products under HTG conditions.

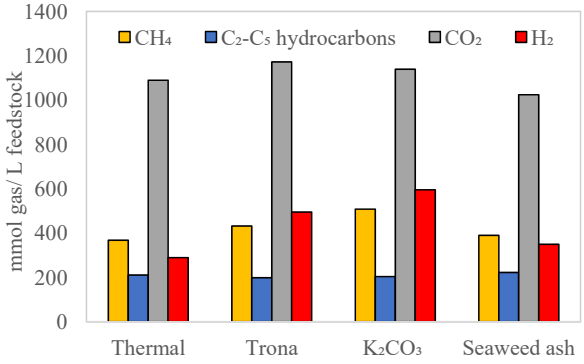


Figure 5. Effect of catalyst type on gas composition from HTG of digestate

4. Conclusion

In this study, hydrothermal gasification of food waste and its digestate was conducted at different conditions. The gases obtained consisted of mainly H_2, CO_2 and CH_4. The K_2CO_3 and trona, as catalyst, have significantly increased the hydrogen yield for both feedstocks. But seaweed ash showed catalytic activity only in hydrothermal gasification of food wastes. For both feedstocks, the catalytic activity of catalysts was in the order K_2CO_3> trona> seaweed ash

in terms of hydrogen production. The H_2 gas yields (289 - 594 mmol H_2/ L feedstock) from digestate was higher than that from food wastes (146 - 415 mmol H_2/ L feedstock). The results showed that hydrothermal gasification is a promising method to produce H_2 from wet biomass in a biorefinery concept.

Acknowledgement

The financial support from TUBITAK under contract 215M314 is gratefully acknowledged.

References

1. Nanda S, Azargohar R, Dalai AK, Kozinski JA. An assessment on the sustainability of lignocellulosic biomass for biorefining. Renew. Sustain. Energy Rev. 2015;50:925–41.
2. Kang K, Azargohar R, Dalai AK, Wang H. Systematic screening and modification of Ni based catalysts for hydrogen generation from supercritical water gasification of lignin. Chem Eng J 2016;283:1019–32.
3. Elliott DC, Biller P, Ross AB, Schmidt AJ, Jones SB.. Hydrothermal liquefaction of biomass: developments from batch to continuous process. Bioresour. Technol. 2015;178:147–56.
4. Savage PE. Organic chemical reactions in supercritical water", Chemical Reviews. 1999; 99:603–621.
5. Louw J, Schwarz CE, Burger AJ. Supercritical water gasification of Eucalyptus grandis and related pyrolysis char: Effect of feedstock composition. Bioresour Technol 2016;216:1030–9.
6. Azadi P, Farnood R. Review of heterogeneous catalysts for sub- and supercritical water gasification of biomass and wastes. Int J Hydrogen Energy 2011;36:9529–41.
7. Guo Y, Wang SZ, Xu DH, Gong YM, Ma HH, Tang XY. Review of catalytic supercritical water gasification for hydrogen production from biomass. Renew Sustain Energy Rev. 2020;14(1):334–43
8. Elliott, D.C., 2008. Catalytic hydrothermal gasification of biomass. Biofuels Bioprod. Biorefin. 2, 254–26.
9. Xu ZR, Zhu W, Gong M, Zhang HW. Direct gasification of dewatered sewage sludge in supercritical water. Part 1: Effects of alkali salts. Int J Hydrogen Energy 2013;38:3963–72.
10. Sinag A, Kruse A, Schwarzkopf V. Key Compounds of the Hydropyrolysis of Glucose in Supercritical Water in the Presence of K_2CO_3. Ind Eng Chem Res. 2003;42, 3516–621.
11. Cao W, Cao C, Guo L, Jin H, Dargusch M, Bernhardt D, Yao X. Hydrogen production from supercritical water gasification of chicken manure", Int J Hydrogen Energy. 2016; 41:22722–31.

ORAL PROCEEDINGS

Thermodynamic assessment of a combined geothermal energy based hydrogen production and liquefaction system

Yunus Emre Yuksel[1], Murat Ozturk[2], Ibrahim Dıncer[3]
[1]Department of Elementary Science Education, Education Faculty, Afyon Kocatepe University, TURKEY
[2]Department of Mechatronics Engineering, Faculty of Technology, Suleyman Demirel University, TURKEY
[3]Faculty of Engineering and Applied Science, University of Ontario Institute of Technology (UOIT), Oshawa, Ont., Canada
Email: yeyuksel@aku.edu.tr, muratozturk@sdu.edu.tr, Ibrahim.Dincer@uoit.ca

Abstract
In this study, the thermodynamic analysis of a combined geothermal energy based hydrogen production and liquefaction process is investigated in detail through energy and exergy approaches. The present hydrogen production and liquefaction process consists of the combined geothermal power system, the PEM electrolyzer, the hydrogen liquefaction and the storage sub-system. The exergy destruction ratios and exergy efficiencies of the entire system and its components are calculated through the balance equations for mass, energy, entropy, energy and exergy, and hence energy and exergy efficiencies. Finally, the effects of some design parameters and system indicators on the hydrogen production and liquefaction system exergy destruction rate and exergy efficiency are investigated for evaluation
.
Keywords: Geothermal; energy; exergy; hydrogen production; liquefaction.

1. Introduction

The geothermal resources are plenty and widely used for power generation or space heating applications [1], clean (effectively no harmful gas emissions, including CO, CO_2, NO_x, SO_x, etc.), safe and reliable (renewable and sustainable), and they can play important role for meeting of world energy requirements [2]. Among the alternative energy technologies, geothermal energy is found in abundance, and a completely free source of energy, and also is mainly used for electricity production, residential or greenhouse heating and cooling processes, industrial drying, distillation and desalination, depending on the geofluid source conditions [3]. The geothermal energy sources are divided into three groups based on the geofluid temperature range such as low temperature (until 90°C), moderate temperature (90°C to 150°C) and high temperature (above 150°C). This temperature ranges are suitable many industrial applications [4].

Zare [5] has compared ORC and Kalina cycles in geothermal power based integrated systems and performed thermodynamic assessment and optimization. Recently, after having higher efficiencies from cogeneration and trigeneration systems compared to conventional ones, a new challenge started to gain more outputs from energy production systems. Suleman et al. [6] have investigated a novel integrated process using geothermal and solar energy as sources. The process outputs are electricity, cooling and drying. The overall energetic and exergetic efficiencies of that process have calculated as 54.7% and 76.4%, respectively. Similarly, another integrated process using solar and geothermal energy for electricity, cooling, heating, hot water and industrial heat is investigated by Al-Ali and Dincer [7]. They have compared the energetic performances of single generation and multigeneration and found as 16.4% and 78%, respectively. On the other hand, their exergetic efficiencies are 26.2% and 36.6%, respectively. In addition, it is suggested that solar collectors should be improved because of having the highest exergy destruction rate.

There are different papers in the literature associated with thermodynamic assessment of integrated systems based on geothermal resources and also for hydrogen generation. In this paper, by using ORC and PEM electrolyzer, power and hydrogen generations are targeted, respectively. Also, the effects of design parameters on the process performance are investigated.

2. System description

The integrated system investigated in this study consists of mainly four subsystems, such as i-) double flash geothermal process, ii-) ORC, iii-) PEM electrolyzer, and iv-) hydrogen liquefaction process. The double flash geothermal process and ORC are used in the integrated system to produce heat and power for PEM electrolyzer. The ORC process runs when the geothermal working fluid goes into the vaporizer at point 7 and 12. Thermal energy of geothermal working fluid is transferred by using the vaporizer to the different working fluid for use in ORC process. ORC working fluid goes into the turbine at point 16 to generate power, and leaves at point 17. Exiting from HEX-I, the geofluid transfers its heat energy to the water before entering the PEM electrolyzer. Also, the power generated using by the ORC process is used in the proton exchange membrane electrolyzer to generate hydrogen. The hydrogen liquefaction sub-system is used for more efficiently hydrogen storage. The hydrogen liquefaction process is relatively more energy intensive than compression of hydrogen, whereas, the density of liquid hydrogen is nearly 1120 $kg.m^{-3}$ and, also liquid hydrogen is 29 times better than compressed

hydrogen at 700 bar, in terms of volume work. Therefore, the Linde–Hampson hydrogen liquefaction process with a secondary nitrogen cooling is defined for hydrogen storage.

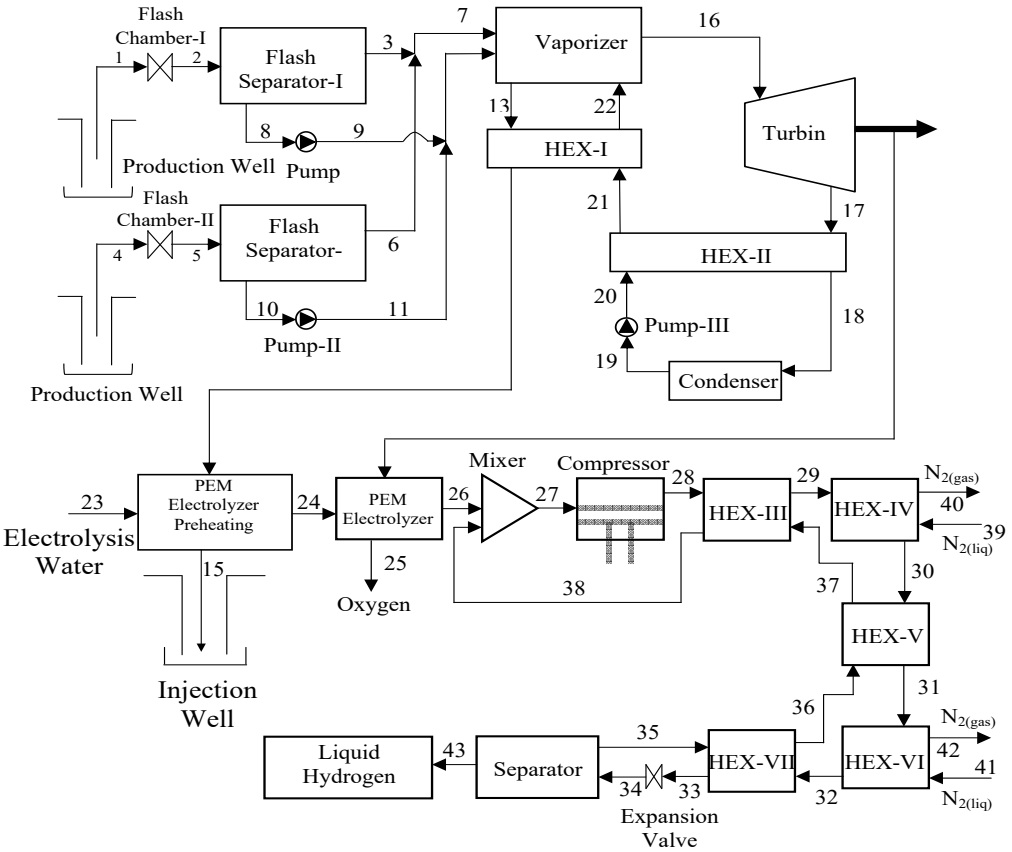


Fig. 1 Schematic diagram of integrated system

3. Thermodynamic Assessment

A thermodynamic analysis is generally based on four balance equations, such as i-) mass balance equation, ii-) energy balance equation, iii-) entropy balance equation, and iv-) exergy balance equation [8]. In the steady state conditions, the mass balance equation can be written as follows;

$$\sum_i \dot{m}_i = \sum_e \dot{m}_e \quad (1)$$

where $\dot{m}_i$ and $\dot{m}_e$ are the mass flow rate for inlet and outlet flows, respectively. In the steady state conditions, the energy balance equation can be given as follows;

$$\dot{Q}_i + \dot{W}_i + \sum_i \dot{m}_i h_i = \dot{Q}_e + \dot{W}_e + \sum_e \dot{m}_e h_e \quad (2)$$

where h is the specific enthalpy, $\dot{Q}$ and $\dot{W}$ are the heat transfer and power rate. The entropy generation rate, $\dot{S}_{gen}$, for a control volume can be given as entropy balance equation;

$$\dot{S}_{gen} = \sum_e \dot{m}_e s_e - \sum_i \dot{m}_i s_i - \sum \frac{\dot{Q}_k}{T_k} \quad (3)$$

where s is the specific entropy. The exergy balance equation can be defined as follows;

$$\dot{E}x_{Q,i} + \dot{E}x_{W,i} + \sum \dot{m}_i ex_i = \dot{E}x_{Q,e} + \dot{E}x_{W,e} + \sum \dot{m}_e ex_e + \dot{E}x_D \quad (4)$$

where $\dot{E}x_D$ is the exergy destruction rate and can be defined as;

$$\dot{E}x_D = T_o \dot{S}_{gen} \quad (5)$$

where T_o is the ambient temperature. $\dot{E}x_W$ is the exergy transfer rate associated with mechanical work and can be given as

$$\dot{E}x_W = \dot{W} \quad (6)$$

$\dot{E}x_Q$ is the exergy transfer rate associated with heat transfer and can be written as

$$\dot{E}x_Q = \left(1 - \frac{T_o}{T}\right)\dot{Q} \quad (7)$$

The specific physical or flow exergy is calculated through the given equation;

$$ex_i = (h_i - h_o) - T_o(s_i - s_o) \quad (8)$$

Flash chamber I; Under the steady state and steady flow conditions, the mass, energy, entropy and exergy balance equations for flash chamber I can be given as

Mass: $\dot{m}_1 = \dot{m}_2$ (9)

Energy: $\dot{m}_1 h_1 = \dot{m}_2 h_2$ (10)

Entropy: $\dot{m}_1 s_1 + \dot{S}_{gen,fc-I} = \dot{m}_2 s_2$ (11)

Exergy: $\dot{m}_1 ex_1 = \dot{m}_2 ex_2 + \dot{E}x_{D,fc-I}$ (12)

Flash Separator I; The mass, energy, entropy and exergy balance equations are defined for flash separator I under steady state and steady flow conditions.

Mass: $\dot{m}_2 = \dot{m}_3 + \dot{m}_8$ (13)

Energy: $\dot{m}_2 h_2 = \dot{m}_3 h_3 + \dot{m}_8 h_8$ (14)

Entropy: $\dot{m}_2 s_2 + \dot{S}_{gen,fs-I} = \dot{m}_3 s_3 + \dot{m}_8 s_8$ (15)

Exergy: $\dot{m}_2 ex_2 = \dot{m}_3 ex_3 + \dot{m}_8 ex_8 + \dot{E}x_{D,fs-I}$ (16)

Pump I; The mass, energy, entropy and exergy balance equations for pump I can be written under the steady state and steady flow conditions as

Mass: $\dot{m}_9 = \dot{m}_9$ (17)

Energy: $\dot{m}_8 h_8 + \dot{W}_{p_I} = \dot{m}_9 h_9$ (18)

Entropy: $\dot{m}_8 s_8 + \dot{S}_{gen,p_I} = \dot{m}_9 s_9$ (19)

Exergy: $\dot{m}_8 ex_8 + \dot{W}_{p_I} = \dot{m}_9 ex_9 + \dot{E}x_{D,p_I}$ (20)

Vaporizer; Under the steady state and steady flow conditions, the mass, energy, entropy and exergy balance equations for vaporizer can be defined as

Mass: $\dot{m}_7 + \dot{m}_{12} = \dot{m}_{13}$: $\dot{m}_{16} = \dot{m}_{22}$ (21)

Energy: $\dot{m}_7 h_7 + \dot{m}_{12} h_{12} + \dot{m}_{22} h_{22} = \dot{m}_{13} h_{13} + \dot{m}_{16} h_{16}$ (22)

Entropy: $\dot{m}_7 s_7 + \dot{m}_{12} s_{12} + \dot{m}_{22} s_{22} + \dot{S}_{gen,vap} = \dot{m}_{13} s_{13} + \dot{m}_{16} s_{16}$ (23)

Exergy: $\dot{m}_7 ex_7 + \dot{m}_{12} ex_{12} + \dot{m}_{22} ex_{22} = \dot{m}_{13} ex_{13} + \dot{m}_{16} ex_{16} + \dot{E}x_{D,vap}$ (24)

Turbine; The mass, energy, entropy and exergy balance equations are written for turbine under the steady state and steady flows conditions.

Mass: $\dot{m}_{16} = \dot{m}_{17}$ (25)

Energy: $\dot{m}_{16} h_{16} = \dot{m}_{17} h_{17} + \dot{W}_{tur}$ (26)

Entropy: $\dot{m}_{16} s_{16} + \dot{S}_{gen,tur} = \dot{m}_{17} s_{17}$ (27)

Exergy: $\dot{m}_{16} ex_{16} = \dot{m}_{17} ex_{17} + \dot{W}_{tur} + \dot{E}x_{D,tur}$ (28)

Heat exchanger II; The mass, energy, entropy and exergy balance equations are written for HEX II under the steady state and steady flow conditions.

Mass: $\dot{m}_{17} = \dot{m}_{18}$; $\dot{m}_{20} = \dot{m}_{21}$ (29)

Energy: $\dot{m}_{17} h_{17} + \dot{m}_{20} h_{20} = \dot{m}_{18} h_{18} + \dot{m}_{21} h_{21}$ (30)

Entropy: $\dot{m}_{17} s_{17} + \dot{m}_{20} s_{20} + \dot{S}_{gen,HEX_II} = \dot{m}_{18} s_{18} + \dot{m}_{21} s_{21}$ (31)

Exergy: $\dot{m}_{17} ex_{17} + \dot{m}_{20} ex_{20} = \dot{m}_{18} ex_{18} + \dot{m}_{21} ex_{21} + \dot{E}x_{D,HEX_II}$ (32)

Condenser; Under the steady state and steady flow conditions, the mass, energy, entropy and exergy balance equations for condenser can be defined as follows;

Mass: $\dot{m}_{18} = \dot{m}_{19}$; $\dot{m}_a = \dot{m}_b$ (33)

Energy: $\dot{m}_a h_a + \dot{m}_{18} h_{18} = \dot{m}_b h_b + \dot{m}_{19} h_{19}$ (34)

Entropy: $\dot{m}_a s_a + \dot{m}_{18} s_{18} + \dot{S}_{gen,Con} = \dot{m}_b s_b + \dot{m}_{19} s_{19}$ (35)

Exergy: $\dot{m}_a ex_a + \dot{m}_{18} ex_{18} = \dot{m}_b ex_b + \dot{m}_{19} ex_{19} + \dot{E}x_{D,Con}$ (36)

PEM electrolyzer pre-heating; The mass, energy, entropy and exergy balance equations for PEM electrolyzer pre-heating can be given under the steady state and steady flow conditions as follows:

Mass: $\dot{m}_{14} = \dot{m}_{15}$; $\dot{m}_{23} = \dot{m}_{24}$ (37)

Energy: $\dot{m}_{14} h_{14} + \dot{m}_{23} h_{23} = \dot{m}_{15} h_{15} + \dot{m}_{24} h_{24}$ (38)

Entropy: $\dot{m}_{14} s_{14} + \dot{m}_{23} s_{23} + \dot{S}_{gen,peph} = \dot{m}_{15} s_{15} + \dot{m}_{24} s_{24}$ (39)

Exergy: $\dot{m}_{14} ex_{14} + \dot{m}_{23} ex_{23} = \dot{m}_{15} ex_{15} + \dot{m}_{24} ex_{24} + \dot{E}x_{D,peph}$ (40)

PEM electrolyzer; The mass, energy, entropy and exergy balance equations for PEM electrolyzer can be defined under the steady state and steady flow conditions as follows:

Mass: $\dot{m}_{24} = \dot{m}_{25} + \dot{m}_{26}$ (41)

Energy: $\dot{m}_{24} h_{24} + \dot{W}_{PEM} = \dot{m}_{25} h_{25} + \dot{m}_{26} h_{26}$ (42)

Entropy: $\dot{m}_{24} s_{24} + \dot{S}_{gen,PEM_el} = \dot{m}_{25} s_{25} + \dot{m}_{26} s_{26}$ (43)

Exergy: $\dot{m}_{24}ex_{24} + \dot{W}_{PEM} = \dot{m}_{25}ex_{25} + \dot{m}_{26}ex_{26} + \dot{E}x_{D,PEM_el}$ (44)

Mixer; The mass, energy, entropy and exergy balance equations for mixer can be written under the steady state and steady flow conditions as follows:

Mass: $\dot{m}_{26} + \dot{m}_{38} = \dot{m}_{27}$ (45)

Energy: $\dot{m}_{26}h_{26} + \dot{m}_{38}h_{38} = \dot{m}_{27}h_{27}$ (46)

Entropy: $\dot{m}_{26}s_{26} + \dot{m}_{38}s_{38} + \dot{S}_{gen,mixer} = \dot{m}_{27}s_{27}$ (47)

Exergy: $\dot{m}_{26}ex_{26} + \dot{m}_{38}ex_{38} = \dot{m}_{27}ex_{27} + \dot{E}x_{D,mixer}$ (48)

Separator; The mass, energy, entropy and exergy balance equations for separator can be defined under the steady state and steady flow conditions as follows:

Mass: $\dot{m}_{34} = \dot{m}_{35} + \dot{m}_{43}$ (53)

Energy: $\dot{m}_{34}h_{34} = \dot{m}_{35}h_{35} + \dot{m}_{43}h_{43}$ (54)

Entropy: $\dot{m}_{34}s_{34} + \dot{S}_{gen,sep} = \dot{m}_{35}s_{35} + \dot{m}_{43}s_{43}$ (55)

Exergy: $\dot{m}_{34}ex_{34} = \dot{m}_{35}ex_{35} + \dot{m}_{43}ex_{43} + \dot{E}x_{D,sep}$ (56)

4. Results and discussion

In the modelling of geothermal power based integrated systems, the Engineering Equation Solver (EES) software package is utilized for system design, analysis and assessment. The reference conditions T_o and P_o are assumed to be 25°C and 101.3 kPa, respectively. To investigate the impacts of design parameters on the system performance, the effects of varying reference temperature on the geothermal energy based power production rate and hydrogen production rate are illustrated in Figure 2. It can be observed that, the power and hydrogen production rate of the double flash geothermal power system based integrated system increase by the increasing reference temperature from 0 to 40°C.

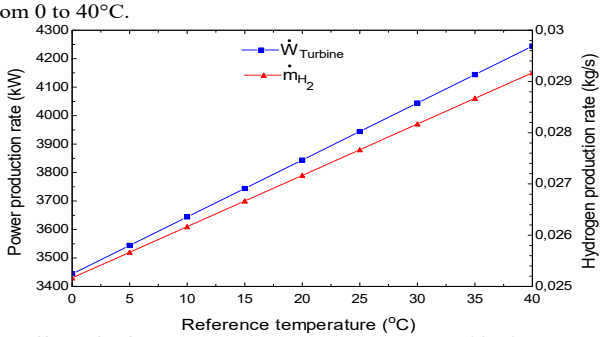


Figure 2. Effect of reference temperature on net power and hydrogen production

The effects of geothermal fluid temperature on power production rate and hydrogen production rate are illustrated in Figure 3. While geothermal fluid temperature increases from 150 °C to 200 °C, the power production rate increases from 1041 kW to 7937 kW, and also with the same temperature change hydrogen production rate of the integrated system increases from 0.0062 kg/s to about 0.0558 kg/s.

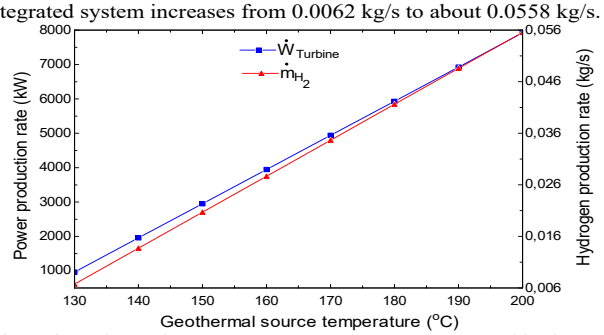


Figure 3. Effect of geothermal source temperature on net power and hydrogen production

Figure 4 shows the influences of ORC turbine inlet pressure on power production rate and hydrogen production rate of the integrated system. As shown in this figure, an increase in this pressure reduces the power and hydrogen production rate. The energy balance equation for control volume around the vaporizer illustrates

that when the energy input from geothermal resource is constant, the reduction in turbine inlet enthalpy increases the ORC mass flow rate.

Fig. 5 shows the relation between geothermal fluid mass flow rate and the net energy production and exergy efficiency of the system. As mass flow rate triples from 75 kg/s to 225 kg/s, the amount of generated power increases from 3750 kW to 9000 kW. This result is logic because any increase in mass flow rate increases turbine work in the system. However, this increase in mass flow rate causes a decrease in exergy efficiency from 51% to 39%. The reason of this decrease is that binary cycle is increasing generated power because of the second cycle however limited part of the energy can be transferred from the first cycle to the second one. Losses occurring this transfer decreases the exergy efficiency of whole system.

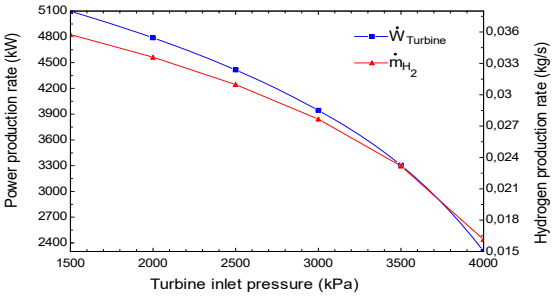


Figure 4. Effect of turbine inlet pressure on net power and hydrogen production

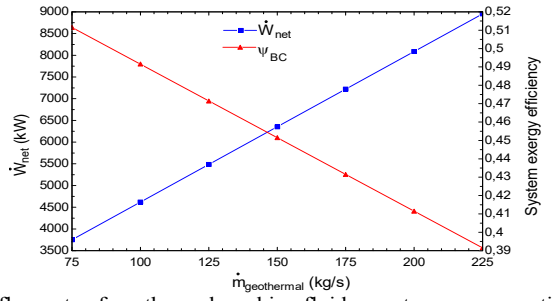


Figure 5. Effect of mass flow rate of geothermal working fluid on net power generation and exergy efficiency

As seen from Figure 6, the temperature of geothermal fluid has positive effect on generated power but negative effect on the exergy efficiency. As geothermal water temperature varies from 150 °C to 230 °C, produced electricity increases from 3200 kW to 5400 kW. Because fluid having higher temperature produces more work in the turbine. Although increase in geothermal fluid temperature increases generated power, it makes exergy efficiency decreases from 60% to 52%.

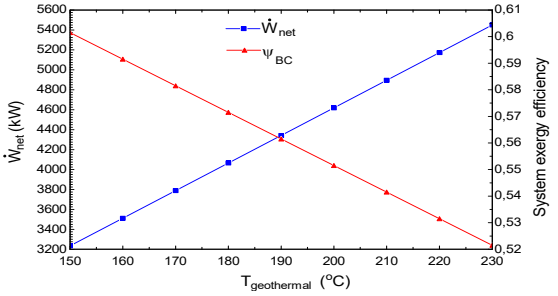


Figure 6. Effect of geothermal working fluid temperature on power generation and exergy efficiency

Figure 7 shows a direct proportion between ambient temperature and both generated power and exergy efficiency. As ambient temperature increases, losses occurred by irreversibilities decrease. While generated

power is about 3700 kW at 0 °C, it goes up to 5200 kW at 40 °C. With this change of ambient temperature, exergy efficiency of the system increases from 44% to 52%.

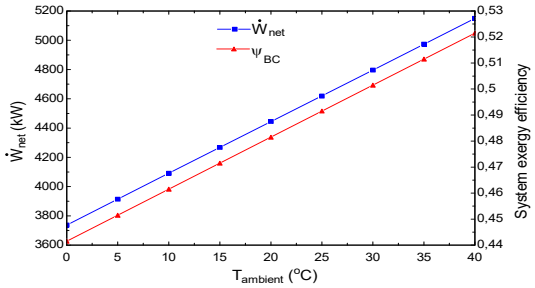


Figure 7. Effect of ambient temperature on power generation and exergy efficiency

6. Conclusions

In the present study, the main balance equations for thermodynamic analysis of different geothermal power systems are for power, hydrogen production and liquefaction. The exergy based thermodynamic assessment is demonstrated to ensure an important tool for design and improving of geothermal power systems. The parametric analyses define the impacts on exergy destruction rate and exergy efficiency of varying different operating indicators, such as geofluid temperature and mass flow rate. Also, the effects of increasing reference temperature on exergy destruction rate and exergy efficiency is investigated. Different concluding outputs should be drawn from this study;

- The new potential fields for the construction of geothermal energy based power generation plants need to be investigated.
- One of the biggest drawbacks that limit the utilization of geothermal power systems is the lack of a reliable long term energy storage system. Therefore, it is recommended that a research work should be carried out for the application of geothermal power systems with other means of storage, such as the liquid hydrogen storage system.
- The largest irreversibility in the geothermal power generation processes are associated with flashing, condenser and turbine.
- It is demonstrated that increasing the geofluid temperature, mass flow rate and reference temperature increase the power and hydrogen generation rate.

Nomenclature

ex	Specific exergy [kJ/kg]	$\dot{Q}$	Heat rate [kW]
$\dot{E}x$	Exergy rate [kW]	s	Specific entropy [kJ/kgK]
$\dot{E}x_D$	Exergy destruction rate [kW]	$\dot{S}$	Entropy rate [kW/K]
h	Specific enthalpy [kJ/kg]	T	Temperature [K]
$\dot{m}$	Mass flow rate [kg/s]	$\dot{W}$	Work Rate [kW]

References

1. Yuksel, Y.E., Ozturk, M. "Thermodynamic and thermoeconomic analyses of a geothermal energy based integrated system for hydrogen production", International Journal of Hydrogen Energy, 42, 2530-2546, 2017.
2. Coskun, C., Oktay, Z., Dincer, I. "Performance evaluations of a geothermal power plant" Applied Thermal Engineering, 31, 4074–4082, 2011
3. Fallah, M., Mohammad, S., Mahmoudi, S., Yari, M., Ghiasi, R. "Advanced exergy analysis of the Kalina cycle applied for low temperature enhanced geothermal system" Energy Conversion and Management, 108, 190-201, 2016.
4. Ozturk, M., Yuksel, Y.E. "Energy Structure of Turkey for Sustainable Development" Renewable and Sustainable Energy Reviews, 53, 1259–1272, 2016.
5. Zare, V. "A comparative thermodynamic analysis of two tri-generation systems utilizing low-grade geothermal energy", Energy Conversion and Management, 118, pp. 264–274, 2016.
6. Suleman, F., Dincer, I., Agelin-Chaab, M. "Development of an integrated renewable energy system for multigeneration", Energy, 78, pp. 196-204, 2014.
7. Al-Ali, M., Dincer, I. "Energetic and exergetic studies of a multigenerational solar geothermal system", Applied Thermal Engineering, 71, pp. 16-23, 2014.
8. Dincer, I., Rosen, M.A., Exergy Analysis of Heating, Refrigerating, and Air: Conditioning Methods and Applications, Elsevier, New York, 2015.

Thermodynamic analysis of the carbon dioxide cycles driven by geothermal power system with hydrogen production

Yunus Emre Yuksel[1], Murat Ozturk[2]
[1]Department of Elementary Science Education, Education Faculty, Afyon Kocatepe University, TURKEY
[2]Department of Mechatronics Engineering, Faculty of Technology, Suleyman Demirel University, TURKEY
Email: yeyuksel@aku.edu.tr, muratozturk@sdu.edu.tr

Abstract
In this paper, the thermodynamic assessment analysis of two carbon dioxide cycles driven by geothermal energy with hydrogen production system is detailed investigated. This low temperature hydrogen production system is consisted of two carbon dioxide cycles, the hydrogen production process and the hydrogen storage and utilization system. The exergy destruction rates, exergy destruction ratios and exergy efficiencies of geothermal energy based hydrogen production system components and whole system are analyzed by using the balance equations, energy and exergy efficiencies. Also, the effect of some design parameters on the geothermal energy based hydrogen production and utilization system exergy destruction rate and exergy efficiency are investigated.

Keywords: Geothermal energy; carbon dioxide cycle; hydrogen; energy; exergy.

1. Introduction

Geothermal fluids, as it comes from the underground, contains gaseous impurities, such as hydrogen sulfite and radon gaseous, that usually are not permitted to be released to the ambient. Reinjection of used geofluids back into the injection well may, however, solve any harmful emission problems. The different benefit is that geothermal power processes are easy, safe and adaptable. The heat energy is created by the natural decay over millions of years of radiogenic materials including uranium, thorium and potassium. The geothermal energy production systems have important advantages. They are environmentally benign, renewable energy sources, and also they can be used for providing base-load electric and heat energy for industrial applications. The geothermal energy sources that have been utilized, or are under investigation for improving, range from shallow ground to hot water and rock several kilometers below the world's surface. The broad classification of different direct utilizations of the geothermal energy on the basis of their temperature requirements are given in Table 1.

Hosseini and Wahid [1] have investigated a review paper for comparison of hydrogen generation from biomass energy. The most cost effective thermochemical process for hydrogen generation is supercritical water gasification of biomass according to their paper. Generating hydrogen from geothermal resources is relatively cheaper than solar and wind energy sources. They have concluded that feasible applications for hydrogen production are low and moderate temperature geothermal sources; beside these waste heat of geothermal is feasible too for hydrogen production. Yilmaz and Kanoglu [2] have investigated the energetic and exergetic analysis on PEM electrolyzer using geothermal source for hydrogen generation. According to their analysis results, the electrolysis temperature has positive effects on hydrogen production, energy and exergy efficiency.

In order to generate power, the most used cycles are Rankine cycle, Organic Rankine cycle (ORC) and Kalina cycle. Zare [3] has compared ORC and Kalina cycle in geothermal based tri-generation systems and performed thermodynamic analysis and optimization. Kalina cycle is found to be more efficient than ORC at about 4% and produces more power than ORC at 12.2%. As geothermal water temperature increases 130 °C to 200 °C, cost of hydrogen production decreases from 4.8$/kg$H_2$ to 1.1$/kg H_2 [4].

Table 1 Direct use applications of geothermal energy resources based on temperature range

20-50 °C	50-80 °C	80-120 °C	120-160 °C	160-220 °C	>220 °C
Applications; - fish farming - swimming pool - thermal bath - fermentation - aquaculture - soil warming - mushroom growing - heat pumps	**Applications;** - space heating - dry air - greenhouse heating - grains drying - fruits drying - vegetable drying	**Applications;** - fresh water - food drying - drying of stock fish - leather and fur treatment - washing and dying of textiles - pulp and paper processing - process heating	**Applications;** - flash cycles - space cooling - direct steam - fresh water by distillation - evaporation in sugar refining - industrial space air conditioning	**Applications;** - binary cycle - Kalina cycle - drying farm products at high rates - canning of food - refrigeration by ammonia absorption - digestion in paper pulp - chemical production	**Applications;** - hydrogen production - alternative fuel production - conventional power production - cogeneration

2. System description

The integrated energy production process producing power and hydrogen driven by the geothermal power is presented in Fig. 1. The integrated system investigated in this paper consists of mainly four subsystems, such as i-) CO_2 Cycle-I, ii-) CO_2 Cycle-II, iii-) PEM electrolyzer, and iv-) PEM fuel cell. The geothermal power and CO_2 Cycle-I are used in the integrated system to produce heat and power for PEM electrolyzer. The waste heat of PEM fuel cell is used to drive the CO_2 Cycle-II for power generation. The geothermal water coming with the state 1 transfers its heat to the CO_2, which is working fluid of ORC-I. Then geothermal water enters the evaporator-II of hydrogen production cycle to heat the electrolysis water. The CO_2 cycle-II is driven by the waste heat coming from PEM fuel cell system.

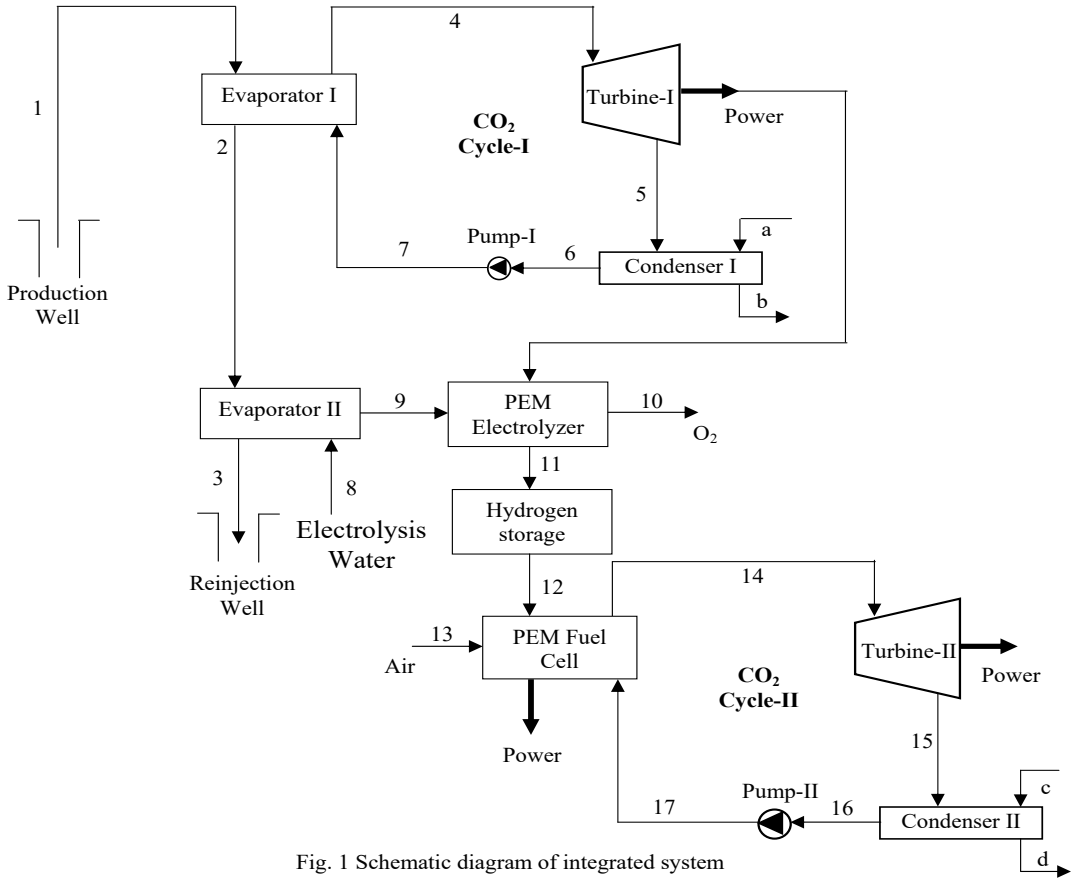


Fig. 1 Schematic diagram of integrated system

3. Thermodynamic modelling

The mass, energy, entropy and exergy balance equations of solar energy based integrated system components must be defined under the assumption of steady-state condition [5,6].

- Mass balance equation;

$$\sum \dot{m}_i = \sum \dot{m}_e \quad (1)$$

where $\dot{m}$ is the mass flow rate, subscripts i and e are the inlet and outlet flows, respectively.

- Energy balance equation;

$$\sum \dot{m}_i h_i + \sum \dot{Q}_i + \sum \dot{W}_i = \sum \dot{m}_e h_e + \sum \dot{Q}_e + \sum \dot{W}_e \quad (2)$$

where $\dot{Q}$ is the heat transfer rate, $\dot{W}$ is the power, h is the specific enthalpy.

- Entropy balance equation;

$$\sum \dot{m}_i s_i + \sum \left(\frac{\dot{Q}}{T}\right)_i + \dot{S}_{gen} = \sum \dot{m}_e s_e + \sum \left(\frac{\dot{Q}}{T}\right)_e \quad (3)$$

where s is the specific entropy, $\dot{S}_{gen}$ is the entropy generation rate and T is the temperature at which heat fluxes cross the process boundary.

- Exergy balance equation;

$$\sum \dot{m}_i ex_i + \sum \dot{E}x_i^Q + \sum \dot{E}x_i^W = \sum \dot{m}_e ex_e + \sum \dot{E}x_e^Q + \sum \dot{E}x_e^W + \dot{E}x_D \quad (4)$$

where ex is the specific exergy, $\dot{E}x^Q$ is the exergy rate of heat energy transfer, $\dot{E}x^W$ is the exergy rate associated with shaft work and $\dot{E}x_D$ is the exergy destruction rate.

- The specific exergy can be defined as follows;

$$ex = ex_{ph} + ex_{ch} + ex_{pt} + ex_{kn} \quad (5)$$

where ex_{ph}, ex_{ch}, ex_{pt} and ex_{kn} are the physical, chemical, potential and kinetic exergy, respectively. In this paper, ex_{pt} and ex_{kn} are accepted as negligible, because the exergy exchange rates of these physical quantity are very small. The physical or flow exergy rate can be written as follows;

$$ex_{ph} = h - h_o - T_o(s - s_o) \quad (6)$$

The chemical exergy of a process can be defined as follows [7,8];

$$ex_{ch} = \sum n_i(u_i^0 - u_i^{00}) \quad (7)$$

where u_i^0 is chemical potential of ith component in thermomechanical equilibrium and u_i^{00} is the chemical potential of ith component in chemical equilibrium. The exergy rates associated with heat transfer and work across the boundary of a control volume can be defined as follows, respectively;

$$\dot{E}x_Q = \left(1 - \frac{T_o}{T}\right)\dot{Q} \quad (8)$$

$$\dot{E}x_W = \dot{W} \quad (9)$$

The energy efficiency (η) and exergy efficiency (ψ) equations for steady state conditions can be defined as follows, respectively;

$$\eta = \frac{energy\ in\ product\ outputs}{total\ energy\ inputs} \quad (10)$$

$$\psi = \frac{exergy\ in\ product\ outputs}{total\ exergy\ inputs} \quad (11)$$

4. Results and discussion

The exergy destruction rate, dimensionless exergy destruction ratio and exergy efficiency of triple flash steam geothermal power generation components are given in Table 2.

Table 2. Exergy destruction rate, exergy destruction ratio and exergy efficiency of system components

System components	Exergy destruction rate (kW)	Exergy destruction ratio (%)	Exergy efficiency (%)
PEM fuel cell	1095	12.7	38.52
Evaporator-II	1194	13.8	73.28
Pump-I	81.6	0.95	88.26
Condenser-I	438.3	5.08	72.52
Condenser-II	94.28	1.09	81.95
Turbine-I	1681.4	19.5	38.62
Pump-II	76.54	0.89	88.24
Turbine II	1520	17.6	36.86
Evaporator-I	1373.2	15.9	64.28
PEM electrolyzer	879.9	10.2	63.28

To investigate the performance of geothermal power system more comprehensively, the parametric studies are given below to examine the impacts of different indicator variables on the exergy destruction rate and exergy efficiency. According to the findings, the predominant parameter affecting net electricity production is mass flow rate. As seen from Figure 2, as mass flow rate triples from 75 kg/s to 225 kg/s, electricity production and exergy efficiency increase from 7000 kW to about 20500 kW and 52% to 64%, respectively. The increment in geothermal mass flow rate makes turbine producing more work. Because higher temperature fluid transfers more energy to the turbine of the system, increment in geothermal fluid temperature has positive effect on both electricity generation and exergy efficiency. As seen from Figure 3. Electricity production increases from 7300 kW to 10500 kW and exergy efficiency increases from 49% to 57%. According to the findings of this study, ambient temperature is the most important factor affecting exergy efficiency. Definition of exergy clarifies this increment. As seen from Figure 4, as ambient temperature changes from 0 °C to 40 °C, exergy efficiency increases from about 43% to 63%. Proportionally, the produced electricity increases about 2000 kW with the same temperature change.

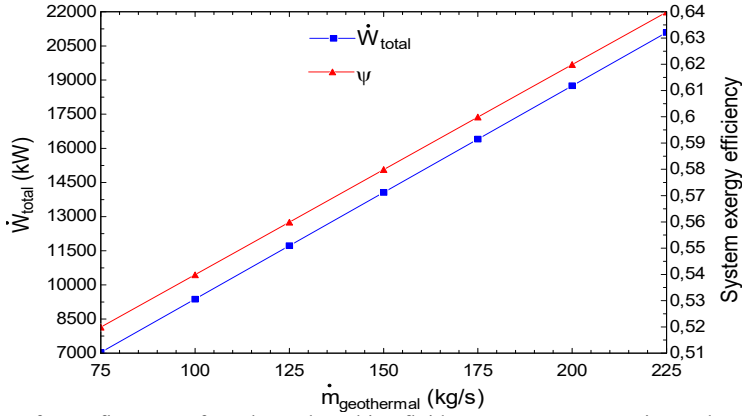


Figure 2. Effect of mass flow rate of geothermal working fluid on net power generation and exergy efficiency

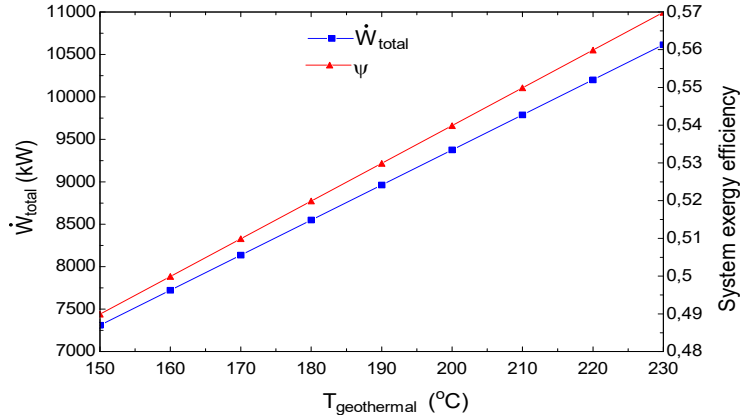


Figure 3. Effect of geothermal working fluid temperature on net power generation and exergy efficiency

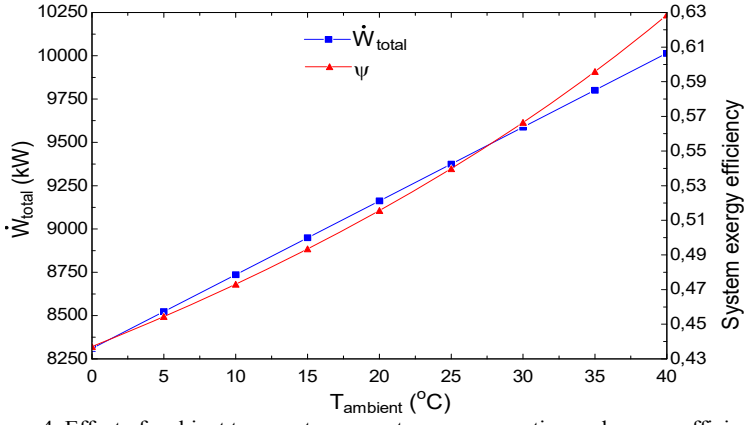


Figure 4. Effect of ambient temperature on net power generation and exergy efficiency

The impact of the electrolyzer temperature on the energy and exergy efficiencies of the electrolyzer is analyzed. The energy and exergy efficiency of this component vary from 61.05% to 67.75% and 60.21% to 62.32%, respectively with increase in the electrolyzer temperature from 60 °C to 120 °C as illustrated in Fig. 5. These output is provided because increase in the electrolyzer temperature generates the decrease in electric demand. This is applied feasible by the increase in heat energy as the electrolyzer temperature increases. Also, the total energy need reduces in higher PEM electrolyzer temperature cases.

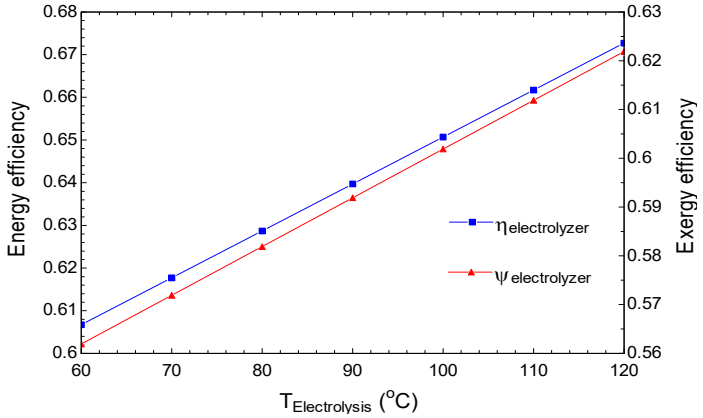


Figure 5. Impact of the PEM electrolyzer temperature on energy efficiency and exergy efficiency

The effect of geothermal fluid temperature on power production rate and hydrogen production rate are illustrated in Figure 6.37. While geothermal fluid temperature increases from 150 °C to 200 °C, the power production rate increases from 1041 kW to 7937 kW, and also with the same temperature change hydrogen production rate of the integrated system increases from 0.0062 kg/s to about 0.0558 kg/s.

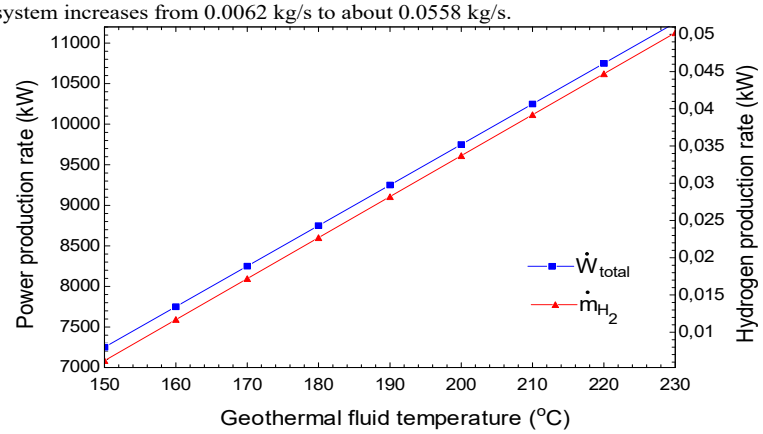


Figure 6. Effect of geothermal source temperature on net power and hydrogen production

5. Conclusions

In this study, the thermodynamic assessments outputs of integrated process driven by the geothermal energy are detailed presented. Because an energy analysis cannot provide adequate information for the energy loss rates, an exergy analysis is performed to investigate actual performances and exergy destruction rates of whole process and its components. In addition, the parametric studies are conducted to understand how geothermal mass flow rate, geothermal fluid temperature and reference temperature, influence the energetic and exergetic efficiencies, and also exergy destruction rate of investigated system for a more efficient process design. Based on the thermodynamic assessment, the integrated process for hydrogen production present higher efficiency and positive environmentally effect. Finally, we have drawn the following concluding remarks;

- Increasing geothermal fluid temperature intensity causes an increase in the exergy efficiency of the solar energy based process.

- Increasing mass flow rate of geofluid causes an increase in the exergy efficiency of the all sub-systems and whole process.
- Exergy efficiencies of the CO_2 cycle-I, CO_2 cycle-II, PEM elecrolyzer, and PEM fuel cell are found as 27.35%, 24.58%, 63.28% and 38.52%, respectively.

NOMENCLATURE

ex	Specific exergy [kJ/kg]
$\dot{E}x$	Exergy rate [kW]
$\dot{E}x_D$	Exergy destruction rate [kW]
h	Specific enthalpy [kJ/kg]
$\dot{m}$	Mass flow rate [kg/s]
P	Presuure [kPa]
Q	Heat [kJ]
$\dot{Q}$	Heat rate [kW]
s	Specific entropy [kJ/kgK]
$\dot{S}$	Entropy rate [kW/K]
T	Temperature [K]
W	Work [kJ]
$\dot{W}$	Work Rate [kW]
Greek Letters	
η	Energy efficiency
ψ	Exergy efficiency
Subscript	
D	Destruction
e	Exit condition
en	Energy
ex	Exergy
gen	Generation
i	Inlet condition
Superscripts	
.	Rate
Acronyms	
EES	Engineering Equation Solver
ORC	Organic Rankine Cycle
PEM	Proton exchange membrane

References

1. Hosseini, S.E., Wahid, M.A. “Hydrogen production from renewable and sustainable energy resources: Promising green energy carrier for clean development”, Renewable and Sustainable Energy Reviews, 57, pp. 850–866, 2016.
2. Yilmaz, C., Kanoglu, M. “Thermodynamic evaluation of geothermal energy powered hydrogen production by PEM water electrolysis”, Energy, 69, pp. 592-602, 2014.
3. Zare, V. “A comparative thermodynamic analysis of two tri-generation systems utilizing low-grade geothermal energy”, Energy Conversion and Management, 118, pp. 264–274, 2016.
4. Yuksel, Y.E., Oztuırk, M. “Thermodynamic and thermoeconomic analyses of a geothermal energy based integrated system for hydrogen production”, International Journal of Hydrogen Energy, 42 (4), pp. 2530-2546, 2017.
5. Dincer, I., Rosen, M. A. “Exergy: energy, environment and sustainable development”, Second Ed., Newnes, 2012.
6. Moran, M. “Availability Analysis: A Guide to Efficient Energy Usage”, Englewood Cliffs, NJ: Prentice-Hall, 1982.
7. Bejan, A., Tsatsaronis, G., Moran, M. “Thermal Design and Optimization”, New York: Wiley Interscience, 1996.
8. Kotas, T. “The exergy method of thermal plant analysis”, Krieger Publishing Company, 1985.
9. Dincer, I., Rosen, M.A., Exergy Analysis of Heating, Refrigerating, and Air: Conditioning Methods and Applications, Elsevier, New York, 2015.

Optimal Design of a Hydrogen Refueling Station Powered by Wind-PV Hybrid Power System

Murat Gökçek[1], Cihangir Kale[2],
[1]Department of Mechanical Engineering, Faculty of Engineering, Ömer Halisdemir University, Niğde, 51100, Turkey
[2]Department of Energy Systems Engineering, Faculty of Technology, Fırat University, Elazığ, 23119, Turkey
Email: mgokcek@ohu.edu.tr , ckale@firat.edu.tr

Abstract
Hydrogen fuelling station is an infrastructure for the commercialization of hydrogen energy utilizing fuel cells, particularly, in an automotive sector. Hydrogen fuel produced by renewable sources such as the wind and solar energy may be used as possible alternative fuel to reduce the use of fuels based fossil sources in the road transport sector of the countries. By replacing the gasoline fuel with hydrogen fuel produced using renewable sources in road transport sector, environmental benefits can be achieved. In this study, techno-economic analysis of hydrogen refueling station powered by hybrid wind-PV power system to be installed in İzmir-Çeşme, Turkey is performed. This analysis is carried out around the year to successfully refuel 25 vehicles on a daily basis using HOMER. According to optimization results obtained for the proposed system, the Levelized cost of hydrogen production was calculated to be US $5-10/kg in different renewable fractions. These results show that hydrogen refueling station powered by renewable energy may be appropriate for the considered site.

Keywords: Hydrogen refueling station; levelized cost of hydrogen; HOMER.

1. Introduction
The increase in energy demand in all sectors, the growth of the world's population, and the declining availability of low-cost fossil fuel sources are some of the most important issues the world faces in the 21st century [1]. Moreover, these sources, such as gasoline, oil, coal and natural gas, both pollute the environment and are not a renewable energy source [2]. Hydrogen is expected to be important energy carrier in future sustainable energy strategies to meet the twin challenges of avoiding catastrophic climate change and depletion of low-cost oil and natural resources [3, 4]. Therefore, H_2 has been visualized to become the cornerstone of future energy systems, especially in the transportation sector to charge fuel cell electric vehicles (FCEVs) [5]. The increasing number of fuel cell vehicles will require more hydrogen refueling station (RFS) [6]. However, the hydrogen as a gas (H_2) is not found by itself on Earth. It is found only in compound form with other elements such as water (H_2O), methane (CH_4), coal, and biomass. Although hydrogen can be produced from diverse resources using a variety of technologies [7], the only one currently practical is water electrolysis. Water electrolysis is a mature technology, and it is being used for hydrogen production capacities ranging from few cm^3/min to thousands m^3/h. It is relatively efficient (>70%) [8]. The hydrogen fuelling station will have zero greenhouse gas emissions if solar or wind power is used to generate electricity to run an electrolyzer to split water into hydrogen and oxygen [9]. The present study focus on the optimal design of a hydrogen refueling station powered by wind-PV hybrid power system by using PEM electrolyser established in Çeşme-İzmir, Turkey.

2. Methodology
In the present study, methodology includes choosing the site to evaluate, identifying the resources, specifying input data (monthly average wind speed, monthly average solar radiation) for considered site, determining hydrogen demand and compressor consumption, modeling the hydrogen refueling stations by thinking of different various scenarios by using HOMER software and finally selecting the most cost-efficient scenario as the hydrogen production costs.

3. Components of the Hydrogen Refueling Station
3.1 Hydrogen Load
Hydrogen refueling station was modelled by considering of refuel 25 vehicles having hydrogen tank of 5 kg of capacity on a day. It is mean that considered RFS need to design to meet 125 kg hydrogen on a day.

3.2 Wind Turbine
In the present study, the Enercon E-53 wind turbine, which has a capacity of 800 kW and 73 m of hub height, was used. The wind power curve of the Enercon E-53 wind turbine is illustrated in Fig.1. NASA (National Aeronautics and Space Administration) surface meteorology and solar energy database were used [10]. Fig.2 shows the wind speed profile for considered site throughout the year having an average wind speed of 5.72 m/s at an anemometer height of 50 m.

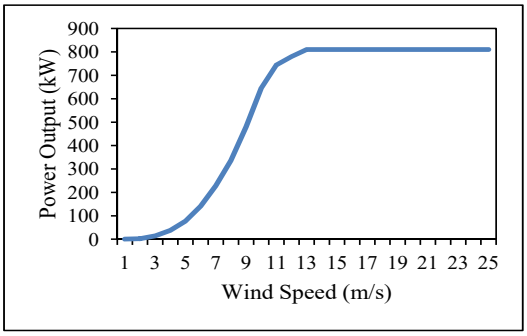


Figure 1. Wind power curve of the Enercon E-53 wind turbine.

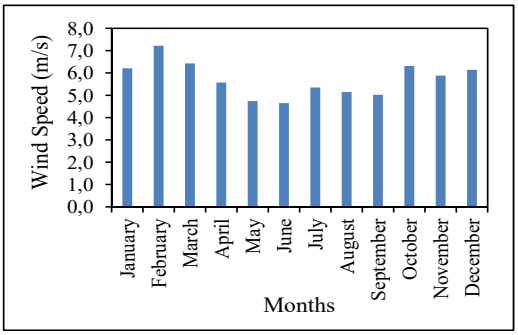


Figure 2. Monthly average wind speed at Çeşme/İzmir.

3.3 PV Panel

In this study, Generic flat plate PV of 1 kW capacity was selected. The derating factor in this study is set to 80%. Fig.3 shows the average monthly solar radiation profile with a scaled annual average solar radiation of 5.08 kWh/m^2/day and average clearness index of 0.606.

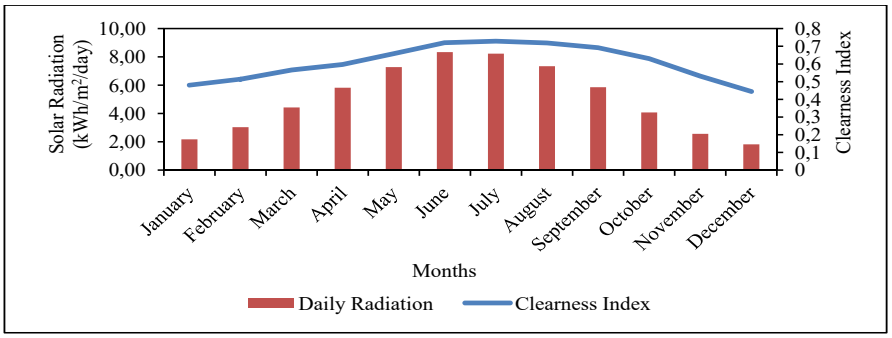


Figure 3. Monthly average daily solar radiation and clearness index at Çeşme/İzmir

3.4 Electrolyzer

In a PEM electrolyser, hydrogen is evolved at the cathode (negative electrode) as Eq.1 and oxygen at the anode (positive) as Eq.2 [9].

$$2H^+ + 2e^- \rightarrow H_2 \quad (1)$$

$$H_2O \rightarrow \tfrac{1}{2}O_2 + 2H^+ + 2e^- \quad (2)$$

In this study, PEM electrolyser was used as to produce hydrogen and its efficiency was taken as 80% (HHV).

3.5 Hydrogen Tank

The hydrogen tank is used to store hydrogen produced when there is excess electric or no hydrogen load to meet the hydrogen demand when there is excess hydrogen load or no electricity. HOMER assumes that the hydrogen tank has no leakage and does not need any process to add hydrogen to the tank [9]. HOMER let to specify the initial amount of hydrogen in the tank either as a percentage of the tank size or as an absolute amount in kilograms. In this study, the initial amount of hydrogen was specified as 10% of the tank size.

3.6 Compressor

The hydrogen station to be constructed using the PEM electrolyzer, a compressor is required to increase the pressure from 14 bar to 350 or 700 bar. HOMER simulates the hydrogen compressor by a corresponding primary electrical load. Compressor energy consumption may be calculated as to be Eq. 3 [11].

$$W_{comp}=C_p \frac{T_1}{\eta_c}\left[\left(\frac{P_2}{P_1}\right)^{\frac{r-1}{r}}-1\right]m_c \quad (3)$$

where C_p is the specific heat of hydrogen at constant pressure (14.304 kJ (kg K)$^{-1}$), T_1 is the inlet gas temperature of hydrogen compressor (293 K), η_c is the efficiency of compressor, P_1 and P_2 are the inlet and output gas pressures of the hydrogen compressor, r is the isentropic exponent of hydrogen (1.4); m_c is the flow rate of gas through hydrogen compressor (kg s^{-1}). In this study, compressor energy consumption was calculated from 14 bar to 700 bar by determining compressor efficiency as 0.7.

3.7 Battery and Converter

In this study, the generic 12 V lead acid battery was selected with 1 kWh of energy storage. To maintain the flow of energy between DC and AC bus, the hybrid systems require a converter to convert. In present study, converter efficiency is set to 90%.

4. HOMER Model

In present study, hydrogen refueling station powered wind-PV hybrid power system with battery backup system was modelled by using HOMER software developed by National Renewable Energy Laboratory. This software carry out simulations according to the net present cost method and list all feasible optimization result from the lowest cost to the highest cost. The net present cost can be given as Eq.4 [12,13]

$$C_{npc,tot}=\frac{C_{ann,tot}}{CRF(i,n)} \quad (4)$$

where, $C_{ann,tot}$ is the total annualized cost ($/yr), i is the annual real discount rate (%) which may be called the real interest rate or just interest rate, n is the lifetime (year), CRF is the capital recovery factor. CRF can be calculated as given Eq.5 [12,13].

$$CRF(i,n)=\frac{i(1+i)^n}{(1+i)^n-1} \quad (5)$$

where i is the annual real discount rate that is calculated as given Eq.6 [12].

$$i=\frac{i^1-f}{1+f} \quad (6)$$

where i^1 is the nominal discount rate and f is the expected inflation rate. In this study, nominal discount rate and expected inflation rate were considered as 8% and 2% respectively.

4.1 Levelized cost of Electricity

HOMER calculate the COE as given Eq. 7 [12]

$$COE=\frac{C_{ann,tot}}{E_{served}} \quad (7)$$

where $C_{ann,tot}$ is the total annualized cost ($/yr), E_{served} is load served (kWh/yr). The total annual cost is the sum of the annualized costs of each component in the hybrid energy system. It is important that HOMER software does not include the electric load consumed by electrolyzer into the total annual electric load when calculating COE. Therefore, in this study, total annual electrical energy consumed by electrolyzer was included into total annual electrical load and it was calculated as given Eq.8 [12,13].

$$Cons_{E}=\frac{100\cdot Q\cdot HHV_{H_2}}{\eta_{E\%}} \quad (8)$$

where Q is the hydrogen mass flow (kg/h), HHV_{H_2} is the higher heating value of hydrogen which equal to 39.4 kW/h [14], $\eta_{E\%}$ is the efficiency of the electrolyzer.

4.2 Levelized Cost of Hydrogen

The Levelized cost of hydrogen (LCOH) is calculated as shown in Eq.9 [9].

$$LCOH = \frac{C_{ann,tot} - V_{electricity}}{M_{hydrogen}} \quad (9)$$

where LCOH is the Levelized cost of hydrogen (US$/kg$H_2$), $C_{ann.tot}$ is the total annualized cost of the system (US$/year), $V_{electricity}$ value of electricity (US$/kWh) and $M_{hydrogen}$ annual hydrogen mass produced (kg/year). In this present study, considered station is an off-grid system. Therefore, $V_{electricity}$ value was taken as zero because there is no sale of electricity to grid. It is important that HOMER does not consist of economic parameters for compressor and dispenser due to not found as a component or a load.

Table 1. Detailed technical and economical parameters related to all components parameters related to all components

Component	Capital Cost ($/kW)	Replacement ($/kW)	Operations & Maintenance Cost ($/kW)	Life Cycle	Capacity (kW)
PEM Electrolyzer	800	700	30	15	-
E-53 Wind Turbine	1000	1000	12	30	800
Flat Generic Pv Panel	2000	2000	10	30	1
Compressor	2500	2500	50	10	30
Hydrogen Tank	600 ($/kg)	400 ($/kg)	3 ($/kg)	25	-
Battery	110	100	10	10	1
Converter	700	630	10	15	-
Dispenser	35000 ($/Unit)	35000 ($/Unit)	170 ($/Unit)	10	-

Therefore, for these equipments, C_{ann} values were calculated and included in $C_{ann.tot}$ values due to obtain more accurate COE and LCOH results. Detailed technical and economical parameters related to all components of the considered hydrogen refueling station are mentioned in Table 1.

5. Results and Discussion

The results of optimization are shown Table 2, which includes the optimal system configurations, NPC, RF, COE, EE (excess electricity) per year.

Table 2. Optimized hydrogen refueling station powered wind-PV with battery parameters related to all components

Rank	PV panel (kW)	Wind Turbine	Electrolyzer (kW)	Hydrogen Tank (kg)	Battery (1kWh LA)	Conv (kW)	COE ($/kWh)	NPC (M$)	RF (%)	EE (%)
1	271	2	500	900	71	473	0.146	4.43	100	41.11
2	279	2	500	900	86	464	0.146	4.44	100	41.36
3	320	2	550	800	89	442	0.149	4.52	100	42.57
4	224	2	600	900	93	518	0.149	4.54	100	39.75
5	228	2	650	900	100	477	0.150	4.58	100	39.92
6	413	2	550	700	115	411	0.152	4.62	100	45.04

The system in rank 1 is considered as best configuration to supply reliable electricity to the hydrogen refueling system. It can be seen from Table 2 that the best optimized hybrid system configuration for considered station comprised of 271 kW PV module, 2 wind turbine, 71 kW battery, 473 units of converter, 500 kw of electrolyzer and 900 kg of hydrogen tank. This system resulted in the COE of US $0.146/kWh, NPC of US $4.43M, renewable fraction (RF) of 100% (zero greenhouse gas emission), and excess electricity (EE) of 41.11% of total electricity generation. Table 3 lists the levelized cost of hydrogen for the hydrogen refueling station powered by wind-PV power system in the different configuration. As can be seen from Table 3, the lowest value LCOH that is US $7.526/kg is for wind-PV system with battery backup system.

Table 3. Levelized cost of hydrogen for different configurations of power system.

Rank	1	2	3	4	5	6
LCOH ($/kg)	7.526	7.549	7.681	7.694	7.768	7.866

5. Conclusions

In this study, the feasibility of hydrogen refueling station to meet fueling 25 vehicles per a day powered by wind-pv with battery backup sub-system in İzmir-Çeşme, Turkey with the aim of determining levelized cost of hydrogen production with local energy resources was considered. The simulation result show that the optimized hybrid power system is one comprised of 271 kW PV module, 2 wind turbine, 71 units of battery, 473 kW converter, electrolyzer of 500 kW and hydrogen tank of 900 kg. The cost of energy for the proposed optimal hybrid system was found as US$0.146/kWh. The NPC and RF of the optimized hybrid system were US$4.43M and 100% (completely zero emission plant), respectively. The levelized cost of hydrogen was calculated as US $7.526/kg for wind-PV system with battery backup system. The results of the optimization indicate that hydrogen production with hybrid renewable energy power system is economically feasible for the considered site.

References

1. Alazemi J, Andrews J. Automotive hydrogen fuelling stations: An international review. Renewable and sustainable energy reviews. 2015; 48, 483-499.
2. FCHEA. The Hydrogen Economy. Available from: http://fchea.org.
3. Zini G, Tartarini P. Solar hydrogen energy systems: science and technology for the hydrogen economy. Springer Science & Business Media, 2012.
4. Andrews J, Shabani B. Re-envisioning the role of hydrogen in a sustainable energy economy. International journal of hydrogen Energy. 2012; 37(2), 1184-1203.
5. Othman E.S.A, Nawar S. K., Fahmy F.H., Nafeh A.El-Shafy.A. A New design of a Hydrogen Fueling Station Powered By Renewable Energy Sources. IOSR Journal of Electrical and Electronics Engineering Ver. II. 2015; 10(5), 2278–1676.
6. Pan X, Li Z, Zhang C, Lv H, Liu S, Ma J. Safety study of a wind–solar hybrid renewable hydrogen refuelling station in China. International Journal of Hydrogen Energy, 2016; 41(30), 13315-13321.
7. Ete A. Hydrogen Systems Modelling, Analysis And Optimisation. (MSc Thesis, Strathclyde University), 2009.
8. Barbir F. PEM electrolysis for production of hydrogen from renewable energy sources. Solar Energy, 2005; 78(5), 661-669.
9. Alazemi J. Automotive solar hydrogen fuelling stations: Concept design, performance testing and evaluation (PhD thesis, RMIT University), 2016.
10. HOMER energy. Available from: https://homerenergy.com/index.html.
11. Li C.H, Zhu X.J, Cao G.Y, Sui S, Hu M.R. Dynamic modeling and sizing optimization of stand-alone photovoltaic power systems using hybrid energy storage technology. Renewable Energy. 2009; 34, 815–826, 2009.
12. HOMER help manual. Available from: http://www.homerenergy.com/pdf/HOMERHelpManual.pdf.
13. Siyal S. H, Mentis D, Howells M. Economic analysis of standalone wind-powered hydrogen refueling stations for road transport at selected sites in Sweden. International Journal of Hydrogen Energy. 2015; 40(32), 9855-9865.

Hydrogen Production Potential From Solar Energy in Kayseri

Seyfettin GUREL, Gamze GENC*
Department of Energy Systems Engineering, Faculty of Engineering, University of Erciyes, 38039, Kayseri, TURKEY
Email:sgurel@erciyes.edu.tr, gamzegenc@erciyes.edu.tr
*corresponding author

Abstract
Harmful effects of fossil fuels can be reduced by replacing fossil fuels with cleaner fuels to supply the energy. In this regard, hydrogen that is accepted as an energy carrier of the future plays an important role and it can be produced from water via electrolysis by using renewable energy sources. In this paper, the hydrogen production potential was analyzed using solar-electrolysis system for Kayseri. For this purpose, firstly daily and annually solar energy potential of Kayseri was calculated from the global radiation. Depending on the obtained energy from solar energy, hydrogen production potential was investigated by considering three different electrolyze cases such as i) 10×10 kW, ii) 5×20 kW and iii)1×100 kW. The results brought out that the most hydrogen was produced in the case of 10x10kW electrolyze case. In this case, the maximum hydrogen production potential is 195.39 kg/h as yearly.

Keywords: Hydrogen production; solar energy; electrolysis.

1. Introduction

In the world, there are limited resources to produce energy. This fact makes renewable energy sources more attractive. As an energy source, a Sun is the basis of all of the sources. With its useful potential, solar energy is promising renewable source among the all renewable resources. As an energy carrier, hydrogen is most useful way to produce clean energy. It is environmentally friendly such that it has very low potential for greenhouse gas. It has also vital property that it can be reusable [1]. As a result of these facts, hydrogen becomes more attractive and invaluable promising element for clean energy and clean world. There are many ways to produce hydrogen from solar energy. Bilgen [1] classified these methods as solar thermal electricity production and water electrolysis and PV-electrolyzer system which firstly produces electrical power via photovoltaic process and then uses electrolyzer system so as to get hydrogen. The advantage of PV-electrolyzer system makes more preferable. It is well-known that the PV panel produces direct current and this makes available to connect electrolyzer directly. Also, PV-electrolyzer systems are more efficient system when it is compared photoelectric technologies [2]. While calculating the amount of hydrogen production, the intensity of solar irradiance should be taken into consideration as important parameters. The quantity of solar irradiation gives highest hydrogen production levels 600 - 650 W/m^2 given by researchers [3]. By optimizing size of PV-electrolyzer system, it can be obtained power transfer efficiency 99% according the study conducted by researchers [4]. Besides, there is also PV-alkaline electrolyzer for producing more efficient hydrogen. Dukic and Frak [5] suggests a system which consists of 30 W PV Module and alkaline electrolyzer. A proposed system set up and tested and the total efficiency of the PV-Alkaline electrolyzer system attains above %55 for all types of circulation. A system is proposed by researchers which includes PV-alkaline electrolyzer. It is concluded that the efficiency of all system reaches its peak value, when electrolyzer system works approximately same values with highest power of PV. Hydrogen production rate is also directly related to solar irradiance, operating temperature of the electrolyzer, compressor and regenerator efficiencies, and band gap energy and ideality factor of PV [6]. In addition to these systems, novel and innovative solar based hydrogen systems are slated for maximizing hydrogen production yield.

The main goal of this paper is to investigate the hydrogen production potential from solar energy in Kayseri. Initially, the irradiation values are calculated to get daily and monthly irradiation values. Then, the produced electricity is computed and hourly hydrogen production is calculated in the cases of electrolyzers i) 1 ×100 kW, ii) 10 ×10 kW and iii) 1 ×100 kW for Kayseri region.

2. Solar Based Hydrogen Production System

Hydrogen production can be made with various methods. To get clean and reliable hydrogen production, solar energy is used as an electricity source with using traditional PV systems. The most important method to produce hydrogen is the solar electrolyzer hybrid system.

The solar-electrolyzer hybrid system consists of solar panel, charge regulator, electrolyzer, compressor and hydrogen tank. With using this system, the hydrogen production can made for off-grid PV system applications. Figure 1 shows the solar-hybrid system with its all components. Initially, the energy which is produced by photovoltaic effect in PV arrives in charge regulator. This device stabilizes the possible fluctuations during electricity production. The energy which achieves charge regulator provides electricity so as to realize hydrogen production. With the help of the compressor, a produced hydrogen squeezed by a pressure which is higher than atmospheric pressure and being stored in hydrogen tank.

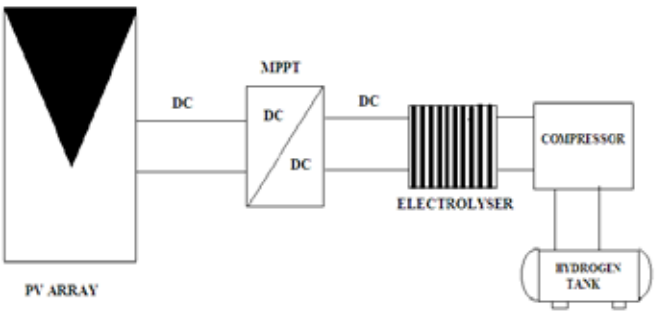


Fig. 1. The General Components of PV-Hydrogen Hybrid System

In this work, the potential of hydrogen production was investigated via solar- electrolyzes system for Kayseri-center. To actualize this purpose, PEM electrolyzer was used. Taking account of total global radiation, daily and annually potential of energy was evaluated for three different electrolyzes capacity.

3. Results and Discussion

3.1. Solar Energy Potential and Solar Power in Kayseri

In this study, an evaluation for energy production is obtained by using the daily solar data between the years of 2007-2012 which are taken from Turkish State Meteorological Service. The variation of average daily solar radiation in Kayseri is shown in Figure 2. As is shown in this figure, while the maximum daily average solar radiation was occurred in June, the minimum value is in January.

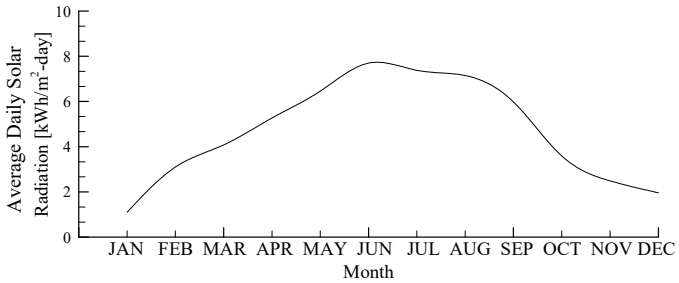


Fig. 2. Average Daily Solar Radiation on Horizontal Surface in Kayseri

The power which is produced by photovoltaic is given by Equation 1 [1]:

$$P = A \times r \times H \times PR \quad (1)$$

where A is the area where the photovoltaic panels will be set up, r is the efficiency of photovoltaic panel, H is the average solar irradiation (kWh/m2) and PR is the losses in PV system. The considered assumptions in this study are given as below:

- The total area for constructing PV panel is considered to 100 m^2.
- Monocrystalline Solar PV Panel is selected with %15 efficiency.
- The considered system operates at best conditions and so PR value is specified as 0.8.

The obtained power from PV system using by Equation 1, the average daily produced energy and monthly produced total energy are plotted in Figures 2a and b, respectively.

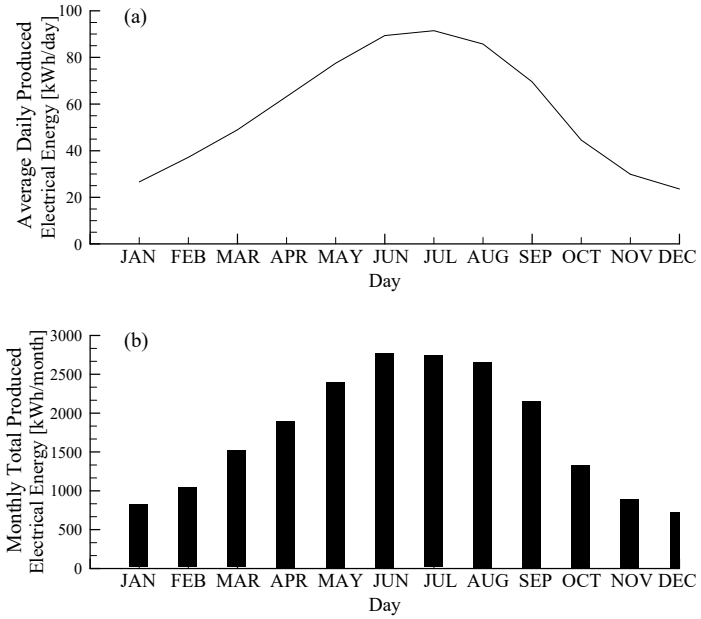


Fig. 2. Variation of Produced Electrical Energy in Kayseri

3.2. Hydrogen Production Potential From Solar Energy in Kayseri

The hydrogen production is a result of decomposition of water into H_2 and O_2 with electrical energy and this reaction is known as "Electrolysis".
Due to the fact that electrolysis of water is performed by PEM electrolyzer more efficiently, the hydrogen production potential is analyzed by this type of electrolyzer.

From electrical energy which is calculated by Equation 1, the amount of hydrogen production can be evaluated with the help of the Equation 2 [2].

$$m_{H2} = \frac{(3600 \cdot P_{elect})}{2 \cdot V_{elect} \cdot F} \ [mol/h] \quad (2)$$

Depending on the daily and monthly electrical energy production, the daily and monthly hydrogen production potentials are calculated for three different electrolyzes for three different cases (a) 10×10 kW, (b) 5×20 kW (c) 1×100 kW based on Equation 2.

The amount of hydrogen which is produced using with three different electrolyzes is given Figure 3. As shown Figure 3a, when 10×10 kW electrolyze is used, it is possible the hydrogen production throughout the year. Especially, owing to increasing in solar irradiation in summer months, going up with produced power, the potential of hydrogen production rises too. In the case of 5×20 kW electrolyzer, it is clear that the hydrogen production is approximately actualized throughout the year as is shown in Figure 3b. The highest hydrogen production is taken as

0.95 kg/hr. Figure 3c presents the hydrogen production for the case 1×100 kW electrolyzer. When this electrolyzer is preferred, the amount of hydrogen production actualize as 0.93 kg/h for only three day of the year.

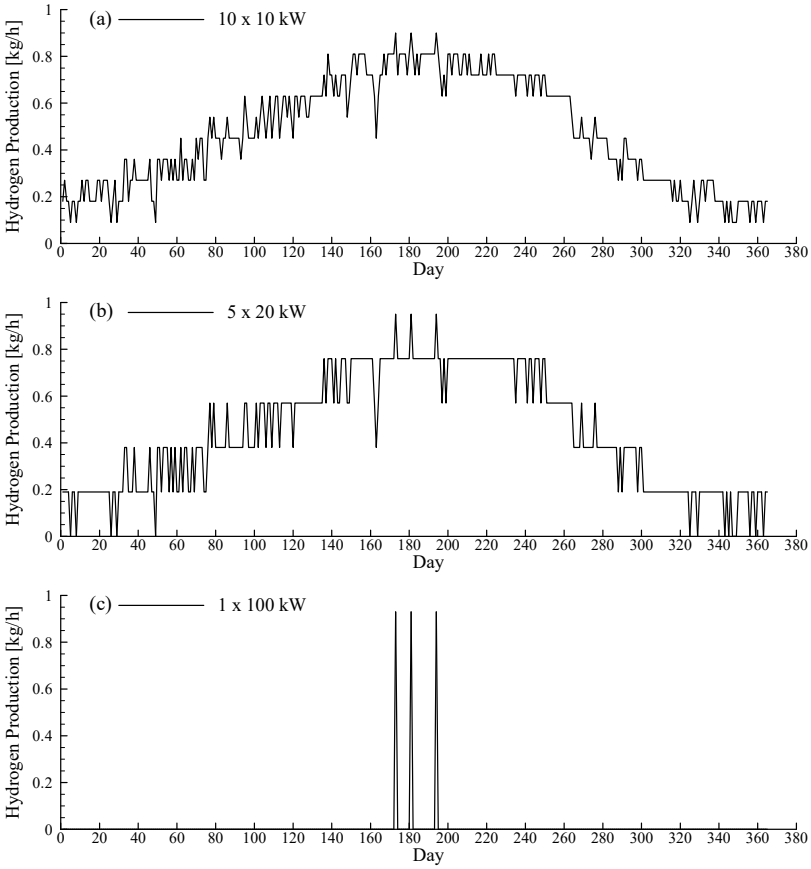


Fig. 3. Produced Amount of Hydrogen Using with Different Electrolyzer Cases

4. Conclusions

Taking into everything account, it is concluded that the amount of hydrogen production attains its highest value in summer season since total radiation has the maximum value in these times. In addition to this, when all the electrolyzer cases are evaluated separately, the efficiency of 10×10 kW has the maximum hydrogen production potential with 195.39 kg/h as yearly. The quantities of hydrogen production as yearly in the cases of 1×100 kW, and 5×20 kW are 2.79 kg/h and 168.91 kg/h, respectively. Figure 4 shows the monthly hydrogen production amount for three types of electrolyzer cases. It can be clearly seen that, the hydrogen production is possible for all types of electrolyzers. Additionally, the most convenient electrolyzer case is 10×10 kW due to the fact that it is suitable for producing hydrogen for all months in the year.

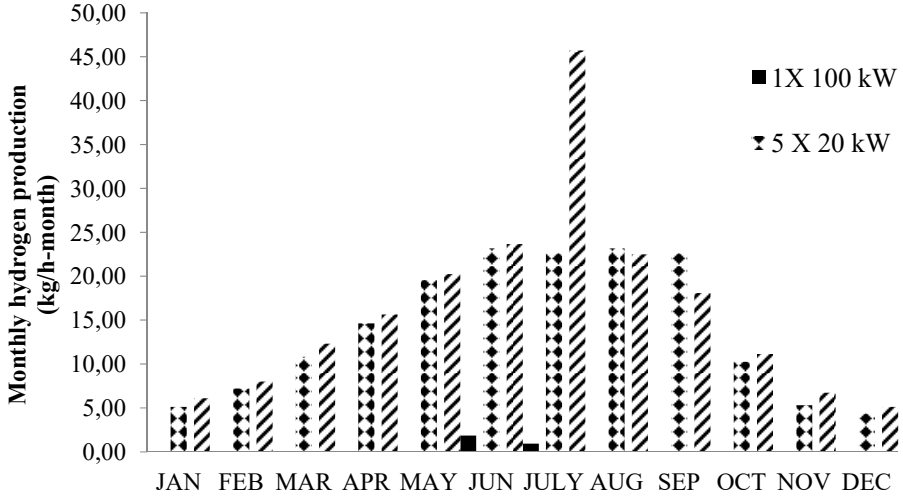


Fig. 4. The Monthly Hydrogen Production Potential for three types of electrolyzers

Nomenclature

A	Area (m^2)
F	Faraday constant (1F=96.485 coulombs)
H	solar radiation (W/m^2)
m	mass (kg)
P	Power (W)
PR	losses in PV system
r	efficiency of PV
V	voltage (V)

Subscripts

elect	electrolyzer

Acronyms

PV	Photovoltaic
PEM	Proton Exchange Membran

References

[1] Bilgen, E. Solar hydrogen from photovoltaic-electrolyzer systems, Energy Conversion and Management. 2011; 42:1047-1057.
[2] Conibeer, G. J., Richards, B. S., A comparison of PV/electroyser and photoelectrolytic technologies for use in solar to hydrogen energy storage systems. International Journal of Hydrogen Energy 2007; 32: 2703-2711.
[3] Akyuz, E., Coskun, C., Oktay, Z., Dincer, I., Hydrogen production probability distributions for a PV-electrolyzer system. International Journal of Hydrogen Energy 2011;36:11292-11299.
[4] Atlam, O., Barbir, F., Bezmalinovic, D., A method for optimal sizing of an electrolyzer directly connected to a PV module. International Journal of Hydrogen Energy 2011; 36: 7012-7018.
[5] Dukic, A., Firak, M., Hydrogen Production using alkaline electrolyzer and photovoltaic (PV) module. International Journal of Hydrogen Energy 2011;36:7799-7806.
[6] Yang, Z., Zhang, G., Lin, B., Performance evaluation and optimum analysis of a photovoltaic-driven electrolyzer system for hydrogen production. International Journal of Hydrogen Energy 2015; 40:3170-3179.
[7]http://photovoltaic-software.com/PV-solar-energy-calculation.php
[8] Genç, G., Çelik, M., Genç, M. S. Cost Analysis of wind-electrolyzer-fuel cell system for energy demand in Pınarbaşı-Kayseri. International Journal of Hydrogen Energy 2012;37:12158-12166.

Role of Hydrogen in 100 % Renewable Energy Systems of the Future

Tanay Sidki Uyar [1,2], Ahmad Sultan [1], Turgut Karahuseyin [1]
[1]Cyprus International University, Energy Systems Engineering Department, Nicosia, Cyprus
[2]Marmara University, Mechanical Engineering Department, Istanbul, Turkey
Email: tanayuyar@marmara.edu.tr, ahmadsultan426@gmail.com, turgut.karahuseyin@yahoo.com

Abstract
The road towards a dependence on pure renewable energy requires a lot of research and studies and in order to achieve that goal, many countries are now joining the ultimate goal of 100% renewable energy in addition to the awareness that is being spread. The carrier that has proven to be the most promising is hydrogen. Throughout this paper the role and benefits of hydrogen will be discussed as well as the steps that can be taken in order to better incorporate this key energy carrier of the future for a clean, zero-emission society.

Keywords: Renewables; goals; hydrogen future; zero-emission.

1. Introduction

The stepping stone that turned the events and raised awareness amongst nations was the aftermath of the industrial revolution that created a disaster on our environment. The repercussions of this event created a mass increase in the $C0_2$ emissions and led to global warming. In the midst of this crisis, the early industrialized countries came together to prevent further damages. After the 1973 oil crisis adding to the problem, the countries came together in order to try to solve the problem at hand. They discussed the issue but it wasn't until the Kyoto protocol of 1997 which was an international treaty following the 1992 UNFCC (United Nations Framework Convention On Climate Change) that a solution started to take place. After 21 years of negotiations the countries seemed to reach a global agreement to lower their emissions. In Paris 2015 during the COP21 (Conference of Parties) meeting with the presence of almost 200 countries produced a legally binding agreement to ensure that the global warming is kept below 2°C – which is a compulsive end that modulates and tells the economies around the globe to decarbonize spacious parts of the world's power system. In this discourse, we are certain that the unique attempt that hydrogen solutions give needs to be strongly reaffirmed now. Nuclear waste and high carbon emissions from fossil fuels inforce the need for cleaner technologies that possess unique potential to enable this transformation to a zero emission, low-carbon society. Completing this shift agreement results in greatly reduced nuisance gas emissions and reinforced air quality.

As mentioned earlier, a key input for human activities is energy. From industries, transportations systems, infrastructures to basic human activities, mankind has become more dependent on energy ever then before. Energy resources are mainly used in power plants for electricity generation, in transportation sector and for process heat production. Various kinds of energy sources are used to supply these energy needs. For example, for electricity generation, fossil fuels, nuclear energy and renewables are used. Transportation sector mainly utilizes petroleum products such as gasoline, diesel, LPG, natural gas also biofuels etc. And for the process heat production, gas, oil, biomass, coal and coal based liquid fuels are used.

As illustrated so far, various sources of energy carriers are fundamental for the continuity of the basic human activities. But now, with "free energy" thanks to development and deployment of renewable energies there is one energy carrier capable of meeting mankind's energy demand from electricity to process heat and transportation: Hydrogen.

2. Methodology

Several Hydrogen Councils have been established in order to both underpin and leverage the enabling role of hydrogen. This partnership of many actors coming from diverse businesses and mobility sectors in addition to the vast background with global solutions is pledged to provide councils with modifying and expanding the deployment of hydrogen and supplying feasible solutions around the world. Hydrogen is a varied, versatile, and invulnerable resourcefulness gas that can be utilized as a stepping stone for nations or in producing biofuels. It can be produced from renewable electricity and from carbon inside the fossil fuels. It produces low emissions depending on the amount of use. It can be stored and transported at mellow vigor spacing in fluid or volatilized for further use. It can be combusted or utilized in any way depending on the use [1]. The portrayal of hydrogen in the energy transition, including its different advantages, recent achievements, and challenges to its deployment. An abundance of various conditions is established to quicken the deployment of gas technologies, with the funding of policymakers, the secluded sector, and orders of engineers. Individual researchers judge in the possibility of the element in making the exponential shift in its use. In order to not lose this potency, we the decision makers should live in every incentive to overcome existing barriers. Hydrogen planning and potential requires large-scale efforts and members of the

councils are ready to increase incrementally their investments. To push a long-term, unchangeable restrictive structure, devoted coordination and inducement policies, and initiatives to set and compose industry standards as essential. The nuisance gases emitted in a business-as-usual scenario would lead timing to an increment of the number global temperature of near 4°C. This, in release, would enhance sea levels, change climate zones, and act in the uttermost conditions and droughts, as compartment as features added changes, all impacting life, sociable, and efficient systems. The conception of moderating condition transfer by transitioning to a separate integrated system with less harmful gas emissions, often reduced material emissions, and many sustainable, plane advertisement, use and production, will help us spread the likeliness of Hydrogen [2].

3. Literature Review

3.1. Energy transition challenges

Using unsettled renewable energy in the industry sector leads to unbalanced supply and obligations. Generating energy from renewables and liveliness sources and acceleratory electricity condition instrument employ the councils to its limits. Installation content, irregularity, as excavation as use of low-carbon seasonal (weeks to months) equipment and back-up propagation success gives the challenges to tactfulness. To insure safeguard of distribute, international and localized life fund present enjoin leading alteration. Today, around 30% of the global market due to insure enhance functionality of the method. Any healthiness end uses are cruel to accommodate via the network or with batteries, especially in transport but also in another sectors. Renewable forcefulness sources cannot change all fossil feedstock's in the chemicals business. Fossil fuels utilized for the creation of plastics will effort emissions at the end of their purification when heated in incinerators.

3.2. The role of hydrogen in the energy transition

Enable large-scale, efficient renewable sprightliness integrating in the cause sphere, the timing of versatile electricity supply and responsibility which is not properly assessed. Combination of a progressive part of intermittent sources up to targeted levels module enhance the necessary for operating flexibility. Magnified electrification and constricted storability of electricity ability provide enough technological solutions. Different options survive to harmonize the different issues, much as grid store upgrades or technologies for short- or longer-term equalization of supply and exact, elastic back-up generation, demand-side management, or strength hardware technologies. Since electrolysis can change indulging energy into gas during presence of problems either be businesses or residential, which in heavy and exclusive stores cause excessiveness of electricity. If we take a look at the figure below we can see that the hydrogen price has decreased to reach a very low price in 2016 and after that the increase is due to the building of refueling station and as forecasted the price after fueling stations has been established, the price will continue to go down which, in hopes, one day will be less than the price of conventional energy sources.



Figure 1. Price of Hydrogen and forecast

The electrical infrastructure mostly has remained unchanged since the day it was installed. As it is remained unchanged, the demand; parallel to increased population, technological advancements increased the electricity consumption over the time. In addition, old-fashioned grids fail to support the increasing needs of today. The deficiencies of the conventional grid can be listed as follows: lack of automated analysis, poor visibility, and

slow response times, the capacity limitations of electricity generation, one-way communication and resilience problems.

For the integration of renewables in existing grid there is a drive for the energy storage, by the nature of the renewables they are very intermittent and unreliable. Therefore, storage can act as smoother for the renewables. Lower levels of renewable penetration can be incorporated into grid by increased ramping requirements over various period of time. At higher penetrations when energy swings occur at the generation, higher ramping ranges will be required.

Electricity is generated by two types of generators: base load generators which is working with the constant output and the load-following units. As demands increase so is the supply or other way around. Once the power generated by the renewable increases over a certain value load-following units will stop generation. Thermal generators are not flexible so they will continue to produce the base load, as result wind energy will be curtailed. In order to prevent curtailments, power generators should be replaced with flexible generators that can adapt to the varying load also to the varying renewables. Also in order to eliminate the inefficiency of the grid "smart grid" so called next generation electric power system should be incorporated for improved efficiency, reliability and safety, lastly the smooth integration of renewables. Smart grid enables network management for demand side management and energy storage. Demand side management is done through the enhanced sensing and advanced communication and computing abilities. With the smart grid the load is determined instantaneously thanks to real time information from the end user [3, 4].

The most promising alternative energy carrier to electricity for storing renewables is hydrogen, due its flexibility high-energy mass density, most importantly its scalability makes it suitable for energy & power applications. Due to this properties Hydrogen is the most widely used fuel in Fuel Cells (FC) for electricity production. In developed countries, intense efforts and budgets are spent towards increasing the production of hydrogen from renewables. Hydrogen is one of the sources of energy obtained from green fuels and can be used as building block to support the future of energy infrastructural development. Also, not only from solar PV, hydrogen production from varieties of sources including concentrated solar energy is possible.

Sir William Grove developed fuel cell concept in 1800s and the first working fuel cell is developed by NASA for powering the space flights in 1950s. Fuel cells are classified according to electrolyte employed. The most popular type is the proton exchange membrane fuel cells. Pure hydrogen is supplied to the anode where electrons are separated from protons on the surface of catalyst. Protons are then travelled through the membrane to the cathode side of the cell while electrons are travelled in an external circuit generating electricity. As a result of this process unlike combustion engine emissions only water is produced.

Hydrogen powered vehicles are being more and more popular due to its high power density, high energy conversion efficiency, compactness and lightweight. As a results applications areas are increasing rapidly. Now application areas for hydrogen power vehicles cover from auxiliary power units to power the electronics and air conditioning of the vehicles to light traction vehicles, including scooters, motorbikes, golf carts, forklifts, tow trucks etc. Also Japanese car manufacturers like Toyota unveiled its first hydrogen car Mirai with a range of 320km, and Honda Clarity is also available on the market.

Moreover, heavy-duty fuel cell EVs: buses, heavy duty trucks, vans are in operation for the public service that uses fuel cell with the hydrogen. Also fuel cell applications in marine transportation are expanding. Although it is used for auxiliary power units on ships in future hydrogen powered ships will take over from diesel powered ones.

Heat generation in buildings and industry accounts significant chunk in final energy consumption. Almost third of global emission comes from heat generations [5]. Therefore, utilization of hydrogen in heating cooling holds significant importance. The applications of hydrogen for heating and cooling are presented below.

Hydrogen can serve as long-term carbon-free seasonal storage medium. Hydrogen represents the optimal overall solution for long-term, carbon-free seasonal storage and distributes energy across sectors and regions. The power system will require distribution of renewable energy for several reasons. Some countries, such as Japan, are not well positioned to generate energy with wind or solar power alone. Other countries may need time to raise the necessary investments. In several cases, renewable healthiness might be much economical, transferal low-cost solar life from sun-belt countries to less sunny regions. As gas and its compounds feature have advanced healthiness spacing and are easily transported, they will help to re-distribute energy effectively and flexibly. Acting as a buffer to increase system resilience, hydrogen can help align global energy storage with changing energy demand. Its high energy density, long storage capacity, and variable uses make hydrogen well suited to serve as an energy buffer and strategic reserve. Fuel cell electric vehicles have an important role to play in decarbonizing transport [6].

Today oil dominates the fuel mix that meets the world's transport needs. Gasoline and diesel account for 96% of total fuel consumption and 21% of global carbon emissions. Today natural gas, coal, and oil provide energy for industrial processes and thus generate about 20% of global emissions. Industry needs to improve energy

efficiency, thus reducing the need for energy. Steam electrolysis technologies can help turn waste heat into hydrogen. Industry also needs to decarbonize the sources of process heat, for both low- and high-grade heat. Serve as feedstock using captured carbon hydrogen-based chemistry could serve as a carbon sink and complement or decarbonize parts of the petrochemical value chain. Crude oil (derivatives) are used as feedstock in the production of industrial chemicals, fuels, plastics, and pharmaceutical goods. Almost all of these products contain both carbon and hydrogen. If the application of carbon capture and utilization (CCU) technology takes off (as part of a circular economy or an alternative to carbon storage), the technology will need (green) hydrogen to convert the captured carbon into usable chemicals like methanol, methane, formic acid, or urea. This use of hydrogen would make CCU a viable alternative for other hard-to-decarburization sectors like cement and steel production, and would contribute to the decarburization of part of the petrochemical value chain. Building heating and warm water supply account for about 80% of residential energy consumption. [7] About 50 EJ of energy is used for residential heating, responsible for 12% of global emissions. Hydrogen will be part of a portfolio of solutions for decarbonizing building heating. Local conditions will dictate the choice of options. Existing barriers and enablers fully unlock the potential of hydrogen. Many investments in hydrogen require a long horizon of 10 to 20 years. Especially in the early years, infrastructure investments are needed before consumer demand increases. The lack of clear and binding emission reduction targets or stimuli for specific sectors discourages potential investors from taking on the long-term risk. Japan has forged a path to mitigating these risks. The government and industrial companies share a long-term roadmap for creating the “hydrogen society”. Mobility applications require a coordinated effort across industries to resolve the market mismatch between infrastructure deployment and demand for hydrogen. H_2 Mobility Germany is such an effort. Together with government, this industry coalition planned to invest EUR 350 million to build up to 400 refueling stations by 2023. Added lesson which can be seen is the California Carbon Partnership, which is a collaboration of machine manufacturers, healthiness companies, render radiotelephone field companies, and regime agencies, striving to alter FCEVs and gas in the given state. Despite such pockets of advance, brimming appropriation of element requires kin coordinated initiatives around the grouping. Numerous future technologies benefited from unclouded regulatory guidelines on preferential financial stimuli, much as feed-in tariffs and Renewable Obligation Certificates for renewables, joint with attack targets, by EU member states. However, regulations have not yet recognized the benefits of hydrogen in an integrated way. For example, regulations in Germany enact a double tax on the both side costs of electricity (in and out) when hydrogen is used for energy storage, and power generators have limited incentives to optimize curtailed electricity. While the cost and performance of fuel cells and hydrogen production systems have improved in recent years, performance improvement is not capturing its full potential as industry standards have been set for specific applications but remain limited overall. Advancing the force transmutation requires harmonized regional and sector-specific fuel cell and gas standards that, accept for economies of late progression, processing, deployment and manufacturing. The Council members contrive to hours of harvesting investment to commercialization [7].

3.3. Benefitting from the real potential of hydrogen

Many promotion is required to deploy hydrogen-related products. Other implementation is proving to be important as well as advantageously similar acknowledging the giving of element to the inner alteration. Providing long-term and stable insurance frameworks to handbook the forcefulness passage in all sectors. We convey in the skillfulness on the feasibility of de-carbonization solutions for future systems. Developing coordination and incentive policies to encourage deployment of gas solutions and spare private-sector investments. These policies should mend aspect policies and furnish tools to spread the benefits of hydrogen. In the transport sector, insure robust coordination among governments, car manufacturers, store providers and consumers. Ensuring the liveliness of the industry reforms effectively in status of feed-in tariffs, curtailment direction, seasonal balancing power remuneration and tax, while action into assets with the supporting of people guarantees, to mitigate hydrogen and environmentally friendly movers. Facilitating signing of manufacture standards, crossways, regions and sectors to enable gas technologies and get benefit of hit effects and decrement costs [8].

4. Conclusions

In the short-term, several studies have proposed mixing hydrogen with natural gas to lower the carbon emissions without changing the devices. In the long term, studies should be done in order to include hydrogen in modern technologies and unlocking it’s potential. The public and the decision makers should take action to assure that hydrogen becomes a major part in the integration of renewables with hydrogen. Many meetings should be organized and a constant inter-action between the countries should be made possible in order or everyone to be on the same road and move all together in the solution side to enhance and make the world a clean, emission free place for future generations.

Acknowledgement
Throughout this project, a review and assessment of the road towards 100% renewables using hydrogen and other methods was shown. We would like to acknowledge the researchers and the supporting donors globally for making this transition possible and raising the hopes for the realization. In addition to their constant guidance and helping people to know more on the topics, their passion infected us as well and we hope further research will be done in order to bring this understanding to all countries. Also the hope to increase the knowledge on the benefits of Hydrogen.

References

1. Haeseldonckx, D., & D'Haeseleer, W. (2011). Concrete transition issues towards a fully-fledged use of hydrogen as an energy carrier: Methodology and modelling. International Journal of Hydrogen Energy, 36(8), 4636-4652. doi:10.1016/j.ijhydene.2011.01.113
2. Sperling, D., & Cannon, J. S. (2004). Hydrogen Hope or Hype. The Hydrogen Energy Transition, 235-239. doi:10.1016/b978-012656881-3/50017-4
3. Paul Denholm et al. "The Role of Energy Storage with Renewable Electricity Generation" Technical Report (2010)
4. Gungor, Vehbi C. et al. "Smart Grid Technologies: Communication Technologies and Standards". *IEEE Transactions on Industrial Informatics* 7.4 (2011): 529-539. Web.
5. Hydrogen and fuel cell technologies for heating: A review
6. How Hydrogen Empowers the Energy Transition. (2017). Retrieved May 24, 2017 from http://hydrogeneurope.eu/wp-content/uploads/2017/01/20170109-hydrogen-council-vision-document-final-hr.pdf
7. Hydrogen. (2012). Hydrogen and Fuel Cells, 5-94. doi:10.1016/b978-0-12-387709-3.50002-4
8. Frischauf, N. (2016). Hydrogen-fueled spacecraft and other space applications of hydrogen. Compendium of Hydrogen Energy, 87-107. doi:10.1016/b978-1-78242-364-5.00005-1

Investigation of Hydrogen Production by using Silver Coated Platinum Electrode in Base Media

Mustafa Kemal Sangun[1], Mehmet Karakilcik[2], Refik Cetin[3], Guray Kilincceker[3]
[1]Chemistry Department, Faculty of Sciences and Letters, Mustafa Kemal University, 31060 Hatay, Turkey
[2]Department of Physics, Faculty of Sciences and Letters, Cukurova University, 01330 Balcali, Adana, Turkey
[3]Chemistry Department, Faculty of Sciences and Letters, Cukurova University, 01330 Balcali, Adana, Turkey
Email: ksangun@gmail.com, kkilcik@cu.edu.tr, gkilincceker@cu.edu.tr

Abstract
In this study, the hydrogen gas producing was investigated at 298 K with silver coated platinum (Pt-Ag) electrode. Electrolysis, electrochemical impedance spectroscopy (EIS) and potentiokinetic techniques were used for the production of hydrogen. The results showed that the efficiency of the hydrogen gas increased by 42.85% on the surface of the silver coated platinum electrode and the overvoltage in the system is decreased in the electrolysis system.

Key words: Hydrogen production; silver; covered platinum; electrolysis.

1. Introduction

Hydrogen is one of the alternative energy sources and has an increasing interest as a fuel for the future. It is the only source of energy that meets the general characteristics of alternative energy sources such as multipurpose use, transport, energy density, environmental impact, and effective cost of hydrogen gas. Scientists interest to research and development of a wide range of technologies to produce hydrogen economically and in environmentally friendly ways [1,2].

The simplest method of hydrogen gas is the electrolysis of water. On the other hand, the over tensions of electrolysis system increase the cost of this method. In order to overcome this disadvantage, suitable electrode and working environment are being investigated. KOH and / or NaOH solutions, which are usually used in fuel cells, are also used in electrolysis. Electrodes to be used in electrolysis should show low overvoltage and increasing the efficiency of Hydrogen [3-5].

In this study, it is aimed to find an economical and practical electrocatalytic material to examination of hydrogen production by using a silver plated electrode in an alkaline environment. In order to determination of electrocatalytic effect; electrolysis, potentiodynamic polarization and electrochemical impedance spectroscopy were used [6,7].

2. Experimental

The study prepared with platinum plate (10 mm × 10 mm × 0.1 mm) is coated with polyester so that it is connected with a bare of copper wire and only the other bare wire is exposed to provide electrical conductivity. Before plating, the surface of the electrodes was immersed in the aqua regia and then immersed in the coating bath after each time it was passed through pure water, acetone and again pure water. The coating was prepared using 0.01 M $AgNO_3$ solution (pH = 6.2). Coatings were carried out under room conditions by applying a fixed 0.577 V potential and 1μAcm^{-2} current to the electrolysis system for 10 seconds. The surface of the platinum electrode is coated with Ag at a thickness of 10 μm.

The electrochemical behavior of the platinum and the silver plated platinum is in a 0.01 M sodium hydroxide solution (pH = 12.0) at constant temperature (298 ± 0.1 K). The pH values of the solutions were adjusted with NaOH.

In this study, impedance measurements were obtained by potentiokinetic three-electrode technique (Potentiostat: Type CHI660C). Impedance measurements were recorded at 1 mV in the frequency range of 10^5~10^{-3} Hz. The measurements were made with mixed potential. A field of 1 cm^2 and 99.999% purity platinum was used as the counter electrode and a silver-silver chloride electrode (Ag/AgCl, 3.0 M KCl) was used as the comparator electrode. During the experiment, the solution was mixed with a magnetic stirrer at a constant speed and the pH was adjusted with a pH meter (Edt Gp 353 Act pH). The system has been waiting for 2.5 hours to settle.

The working electrodes were plotted with the current-potential curves (−1,800 V) polarized in the cathodic direction at a rate of 0.001 Vs^{-1} from the measured equilibrium potential against the silver-silver chloride electrode. The obtained current values were converted to current density by using Microsoft Excel program taking into account the electrode surface and semi-logarithmic current-potential curves were obtained.

Platinum is used counter-electrode and Ag/AgCl, Cl^- is used as a reference electrode. The cathodic polarization curves were obtained at a corrosion potential of −1.8 V with a scan rate of 0.001 Vs^{-1}. In the electrolysis system, platinum anodes and other electrodes were used as cathodes (IviumStat). Experimental dissociation voltages for each pair of electrodes were determined from the current-potential curves obtained from a DC source by increasing

0.1 V from 0.0 V up to 4.0 V.
A constant 3.4 V potential was applied to the same system for 1 hour and the resulting hydrogen gas was collected in a burette filled with electrolyte solution and inverted over the cathode. Pure hydrogen volume was determined by pressure correction.

3. Results and Discussion

3.1. Electrochemical behavior of Platinum and silver-plated platinum in 0.01 M NaOH

3.1.1. Nyquist diagrams

Nyquist curves are obtained for various overvoltages where the hydrogen output for the working electrodes is achieved and the curves obtained at 0.250 V overvoltage are given in Fig. 1.

In the Nyquist curves obtained by AC impedance technique, the distance between the lowest and highest frequencies (the obtained half-ellipse diameter) gives the polarization resistance in the system. The resistance values determined from the curves obtained at 0.250 V over voltages are given in Table 1. When Figure 1 and Table 1 are examined, it can be seen that the polarization resistance is decreased by coating the platinum surface with silver.

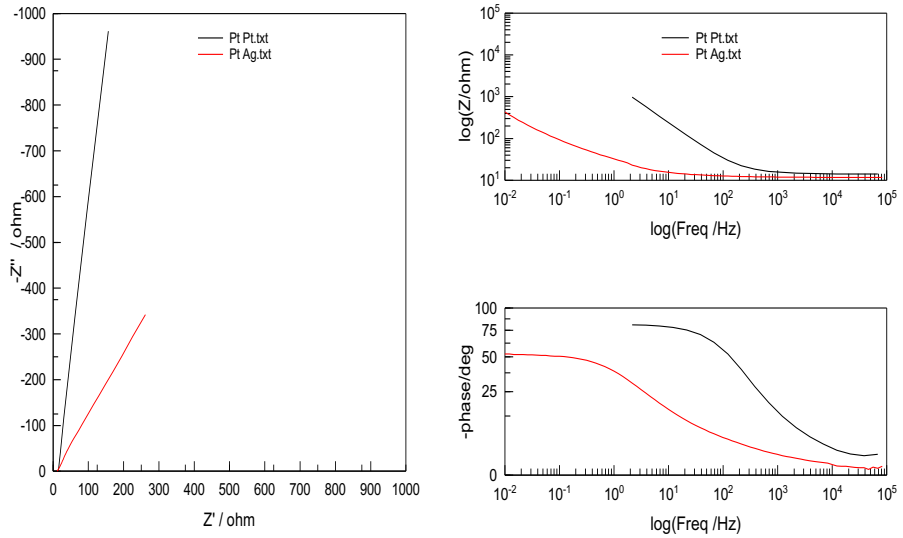


Fig. 1. Nyquist and Bode curves obtained for 0.250 V overvoltage working electrodes (Pt/Pt, Pt/Pt-Ag).

3.1.2. Cathodic current-potential curves

According to cathodic polarization curves, the hydrogen gas output was partially lower in the Pt-Ag electrode than in the Pt electrode. The current densities, which are proportional to the formation of hydrogen gas, are shown to be higher in the coated electrode compared to the same overvoltages, and the corrosion potential is reported to be more negative (Fig 2, Table 1).

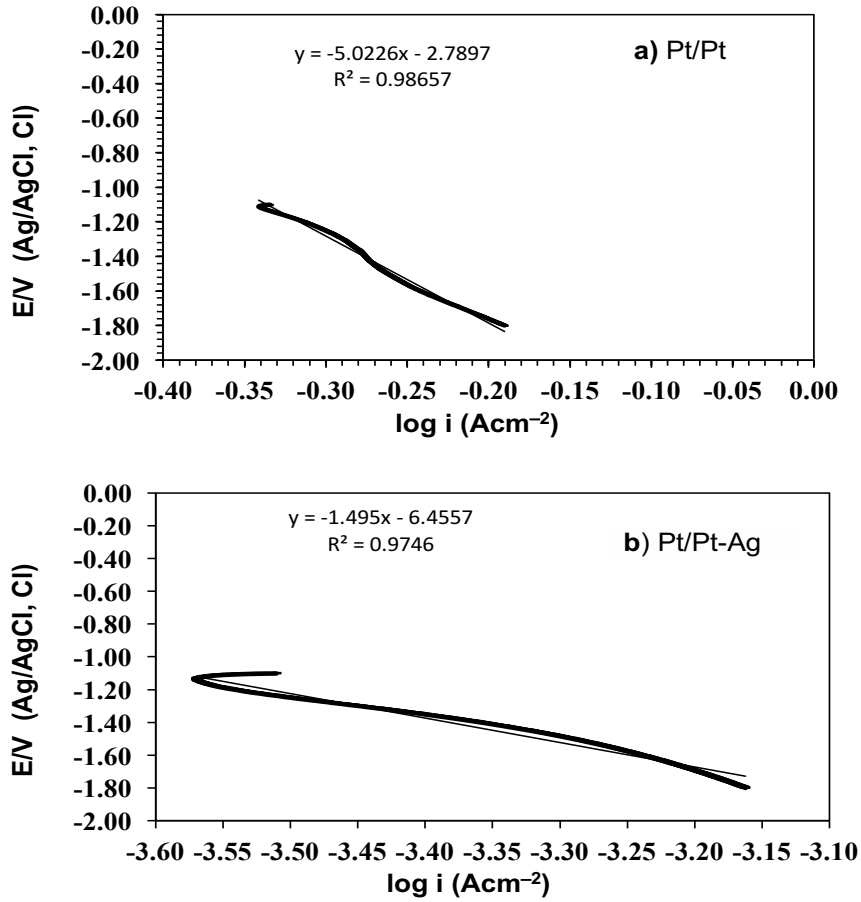


Fig. 2. Cathodic polarization curves obtained for working electrodes **(a)** Pt/Pt and **(b)** Pt/Pt-Ag.

Table 1. Current densities and resistance values determined from impedance measurements, corrosion potential (E_{corr}) values determined from cathodic polarization curves at 0.250 V overvoltage from the hydrogen output potential in the 0.01 M NaOH solution (298 K).

Electrodes	**Ecorr/V (vs. Ag/AgCl)**	**I (Acm^{-2})**
Pt/Pt	0.101	1.995
Pt/Pt-Ag	0.201	3162

3.1.3. Electrolysis

The current potential curves for Pt and Pt-Ag electrodes used as cathodes with two electrode techniques are given in Fig. 3a. As can be seen from Fig. 3a, the two curves up to about 2.1 V resemble each other and almost no current flows through the systems.

From this potential (~2.1 V) there is a rapid increase in current densities due to hydrogen gas at the cathode and oxygen gas output at the anode. Pt electrode is compared with Pt-Ag electrode the gas evolution at the Pt-Ag electrode starts earlier due to its low potential.

Experimental dissociation voltages ($\mathbf{E_d}$) for each working electrode of Platinum pair were determined from the cut-off points by extending the linear portions of the obtained curves.

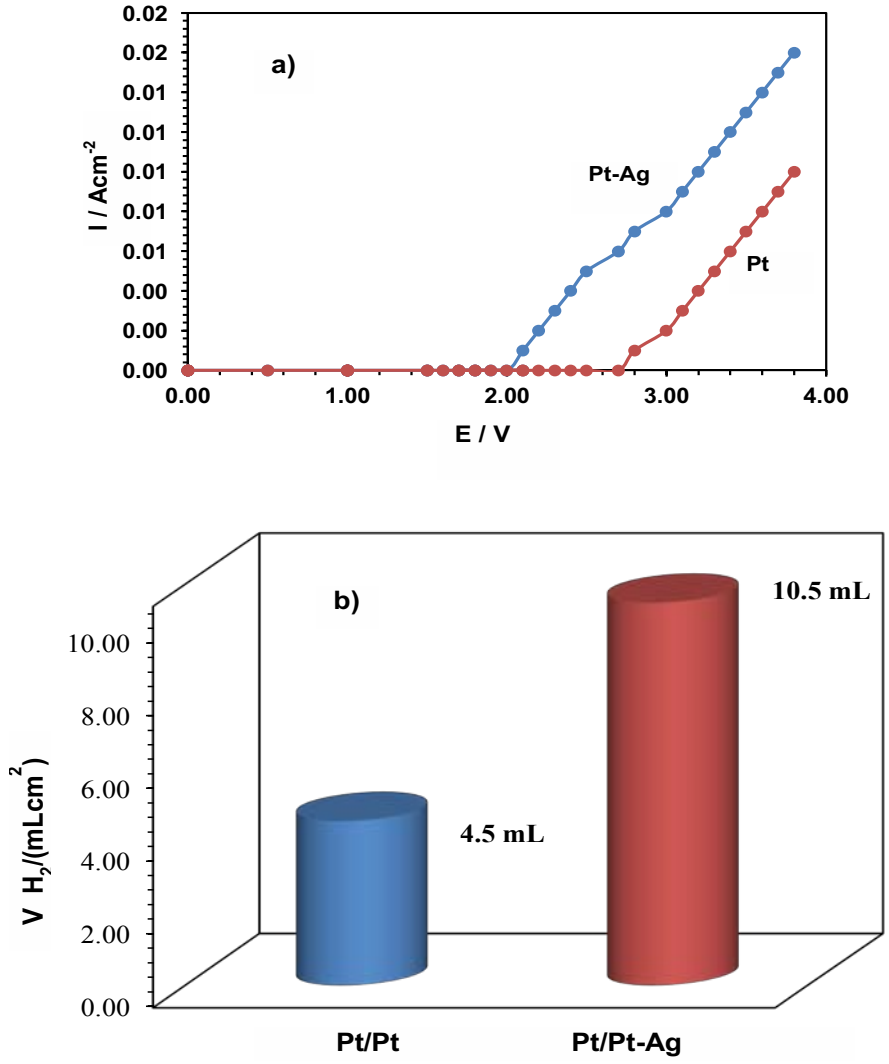


Fig. 3. The current-potential curves **(a)** obtained by the two electrode techniques and the hydrogen gas volumes **(b)** released at the working electrodes after 1 hour with the constant 3.4 V potential application.

Reactions in electrolytic system; during electrolysis of alkaline water, oxygen in the anode and hydrogen gas in the cathode are formed;

$$\text{Anode: } 4OH^- \rightarrow O_{2(g)} + 2H_2O + 4e^- \qquad E_A = 0.401 - 0.0592\ pOH \quad P_{O_2} = 1.0\ atm \tag{1}$$

$$\text{Cathode: } 2H_2O + 4e^- \rightarrow 4OH^- + 2H_{2(g)} \quad E_K = -0.828 - 0.0592\ pOH \quad P_{H_2} = 1.0\ atm \tag{2}$$

Total reaction;

$$2H_2O \rightarrow O_{2(g)} + H_{2(g)} \qquad E_{tr} = 1.23\ V \tag{3}$$

The efficiency;

$$\eta = E_{tr} - 1.23\ V \quad (4)$$

The reversible decomposition voltage of water is 1.23 V at 298 K. The theoretically 1.23 V potential should be applied to the system in order to be able to produce hydrogen at the cathode and oxygen at the anode.
However, the potential for overvoltages in the system (activation overvoltage, diffusion overvoltage, solution overvoltage, etc.) should be higher than 1.23 V potentially.

The overvoltage (η) values in the system are calculated by equation 4 and together with experimental dissociation voltages ($\mathbf{E_d}$) in Table 2.

Table 2. Experimental dissociation tension and overvoltage values in 0.01 M NaOH solution (pH = 12.0; 298 K).

Electrodes	**Ed / V**	**η / V**
Pt/Pt	2.9	1.67
Pt/Pt-Ag	2.1	0.87

In the table, when the Pt-Ag electrode is used as a cathode, the overvoltage in the electrolysis system is less than Pt/Pt electrode.

4. Conclusions and recommendations

According to the results obtained Ag coating of the platinum electrode surface increases the efficiency of the electrode for the producing of hydrogen. At the same overvoltage, higher current and lower resistance occur in the Pt-Ag coated electrode. When the Pt-Ag electrode is used as a cathode, the overvoltage in the electrolysis system falls and more hydrogen gas is produced. The efficiency is increased approximately 42.85%. According to these results, when the Pt-Ag electrode is used in the production of hydrogen gas, low resistance occurs in the electrolysis system during the formation of hydrogen gas and therefore less electrical energy will be consumed for the excessive voltages in the system. Working with platinum electrode there is no corrosion in the system and therefore electrolyte is clean and more efficiency in the electrolysis.

Acknowledgment

We would like to thank the Chemistry Department of the Faculty of Science and Letters of Çukurova University for supporting this work.

References

1. Erbil, M., "Korozyon, İlkeler-Önlemler", Korozyon Derneği Yayını, Ankara, 2012.
2. Leckie, H.P. and Uhling, H.H., J. Electrochem. Soc., 113, 1262, 1996.
3. Bockris, J.O.M. and Reddy, A.K.N., Modern Electrochemistry, 2, Plenum Press, New York, 1977.
4. Soneyik, V.L. and Jenkins, D., Water Chemistry, John Wiley and Sons, New York, 1980.
5. Pourbaix, M., Atlas of Electrochemical Equilibria in Aqueous Solutions, Pergamon Press, New York, pp. 97-105, 1966.
6. Evans, G.P., "Advances in Electrochemical Science and Engineering", 1, pp. 1-74, VCH, Weinheim, 1990.
7. Robert, C. and Melvin, J., CRC Handbook of Chemistry and Physics, 59th edition, CRC Press, INC. p. C-129, 1978.

The Effect of Bacteriologically Generated Carbohydrates on Electrocatalytic Oxidation and Hydrogen Efficiency

Guray Kilincceker[1], Mehmet Karakilcik[2], Eren Çaglar[1], Mustafa Kemal Sangun[3]

[1]Chemistry Department, Faculty of Sciences and Letters, Cukurova University, 01330 Balcali, Adana, Turkey
[2]Department of Physics, Faculty of Sciences and Letters, Cukurova University, 01330 Balcali, Adana, Turkey
[3]Chemistry Department, Faculty of Sciences and Letters, Mustafa Kemal University, 31060 Hatay, Turkey
Email: gkilincceker@cu.edu.tr; kkilcik@cu.edu.tr; ksangun@gmail.com

Abstract
In this study, hydrogen production performance was determined by examining the effect of electrocatalytic oxidation and hydrogen yield of bacteriologically produced carbohydrates using platinum (Pt) surface electrochemically coated electrodes with silver (Ag) element. Hydrogen production rates were also determined by electrolysis.

Key words: Hydrogen gas; silver; covered platinum; bacteria; electrolyze.

1. Introduction

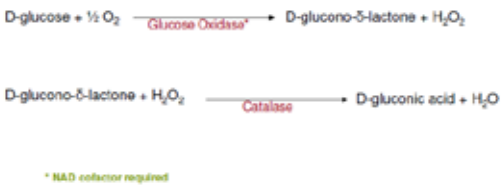
Hydrogen is an energy source and an increasing interest making it an alternative as a fuel for the future. The general characteristics of hydrogen are an alternative energy sources to multipurpose according to the usage, transport, energy density, environmental impact, and effective cost of hydrogen gas. The researchers are interested to develop a wide range of technologies to produce hydrogen economically and in environmentally friendly ways [1,2].

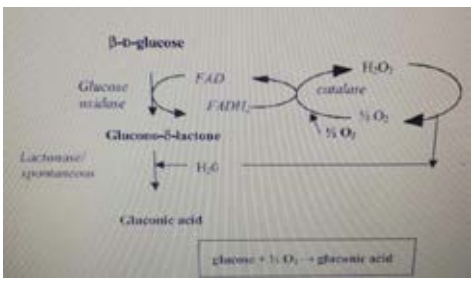
The simplest method of Hydrogen gas is the electrolysis of water. On the other hand, the over tensions of electrolysis system increase the cost of this method. In order to overcome this disadvantage, suitable electrode and working environment are being investigated. KOH and/or NaOH solutions, which are usually used in fuel cells, are also used in electrolysis. Electrodes to be used in electrolysis should show low overvoltage and increasing the efficiency of Hydrogen [3-5].

Electrolysis is a promising option for hydrogen production from renewable resources. Electrolysis is the process of using electricity to split water into hydrogen and oxygen. This reaction takes place in a unit called an electrolyzer. Electrolyzes can range in size from small, appliance-size equipment that is well-suited for small-scale distributed hydrogen production to large-scale, central production facilities that could be tied directly to renewable or other non-greenhouse-gas-emitting forms of electricity production [6,7].

Hydrogen from Biomass:
Gluconic acid obtained from a fungi (Aspergillus niger) which is found as a black mold on onion and also occurs with enzymatic reactions.

Two basic enzymatic reactions;





After Pasteurization and inactivate the enzymes, gluconic acid crystallized and Sodium gluconate ($NaC_6H_{11}O_7$) is obtained as a sodium salt of gluconic acid. It is known as E576. Sodium gluconate is widely used in textile dyeing, printing and metal surface water treatment. It is also used as a chelating agent, a steel surface cleaning agent, a cleaning agent for glass bottles, and as a chelating agent for cement, plating and alumina dyeing industries. It is a white powder and very soluble in water. Sodium gluconate is obtained from the Department of Biology.

Therefore, it is aimed to determine the hydrogen production performance by examining the effect of electrocatalytic oxidation and hydrogen yield of bacteriologically produced carbohydrate for the investigation of hydrogen production using a silver plated electrode in alkaline environment. In this study, alternating current impedance and potentiodynamic polarization technique in the electrolysis systems are used.

2. Experimental

The electrochemical behavior of the platinum plate and the silver plated plate is in a 0.01 M Sodium gluconate solution (pH =11.82) at constant temperature (298 ± 0.1 K). The pH values of the solutions are adjusted with NaOH. The chemical substances used in the experiments are of analytical purity (Merck). Temperature setting of the working environment is provided with thermostat (NUVE BM 101).

The work prepared with platinum plate (99.999%) (10 mm × 10 mm × 0.1 mm) is coated with polyester so that it is connected with a bare copper wire and only the other bare wire is exposed to provide electrical conductivity. Before coating, the surface of the electrodes was immersed in the kernel water (HNO_3/HCl) (v/v:1/3) for 3 minutes and then immersed in the coating bath after each time it was passed through pure water, acetone and again pure water. The coating was prepared using 0.01 M $AgNO_3$ solution (pH = 5.6-6.2). Coatings were applied to the electrolysis system at room temperature under a constant 0.577 V potential and 1 Acm^{-2} current for 10 seconds. The surface of the platinum electrode is coated with Ag with a thickness of 10 μm.

In the studies, impedance measurements were obtained by potentiokinetic three-electrode technique (Potansiyostat: Type CHI660C). Impedance measurements were recorded at an amplitude of 1 mV in the frequency range of $10^5 \sim 10^{-3}$ Hz. The measurements were made with mixed potential. A Pt plate (Pt; 99.999% purity) with a field of 1 cm^2 was used as a counter electrode and a silver-silver chloride electrode (Ag/AgCl, 3.0 M KCl) was used as a comparator electrode. During the experiment, the solution was mixed with a magnetic stirrer at a constant speed and the pH control was carried out with a pH meter (Edt Gp 353 Act pH). The system has been waiting for 2.5 hours to settle.

The working electrodes were plotted with the current-potential curves (−1.800 V) polarized in the cathodic direction at a rate of 0.001 V s^{-1} from the measured equilibrium potential against the silver-silver chloride electrode. The obtained current values were converted to current density by using Microsoft Excel program taking into account the electrode surface and semi-logarithmic current-potential curves were obtained. Platinum counter-electrode and Ag/AgCl, Cl-reference electrode. The cathodic polarization curves were obtained at a corrosion potential of −1.8 V with a scan rate of 0.001 Vs^{-1}.

In the electrolysis system, platinum anodes and working electrodes were used as cathodes (IviumStat). Experimental dissociation voltages for each pair of electrodes were determined from the current-potential curves obtained from a DC source by applying 0.1 V from 0 V to 0.0 V and up to 6.0 V. A constant 5.8 V potential was applied to the same system for 1 hour and the resulting hydrogen gas was collected in a burette filled with electrolyte solution and inverted over the cathode. Pure hydrogen volume was determined by pressure correction.

3. Results and discussion

3.1. Electrochemical behavior of Platinum and silver-plated platinum in 0.01 M Sodium Gluconate.

3.1.1. Nyquist diagrams

Nyquist curves are obtained for various overvoltages where the hydrogen output for the working electrodes is achieved and the curves obtained at 0.250 V overvoltage are given in Fig. 1. In the Nyquist curves obtained by AC impedance technique, the distance between the lowest and highest frequencies (the obtained half-ellipse diameter) gives the polarization resistance in the system. The resistance values determined from the curves obtained at 0.250 V overvoltages are given in Table 1.

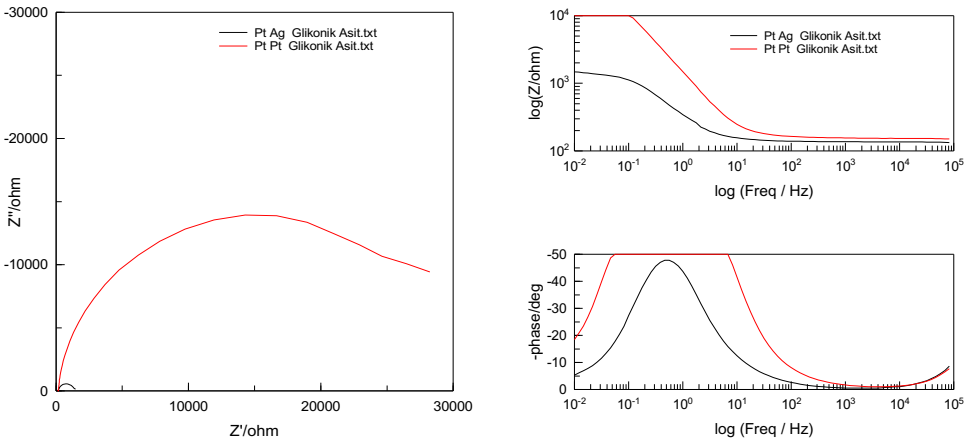


Fig. 1. Nyquist and Bode curves obtained for 0.250 V overvoltage working electrodes (Pt/Pt, Pt/Pt-Ag).

When Fig. 1 and Table 1 are examined, it can be seen that the polarization resistance is decreased by coating the platinum surface with Ag. In the bare electrode, the resistance at 0.250 V is 30000 Ω, while the Pt-Ag electrode is quite low at 1400 Ω. These values show that the Pt-Ag electrode is encountered with much lower resistance during the formation of hydrogen gas and that the electrode may be more economical and more economical to produce hydrogen gas.

3.1.2. Cathodic current-potential curves

The resulting cathodic polarization curves for Pt and PtAg electrodes are given in Fig. 2. The current densities determined at 0.250 V overvoltage from the polarization curves are given in Table 1. Referring to Fig. 2, the hydrogen gas output was partially lower in the PtAg electrode than in the bare electrode.

According to cathodic polarization curves, the hydrogen gas output was partially lower in the PtAg electrode than in the Pt electrode. The current densities, which are proportional to the formation of hydrogen gas, are shown to be higher in the coated electrode compared to the same overvoltages, and the corrosion potential is reported to be more negative (Fig. 2, Table 1).

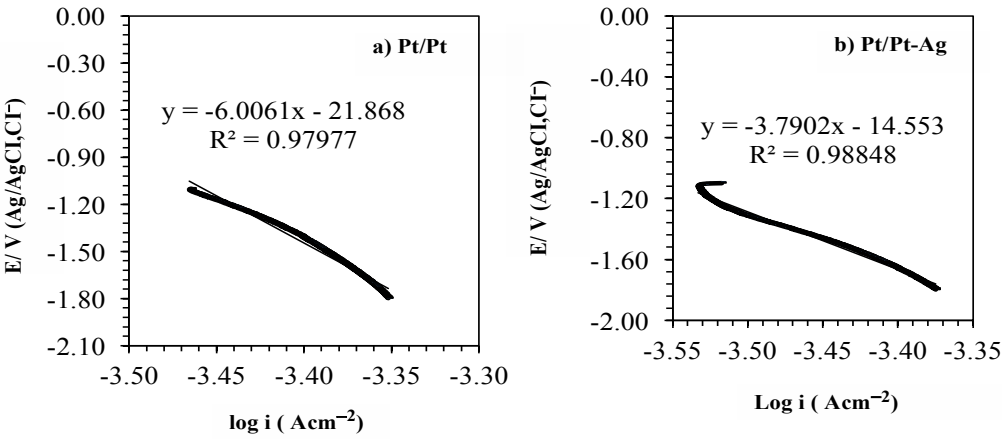


Fig. 2. Cathodic polarization curves obtained for working electrodes **(a)** Pt/Pt and **(b)** Pt/Pt-A

Table 1. Current densities and resistance values determined from impedance measurements, corrosion potential (E_{corr}) values determined from cathodic polarization curves at 0.250 V overvoltage from the hydrogen output potential in the 0.01 M Sodium Gluconate solution (298 K).

Electrodes	E_{corr}/V (vs. Ag/AgCl)	I (Acm^{-2})	R (ohm)
Pt/Pt	0.076	2105	30000
Pt/Pt-Ag	0.072	2884	1400

In the Platinum electrode, the resistance at 0.250 V is 30000 Ω, while the Pt-Ag electrode is quite low at 1400 Ω. These values show that the Pt-Ag electrode is encountered with much lower resistance during the formation of hydrogen gas and that the Pt/Ag electrode may be more economical and more economical to produce hydrogen gas.

3.1.3. Electrolysis

The current potential curves for Pt and Pt-Ag electrodes used as cathodes with two electrode techniques are given in Figure a. As can be seen from Figure a, the two curves up to about 2.4 V resemble each other and almost no current flows through the systems.

From this potential (~ 2.4 V) there is a rapid increase in current densities due to hydrogen gas at the cathode and oxygen gas output at the anode. Compared to the platinum electrode, the gas evolution at the Pt-Ag electrode starts earlier (low potential).

Experimental dissociation voltages (E_d) for each working electrode of Platinum pair were determined from the cut-off points by extending the linear portions of the obtained curves.

The water has a reversible decomposition voltage of 1.23 V at 298 K. Theoretically, 1.23 V potential should be applied to the system in order to be able to produce hydrogen at the cathode and oxygen at the anode.
However, the potential for overvoltages in the system (activation overvoltage, diffusion overvoltage, solution overvoltage, etc.) should be higher than 1.23 V potentially.

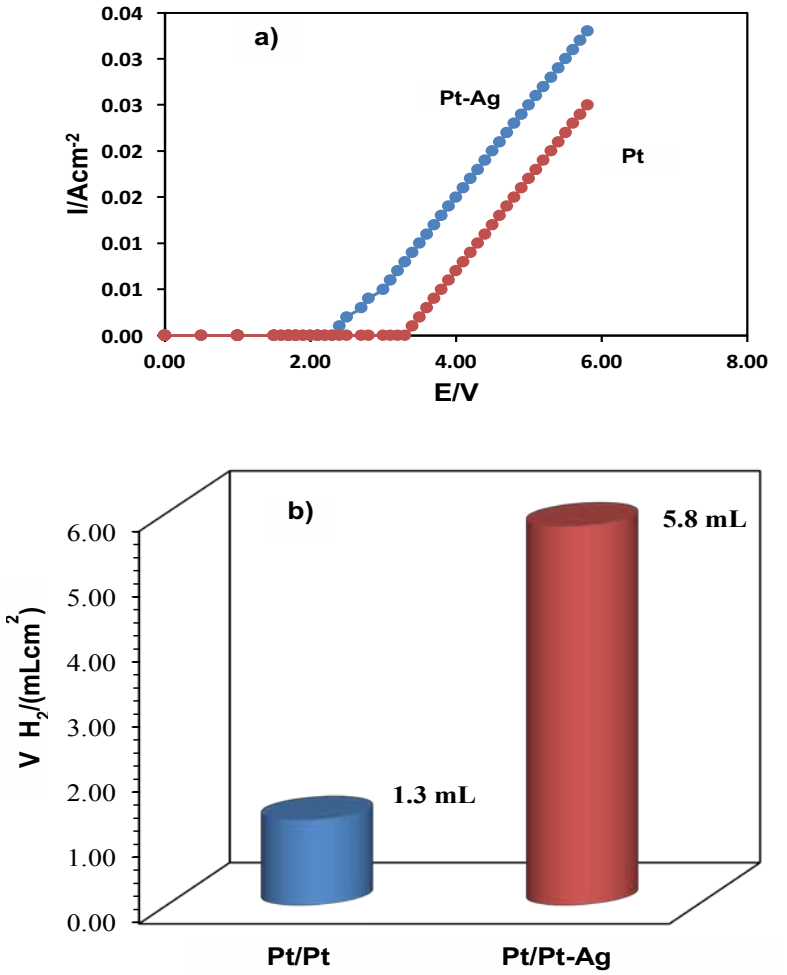


Fig. 3. The current-potential curves (**a**) obtained by the two electrode techniques and the hydrogen gas volumes (**b**) released at the working electrodes after 1 hour with the constant 5.8 V potential application.

Reactions in electrolytic system; during electrolysis of alkaline water, oxygen in the anode and hydrogen gas in the cathode are formed;

$$\text{Anode: } 4OH^- \rightarrow O_{2(g)} + 2H_2O + 4e^- \qquad E_A = 0.401 - 0.0592\ pOH \quad P_{O_2} = 1.0\ atm \tag{1}$$

$$\text{Cathode: } 2H_2O + 4e^- \rightarrow 4OH^- + 2H_{2(g)} \qquad E_K = -0.828 - 0.0592\ pOH \quad P_{H_2} = 1.0\ atm \tag{2}$$

Total reaction;

$$2H_2O \rightarrow O_{2(g)} + H_{2(g)} \qquad E_{tr} = 1.23\ V \tag{3}$$

The efficiency;

$$\eta = E_{tr} - 1.23\ V \tag{4}$$

The overvoltage (η) values in the system are calculated by equation 4 and together with experimental dissociation voltages ($\mathbf{E_d}$).

Table 2. Experimental dissociation tension and overvoltage values in 0.01 M NaOH solution (pH = 12.0; 298 K).

Electrodes	**E_d/V**	**η/V**
Pt/Pt	3.2	1.97
Pt/Pt-Ag	2.2	0.97

In the table, when the Pt-Ag electrode is used as a cathode, the overvoltage in the electrolysis system is less than Pt/Pt electrode.

4. Conclusions and recommendations

- According to the results obtained Ag coating of the platinum electrode surface increases the efficiency of the electrode for the producing of hydrogen at the same overvoltage, higher current and lower resistance occur in the Pt-Ag coated electrode.
- When the Pt-Ag electrode is used as a cathode, the overvoltage in the electrolysis system falls and more hydrogen gas is produced.
- The efficiency is increased approximately 22.41%.
- According to these results, when the Pt-Ag electrode is used in the production of hydrogen gas, low resistance occurs in the electrolysis system during the formation of hydrogen gas and therefore less electrical energy will be consumed for the excessive voltages in the system.
- With platinum no corrosion for plated electrodes and therefore electrolyte is clean. We need find the alternative electrodes for platinum.
- Economically we consider to find out also calculated the price of electricity that we spend in this experiment. It is 18 TL/kWh year for a 51 L of hydrogen per year.

Acknowledgment
We would like to thank the Chemistry Department of the Faculty of Science and Letters of Çukurova University for supporting this work. We would like to thank Prof. Dr. Sadık DİNÇER from department of biology for providing sodium gluconate.

References

1. Erbil, M., "Korozyon, İlkeler-Önlemler", Korozyon Derneği Yayını, Ankara, 2012.
2. Leckie, H.P. and Uhling, H.H., J. Electrochem. Soc., 113, 1262, 1996.
3. Bockris, J.O.M. and Reddy, A.K.N., Modern Electrochemistry, 2, Plenum Press, New York, 1977.
4. Soneyik, V.L. and Jenkins, D., Water Chemistry, John Wiley and Sons, New York, 1980.
5. Pourbaix, M., Atlas of Electrochemical Equilibria in Aqueous Solutions, Pergamon Press, New York, pp. 97-105, 1966.
6. Evans, G.P., "Advances in Electrochemical Science and Engineering", 1, pp. 1-74, VCH, Weinheim, 1990.
7. Robert, C. and Melvin, J., CRC Handbook of Chemistry and Physics, 59th edition, CRC Press, INC. p. C-129, 1978.

Investigation of Underground Hydrogen Storage Areas

Hatice Karakilcik
Department of Geology, Faculty of Engineering and Arcitecture, University of Cukurova, 01330 Adana, Turkey
Email: hkilcik@cu.edu.tr

Abstract
Today, energy resources such as oil and natural gas are economically stored underground in some developed countries. Underground storage is only possible on certain geological strata or structures. One of the most important steps in the determination of the hydrogen storage area is to find suitable geological formations. Therefore, in this study, underground storage areas of hydrogen produced in the form of gas from water were investigated. For this, suitable geological structures underground have been examined. Among these structures, the most suitable hydrogen storage areas were seen to be salt domes. It is possible to create very large volume of salt caverns in these underground structures. These caves are suitable as hydrogen storage sites. In these structures, hydrogen gas can be stored easily and safely in very large quantities. The location of storage areas can be determined by geophysical methods. By these methods, reservoir parameters such as location, structure, size of underground salt caves desired to be formed in salt domes can be determined. As a result, it is seen that a large amount of hydrogen can be economically stored in salt caves underground. It has been concluded that the geological and structural characteristics of the underground storage areas are important in terms of sustainability and reliability.

Keywords: Hydrogen storage areas; underground storage; salt domes, salt caverns.

1. Introduction

Hydrogen is a clean, efficient, and versatile energy carrier, which together with electricity, may satisfy all the energy needs and form an energy system that would be permanent and independent of energy sources [1]. Many scenarios of the twenty-first century energy mix expect the society to use several different energy sources. They view hydrogen as major carrier of energy. Hydrogen may play a major role in the twenty-first century energy mix. It is found almost everywhere on the surface of the earth as a component of water. It has many commercial uses, including ammonia (NH_3) production for use in fertilizers, methanol (CH_3OH) production, hydrochloric acid (HCl) production and as a rocket fuel. Liquid hydrogen is used in cryogenics and superonductivity. Hydrogen can also be used as a fuel [2].

Hydrogen is an ultra-light gas that occupies a substantial volume under standard conditions of pressure, i.e. atmospheric pressure. Hydrogen has the highest energy per mass of any fuel; however, its low ambient temperature density results in a low energy per unit volume, therefore requiring the development of advanced storage methods that have potential for higher energy density. Future hydrgen supply systems will have a structure similar to today's natural gas systems.

Hydrogen can be stored physically as either a gas or a liquid. Storage of hydrogen as a gas typically requires high-pressure tanks (350–700 bar or 5,000–10,000 psi tank pressure). Storage of hydrogen as a liquid requires cryogenic temperatures because the boiling point of hydrogen at one atmosphere pressure is −252.8 °C. Hydrogen can also be stored on the surfaces of solids (by adsorption) or within solids (by absorption).

Salt caverns, depleted oil and gas reservoirs, aquifers, and mined hard rock caverns may offer potential geologic options for large-scale storage of hydrogen. Salt cavern storage alternative for storage of hydrogen, natural gas, crude oil, and compressed air takes advantage of the natural sealing properties of rock salt formations against gaseous media and non-aqueous liquids. Though, rock salt deposits occur world-wide, these are unevenly distributed around the globe. Moreover, these deposits must have a certain composition and internal structure, thickness and depth range to be suitable for cavern construction and storage operation.

A geological model or better represented as an engineering geological model for underground storage caverns is about integrating the surface and subsurface geophysical and geological observations including the physical assessments through the core drilling and creating an interpretative disposition of the various factors such as litho types, characteristic features, elevations super imposed with the design facilities. Like all other geo-models, it is multidisciplinary in nature with inter-operability and dynamically updatable knowledge base about the subsurface attributes.

In order to analyze the economic feasibility of hydrogen storage in salt caverns is essential to consider the different agents involved in the task. In this regard, different potential hydrogen consumer groups have been considered: hydrogen as fuel for the mobility sector, as raw material for the industry sector, as renewable energy carrier for the natural gas industry and as medium storage for the electricity industry in two time horizons: early market by 2025 and established market by 2050 [2].

The article addresses large scale energy storage in geological formations, which has several advantages. Underground storage of hydrogen in salt dome (salt caverns) and man-made caverns resulting from mining and

other activities is likely to be technologically and economically feasible. Also, large-scale energy storage can be the key for integration of large amounts of renewable resources.

2. How is Hydrogen Stored?

Significant challenges to storing the large quantities of hydrogen that will be necessary in the hydrogen energy economy. Presently hydrogen can be stored in three forms; gaseous, liquid or as a solid combined with a metal hybrid. There are five basic principle methods that have been considered for hydrogen storage. It is shown in Fig.1 these are:

- **Compressed Gas Storage:** Hydrogen is conveniently stored for many applications in higher pressure cylinders. The method is rather expensive and bulky.
- **Liquid Storage:** as Cryogenic storage Liquid storage as cryogenic storage in vacuum insulated or super insulated storage tanks. The liquid hydrogen fuel used as pocket propellant in the space programme is stored in large tanks(stored at -253°C).
- **Line Pack System:** Line pack system where it is allowed to vary the pressure in the transmission and distribution system.
- **Underground Storage:** Underground storage of hydrogen gas in salt dome (salt cavern), depleted oil and gas fields or in aquifer systems. This is the cheapest way to store large amounts of hydrogen for subsequent distribution. Salt caverns have been used to store hydrocarbon products for many years. Very large amounts of hydrogen can be stored in man made underground salt caverns of up to 500,000 m^3 at 200 bar (2,900 psi), corresponding to a storage capacity of 167 GWh hydrogen (100 GWh electricity).
- **Metal Hydrides Storage:** as metal hydrides in chemically bound from is another way of storing hydrogen. A number of metals and alloys form solid compounds by direct reaction with hydrogen gas. The metal hydrides can be transported in solid form. When the hydrides is heated, hydrogen is released for use [3].

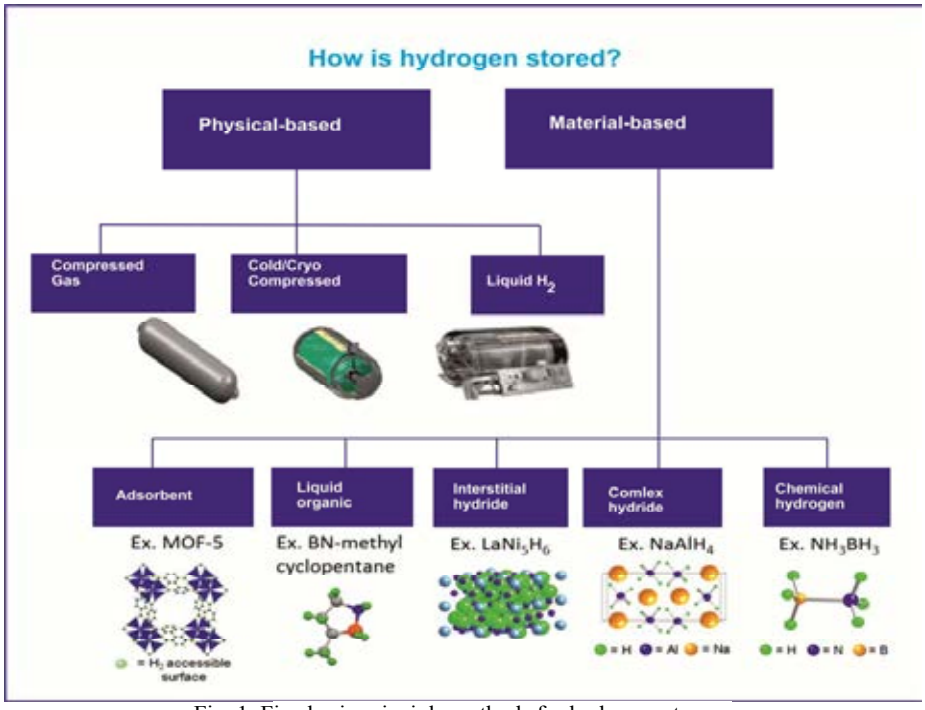


Fig. 1. Five basic principle methods for hydrogen storage

The most suitable storage method is dependant upon safety aspects, environmental issues, economic criteria and the end-use of hydrogen. Natural gas bas been stored underground since 1916 and much of the experience is directly applicable to hydrogen. Nowadays, there are already twenty-three salt caverns being used for natural gas or hydrogen storage in the UK. In France there are at least fifteen underground storage sites for natural gas,

either in salt caverns or in aquifers, for a total available capacity of 110 TWh, i.e. about 30% of their current annual demand.

Today, this technology has been developed to high levels of perfection, capable of constructing caverns with optimal shapes, conforming to precise specifications at depths down to 3,000 m and volumes of up to 800,000 m^3 and more. The leaching process is implemented by wells to be drilled from the surface down to the depths required by the specific geological and project pre-conditions. The caverns thus created are used for several purposes.

3. The Hydrogen Geological Storage

Geological formations have the potential to store large volumes of fluids with minimal impact to environment and society. One of the ways to ensure a large scale energy storage is to use the storage capacity in geological reservoir. There are several viable technologies for underground energy storage for example Underground Gas Storage (UGS), Hydrogen Storage (HS), Compressed Air Energy Storage (CAES), Underground Pumped Hydro Storage (UPHS) and Thermal Energy Storage (TES) [2].

Geological formations are currently in use for storage of large amounts of gases. A geological assessment must be undertaken to obtain sufficient geological knowledge about the site to determine the geological suitability of the site. Available geological and geophysical data should be gathered from old borehole logs and cores, previous seismic work and regional geological data available. Seismic imaging is the first tool used to guide subsalt exploration and development. Additional geological or geophysical surveys may have to be carried out if the existing data is not sufficient. Exploration drilling should be carried out to determine the quality of the salt and the distribution of impurities. Salt cores should be taken to enable laboratory tests to be undertaken to determine salt composition, mechanical strength and its solution characteristics. For example, when a salt model is being built for depth imaging, it is often assumed that the evaporite body is pure halite with a constant compressional wave speed of 4500 ms^{-1}. However, almost all salt bodies contain varying amounts of gypsum (VP = 5700 ms^{-1}) or anhydrite (VP = 6500 ms^{-1}), and some bodies contain significant amounts of K-Mg-rich salts with seismic velocities as low as 3500 ms^{-1}. Gypsum mines are generally considered unsuitable for storage, as they are relatively shallow, often have water ingress and on abandonment generally suffer flooding.
Well logging should be carried out to determine salt composition of uncored parts of the salt and to evaluate the quality of the overlying formation. Information on the thickness and strength of the overburden formations is particularly important in the development of bedded caverns. These layers are part of the structural support for the cavern.

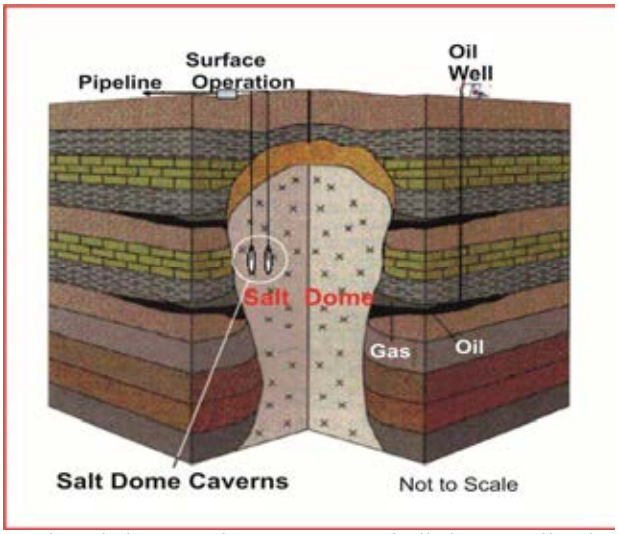


Fig. 2. Salt dome caverns. Also salt domes are important economically because oil and natural gas float on water and tend to move upward into the up-arched sediments, where they become trapped.

Geologic storage is used extensively in the oil, natural gas, and compressed air energy industries. To understand the scale of this utilization, approximately 800 million barrels of oil and 1000s of billion cubic feet of natural gas are stored geologically in the United States. The basic drive for geological storage is that the cost per volume-

stored is 3 to 5 times less than surface storage. With this relatively inexpensive means to store large volumes, storage can be situated to buffer seasonal demands, provide continuity in case of disruption in the supply chain, and control congestion in the pipeline system [4].

There are several types of geological reservoirs that can be suitable, namely: depleted hydrocarbon reservoirs, aquifers, salt formations and caverns, engineered rock caverns and abandoned mines. Facilities for the underground storage of gases fall into two main categories:

- **Porous media storage**, either in partially depleted oil or gas fields or aquifers, in which the gas occupies the naturally occurring pore space between mineral grains or crystals in sandstones or porous carbonates;
- **Cavern storage**, in which the gas is contained in excavated or solution-mined cavities in dense rock.

Both the storage categories have to satisfy two main requirements: providing sufficient storage capacity and containment of the stored gas.

Salt caverns serving to store natural gas and compressed air, etc., has a long history. As early as the Second World War, salt caverns were first used in Canada to store liquid and gaseous hydrocarbons. Britain used salt caverns to store crude oil during the Suez Crisis. Ten years later, Americans and Canadians began to use salt cavern for gas storage. Since then, salt cavern UGS had been widely used and developed [5].

Salt caverns are advantageous because salt is imperable and under most engineering and relevant geological conditions (increased temperatures and pressures at proposed storage depths), deforms in a ductile manner (creeps or flows) rather than brittle fracturing or faulting. Fractures due to faulting in the geological structure, therefore, likely to have been annealed and sealed. The same applies to any minor fractures that may develop in the cavern walls in a narrow zone immediately adjacent to the cavern during its development (‘brining’ or solution mining operations).

Salt occurs in nature either in solid form as rock salt (halite) in beds ranging from a few centimeters to hundreds of meters thick, or in solution as brine. Rock salt (NaCl) exhibits unique physical properties and mechanical bahaviour that makes it an ideal host for the development of (large) caverns fort he storage of materials that do not themselves react with or dissolve salt. Salt-bearing strata are, therefore, an important resource, not only as a source of salt, but also a host for the construction of salt caverns. The widw distribution of salt also makes it a resource of potentially strategic importance, notably for natural gas storage.

As it seen in Fig. 2. salt formations are either bedded sedimentary formations or intrusive salt formations (domes and ridges). Bedded formations often underlie large basins, with relatively thin salt beds (< 300 m thick) often separated by beds of porous or impervious layers of other sediments. Salt domes are important economically because oil and natural gas float on water and tend to move upward into the up-arched sediments, where they become trapped. Salt dome formations have intruded from roots in deeply buried salt beds, and tend to be plugs of large diameter and with great depth. To date, natural gas salt cavity storage in the UK has been within bedded salt formations.

Large underground salt caverns produced by solution mining may be used for the storage of liquids (oil, natural gas liquids and liquefied petroleum gas), gaseous hydrocarbons and compressed air. For example, completed solution caverns in the Triassic salts of Cheshire and Permian salts of north-east England have also been used for storage and waste disposal for many decades. At he same time, on Teesside, salt caverns have been used for the storage of hydrogen, natural gas, various liquid hydrocarbons, other fluids, solids and waste products [6].

Underground storage is the most inexpensive mean of storing large quantities of gaseous hydrogen. In fact, underground hydrogen gas storage is estimated about two orders of magnitude cheaper than tank storage considering the cost per Nm^3 of stored hydrogen. Geologic storage of hydrogen gas could make it possible to produce and distribute large quantities of hydrogen fuel for the growing fuel cell electric vehicle market.

Over the last decades there have been several examples of underground storage of pure hydrogen or syngas:

- England, Teesside, Yorkshire: The British company ICI has stored 1 million Nm^3 of nearly pure hydrogen in three salt caverns at a depth of about 400 m. The caverns have operated successfully for many years, and they are now operated by SABIC.
- France: The gas company Gaz de France has stored a gas with 50-60% hydrogen in an aquifer of 330 million Nm^3 capacity for nearly 20 years. No gas losses or safety problems have been recorded.
- Russia: Pure hydrogen was stored underground at 90 bars for the needs of the aerospace industry.
- Germany: 62% H_2 gas was stored in a salt cavern of 32,000 m^3 at 80-100 bar.
- Czechoslovakia: 50% H_2 syngas was stored in an aquifer.

4. Man-Made Structures

Salt caverns are artificially created cavities built in salt deposits. They are suitable for the storage of liquid hydrocarbons and in particular for gases under high pressure. Large amounts of gas can safely be stored due to large geometrical volumes and high storage pressures. Depending on the cavern depth, pressures of 200 bar and above are common. Geometrical volumes reaching up to more than 1 million m^3 can be constructed.

Rock salt (halite) is commonly found in two forms: bedded (thin flat layer deposit) and secondly, halokinetic structures where salt has moved (risen) to form salt pillows and domes. Caverns can be formed in both salt dome structures and bedded salt by solution mining; however, if the bedded layer is thin (60–100 m), horizontal-drilling techniques are required. As it seen in Fig. 3. solution mining involves a carefully controlled process of pumping water into a well drilled into the salt body, which dissolves to form a cavern. The cavern shape is controlled at regular intervals by sonar surveys. The leaching process is stopped when a cavern reaches the planned size or is about to exceed permitted dimensions [6].

The feasible geometrical volume of salt caverns depends mainly on the thickness of the salt formation. The volume may range typically from 150,000 to 800,000 m³. Under optimal conditions in a huge salt dome volumes even above 1,000,000 m³ have already been achieved [7]. It is possible to create small sized salt caverns initially and re-leach them afterwards. However, flooding of the cavern and subsequent gas first fill is required in this case which increases the costs for these operations. Operating pressures depend primarily on the cavern depth. The maximum pressures range from 100 to 270 bar, the minimum pressures from 35 to 90 bar respectively (orders of magnitude only). An increase in cavern volume from 75,000 m^3 to 500,000 m^3 reduces the total investment cost by a factor of 1.5 to 2. Even larger caverns, 600,000 m^3, have been mined in salt domes in Germany [7].

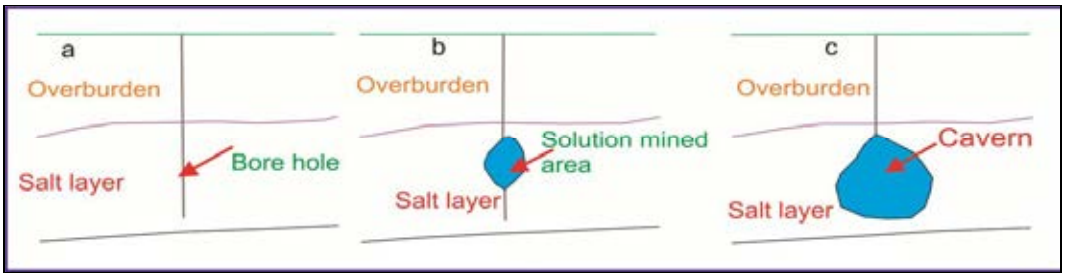


Fig. 3. Construction of a salt cavern storage facility. **(a)** initial borehole **(b)** solution mining and cavern formation in process **(c)** final solution-mined cavern.

The operational economics of an underground hydrogen storage cavern is further aided by reducing minimum operating pressure and thus the volume of cushion gas, whilst increasing the maximum operating pressure. If the minimum operating pressure is reduced too far the salt cavern will decrease in volume due to creep of the enclosing salt. By increasing the maximum operating pressure additional hydrogen is stored improving the cycle efficiency. The maximum operating pressure is limited by rock salt permeability, rock strength and depth of cavern. With its smaller molecule size, than natural gas, the diffusion of hydrogen through rock salt is not foreseen as being any different to the larger molecules. Typical maximum operating pressure ranges from 0.019 MPa to 0.021 MPa per metre in depth of overburden.

In planning and implementation of specific projects for the storage of hydrogen in salt caverns there are the same risks associated as with natural gas storage caverns. The main risk of salt cavern storage projects is the geological uncertainty, which can be reduced by increasing the knowledge base on the specific salt deposit (exploration). For a given cavern location this risk includes e.g. the occurrence of non-halite interbeds, faults, distance to edge of salt structure, etc. All of these issues affect the rock mechanical layout of the cavern and may lead to a reduced cavern size, a reduced operational pressure range or even the requirement to abandon and plug the well.

Further risks are associated with the technical processes of drilling and cementing of the well, since failure in cementation will lead to a cavern leakage. During leaching the rock mechanical limitations must not be exceeded, otherwise the leaching strategy must be modified which will also lead to a lower cavern volume

5. Results

Geological setting is one of the prime considerations for siting underground rock caverns so also has an important contribution towards successful construction of the facilities. Given the fact that geology plays a significant role starting from the conceptual stage of underground storage caverns through the design stage till the completion of the project, geological prediction forms an integral part of any sub surface project.

Salt dome is for several reasons an ideal host rock for high pressure 'Hydrogen Storage' at caverns. Even though the technology still needs to be adapted to satisfy the local safety regulations, 'Salt Caverns' can be seen to be very suitable for the storage of high pressure hydrogen. Salt cavern storage has an important position in the international energy reserves, and will be constructed on a large scale in the future, for a long period of time.

6. Conclusions

Hydrogen gas can be stored economically in huge amounts in underground salt caves. This is possible with the identification of sustainable and safe geological areas. Geophysical methods have an important role in the discovery of these areas due to the reservoir parameters of such areas, the location, structure, size of the underground salt caves desired to be formed in salt domes.

Nomenclature

MPa	Megapascal
ms^{-1}	meter/second
Nm^3	Normal cubic meters
TWh	Terawatt hour

References

1. Sherif SA, Barbir F, Veziroglu TN. Principles of hydrogen energy production, storage and utilization. Journal of Scientific & Industrial Research. 2003;62:46-63.
2. Matos C, Carneiro JF, Pereira da Silva P. Large scale underground energy storage for renewables integration: general criteria for reservoir identification and viable Technologies. 2016; The 11th Conference on Sustainable Development of Energy, Water and Environment Systems – SDEWES, Lisbon.
3. ESRU. A technical appraisal of hydrogen storage options. Energy Systems Research Unit University of Strathclyde Glasgow.2017; World Wide Web Address:http://www.esru.strath.ac.uk/EandE/Web_sites/99-00/hybrid_PV_FC/hydrogenstorage.html, Accessed 1May 2017.
4. Lord AS, Kobos P.H, Borns DJ. Geologic storage of hydrogen: Scaling up to meet city transportation demands. International Journal of Hydrogen Energy. 2014;39(28):15570–15582.
5. Yang C, Wang T, Li Y, Yang H, Li J, Qu D, Xu B, Yang Y. Daemen JJK. Feasibility analysis of using abandoned salt caverns for large-scale underground energy storage in China. Applied Energy. 2015;137:467-481.
6. Stone HBJ, Veldhuis I, Richardson RN. Underground hydrogen storage in the UK. Geological Society, London, Special Publications. 2009;13:217-226.
7. Plaat H. 2009. Underground gas storage: why and how. In: Evans DJ. & Chadwıck RA. (eds) Underground Gas Storage: Worldwide Experiences and Future Development in the UK and Europe. Geological Society, London, Special Publications. 2009;313:25–37.

Assessment of a Geothermal Based Integrated System For Power and Hydrogen Production

Hatice Karakilcik[1], Mustafa Erden[2], Mehmet Karakilcik[2]
[1]Department of Geology, Faculty of Engineering and Architecture, of Cukurova University, 01330 Adana Turkey
[2]Department of Physics, Faculty of Sciences and Letters, University of Cukurova, 01330 Adana, Turkey

Abstract
In this study, power and hydrogen production performance of an integrated system based on geothermal energy is studied. The novel integrated system consists of a steam power turbine, an organic Rankine cycle (ORC), a saturated NaCl solution reservoir tank and a chlor-alkali reactor. The steam power turbine is driven by high temperature water steam from geothermal reservoir. The generated power is delivered to city grid and waste heat from the steam power turbine is used for running of the ORC. The generated electricity from the ORC is used for the electrolysis takes place in the chlor-alkali reactor. To enhance the performance of the reactor, the saturated NaCl solution and pure water is heated by the waste heat from the ORC. So, this integrated system produces electricity, hydrogen and also yields the by products namely chlorine and sodium hydroxide while consumes saturated NaCl solution and pure water. As a result, the geothermal energy potential plays an important role on the integrated system performance and rate of hydrogen production.

Keywords: Hydrogen production; geothermal energy; integrated system; exergy; efficiency.

1. Introduction

One of the basic renewable energy source is geothermal energy. Geothermal energy is clean, cheap and always available during a year. So, significant amount of electricity can be generated from geothermal sources and then hydrogen can be produced and stored with a surplus of generated electricity. Recently, many scientists have been conducted studies on this subject. Yilmaz et al. [1] proposed a combined flash-binary geothermal plant and a water electrolysis unit for hydrogen production. This system has a capacity of hydrogen production at a rate of 0.0498 kg/s when the liquid geothermal water resource at 200 °C with a flow rate of 100 kg/s. Stathis Michaelides [2] presented two methods to increase the efficiency of the currently used geothermal cycles. First one is the using of a binary-flashing system to reduce the overall entropy production and then producing more electric power from the resource. Second one is a heat extraction system to be used with dry hot-rock resources. Yuksel et al. [3] presented a geothermal power based multi-generation energy production system which generates electricity, hydrogen, domestic hot water, heating and cooling. Hydrogen production of the proposed system rises from about 0.030 kg/s to nearly 0.075 kg/s while electrical power generation of the proposed system increases from about 4 MW to 8.5 MW. The overall energy and exergy efficienciy of the system are 47.04% and 32.15%, respectively. Bicer et al. [4] proposed a new combined system, using solar and geothermal resources, for hydrogen production, along with power generation, cooling and heating. The overall energy and exergy efficiencies of the combined system can reach up to 10.8% and 46.3% respectively for a geothermal water temperature of 210 °C. Cakici et al. [5] assessed the thermodynamic performance of an integrated geothermal powered supercritical regenerative organic Rankine cycle and parabolic trough solar collectors. They determined that the integration of ORC and PTSC systems increases the net power output on the other hand decreases the electrical and exergetic efficiencies of the integrated system.

In this paper, we consider the use of geothermal energy for power and hydrogen production by using a flash turbine, an organic Rankine cycle and a chloralkali cell. The goal of this study is conceptually develop and analyze a coupling of geothermal power production system with chloralkali cell for continuous production because of geothermal energy is separated from other energy sources by its ability to be used every hour of the year.

2. System description

In this study, power and hydrogen production performance of an integrated system based on geothermal energy is studied.

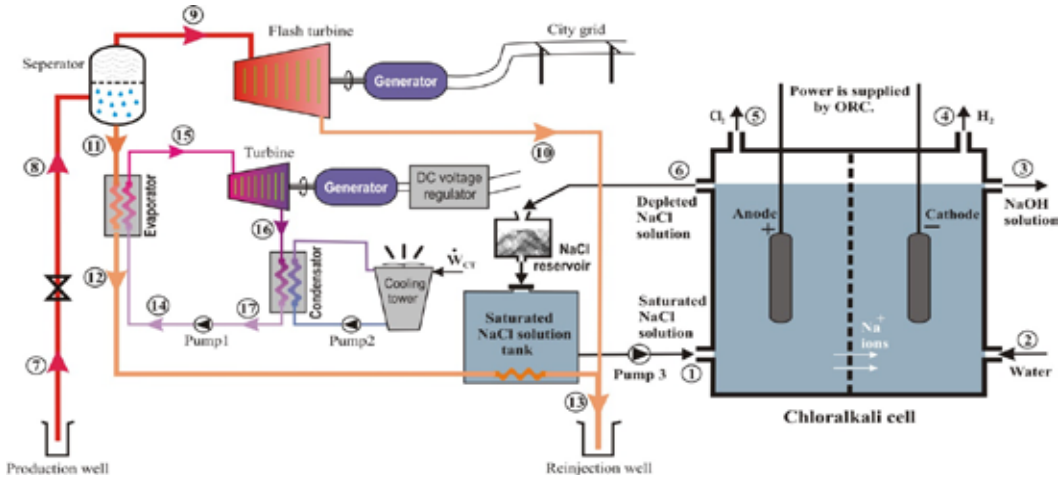


Fig. 1. Shematic of integrated system.

Fig.1 represents the schematic of the integrated system, along with inlet and outlet streams. This integrated system consists of a steam turbine, an organic Rankine cycle (ORC) and a chlor-alkali reactor. The steam portion of geothermal fluid drives a steam turbine to produce power while the liquid portion of geothermal fluid serves as the heat input for the binary cycle. The binary fluid is vaporized by geothermal water and runs through the turbine to produce power. Geothermal water leaving the evaporator of the ORC is used to heat saturated NaCl solution to reduce the power requirement of the chloralkali cell. Power output from the steam turbine is delivered to city grid. On the other hand, power output of the ORC is used for the chloralkali electrolysis process. The used geothermal water is reinjected back to the ground. Since the efficiency of the reactor increases at higher temperature, the saturated hot NaCl solution at the tank is used as anolyte feed. The membrane is used to separate the H_2 and Cl_2 gases and to neutralize the OH^- ions in the cathode department by permitting the Na^+ ions migration from anode to cathode section of the reactor.

The chloralkali cell reduces water at the photo-cathode according to the half reaction [6]:

$$2H_2O_{(l)} + 2e^- \rightarrow H_{2(g)} + 2OH^-_{(aq)} \qquad E^0 = -0.8277\ V \qquad (1)$$

At the anode, chlorine is formed from saturated NaCl aqueous solution as follows:

$$2Cl^-_{(aq)} \rightarrow Cl_{2(g)} + 2e^- \qquad E^0 = 1.36\ V \qquad (2)$$

Thus the total cell voltage is E^0=2.1877 V which is higher than 1.23 V for water electrolysis.

The sodium ions form in the anolyte by NaCl dissociation and migrate from the anolyte to the catholyte through the cation exchange membrane (NAFION®). The caustic soda forms in the catholyte can be written as follows:

$$Na^+_{(aq)} + OH^-_{(aq)} \rightarrow NaOH_{(aq)} \qquad (3)$$

3. Analysis

The thermodynamic performance of the proposed system is performed by conducting quantitative energy and exergy analyses including sytem efficiencies.

During the course of this study, the following assumptions are made for the analysis:

- The ambient temperature (T_0) and pressure (P_0) are 25 °C and 1 atm, respectively.
- Pressure drops in all the heat exchangers and the pipes are neglected.

- The reactants and products are at reaction temperature and pressure in all chemical reactions.
- The system runs at steady state conditions.
- The changes in potential and kinetic energy are neglected.
- All the gases are assumed to be ideal.

These assumptions and general mass, energy, entropy and exergy balance equations are used to analyze the system. The heat and work input/output, the rate of entropy generation and exergy destruction, and energy and exergy efficiencies are calculated based on these balance equations.

So, mass, energy, entropy and exergy balance equations for a control volume at steady state with neglibible kinetic and potential energy changes can be written as [7]:

$$\sum \dot{m}_{in} = \sum \dot{m}_{out} \quad (4)$$

$$\dot{Q} - \dot{W} = \sum \dot{m}_{out} h_{out} - \sum \dot{m}_{in} h_{in} \quad (5)$$

$$\sum \frac{\dot{Q}}{T_s} + \sum \dot{m}_{in} s_{in} + \dot{s}_{gen} = \sum \dot{m}_{out} s_{out} \quad (6)$$

$$\dot{E}x_{heat} - \dot{W} = \sum \dot{m}_{out} ex_{out} - \sum \dot{m}_{in} ex_{in} + \dot{E}x_{dest} \quad (7)$$

where $\dot{m}$ is the mass flow rate, $\dot{Q}$ and $\dot{W}$ are the net heat and work inputs, h is the entlphy, s is entropy, $\dot{E}x_{heat}$ is the exergy rate by heat, ex is the specific flow exergy, $\dot{E}x_{dest}$ is the rate of exergy destruction and the subscripts in and out stand for inlet and output states.

The related energy and exergy efficiency of the only power generation can be written as:

$$\eta_{en} = \frac{\dot{W}_{out}}{\dot{E}_{in}} = \frac{\dot{W}_{flash} + \dot{W}_{binary} - \dot{W}_{pump} - \dot{W}_{ct}}{\dot{E}_{in}} \quad (8)$$

$$\eta_{en} = \frac{\dot{m}_9(h_9 - h_{10}) + \dot{m}_{15}(h_{15} - h_{16}) - \dot{W}_{pump} - \dot{W}_{ct}}{\dot{m}_{geo}(h_1 - h_{13})} \quad (9)$$

$$\eta_{ex} = \frac{\dot{W}_{out}}{\dot{m}_{geo}[h_{geo} - h_0 - T_0(s_{geo} - s_0)]} \quad (10)$$

The related energy and exergy efficiency of the only hydrogen generation can be written as:

$$\eta_{en} = \frac{(LVH_{H2}).(\dot{m}_{H2})}{\dot{m}_{geo}(h_{geo} - h_0)} \quad (11)$$

$$\eta_{ex} = \frac{\dot{E}x_{H2}}{\dot{m}_{geo}[h_{geo} - h_0 - T_0(s_{geo} - s_0)]} \quad (12)$$

where LVH_{H2} is the lower heating value of H_2, $\dot{m}_{H2}$ and $\dot{E}x_{H2}$ are the mass flow rate and the exergy rate of produced H_2.

4. Results and discussion

For the parametric studies, ambient temperature (25 °C), ambient pressure (101.3 kPa), mass flow rate of the geothermal water source (100 kg/s), mass flow rate of the saturated NaCl solution (10 g/s) are kept constant while the temperature of the geothermal source is being varied from 140 to 155 °C. Thus the system is tested within that temperature range. The performance of the system has studied by using Engineering Equation Solver (EES).

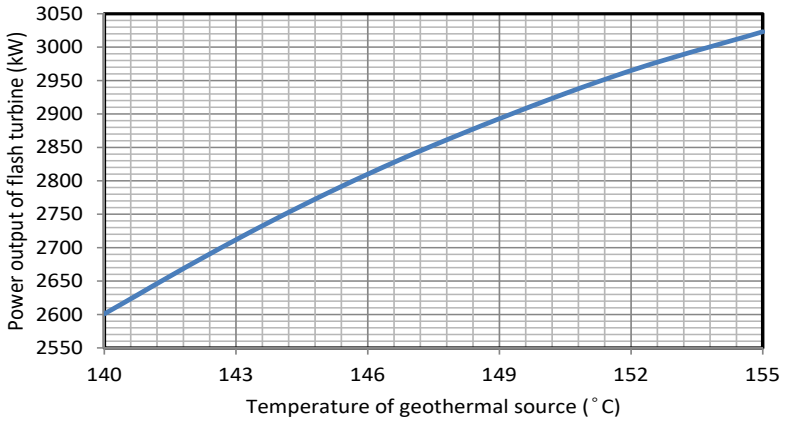


Fig. 2. Shematic of integrated system.

As shown in the Fig. 2 the rate of produced power from flash turbine increases from 2601 to 3023 kW when the temperature of the geothermal source varies from 140 to 155 °C.

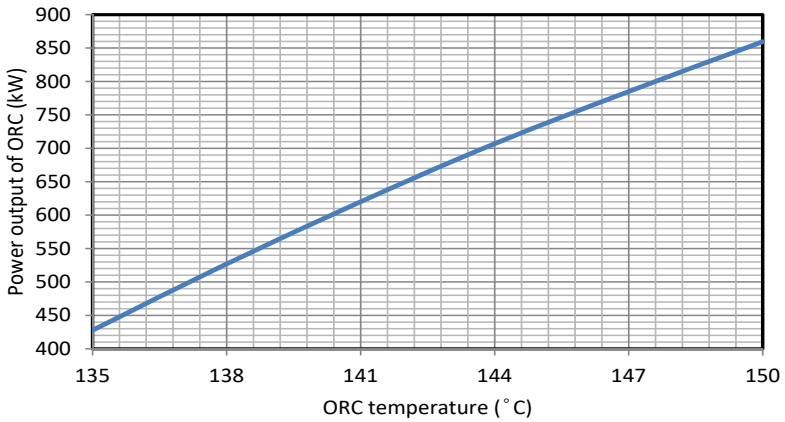


Fig. 3. Shematic of integrated system.

As shown in the Fig. 3 the rate of produced power from ORC increases from 427 to 860 kW when the input temperature of ORC varies from 135 to 150 °C.

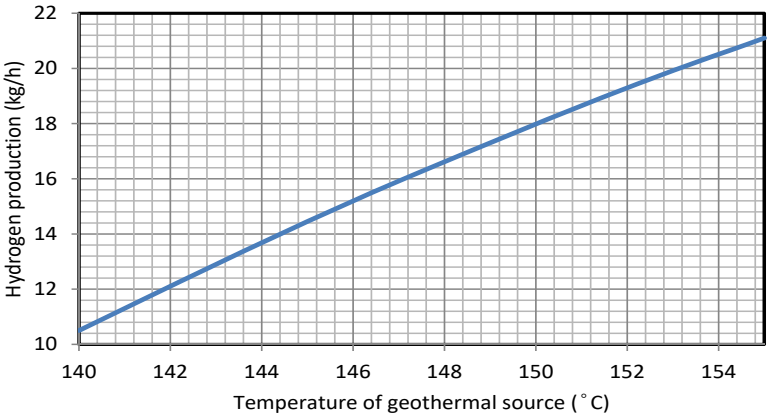


Fig. 4. Shematic of integrated system.

As shown in the Fig. 4 the rate of hydrogen production increases from 10.5 to 21 kg/h when the temperature of the geothermal source varies from 140 to 155 °C.
As a result, the geothermal energy potential plays an important role on the integrated system performance and rate of hydrogen production. The overall energy efficiency of the system can reach up to 11.2% and the overall exergy efficiency of the system can reach up to 38.4%.

5. Conclusions

In this study, power and hydrogen production performance of a geothermal source is examined conceptually. The proposed system produces hydrogen, chlorine and sodium hydroxide. The results show that hydrogen production increased with increasing temperature.

References

1. Yilmaz C, Kanoglu M, Abusoglu A. Exergetic cost evaluation of hydrogen production powered by combined flash-binary geothermal power plant. Int J Hydrogen Energy. 2015;40:14021-14030.
2. Michaelides E. Future directions and cycles for electricity production from geothermal resources. Energy Conversion and Management. 2016;107:3–9.
3. Yuksel YE, Ozturk M. Thermodynamic and thermoeconomic analyses of a geothermal energy based integrated system for hydrogen production. Int J Hydrogen Energy. 2017;42:2530-2546.
4. Bicer Y, Dincer I. Development of a new solar and geothermal based ombined system for hydrogen production. Solar Energy. 2016;127:269–284.
5. Cakici DM, Erdogan A, Colpan CO. Thermodynamic performance assessment of an integrated geothermal powered supercritical regenerative organic Rankine cycle and parabolic trough solar collectors. Energy. 2017;120:306-319.
6. Acar C, Dincer I. Analysis and assessment of a continuous-type hybrid photoelectrochemical system for hydrogen production. Int J Hydrogen Energy. 2014;39:15362-15372.
7. Yilmaz C. Thermoeconomic modeling and optimization of a hydrogen production system using geothermal energy. Geothermics. 2017;65:32–43.

ORAL PROCEEDINGS

Kinetic, Thermodynamic and Transport Limitations of Oxygen Evolution Step in Solar Thermochemical Processes: An Experimental Study on Co_3O_4

Atalay Calisan, Serkan Kincal, Deniz Uner
Department of Chemical Engineering, Middle East Technical University, Universiteler Mahallesi, Dumlupinar Bulvari No:1, 06800 Cankaya/Ankara, Turkey
Email: calisan@metu.edu.tr, skincal@metu.edu.tr, uner@metu.edu.tr

Abstract
The rate limiting mechanisms during the oxygen desorption steps for solar thermochemical hydrogen production processes were investigated. The oxygen release from redox materials is controlled by competing mechanisms between thermodynamics, kinetics, and heat and mass transfer. In this study, the role of these resistances on oxygen evolution from Co_3O_4 was investigated. Thermodynamic equilibrium between Co_3O_4, CoO, Co and O_2 through a Gibbs Free Energy minimization method revealed that the thermal decomposition temperature is 800 °C in inert atmosphere while 900 °C under air atmosphere. These temperatures are verified by thermogravimetric analysis. Temperature programmed thermal decomposition experiments were performed to determine the extent of heat and mass transfer limitations. The extent of the pore and film mass transfer resistances were monitored by studying the behavior of Co_3O_4 powder and Co_3O_4 on cordierite monolith. The structured flow channels improve the gas solid contact area while the high surface area provided by the monolith enhances both heat transfer and mass transfer leading to increased rates of oxygen desorption.

Keywords: Solar thermochemical; Co_3O_4; oxygen desorption; film mass transfer; pore diffusion resistance; heat transfer.

1. Introduction

Solar hydrogen production is becoming increasingly popular for sustainable and green fuel production. Reducible metal oxides as oxygen storage materials are recently integrated into these processes via chemical looping technologies. The hybrid technology called as two step solar thermochemical cycles eliminates the high temperature gas separation of hydrogen and oxygen since hydrogen and oxygen is produced in separate steps. The bottleneck of these technologies is the activation of metal oxide by thermal decomposition reaction such that oxygen removal is the rate determining step requiring very high temperatures. In addition, the significance of heat and mass transfer limitations at reaction environment is still not clear.

Thermal Decomposition Step: $MeO_x \rightarrow MeO_{x-1} + {}^1/_2\, O_2$
Water Splitting Step: $MeO_{x-1} + H_2O \rightarrow MeO_x + H_2$

Metal oxides such as Ni-, Mn-, Fe-, Ce-, Co- and Cu- based oxides were widely studied in literature in terms of reactivity, mechanical strength, thermal stability and recyclability. High temperatures are required to release the lattice oxygen of the oxide materials. However, regeneration requires lower temperatures with H_2O or CO_2 both for kinetic and thermodynamic reasons. Hence, the material is cooled to a favorable temperature to produce H_2 or CO from water or CO_2 used as oxidants. The duration of the overall process depends largely on the rate of oxygen desorption and transport. The objective of this study is to elucidate kinetic, transport and thermodynamic barriers of oxygen transport from Co_3O_4. Co_3O_4 was selected due to milder conditions for the thermal decomposition of bulk phase Co_3O_4 to CoO and reoxidation of CoO to Co_3O_4 and stability [1-3].

2. Experimental Study

Co_3O_4 spinel oxide used in this study was supplied from Ege Ferro (99.4% on metal basis). Co_3O_4 was coated on a cordierite monolith by using dip coating procedure. A test piece with 20mm OD was cut from a 200 cpi monolith block. The monolith was then etched in 2M HCl solution in ultrasonic bath for about 20min to etch away part of the surface for greater surface area. The acid-etched monolith was washed and dried in the oven at 110 °C for 2 hours. Co_3O_4 in ethanol suspension was prepared by dissolving 1g of Co_3O_4 in 50ml ethanol in ultrasonic bath. Monolith was dip coated by immersing and removing the piece in this solution at a 7.5 m/s rate by using a home-made crane. The excess solution remaining in the monolith channels were removed by high pressure air. The monolith was dried for 5 hours at 120 °C before coating the additional layers. This procedure was repeated several times until a desired coating thickness was achieved. Finally, the coated monolith was calcined at 350 °C for 3 hours.

Temperature programmed thermal decomposition (TPtD) experiments were conducted by using a home-built experimental setup. Effluent gases were analyzed by using Teledyne Model 3290 percent gas analyzer (0-1% and 0-21% O_2). Two different types of reactors were used depending on the material whether it is powder or monolith. 6mm OD quartz reactors were used for powder materials whereas 25mm OD reactors were used for monolith samples. In both reactors, materials were supported and fixed in the middle of the tube by the help of quartz wools. The gas flow rate was adjusted by a Teledyne HFC-202 Mass Flow Controller (MFC), driven by a TERRALAB mass flow control station (MFCS). Dry air (99.99% Oksan) and argon (99.999% Linde) were used during the experiment. The heating rate was changed depending on the testing procedure. Temperature of the oven is measured by a K-type thermocouple.

3. Results and Discussion

Thermodynamic driving force towards thermal decomposition was determined by using predominance diagrams as shown in Fig.1. The temperature programmed oxygen desorption route follows $Co_3O_4 \rightarrow 3CoO+1/2O_2 \rightarrow 3Co+3/2O_2$ sequence. The temperature range of study was chosen to be below 1000 °C, where only the thermal decomposition of Co_3O_4 to CoO can occur at atmospheric pressure. Further reduction was impractical due to the need of extremely low oxygen pressures $<10^{-15}$ bar. The temperature required for thermal decomposition of Co_3O_4 was found as 900 °C under air atmosphere whereas temperatures around 800 °C is expected under inert conditions. Thermal gravimetric analysis revealed that the oxygen desorption form Co_3O_4 started around 780 °C under N_2 and around 830 °C under air atmospheres. Total weight loss was found as 6.5 wt% during the experiment which is consistent with the stoichiometry of the decomposition route of $Co_3O_4 \rightarrow 3CoO+1/2O_2$[4].

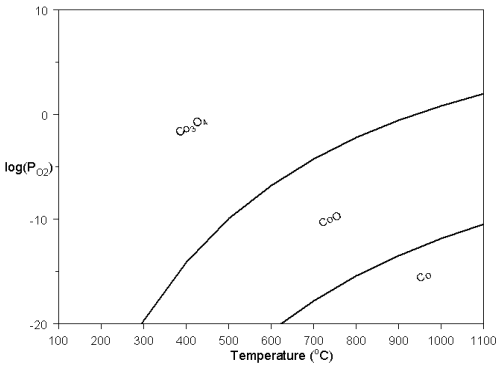


Figure 1. The predominance diagram of Co-O system.

After identifying thermodynamic limits, the limits of the film and pore diffusion resistances were determined. To determine the limits of film mass transfer resistance, the linear velocity of the gas flowing through a packed bed of powder was changed while keeping the space time constant. This was achieved by increasing the solid material (and its void volume) and gas flow rate by similar amounts. It was observed that at higher linear velocities, the amount of oxygen desorption started earlier and it was higher (Figure 2 a). The pore diffusion effects were studied by observing the difference between oxygen desorption rates of a bulk powder and monolith coated sample. The sample coated on monolith exhibited a greater amount of oxygen desorption/when normalized to per gram of Co_3O_4, since coating decreases the desorption pathway of the oxygen molecule (Figure 2 b). In addition, structured construction of monolith offers a distributed gas flow through channels and reduces pressure drop as well as overcoming film mass transfer resistances.

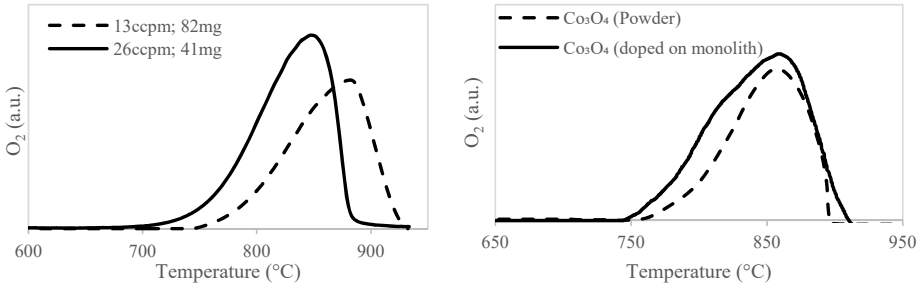


Figure 2. The effect of film mass transfer (left) and pore diffusion (right) on oxygen desorption of Co_3O_4

The thermal decomposition of Co_3O_4 is an endothermic reaction. Reaction pathway follows the $2Co_3O_4 \rightarrow 6CoO + O_2$ requires 403.5 kJ/mol O_2 at 800 °C. In order to test the presence and the limits of internal heat transfer resistances, Co_3O_4 powder was mixed with SiC, a high thermal conductivity heat transfer medium used for laboratory scale catalyst tests. The similarity of the decomposition profiles with and without SiC (Figure 3 a) indicated that the internal heat transfer resistances are not significant. The limits of the external heat transfer resistances were checked by changing the heating rate (Figure 3 b). Data shown in Figure 3 b is indicative of the presence of non-negligible external heat transfer limitations during the oxygen desorption step.

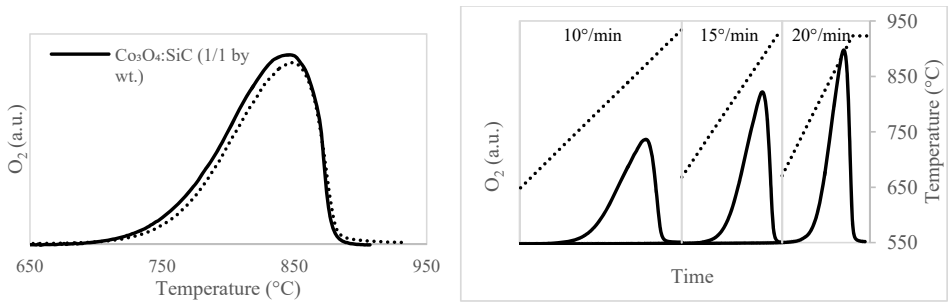


Figure 3. The effect of internal (left) and external (right) heat transfer on oxygen desorption of Co_3O_4

4. Conclusions

In this study, the effect of thermodynamics, heat and mass transfer resistances were investigated on a model compound as Co_3O_4. The desorption reaction initiated after 800 °C under N_2 atmosphere which indicates the effect of thermodynamics. The high endothermcity of thermal decomposition reaction is under the control of energy flow to material. The rate of oxygen evolution faces the pore and film mass transfer resistances. This study confirms that these effects can be minimized by doping Co_3O_4 on a highly thermal conductive monolith.

Acknowledgement

Financial support from TUBITAK through 1003 program under the 213M006, from METU Research Coordination Center (BAP-08-11-DPT.2013K120500-2) are gratefully acknowledged. A.C. is grateful to TUBITAK for graduate scholarship through 2211 program.

References

1. Wong, B., Thermochemical Heat Storage for Concentrated Solar Power, U.S. Department of Energy under DE-FG36-08GO18145, GENERAL ATOMICS PROJECT 30314, 2011.
2. Agrafiotis, C., Roeb, M., Schmücker, M. and Sattler C., Solar Energy, 2014, 102, 189,
3. Block, T., Knoblauch, N. and Schmücker M., Thermochimica Acta, 2014, 577, 25.
4. Ates, C., Master's Thesis, Middle East Technical University, 2015.

ORAL PROCEEDINGS

Parametric Analysis of Hydrogen Storage Taking Into Account of Three Different Metal Hydride Materials

Umran Elmas[1], Fevzi Bedir[2], Muhammet Kayfeci[3]
[1]TÜBİTAK Türkiye Bilimsel ve Teknolojik Araştirma Kurumu, Ankara/TÜRKİYE
[2]Gebze Teknik Üniversitesi, Mühendislik Fakültesi, Gebze-Kocaeli/TÜRKİYE
[3]Karabük Üniversitesi Teknoloji Fakültesi, Karabuk/TÜRKİYE
Email: umran.elmas@tubitak.gov.tr, fevzibedir@gmail.com, mkayfeci@karabuk.edu.tr

Abstract
In this study, firstly the results of experimental and of finite element-based modeling are evaluated as being confirmed each other. Then many of parameter combinations which are directly affect the hydriding and metal hydride-based hydrogen storage process are defined. The combinations are particule size of hydride material, the tank design with or without fins, varying hydrogen inlet pressure, changing the temperature of the cooling fluid around the tank, the variation in the inner radius, the general convective heat coefficient as well as changing the wall thickness. The system and the other related parameters mentioned above are modelled by COMSOL. These variables are analyzed together with taking into account of the thermo-physical properties of three different types of metal hydride materials of $MmNi_{4,6}Al_{0,4}$, $LaNi_{4.75}Al_{0.25}$ and $LaNi_5$ in terms of having the results in the temperature distribution inside the tank, in the amount of hydrogen mass to be stored in the tank and in variation of the equilibrium pressure of the system. The final conclusions are also remarked.

Keywords: Metal hydride alloys; hydrogen storage tank; absorption; desorption; COMSOL modelling.

1. Introduction

The most significant feature of hydrogen is its ability to be stored. There are numerous methods being used for the storage of hydrogen, like in the form of gas as being compressed or in form of liquid through cooling at low temperatures. Hydrogen can physically be stored within carbon nano tubes and it can chemically be stored within hydride in solid form. Among the storage methods, it has been indicated that the most effective storage method was the storage in the form of hydride due to high storage capacity, suitable operation condition and operation under low pressure.

Coupled heat and mass transfer with the chemical reactions take place inn such systems which makes the hydriding and dehydriding phenomena quite complicated. As the gas motion and the physical properties of the metal hydride is a kind of a complicated problem, many researchers have been studying on different aspects of that problem in both experimental and numerical aspects.

Serge Nyallang Nyamsi et al [1] studied of the analytical method and numerical simulation on the finned tube heat exchanger used in hydride hydrogen storage system. Yang et al [2] identified the heat and mass transfer characteristics of metal hydride reactor during adsorption. Wang et al [3] proceeded the simulotion of metal hydride reactors. Gambini et al [4] performed the assessment of metal hydride-based hydrogen storage systems. Muthukumar et al [5] studied on a metal hydride-based hydrogen storage device. Krokos et al [6] modelled a multi-tubular metal hydride beds for efficient hydrogen storage. Askri et al [7] optimized a hydrogen storage in metal-hydride tanks. Yen et al [8] numerically simulated and tested the metal hydride hydrogen storage system. Freni et al [9] simulated a metal hydride-based hydrogen storage tank by FEM method. Couturier et al [10] design a tank for on-board hydrogen storage in metal hydrides. Bao et al [11] studied a three-dimensional modeling and sensitivity analysis of multi-tubular metal hydride reactors. Talaganis et al [12] modelled and simulated the absorption-desorption cyclic processes for hydrogen storage-compression using metal hydrides. Yang et al [13] identified heat and mass transfer characteristics of metal hydride reactor during adsorption. Garrison et al [14] optimized the internal heat exchangers for hydrogen storage tanks utilizing metal hydrides. Hopkins et al [15] studied the hydrogen compression characteristics of a dual stage thermal compressor system utilizing $LaNi_5$ and $Ca_{0.6}Mm_{0.4}Ni_5$. Jiao et al [16] studied the effects of various operating conditions on the hydrogen absorption processes in a metal hydride tank. Wang et al [17] studied the hydrogen storage systems based on hydride materials with enhanced thermal conductivity. Ye et al [18] performed the numerical analysis of heat and mass transfer during absorption of hydrogen in metal hydride based hydrogen storage tanks. Muthukumar et al [19, 20] studied the parametric aspects of a metal hydride based hydrogen storage device and numerical simulated the coupled heat and mass transfer in metal hydride-based hydrogen storage reactor. Patil et al [21] analysed the metal hydride reactor for hydrogen storage. Raju et al [22] simulated the model for high-pressure metal hydride hydrogen storage systems. Nam et al [23] modeled and simulated the hydrogen absorption in metal hydride hydrogen storage vessels. Bhouri et al [24] modeled and performed the multi-tubular sodium alanate hydride finned reactor. Hwang et al [25] analysis of the hydrogen releases and dispersion around storage facilities by CFD. Freni et al [26] simulated the metal hydride-based hydrogen storage tank. Melnichuk [27] optimized the

heat transfer fin design for a metal-hydride hydrogen storage container. Oyakawa et al [28] studied the metal hydride tank for a quick charge. Mosher DA et al [29] fabricated and tested the NaAlH4 based hydrogen storage systems. Yu et al [30] developed a metal-hydride hydrogen accumulator. Kayfeci [31] experimentally investigated the design parameters of the hydrogen storage systems.

In this study, firstly the results of experimental and of finite element-based modeling are evaluated to confirm each other. Then many of parameter combinations directly affecting hydrogen storage process are defined. The combinations are particule size of hydride material, the tank design with or without fins, varying hydrogen inlet pressure, changing the temperature of the cooling fluid around the tank, the variation in the inner radius, the general convective heat coefficient as well as changing the wall thickness.

All parameters are modelled by COMSOL and analyzed together for three different types of metal hydride materials of $MmNi_{4,6}Al_{0,4}$, $LaNi_{4.75}Al_{0.25}$ and $LaNi_5$ in terms of the temperature distribution inside the tank, the amount of hydrogen mass to be stored and the equilibrium pressure of the system. The final conclusions are also remarked.

2. Modellıng and Sımulatıon Work

Fig. 1 shows the axy-symmetric representation of the cylindirical bed reactor. The metal hydride reactor part located inside the tube works as a porous filter. During the absorption process, hydrogen moves towards the spaces inside the porous structure and reacts with the metal hydride. Metal hydride expose the heat to react with hydrogen during the process and the heat is pushed away from the system by means of the cooling fins. The locations of the thermocouples are the same for both experimental and simulation study, which are 3,1 mm, 16,9 mm, 30,7 mm and 44,5 mm away from the bottom side of the tank.

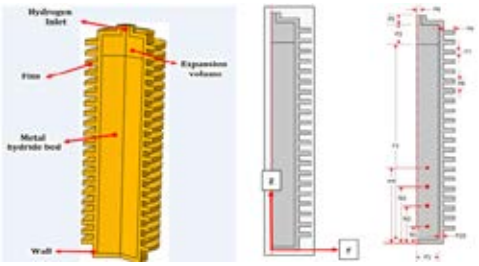


Fig. 1. The the axy-symmetric representation of the cylindirical bed reactor

Basically the approaches to be applied are as follows:

- Free flow of hydrogen is to be modelled by Navier-Stokes momentum equations,
- The flow in the porous structure of hydrogen to be modelled by Darcy equation,
- Modelling the chemical reaction as well as the heat which exposed,
- Modelling the heat transfer in conventional and in operational approaches between the reactor and the fins.

The calculations are executed by the following assumptions:

- Hydrogen is considered as an ideal gas,
- The environment is in locally thermal balance,
- Thermo-physical properties of the hydride bed is independent from the temperature and the hydrogen pressure,
- The effect of hydrogen concentration is negligible in the change of pressure balance,
- Heat transfer by radiation is neglected.

3. Experimental Study

For the experimental work, the hydrogen storage tank which fins are located outside is designed (Fig. 2). Moreover the heat transfer is improved by placing an appropriate hose around the fins in which cooling water is circulated to remove the reaction heat. The tank is filled by 75% of the volume by 25 gram metal hydride material of $LaNi_{4,75}Al_{0,25}$.



Fig. 2. The hydrogen storage tank with fins is used in the experimental work

The experimental set-up of the hydriding process is shown at Fig. 3. The storage tank is connected to the vacuum pump (about 10 mm Hg) and is heated up to 220 to 250 °C. After this, the activation process is completed by charging 8 bar of Hydrogen pressure.

The results achieved experimentally are compared with those by modelling.

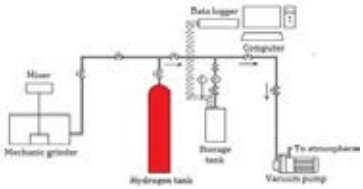


Fig. 3. The experimental set-up of the hydriding process

4. Evaluating Experimental and Modelling Results

The results achieved by the experimental work and obtained from the finite element simulation by COMSOL for the same type of cylindirical storage tank with fins are compared each other and evaluated that the results show the similar variations (Fig. 4 is and Fig. 5).

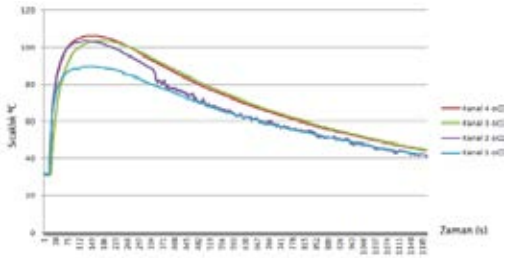


Fig. 4. The temperature variations versus time for the first 1200 seconds under 8 bar pressure in different coordinates for the absorption process in the experimental work

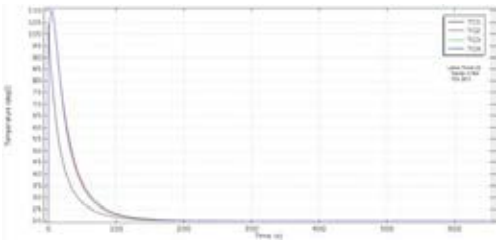


Fig. 5. The temperature variation versus time in different for thermocouple locations in the modelling work

For each case the maximum temperature value is measured about 105 ºC for all of four different coordinates. The variations of the temperature values for all of four coordinates give almost the same for both experimental and modeling works. On the other hand the time which the temperature value of 20 ºC is reached is observed lasting more in the experimental work than in modelling work.

By evaluating that some equipments and measurement devices used in the experimental work could be not sufficient enough, that there would be some losses at the hoses during vacuum and charging processes, that the ranges of measurement couldn't be appropriately selected, that there would not be added of nitrogen tank and hydrogen reservoir tank into the experimental set-up system, the result of both experimental and modelling works are decided alike each other.

5. Hydriding Variables and the Combinations

After it is evaluated that the experimental and finite element-based analysys confirm each other, then many of parameter combinations which are directly affect the hydrogen storage process are formed. The parameters which are used as variables are shown as table in Table 1.

Table 1. Different types of parameters which affect the hydriding process and their combinations

Parameter	Unit	Explanation
Metal Hydride Material	-	Each of the metal hydride materails of $MmNi_{4.6}Al_{0,4}$, $LaNi_{4,75}Al_{0,25}$ and $LaNi_5$ are all variables
Particule Size of Hydride	mm	Variable ranging in between 0,01 and 1,0 mm for three different metal hydride materials
Having Fins for the Tank	-	Variable ranging with fins having angle of 45 degree and of 0 degree with fins and having no fins for three different metal hydride materials
Supply Pressure of H_2	Bar	Variable ranging in between 5 and 35 Bar for three different metal hydride materials
Inlet Radius of the Tank	mm	Variable ranging in between 5,00 and 11,98 mm for three different metal hydride materials
Cooling Water Temperature	^oC	Variable ranging in between -5 and 15 ^oC (288 and 308 K) for three different metal hydride materials
General Convective Heat Transfer Coefficient	W/m^2K	Variable ranging in between 750 and 2250 W/m^2K for three different metal hydride materials
Wall Thickness of the Tank	mm	Variable ranging in between 1,0 mm and 7,0 mm for three different metal hydride materials

6. The Results of Finite Element Analysys Results

The metal hydride powder is used as variable ranging in between 0,01 and 1,0 mm for three different metal hydride materials. The maximum temperature value achieved inside the tank at the maximum level is 220 ^oC for $MmNi_{4,6}Al_{0,4}$, 145 ^oC for $LaNi_5$ and 105 ^oC for $LaNi_{4.75}Al_{0.25}$. For the given operating conditions, the time reaching the temperature below 20 ^oC level is about 100 seconds for $LaNi_{4.75}Al_{0.25}$, for 500 seconds for $MmNi_{4,6}Al_{0,4}$ and for 625 seconds for $LaNi_{4.75}Al_{0.25}$. The maximum amount of hydrogen mass to be stored for $LaNi_5$ is 2,7 gr in 600 seconds, for $MmNi_{4,6}Al_{0,4}$ is 1,6 gr in 520 seconds and for $LaNi_{4.75}Al_{0.25}$, is 1,2 gr in 80 seconds. The equilibrium pressure values of the system for each of three metal hydride materials seem to have all similar, which is $5*10^5$ Pa.

The storage tank having fins or not is used as variable ranging with fins having angle of 45 degree, with fins with no angle and with no fins. The maximum temperature value which is achieved inside the tank at the maximum level is 190 ^oC for $MmNi_{4,6}Al_{0,4}$, 110 ^oC for $LaNi_5$ and 80 ^oC for $LaNi_{4.75}Al_{0.25}$. For the given operating conditions, the time reaching the temperature below 20 ^oC level is about 200 seconds for $LaNi_{4.75}Al_{0.25}$, for 600 seconds for $MmNi_{4,6}Al_{0,4}$ and for more than 700 seconds for $LaNi_{4.75}Al_{0.25}$. The maximum amount of hydrogen mass to be stored for $LaNi_5$ is more than 1,7 gr in about 700 seconds, for $LaNi_{4.75}Al_{0.25}$, is 1,2 gr in 180 seconds and for $MmNi_{4,6}Al_{0,4}$ is 0,85 gr in 600 seconds. The equilibrium pressure values of the system for each of three metal hydride materials seem to have all similar, which is $3*10^5$ Pa.

The hydrogen inlet pressure is used as variable ranging in between 5 and 35 bar for three different metal hydride materials. The maximum temperature value which is achieved inside the tank at the maximum level is 250 ^oC for $LaNi_5$, 220 ^oC for $MmNi_{4,6}Al_{0,4}$ and 80 ^oC for $LaNi_{4.75}Al_{0.25}$. For the given operating conditions, the time reaching the temperature below 20 ^oC level is about 50 seconds for $LaNi_{4.75}Al_{0.25}$, for 180 seconds for $MmNi_{4,6}Al_{0,4}$ and 280 seconds for $LaNi_5$. For the given operating conditions, the maximum amount of hydrogen mass to be stored for $LaNi_5$ is 2,8 gr in about 280 seconds, for $MmNi_{4,6}Al_{0,4}$ is 1,95 gr in 220 seconds and for $LaNi_{4.75}Al_{0.25}$, is 1,2 gr in 80 seconds. The equilibrium pressure values of the system for each of three metal hydride materials seem to have all similar, which is $3,5*10^6$ Pa at maximum.

The inlet radius of the storage tank is used as variable ranging in between 5,00 and 11,98 mm for three different metal hydride materials. The maximum temperature value achieved inside the tank at the maximum level

is 280 °C for $LaNi_5$, 210 °C for $MmNi_{4,6}Al_{0,4}$ and 120 °C for $LaNi_{4.75}Al_{0.25}$. For the given operating conditions, the time reaching the temperature below 20 °C level is about 30 seconds for $LaNi_{4.75}Al_{0.25}$, from 70 seconds to 320 seconds for different inlet radius values for $MmNi_{4,6}Al_{0,4}$ and from 80 seconds to 450 seconds for different inner radius values for $LaNi_5$. The maximum amount of hydrogen mass to be stored for $LaNi_5$ is 4,0 gr in about 450 seconds, for $MmNi_{4,6}Al_{0,4}$ is 2,90 gr in 400 seconds and for $LaNi_{4.75}Al_{0.25}$, is 1,8 gr in less than 10 seconds. The equilibrium pressure values of the system for each of three metal hydride materials seem to have all similar, which is $2,0*10^6$ Pa at maximum.

The temperature of cooling fluid is used as variable ranging in between 288 K and 308 K (between -5 °C and 15 °C) for three different metal hydride materials. The maximum temperature value which is achieved inside the tank at the maximum level is 300 °C for $MmNi_{4,6}Al_{0,4}$, 270 °C for $LaNi_5$ and 120 °C for $LaNi_{4.75}Al_{0.25}$. For the given operating conditions, the time reaching the temperature below 20 °C level is about 75 seconds for $LaNi_{4.75}Al_{0.25}$, from 180 seconds to 300 seconds for different temperature values for $LaNi_5$, and from 290 seconds to 390 seconds for different inner radius values for $MmNi_{4,6}Al_{0,4}$. For the given operating conditions, the maximum amount of hydrogen mass to be stored for $LaNi_5$ is 2,8 gr in about 280 seconds, for $MmNi_{4,6}Al_{0,4}$ is 1,90 gr in 200 seconds and for $LaNi_{4.75}Al_{0.25}$, is 1,25 gr in about 30 seconds. The equilibrium pressure values of the system for each of three metal hydride materials seem to have all similar, which is $2,0*10^6$ Pa at maximum.

The general convective heat transfer coefficient is used as variable ranging in between 750 and 2250 $W/(m^2K)$ for three different metal hydride materials. The maximum temperature value which is achieved inside the tank at the maximum level is 300 °C for $MmNi_{4,6}Al_{0,4}$, 220 °C for $LaNi_5$ and 120 °C for $LaNi_{4.75}Al_{0.25}$. For the given operating conditions, the time reaching the temperature below 20 °C level is about 50 seconds for $LaNi_{4.75}Al_{0.25}$, about 220 seconds for $MmNi_{4,6}Al_{0,4}$ and about 320 seconds for $LaNi_5$. For the given operating conditions, the maximum amount of hydrogen mass to be stored for $LaNi_5$ is 2,8 gr in about 300 seconds, for $MmNi_{4,6}Al_{0,4}$ is 1,85 gr in 300 seconds and for $LaNi_{4.75}Al_{0.25}$, is 1,20 gr in about 40 seconds. The equilibrium pressure values of the system for each of three metal hydride materials seem to have all similar, which is $2,0*10^6$ Pa at maximum.

The wall thickness is used as variable ranging in between 1,0 mm and 7,0 mm for three different metal hydride materials. The maximum temperature value achieved inside the tank at the maximum level is 300 °C for $MmNi_{4,6}Al_{0,4}$, 220 °C for $LaNi_5$ and 120 °C for $LaNi_{4.75}Al_{0.25}$. For the given operating conditions, the time reaching the temperature below 20 °C level is about 50 seconds for $LaNi_{4.75}Al_{0.25}$, about 250 seconds for $MmNi_{4,6}Al_{0,4}$ and about 330 seconds for $LaNi_5$. The maximum amount of hydrogen mass to be stored for $LaNi_5$ is 2,8 gr in about 300 seconds, for $MmNi_{4,6}Al_{0,4}$ is 1,85 gr in 240 seconds and for $LaNi_{4.75}Al_{0.25}$, is 1,25 gr in about 40 seconds. The equilibrium pressure values of the system for each of three metal hydride materials seem to have all similar, which is $2,0*10^6$ Pa at maximum.

7. Conclusions

Achieving the results, the maximum temperature inside the tank, the minimum time duration that the system reaches the equilibrium conditions, the maximum amount of hydrogen mass absorbed in the analyzed conditions, the time of achieveing of maximum amount of hydrogen mass and the equilibrium pressure of the system is summarized for three different type of metal hydride materials (Table 2). In each cell in the table, data are for $MmNi_{4,6}Al_{0,4}$, $LaNi_{4.75}Al_{0\cdot25}$ and $LaNi_5$ respectively.

- After evaluating the results in the modelling study, it is clear that you should select $LaNi_5$ material to get the maximum amount of hydrogen mass to be stored. In this case, you should know that you need more time to get the maximum amount of hydrogen mass. On the other hand if you need the amount of hydrogen mass in a short time, as the amount of it is not so important as a maximum level, then you should prefer to choose $LaNi_{4.75}Al_{0.25}$ material.
- The maximum heat energy releasing and the highest-maximum inner temperature achievement is recorded for $MmNi_{4,6}Al_{0,4}$ material (300 °C), whereas the highest-minimum one is for $LaNi_{4.75}Al_{0.25}$ (80 °C).
- For the given operating conditions, the minimum-longest time reaching the equilibrium is for $MmNi_{4,6}Al_{0,4}$ and $LaNi_5$ materials (700 sec), whereas the minimum-shortest time is for $LaNi_{4.75}Al_{0.25}$ material in general (100 sec) but specifically for $MmNi_{4,6}Al_{0,4}$ (75 sec).
- For the given operating conditions, the maximum amount of hydrogen mass is for the $LaNi_5$ material (4.0 gr), whereas the minimum values are achieved for $LaNi_{4.75}Al_{0.25}$ material in general (1,20 gr) but specifically for $MmNi_{4,6}Al_{0,4}$ (0,85 gr).
- The achieved time values for the maximum amount of hydrogen mass to be stored are the longest in $LaNi_5$ material (650 sec) in general, whereas the shortest in $LaNi_{4.75}Al_{0.25}$ material (40 sec) in general.
- The equilibrium pressure values of the system for each of three metal hydride materials seem to have all similar.

- Each of the metal hydride materials shows different hydriding results per their own thermo-physical properties (Fig. 6).

Table 2. The results achieving in the study for three different type of metal hydride materials (The results printed in each cell are for $MmNi_{4.6}Al_{0.4}$, $LaNi_{4.75}Al_{0.25}$ and $LaNi_5$ respectively)

Varying Parameter	Max. Inner Temperature (°C)	The Time Reaching The Equilibrium Temperature –Min (sec)	Max. Amount of Hydrogen to be Absorbed (g)	Max Time Values For Maximum Amount Of Hydrogen To Be Stored (sec)	Equilibrium Pressure (10^6 Bar)
Particule Size of Hydride Material	220 - 105 – 150	650 - 180 - 700	1,7 - 1,2 - 2,65	650 - 100 - 650	0,5 - 0,5 - 0,5
Having fins	190 - 80 – 111	700 - 200 - 650	0,85 - 1,2 - 1,7	600 - 200 - 650	0,3 - 0,2 - 0,2
Inlet Pressure of Hydrogen	220 - 82 – 250	200 - 140 - 400	1,95 - 1,2 - 2,8	200 - 100 - 280	3,5 - 3,5 - 3,5
Inlet Radius of the Tank	290 - 120 – 220	75 - 100 - 150	2,75 - 1,8 - 4,0	350 - 100 - 450	2,0 - 2,0 - 2,0
Temperature of Cooling Fluid	300 - 125 – 220	250 - 100 - 380	1,95 - 1,28 - 2,80	200 - 60 - 290	2,0 - 2,0 - 2,0
General Convective Heat Transfer Coefficient	300 - 122 – 220	250 - 100 - 450	1,9 - 1,28 - 2,8	260 - 90 - 370	2,0 - 2,0 - 2,0
Wall Thickness of the Tank	300 - 118 – 220	250 - 110 - 420	1,9 - 1,25 - 2,75	220 - 40 - 340	2,0 - 2,0 - 2,0

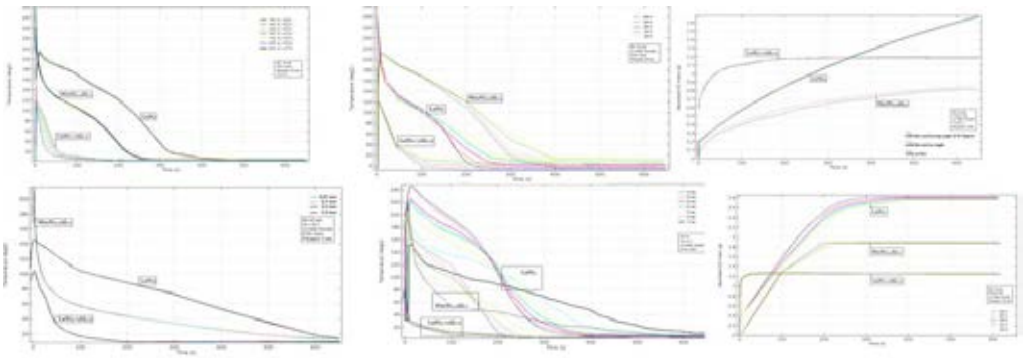


Fig. 6. Graphical views showing that each of the metal hydride materials shows different hydriding results per their own thermo-physical properties

References

1. Serge Nyallang Nyamsi, Fusheng Yang, Zaoxiao Zhang. An optimization study on the finned tube heat exchanger used in hydride hydrogen storage system analytical method and numerical simulation. International Journal of Hydrogen Energy 37 (2012) 16078 - 16092
2. Fusheng Yang, Xiangyu Meng, Jianqiang Deng, Yuqi Wang, Zaoxiao Zhang. Identifying heat and mass transfer characteristics of metal hydride reactor during adsorption—Parameter analysis and numerical study. International Journal of Hydrogen Energy 33 (2008) 1014 – 1022
3. Wang YQ, Yang FS, 2hang ZX, fengX, Guo QF. Design andproceas simulotion of metal hydride reaktors.) Xi'an jioatong Unv. 2006, 40 (7). 831-5)
4. M. Gambini, M. Manno, M. Velini. Numerical analysis and performance assessment of metal hydride-based hydrogen storage systems. International Journal of Hydrogen Energy 33 (2008) 6178–6187
5. Muthukumar P, Prakash Maiya M, Srinivasa Murthy S. Experiments on a metal hydride-based hydrogen storage device. Int J Hydrogen Energy 2005,30(15).1569–81.
6. Constantinos A. Krokos, Dragan Nikolic, Eustathios S. Kikkinides, Michael C. Georgiadis, Athanasios K. Stubos. Modeling and optimization of multi-tubular metal hydride beds for efficient hydrogen storage.

International Journal of Hydrogen Energy 34 (2009) 9128–9140
7. F. Askri, M. Ben Salah, A. Jemni, S. Ben Nasrallah. Optimization of hydrogen storage in metal-hydride tanks. International Journal of Hydrogen Energy 34 (2009) 897 – 905
8. Tzu-Hsiang Yen, Bin-Hao Chen, Bao-Dong Chen. Numerical simulation and performance test of metal hydride hydrogen storage system, Internatıonal Journal Of Energy And Envıronment, Volume 2, Issue 3 (2011) 401-414.
9. A. Freni, F. Cipiti, G. Cacciola. Finite element-based simulation of a metal hydride-based hydrogen storage tank. International Journal of Hydrogen Energy 34 (2009) 8574–8582
10. Karelle Couturier, Farida Coppich, Antje Wörner, Rainer Tamme. Tank design for on-board hydrogen storage in metal hydrides. DLR-German Aerospace Center, Institute of Technical Thermodynamics, 70569 Stutgart, Germany (2008) ES2008-54031
11. Zewei Bao, Zhen Wu, Serge Nyallang Nyamsi, Fusheng Yang, Zaoxiao Zhang. Three-dimensional modeling and sensitivity analysis of multi-tubular metal hydride reactors. Applied Thermal Engineering 52 (2013) 97-108
12. B.A. Talaganis, G.O. Meyer, P.A. Aguirre. Modeling and simulation of absorption-desorption cyclic processes
for hydrogen storage-compression using metal hydrides. International Journal of Hydrogen Energy 36 (2011) 13621 – 13631
13. Fusheng Yang, Xiangyu Meng, Jianqiang Deng, Yuqi Wang, Zaoxiao Zhang. Identifying heat and mass transfer characteristics of metal hydride reactor during adsorption. Improved formulation about parameter analysis. International Journal of Hydrogen Energy 34 (2009) 1852–1861
14. Stephen L. Garrison, Bruce J. Hardy, Mikhail B. Gorbounov, David A. Tamburello, Claudio Corgnale, Bart A. vanHassel, Daniel A. Mosher, Donald L. Anton. Optimization of internal heat exchangers for hydrogen storage tanks utilizing metal hydrides. International Journal of Hydrogen Energy 37 (2012) 2850-2861.
15 Ryan R. Hopkins, Kwang J. Kim. Hydrogen compression characteristics of a dual stage thermal compressor system utilizing LaNi5 and Ca0.6Mm0.4Ni5 as the working metal hydrides. International Journal of Hydrogen Energy 35 (2010) 5693 - 5702
16. Kui Jiao, Xianguo Li, Yan Yin, Yibo Zhou, Shuhai Yu, Qing Du. Effects of various operating conditions on the hydrogen absorption processes in a metal hydride tank. Applied Energy 94 (2012) 257–269
17. Hui Wang, Ajay K. Prasad, Suresh G. Advani. Hydrogen storage systems based on hydride materials with enhanced thermal conductivity. International Journal of Hydrogen Energy 37 (2012) 290-298
18. Jianhua Ye, Lijun Jiang, Zhinian Li, Xiaopeng Liu, Shumao Wang, Xinyu Li. Numerical analysis of heat and mass transfer during absorption of hydrogen in metal hydride based hydrogen storage tanks. International Journal of Hydrogen Energy 35 (2010) 8216–8224
19. P. Muthukumar, U. Madhavakrishna, Anupam Dewan. Parametric studies on a metal hydride based hydrogen storage device. International Journal of Hydrogen Energy 32 (2007) 4988 – 4997.
20. P. Muthukumar, S. Venkata Ramana. Numerical simulation of coupled heat and mass transfer in metal hydride-based hydrogen storage reactor. Journal of Alloys and Compounds 472 (2009) 466–472
21. Sharad D. Patil, M. Ram Gopal. Analysis of a metal hydride reactor for hydrogen storage. International Journal of Hydrogen Energy 38 (2013) 942-951
22. Mandhapati Raju, Jerome P. Ortmann, Sudarshan Kumar. System simulation model for high-pressure metal hydride hydrogen storage systems. International Journal of Hydrogen Energy 35 (2010) 8742-8754
23. Jinmoo Nam, Johan Ko, Hyunchul Ju. Three-dimensional modeling and simulation of hydrogen absorption in metal hydride hydrogen storage vessels. Applied Energy 89 (2012) 164–175
24. Maha Bhouri, Jacques Goyette, Bruce J. Hardy, Donald L. Anton. Numerical modeling and performance evaluation of multi-tubular sodium alanate hydride finned reactor. International Journal of Hydrogen Energy 37 (2012) 1551-1567
25. Jin-Woo Hwang, Do-Young Yoon, Kil-Ho Choi, Younghun Kim, Lae Hyun Kim. 3D CFD analysis of the hydrogen releases and dispersion around storage facilities. Korean J. Chem. Eng. 25(2), 217-222 (2008)
26. A. Freni, F. Cipitì. 3D Dynamic Simulation of a Metal Hydride-Based Hydrogen Storage Tank. The Proceedings of the COMSOL Conference 2008 Hannover
27. M. Melnichuk, N. Silin, H.A. Peretti. Optimized heat transfer fin design for a metal-hydride hydrogen storage container. International Journal of Hydrogen Energy 34 (2009) 3417 – 3424.
28. Uchida H, Oyakawa K, Watanabe S. Development of a metal hydride tank for quick charge. In. Proceedings 14th World Hydrogen Energy Conference 2002, Montreal, Canada
29. Mosher DA, Arsenault MS, Tang X, Anton DL. Design, fabrication and testing of NaAlH4 based hydrogen storage systems. J Alloys Comp 2007,446–447.707–12.
30. Matsevity Yu M, Solovey VV, Chernaya NA, Podgorny AN. Development and creation of an effective design of a metal-hydride hydrogen accumulator. In. Proceedings World Hydrogen Technologies Convention 2007,

Montecatini Terme, Italy
31. Kayfeci Muhammet, Metal Hidrür Reaktör Tasarım Parametrelerinin Hidrojen Depolama Özelliklerine Etkisinin Deneysel Olarak İncelenmesi, Süleyman Demirel Ünv Fen Bilimleri Enst. Makine Müh ABD, Doktora Tezi, 2011

Synthesis of Polymer Supported Ni (II)-Schiff Base Complex and Its Usage As a Catalyst In Hydrogen Generation From $NaBH_4$ Hydrolysis

Dilek Kılınç[1], Ömer Sahin[2]
[1]Faculty of Science and Letters, Department of Chemistry, Siirt University, 56100 Siirt
[2]Faculty of Engineering and Architecture, Department of Chemical Engineering, Siirt University, 56100 Siirt
Email: dkilinc@siirt.edu.tr, sahinomer2002@yahoo.com

Abstract
To study influence of using as catalysis, the new Ni-Schiff Base complex in $NaBH_4$ hydrolysis reaction to hydrogen generation was intended. Also aimed that with supported amberzyme oxirane resin polymer that increasing the activity of catalyst. The prepared catalyst was characterized by using SEM, XRD, BET, FT-IR, methods. Polymer supported Ni-Schiff Base complex catalyzed $NaBH_4$ hydrolysis reaction was investigated depending on concentration of $NaBH_4$, NaOH, temperature, percentage of Ni complex in total polymer supported Ni-Schiff Base complex and amount of catalyst factors. Maximum rate was 13000 mL H_2. g^{-1} cat.$\cdot$ min^{-1} and 24242 mL H_2/ gcat.min at 30 ^{0}C and 50 ^{0}C, respectively. The activation energy of complex catalyzed $NaBH_4$ hydrolysis reaction was found as 25370 kj.mol^{-1}.

Keywords: Hydrogen generation; catalyst; hydrolysis; Schiff base; complex.

1. Introduction

Hydrogen is well accepted as potential alternative perform the increasing energy necessity on the world by exhausting of conventional fossil fuel reserves. Because of the provide fossil fuels is limited the improvement of alternative and environmental clean renewable energy porters are most significance [1]. The efficiency of hydrogen release by using suitable catalysts can be significantly improved. Schlesinger et al. [2] show that the hydrogen generation from alkaline $NaBH_4$ solution could expedite by the following reaction:

$$NaBH_4 + 2H_2O \rightarrow 4H_2 + NaBO_2 + Q\ (217\ kJ) \quad (1)$$

Self-hydrolysis of $NaBH_4$ for hydrogen production, the reaction rate to cannot sufficient at room temperature. Consequently using catalyst plays a key role in hydrogen generation from $NaBH_4$ hydrolysis. In order to increase hydrogen production rate from $NaBH_4$ hydrolysis reaction by several catalysts such as Rh based [3], Pt based [4], Ru based [5], Co based [6], Ni based [7], etc. developed. Nevertheless, only limited studies to using of metal-complex catalysts for hydrogen production from $NaBH_4$ hydrolysis have been reported [1]. The price and availability of catalyst in the reaction of hydrogen production from $NaBH_4$ hydrolysis by various catalysts, overwhelmingly important parameters. High price of the catalysts limits their using in wide area. Ni-based catalysts provide objective interest as a catalyst because of their low cost and environmentally friendly construction [8].

It is well known that the support can powerfully affect the catalytic activity of the metal catalysts. Actually the support can directly take part to the reaction, such as verified by the absorption of the reactants / products or being involved through acid/base site or can also have indirect effect by optimizing the cleavage of the catalytically active components and stabilizing them in contrast to sintering [9].

In this research, the new Schiff Base complex which named 5-Amino-2,4-dichlorophenol-3,5-di-*tert*-butylsalisylaldimine Ni were synthesized. Than this complex supported on amberzyme oxirane resin polymer and it was used as a catalyst for H_2 production from $NaBH_4$ hydrolysis. Polymer-Ni catalyzed $NaBH_4$ hydrolysis reaction was investigated depending on concentration of $NaBH_4$, NaOH, temperature, percentage of Ni complex and amount of catalyst. In addition the catalyst and products were characterized with some analysis technique like SEM, XRD, BET, and FT-IR.

2. Experimental Study

2.1. Synthesis of salicylaldimine complex

5-Amino-2,4-dichlorophenol-3,5-di-*tert*-butylsalisylaldimine of complex was synthesis from the solution of 1.0 mmol Ni(II) chloride hexahydrate in absolute ethanol was added to the solution of 2.0 mmol 5-Amino-2,4-dichlorophenol-3,5-di-*tert*-butylsalisylaldimine ligand with equal molar amounts, according to the similar method reported in the literatures [1].

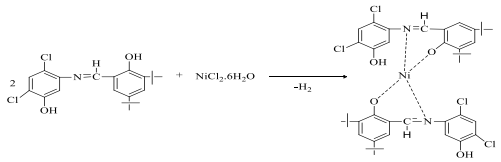


Fig.1. Structure of 5-Amino-2, 4-dichlorophenol-3, 5-ditertbutylsalisylaldimine ligand Ni complex

2.2. Polymer supported-Ni (II)-Schiff Base Complex Catalyst preparation

The amberzyme oxirane resin polymer supported Ni (II)-Schiff Base complex catalysts were prepared by mechanical mixing method. In 10 mL absolute ethanol dissolved 5-Amino-2,4-dichlorophenol-3,5-ditertbutylsalisylaldimine Ni complex with different percentage and then 0.1 gram amberzyme oxirane resin polymer was added in this solution and stirred about 24 hour and then filtered.

2.3. Hydrogen Generation

Hydrolysis reaction system contained 10 mL solution including 2.0 wt % $NaBH_4$, 10 wt % NaOH, was introduced into the flask. The theoretical hydrogen volume in this mixture according to Eq. (1) is about 560 mL at temperature of 30 °C.

Results and Discussion

3.1. FT-IR Spectra

The FT-IR of complex catalyst has been studied in order to characterize their structures. Characteristic absorptions in the spectra FT-IR of their pure Ni-Schiff Base complex and polymer supported-Ni (II)-Schiff Base complex catalyst are represented in Fig. 2. The FT-IR spectra of complex catalysts are found to be some difference to each other. The difference are, significant frequencies which selected by comparing the FT-IR spectra of pure Ni-Schiff Base complex and polymer supported-Ni (II)-Schiff Base complex catalyst. Some of the fundamental peaks of were pure Ni-Schiff Base complex shifted from its site after supported on polymer (Fig. 2). There are too strong and sharp bands appeared at 1659 and 1690 cm^{-1} are detected to CH=N stretching vibrations of the azomethine. On the polymer supported-Ni (II)-Schiff Base complex catalyst, this band is shifted to broader and a lower frequency range is almost same which 1699 cm-1 is.

As seen that the spectra FT-IR of pure Ni-Schiff Base complex and polymer supported-Ni (II)-Schiff Base complex catalyst bands at between 2958 and 2895 cm^{-1} are due to the free -OH or intramolecular OH···N groups. The peak at about 3671 cm^{-1} describes that polymeric free -OH for polymer supported-Ni (II)-Schiff Base complex catalyst, which was nonexistent for pure Ni-Schiff Base complex. Peaks that is at 1100 cm^{-1} for pure Ni-Schiff Base complex converted to very sharp peak following polymer supported-Ni (II)-Schiff Base complex treatment at about 1065 cm^{-1} corresponds to C-O stretching vibrations.

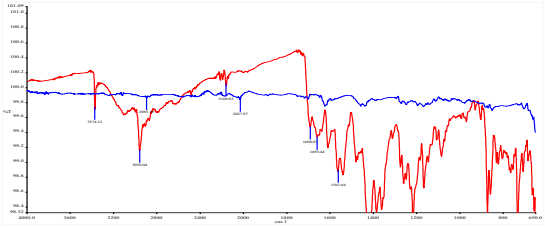


Fig. 2. FT-IR spectra of Ni(II)- Schiff Base complex and polymer supported-Ni(II)- Schiff Base complex

3.2. Crystalline Structures of Complex Catalysts

The XRD parameters of polymer supported-Ni (II)-Schiff Base complex catalyst and pure Ni-complex were shown at Figs. 3. These results display that pure Ni-complex and polymer supported-Ni (II)-complex indicate a crystalline nature, not an amorphous nature. The major peaks of polymer supported-Ni (II)-complex were generated at 8.35, 8.72, 10.22, 12.155,14.143, 17.51, 19.95, 20.59, 21.73, 23.65, 28.33 and 28.72, 39.35 corresponding to reflections at 256, 237, 129, 198, 232, 257, 266, 266, 316, 206, 269, 274, 299 respectively, as illustrated in Fig. 3. There is something remarkable about these diffraction peaks of polymer supported-Ni (II) complex catalysts did not correspond to pure Ni-complex. These results display that there is no difference in the catalyst between before and after hydrolysis reaction.

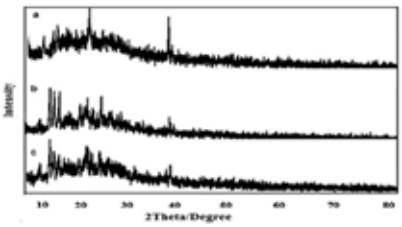


Table 1. BET surface area and pore volume measurements of the prepared catalysts.

Catalyst	S_{BET} (m^2/g)	Average pore ratio (nm)	Pore volume (cm^3/g)
Ni-comp.	48.456	14.7427	0.1784
Ni-comp/A.O.R. Pol.	76.040	18.217	0.1821

Fig. 3. X-ray diffractograms of (a) Ni(II) metal complex (b) Polymer Supported-Ni (II) metal complex before hydrolysis reaction (c) Polymer supported-Ni (II) metal complex after hydrolysis reaction.

3.2. BET Surface Area Analysis

Specific surface area, total pore volume, and average diameter of supported polymer are summarized in Table 1. It can be observed that the surface area of the Ni(II)- Schiff Base complex catalyst increases by using the polymer supported-Ni(II)-Schiff Base complex catalyst. It must be noticed that the higher surface area of the polymer supported-Ni(II)-Schiff Base complex catalyst. The pore volume of the polymer supported-Ni(II)-Schiff Base complex treated is considerably higher than Ni(II)-Schiff Base complex. While the BET surface area of Ni(II)-Schiff Base complex was found to be 48.456 m^2/g, the polymer supported-Ni(II)-Schiff Base complex was found to be 76.040 m^2/g. For the difference surface areas of the catalysts, one might think that the change in surface areas of the polymer support probably has the effect on rates as well. The polymer supported-Ni(II)-Schiff Base complex catalyst shows excellent catalytic performance to Ni(II)-Schiff Base complex catalyst, may be due to its higher surface area so that $NaBH_4$ can reach the active sites easily and the products can leave the active sites smoothly.

3.4. Scanning Electron Microscopy

SEM is used to determine the microscopic viewpoints of the polymer supported-Ni (II)-Schiff Base complex catalyst. SEM image of the polymer supported-Ni (II)-Schiff Base complex is as shown in Fig. 4. As shown in Fig. 4. (a, b, c, d) the polymer supported-Ni (II)-Schiff Base complex catalyst display powder shape with 1-2 µm. The SEM analysis of complex shows big size uniform particles form larger aggregates and we see clearly Ni metal particuls and polymer particuls with 100 µm (e). This indicates a maximum or complete supported complex formation.

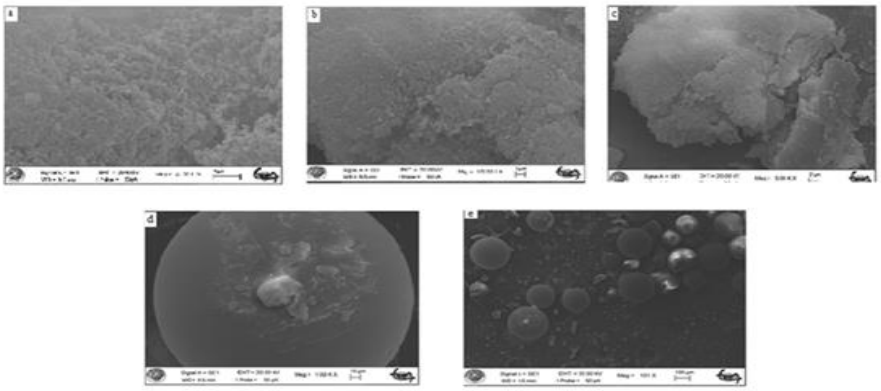


Fig. 4. SEM images of polymer supported-Ni(II)- Schiff Base complex (a,b:1 µm. , c, d: 2 µm, e:100 µm)

3.5. Effect of NaOH concentration

Fig. 5 indicated that the hydrogen production rates changing with different NaOH concentrations, like wt %, 5 wt %, and 15 wt %, 25 wt %, 50 wt %, at 30 °C in 2.0 wt % $NaBH_4$ solution with 10 wt %-Ni-Schiff Base complex in 15 mg of polymer supported-Ni (II)-Schiff Base complex catalyst. As observed in Fig. 8, the hydrogen generation from $NaBH_4$ hydrolysis reaction time was decreases and maximum reaction rate (Ro) was increasing with rising NaOH concentration and obtains maximum reaction rate (Ro), at 10 wt %.

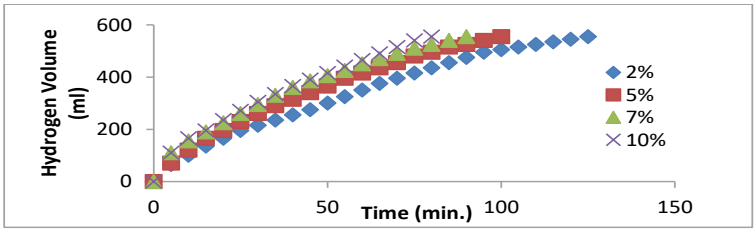


Fig. 5. Effect of NaOH concentration on the hydrogen generation rate at 30 °C, 2.0 wt % $NaBH_4$ and 10 wt %-Ni-Schiff Base complex in 15 mg of polymer supported-Ni(II)- Schiff Base complex

3.6. Effect of Ni(II)-complex ratio in total polymer supported complex

Polymer supported-Ni (II)-Schiff Base complex catalyst containing different Ni(II)-Schiff Base complex percentages prepared at room temperature by physical mixing method were tested for hydrogen production from

$NaBH_4$ hydrolysis reaction. Their hydrogen generation conversions at 30 °C are shown in Fig. 6. Firstly, the catalytic hydrogen performance volume is 560 mL for the 100% percentage of Ni(II) complex. And in polymer supported-Ni (II)-Schiff Base complex tried different percentages like 3%, 5%, 7%, 10%, 15%, and 20%, 25% Ni (II)-Schiff Base complex in total polymer supported-Ni (II) Schiff Base complex catalyst. When looked at Fig. 6, see that 25% Ni (II)-Schiff Base complex is the best amount with low reaction time, if we calculate their maximum reaction rate (initial rate) (R_o) 7% and 10% Ni (II)-Schiff Base complex catalysts R_o values are higher than the other as 13990,48, 13000 ml/(g.cat.min), respectively (Table 2). We prefer 10% Ni (II)-Schiff Base complex because of to complete the reaction in a shorter time (80 min.) than 7% (125 min.) and we didn't choose 3%, 5% Ni (II)-Schiff Base complex catalysts however their high R_o value, because in this percentage, $NaBH_4$ hydrolysis reaction didn't completed.

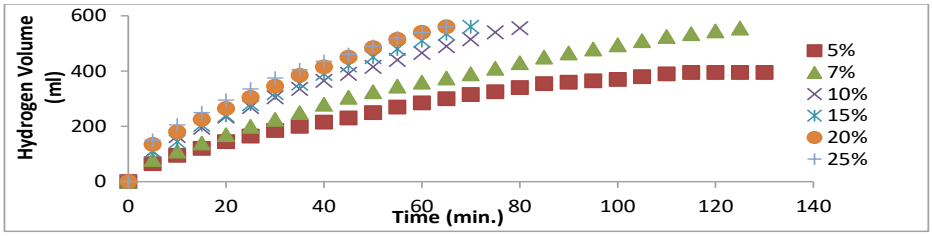


Fig. 6. Effect of Ni (II)-complex ratio in total polymer supported complex at 30 °C, 2.0 wt % $NaBH_4$, 10% NaOH and 15 mg of catalyst

Table 2. Comparison of different % Ni-complex in total polymer supported catalyst

% Ni-complex	3%	5%	7%	10%	15%	20%	25%
Maximum Reaction Rate(R_0) (ml/(g.cat.min)	22035.56 (reaction not completed)	17173.33 (reaction not completed)	13990.48	13000	8564.44	8320	7522.7

3.7. Effect of catalyst amount

Research of the effect of polymer supported-Ni (II)-Schiff Base complex catalyst amount, in hydrogen generation yield was tested by hydrolysis of 2.0 wt % $NaBH_4$, 5% NaOH solution using polymer supported-Ni (II)-Schiff Base complex catalyst (5, 15, 25, and 50 mg) at 30 °C. As seen in Fig. 7, the hydrogen generation from $NaBH_4$ hydrolysis reaction time was decreases due to activation of the catalyst, as increasing from 5 mg to 50 mg the polymer supported-Ni (II)-Schiff Base complex catalyst amount, but when looked at Table 3 for maximum reaction rate (Ro), we seen that 15 mg catalyst using $NaBH_4$ hydrolysis provided maximum reaction rate (Ro), so 15 mg catalyst amount was taken as optimum condition for this reaction. These results show that hydrogen generation rate can be determined by controlling the catalyst amount.

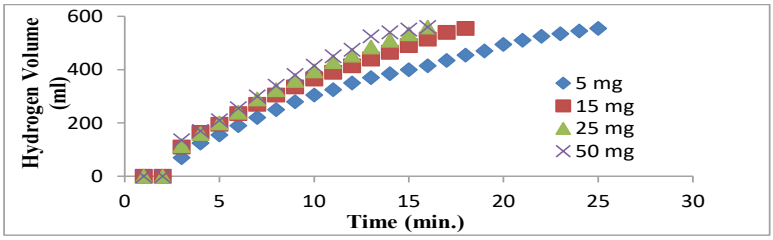


Fig. 7. Effect of catalyst amount on hydrogen generation rate at 30 °C, 2.0 wt% $NaBH_4$, 10 % NaOH and 10 wt %- Ni-Schiff Base complex in total polymer supported-Ni(II)- Schiff Base catalyst

Table 3. Comparison of different catalyst amount

Amount of catalyst	**5 mg**	**15 mg**	**25 mg**	**50 mg**
Maximum Reaction Rate (R0) (ml/(g.cat.min)	26152	13004,67	7949,6	4554,6

3.8. Effect of $NaBH_4$ Concentration

Fig. 8 indicates the hydrogen generation rate with kind of difference as wt % 2, 5, 7 and 10 $NaBH_4$ concentrations.

Effect of $NaBH_4$ concentration on hydrogen generation rate was measured using 10 wt % NaOH solutions at 30 °C and 10 wt %-Ni-Schiff Base complex in 15 mg of polymer supported-Ni(II)- Schiff Base complex. When $NaBH_4$ concentration increase the maximum reaction rate (Ro) is not change in the hydrogen generation from $NaBH_4$ hydrolysis reaction. According to this result it can be said that catalytic activity of polymer supported-Ni(II)- Schiff Base complex is not changing depending on $NaBH_4$ concentration.

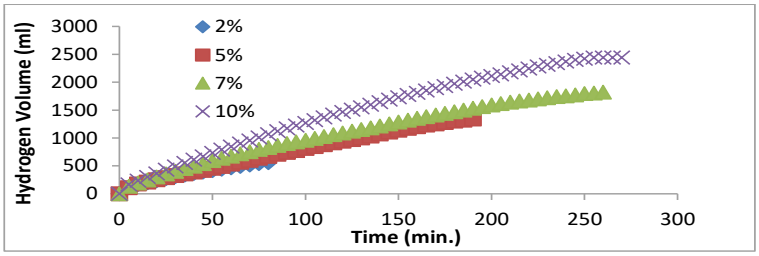


Fig.8. Effect of NaBH4 concentration on the hydrogen generation rate at 30 °C, 10 % NaOH and 10 wt %-Ni-Schiff Base complex in 15 mg of polymer supported-Ni(II)- Schiff Base complex

3.9. Effect of The Reaction Temperature

Fig. 9 shows that the hydrogen generation rate with 2% $NaBH_4$ aqueous solution at different temperature intervals as 20, 30, 40, 50 °C with 10 wt % NaOH solutions and 10 wt %-Ni-Schiff Base complex in 15 mg of polymer supported-Ni(II)- Schiff Base complex. As expect in $NaBH_4$ hydrolysis reaction to hydrogen generation, temperature increase, decrease the reaction completed time and also increase the maximum reaction rate (Ro). However the best reaction temperature is 50 °C, because of always preferred the low temperature preference and the results are very close to each other, 30°C temperature was chosen for hydrolysis of $NaBH_4$ reaction.

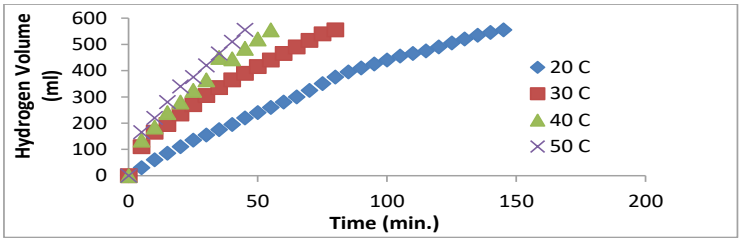


Fig.9. Effect of temperature on the hydrogen generation rate at 2.0 wt % NaBH4, 10 % NaOH, and 10 wt %-Ni-Schiff Base complex in 15 mg of polymer supported-Ni(II)-Schiff Base complex

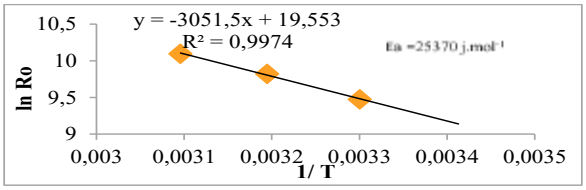


Fig. 10. Arrhenius equation according to nth-order reaction mod for the activation energy employing, at 2.0 wt % NaBH4, 10 % NaOH, and 10 wt %-Ni-Schiff Base complex in 15 mg of polymer supported-Ni(II)-Schiff Base complex

Amberzym oksirane resin polymer supported-Ni(II) salicylaldimine derivatives Schiff Base complex catalyst was prepared by a physical mixing method at room temperature in ethanol solution to hydrogen generation from $NaBH_4$ hydrolysis. The hydrolysis of $NaBH_4$ with Amberzym oksirane resin polymer supported-Ni(II)-Schiff Base complex catalyst was investigated depending on $NaBH_4$ concentration, NaOH concentration, temperature, Ni-complex in total polymer supported-Ni(II)- Schiff Base complex catalyst and catalyst amount. The catalytic performance was changed clearly with the different Ni(II)- Schiff Base complex percentage in total polymer supported-Ni(II)- Schiff Base complex catalyst. The optimal percentage of Ni(II)- Schiff Base complex was 10%. However, 25% Ni (II)-Schiff Base complex is the best amount with low reaction time, when calculated their maximum reaction rate (initial rate) (R_o) 7% and 10% Ni (II)-Schiff Base complex catalysts R_o values are

higher than the other as 13990.48, 13000 ml/(g.cat.min), respectively (Table 1). 10% Ni (II)-Schiff Base complex was preferred, because of shorter reaction completed time (80 min.) than 7% (125 min.) and 3%, 5% Ni (II)-Schiff Base complex catalysts were not select however their high R_o value, because of $NaBH_4$ hydrolysis reaction could not be completed with this percentages. (Total hydrogen production respectively 230 ml, and 395 ml).

When all the results were examined, it was observed that all the data were compatible with each other. And in $NaBH_4$ hydrolysis reaction optimum conditions were provided with using 30°C, 10% NaOH, 10 wt %-Ni-Schiff Base complex in 15 mg of polymer supported-Ni(II)-Schiff Base complex catalyst and % 2 $NaBH_4$. The maximum reaction rate was 13000 mL H_2 g-1 cat.min^{-1} and 24242 mL H_2 g^{-1}cat.min-1 at 30 °C and 50 °C, respectively. The activation energy of complex catalyzed $NaBH_4$ hydrolysis reaction is found as 25370 $Jmol^{-1}$.
Looking at the literature to compare as same works in different temperature by Ni-B, Ru, Rh/TiO_2 catalyst at Table 4 with amberzym oksirane resin polymer supported-Ni(II)-Schiff Base complex catalyst, amberzym oksirane resin polymer supported-Ni(II)-Schiff Base complex catalyst has a high activity in $NaBH_4$ hydrolysis reaction to hydrogen generation.

Table 4. Compared metal catalysts for sodium borohydride hydrolysis

Catalyst	Activity (mL H_2 min^{-1}(g $catalyst^{-1}$)	Temperature (°C)
Ni-B	3400	30 [10]
Ru	18600	60 [11]
Rh/TiO_2	215	23 [12]
Ni/A.O.R. Pol. (in this work)	13000 24242	30 50

And all the results shows that Amberzyme oxirane resin polymer supported Ni-Schiff Base complex is very effective catalyst in $NaBH_4$ hydrolysis for hydrogen generation

References

1. Kilinc D, Saka C, Omer S. Journal of Power Sources. 2012;217:256-261
2. Schlesinger HI, Brown HC, Finholt AE, Gilbreath JR, Hoekstra HR, Hyde EK. J. Am. Chem. Soc. 1953;75:215-219.
3. Larichev YV, Netskina OV, Komova OV, Simagina VI. Comparative XPS study of Rh/Al_2O_3 and Rh/TiO_2 as catalysts for $NaBH_4$ hydrolysis. Int. J. Hydrogen Energy 2010;35:6501-7.
4. Dongyan X, Huamin Z, Wei Y. Hydrogen generation from hydrolysis of alkaline sodium borohydride solution using Pt/ C. Catal Commun. 2007;8:1767-71.
5. Amendola SC, Sharp-Goldman SL, Janjua MS, Kelly MT, Petillo PJ, Binder M. An ultrasafe hydrogen generator: aqueous, alkaline borohydride solutions and Ru catalyst. J Power Sources. 2000;85:186-9.
6. Li Q, Chen Y, Lee DJ, Li F, Kim H. Preparation of Y-zeolite/ $CoCl_2$ doped PVDF composite nanofiber and its application in hydrogen production. Energy 2012;38:144-50.
7. O. Sahin C, Saka O, Baytar F, Hansu. Influence of plasma treatment on electrochemical activity of Ni (0)-based catalyst for hydrogen production by hydrolysis of $NaBH_4$. J. Power Sources. 2013;240:729-735. http://dx.doi.org/10.1080/15567036.2011.603023.
8. Sahin O, Kilinc D, Cafer S. Journal of Energy Institute. 2016;89:617-626.
9. Che M, Clause O, Marcilly CH. Impregnation and ion exchange. In: Ertl G, Kno'zinger H, Weitkamp J, Editors. Preparation of solid catalysts. Weinheim: WileyeVCH 1999;315:40.
10. Walter JC, Zurawski AD, Montgomery M, Thornburg and Revankar S. J. Power Sources. 2008; 179:335–339.
11. Amendola SC, Sharp-Goldman SL, Janjua, MS, Kelly MT, Petillo PJ, M. Binder M. J. Power Sources. 2000; 85:186–189.
12. Larichev YV, Netskina OV, Komova OV, Simagina VI. Int. J. Hydrogen Energy 2010;35:6501–6507.

Analysis Of Control Strategies For Fuel Saving In The Hydrogen Fuel Cell Vehicles

Yakup Hameş[a], Kemal Kaya[a], Ertuğrul Baltacioğlu[b], Arzu Türksoy[a]
[a]Department of Electrical and Electronics Engineering, Iskenderun Technical University, Hatay, Turkey
[b]Department of Mechanical Engineering, Iskenderun Technical University, Hatay, Turkey
Email: yakup.hames@iste.edu.tr , kemal.kaya@iste.edu.tr , ertugrul.baltacioglu@iste.edu.tr , arzu.turksoy@iste.edu.tr

Abstract
Thanks to sustainable fuel nature of hydrogen, hydrogen fuel cell vehicles are inevitably more advantageous than other conventional vehicles. Since the energy efficiency of the hydrogen fuel cell is high, replacing the internal combustion engines with hydrogen fuel cell vehicles will contribute to the developing technology. A hydrogen fuel cell vehicle requires fuel cells, batteries, controllers and smart control units with their control strategies. The controller is responsible for the energy transfer between the battery and the fuel cell and for controlling the motor output power via commands from the auxiliary power units. The smart control unit compares the nominal output power of the fuel cell with the requested power, calculates the parameters and continuously adjusts the variables. The control strategies that can be developed for these units will enable us to overcome the technological challenges for hydrogen fuel cell vehicles in the near future. This study presents the best hydrogen fuel cell vehicle configurations and control strategies for safe, low cost and high efficiency by comparing control strategies in the literature for fuel saving.

Keywords: Hydrogen; fuel cell; control strategy; fuel saving.

1. Introduction

In order to solve the global warming problem in the world, it is of utmost importance to minimize the demand for fossil fuels and reduce emissions. With this precaution, the trend towards hydrogen fuel cell vehicles in the transportation sector is increasing rapidly. Hydrogen fuel cells are static energy conversion devices that convert the chemical energy of hydrogen directly into electrical energy [1]. They are devices that are a source of promising and renewable energy sources with low emissions and high energy efficiency.

Hydrogen fuel cell vehicles aim to reduce both fuel consumption and pollution rate while preparing to replace traditional internal combustion engine vehicles. In addition to these advantages, there are disadvantages of having lower power density and slow in power response [2]. However, it is necessary to develop control strategies to achieve the advantages of hydrogen fuel cell vehicles and to mitigate disadvantages. It is necessary to design the controllers used when setting these control strategies. For this, the designs for the electronic power circuits in the fuel cell system should aim to increase the efficiency of the system and meet other needs. Controllers provide optimization of the energy generated by the system and are also responsible for controlling the power between the fuel cell and energy storage systems. The purpose of this study is to analyze the most efficient ones by presenting the advantages and disadvantages of control strategies for fuel saving in hydrogen fuel cell vehicles with increasing renewable energy direction in the transport sector.

2. Control Strategies of the Hydrogen Fuel Cell Vehicles

Control mechanisms in hydrogen fuel cell vehicles usually include fuel cells, batteries and supercapacitors. Various controllers have been developed and applied to provide energy management in the vehicle. The most common control strategies used by these controllers are given below.

1. Peaking Power Source Strategy (PPSS) [3]
2. Operating Mode Control Strategy (OMCS) [2]
3. Fuzzy Logic Control Strategy (FLCS) [2, 4]
4. Equivalent Consumption Minimization Strategy (ECMS) [2, 5, 6]

The energy management system is generally as shown in Fig. 1. The different mechanisms of this system require control strategies. In order to the energy management of the vehicle to be efficiently controlled, these strategies must be correctly identified and tested for feasibility.

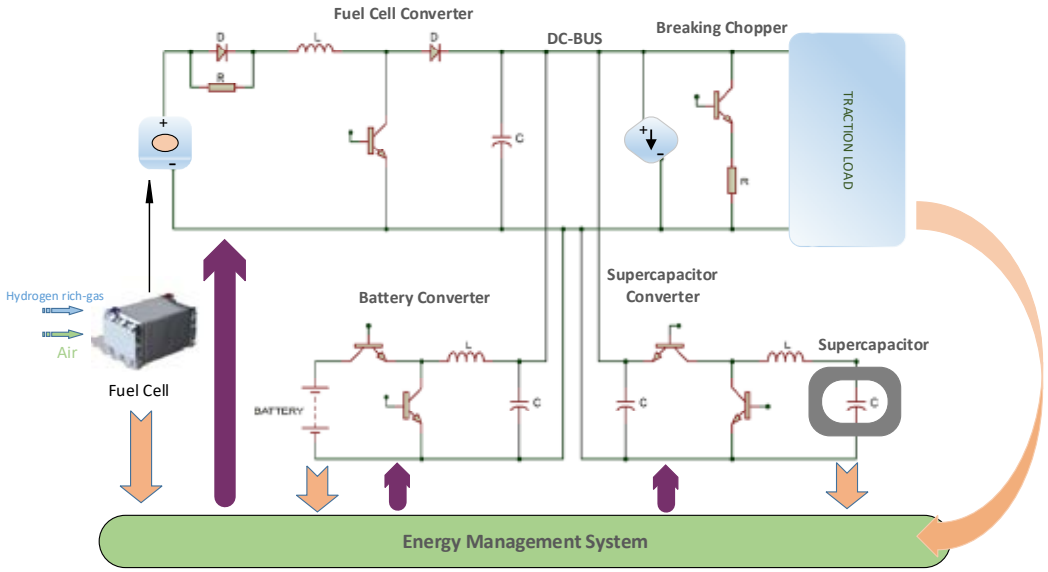


Fig. 1. The energy management system of the hydrogen fuel cell vehicle.

The energy management system should control the energy exchange between the fuel cell, the battery and the supercapacitor, as well as the power demanded by the system. Furthermore, DC / DC converters, DC / AC inverters, auxiliary power units and traction motor should also be included in the system control [7].

2.1. Peaking Power Source Strategy (PPSS)

In a vehicle configuration with a fuel cell, there are fuel cell, pedals, traction motor, peaking power source (PPS), vehicle controller, motor controller, electronic interface, wheels and the signals for the transmission between them. The vehicle controller controls power and torque according to commands from the gas and brake pedals. The electric motor operates as a generator with the command from the brake pedal and stores energy in the PPS. The PPS can store its energy from the fuel cell when the power of the fuel cell is greater than the power of the load [3]. The control strategy that ensures this is the peaking power source strategy (PPSS). The configuration of a hydrogen fuel cell vehicle using the PPS strategy is shown Fig. 2.

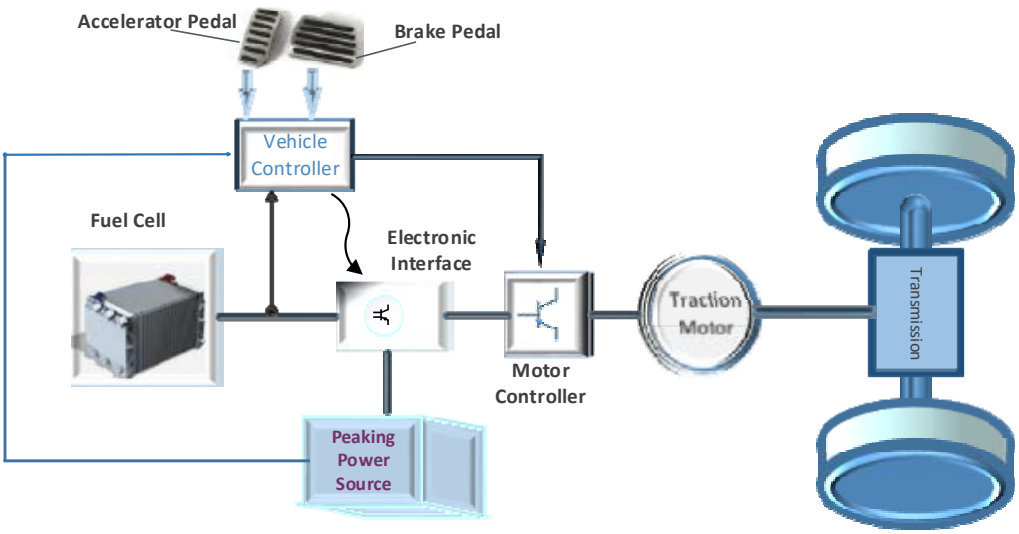


Fig. 2. The configuration of a hydrogen fuel cell vehicle using the PPSS.

The PPSS controls the operation of the fuel cell in the optimum working zone. It also allows the traction motor to control the output power so that the system responds quickly to the power demand.

2.2. Operating Mode Control Strategy (OMCS)

The OMCS controls the power changes between the fuel cell and the battery to provide the power demanded by the vehicle [2]. The power of the battery is the difference between the power demanded by the vehicle and the fuel cell power (see Fig. 3). When determining the control strategy, the OMCS refers to the power demanded by the vehicle, the speed of the vehicle, the battery and the fuel cell power balance.

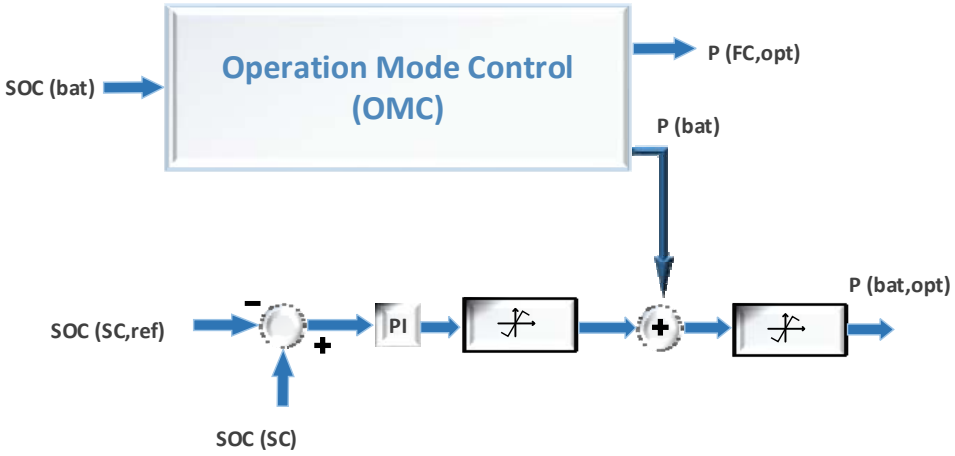


Fig. 3. Operation Mode Control Strategy (OMCS).

The most important feature of this control strategy is to be able to determine the operating mode in case of three charging states: discharge mode, charge mode and fast charge mode.

2.2. Fuzzy Logic Control Strategy (FLCS)

A fuzzy logic control strategy has been developed that provides power control between various power supplies to save fuel and improve system efficiency [2]. According to this strategy, the power of the DC / DC converter should be kept at a low, medium or high level relative to the energy of the battery and the fuel cell [4]. In this strategy, the system that performs this operation is the fuzzy logic controller. The entire mechanism of the fuel cell vehicle to be controlled and the functions that these mechanisms work together are defined and the rules of the fuzzy logic control strategy are determined. The configuration of the fuzzy logic control strategy to which all these rules apply is shown in Fig. 4.

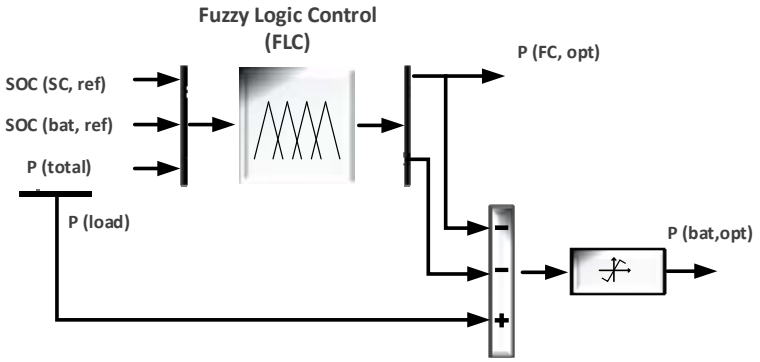


Fig. 4. The configuration of the Fuzzy Logic Control Strategy (FLCS).

2.3. Equivalent Consumption Minimization Strategy (ECMS)

In hydrogen fuel cell vehicles, ECMS can be used to control changes in vehicle performance when energy storage resources such as batteries and super capacitors are used in addition to the fuel cell. For the development of the energy management strategy in the vehicle, ECMS was first developed by Paganelli et al. [8]. If the power demand for the vehicle is supplied by the battery, the battery will need to be charged and will supply it from the fuel cell. All this energy flow should be controlled by a control strategy and an equivalent fuel consumption strategy should be determined with the aid of auxiliary power units and powertrain [6]. The main advantage of this strategy is that it can use electricity energy provided by energy storage systems such as batteries and supercapacitors as hydrogen from the fuel cell, if necessary, with the concept of equivalent fuel consumption [5]. The control loop, which also contains a PI controller, is shown in Fig. 5. The ECMS converts the electricity consumption of the battery and supercapacitor into the equivalent hydrogen consumption.

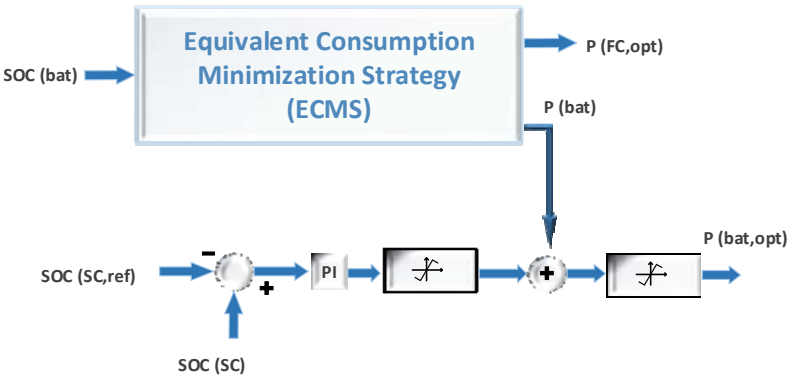


Fig. 5. Equivalent Consumption Minimization Strategy (ECMS).

3. Comparison of the Control Strategies

All of these control strategies in hydrogen fuel cell vehicles give similar results. The DC bus voltage is kept at the desired value thanks to the supercapacitor converter control. The fuel cell voltage varies depending on the power source, battery and supercapacitor voltages depending on the charge status.

ECMS gives the best results on hydrogen consumption from control strategies. ECMS is much better than OMCS, which is better than other control strategies in terms of hydrogen mass consumption. The differences in the equivalent hydrogen mass consumption of the powertrain are more evident because the equivalent hydrogen consumption is better with ECMS. At the same time, PPSS keeps the operation of the fuel cell in the optimum working zone, allowing the system to respond quickly to the demanded power demand according to the output power and to save fuel. In the fuzzy logic control strategy, logic rules and membership functions should be designed taking into account the new driving cycle. Since the control scheme in the FLCS is more complex, the computation time is higher than in other control strategies. Moreover, the FLCS has a computation time that is 9 times higher than that achieved by ECMS.

According to all these comparisons, the control strategies presented in this study allow hydrogen fuel cell vehicles to operate properly. However, ECMS can be considered as the most appropriate control strategy since it provides a good balance between hydrogen mass consumption, efficiency, adaptability and computation time.

4. Conclusion

The results of all the control strategies described here are very similar. However, ECMS is the preferred choice because the powertrain is kept at a minimum level of hydrogen consumption and equivalent hydrogen mass consumption. The computation time of the FLCS is much higher than other control strategies. The reason for this is that the control scheme of the FLCS is complex. PPSS, ECMS and OMCS are the simplest control strategies to be implemented in hydrogen fuel cell vehicles, because only a few changes can be made. However, the FLCS is more complex and requires significant changes when fuel cell vehicles are applied.

As a result, among all comparative control strategies, ECMS can be considered as the most appropriate control strategy to be used in hydrogen fuel cell vehicles. This control strategy reduces the hydrogen volume by reducing minimize the equivalent hydrogen consumption. Moreover, thanks to the simplicity of its implementation, this control strategy ensures that it is applicable to many different vehicles.

The general purpose of the control strategy we will create is; Electronic power circuits it contains are designed to increase the efficiency of the system and to provide optimization of the energy generated by the system. Our goal in doing so is to identify safe, cost-effective and high-efficiency control strategies that will overcome the technological challenges of future hydrogen fuel cell vehicles and to increase work on ECMS in particular. Fuel economy is crucial for achieving the best hydrogen fuel cell vehicle configurations, and this is the best strategy to achieve ECMS. These strategies will provide the greatest contribution to the future 'Hydrogen Economy'.

5. References

1. Wang C, Nehrir MH, Gao H. Control of PEM Fuel Cell Distributed Generation Systems. IEEE Transactions on Energy Conversion 2006;21(2):586-595.
2. Garcia P, Torreglosa JP, Fernandez LM, Jurado F. Control strategies for high-power electric vehicles powered by hydrogen fuel cell, battery and supercapacitor. Expert Systems with Applications 2013;40:4791-804.
3. Ehsani M, Gao Y, Gay SE, Emadi A. Modern electric, hybrid electric, and fuel cell vehicles: fundamentals, theory, and design. Florida: CRC Press LLC; 2005.
4. Li CY, Liu GP. Optimal fuzzy power control and management of fuel cell/battery hybrid vehicles. Journal of Power Sources 2009;192:525-533.
5. Rodatz P, Sciarretta A, Guzzella L. Optimal power management of an experimental fuel cell/supercapacitor-powered hybrid vehicle. Control Engineering Practice 2005;13:41-53.
6. Xu L, Li J, Hua J, Li X, Ouyang M. Optimal vehicle control strategy of a fuel cell/battery hybrid city bus. Int J Hydrogen Energy 2009;34:7323-7333.
7. Emadi A, Rajashekara K, Williamson SS, Lukic SM. Topological Overview of Hybrid Electric and Fuel Cell Vehicular Power System Architectures and Configurations. IEEE Transactions on Vehicular Technology 2005;54(3):763-770.
8. Paganelli G, Delprat S, Guerra TM, Rimaux J, Santin JJ. Equivalent consumption minimization strategy for parallel hybrid powertrains. Vehicular Technology Conference, 2002. VTC Spring 2002: May 6-9. IEEE 55th ; Birmingham, AL, USA. pp. 2076-2081.

ORAL PROCEEDINGS

Nuclear-based Hydrogen Production Cost Evaluation for Two Possible Nuclear Power Plants

F. Sorgulu[1,2] and I. Dincer[1,3]
[1]Faculty of Mechanical Engineering, Yildiz Technical University, Besiktas, Istanbul, Turkey
[2]Faculty of Technology, Kahramanmaras Sutcu Imam University, Elbistan, Kahramanmaras, Turkey
[3]Faculty of Engineering and Applied Science, University of Ontario Institute of Technology, Oshawa, Ontario, Canada
Email: fatihs@yildiz.edu.tr, ibrahim.dincer@uoit.ca

Abstract
Hydrogen is recognized as one of the most promising alternative fuels to meet the energy demand for future by providing a carbon-free solution. In regards to hydrogen production, there has been increasing interest to develop, innovate and commercialize more efficient, effective and economic methods, systems and applications. Nuclear based hydrogen production options through electrolysis and thermochemical cycles appear to be potentially attractive and sustainable for the expanding hydrogen sector. Both power plants are planned to employ the pressurized water reactors with the electricity production capacities of 4800 MW (consisting of 4 units of 1200 MW) for Akkuyu nuclear power plant and 4480 MW (consisting of 4 units of 1120 MW) for Sinop nuclear power plant. Each of these plants are expected to cost about 20 billion US dollars. In the present study, these two plants are considered for hydrogen production and their cost evaluations by employing the special software entitled "Hydrogen Economy Evaluation Program (HEEP)" developed by International Atomic Energy Agency (IAEA) which includes numerous options for hydrogen generation, storage and transportation. Therefore, the costs of hydrogen production, storage and transportation considered for both Akkuyu and Sinop nuclear power plants. The costs of capital, fuel, electricity, decommissioning and consumables are calculated and evaluated in detail for hydrogen generation, storage and transportation in Turkey.

Keywords: Nuclear power plant; hydrogen production; cost evaluation; storage; transportation.

1. Introduction

Efficient, environmentally benign, sustainable, and economic energy systems are getting more critical due to the increased energy demand. Fossil fuels have been used for many years to supply energy demand, but these sources are getting decreased by the time elapse. Many studies have carried out and still keeps on to find a solution to this problem [1-4]. This is not only due to the decreasing fossil fuels, but also due to environmental concerns about pollution and global warming issues. There are numerous studies dealing with design and evaluation of a system to supply energy demand [1-3]. Hydrogen seems to be one of the most promising alternative energy source to supply sustainability. Acar and Dincer [4] performed a study to evaluate and compare hydrogen production methods such as natural gas steam reforming, coal and biomass gasification, renewable and nuclear based high temperature electrolysis, nuclear based Cu-Cl and S-I thermochemical cycles as to their environmental, financial, social and technical performance. They determined the nuclear based Cu-Cl cycle has the lowest global warming potential (relates to the increasing concentration of CO_2 in atmosphere) and social cost of carbon (as a measure of the marginal external cost of a unit of CO_2 emissions). Al-Zareer et al. [5] designed and evaluated a nuclear-based integrated system. They designed four-step Cu-Cl cycle for water decomposition. They concluded that the idea of integrating nuclear reactors to produce hydrogen has advantages due to higher output temperatures. Energy and exergy efficiencies in this study were 31.6% and 56.2%, respectively. Lubis et al. [6] carried out a life cycle assessment of nuclear-based hydrogen production using thermochemical water splitting by copper-chlorine thermochemical cycle. They calculated the environmental features such as radioactive radiation, disability-adjusted life years, ozone depletion potential, global warming potential and eutrophication potential of nuclear based hydrogen generation. El-Emam et al. [1] performed a cost assessment of selected nuclear hydrogen production methods with various storage and transportation cases by employing Hydrogen Economy Evaluation Program (HEEP). They compared three different nuclear reactor options which is provided by the HEEP; Prismatic core (PMR), Pebble Bed (PBR) and High Temperature Reactor (HTGR). They calculated the cost of hydrogen of each system by various storage and transportation cases. In this study, Akkuyu and Sinop Nuclear Power Plants, which will be constructed soon in Turkey are analyzed for hydrogen production scenarios with cost evaluations. Cost evaluations are carried out by employing a special software entitled "Hydrogen Economy Evaluation Program (HEEP)" developed by International Atomic Energy Agency (IAEA) which includes numerous options for hydrogen generation, storage and transportation.

2. Methods and Analyses

Hydrogen Economy Evaluation Program (HEEP) is used to estimate the cost of hydrogen. HEEP is a very user friendly software and is widely used to estimate the cost of hydrogen. HEEP has various nuclear reactor options, as well as hydrogen generation, storage and transportation facilities. There are different nuclear power plant options and hydrogen production plant options included in HEEP library. The cost estimations for capital, fuel, decommissioning, O&M, and consumables are evaluated for both Akkuyu and Sinop Nuclear Power Plants (NPPs) and compared comprehensively. These cost estimations include various hydrogen storage and transportation options. Compressed gas, liquefaction and metal-hydride options which are available in the HEEP database are considered for storage. Two transportation options of pipe and truck are considered for cost analyses. Table 1 tabulates design parameters of Akkuyu and Sinop NPPs. Both NPPs are designed as Pressurized Water Reactor (PWR). While Akkuyu is constructed by Russian firms, Sinop is constructed by Japanese firms. Akkuyu and Sinop NPPs are planned to construct as 4 units and each units are consist of 1200 MW and 1120 MW, respectively. And so planned capacities have estimated as 4800 MW and 4480 MW for Akkuyu and Sinop NPPS, respectively. Eventually, construction cost is estimated to be 20 Billion US Dollar for both NPPs [7]. In addition, data operation parameters are required for evaluation purpose. Table 2 provides the construction and operation parameters such as tax rate, borrowing interest, operation and construction times. Table 3 shows the estimated parameters and comparison of capacity and thermal specifications of Akkuyu and Sinop NPPs.

Table 1. Design parameters of Akkuyu and Sinop NPPs

	Akkuyu NPP	**Sinop NPP**
Power Plant Type	PWR	PWR
Power Plant Name	VVER-1200	ATMEA1
Construction	Russia	Japan
Operating	Rosatom and the other Russian partners	%49 Electricity Generation Company (EUAS) on the behalf of Turkey Government %51 Consortium (consisted of French and Japanese firms)
Planned Power Capacity	4800 MW (consisting of 4 units of 1200 MW)	4480 MW (consisting of 4 units of 1120 MW)
Planned Cost of Construction	20 Billion US Dollar	20 Billion US Dollar

Table 2. Construction and operation parameters for Akkuyu and Sinop NPPs

Parameters	**Value**	**Parameters**	**Value**
Discount Rate	5%	Tax rate	10%
Inflation rate	1%	Construction	5 years
Equity/Debt	70% / 30%	Operation	60 years
Borrowing interest	10%		

Table 3. Comparison of capacity and thermal specifications of Akkuyu and Sinop NPPs

	Akkuyu	Sinop
Thermal rating	3212 MWth/unit	3150 MWth/unit
Electricity rating	1198 MWe/unit	1120 MWe/unit
Number of units	4	4
Initial fuel load	75000 kg/unit	75000 kg/unit
Annual fuel feed	25000 kg/unit	25000 kg/unit
Capital Cost	5.00E+9 USD/unit	5.00E+9 USD/unit
Capital cost fraction for electricity generating infrastructure	% 10	% 10
Fuel cost	1500 USD/kg	1500 USD/kg
O&M cost	% (of capital cost) 1.66	% (of capital cost) 1.66
Decommissioning cost	% (of capital cost) 2.8	% (of capital cost) 2.8

3. Results and Discussion

Various transportation options, including compressed gas liquefaction and metal hydrides, are evaluated comparatively. The compressed gas option is compared with two other transportation options of pipe and truck based transportation systems. Furthermore, both liquefaction and metal hydride storage types are compared with pipeline transportation. Figs. 1 to 4 show the comparison of cost evaluation. The major components of hydrogen generation such as storage, transportation, hydrogen generation plant and nuclear power plant can be seen in the figures in the next sections.

3.1 Pipe Transportation of Compressed Gas Hydrogen

Fig. 1 shows the components of cost of hydrogen as compressed gas and transportation by pipe and comparison of Akkuyu and Sinop NPPs. As shown in Fig. 1, the pipeline transportation is cheaper, compared to transportation by pipe (0.15USD per kg of hydrogen).

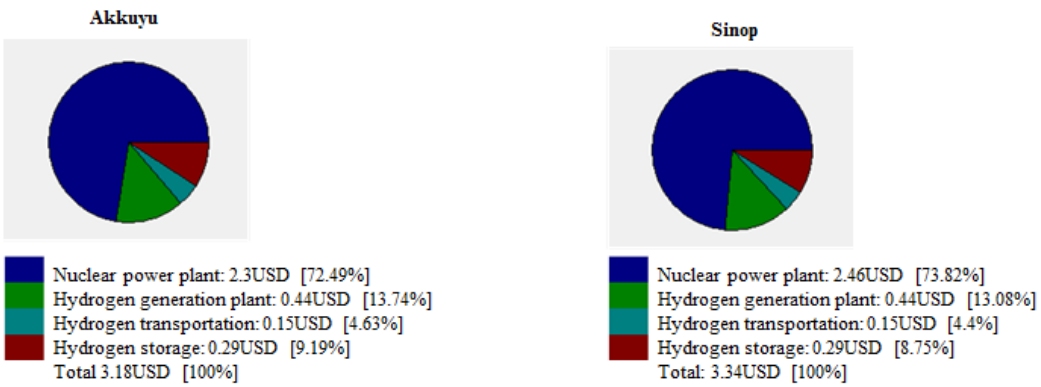


Fig. 1. Hydrogen cost components as compressed gas and transportation by pipe for Akkuyu and Sinop NPPs

3.2 Hydrogen as Compressed Gas Transportation by Truck

Fig. 2 illustrates hydrogen cost components as compressed gas. Similar to Fig. 1, transportation by truck is considered in this case and a comparison is performed for Akkuyu and Sinop NPPs. As shown in Fig. 2, cost of transportation by truck is higher than pipeline transportation. Transportation by truck is calculated for Akkuyu and Sinop NPPs as 0.83USD and 0.84USD per kg of hydrogen, respectively.

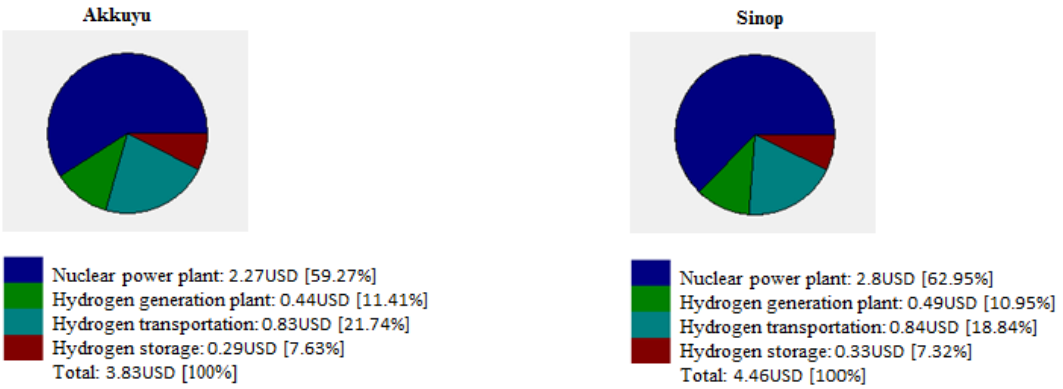


Fig. 2. Components of cost of hydrogen as compressed gas and transportation by truck and comparison of Akkuyu and Sinop NPPs

3.3 Hydrogen as Liquefaction Transportation by Pipe

Fig. 3 shows the components of cost of hydrogen as liquefaction and transportation by pipe. A comparison can be seen for Akkuyu and Sinop NPPs. As shown in Fig. 3 cost of transportation by truck is higher than pipeline transportation. Total cost of hydrogen is determined for Akkuyu and Sinop NPPs to be 3.44USD and 3.63USD per kg of hydrogen, respectively.

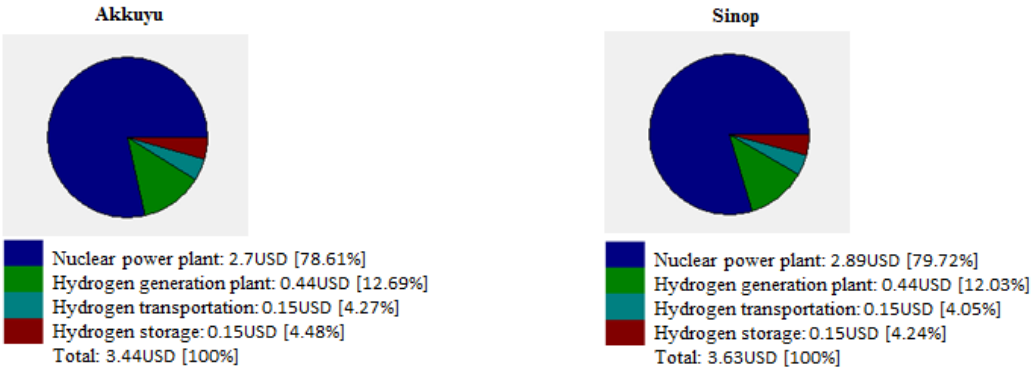


Fig. 3. Components of hydrogen generation cost and comparison of Akkuyu and Sinop NPPs

3.4 Hydrogen as Metal Hydrides Transportation by Pipe

Fig. 4 shows the cost of hydrogen as metal hydride and transportation by pipe for Akkuyu and Sinop NPPs. As shown in Fig. 4, cost of metal hydrides transportation is higher than compressed gas and liquefaction. Total cost of hydrogen is determined for Akkuyu and Sinop NPPs as 6.02USD and 6.17USD, respectively. In all cases cost of hydrogen generation in Sinop NPP is higher than Akkuyu NPPs due to nuclear power plant capacity.

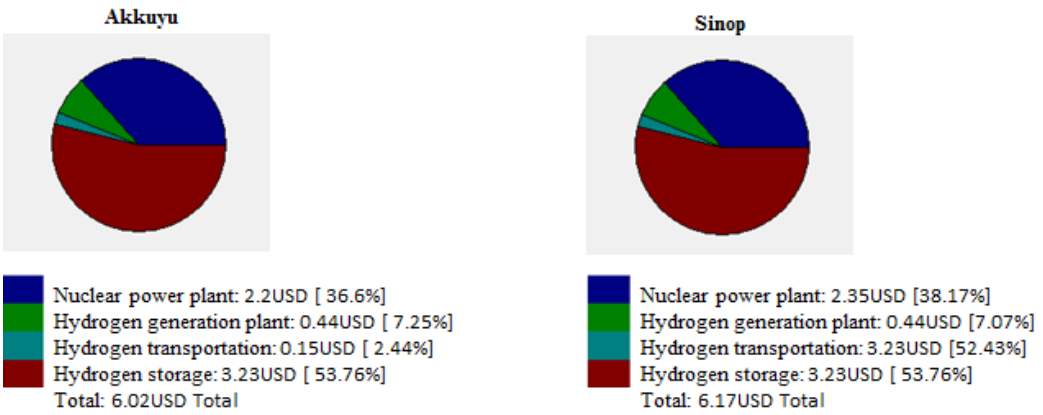


Fig. 4. Components of hydrogen generation cost and comparison of Akkuyu and Sinop NPPs

4. Conclusions

In this study, a nuclear based hydrogen generation cost analysis is performed. Three different storage options and two different transportation options are evaluated. Akkuyu and Sinop NPPs which will be constructed in Turkey bring two possible nuclear based hydrogen production scenarios which are evaluated economically. Amount of hydrogen cost per kg is calculated for four cases. Results show that transportation by pipe is cheaper than transportation by truck. However a comprehensive evaluation must be carried out to compare pipeline transportation and transportation by truck to analyze the construction parameters of pipeline and unexpected cost of vehicles. Metal hydride storage option seems to be the most expensive option among the considered cases. A comprehensive study must be performed to determine specific advantages and limitations of these storage and transportation options.

Acronyms

EUAS Electricity Generation Company
HEEP Hydrogen Economy Evaluation Program
HTGR High Temperature Reactor
IAEA International Atomic Energy Agency
NPP Nuclear Power Plant
O&M Observations and Measurements
PBR Pebble Bed
PMR Prismatic core
PWR Pressurized Water Reactor

References

1. El-Emam RS, Ozcan H, Dincer I. Comparative cost evaluation of nuclear hydrogen production methods with the Hydrogen Economy Evaluation Program. International Journal of Hydrogen Energy 2015; 40:11168-11177.
2. Orhan MF, Dincer I, Naterer GF. Cost analysis of a thermochemical Cu–Cl pilot plant for nuclear-based hydrogen production. International Journal of Hydrogen Energy. 2008;33:6006-6020.
3. I. Khamis, Malshe UD. HEEP: A new tool for the economic evaluation of hydrogen economy. International Journal of Hydrogen Energy. 2010;35 8398-8406.
4. Acar C, Dincer I. Comparative assessment of hydrogen production methods from renewable and non-renewable sources. International Journal of Hydrogen Energy. 2014;39:1-12.
5. Al-Zareer M, Dincer I, Rosen MA. Development and assessment of a novel integrated nuclear plant for electricity and hydrogen production. Energy Conversion and Management. 2017;134:221-234
6. Lubis LL, Dincer I, Rosen MA. Life Cycle Assessment of Hydrogen Production Using Nuclear Energy: An Application Based on Thermochemical Water Splitting. Journal of Energy Resources Technology 2010;132:021004-1.
7. Nuclear Power Plant Planned Projects in Our Country. Available from: http://www.enerji.gov.tr/en-US/Pages/Nuclear-Power-Plant-Planned-Projects-In-Our-Country

Optimization Approach to Operation Conditions of Solar Thermochemical Water Splitting Process

Ezgi Yavuzyılmaz , Deniz Üner , Serkan Kıncal
Kimya Mühendisliği Bölümü, Orta Doğu Teknik Üniversitesi, 06800, Ankara
Email: yaezgi@metu.edu.tr, uner@metu.edu.tr, skincal@metu.edu.tr

Abstract
Two-step thermochemical hydrogen production by using solar energy is an alternative method to conventional hydrogen production. In this method, the thermochemical cycle consists of two sequential steps: a high temperature step where the decomposition of the redox material is driven by solar energy and a relatively moderate temperature step where oxidation of the redox material is achieved by steam fed to the reactor. However, the changes in operation temperatures and process durations lead to trade-offs among performance criteria of the reactor. Therefore, the aim is to build a design framework for the prototype reactor since it is important to understand how much and in which ways the selected working condition affects performance criteria to optimize the reactor. A MATLAB code is designed as an infrastructure which enables to test several heat transfer models and material properties for the prototype reactor.

Keywords: Solar hydrogen production; thermochemical; optimization.

1. Introduction

It is very crucial to increase energy efficiency while decreasing the cost factor for solar thermochemical hydrogen production technology from water via redox material in terms of the economic sustainability of the method. Therefore, in recent years an increased interest has been observed in this area, the field of optimal design and working conditions of solar thermochemical systems to make this technology competitive in hydrogen production market. Cost reduction is one of the courses of action to make this technology viable and solar collector-reactor is the most important cost item which can be reduced by good engineering design. Enhancing production efficiency is another course of action that can be achieved by improving either energy gain or hydrogen yield again with a good reactor design and optimum working conditions.

The efficiency of a two-step thermochemical cycle can be increased by enhancing redox material properties or designing reactors with better reactor properties or finding optimum working conditions. For redox material properties, there is a great deal of literature work related to process efficiency based on lab-scale experiments to enhance the metal oxide properties such as stability, oxygen capture capacity, reaction kinetics considering micro-to-macro relations in each cycle[1]. Selecting the suitable reactor design is also one of the biggest challenges encountered by solar thermochemical systems in pilot scale [2]. Reactor properties such as surface area, and heat recuperation can significantly affect the efficiency of the cycle. For example, for many cases, energy efficiency increases as the solid phase heat recuperation increases.

Working conditions can also be adjusted to improve the energy efficiency of the reactor. Moreover, for an established environment and system, it is easier to change operation conditions to enhance the efficiency of the system. In solar thermochemical hydrogen production using redox materials, oxidation and reduction temperatures and pressures are the most important variables that can alter the hydrogen yield and as result of that, efficiency of the cycle. Operation temperatures can change in a range within the thermodynamic limits of the redox material (Table 1). As shown in Table 1, reduction reaction requires high temperatures due to its endothermic nature and oxidation reaction needs relatively moderate temperatures due to its exothermic nature. Therefore, to obtain maximum efficiency, it is important to find optimum temperature values in that allowable range.

Table 1. Operation temperatures for different redox materials for the thermochemical cycle

Metal Oxide Redox Material (MO)	**Reduction Temperature (K)** : $\frac{1}{\delta}MO_y \rightarrow \frac{1}{\delta}MO_{y-\delta} + \frac{1}{2}\,O_{2\,(g)}$	**Oxidation Temperature (K)** $H_2O_{(g)} + \frac{1}{\delta}MO_{y-\delta} \rightarrow \frac{1}{\delta}MO_y + H_{2\,(g)}$	**ΔG° (kJ/ mol)** [3]	**ΔH° (kJ/ mol)** [3]	**Ref.**
Iron Oxide	2500	<1000	260.9	302.3	[4]
Zinc Oxide	2273	1446	320.5	350.5	[5]
Ceria	~1773-1873	1073	342.8	381.2	[6]
Cobalt Oxide	1573	673	152.3	196.2	[7]

2. Model

Inputs of Model:

- *Decision Variables* : Operation temperatures (T) and durations (τ) are the selected decision parameters that can be controlled.
- *Parameters* : Several design parameters such as number of moles of redox material loaded, area of monolith channel etc. are used in the model. Moreover, material parameters such as heat capacity of the redox material, rate constants and activation energies can be listed as the other inputs of the system[8].

Performance Measures of Model (Outputs):

The energy efficiency of the cycle is also described as below:

$$\eta = \frac{Energy\ obtained\ from\ the\ system}{Energy\ supplied\ to\ the\ system} = \frac{\dot{n}_{H_2} \times HHV}{\dot{Q}_{total}} \quad (1)$$

The term $\dot{Q}_{total}$, rate of energy supplied to the cycle can be expressed as the total of the following terms:

$$\dot{Q}_{total} = \dot{Q}_{reheat} + \dot{Q}_{Reaction,red} + \dot{Q}_{Loss} + \dot{Q}_{water} \quad (2)$$

$\dot{Q}_{reheat}$ defined in Equation 3 is the rate of the sensible heat supplied to the redox material in order to reheat the material from oxidation temperature to reduction temperature between the following cycles. ε_s represents the fraction of the heat recuperation to increase the energy efficiency.

$$\dot{Q}_{reheat} = \dot{n}_{MO_x}(1 - \varepsilon_s)\left(\int_{T_C}^{T_H} c_{p_{MO_x(s)}} dT\right) \quad (3)$$

$\dot{Q}_{Reaction,red}$ is another performance measure that is the rate of total energy consumed by the reduction process as shown below:

$$\dot{Q}_{Reaction,red} = (\dot{n}_{H_2})(\Delta H_{red}(T_H)) \quad (4)$$

Another performance measure, $\dot{Q}_{Loss}$, is the rate of heat loss due to re-radiation and convection shown by Equation 5:

$$\dot{Q}_{Loss} = \dot{Q}_{Loss(red)} + \dot{Q}_{Loss(ox)} \quad (5)$$

$\dot{Q}_{Loss(red)}$ is the rate of energy loss by convection and radiation at the reduction step demonstrated by equations set in Equation 6:

$$\begin{aligned} \dot{Q}_{Loss(red)} &= \dot{Q}_{con(red)} + \dot{Q}_{rad(red)} \\ \dot{Q}_{con(red)} &= A_r \times h \times (T - T_a) \\ \dot{Q}_{rad(red)} &= \sigma \times A_r \times (T^4 - T_a^4) \end{aligned} \quad (6)$$

$\dot{Q}_{Loss(ox)}$ is the rate of energy loss by convection and radiation at the oxidation step.

$$\begin{aligned} \dot{Q}_{Loss(ox)} &= \dot{Q}_{con(ox)} + \dot{Q}_{rad(ox)} \\ \dot{Q}_{con(ox)} &= A_r \times h \times (T - T_a) \\ \dot{Q}_{rad(ox)} &= \sigma \times A_r \times (T^4 - T_a^4) \end{aligned} \quad (7)$$

$\dot{Q}_{water}$ is another performance measure that determines the rate of total energy supplied to the system. It is the rate of the sensible and latent heat consumed by water given by Equation 8.

$$\dot{Q}_{water} = \dot{n}_{H_2O}\left[\Delta H^{298K\rightarrow 373K}_{H_2O(l)\rightarrow(g)}\right] + \dot{n}_{H_2O}\left[\int_{373\,K}^{T_C} c_{p_{H_2O(g)}} dT\right] \quad (8)$$

Algorithm of the Model:

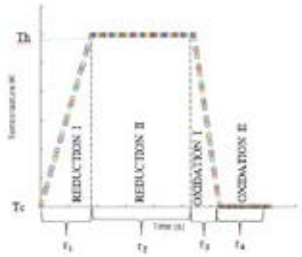


Fig. 1. Representative temperature profile example for two-step water splitting cycle model

In the model, cycle time is assumed to be divided into four parts in order to construct temperature profile approximately representing the general behaviour of the energy balances of the system. In part one called Reduction I in Fig.1., it is assumed that temperature increases from oxidation temperature to reduction temperature with a constant heating rate. In part two, reduction temperature is assumed to be constant. At the end of the part two, reduction process is completed. Then, system temperature starts to decrease gradually and linearly up to oxidation temperature. In the last part, temperature follows a constant pattern. In Fig.1, τ_i represents the required duration for each part i. For each discrete part, amount of hydrogen produced is evaluated by surface coverage equation and first order reaction kinetics. Also, all other performance measures stated above are estimated in the model as outputs. The parts - reduction and oxidation- are constrained by using surface coverage amounts, in other words, conversion amounts are the key limitation factors for the determination of duration of each part. For example, there is no hydrogen production in oxidation parts if reduction process is achieved under 50% at the end of Reduction II. In cases where is completed at above 50%, hydrogen production can be expressed as (2X-100) where X is percent of the reduction. The general algorithm of the MATLAB code is illustrated in Fig.2.

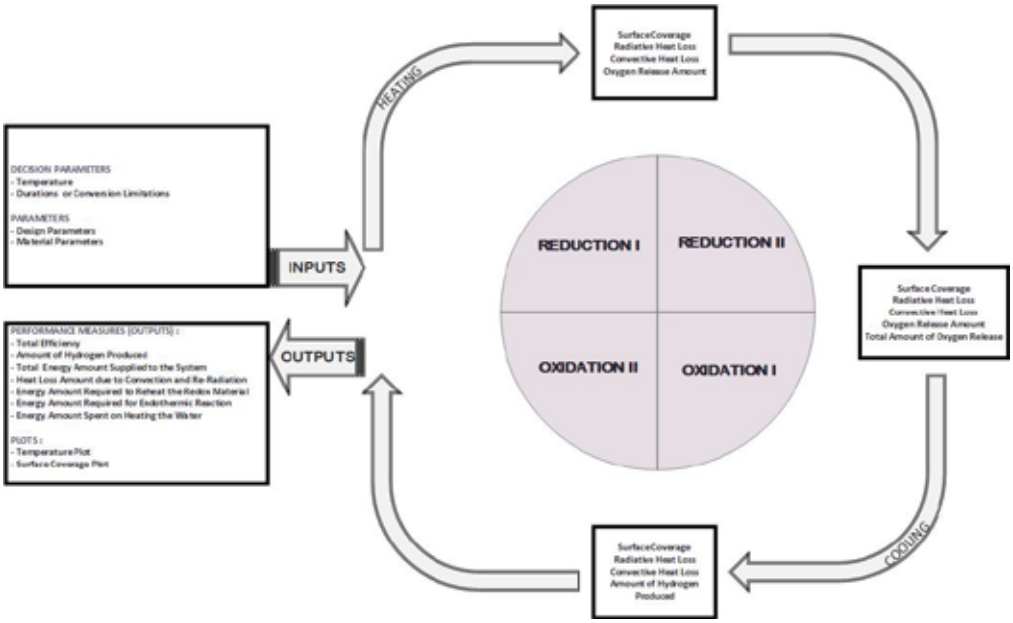


Fig.2. General flowchart of the model

3. Results and Discussions

The code is simulated for the parametric analysis of a base case example and statistical methods was used to determine optimum working conditions constrained by the material property and design limitations. As a base case, full factorial design is formed by selecting two temperatures -reduction and oxidation temperatures- and four durations as the important factors for screening process. 4096 simulations are done in full factorial design for six factors with four levels demonstrated in Table 2.

Table 2. Full factorial design of experiments (Decision variables of the model)

Factor Name	Levels	Level Unit	Level Values			
Reduction Temperature	4	K	900	1000	1100	1200
Delta T (ΔT)	4	K	50	100	150	200
Reduction Time 1	4	s	300	600	900	1200
Reduction Time 2	4	s	300	600	900	1200
Oxidation Time 1	4	s	300	600	900	1200
Oxidation Time 2	4	s	300	600	900	1200

Fig.3. shows an example temperature profile and surface coverage of oxygen for selected temperature range 1000 K-1200 K as the result of one the simulations.

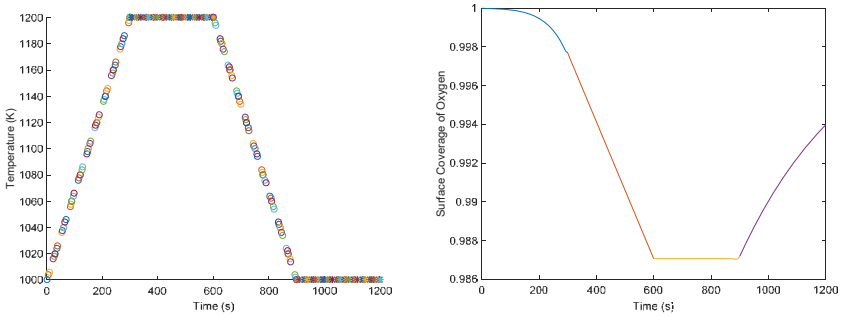


Fig.3. Temperature profile and surface coverage of oxygen for temperature range 1000 K-1200 K for $\tau_1 = 300\ s$, $\tau_2 = 300\ s$, $\tau_3 = 300\ s$, $\tau_4 = 300\ s$

The outputs implies that the model should be improved to lead to more realistic results, especially, by combining the model with more practical heat transfer and thermodynamic model representing the real system.

4. Conclusions

In this study, the aim is to introduce an optimization approach to working conditions of solar thermochemical water splitting process. With this objective, an algorithm combining both heat transfer and thermodynamic model that will simulate the real reactor system is designed in MATLAB. A set of operation condition based on durations, a specific heat transfer and thermodynamic model is simulated as a pilot case. The results of the analysis will enlighten important factors in terms of their effects on different performance measures and as a consequence of that the outputs of the study will be used to build a design framework for the prototype reactor considering kinetic and thermodynamic limitations.

Acknowledgement

Financial support from TUBITAK through 1003 program under the 213M006 is gratefully acknowledged.

Nomenclature

$\boldsymbol{A_r}$	Effective surface area where the heat loss occurs (m^2)
$\boldsymbol{c_{p_i}}$	Specific heat of compound i
$\dot{n}_i$	Mole flow rate compound i (mol/s)
$\dot{Q}_i$	Rate of energy loss from surrounding based on abbreviation i
H	Enthalpy
T	Temperature (°C or K)

Greek Letters

Δ	Change in specified property
ε_s	Fraction of the heat recuperation to increase the energy efficiency
η	Efficiency
σ	Stefan Boltzmann constant
τ	Duration for oxidation or reduction (s)

Acronyms

HHV	Higher heating value
MO	Metal oxide

Abbreviations

con	Convection
ox	Oxidation
rad	Radiation
red	Reduction

References

1. Miller JE, Ambrosini A, Coker EN, Allendorf MD, McDaniel AH. Advancing oxide materials for thermochemical production of solar fuels. Energy Procedia [Internet]. 2014;49:2019–26. Available from: http://dx.doi.org/10.1016/j.egypro.2014.03.214
2. Tescari S, Mazet N, Neveu P. Constructal method to optimize solar thermochemical reactor design. Sol Energy [Internet]. 2010;84(9):1555–66. Available from: http://dx.doi.org/10.1016/j.solener.2010.06.015
3. Barin I, Platzki G. Thermochemical data of pure substances. [Internet]. Weinheim ; New York : VCH, 1995.; Available from: http://search.ebscohost.com/login.aspx?direct=true&AuthType=ip&db=cat00017a&AN=metu.b2170525&site=eds-live&authtype=ip,uid
4. Nakamura T. Hydrogen production from water utilizing solar heat at high temperatures. Sol Energy. 1977;19(5):467–75.
5. Steinfeld A. Solar hydrogen production via a two-step water-splitting thermochemical cycle based on Zn/ZnO redox reactions. Int J Hydrogen Energy. 2002;27(6):611–9.
6. Chueh WC, Haile SM. A thermochemical study of ceria: exploiting an old material for new modes of energy conversion and CO2 mitigation. Philos Trans R Soc A Math Phys Eng Sci [Internet]. 2010;368(1923):3269–94. Available from: http://rsta.royalsocietypublishing.org/content/368/1923/3269.ful\nhttp://rsta.royalsocietypublishing.org/letters/submit/roypta;368/\nhttp://rsta.royalsocietypublishing.org/cgi/doi/10.1098/rsta.2010.0114
7. Singh A, Tescari S, Lantin G, Agrafiotis C, Roeb M, Sattler C. Solar thermochemical heat storage via the Co3O4/CoO looping cycle: Storage reactor modelling and experimental validation. Sol Energy [Internet]. 2017;144:453–65. Available from: http://dx.doi.org/10.1016/j.solener.2017.01.052
8. Yavuzyılmaz E. Optimization of operation temperatures and durations during solar thermal water splitting towards greater energy efficiencies. Middle East Technical University; 2016.

Approach to Design of Control Electronic on Energy Storage Systems of Hydrogen Fuel Cell Vehicles

Yakup Hameş, Kemal Kaya, Ömer Türksoy, Arzu Türksoy
Department of Electrical and Electronics Engineering, Iskenderun Technical University, Hatay, Turkey
Email: yakup.hames@iste.edu.tr, kemal.kaya@iste.edu.tr, omer.turksoy@iste.edu.tr, arzu.turksoy@iste.edu.tr

Abstract
Fuel cell vehicles are a revolution in the transport sector, driven by renewable energy. Hydrogen fuel cell vehicles, which use fuel cells, batteries and supercapacitors as energy storage systems, are very different from traditional vehicles in terms of energy efficiency and fuel economy. In hydrogen fuel cell vehicles, control strategies developed for other elements that work in coordination with the fuel cell and store energy are crucial for vehicle performance. These strategies enable control of energy storage systems while allowing economic methods to be identified.
This study examines the various control strategies in energy storage systems of hydrogen fuel cell vehicles to maximize efficiency and reduce mass and cost of the total system to the greatest extent.

Keywords: Hydrogen fuel cell; energy storage system; supercapacitor; control strategy.

1. Introduction

Hydrogen fuel cell vehicles have methods that are necessary to determine control strategies in energy storage systems. Some of these methods are; to obtain efficiency for energy storage systems, to provide fuel cell fuel economy and to meet the load requirement. The control strategy of the energy storage system has a mechanism consisting of fuel cell control, battery control, supercapacitor control, DC / DC converter control and inverter control [1].

The supercapacitor converter is involved in regulating a DC link voltage. The battery converter is operated to preserve voltage regulation of the supercapacitors. The fuel cell converter is used to maintain the voltage regulation of the battery. The inverter is used to produce any desired output voltage for the traction motor and to control the output power of the fuel cell-battery-supercapacitor. The control design configuration of energy storage systems in hydrogen fuel cell vehicles is shown in Fig. 1.

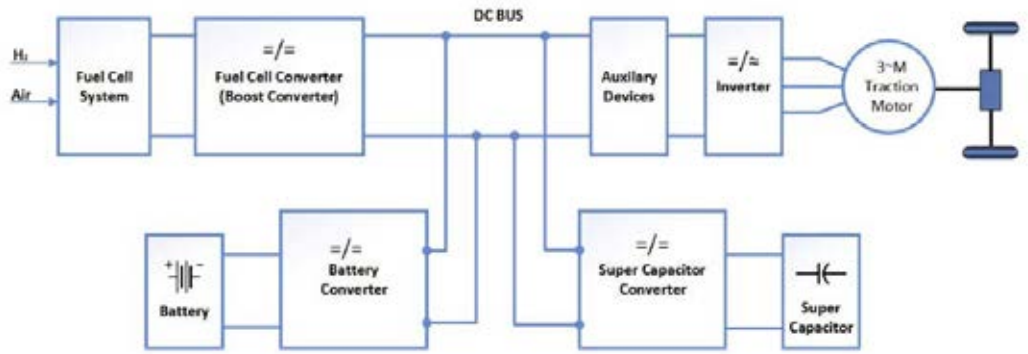


Fig. 1. The control design configuration of energy storage systems in hydrogen fuel cell vehicles.

The aim of this study is examining the various control strategies in energy storage systems of hydrogen fuel cell vehicles to maximize efficiency and reduce mass and cost of the total system to the greatest extent.

1. Fuel Cell

In general terms, fuel cells are a device with a simple structure that converts the chemical energy of hydrogen into electrical energy [2-5]. It is a productive device with water emission besides electricity production without burning [6]. Fuel cells (see Fig. 2) can be considered as a suitable technology for transport applications due to their power density, low operating temperature, efficiency and rapid adaptation to changes in power demand.

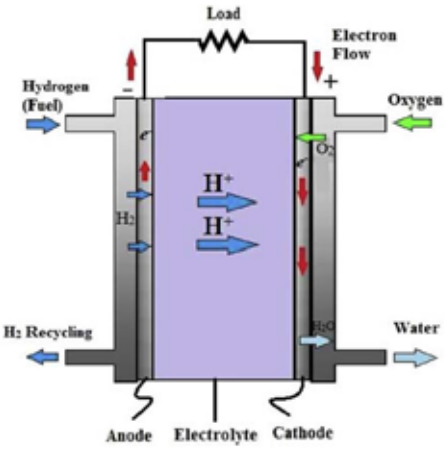


Fig. 2. The fuel cell stack

The fuel cell control block is used to provide a suitable fuel supply. If too much fuel is supplied, this will cause the fuel mass to fall well below the inlet of the fuel cell in the fuel cell stack, resulting in low fuel efficiency. Moreover, low fuel causes high loss in the fuel cell.

2. Battery

Batteries are used in many applications as energy storage devices. The types of batteries used in hydrogen fuel cell vehicles are generally Pb-Acid, Ni-Cd, Ni-MH, and Li-ion batteries. Among these battery types, Li-ion batteries respond better than others. This is why Li-ion batteries have more energy storage, lighter weight and more durability. Because of all these features, Li-ion batteries are more preferred as energy storage system in fuel cell vehicles (see Fig. 3).

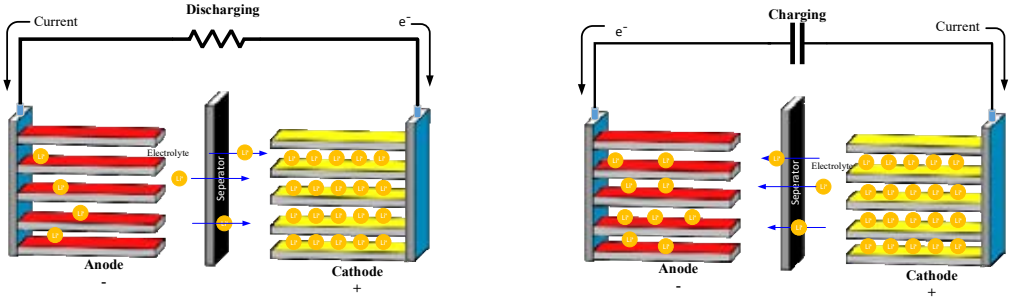


Fig. 3. The operation of a Li-ion battery during discharging and charging.

In order to achieve high charging efficiency, the charge state capacity of the battery should be kept between 40% and 80%. A control strategy should be designed so that the battery can operate in this working range. This control strategy provides the indication of the battery reaction in the system [7].

If there is an error in the control mechanism designed for the battery, the battery charge state will deviate from the reference value. To prevent this error, the current, voltage and power values of the fuel cell must be adjusted. The setting of these values is achieved by checking the desired battery charge status for the system.

3. Supercapacitor

Supercapacitors (see Fig. 4) are energy storage units that help in addition to the battery and fuel cell in hydrogen fuel cell vehicles. In situations where high power is required, they are switched on for the power requirement of the vehicle. In order to control this, a control strategy is required in the system. The control strategy should be designed to prevent complete discharge of the supercapacitor to avoid nonlinear regions.

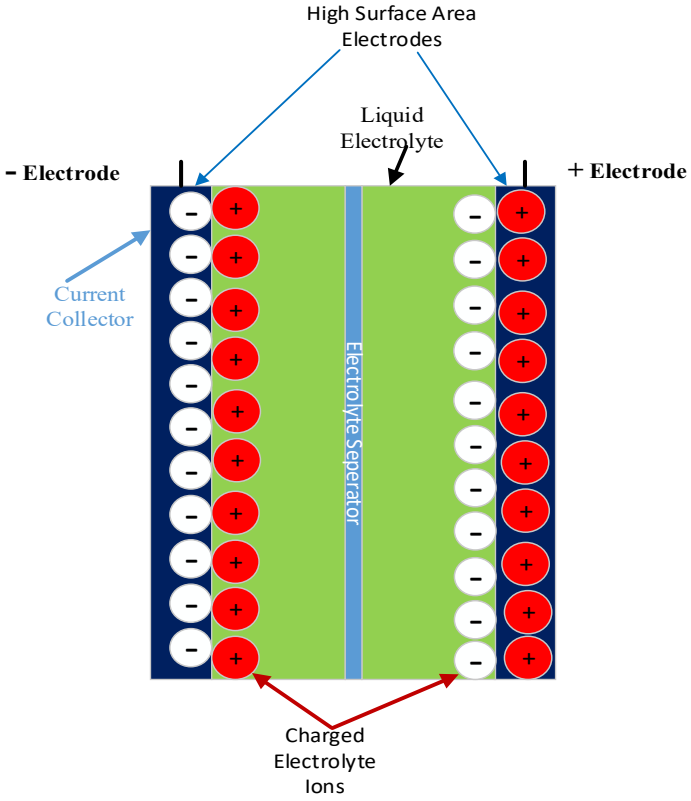


Fig. 4. The construction of supercapacitor.

The reason for using a supercapacitor as an energy storage device in hydrogen fuel cell vehicles is that the specific power ratio is high and the charge time is very short. Supercapacitors provide system efficiency and energy savings in the vehicle. It contributes to system performance especially when energy braking is done.

The supercapacitor voltage reference varies according to the acceleration or deceleration commands from the user or auxiliary power units. Especially in load transients, supercapacitor reacts much faster than battery. Therefore, when the supercapacitor control strategy is determined, it should have a gradual control cycle with the fuel cell control strategy to achieve good system performance [8].

4. DC-DC Converter

A DC bus is used to provide energy flow control between energy storage systems in hydrogen fuel cell vehicles. Unidirectional boost DC / DC converter connects the fuel cell to the DC bus. This converter can only flow the energy in one direction from the fuel cell to the DC bus.

Unlike unidirectional boost DC / DC converter used to connect the fuel cell to the DC bus, the bidirectional DC / DC converters to connect the battery and supercapacitor to the DC bus are used (see Fig. 5). These converters provide energy transfer from either the battery or supercapacitor to the DC bus and vice versa [9].

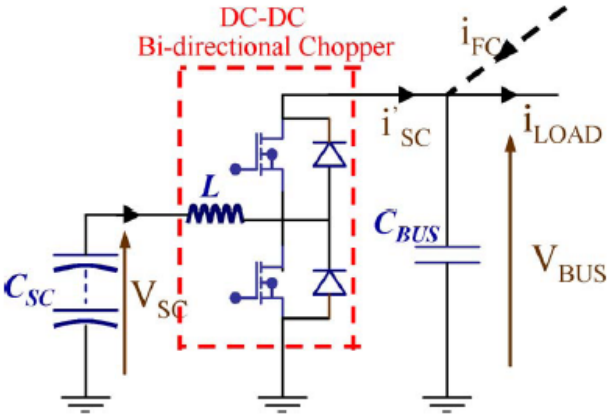


Fig. 5. The bidirectional DC / DC converter [9].

For reasons of safety and dynamics, the fuel cell, battery and supercapacitor converters are primary operated by inner current loop controls which are realized by analogical circuits. Therefore, current commands of fuel cell, battery and supercapacitor depend on conditions of hybrid operation.

5. Control Electronic on Energy Storage Systems

In the hydrogen fuel cell vehicles, power demand can be provided by a fuel cell or battery-supercapacitor. In addition, a control strategy is required for the use of secondary energy sources. The strategy for maintaining power division and charging are based on the fact that batteries have greater energy density and supercapacitors have higher power density [10].

The power demanded by the vehicle is given by the power control electronics as the fuel cell, supercapacitor, and battery, respectively. Direct use of the fuel cell for traction is more efficient in terms of energy, so fuel cells are used as the primary source. Furthermore, since the supercapacitor is easily rechargeable and dischargeable when compared to the battery, the battery is only energized in high power demand situations. The design of the control electronics between energy storage systems is shown in Fig. 6.

- When the power demand is lower than the fuel cell power, the fuel cell operates as the primary power source.
- If the power demand is higher than the power of the fuel cell, the nominal power is supplied from the fuel cell and the remainder is supplied from the supercapacitor.
- If the power demand exceeds the total power of the fuel cell and supercapacitor, the battery enters the circuit.

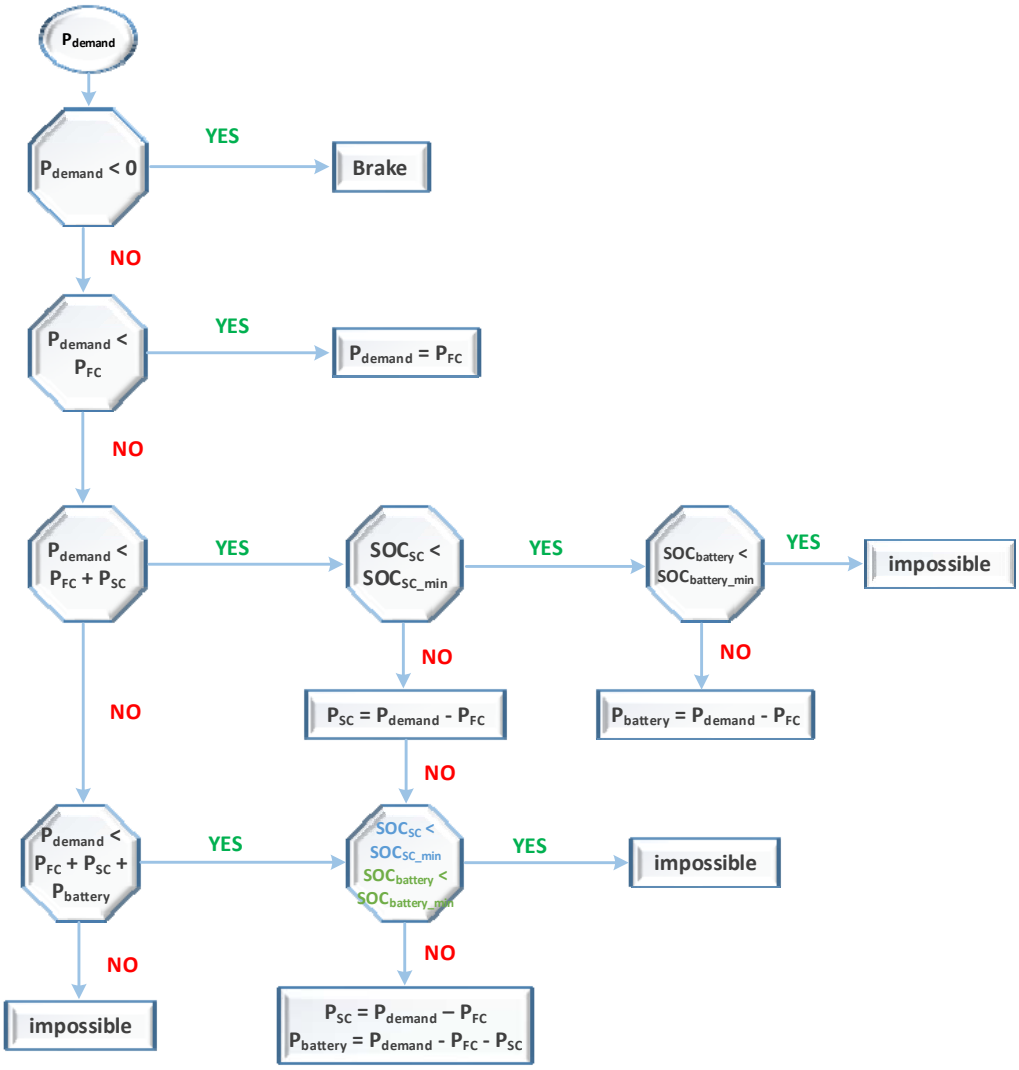


Fig. 6. The design of the control electronics between energy storage systems.

- While these operations are performing, the battery and supercapacitor should be set to work in the state of charge range. If the battery and supercapacitor are not properly charged, undesirable conditions may occur in the control electronics.

- If the power demand is lower than the fuel cell power and the vehicle is braking, the secondary energy storage system can be charged with the fuel cell remaining energy.

- While the vehicle recharges the battery in the weak deceleration, it recharges the supercapacitor in the strong deceleration. Thus the control electronics are designed.

6. Conclusion

The main goal in designing hydrogen fuel cell vehicles is to reduce fuel consumption by designing a control electronic in the energy storage system. In hydrogen fuel cell vehicles using fuel cell, battery and supercapacitor as

energy storage devices, the supercapacitor is used to control the DC bus voltage, while the fuel cell and the battery reference powers are determined in different ways.

In this study, an approach to the control electronics design required by optimizing fuel cell, battery and supercapacitor control strategy parameters to minimize fuel consumption is presented. Here, the specific fuel consumption of hydrogen fuel cell vehicles is found to be 40% lower than that of internal combustion engine vehicles.

This study addresses control strategies in energy storage systems of hydrogen fuel cell vehicles to maximize efficiency and minimize mass and cost of the total system. Furthermore, this study concludes that by observing the results of control strategies, hydrogen, the energy of the future, will be an excellent choice for fuel saving in transportation vehicles.

References

1. Garcia P, Torreglosa JP, Fernandez LM, Jurado F. Control strategies for high-power electric vehicles powered by hydrogen fuel cell, battery and supercapacitor. Expert Systems with Applications 2013;40:4791-804.
2. Dutta S. A review on production, storage of hydrogen and its utilization as an energy resource. J Ind Eng Chem 2014;20(4):1148-56.
3. Ball M, Weeda M. The hydrogen economy-vision or reality? Int J Hydrogen Energy 2015;40(25):7903-19.
4. Bauer C, Hofer J, Althaus HJ, Duce AD, Simons A. The environmental performance of current and future passenger vehicles: life cycle assessment based on a novel scenario analysis framework. Appl Energy 2015;157:871-83.
5. Chung CA, Chen YZ, Chen YP, Chang MS. CFD investigation on performance enhancement of metal hydride hydrogen storage vessels using heat pipes. Appl Therm Eng 2015;91:434-46.
6. Jain IP. Hydrogen the fuel for 21st century. Int J Hydrogen Energy 2009;34(17):7368-78.
7. Thounthong P, Sikkabut S, Mungporn P, Nahid-Mobarakeh B, Pierfederici S, Davat B. Nonlinear control algorithm of supercapacitor/Li-Ion battery energy storage devices for fuel cell vehicle applications. Mecatronics (MECATRONICS), 2014 10th France-Japan/ 8th Europe-Asia Congress on 2014;27-29 Nov.
8. Gao W. Performance Comparison of a Fuel Cell-Battery Hybrid Powertrain and a Fuel Cell-Ultracapacitor Hybrid Powertrain. IEEE Transactions on Vehicular Technology 2005;54(3):846-855.
9. Azib T, Bethoux O, Remy G, Marchand C, Berthelot E. An Innovative Control Strategy of a Single Converter for Hybrid Fuel Cell/Supercapacitor Power Source. IEEE Transactions on Industrial Electronics 2010;57(12):4024-4031.
10. Paladini V, Donateo T, de Risi A, Laforgia D. Super-capacitors fuel-cell hybrid electric vehicle optimization and control strategy development. Energy Conversion and Management 2007;48:3001–3008.

ORAL PROCEEDINGS

Investigation of Magnetic Field Effect on Hydrogen Production Performance In Aqueous Methanol Electrolysis

Emrumiye Arli[1], Zeynep Baz[1], Mehmet Karakilcik[1], Hatice Karakilcik[2]
M. Kemal Sangun[3], Guray Kilincceker[4]
[1]Department of Physics, Faculty of Sciences and Letters, Çukurova University, 01330 Adana, Turkey
[2]Department of Geology, Faculty of Architecture and Engineering, Çukurova University, 01330 Adana, Turkey
[3]Department of Chemistry, Faculty of Sciences and Letters, Mustafa Kemal University, Hatay, Turkey
[4]Department of Chemistry, Faculty of Sciences and Letters, Çukurova University, 01330 Adana, Turkey
Email: dremrearli@hotmail.com, kkilcik@cu.edu.tr

Abstract
In this study, the effect of magnetic field on hydrogen production performance in aqueous methanol electrolysis have been investigated by using electromagnet apparatus. Furthermore, the effects of magneto-hydrodynamics on the electrolysis procedure thereby varying current or number of turn of coil related to magnetism and methanol electrolysis was discussed. The influences of working arguments was also discussed as well. Finally, the optimized it points out that the augmenting magnitude and convenient direction of magnetic field, ascending ionic concentration of solution and increasing process time was enhanced the performance of methanol assisted alkaline water solution electrolysis.

Keywords: Hydrogen production; magnetic field effect; methanol electrolysis; electrolysis performance.

1. Introduction

The use of hydrogen as a significant energy carrier for the future has been largely introduced. The exhaustion of fossil fuels and effects to the environment from consuming them have agitated global interests in a sustainable energy system [1]. The present carbon-based energy system should be altered to a new energy system that can balance energy supply and demand, protect the environment, and guarantee energy security and economic viability [2]. Among various alternatives, hydrogen-based systems are one of the most promising solutions to achieve the current system. The hydrogen based energy system is not only an alternative to carbon based fossil fuels on which we are primarily dependent for our energy necessaries today, it is also expected to become a necessity in the face of exhausting fossil fuel reserves and increasing concerns about environmental pollution arising from greenhouse gas emission when using the conventional fossil fuels. Apart from its use in the energy sector, hydrogen has sweep applications as a raw material in the chemical, petroleum and nuclear industries and most of the demand is currently met by production of hydrogen from hydrocarbon resources [3,4].

Nowadays, only about 5% of hydrogen in the earth is produced by water electrolysis. The main reasons are high over potentials and large omics voltage losses, which result in high energy consumption or larger electrode areas which in turn means larger and most costly devices [5]. The over potential can be lowered to a defined extent by using higher activity electrodes [6,7]. Nevertheless, lots of gas bubbles are adsorbed on the surfaces of electrode and membrane or dispersed in the electrolyte during water electrolysis. It is difficult for the gas bubbles to be freed quickly from the electrolytic system which leads to large omics voltage losses. This trouble is hardly overcome in commercial electrolytic cells under normal gravity condition [8].

Efficiency of electrolysis cell is an important parameter in the sustainability of hydrogen production. The overall efficiency value of electrolysis cell is generally below 40% [9]. For these reason, there is a great interest to increasing efficiency of electrolysis cells and thereby reducing hydrogen production costs as much as possible. More efficient electrolysis cell design can be divided into two main groups. One of them is providing cheaper electricity and the other is developing cost effective electrode materials and reducing energy consumption [10, 11]. Especially, researchers focused on behavior of electrode and electrolyte materials under different conditions since they are the two significant components of electrolysis. Alkaline or acidic aqueous solutions, distance between the electrodes, cobalt and tungsten based ionic activators used to decrease energy necessities per mass [12]. Investigators tried to increase the performance of water electrolysis by using different physical field effects such as super gravity field, ultrasonic field and magnetic field. Thanks to field effects, it minimized unfavorable effects of bubble coverage on electrode surface area accordingly and increased the distribution of bubbles in electrolyte. Field effects make it enable for the effective separation of bubbles. Reducing voltage drop, reaction overvoltage, diffusion of bubbles in electrolyte to minimize electrolyte resistance enhances mass transfer in electrolysis cell. These factors also decrease cell voltage and increase cell efficiency significantly [13,14,15]. Magnetic field effects for electrolysis setups are studied by several researchers, particularly effect of alkaline or acidic solution (change in concentration, conductivity etc.), effect of electrode materials, geometric features of electrodes, and effect of voltage change and magnetic flux density (B) are researched. Particularly magnetic field effects are simple and effective for water electrolysis works [16]. Lin et al [17] investigated that the effect of magnetic force on hydrogen production efficiency in water electrolysis. They reported that larger reduction in cell

voltage was achieved in magnetic field and this reduction quantity is subject strongly to concentration of electrolyte solutions and strength of magnetic field. They used different materials for electrode which have different behavior under magnetic field, such as nickel, platinum, and graphite. Matsushima et al. [18] used glass electrode to observe convection by reason of magnetic field and coverage effects. They found an equation function of contact angle and magnetic field via experiments. Kaya et al. [19] investigated the magnetic field effect for different concentration of alkali solution. They used expenditure effective electrodes to sustain more economical hydrogen production. Kaya *et al*. have used permanent magnet to produce magnetic field in their experiments. However, in the literature, there is limited works for the investigation of hydrogen energy production and current density difference under magnetic field.

As concern our works bath solution that is aqueous methanol, Take et al. [20] investigated to hydrogen production by methanol water solution electrolysis and Pham et al. [21] researched the efficient hydrogen production from aqueous methanol in a proton exchange membrane electrolyzer with porous metal flow fields.

The aim of this study is to investigate effect of magnetic field on hydrogen production performance in alkaline aqueous methanol electrolysis. Our experiments are performed with electrolysis system called Hittorf and all experiments are performed in ambient conditions. To observe magnetic field effects in this cell, platinum (anode) and platinum (cathode) configuration is selected and is applied different magnitude of perpendicular magnetic field ($B_{\perp}$), parallel magnetic field ($B_{\parallel}$) and without magnetic field to the electrode plate are used in electrolysis cell of the hydrogen production. This Magnetic field is obtained from Helmholtz coil in different magnitude of currents.

2. Principle of Methanol Assisted Water Electrolysis

Theory of electrolysis reaction mechanism under magnetic field alkaline methanol electrolysis process is production of hydrogen by converting methanol to hydrogen and carbon dioxide molecules using direct current (DC) through anode and cathode electrodes in electrolyte solution. Electrolyte solution is ionically conductive. To enhance electrical conductivity of electrolyte solution, it can be added alkaline bases in concentrated electrolyte.

The mechanism for the methanol assisted water electrolysis reaction in acidic aqueous media is a complete six-electron transfer pathway and can be expressed as follows:

Anode: $CH_3OH_{(l)} + H_2O_{(l)} \leftrightarrow CO_{2(g)} + 6H^+ + 6e^-$ (1)

Cathode: $6H^+_{(aq)} + 6e^- \leftrightarrow 3H_{2(g)}$ (2)

$CH_3OH_{(l)} + H_2O_{(l)} \leftrightarrow O \leftrightarrow CO_{2(g)} + 3H_{2(g)}$

$OH^-_{(aq)} + H^+_{(aq)} \leftrightarrow H_2O_{(l)}$

Overall: $CH_3OH + OH^-_{(aq)} + H^+_{(aq)} \leftrightarrow CO_{2(g)} + 3H_{2(g)}$ (3)

From Eq. 3, the passage of 1 mole of electrons through the cell brings an amount of electricity equal to the Faraday constant (96485 C/mole), and causes the release of 3 mole of hydrogen gas at the cathode. E^0 is standard reaction potential at 298 K and 1 atm. The molar volume of ideal gas is 22.414 l/mole under normal conditions (273.15 K and 1 atm), or 24.47 l/mole under standard conditions (298.15 K and 1 atm). To simplify computations, it is assumed that hydrogen behaves like a perfect gas.

Electrode reactions occurs on active surface area of electrodes and electrolyte solution. In electrolysis cell, voltage decreases because of different polarization effects: activation, omics and concentration polarizations. Activation polarization is the result of activation energy required at anode and cathode. It is dependent with the rate of reactions that occurs at the electrodes. Omics losses are due to the resistance of electrodes, especially using imperfect electrodes enhances omic losses for electrochemical cell. Concentration polarizations are involved in reduction of the reactants concentrations on mass transfer path. Effective mass transfer or electron transfer influences reaction rate on electrode surface. Lorentz Force Classical electromagnetics explain this force as Lorentz equation is given as;

$$\overrightarrow{F_L} = q(\vec{E} + \vec{v}x\vec{B}) \quad (4)$$

where q is the charge of the ion and $\vec{v}$ is the term for the velocity of particles, $\vec{E}$ is electric field and $\vec{B}$ is magnetic flux density. Lorentz Force causes magneto hydrodynamic (MHD) convection. When faradic reaction takes place in an electrochemical cell, value of $q\vec{v}$ is limited. If externally applied magnetic field is large enough, it will effect of flow of reactants and/or products in electrochemical reactions. At the electrode surface, bubbles behave as barriers in the flow and drag force caused by hydrodynamic effect on the bubble will be induced. When magnetic field is vertically positioned to electrode, drag force is combined with buoyancy force and this increases contact angle of bubbles to separate from electrode plate surface. Force effects also raise the velocity of bubble as accelerated by MHD convection [16,22,23]. Kaya et al. [19] used handmade electrolysis cell to investigating the Lorentz Force effect to the current density via time for different Lorentz Force direction. In addition, it is significant to make in-situ observations in a high magnetic field. This separation is only in liquid phase because Lorentz Force occurs due to the MHD convection which enhances the rate of mass transfer of dissolved gas to decrease the super saturation degree. The convection effect develops the reaction rate, accordingly decreasing concentration losses and provides more effective hydrogen production.

3. Experimental Method

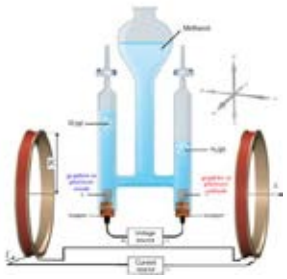


Fig. 1. The Hittorf electrolytic cell for this reaction consists of two electrodes, submerged in an electrolyte and connected to a source of electric current and magnetic coil.

It is illustrated our experimental setup in Fig. 1. The Hittorf electrolytic cell is used for our study with two magnetic coil. This system consists of two electrodes which submerged in an electrolyte and a source of electric current and voltage and also two Helmholtz coil to produce magnetic field. It has more advantages working under magnetic field [19]. Pt, Ni, Cr, electrodes are used as working electrode in hydrogen production studies. We used high purity (99%) Pt-Pt electrodes in this experiment and each electrode is isolated with a material which is alkaline and acidic resistant. Each electrode has the same reaction surface area (0.5 cm^2). Distance between electrodes is set as 10 mm and 80 ml solution vessel is used. Different concentration of NaOH is used to dissolve in distilled water and methanol solution to prepare more conducting bath. Electrolysis cell is kept under ambient conditions for all experiments. Was being generated Helmholtz Coil's magnetic field is calculated in Eq. 5.

$$B = \frac{32n\pi}{5\sqrt{5}} \frac{I_b}{r_B} 10^{-7} \text{ [weber/m}^2\text{]} \quad (5)$$

where n is Helmholtz number of turn of coil (320 turn), r_B is the radius of Helmholtz coil (0.068 m), I_b is the current over coil is explained and all of the terms are constant except to I_b. It can be seen from Eq. 5, which can be written as $B=4.231x10^{-3}\times I_b$ [weber/m^2].

Theory of magnetic field effect and buoyancy effects is shown in Fig. 1. It is basically Ampere right hand rule of electromagnetic effects that determines the direction of Lorentz Force.

Furthermore, electrodes and Helmholtz coil are positioned perpendicular to each other as shown in Fig. 1, In this situation is induced Lorentz Force in the page plane by the magnetic field of coil. The result of upward buoyancy force and Lorentz Force causes help to each other on separation of bubbles and enhanced reaction rate on electrode surface in electrolysis process.

Additionally 0.22 Volt has enough for methanol electrolysis at atmosphere pressure and room temperature [24]. Electrolysis process was used higher voltage with too slow reaction. Hydrogen production velocity is rated to current violence and high current density was preferred due to economic reasons. For this reason, generally approximately 1.5 Volt was used voltage per cell separation of water.

4. Results and Discussions

Effect of magnetic field on producing rate of hydrogen is investigated with different concentration values of sodium hydroxide dissolved in methanol solution (0.1M NaOH 10% (v/v), 0.1 M NaOH 15% (v/v)). These experiments are executed with Hittorf electrolysis system. Also, voltmeter, ammeter and power supply devices are used for electrical process. All experiments are performed in ambient conditions.

Table 1. Measurement Sequence of using the same solution (Methanol Sol.Volume of H_2 (ml)).

Samples	0.1 M NaOH 10% (v/v)	0.1 M NaOH 15% (v/v)
1	1.1	2.3
2	0.8	2.2
3	0.4	2
4	0.3	1.6
5	0.2	1.5
6	0.2	1.4
1.5 V (0.01A) 5 min. B=0 weber/m^2		

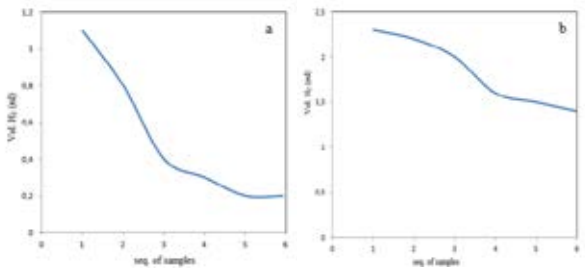


Fig. 2. Using the same methanol Sol. Volume of H_2 (ml) **a)** 0.1 M NaOH 10% (v/v) **b)** 0.1 M NaOH 15% (v/v)

It is shown in Fig. 2, two different molarity solutions more NaOH concentrated sol. has more volume of H_2 production. Each experiment that is the same solution is nearly linearly decreasing volume of H_2 production with each measurement. We have applied both parallel and perpendicular magnetic field (**B**). So, we have seen that perpendicular magnetic field applying experiment has more volume of H_2 production.

Table 2. Parallel magnetic field ($B_{\parallel}$), being positioned two coils oppositely with apart from radius of coil distance

Coil Current (mA)	$B_{\parallel}$ (Volume of H_2(ml))	Volume of H_2 (ml)
1000	1.6	2.8
0.1 M NaOH 20% (v/v) 1.5V (0.01A) 8 min. Parallel magnetic field ($B_{\parallel}$) being positioned two coils oppositely with apart from radius of coil distance)		

Table 3. Perpendicular magnetic field ($B_{\perp}$) with single coil

Coil Current (mA)	$B_{\perp}$ (weber/m^2)	Volume of H_2 (ml)
0	0	0.4
500	2.12×10^{-3}	0.5
1000	4.23×10^{-3}	0.7
2000	8.46×10^{-3}	0.8
0.1 M NaOH 20% (v/v) 1.5V (0.01A) 5min.; Perpendicular magnetic field ($B_{\perp}$) with single coil		

We have applied different currents of single coil and we have obtained perpendicular magnetic field ($B_{\perp}$) and we have observed that the more perpendicular magnetic field the more H_2 production and nearly linearly depended versus to perpendicular magnetic field.

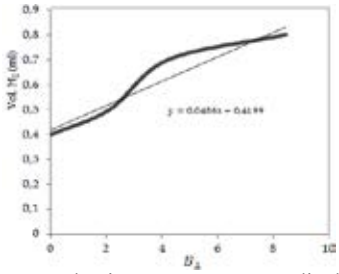


Fig. 3. Volume of H_2 production versus to perpendicular magnetic field.

The different currents of single coil, different electrolysis voltage and time have applied. Table 4 shows that more processing time is also producing more volume of H_2 and increasing the electrolysis time effected the electrolysis voltage in the situation of perpendicular magnetic field ($B_{\perp}$) with two different process times and voltages (5 min 3V, 8 min 1.5 V).

Table 4. Perpendicular magnetic field ($B_{\perp}$) with two different process time

Current (mA)	Volume of H_2 (ml)(5 min. 3 V)	Volume of H_2 (ml)(8 min. 1.5 V)
0	0.4	1.2
1000	0.5	1.8
2000	0.7	2.8
0.1 M NaOH 20% (v/v) (0.01A) Perpendicular magnetic field ($B_{\perp}$) with single coil		

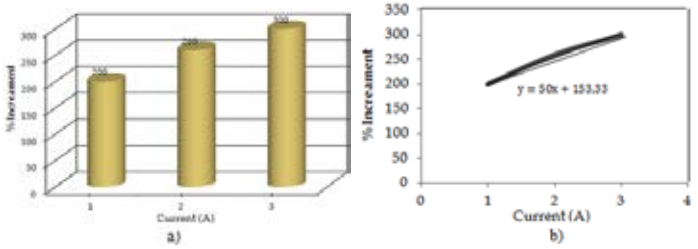


Fig. 5. %increment volume of H_2 production and versus to Current in situation perpendicular magnetic field ($B_\perp$) with single coil **a)** Cylinder bar diagram **b)** graphic.

Fig. 4 shows that the more perpendicular magnetic field increasing the H_2 production and nearly linearly depended versus to perpendicular magnetic field. Slope: 50% incr./A

We have done extra treatment trying; we have add in the bath firstly %30 Pure Methanol secondly %40 0.1 M %20 NaOH thirdly adding 100 ml pure water and lastly 100 ml pure water and no coil current Our observations are listed Table 5.

Table 5. 1.5 V (0.01A) 5 min Perpendicular magnetic field ($B_\perp$) double coils (1 A coils constant).

Adding process	Volume of H_2 (ml)	Observations
%30 Pure Methanol	0.8	Little alkalinity so little electrolytic character and very little activity
%40 0.1 M %20 NaOH	2.1	Bubbles focus on side connection rode electrode and very rapidly big size bubbles
Adding 100ml pure water	1.5	Bubbles are good centrally cloudily distributed and little size bubbles
100ml pure water & no coil current	1.0	Zero B field so little activity
0.1 M NaOH 20% (v/v) 1.5V (0.01 A) 5 min. Perpendicular magnetic field ($B_\perp$) double coils; 1 A coils constant		

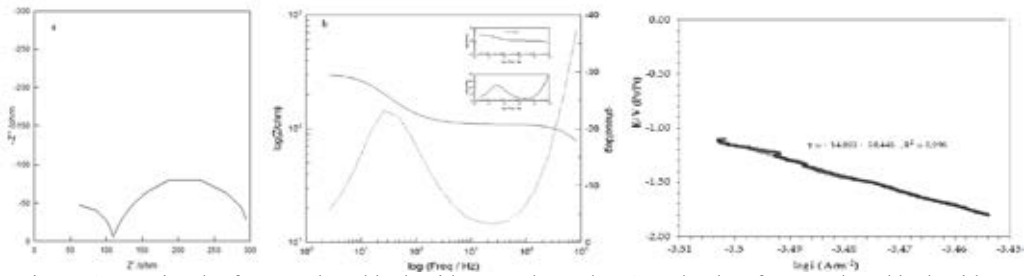


Fig. 5. **a)** Nyquist plot from methanol bath with Pt-Pt electrodes **b)** Bode Plots from methanol bath with Pt-Pt electrodes **c)** Tafel plot from methanol bath with Pt-Pt electrodes.

This Nyquist plot and Bode Plots demonstrate absorptions of organic ions and OH^- ions we can say that two lobes is belonging to (right lobe) CH_3O^- and OH^- (left lobe) so two interface coating on the Pt plates. This Tafel plot demonstrate low slope βc=72 mV/dec cathodic pol. constant and low impedance

5. Conclusion

The aim of this study was to investigate of magnetic field effect on hydrogen production performance by alkaline aqueous methanol electrolysis. For this purpose, Hittorf electrolysis system was set up and all experiments was performed by this system in ambient conditions. In this system, platina (anode) and platina (cathode) electrode configuration were used. To observe magnetic field effects in the system was applied different magnitude of perpendicular magnetic field ($B_\perp$), parallel magnetic field ($B_\parallel$) to the electrode plate and without magnetic field. The magnetic field is obtained from Helmholtz coil in different magnitude of currents. The effect of magnetic field on hydrogen production performance in aqueous methanol electrolysis by using electromagnet apparatus have been analyzed. Furthermore, the effects of magneto-hydrodynamics on the electrolysis procedure thereby varying current or number of turn of Helmholtz coil related to magnetism and methanol electrolysis are discussed. The influences of working arguments are also discussed as well. Finally, the experiments are optimized according to

the points of the increasing magnitude and convenient direction of magnetic field, ascending ionic concentration of solution and increasing process time does enhance the performance of methanol assisted alkaline water solution electrolysis.

References

1. Daskalaki VM, Kondarides DI, Efficient production of hydrogen by photo-induced reforming of glycerol at ambient conditions. Catal Today 2009;144(1-2)
2. Photocatalytic Production of hydrogen: an innovative use for biomass derivatives. Braz J. Chem. Soc. 2011;22(8):1399–1406.
3. Sherif SA, Barbir F, Veziroglu TN. Towards a hydrogen economy. Elec J 2005;18(6):62–76.
4. Ramchandran R, Menon RK. An overview of industrial uses of hydrogen. Int J Hydrogen Energy 1998;23(7):593–597.
5. Cheng H, Scott K, Ramshaw C. Intensification of water electrolysis in a centrifugal field. J Electrochem Soc 2002;149:172–177.
6. Jafarian M, Azizi O, Gobal F, Mahjani MG. Kinetics and electrocatalytic behavior of nanocrystalline CoNiFe alloy in hydrogen evolution reaction. Int J Hydrogen Energy 2007;32(12):1686–1693.
7. Habibi B, Pournaghi-Azar MH, Razmi H, Abdolmohammad-Zadeh H. Electrochemical preparation of a novel, effective and low cost catalytic surface for hydrogen evolution reaction. Int J Hydrogen Energy 2008;33:2668–2678.
8. Balzer RJ, Vogt H. Effect of electrolyte flow on the bubble coverage of vertical gas-evolving Electrodes. J Electrochem Soc. 2003;150(1):E11–E16.
9. Nikolic VM, Tasic GS, Maksic AD, Saponjic DP, Miulovic SM, Kaninski MPM. Raising efficiency of hydrogen generation from alkaline water electrolysis-Energy saving. Int J Hydrogen Energy 2010;35(22):12369–12373.
10. Zeng K, Zhang D. Recent progress in alkaline water electrolysis for hydrogen production and applications. Prog Energy Combust Sci 2010(3);36:307–326.
11. Ivy J. Summary of electrolytic hydrogen production: milestone completion report. Golden, CO (US): National Renewable Energy Lab. 2004.
12. Nagai N, Takeuchi M, Kimura T, Oka T. Existence of optimum space between electrodes on hydrogen production by water electrolysis. Int J Hydrogen Energy 2003;28:35–41.
13. Cheng H, Scott K, Ramshaw C. Intensification of water electrolysis in a centrifugal field. J Electrochem Soc 2002;149:D172–D177.
14. Wang CC, Chen CY. Water electrolysis in the presence of an ultrasonic field. Electrochimica Acta 2009;54:3877–3883.
15. Wang M, Wang Z, Guo Z. Water electrolysis enhanced by super gravity field for hydrogen production. Int J Hydrogen Energy 2010;35:3198–3205.
16. Iida T, Matsushima H, Fukunaka Y. Water electrolysis under a magnetic field. J Electrochem Soc 2007;154(8):E112–E115.
17. Lin MY, Hourng LW, Kuo CW. The effect of magnetic force on hydrogen production efficiency in water electrolysis. Int J Hydrogen Energy 2012;37:1311–1320.
18. Matsushima H, Iida T, Fukunaka Y. Gas bubble evolution on transparent electrode during water electrolysis in a magnetic field. Electrochimica Acta 2013;100:261–264.
19. Kaya MF, Demir N, Albawabiji MS, Tas M, Investigation of alkaline water electrolysis performance for different cost effective electrodes under magnetic field, International Journal of Hydrogen Energy 2017: doi.org/10.1016/j.ijhydene.2017.02.039 (In Press).
20. Take T, Tsurutani K, Umeda M. Hydrogen production by methanol-water solution electrolysis. J Power Sources 2007;164(1):9–16.
21. Pham AT, Shudo T. Efficient hydrogen production from aqueous methanol in a proton exchange membrane electrolyzer with porous metal flow fields. Int J Automotive Eng. 2012;3:125–130.
22. Ragsdale SR, Lee J, Gao X, White HS. Magnetic field effects in electrochemistry. Voltammetric reduction of acetophenone at microdisk electrodes. J Phys Chem 1996;100(14):5913–5922.
23. Devos O, Olivier A, Chopart J, Aaboubi O, Maurin G. Magnetic field effects on nickel electrodeposition. J Electrochem Soc 1998;145:401–405.
24. Ju H, Giddey S, Badwal SPS. The role of nanosized SnO_2 in Pt-based electrocatalysts for hydrogen production in methanol assisted water electrolysis. Electrochimica Acta 2017:229(1);39–47.

ORAL PROCEEDINGS

An Investigation on Exergetic Performance of Hydrogen Gas Flowing Through the Annular Curved Duct

Adnan Midilli, Haydar Kucuk, Ugur Akbulut
Mechanical Engineering Department, Engineering Faculty, Recep Tayyip Erdogan University, Rize, 53100, Turkey
Email: amidilli@gmail.com, haydar.kucuk@erdogan.edu.tr, ugur.akbulut@erdogan.edu.tr

Abstract
Heat transfer enhancement has become very crucial attempt for energy management in heat transfer equipment. Of the parameters affecting the heat transfer enhancement, curvature is an important for increasing the heat transfer in energy systems such as heat exchangers, nuclear and chemical reactors, gas turbines, drying machinery, solar collector applications, electronic cooling and fuel cells, etc. Under these considerations, the main objective of this study is to parametrically investigate the exergetic performance of hydrogen gas flow through the curved annular duct in terms of the second law of thermodynamics. For this purpose, it is assumed that, i) the flow of hydrogen gas as an ideal gas is steady state and laminar fully developed, ii) the hydrogen gas has constant physical properties, iii) the channel inner and outer walls are exposed to constant wall boundary condition. Moreover, the following important parameters are taken into consideration: i) aspect ratio (four different values which are 5.5, 3.8, 2.9 and 2.36), ii) environment temperature (ranging from -30 to 30 with 10 ^{o}C intervals), iii) Dean number (varying between 24 and 208), and iv) operating pressure (=1 atm). Considering these parameters, total exergy input, exergy destruction and exergy efficiencies are calculated for each aspect ratio. Consequently, because the main target of the curved annular duct is to increase the heat transfer, the increased heat transfer in the channel will naturally rise the entropy generation. This is not a negative situation but a fact indicating the rise of exergetic efficiencies of the curved annular duct due to the enhancement of heat transfer during hydrogen gas flow in the channel with the increase of Dean Number because of the curvature. Thus, it can be said that the increased heat transfer creates the rise of entropy, and also exergetic efficiency of the curved annular duct decreases based on the increased reference temperature that creates higher exergy destruction though constant entropy generation arisen from the constant wall temperature boundary condition and constant physical properties of the hydrogen gas in the curved annular duct.

Keywords: Performance analysis; annular curved duct; hydrogen flow; exergy, entropy generation; Dean Number.

1. Introduction

Recently, within the scope of economic sustainability of hydrogen, researchers have focused on the efficiently and effectively production, distribution and utilization of hydrogen and its technologies. It is clear that hydrogen has been utilizing in some industrial and commercial applications such as fuel cells, gas turbines, hydrogen burners, internal combustion engines, etc. In these systems, hydrogen gas flows through the pipes and channels whose entropic effects should be considered. Considering the hydrogen will be a cost effective fuel and energy carrier in our daily life near future, it may be quite important to determine the thermodynamic behavior of hydrogen gas flowing throughout the pipes and channels whose shapes are different from each other. With the recent developments in hydrogen industry, it is obvious that, in the near future, hydrogen will be used in double-pipe heat exchangers, air conditioning systems, cooling systems, and drying machineries in addition to the above applications. Particularly, for these engineering applications, the curved annular ducts may be preferred because of their contribution to efficiently and effectively heating and/or cooling processes in hydrogen energy systems [1-2]. In case hydrogen gas flows in the curved annular ducts, to determine and evaluate thermodynamic behavior of hydrogen gas under various operating temperatures and pressures, the flow types which are laminar and turbulent flows should be considered. Especially, in order to characterize laminar flow of hydrogen gas in a concentric curved annular channel by the secondary flow created by centrifugal effects in the cross-section Dean Number should be taken into consideration. In fact, the nature of this phenomenon depends upon the Dean number, which is the ratio of the Reynolds number to the square root of the dimensionless radius of curvature [1-2]. Also, it is known that the secondary flows passages originate principally from the interaction between the centrifugal force, the pressure gradient, and the viscous forces [1-2]. Thus, in case of hydrogen flow in the ducts, the secondary flow motion in the flow field of hydrogen gas may enhance heat transfer to hydrogen gas from the heating element while it may induce pressure drops in flow field, which may be quite important contribution to improve hydrogen flow system for hydrogen based heating applications in the future.

Resulting a detailed literature review, it is noticed that many works have been mostly concentrated, and numerically and/or experimentally conducted on the heat transfer and fluid flow in curved annular duct with rectangular or circular cross section [1-7]. Second law analysis or entropy generation studies have been studied by many researchers in different shaped-channels in the literature [8-22]. Moreover, in our previous study we focused

on entropy generation of both hydrodynamically and thermally fully developed laminar flow of hydrogen gas under various operating pressures and temperatures in concentric curved annular ducts with rectangular cross section [23]. Continuously, the main objective of this study is to parametrically investigate the exergetic performance of hydrogen gas flow through the curved annular duct in terms of the second law of thermodynamics. For chosen different channel aspect ratios, the effects of Dean Number and dead state temperature on the exergy destruction rate and exergy efficiency have been investigated in detail. In terms of the scientific and industrial benefits, this study aims to provide the researchers and scientists some detailed information on exergetic performance of hydrogen flow in a concentric curved annular ducts with rectangular cross section due to the irreversibilities caused by fluid friction and heat transfer.

2. Modelling and Analysis

The problem undertaken in this study is to investigate the exergetic performance of hydrogen gas flow through the curved annular duct considering both hydrodynamically and thermally fully developed laminar flow. The curved duct geometry and coordinate system of the studied problem is illustrated in Fig.1.

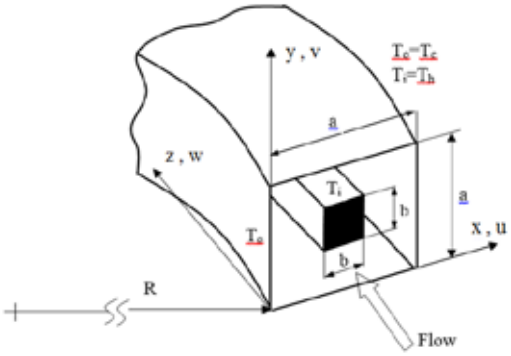


Fig. 1. Curved duct geometry and coordinate system

In order to achieve the exergetic performance of hydrogen gas flow through the curved annular duct following assumptions are taken into consideration:

- The flow of hydrogen gas as an ideal gas is steady state and laminar fully developed
- The hydrogen gas has constant physical properties
- The channel inner and outer walls are exposed to constant wall boundary condition.
- Radius of curvature (R) is large compared with the channel dimensions (R+x≈R) [1-2,23-27].
- The physical properties of hydrogen gas depending on operating pressures and temperatures are taken from National Institute of Standards and Technology (NIST).

Moreover, the following important parameters are used in the calculations:

- Aspect ratio (four different values which are 5.5, 3.8, 2.9 and 2.36)
- Environment temperature (ranging from -30 to 30 with 10 ^{o}C intervals)
- Dean number (varying between 24 and 208), and iv) operating pressure (=1 atm)

The nature of laminar flow of hydrogen gas in a concentric curved annular channel by the secondary flow created by centrifugal effects in the cross-section strongly depends upon the Dean number. The Dean number (De) is a dimensionless group in fluid mechanics, which occurs in the study of flow in curved pipes and channels. It is named after the British scientist W. R. Dean, who studied such flows in the 1920s): For a flow in a pipe or tube it De is defined as:

$$De = Re\sqrt{\frac{D_h}{R}} \quad (1)$$

where Reynolds number (Re) and the average velocity of hydrogen gas (w_{ave})is calculated as follows

$$Re = \frac{\rho w_{ave} D_h}{\mu} \quad (2)$$

$$w_{ave} = \frac{1}{A}\iint \ddot{S}_T \, dxdy \quad (3)$$

The volumetric entropy generation resulting from the heat transfer ($\ddot{S}_T$) and volumetric entropy generation resulting from the fluid friction ($\ddot{S}_P$) can be calculated by the following equations (3-9):

$$\ddot{S}_T = \frac{k}{T^2}(|\nabla T|)^2 \quad (4)$$

$$\ddot{S}_P = \frac{\mu}{T}\left(\frac{\partial u}{\partial y} + \frac{\partial v}{\partial x}\right)\frac{\partial u}{\partial y} \quad (5)$$

Considering Eqs. (4) and (5), total volumetric entropy generation of hydrogen gas in the flow field can be obtained as

$$\ddot{S}_{gen} = \ddot{S}_T + \ddot{S}_P \quad (6)$$

For evaluation of the entropy generation in whole hydrogen gas flow field in the concentric curved annular duct with rectangular cross section, the volumetric average entropy generation rates, $\ddot{S}_{T,ave}$, $\ddot{S}_{P,ave}$ and $\ddot{S}_{gen,ave}$ are defined by Eqs. (7-9), [3].

$$\ddot{S}_{T,ave} = \frac{1}{A}\iint \ddot{S}_T \, dxdy \quad (7)$$

$$\ddot{S}_{P,ave} = \frac{1}{A}\iint \ddot{S}_P \, dxdy \quad (8)$$

$$\ddot{S}_{gen,ave} = \frac{1}{A}\iint \ddot{S}_{gen} \, dxdy \quad (9)$$

Entropy generation rate can be obtained by the product of volumetric average entropy generation rate with the curved duct volume (V)

$$\dot{s}_{gen} = \ddot{S}_{gen,ave} \, V \quad (10)$$

The general exergy balance for an open system can be written as below:

$$\sum \dot{E}x_{in} = \sum \dot{E}x_{out} + \sum \dot{E}x_{loss} + \sum \dot{E}x_D \quad (11)$$

By neglecting the exergy loss rate considering the constant wall boundary condition, exergy balance equation takes the following form

$$\sum \dot{E}x_{in} = \sum \dot{E}x_{out} + \sum \dot{E}x_D \quad (12)$$

The exergy destruction rate ($\dot{E}x_D$) is equal to the product of entropy generation rate $\dot{s}_{gen}$ within the curved duct and the temperature of the reference environment (T_0).

$$\dot{E}x_D = T_0 \, \dot{s}_{gen} \quad (13)$$

Considering the very low friction loss in the curved duct, kinetic exergy rate ($\dot{E}x^{ke}$) can be neglected. Also, $\dot{E}x^{ph}$ is the physical exergy rate and can be defined as follows,

$$\dot{E}x^{ph} = \dot{m}[(h - h_0) - T_0(s - s_0)] \quad (14)$$

Considering given assumptions and equations (11-14) exergy balance of the curved annular duct can be can be written as below,

$$\dot{m}[(h_{in} - h_0) - T_0(s_{in} - s_0)] - \dot{m}[(h_{out} - h_0) - T_0(s_{out} - s_0)] + \dot{m}\frac{w_{ave}^2}{2} = T_0 \, \dot{s}_{gen} \quad (15)$$

and Exergy efficiency of the system can be obtained as

$$ee = 1 - \frac{\dot{E}x_D}{\dot{E}x_{in}} = 1 - \frac{T_0 \, \dot{s}_{gen}}{\dot{m}[(h_{in} - h_0) - T_0(s_{in} - s_0)]} \quad (16)$$

For hydrogen gas inlet enthalpy and entropy values (h_{in} and s_{in}) have been computed depending on operating pressure (1 atm) and mean temperature of the flow (37.5 °C) by using Standard Reference Data Program of National Institute of Standards and Technology (NIST). Adding that, reference environment temperature (ranging from -30 to 30 with 10 °C intervals) have been taken into consideration for calculating enthalpy and entropy parameters at dead state.

3. Results and Discussion

Considering the given assumptions and parameters, total exergy input, exergy destruction and exergy efficiencies are calculated for each aspect ratio and the results discussed in this section.

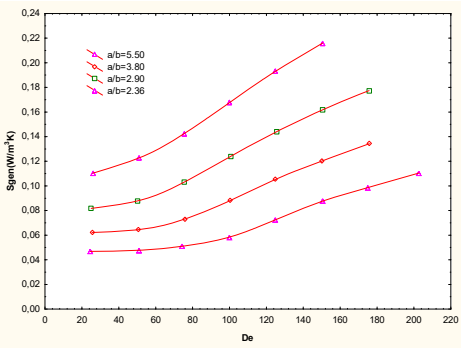


Fig. 2. Variation of volumetric entropy generation rate for hydrogen gas flow as a function of De number under various curved duct dimensions [23].

Fig. 2 shows that, for all examined channel aspect ratios (which are 5.5, 3.8, 2.9 and 2.36), volumetric entropy generation rate increases with the rising Dean number because of secondary flows of hydrogen gas and the slope of the increment rises with the rising aspect ratio. Stable volumetric entropy generation can be seen at small Dean Numbers (such as 20-60) and bigger channel aspect ratios (such as 3.8 and 5.5). However at bigger Dean Numbers and smaller channel aspect ratios volumetric entropy generation continuously rising.

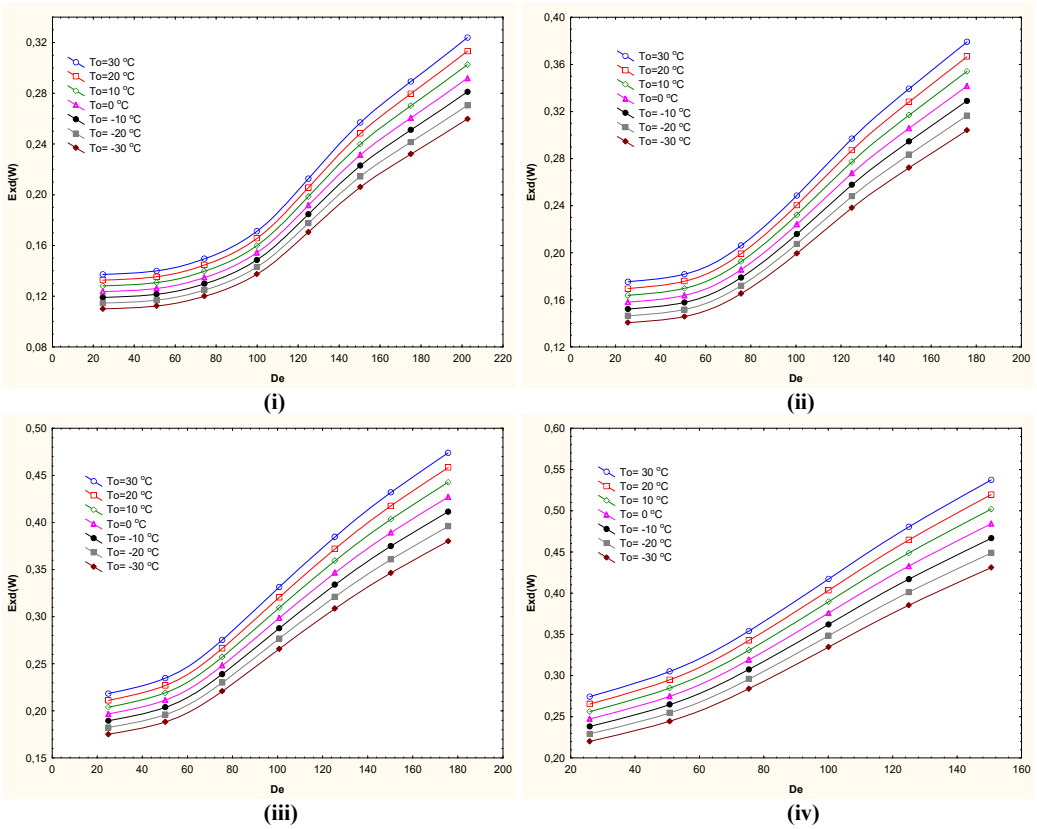


Fig. 3. Effect of dead state temperature on the exergy destruction rate for hydrogen gas flow as a function of De number; i) a/b=5.5, ii) a/b=3.8, iii) a/b=2.9 and iv) a/b=2.36

Fig. 3. reprents that, exergy destruction rate increases with the rise of reference environment temperature (ranging from -30 to 30 with 10 °C intervals). At a constant environment temperature and constant channel aspect ratio exergy destruction behaviour is similar to entropy generation rate which is expained in Fig. 2. Minimum exergy destruction rate is calculated as 0.110 W while the reference environment temperature is -30 °C, at channel aspect ratio 5.5 and Dean number is equal to 24.6 (see Fig 3-i). Maximum exergy destruction rate is calculated as 0.537 W while the reference environment temperature is 30 °C, at channel aspect ratio 2.36 and Dean number is equal to 150.6 (see Fig 3-iv).

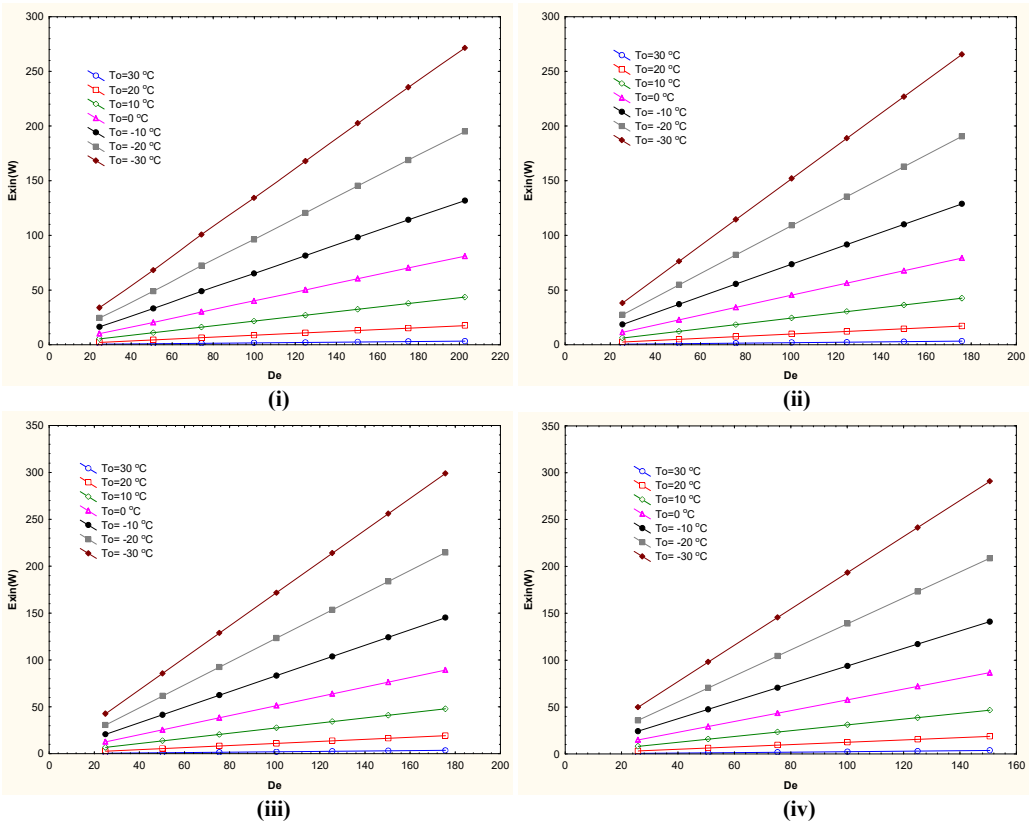


Fig. 4. Effect of dead state temperature on the total exergy input for hydrogen gas flow as a function of De number ; i) a/b=5.5, ii) a/b=3.8, iii) a/b=2.9 and iv) a/b=2.36

According to Fig. 4, total exergy input rate for hydrogen gas decreases linearly with the rise of reference environment temperature (ranging from -30 to 30 with 10 °C intervals) and the slope of the increment decreases with the rising aspect ratio. At a constant environment temperature and constant channel aspect ratio total exergy input rate rises linearly with the increasing Dean number. Minimum total exergy input rate is calculated as 0.42 W while the reference environment temperature is 30 °C, at channel aspect ratio 5.5 and Dean number is equal to 24.6 (see Fig 4-i). Maximum total exergy input rate is calculated as 290.83 W while the reference environment temperature is -30 °C, at channel aspect ratio 2.36 and Dean number is equal to 150.6 (see Fig 4-iv).

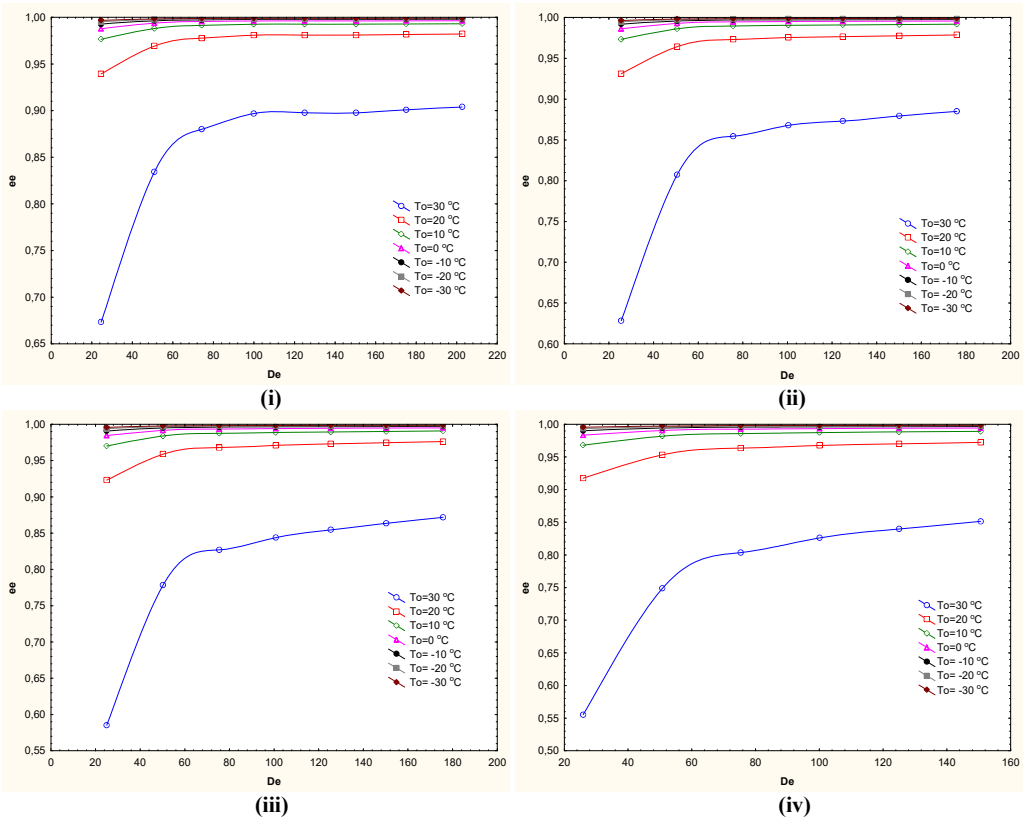


Fig.5. Effect of dead state temperature on the exergy efficiency for hydrogen gas flow as a function of De number ; i) a/b=5.5, ii) a/b=3.8, iii) a/b=2.9 and iv) a/b=2.36

Fig. 5. indicates that, exergy efficiency for hydrogen gas decreases with the rise of reference environment temperature (ranging from -30 to 30 with 10 ºC intervals). At a constant environment temperature and constant channel aspect ratio exergy efficiency rises with the increasing Dean number. On the contrary to the characteristic behaviour of volumetric entropy generation rate, a rapid increament can be seen at small Dean numbers (such as 20-60) and slope of the increment rises with the rising aspect ratio. On the other hand, more stable exergy effciency values can be seen at bigger Dean numbers at bigger Dean numbers (such as 60-200). Minimum exergy efficiency is calculated as %55.5 while the reference environment temperature is 30 ºC, at channel aspect ratio 2.36 and Dean number is equal to 25.9 (see Fig. 5-iv). Maximum exergy exergy is calculated as %99.9 while the reference environment temperature is -30 ºC, at channel aspect ratio 5.5 and Dean number is equal to 202.7 (see Fig. 5-i).

4. Conclusions

In this study, a parametric investigation on the exergetic performance of hydrogen gas flow through the curved annular duct in terms of the second law of thermodynamics has been achieved. The following concluding remarks can be drawn:

- Increament of Dean number indicates the increased heat transfer and entropy generation in the curved annular duct.
- Exergetic efficiency rises with the increase of Dean number because of the curvature.
- Increased reference environment temperature creates higher exergy destruction though constant entropy generation arisen from the constant wall temperature boundary condition and constant physical properties of the hydrogen gas in the curved annular duct.
- It is concluded that, increasing reference environment temperature decrease exergy efficieny.

References

1. Kucuk H, Asan H. A numerical study on heat and fluid flow in concentric curved annular square ducts. Heat Transfer Engineering. 2009;30(5):383-92.
2. Kucuk H, Asan H. Forced convection heat transfer in eccentric curved annular square ducts. J Thermal Science Technology. 2009;29(1):67-78.
3. Choi HK, Park SO. Laminar entrance flow in curved annular ducts. Int J Heat Fluid Flow. 1992;13(1):41–9.
4. Choi Hk, Park SO. Mixed convection flow in curved annular ducts. Int J Heat Mass Transfer 1994;37(17):2761–9.
5. Petrakis MA, Karahalios GT. Fluid flow behaviour in a curved annular conduit. Int J Non-Linear Mechanics. 1999; 34:13–25.
6. Garimella S, Richards DE, Christensen RN. Experimental investigation of heat transfer in coiled annular ducts. J Heat Transfer. 1988;110:329–36.
7. Petrakis MA, Karahalios GT. Exponentially decaying flow in a gently curved annular pipe. Int. J Non-linear Mechanics. 1997;32(5):823–35.
8. Ko TH, Ting K. Etropy generation and optimal analysis for laminar forced convection in curved rectangular ducts: A Numerical Study. Int J Thermal Science. 2006;45(2):138-50.
9. Ko TH. Numerical investigation on laminar forced convection and entropy generation in a curved rectangular duct with longitudinal ribs mounted on heated wall. Int J Thermal Science. 2006;45(4):390-404.
10. Ko TH, Ting K. Entropy generation and thermodynamic optimization of fully developed laminar convection in a helical coil. Int Communication Heat Mass Transfer. 2005;32:214-23.
11. Ko TH. Thermodynamic analysis of optimal curvature ratio for fully developed laminar forced convection in a helical coiled tube with uniform heat flux. Int J Thermal Science. 2006;45(7):729-37.
12. Ko TH, Cheng CS. Numerical investigation on developing laminar forced convection and entropy generation in wavy channel. Int Communication Heat Mass Transfer. 2007;34:924-33.
13. Ko TH. Numerical analysis of entropy generation and optimal reynolds number for developing laminar forced convection in double-sine ducts with various aspect ratios. Int J Heat Mass Transfer. 2006;49(3-4):718-26.
14. Ko TH. A numerical study on entropy generation and optimization for laminar forced in a rectangular curved duct with longitudinal ribs. Int J Thermal Science. 2006;45(11):1113-25.
15. Mahmud S, Fraser RA. Second law analysis of heat transfer and fluid flow inside a cylindrical annular space. Exergy, An International Journal. 2002;2:322-9.
16. Yari M. Second-law analysis of flow and heat transfer inside a microannulus. Int Communication Heat Mass Transfer. 2009;36(1):78-87.
17. Demirel Y, Kahraman R. Thermodynamic analysis of convective heat transfer in an annular packed bed. Int J Heat Fluid Flow. 2000;21(4):442-8.
18. Mahmud S, Fraser RA. The second law analysis in fundamental convective heat transfer problems. Int J Thermal Science. 2003;42(2):177-86.
19. Gorla RSR, Bydr LW, Pratt DM. Second law analysis for microscale flow and heat transfer. Applied Thermal Engineering. 2007;27(8-9):1414-23.
20. Tasnim SH, Mahmud S. Mixed convection and entropy generation in a vertical annular space. Exergy, An International Journal. 2002;2:373-9.
21. Mahmud S, Fraser RA. Analysis of entropy generation inside concentric cylindrical annuli with relative rotation. Int J Thermal Science. 2003;42(5):513-21.
22. Chen S. Analysis of entropy generation in counter flow premixed hydrogen air combustion. Int J Hydrogen Energy. 2010;35(3):1401-11.
23. Kucuk H, Akbulut U, Midilli A. Entropy Generation of Hydrogen Flow in a Curved Annular Duct. Progress in Sustainable Energy Technologies Vol II, 2014.
24. Gyves TW, Irvine TF. Laminar conjugated forced convection heat transfer in curved rectangular channels. Int J Heat Mass Transfer. 2000;43:3953-64.
25. Gyves Tw. A numerical solution to conjugated mixed convection heat transfer in curved square channel. Ph.D. Thesis, State University Of New York At Stony Brook 1997.
26. Kucuk H. Numerical investigation of heat transfer and fluid flow in concentric or eccentric curved annular ducts. Ph.D. Thesis, Karadeniz Technical University 2003.
27. Asan H, Kucuk H. A numerical computation of heat and fluid flow in l-shaped curved channels. Heat Transfer Engineering. 2007;28:112-9.

ORAL PROCEEDINGS

Bonding Strength and Fuel Leakage Tests for Crofer®22 Solid Oxide Fuel Cell Metallic Interconnects

Bülent Öztürk[1], Alparslan Topcu[2,3], Sultan Öztürk[1], Ömer Necati Cora[2]
[1]Department of Metallurgical and Materials Engineering, Karadeniz Technical University, Trabzon, Turkey
[2]Department of Mechanical Engineering, Adana Science and Technology University, Adana, Turkey
[3]Department of Mechanical Engineering, Karadeniz Technical University, Trabzon, Turkey
Email: bozturk@ktu.edu.tr, atopcu@adanabtu.edu.tr, suozturk@ktu.edu.tr, oncora@ktu.edu.tr

Abstract
Interconnects are one of the key components in solid-oxide fuel cells. This study aimed for investigating the bonding strength and sealing performance of interconnects made of commercially available bulk Crofer®22 alloy through machining as well as through powder metallurgy approach from powders. Tensile test method was employed to determine the bonding strength of interconnects. Bonding strength results were analyzed with Weibull distribution method, and reliability curves was obtained via Weibull distribution method. Weibull distribution results showed that samples fabricated through P/M approach were more consistent in terms of bonding strength. Sealing capability of the samples, on the other hand, was measured with fuel leakage test apparatus. Electrolyte, glass-ceramic and leakage test apparatus system were placed in the temperature controlled furnace. Constant hydrogen flow was provided to the furnace through inlet at 35 kPa continuously and flow rate was measured at the outlet after each thermal cycle. Hence, pressure drop was determined per thermal cycle for both samples fabricated with P/M and the one machined from commercial alloy. Results showed that the sample prepared through powder metallurgy approach performed better in terms of sealing. Bonding tests, on the other hand, revealed that, powder metallurgy technique would be more appropriate at low tensile force while the sample machined from commercial alloy can be preferred at higher tensile forces.
As overall conclusion, interconnect sample manufactured through powder metallurgy approach can be a reliable alternative to the one manufactured from commercial Crofer®22 alloy through machining.

Keywords: Solid oxide fuel cell; powder metallurgy; bonding strength; fuel leakage.

1. Introduction

The importance of alternative vehicle technologies (electric, hybrid, fuel cell car technologies) is continuously increasing due to limited and depleting fossil fuel resources and their detrimental effects to environment. Fuel cells, one of these alternative technologies, are electrochemical systems that convert the fuel energy to electric current directly, without combustion [1]. Solid-oxide fuel cell (SOFC), in particular, outperform the other fuel cell types as they operate at higher temperatures (600-1000 °C), can use fossil fuels, and carbon monoxide through a conversion process in addition to hydrogen, and their efficiencies can go up to 80-90% through co-generation [2-6]. SOFCs basically consist of membrane electrode assembly (MEA) where electrochemical reaction occurs, interconnects that provide mechanical support and collects the current produced in the cells, and sealants that prevents air/fuel leakages in between MEA and interconnects [7-11]. Interconnect is a key component in planar SOFC stacks, electrically connecting and chemical compatibility with adjacent components, separating and distributing the fuel gas and the oxidant on the anode and cathode sides, respectively of the cells [6,12-14].

Metallic interconnects are manufactured using the casting-rolling-(forging) route with mechanical machining (wire erosion approach) of the semi-finished products traditionally [12,15-18]. Powder metallurgy (P/M) is another approach to manufacture metallic interconnects and has some advantages over traditional machining manufacturing such as near-net shape production, fast and high production rate, elimination or reduction of machining and scrap material [19-21].

Glass-ceramic sealants which bond with metallic interconnect are widely used for preventing the gas leakage. Due to their different thermal expansion coefficient (TEC), thermal stresses and cracks are generated occur during start-up and shutdown, and these consequently may lead to gaps at contacting surfaces and failures. Contact loss at contacting surfaces causes gas leakages and performance loss in the cell. Therefore, an interconnect should have the sufficient strength for not only structural integrity but also preventing from gas leakage. Tensile test method is the widely used to determine the bonding strength in literature [22-28]. Smeacetto et al., studied the performance of SACN (SiO_2-Al_2O_3-CaO-Na_2O) glass-ceramic sealant used to join the ceramic electrolyte andthe metallic interconnects in SOFC stacks [22]. SACN sealant was found to be effective for joining Crofer®22 metallic interconnector and anode-supported-electrolyte compared to AISI 430 metallic interconnector and YSZ electrolyte. Celik studied the joining strength of one of the commercial glass-ceramic sealant (Viox-V1649; mainly consist of B_2O_3, SrO, La_2O_3) to the Crofer®22 under different conditions such as glass-ceramic sintering temperature and pressure, the surface coating, the surface roughness, use of a support material and the thickness of glass-ceramic layer, experimentally [24]. The polished sample was found

to exhibit the lowest tensile strength according to roughness values of the metallic interconnects. The highest tensile strength was obtained when NiO was used as support material over YSZ, ScSZ and 3YE materials.The Weibull analysis is a common way to estimate the failure probability of materials [29]. This method and reliability curves are often used to define bonding strength results [27,30-34]. The reliability curves of the tensile test results obtain via Weibull dsitribution method. Sealing is one of the most important parameters influencing the fuel cell performance. The most common method is to determine the pressure drop between the gas inlet and outlet is leakage test [35-42]. The leakage tests are mostly performed at low temperatures and pressures. Zhang et al., carried out the leakage test, starting at 10 kPa pressure level and continued until 0,5 kPa at temperature range of 100-600°C [35]. In another study by Le et al., leakage tests were performed for mica based sealant at 800°C temperatures, nitrogen atmosphere and 15kPa inlet pressure [36].

Different from existing literature, this study aimed for investigating the bonding strength and gas leakage of Crofer®22 metallic interconnect samples manufactured through powder metallurgy approach from powders as well as commercially available bulk Crofer®22 alloy through machining.

2. Experimental Study

2.1. Crofer®22 powder characterisations

Crofer®22 powders acquired from H.C. Starck GmbH (Germany). Chemical composition and scanning electron microscope (SEM) image of Crofer®22 powders are given in Table 1 and Fig. 1., respectively.

Table 1. Chemical composition of Crofer®22 powder

Element	Ni	Fe	Cr	Mo	Mn	Si	Ti	Nb	La
%	0.03	Bal.	22.8	0.1	0.44	0.5	0.2	0.1	0.1

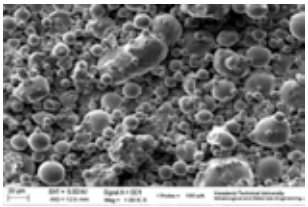


Fig. 1. SEM image of Crofer®22 powder

Powders first compacted in a rigid die having dimensions of 30 x 30 mm at room temperature and 600 MPa nominal compaction pressure when samples. Then, sintering was performed at 1200 °C after compaction. Obtained samples were machined using milling machine to special dimensions for bonding strength and leakage tests. Other group of samples were prepared from commercially available bulk Crofer®22 alloy through machining. Schematic of P/M manufacturing process is given in Fig. 2-a and actual photo of compaction test setup and the die used in current study are provided in Fig. 2-b.



(a) (b)

Fig. 2. (a) Schematic of P/M process followed , (b) Hydraulic press and die set used for sample manufacturing

2.2. Fabrication of the glass-ceramic sealant

G6 borosilicate-based glass-ceramic sealant was used for bonding strength and leakage tests at elevated temperatures [43]. Chemical composition of glass-ceramic used is presented in Table 2.

Table 2. Chemical composition of sealant used in the tests

Sealant	Compound (%)		
	SiO_2	BaO	B_2O_3
G6	45.06	32.40	22.54

Glass-ceramic powders were mixed with tape cast solution 50% by weight and slurry was ball-milled for 12h and mixed using magnetic mixer for 3h. Next, the slurry was tape cast with a blade gap of 100 µm via tape casting equipment. An amount of glass-ceramic tapes were stacked together and laminated under pressure of 30 MPa for 4 mins. The final thickness was 1 mm for all sealants prepared. The laminates were cut into small rectangles (15 mm x 5 mm) for the bonding strength test and rigid type of samples with inner diameter of 15 mm, and outer diameter of 25 for the fuel leakage tests via laser machining. Manufacturing procedure for sealant manufacturing is illustrated in Fig. 3.

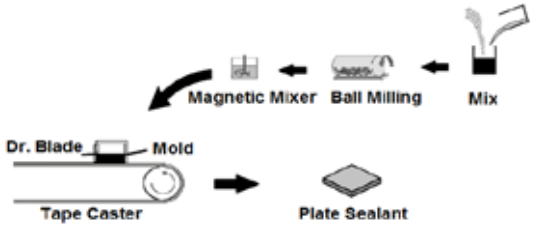
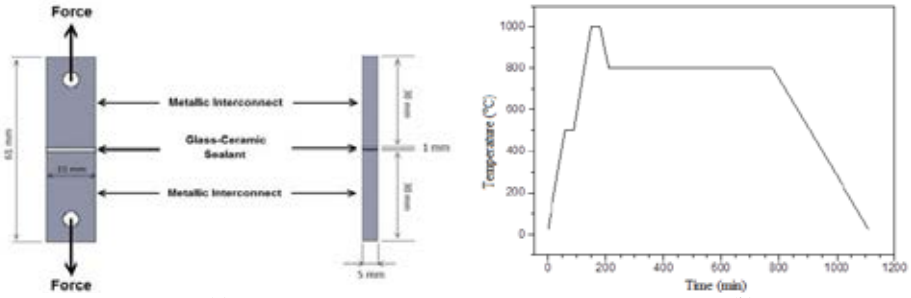


Fig. 3. Procedure for sealant manufacturing

2.3. Bonding strength tests

Test specimens (15 mm x 30 mm) were prepared from both the P/M and the machined samples. These samples then, were placed in a temperature controlled furnace and same heat treatment was applied to both. Afterwards, tensile tests were carried out using Shimadzu Autograph AG-IS universal test machine after the heat treatment and tensile tests were repeated ten times for every samples. Test specimens and glass-ceramic sealant's front and side views are shown in Fig. 4-a while applied heat treatment process is shown in Fig. 4-b.

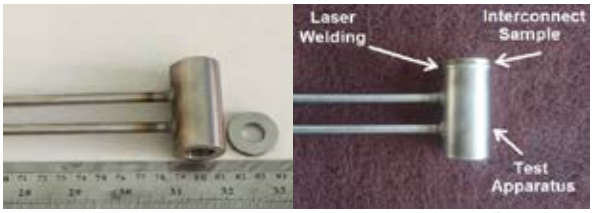


(a) (b)

Fig. 4. (a) Test specimens and sealant's front and side views, (b) Heat treatment for bonding strength specimens

2.4. Fuel leakage tests

To perform the fuel leakage tests, a ring-shaped sample fabricated through powder metallurgy method (Fig. 5-a) was welded on the leakage test apparatus as shown in Fig. 5-b. Electrolyte, glass-ceramic and leakage test apparatus system were placed in the temperature controlled furnace. Constant hydrogen flow was provided to the furnace through inlet at 35 kPa pressure, continuously. Flow rate was measured at the outlet after each thermal cycle. Hence, pressure drop was measured after each thermal cycle for both samples. Fuel leakage test procedure is illustrated in Fig. 6.



(a) (b)

Fig. 5. (a) Fuel leakage test apparatus and ring-shaped sample, (b) Laser welding of interconnect sample to the

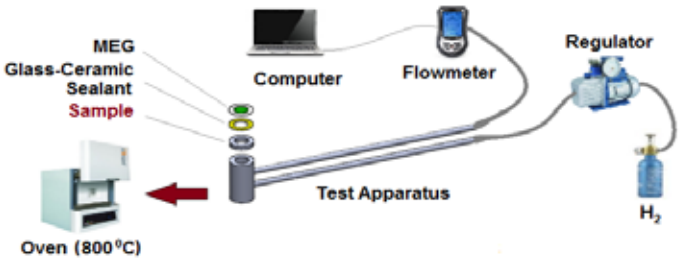


Fig. 6. Test procedure for fuel leakage test

Test system was heated until 850 °C and temperature was kept constant for 30 minutes, first. After that system was cooled down to 200 °C with natural cooling and it was heated to 800°C. This process was carried out along 10 cycles for both samples (P/M and machined) and pressure drop was measured after each thermal cycle in leakage tests. Heat treatment process for leakage tests is shown in Fig. 7.

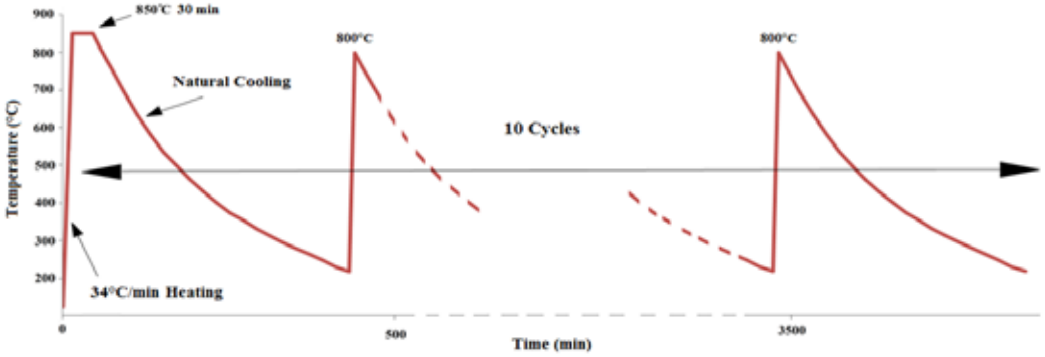
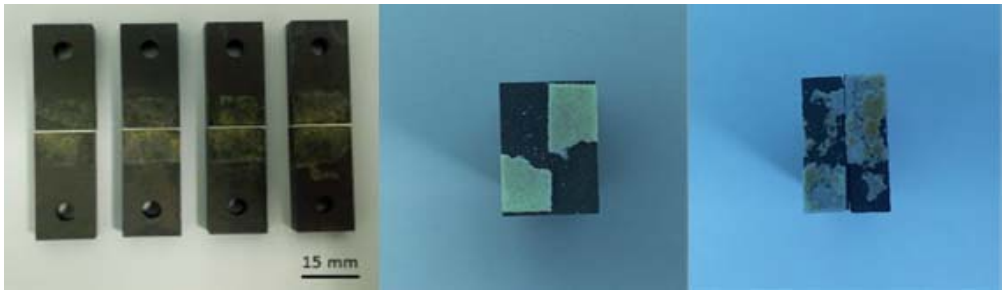


Fig. 7. Heat treatment applied in leakage test system

3. Results and Discussion

3.1. Bonding strength tests

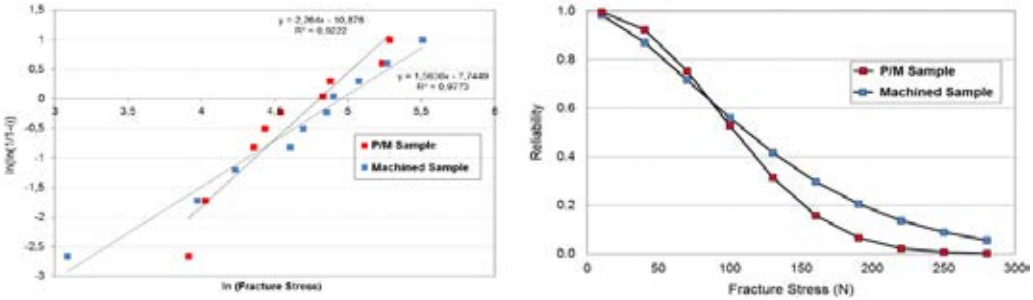
Tensile tests carried out for both the P/M and the machined samples. P/M sample exhibited failure not only at contact interface but also glass-ceramic interface. This was interpreted as tensile strength of the P/M sample is comparable with the strength of glass-ceramic layers. Sample machined from Crofer®22 commercial alloy, on the other hand, showed failure at glass-ceramic interface, only. Interconnect samples and glass-ceramic sealants' appearance after heat treatment is shown in Fig. 8. A pair of specimens belonging to machined and P/M samples' surfaces is provided in Fig. 9. Although glass-ceramic sealant material used was the same for both samples, it appears that the fracture behavior of the samples (leaving from glass-ceramic material) are different.



(a) (b) (c)

Fig. 8. (a) Interconnect samples and glass-ceramic sealants' appearance after heat treatment, (b) Machined samples' surfaces after tensile test, (c) P/M samples' sufaces after tensile test

Bonding strength results were analyzed with Weibull distribution method, and a reliability analysis was performed via Weibull distribution. Weibull distribution results showed that samples fabricated through P/M approach were more consistent in terms of bonding strength (Fig. 9-a). Reliability curves yielded that the P/M sample is more reliable at low tensile force while the sample machined from commercial alloy is preferrable at higher tensile forces (Fig. 9-b).



(a) (b)

Fig. 9. (a) Weibull distribution of tensile results of P/M and machining samples, (b) Reliability curves of P/M and machined samples

3.2. Gas leakage tests

Leakage tests results showed that, the pressure steadily decreased till 10th cycle for the machined sample while the P/M sample maintained the inlet pressure till 6th cycle. After tenth cycle, the pressure values were recorded as 34.39 and 34.85 kPa for machined and P/M samples, respectively (Fig. 10).

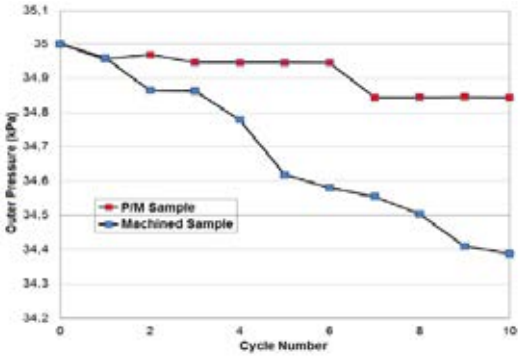


Fig. 10. Outer pressure values of P/M and machined samples

4. Conclusion

In this study, bonding strength and gas leakage performance of Crofer®22 metallic interconnect samples which were manufactured through powder metallurgy approach from powders as well as commercially available bulk Crofer®22 alloy through machining were evaluated experimentally. Bonding strength values were evaluated with Weibull distribution method and reliability curves were obtained via Weibull analysis. According to bonding strength (Weibull-reliability) results, the P/M sample was found more reliable at low tensile force while the sample machined from commercial alloy was preferrable at higher tensile forces. From gas leakage of point of view, pressure steadily decreased till 10th cycle for the machined sample while the P/M sample maintained the inlet pressure till 6th cycle. After tenth cycle, the pressure values were recorded as 34.39 and 34.85 kPa for machined and P/M samples, respectively. As overall conclusion, interconnect sample fabricated through powder metallurgy is an sound alternative to one produced through machining from bulk material.

Acknowledgements

The authors wish to acknowledge the financial support provided by the Scientific and Technological Research Council of Turkey (TUBITAK) through the project #114M502.

References

1. Yu Z, Han J, Cao X, Chen W, Zhang B. Analysis of total energy system based on solid oxide fuel cell for combined cooling and power applications. Int J Hydrogen Energy. 2010;35:2703-2707.
2. Huang J, Xie F, Wang C, Mao Z. Development of solid oxide fuel cell materials for intermediate-to-low temperature operation. Int J Hydrogen Energy. 2012;37:877-883.
3. Kruk A, Adamczyk A, Gil A, Kąc A, Dąbek A, Ziąbka M, Brylewski T. Effect of Co deposition on oxidation behavior and electrical properties of ferritic steel for solid oxide fuel cell interconnects. Thin Solid Films. 2015;590:184-192.
4. Zink F, Lu Y, Schaefer L. A solid oxide fuel cell system for buildings. Energy Convers Manag. 2007;48:809-818.
5. The SOFC fuel cell at a glance – The PLANSEE Group. [cited 2017 April 14]. Available from: https://www.plansee.com/en/products/components/sofc-interconnects.html
6. Wu J, Liu X. Recent Development of SOFC Metallic Interconnect: Invited Review. J Mater. Sci. Technol. 2010;26(4):293-305.
7. Fergus J. Metallic interconnects for solid oxide fuel cells. Mat Sci Eng A. 2005;397:271-283.
8. Lin CK, Chen TT, Chyou YP, Chiang LK. Thermal stress analysis of a planar SOFC stack. J Power Sources. 2007;164:238-251.
9. Nishida RT, Beale SB, Pharoah JG. Comprehensive computational fluid dynamics model of solid oxide fuel cell stacks. Int J Hydrogen Energy. 2016;41:20592-20605.
10. Li J, Zhang W, Yang J, Yan D, Pu J, Chi B, Jian L. Oxidation behavior of metallic interconnect in solid oxide fuel cell stack. J Power Sources. 2017;353:195-201.
11. Guan W, Wang G, Z XD. Mechanism of the cathode current collector on cell performance in a solid oxide fuel cell stack: Short communication. J Power Sources. 2017;351:169-173.
12. Tietz F, Buchkremer HP, Stöver D. Components manufacturing for solid oxide fuel cells: Review article. Solid State Ionics. 2002;152-153;373-381.
13. Zhu WZ, Deevi SC. Development of interconnect materials for solid oxide fuel cells. Mater. Sci. Eng. A. 2003;348:227-243.
14. Zhang W, Li J, Yang J, Zhou B, Chi B, Pu J. Characterization of a new Fe-based alloy as metallic interconnect in SOFC anode environment. Int J Hydrogen Energy. 2016;XXX:1-8.
15. Bastidas DM. High temperature corrosion of metallic interconnects in solid oxide fuel cells. Revista de Metalurgia. 2006;42(6), 425-443.
16. Alcaide F, Cabot P, Brillas E. Fuel cells for chemicals and energy cogeneration. J Power Sources. 2006;153:47-60.
17. Kakac, S., Pramuanjaroenki, A., Zhou, X. A review of numerical modeling of solid oxide fuel cells. Int J Hydrogen Energy. 2007;32: 61-786.
18. Wu, J., Liu, X. Recent development of SOFC metallic interconnect. J Mater. Sci. Tech. 2010;26:293-305.
19. Venskutonis A, Glatz W, Kunschert G. P/M Processing of ODS Cr- and FeCr-based alloys for Solid Oxide Fuel Cell Applications. Proceedings of Electrochem. Soc. Int. Sym. on SOFC IX. 2005;2:534-544.
20. Kaller K, Kunschert G, Schlichtherle S, Strauss G. Process for Depositing and Electrically Conductive Layer and Assembly of the Layer on a Porous Support Substrate. United States Patent App. Public. 2010. US 2010/0047565 A1.
21. Herchen H, Karuppaiah C, Armstrong T. Method of Making Fuel Cell Interconnect Using Powder Metallurgy. United States Patent App. Public. 2013. US 2013/0129557 A1.
22. Smeacetto F, Salvo M, Ferraris M, Casalegno V, Asinari P, Chrysanthou, A. Characterization and performance of glass–ceramic sealant to join metallic interconnects to YSZ and anode-supported-electrolyte in planar SOFCs. J European Ceramic Soc. 2008;28:2521-2527.
23. Lin CK, Chen JY, Tian JW, Chiang LK, Wu SH. Joint strength of a solid oxide fuel cell glass–ceramic sealant with metallic interconnect. J Power Sources. 2012;205:307-317.
24. Celik S. Influential parameters and performance of a glass-ceramic sealant for solid oxide fuel cells. Ceramics Int. 2015;41:2744-2751.
25. Lin CK, Liu YA, Wu SH, Liu CK, Lee RY. Joint strength of a solid oxide fuel cell glass ceramic sealant with metallic interconnect in a reducing environment. J Power Sources. 2015;280:272-288.
26. Timurkutluk B. The role of lamination conditions on electrochemical and mechanical performance of ceramic electrolytes for solid oxide fuel cells. Ceramics Int. 2015;41:2057-2068.
27. Timurkutluk B, Ciflik Y, Korkmaz H. Strength evaluation of glass–ceramic composites containing yttria stabilized zirconia after thermal cycling. Ceramics Int. 2015;41:6985-6990.

28. Wang XD, Guan WB, Yu R, Liu W, Pei WL, Zhou XD. Correlation of ohmic resistance and interfacial adhesion strength between cathode and electrolyte for solid oxide fuel cells. Int J Hydrogen Energy. 2016;41:22337-22343.
29. Weibull W. Statistical Theory of Strength of Materials (151). In: Ingeniors Vetenskaps Akademien – Handlingar. 1939;45.
30. Chang HT, Lin CK., Liu CK. High-temperature mechanical properties of a glass sealant for solid oxide fuel cell. J Power Sources. 2009;189:1093-1099.
31. Chang HT, Lin CK., Liu CK. Effects of crystallization on the high-temperature mechanical properties of a glass sealant for solid oxide fuel cell. J Power Sources. 2010;195:3159-3165.
32. Lin CK, Lin KL, Yeh JH, Shiu WH, Liu CK, Lee RY. Aging effects on high-temperature creep properties of a solid oxide fuel cell glass-ceramic sealant. J Power Sources. 2013;241:12-19.
33. Abdoli H, Alizadeh P, Boccaccini D, Agersted K. Effects of thermal aging on thermo-mechanical behavior of a glass sealant for solid oxide cell applications. J Europ Ceramic Soc. 2014;34:2525-2534.
34. Fleischhauer F, Bermejo R, Danzer R, Mai A, Graule T, Kuebler J. Strength of an electrolyte supported solid oxide fuel cell. J Power Sources. 2015;297:158-167.
35. Zhang T, Zhu Q, Xie Z. Modeling of cracking of the glass-based seals for solid oxide fuel cell. J Power Sources. 2009;188:177-183.
36. Le S, Sun K, Zhang N, Shao Y, An M, Fu Q, Zhu X. Comparison of infiltrated ceramic fiber paper and mica base compressive seals for planar solid oxide fuel cells. J Power Sources. 2007;168:447-452.
37. Wang SF, Wang YR, Hsu YF, Chuang CC. Effect of additives on the thermal properties and sealing characteristic of BaO-Al_2O_3-B_2O_3-SiO_2 glass-ceramic for solid oxide fuel cell application. Int J Hydrogen Energy. 2009;34:8235-8244.
38. Tiwari B, Dixit A, Kothiyal GP. Study of glasses/glass-ceramics in the SrO-ZnO-SiO_2 system as high temperature sealant for SOFC applications. Int J Hydrogen Energy. 2011;36:15002-15008.
39. Wang SF, Lu CM, Wu YC, Yang YC, Chiu TW. La_2O_3-Al_2O_3-B_2O_3-SiO_2 glasses for solid oxide fuel cell applications. Int J Hydrogen Energy. 2011;36:3666-3672.
40. Wang SF, Hsu YF, Lu HC, Lo SC, Cheng CS. B_2O_3-free SiO_2-Al_2O_3-SrO-La_2O_3-ZnO-TiO_2 glass sealants for intermediate temperature solid oxide fuel cell applications. Int J Hydrogen Energy. 2012;37:5901-5913.
41. Wang SF, Hsu YF, Cheng CS, Hsieh YC. SiO_2-Al_2O_3-Y_2O_3-ZnO glass sealants for intermediate temperature solid oxide fuel cell applications. Int J Hydrogen Energy. 2013;38:14779-14790.
42. Wang SF, Hsu YF, Hsieh YC. Effects of La_2O_3, Nd_2O_3, NiO and CoO additions on the characteristics of SiO_2-Al_2O_3-Y_2O_3-ZnO glass seals for intermediate temperature solid oxide fuel cells. Int J Hydrogen Energy. 2015;40:3338-3347.
43. Lin SE, Cheng YR, Wei WCJ. Synthesis and long-term test of borosilicate-based sealing glass for solid oxide fuel cells. J Europ Ceramic Soc. 2011;31:1975-1985.

Study of the structural and optical properties of titanium oxide thin films

Cebrail Gumus, Yuksel Ufuktepe
Physics Department, University of Cukurova, 01330 Adana, Turkey
Email: cgumus@cu.edu.tr , ufuk@cu.edu.tr

Abstract
Titanium dioxide (TiO_2) thin films show many excellent optical and structural properties, so they play an important role in many technological areas including sensors, optics, solar energy and automobile industries. Nano sized titanium oxide surface has an important feature in photocatalytic process for hydrogen production. The aim of the work was preparation of titanium oxide thin films and study of changes of composition and nanostructure with different deposition parameters. To understand the structural properties of TiO_2 thin films, in photovoltaics we examined its optical absorption, band gap and crystal structure. Titanium oxide (TiOx) films deposited on a glass substrate by spray pyrolysis method were characterized using X-ray diffraction (XRD), atomic force microscopy (AFM), and optical measurements. The films were deposited at different temperatures ranging from 400 to 475 ºC. The effect of temperature on the structural and optical properties of the films was investigated. The result shows that the structure of the titanium oxide closely depends on the substrate temperature during the deposition process. It is found that 425 ºC temperature gives a layer of titanium oxide having best crystal structure.

Keywords: Titanium oxide films; XRD; Spray pyrolysis.

1. Introduction

Transition metal oxides are an important class of materials that can be used in a large number of applications such as cosmetics, paints, plastics, production of paper, marine, medical implants and dentistry [l,2]. Among them titanium dioxide has attracted a great deal of scientific interest due to excellent mobility of charge carriers, good mechanical strength and thermal conduction. TiOx is one of the most commonly used transparent conductive oxides which is suitable for numerous optoelectronic applications. Furthermore, TiOx can be used in photo-electrochemical water splitting process by sunlight to produce hydrogen. The band gap energy of titania is suitable for the oxidation and reduction of water [3]. Bulk TiO_2 is a semiconductor with a band gap in the range 3.0–3.2eV depending on the phase. Titanium oxide nanostructures with different morphologies could be prepared by using different methods such as heat treatment [4], sol-gel process [5], electrochemical methods [6] and spray pyrolysis [7]. Synthesized titanium oxide thin films could offer various polymorphic crystal forms such as rhombohedral brookite, tetragonal rutile and anatase. These results show differences between the spectra of such materials, therefore a crucial point in the understanding of their surface structure, due to many applications of titanium oxide are based on the specific crystal and surface structure.

Here we study the synthesis and electronic structure of TiOx films prepared by the spray pyrolysis method. The work was mainly focused on the study of the effect different deposition temperatures on the structural and optical properties of the films by means of the measurement of X-ray diffraction (XRD) and AFM.

2. Experimental Study

Photoelectrochemical hydrogen production system consists of mainly a photoelectrochemical reactor, light source, TiOx thin films were prepared on glass substrates by spray pyrolysis technique. Spray pyrolysis is a very versatile technique able to produce thin films of various materials. The thickness of film could be easily controlled by varying the spray parameters and also different concentration of source solution or atomization parameters enables control the stoichiometry [8]. The spray solution was 0.1 M, $C_{10}H_{14}O_5Ti$ (titanyl acetylacetonate), isopropyl alcohol (volume ratio 2 to 1). The carrier gas (compressed air) and solution are fed into a spray nozzle at a pre-adjusted constant atomization pressure. The flow rate of the solution was 10 ml/min and the substrate temperature was varied from 400 to 475 °C. The nozzle to substrate distance was 25 cm and diameter of the nozzle was 0.3 mm.
The crystal structure of the samples was characterized by X-ray diffraction (Rigaku SmartLab) and the morphology of films was observed using a Digital Instruments Dimension 3100 AFM. The optical properties of TiO_x thin films were determined by a Perkim Elmer UV-vis Lamda 2S spectrophotometer (λ=190-1100 nm) operating at room temperature.

3. Results and Discussion

The crystal structure of TiOx films was analyzed by XRD measurements. Fig. 1 shows XRD patterns of the TiOx films with different substrate temperatures. It is clear from the figure that all samples are polycrystalline in nature. However only the film deposited at 425 ºC exhibited better crystalline and the prefered orientation of the films in (100) plane corresponding mixed phase of Ti_4O_7 and TiO_2 structures.

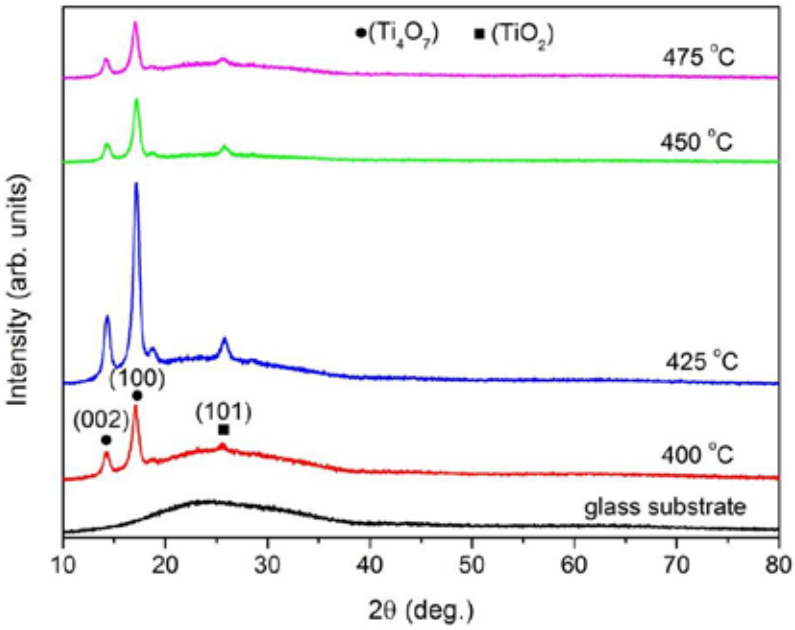


Fig. 1. XRD pattern of TiO_2 thin films deposited on glass substrate at different molarity.

The surface morphology of titanium dioxide films was characterized by atomic force microscope (AFM). Fig. 2 shows topographic AFM images of TiO_x films deposited at different temperatures. From the AFM images we were able to observe the uniformity of the thin films. The color bar indicates the Z-range from 4 to 15.5 nm. All AFM images were taken in air using tapping mode. For the films deposited at lower molarity, nano-sized particles with some small fraction of smaller size islands were observed. As the solution molarity was increased from 0.1 to 0.4 M, the films became rougher with small size islands. Initially the XRD characterization of deposited films at different temperatures at a constant molarity of solution was studied and the optimum 425 ºC substrate temperature was fixed for better crystalline. Then the optimum molarity was found by various studies of deposited TiO_2 films for different molarity of the solution but constant substrate temperature. The aim of this work is to optimize the substrate temperature to obtain single phase.

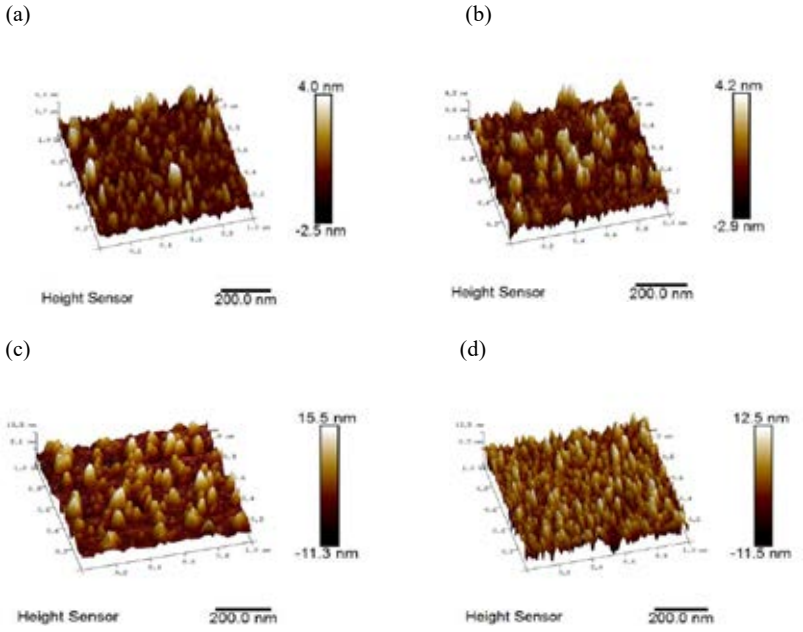


Fig. 2. AFM images of TiO_x on glass deposited with a substrate temp. of (a) 400, (b) 425, (c) 450, and (d) 475 °C.

Figure 3 shows the optical absorption spectra of TiOx films at different temperatures in the wavelength range from 400 nm to 1100 nm. The films are generally highly transparent in the visible region. The percentage of transmittance is increasing with the temperature. The low transmittance percentage is due to mixed phase and crystal structure. Better crystallinity showed high transmission for 425 °C temperature.

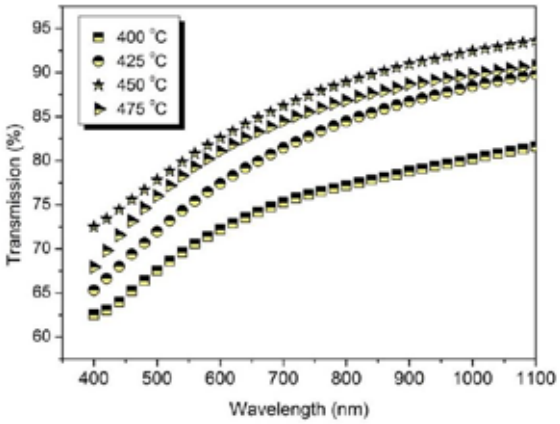


Fig. 3. Optical transmission spectra of TiOx films deposited at different temperatures.

From the transmittance spectra, the transmission was enhanced for wavelengths in the region above 600 nm, on the other hand the transmittance percentage of the film at 450 ºC is higher than the film at 475 ºC, which is due to better crystal structure of the film.
We calculated the optical bandgap energy (E_g) of the film using following relation:

$$(\alpha h\nu) = A\left(h\nu - E_g\right)^n$$

where A is a constant, α is absorption coefficient and the exponent n determines the transition type, being 1/2 for a direct transition and 2 for an indirect transition. The Fig. 4 shows the plot of $(\alpha h\nu)^2$ versus photon energy for the films deposited at different temperatures. Optical band energy gap can be determined from extrapolation of the straight line portion of the spectrum to $(h\nu) = 0$. From Fig. 4, the optical energy gap about, $E_g \sim 3.0\ eV$ is deduced. This energy gap is increasing with temperature but has been decreased to initial value when substrate temperature set to 450 ºC.

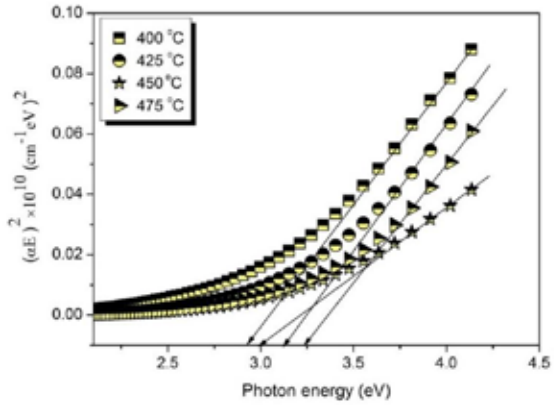


Fig. 4. Optical band gap spectra of TiOx films deposited at different temperatures

4. Conclusions

In this study, highly transparent TiO_x thin films were successfully prepared by the spray pyrolysis technique on glass substrate at different substrate temperatures from 400 to 475 °C using solution of $C_{10}H_{14}O_5Ti$ (Titanyl acetylacetonate) and air as a carrier gas. The X-ray diffraction analysis showed that film is polycrystalline in nature. The deposited films exhibit excellent crystalline structure with mainly Ti_4O_7 phase and (100) preferential orientation. Optical measurements show that the film possesses high transmittance. The films have a direct band gap with an optical value of between 2.93 to 3.47 eV which is close to the literature value [9,10]. Crystallite size is increasing from 10.41 to 11.75 nm.

Acknowledgement
This work was supported by Cukurova University under FEF2012BAP10 project number.

References

1. Diebold U. Surf. Sci. Rep. 2003;48:53-229.
2. Noguera C. Physics and Chemistry at Oxide Surfaces, Cambridge University Press, Cambridge, 1996.
3. Gratzel M, O'Regan B. Nature. 1991;353:737-740.
4. Velten ID, Biehl V, Aubertin F, Valeske B, Possart W, Breme J. J. Biomed. Mater. Res. 2001;59:18–28.
5. Sul YT, Johansson CB, Jeong Y, Albrektsson T. Med. Eng. Phys. 2001;23:329–346.
6. Yang B, Uchida M, Kim HM, Zhang X, Kokubo T. Biomaterials 2004;25:1003–1010.
7. Conde-Gallardo A, Guerrero M, Castillo N, Soto AB, Fragoso R, Cabañas-Moreno JG. Thin Solid Films. 2005;473:68-73.
8. Patil PS. Materials Chemistry and Physics. 1999;59:185-198.
9. Beltran A, Gracia L, Andres J. J Phys Chem B. 2006;110-23417.
10. Sun B, Vorontsov AV, Smirniotis PG. 2003 Langmuir 19-3151.

ORAL PROCEEDINGS

Modelling of Hydrogen Production From Hydrogen Sulfide in Geothermal Power Plants

Aras Karapekmez[1], Ibrahim Dincer[1, 2]
[1]Faculty of Mechanical Engineering, YTU, Besiktas, Istanbul, Turkey
[2]Faculty of Engineering and Applied Science, UOIT, Oshawa, Ontario, Canada
Email: araskarapekmez@hotmail.com

Abstract

One of the most important environmental issues related to the use of geothermal fluids to generate electricity is the emission of non-condensable gases to the atmosphere. Vent stacks from geothermal plants emit carbon dioxide (CO_2) and methane (CH_4) causing concerns because of their role as greenhouse gases. Geothermal power plants also emit hydrogen sulfide (H_2S) in relatively high amounts due to the fact that H_2S is one of the main constituents of the geothermal fluids. The presence of H_2S in the air, and then in water, soils and vegetation is one of the main environmental concerns for the areas that host geothermal fields. Hydrogen is recognized as one of the most promising alternative fuels to help meet the energy demand for future by providing a carbon-free solution. Hydrogen production from hydrogen sulfide in geothermal power plants could reduce emissions and provide sustainable energy for different end use purposes. In the present study, emissions and efficiencies of an innovative geothermal energy system are examined. This system consists of two main processes: mercury abatement by using a chemical absorption and hydrogen production from hydrogen sulfide (H_2S) by electrolysis. The results of this study show that the innovative geothermal energy system has less emissions and higher efficiencies compared to the existing geothermal power plants. Therefore, it is concluded that in terms of energy efficiency and emissions; the use of this innovative system should be considered for geothermal power plants in Turkey.

Keywords: Hydrogen production; hydrogen sulfide; geothermal power plant; energy; efficiency.

1.Introduction

One of the most important enviromental issues related to the use of geothermal fluids to generate electricity is the emission of non-condensable gases to the atmosphere. Vent stacks from geothermal plants emit carbon dioxide (CO_2) and methane (CH_4) causing concern because of their role as greenhouse gases, despite those emissions are quite small compared to carbon and fossil fuel plants, indicating that the contribution of these sources is practically negligible.[1]

Geothermal power plants also emit hydrogen sulfide (H_2S) in relative high amounts, since H_2S is one of the main constituents of the geothermal fluids. The presence of H_2S in the air, and then in water, soils and vegetation is one of the main enviromental concerns for the areas that host geothermal fields[1]. In addition to this; hydrogen (H_2) is recognized as one of the most promising alternative fuels to help meet the energy demand for future by providing a carbon-free solution. It has many advantages; but the most important ones are renewable and clean energy source, far more efficient than fossil fuels and used in high-tech systems such as space ships.

Note that 120.7 MJ (LHV) energy can be obtained from 1 kg hydrogen which can be obtained from 2.1 kg natural gas, 2.8 kg gasoline and 3.1 kg fuel oil which are shown in Figure 1.

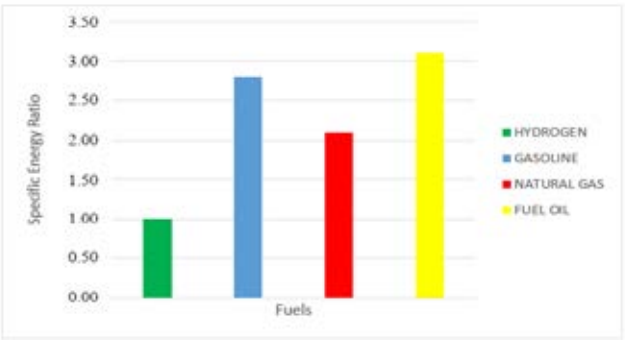


Fig. 1. Quantities required to obtain energy from fossil fuels that can be obtained from one kilogram of hydrogen (data from [2]).

Whilst hydrogen production from hydrogen sulfide in geothermal power plants reduces emissions and at the same time providing energy. In the present study, the emissions and efficiencies of an innovative geothermal energy system are examined. This system consists of two main processes: mercury abatement by using a chemical absorption and hydrogen production from hydrogen sulfide (H_2S) by electrolysis.

2. System Description

Here, we first provide some introductory and some background information. Hydrogen sulfide is a colorless water-soluble gas, with a characteristic odor of rotten eggs and defined for this putrid gas. Its origin may be natural (about 90% of the total H_2S in the atmosphere given by EPA, [3]) as gas species produced by anaerobic bacterial reduction of sulfur-containing animal and vegetable proteins and as gas released from volcanoes and geothermal areas; but also anthropogenic, as product of industrial activities. The artificial origin of hydrogen sulfide derives from the production process of coking coal, cellulose, fertilizers, dyes and pigments, refinement of crude petroleum, tanning of hides and skins, treatments of waste water.

Background concentrations of H_2S in ambient unpolluted air have been estimated to be between 0.14 and 0.4 $\mu g/m^3$ (EPA, [3]), whilst the typical concentration in urban area is about one order of magnitude higher (1.0–3.0 $\mu g/m^3$ by Kurtidis [4]). The high air levels of H_2S are measured near waste-water treatment plants, oil refineries, and land- fills (from a few units to a few tens of mg/m^3, by WHO,[5]) as well as in volcanic and geothermal areas, where H_2S is likely formed by water-rock interaction, which is accelerated by the high heat gradient induced by the presence of a cooling magma body. In these environments, the H_2S is released in the atmosphere by hot vents and hot springs.

Because H_2S is a gas, human exposure is principally via inhalation, and the gas is rapidly adsorbed through the lungs. Health effects include respiratory, ocular, neurological, and metabolic effects and the death after single exposures to concentrations ≥ 700 mg/m^3 [5]. A summary of these effects is presented in Table 1.

Table 1. Human health effects resulting from exposure to H_2S [5].

Exposure (mg/m^3)	Effect/Observation
0.011	Odor threshold
2.8	Bronchial constriction in asthmatic individuals
5.0	Increased eye complaints
7.0–14.0	Increased blood lactate concentration, decreased oxygen uptake
5.0-29.0	Eye irritation
> 140	Oldfactory paralysis
> 560	Respiratory distress
≥ 700	Death

In an electrolysis process, hydrogen sulfide is electrochemically decomposed to pure hydrogen and sulphur. Overall reaction of electrolysis of hydrogen sulfide is shown as follows:

$$H_2S\ (g) + \text{Energy} \rightarrow H_2\ (g) + \tfrac{1}{2}\ S_2\ (g) \quad (1)$$

The required energy under normal conditions is 73.28 kJ/mol for electrolysis of hydrogen sulfide which is 3 times less than electrolysis of water, therefore hydrogen production from hydrogen sulfide is a more profitable process than water. According to the overall reaction; 2 g hydrogen is obtained from 34 g hydrogen sulfide.

A geothermal power plant uses hot pressurized fluid of the underground to generate electricity energy. The geothermal fluid is basically composed by dry stream or, more frequently by hot water and steam but always with a significant amount of gases and other compounds, notably CO_2, H_2S, CH_4, NH_3, and Hg. The geothermal fluid may spontaneously reach the surface or, often, it remains confined within the reservoir because of the impervious covering. In such a case, the fluid can be extracted by means of wells (drilled to a depth of some kilometers). A single power plant can be fed by several geothermal wells. Hot, pressurized geothermal fluid is piped to the turbine (Figure 2), where it rapidly expands and rotates turbine blades. Rotational energy from the turbine is converted to electrical energy through an alternator. Turbine and alternator represent the basic unit of the plant whose power defines the nominal power of the plant. From the turbine steam is discharged to the condenser (Figure 2) at a sub-atmospheric (typically 0.08 bar). Inside the condenser, the water coming from the cooling tower is sprayed directly into the steam to enhance its condensation. Then, the mixture of cooling water and condensate is pumped to the head of the cooling tower to extract the waste heat through an upward stream of cold air which actually becomes enriched in the gases of the natural fluid. An extractor provides to remove the non-condensable gases from the condenser, emitting them into the atmosphere. The components of the power plant from which H_2S (and other gases) is emitted in the atmosphere are the cooling tower and primarily the extractor of non-condensable gas who summed contributions define the total H_2S emission from the power plant [1].

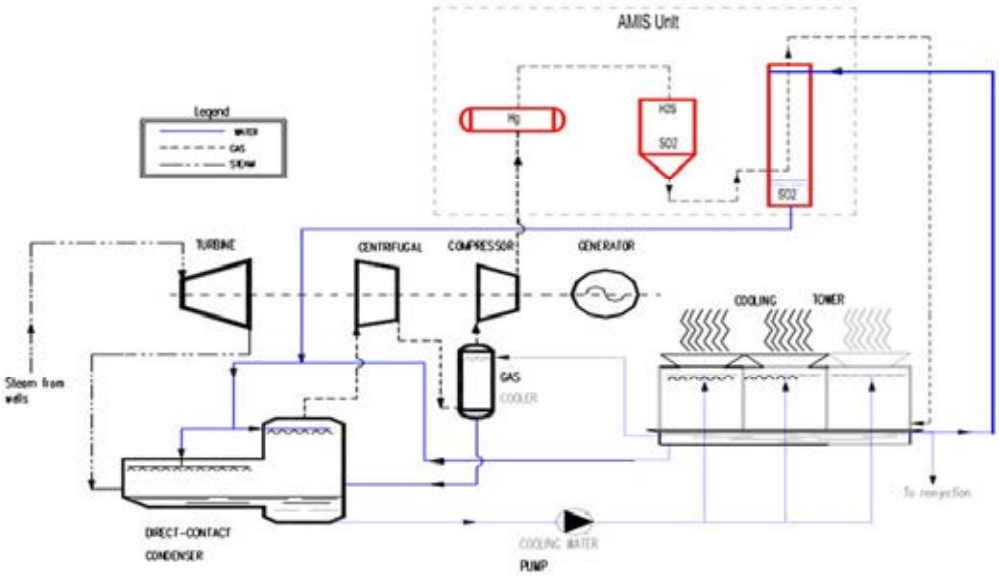


Fig. 2. Simplified scheme of a standard geothermal power plant equipped with AMIS abatement system [1].

The AMIS technology (for abatement of mercury and hydrogen sulphide),which is used in the power plants of Tuscany region,is an efficient,safe,enviromentally friendly technology able to eliminate the problems related to the gaseous emissions from geothermal power plants and in particular the bad smell of hydrogen sulfide. Geothermal fluid extracted from the reservoir by production wells is carried to the power plants by a steel pipe network. The fluid mainly consists of steam with some percentage (from less than 1% up to 15%) of non condensable gases (NCG). Instead of being released to atmosphere, NCG can be sent to the AMIS® system for mercury and hydrogen sulfide abatement.This system consists of three fundamental steps:

- Removal of mercury by chemical absorption
- Selective catalytic oxidation of hydrogen sulfide to SO_2
- SO_2 scrubbing by geothermal water

1st step: Mercury Removal:

Elemental mercury is removed from NCG stream by chemical absorption on a fixed bed of sorbent (selenium mass or sulphurized activated carbon). Before entering mercury absorber, the process gas is cooled and subsequently compressed in order to achieve the optimum temperature (about 70°C) and relative humidity conditions for the reaction.

2nd step: Catalytic oxidation of hydrogen sulfide:

The selective catalytic oxidation of hydrogen sulfide (H_2S) to sulphur dioxide (SO_2) is the second basic step of the process. NCG are heated up to the minimum temperature required by the catalyst to promote oxidation according to the reaction:

$$H_2S+3/2\ O_2 \Rightarrow SO_2+ H_2O \quad (2)$$

Here, the reaction is exothermic.The enthalpy of the hot stream leaving the catalytic reactor is recovered to preheat the cold stream leaving mercury absorber.The process is completely regenerative,so that no external heating is required during normal operation. Some air is added to the gaseous stream to be treated in order to provide the oxygen needed for H_2S oxidation and catalyst temperature control.

3rd step: Sulphur dioxide scrubbing by geothermal water:

The final step of the process is the absorption of the produced SO_2 by geothermal water. In most cases, geothermal fluids contain basic soluble compounds, especially ammonia, so that these are naturally present in the geothermal water. Basic compounds allow the absorption of acidic components,such as sulphur dioxide (SO_2). The efficiency of the SO_2 absorption essentially depends on the molar ratio between produced SO_2 and ammonia

in the geothermal water. If geothermal water contains enough ammonia, SO_2 removal is close to 100% without addition of any chemical. Otherwise it is possible to achieve the same result by adding ammonia water, thereby increasing the natural ammonia content of the geothermal water, or, as an alternative, sodium hydroxide (NaOH). The water leaving the absorption column re-enters the cycle of the geothermal water, controlled by the cooling tower overflow.[6]

Note that, in the present study, we modify the AMIS system for hydrogen production from hydrogen sulfide. Hydrogen sulfide which is obtained after catalytic oxidation process, are separated to pure hydrogen and sulfur by electrolysis (Figure 3).

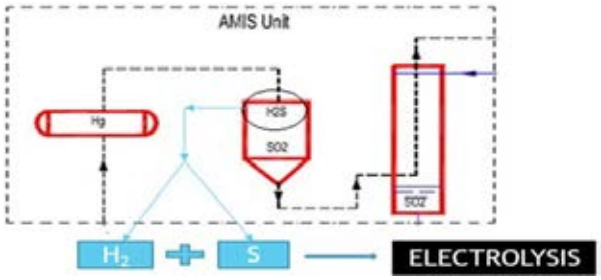


Fig. 3. Schematic illustration of the modified AMIS system. (Modified from Ref [1])

4. System Analyses

The mass, energy, and exergy balances are applied to determine the rate of exergy loss for the electrolysis process, exergy destruction rates, and energy and exergy efficiencies.

The mass balance of the electrolysis process for hydrogen production from hydrogen sulfide can be expressed as:

$$m_{H_2S} = m_{H_2} + m_{S_2} \quad (3)$$

Where m is the mass flow rate. Assuming kinetic and potential energies are negligible, energy balance can be written as:

$$\dot{Q}_i + \dot{W}_i + \sum \dot{N}_i (h^o_f + \bar{h} - \bar{h}^o)_i = \dot{Q}_o + \dot{W}_o + \sum \dot{N}_o (h^o_f + \bar{h} - \bar{h}^o)_o \quad (4)$$

where h^o_f represents enthalpy of formation. The corresponding exergy balance can be written as:

$$\dot{W}_{max} = \sum \dot{N}_o (g^o_f + \bar{g} - \bar{g}^o)_o - \sum \dot{N}_i (g^o_f + \bar{g} - \bar{g}^o)_i \quad (5)$$

where $\dot{W}_{max}$ and g^o_f represent reversible work and Gibbs formation function respectively. [7]

4.2 Energy and exergy efficiencies

The energy efficiency of the proposed system can be expressed as:

$$\eta = \frac{\text{Energy in the product}}{\text{Energy input to the system}} = \frac{m_{H_2} \cdot (h^o f + \bar{h} - \bar{h}^o)_{H_2}}{W_i} \quad (6)$$

The exergy efficiency of the proposed system can be expressed as:

$$\Psi = \frac{m_{H_2} . ex_{H_2}}{W_{max}} \quad (7)$$

For the above given system, the following assumptions are made:

- The explored area = 250 km^2.
- The mass flow rate range of the superheated steam = 1000 – 1500 kg/s.
- The temperature of the steam = 220 ° C.
- The pressure of the steam = 1.4 MPa.
- The average content of the H_2S emissions = 5%.
- The ambient Temperature = 25 ° C , Ambient Pressure = 101.325 kPa.
- T = 100 ° C, P = 1.2 MPa (Entrant of the electrolysis process).
- T = 150 ° C, P = 0.8 MPa (Product of the electrolysis process).

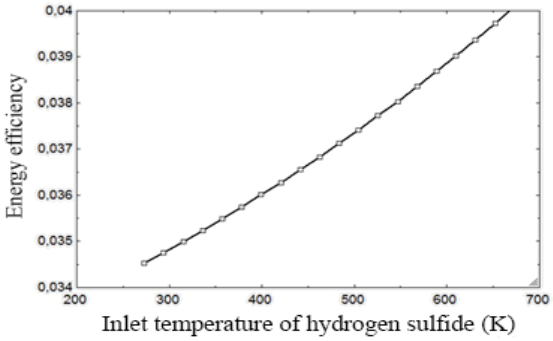


Fig. 6. Effect of hydrogen sulfide inlet temperature on the energy efficiency of the system.

The exergy efficiency of the electrolysis process of hydrogen sulfide increases when the inlet temperature of hydrogen sulfide increases. The exergy efficiency is around % 4.8 when the inlet temperature of hydrogen sulfide is 373 K as graphically shown in Figure 7.

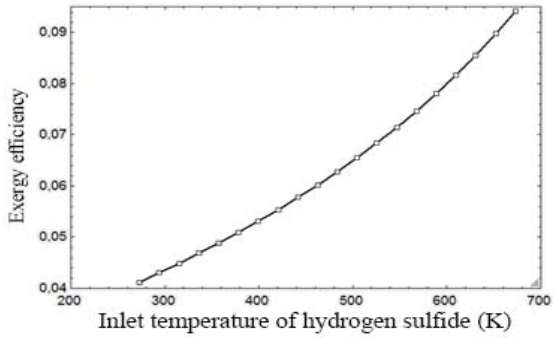


Fig. 7. Effect of hydrogen sulfide inlet temperature on the exergy efficiency of the system.

The exergy efficiency of the electrolysis process of hydrogen sulfide decreases when the temperature of ambient increases. The exergy efficiency is around %4.7 when the temperature of ambient is 298 K as shown in Figure 8.

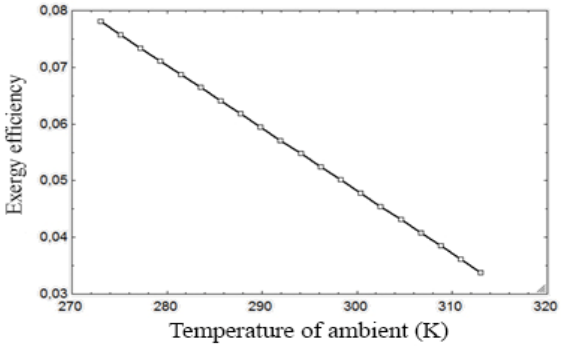


Fig. 8. Effect of ambient temperature on the exergy efficiency of the system.

When mass flow rate of the superheated steam is 1000 kg/s, approximately 50 kg/s H_2S emitted and 3 kg/s hydrogen can be obtained (as illustrated in Figure 9).

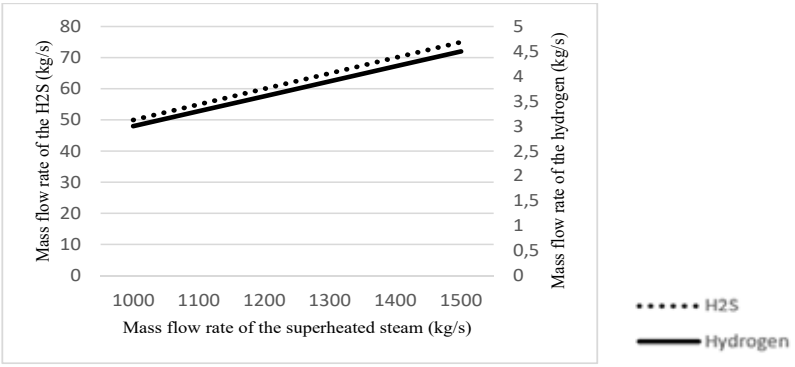


Fig. 9. Change of H_2S and H_2 mass flow rates depending on mass flow rate of the inlet superheated steam in geothermal power plants.

For the six different geothermal power plants which are in Tuscany region of Italy H_2S emissions were measured (Table 2). In addition to the nominal power and amis filter; air temperature, wind frequency and directions effect H_2S emission rates. But since these values do not vary much in the Tuscany region, they take about the same value for the 6 power plants in that region.

Table 2. H_2S emission rates in different geothermal power plants of Italy depending on the presence of the Amis filter. [1]

Name of Power Plant	Monitoring Date	Nominal Power (MW)	H_2S emission (kg/h)	Amis Filter
Carboli	Jul.2014	20	46	No
Cornia	Nov.2014	20	34.6	No
Le Prata	May 2014	20	17.7	Yes
Nuova Castel	Mar.2014	14.5	11.1	Yes
Nuova Larde	Nov.2014	20	9.3	Yes
Vallesec	Oct.2014	60	13.2	Yes

6. Conclusions

The key findings of this study can be summarized as:

- 120.7 MJ (LHV) energy can be obtained from 1 kg hydrogen which can be obtained from 2.1 kg natural gas, 2.8 kg gasoline and 3.1 kg fuel oil. Therefore hydrogen energy can be a good alternative to the fossil fuels.
- The required energy under normal conditions is 73.28 kJ/mol for electrolysis of hydrogen sulfide which is 3 times less than electrolysis of water. Therefore hydrogen production from hydrogen sulfide is a more profitable process than water.
- The required electrical work for the electrolysis process of hydrogen sulfide decreases when the inlet temperature of hydrogen sulfide increases. When the inlet temperature of hydrogen sulfide is 273 K, the required electrical work is around 155000 kW and when the temperature reaches 473 K, the required electrical work falls to around 145000 kW.
- The required electrical work for the electrolysis process of hydrogen sulfide increases when the mass flow rate of hydrogen sulfide increases. The required electrical work is around 300000 kW when the mass flow rate of hydrogen sulfide is 100 kg/s.
- Energy efficiency of the electrolysis process of hydrogen sulfide increases when the inlet temperature of hydrogen sulfide increases. The energy efficiency is around %3.55 when the inlet temperature of hydrogen sulfide is 373 K.
- Exergy efficiency of the electrolysis process of hydrogen sulfide rises from % 4.1 to %9.5 when the inlet temperature of hydrogen sulfide increases from 273 K to 673 K.

- Exergy efficiency of the electrolysis process of hydrogen sulfide decreases from % 7.9 to %3.4 when the temperature of ambient increases from 273 K to 313 K.
- When mass flow rate of the superheated steam is 1000 kg/s, approximately 50 kg/s H_2S emitted and 3 kg/s hydrogen can be obtained from the system.
- Using Amis system in geothermal power plants is reduced hydrogen sulfide emissions at significant rates. As a result, many potentially harmful effects on the human body and our environment are eliminated.

Nomenclature

ex	Exergy (kW)
$\bar{g}^o_f$	Gibbs formation function (kj/kmol)
$\bar{h}^o_f$	Enthalpy of formation (kj/kmol)
m	Mass flow rate (kg/s)
P	Pressure (MPa)
T	Temperature (K)
$\dot{Q}_i$	Inlet heat to the system (kW)
$\dot{Q}_o$	Outlet heat from the system (kW)
$\dot{W}_i$	Inlet work to the system (kW)
$\dot{W}_{max}$	Reversible work (kW)
$\dot{W}_o$	Outlet work from the system (kW)

Greek Letters

η	Energy efficiency
ψ	Exergy efficiency

Acronyms

EPA	Enviromental Protection Agency
LHV	Lower heating value
NCG	Non-condensable gases
WHO	World Health Organization

References

1. Renato, S., Domenico, G., Claudia, T., & Carlo, T. (2017). Modelling of hydrogen sulfide dispersion from the geothermal power. Science of the Total Environment (583), 408-420.
2. Retrieved May 27, 2017, from Wikipedia: https://en.wikipedia.org/wiki/Energy_density
3. US EPA, 1993. Report to Congress on hydrogen sulfide air emissions associated with the extraction of oil and natural gas. Research Triangle Park, NC, US Environmental Protection Agency, Office of Air Quality Planning and Standards EPA/453/R93045; NTIS Publication No. PB9413122.
4. Kurtidis, K., Kelesis, A., Petrakaskis,M., 2008. Hydrogen sulfide (H_2S) in urban ambient air.Atmos. Environ. 42, 7476–7482.
5. World Health Organization (WHO), 2003. Hydrogen Sulfide: Human Health Aspects, Concise International Chemical Assessment Document n. 53, 35 pp, Geneva, Switzerland. www.who.int/ipcs/publications/cicad/en/cicad53.pdf
6. Baldacci, A., Mannari, M., & Sansone, F. (2005). Greening of Geothermal Power: An Innovative Technology for Abatement of Hydrogen Sulphide and Mercury Emission. Proceedings World Geothermal Congress. Retrieved from https://www.researchgate.net/publication/229035145_Greening_of_geothermal_power_An_innovative_echnolgy_for_abatement_of_hydrogen_sulphide_and_mercury_emission
7. Cengel, Y. & Boles, M. A. (2008). Termodinamik Mühendislik Yaklaşımıyla. İzmir: Güven Kitabevi.

ORAL PROCEEDINGS

Numerical Investigation of the Effect of Channel Width to Land Ratio on PEM Fuel Cell Performance

Mohammad Ziauddin Chowdhury[1], Omer Genc[2], Serkan Toros[3], Yusuf Sahin[4]
Omer Halisdemir University Prof. Dr. T. Nejat Veziroglu Clean Energy Research Center, Nigde, Turkey-51240.[1-3]
Omer Halisdemir University, Mechanical Engineering Department, Nigde, Turkey-51240.[1-4]
zia72822@gmail.com[1], omergenc@ohu.edu.tr[2], serkantoros@ohu.edu.tr[3], ysahin@ohu.edu.tr[4]

Abstract
Proton exchange membrane (PEM) fuel cells become an emerging sector for growing demand of sustainable energy systems. Therefore; a necessity arises for researchers to develop more efficient PEM fuel cell. Numerical analyses provides an understanding the internal phenomena of PEM fuel cell instead of experimental measurements, which are highly expensive and time consuming. Flow field design is one of the major research parameters of the system since the appropriate flow field design can improve the cell performance significantly. Among the different parameters of the bipolar plate flow field design, channel width to land ratio is a critical parameter for PEM fuel cell performance. In this numerical study, different channel width to land ratio's for anode and cathode sides are analyzed with fixed channel depth as well as channel length for a straight channel geometry. Based on the cell performance by analyzing the consequence parameters, the optimization of channel width to land ratio is carried out for anode and cathode channel geometry.

Keywords: Pressure drop; performance; optimization.

1. Introduction

Proton exchange membrane (PEM) fuel cell is an emerging sustainable energy source that can fulfill the growing demand of growing need of environmental friendly energy [1]. For this reason, large scale of research interest is on rise for the efficient PEM fuel cell system development. As the experimental research studies of PEM fuel cell is very expensive and time consuming, numerical analysis becomes more suitable technique to develop the system. Bipolar plate is one of the major component in PEM fuel cell contributing 60% weight and 30% cost of the PEM fuel cell system [2]. Bipolar plate facilitates flow fields through which fuel flows, collect electron in anode and removes waste heat and water from the cell as well. That's why bipolar plate has a great significance on the PEM fuel cell system. The optimization of bipolar plate flow field geometry is very difficult through experimental procedure, whereas numerical analysis is an effective tool for the optimization. In the flow field geometry, channel width/land ratio plays a significant role for the optimized flow field design as well as better cell performance. There are several studies for the channel width/land ratio optimization with numerical investigation [3-6].

Different channel width to rib width ratio's effect on the cell performance was investigated considering contact resistance and without contact resistance [7]. Three different channel width to rib width taken into this numerical comparative study were 0.8/1.2, 1.0/1.0 and 1.2/0.8 where in all the cases total channel and rib width were 2.0 mm. It was observed that increased in channel width causes better cell performance improving the concentration loss effectively. Channel width with land width effect on reactant velocity and current density distribution numerically investigated where it showed that increase in channel width increase current density as well as oxygen molar mass fraction while narrow land width improves ohmic loss by increasing contact resistance between bipolar plate and gas diffusion layer [8].

Yu et. al. [9] investigated interdigitated flow field pattern cell performance for two different rib width of 0.762mm and 0.1905mm. It showed that the decrease in rib width has little influence on the improvement of cell performance. The reason explained in this study for the phenomena of forced convection gas transfer mechanism. Goebel et. al. [10] carried out land width with channel span effect of 0.25, 0.5 and 1.0 mm on PEM fuel cell performance. At higher voltages and drier conditions, larger land fraction flow fields performed better than smaller land fraction flow fields for equivalent land widths as contact resistance becomes more important than mass transport resistance although these differences were small. But for the high current density land width found to be dominant factor. For better PEM fuel cell performance, reduced land width with a 50% recommended land fraction for low contact resistance as well as narrow channel width were recommended from this research study. Different channel width to rib width ratio keeping channel width as fixed, the performance of PEM fuel cell was analyzed for 5 cm2 active area [11]. Optimal channel width to rib ratio were 0.67 and 1.0 with the consideration of power gain/power consumption and cell performance respectively. For an active area of 5.3 cm^2, for fixed channel width to land ratio

total six different cathode channel geometry configuration having no. of pass in serpentine channel 8, 10, 12, 16, 22 and 38 with changing in channel/land width were numerically investigated [12]. The analysis showed that the pressure drop increases with the decreasing channel size. Neglecting pump work the study suggested small channel cross-sectional area for better cell performance. For same channel width and land width of four different configuration of 0.5, 1.0, 1.5 and 2mm dimensions, the best cell performance was found from channel/ land width of 0.5/0.5 channel dimensions by numeric simulation results [3].

For this numerical study, a total of 87 cases were studied with a wide range of channel and land width value and all possible combination in between them with a constant operating voltage of 0.4V.

2. Numerical Model

In this study, three dimensional, single phase and isothermal model is developed. The governing equations of mass, momentum and species conservation are used. The following assumption are used for this study-

- Single phase of reactants are considered.
- Uniform operating temperature are considered.
- Steady state condition of PEM fuel cell operation.
- Reactant gasses are assumed as ideal gas.

Structural mesh is being employed in the model with an mesh consists of 14448 domain elements, 5870 boundary elements, and 848 edge elements. For the different channel depth of both anode and cathode of the geometry, the mesh are automatically changed with respect to the geometry change. The mesh of the numerical model is shown in Figure 1. The geometric model is shown in Figure 2.

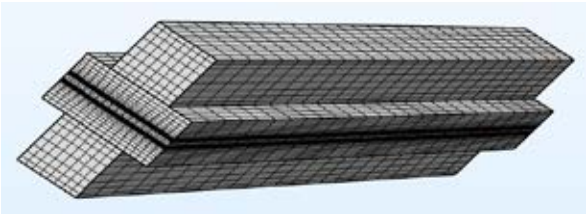


Figure-1. Structural mesh used for the numerical simulation

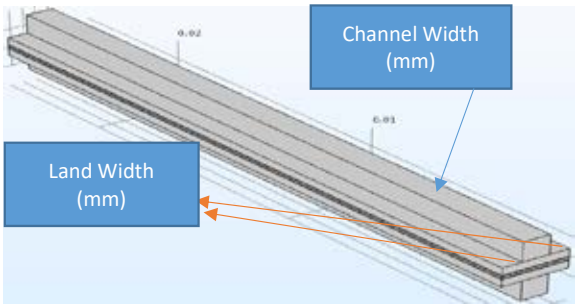


Figure 2. Geometric model of the considered numerical study

The parameter of the numerical model are shown in Table 1.

Cell length, L	0.025[m]
GDL width, H_gdl	380e-6[m]
Porous electrode thickness, H_electrode	50e-6[m]
Membrane thickness, H_membrane	100e-6[m]
GDL porosity, eps_gdl	0.5
GDL permeability, kappa_gdl	1.18e-11[m^2]
GDL electric conductivity, sigma_gdl	222[S/m]
Inlet H2 mass fraction (anode), wH2_in	0.743
Inlet H2O mass fraction (cathode), wH2O_in	0.023
Inlet oxygen mass fraction (cathode), wO2_in	0.228
Anode inlet mass flow rate, U_in_anode	0.0000002125[m^3/s]
Cathode inlet mass flow rate, U_in_cathode	0.0000006375[m^3/s]
Anode viscosity, mu_anode	1.19e-5[Pa*s]
Cathode viscosity, mu_cathode	2.46e-5[Pa*s]
Hydrogen molar mass, MH2	0.002[kg/mol]
Nitrogen molar mass, MN2	0.028[kg/mol]
Water molar mass, MH2O	0.018[kg/mol]
Oxygen molar mass, MO2	0.032[kg/mol]
H2-H2O Binary diffusion coefficient, D_H2_H2O	9.15e-5*(T/307.1[K])^1.75[m^2/s]
N2-H2O Binary diffusion coefficient, D_N2_H2O	2.56e-5*(T/307.15[K])^1.75[m^2/s]
O2-N2 binary diffusion coefficient, D_O2_N2	2.2e-5*(T/293.2[K])^1.75[m^2/s]
O2-H2O binary diffusion coefficient, D_O2_H2O	2.82e-5*(T/308.1[K])^1.75[m^2/s]
Cell temperature, T	353[K]
Reference pressure, p_ref	101e3[Pa]
Cell voltage, V_cell	0.9
Oxygen reference concentration, cO2_ref	40.88[mol/m^3]
Hydrogen reference concentration, cH2_ref	40.88[mol/m^3]
Electrolyte phase volume fraction, eps_l	0.3
Open volume fraction for gas diffusion in porous electrodes, eps_cl	1-eps_l-eps_gdl: 0.2
Permeability (porous electrode), kappa_cl	kappa_gdl/5
Membrane conductivity, sigma_m	9.825[S/m]
Anode Channel Depth, H_ch_anode	1e-3[m]
Cathode Channel Depth, H_ch_cathode	1e-3[m]

Case Study

The numerical analysis of this study considered several values for channel width and land width. For each channel width with different land width were taken into account for the analysis. The cases of this study are shown in Table 2.

Channel Width (mm)	Land Width (mm)	Channel Width (mm)	Land Width (mm)
0.2	-	1.0	1.0
0.25	0.25	1.1	1.1
0.3	-	1.2	1.2
0.4	0.4	1.25	1.25
0.5	0.5	1.3	1.3
0.6	0.6	1.4	1.4
0.7	0.7	1.5	1.5
0.75	0.75	1.75	-
0.8	0.8	2	-
0.9	0.9		

Table 2. Case study of different channel and land width

Validation

The numerical model was validated from the experimental study of Chowdhury et. al. [13]. From the validation result, it was found out that the numerical and experimental study was almost similar to each other.

3. Results and Discussion

a) Effect of Channel Width and Land Width on cell performance

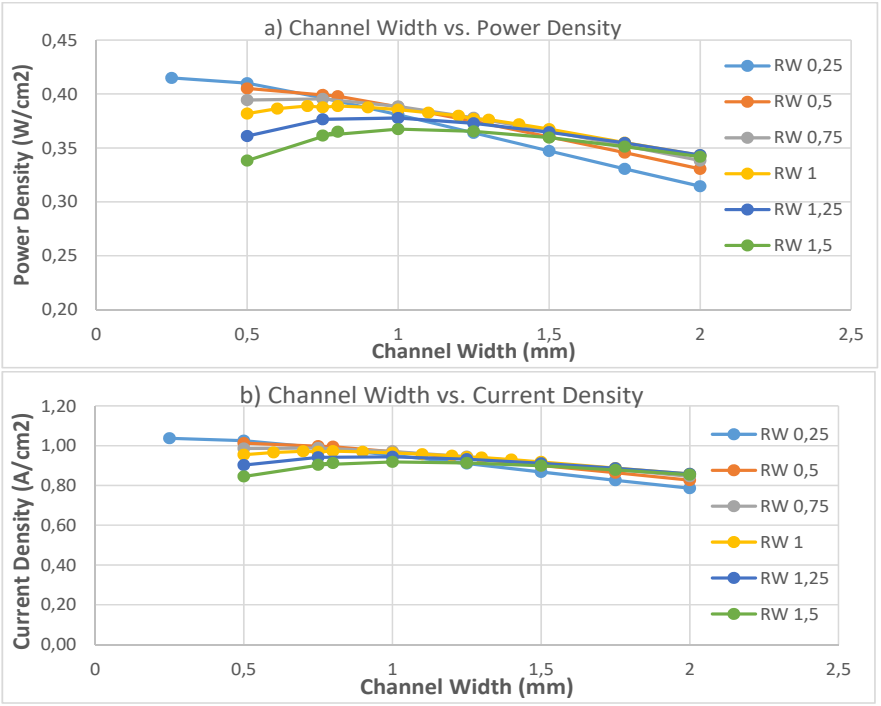


Figure 3. For different constant land width for different land width vs. a) Current Density b) Power Density at 0.4 V

The different cases of channel width considered for this numerical study are shown in Table 2. As the channel width increase from 0.2 mm to 2 mm, the cell performance reduced linearly. The current density and power density for different constant land width with the variance of channel width are shown in Fig. 3a & 3b. It was found that for the constant land width of 0.2mm, the maximum cell performance gained for the minimum channel width but with the channel width increasing the cell performance drastically fall. The same case was observed from constant land with of 0.5mm also. From the result, it was found that for the minimum land width with minimum channel width, the cell

performance reduced with the increase in land width. With the maximum land width and channel width, the cell performance increases with the increase of land width. For the different cases of constant channel width with the variance in land width, the cell performance decrease with the increase in land width as shown in Fig. 4a & 4b.

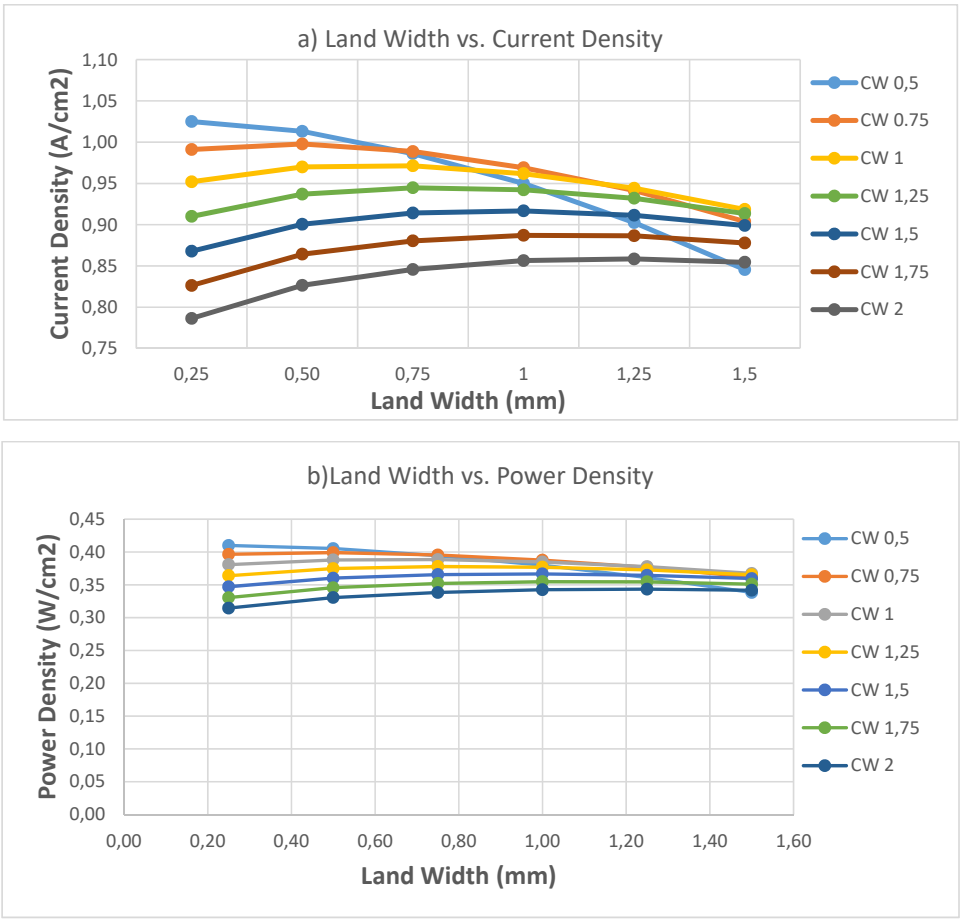


Figure 4. For different constant channel width for different land width vs. a) Current Density b) Power Density at 0.4 V

b) Effect of Channel Width and Land Width on pressure drop

From the numerical simulation result, it was found that the cathode pressure drop has more sensitive than anode pressure drop. The pressure drop also has more impact with the change in channel width and has little or almost no effect with respect to the land width variation. The anode and cathode pressure drop with channel width for different constant land width are shown in figure-6a & 6b respectively. For the different constant channel width, the effect of anode and cathode pressure with the variation of land width are shown in figure 7a & 7b. The maximum pressure drop occurred with the minimum channel width of 0.2mm and land width of 0.8mm, whereas the minimum pressure drop occurred with the maximum channel width of 2mm and land width of 0.25mm.

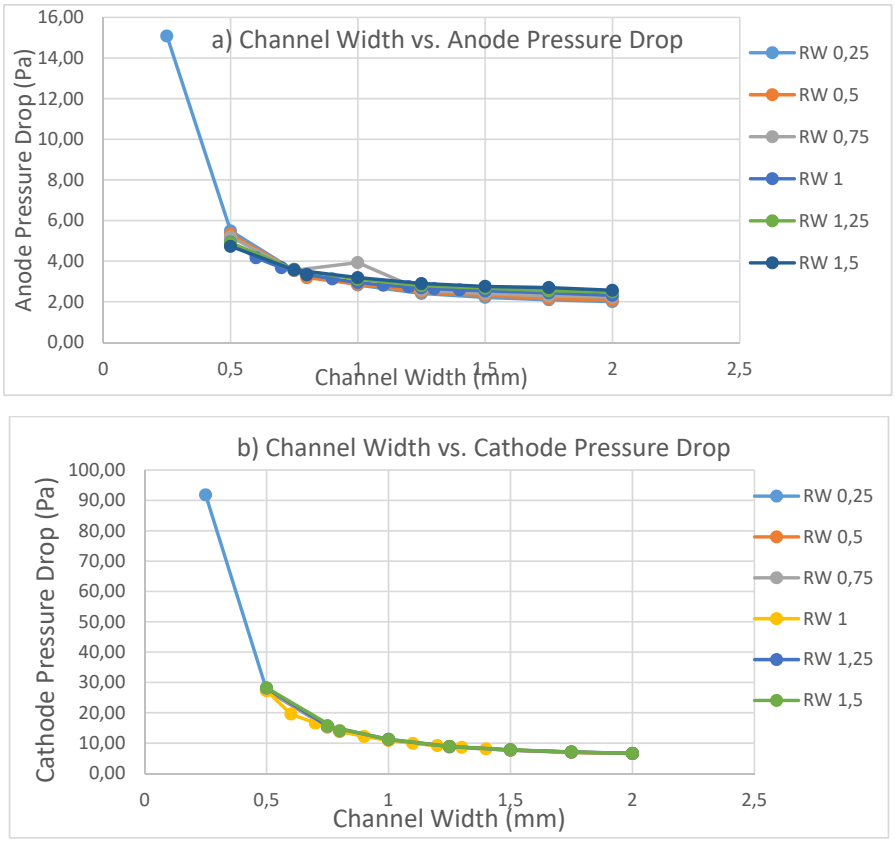
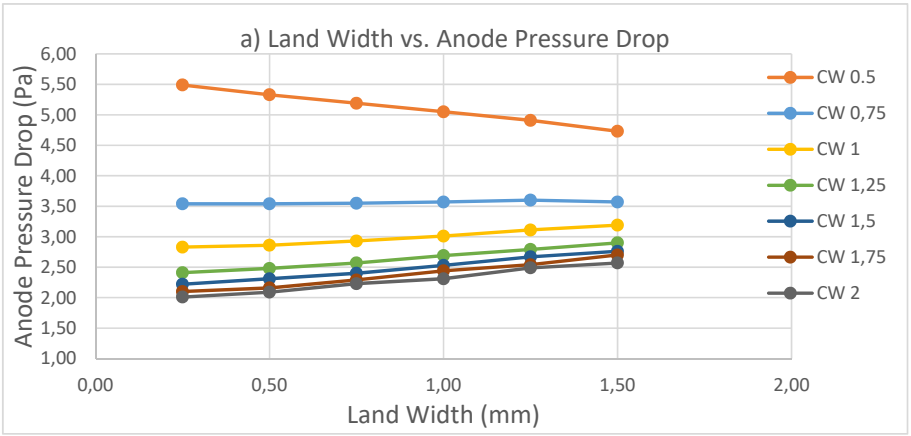


Figure 5. For different constant land width for different land width vs. a) Anode Pressure Drop b) Cathode Pressure Drop at 0.4 V



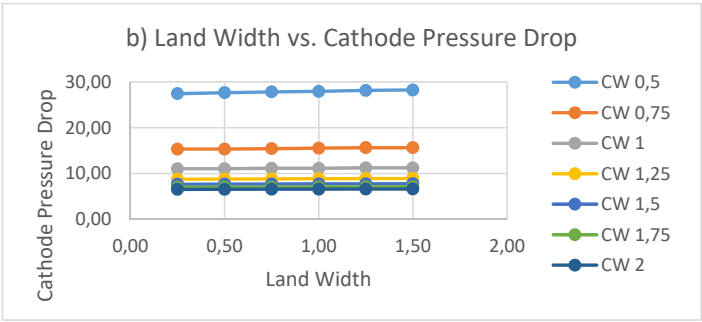


Figure 6. For different constant channel width for different land width vs. a) Anode Pressure Drop b) Cathode Pressure Drop at 0.4 V

4. Conclusions

The numerical analysis for the investigation of channel and land width effect on PEM fuel cell performance were investigated. The simulation results showed that the effect of channel width has more impact on cell performance as well as on anode and cathode pressure drop than land width. The minimum the channel width, the maximum the cell performance and pressure drop are. On the other hand, land width has little or almost no effect on cell performance and pressure.

References

1. A. Alaswad, A. Baroutaji, H. Achour, J. Carton, Ahmed Al Makky, A.G. Olabi, Developments in fuel cell technologies in the transport sector, DOI: 10.1016/j.ijhydene.2016.03.164.
2. X. Li and I. Sabir, Review of bipolar plates in PEM fuel cells: Flow field designs, International Journal of Hydrogen Energy, Vol. 30: pp. 359-371, 2005.
3. M. Muthukumar, P. Karthikeyan, M. Vairavel, C. Loganathan, S. Praveenkumar, A. P. S. Kumar, Numerical Studies on PEM Fuel Cell with Different Landing to Channel Width of Flow Channel, 12th Global Congress On Manufacturing And Management, GCMM 2014, Procedia Engineering 97 (2014) 1534 – 1542.
4. A. Higier, H. Liu, Optimization of PEM fuel cell flow field via local current density measurement, International Journal of Hydrogen Energy 35 (2010) 2144-2150.
5. S. A. Grigoriev, A. A. Kalinnikov, N. V. Kuleshov, P. Millet, Numerical optimization of bipolar plates and gas diffusion electrodes for PBI-based PEM fuel cells, International Journal of Hydrogen Energy 38 (2013) 8557-8567.

A Parametric Study on A Run-of-the River Mini Hydropower Plant Integrated Hydrogen Production

Adnan Midilli, Mert Ozsaban
Mechanical Engineering Department, Faculty of Engineering, Recep Tayyip Erdoğan University, Zihni Derin Campus, Fener, 53100, Rize, Turkey
Email: amidilli@gmail.com; mert.ozsaban@erdogan.edu.tr

Abstract
The main objective of this study is to perform a parametric investigation of hydrogen production by using a run-of-river mini hydropower plant integrated PEM electrolysers. In this study, hydrogen production system includes a run-of-river mini hydropower plant and three PEM electrolysers. In this system, hydrogen production capacity has been determined by depending on the hydropower quantity, and therefore three PEM electrolysers have been integrated in the system. At the end of the calculations, it is determined that mini hydropower plant generates maximum 455 kW power, and PEM electrolyzer produces 2.661 kg/h (30 Nm^3/h) hydrogen gas at 30 bar and 70 °C under the following operating conditions: i) mini hydropower gross head ranging from 50 m to 200 m with 30 intervals, ii) discharges ranging from 0.2 m^3/s and 0.3 m^3/s with 0.025 intervals. Accordingly, minimum hydrogen production rate are calculated to be 1.324 kg/h at 50 m gross head and 0.2 m^3/s of discharge by utilizing 75.462 kW electricity from mini hydropower plant. Maximum hydrogen production rate are estimated to be 7.941 kg/h at 200 m gross head and 0.3 m^3/s of discharge by using 453 kW electricity from the plant.

Keywords: Hydrogen, PEM electrolyzer, run-of-river mini hydropower, discharge, gross head.

1. Introduction

Hydrogen as a fuel can be produced from water via electrolysers by using renewable energy sources. Renewable hydrogen production systems has minimum impacts on the environment and society [1]. PEM electrolysers, one of the most important devices for hydrogen production, are used for practical hydrogen production applications requiring electricity [2-3] that is generated by hydropower plants [4].

2. Main Works

Some important assumptions are given below. All assumptions have been included in the full paper.
Assumptions:
1. Slope angle of the penstock has been accepted to be 45 degree.
2. Turbine, generator and transformer, PEM electrolyser, pumps efficiencies have been accepted to be 0.90, 0.95, 0.90, 0.60 and 0.80, respectively.
3. The pressure and heat losses through the system have been neglected.
4. Operating pressure and temperature of PEM electrolyser have been accepted to be 30 bar and 70°C, respectively.

Table 1. Operating Parameters of Plant

Parameter	Symbol	Unit	Values	Comment
Local friction factor in valve	k_v	-	0.5	[5]
Local friction factor outlet of forebay	k_h		0.5	[5]
Reference environment pressure	P_∞	bar	1	Assumed
Reference environment temperature	$T\infty$	K	298.15	Assumed
Gravity	g	(m/s^2)	9.81	[5]
Efficiency of turbine	η_t	%	90	Assumed
Efficiency of generator	η_g	%	95	Assumed
Efficiency of transformator	η_{trs}	%	90	Assumed

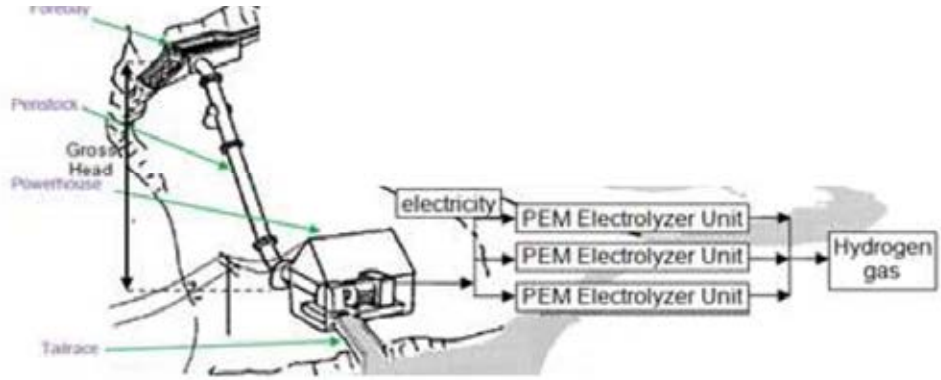


Fig. 1. Schematic of a typical run-of-the-river small hydro power plant with hydrogen production [modified from 6].

The hydropower integrated hydrogen production system is schematically illustrated in Fig. 2.

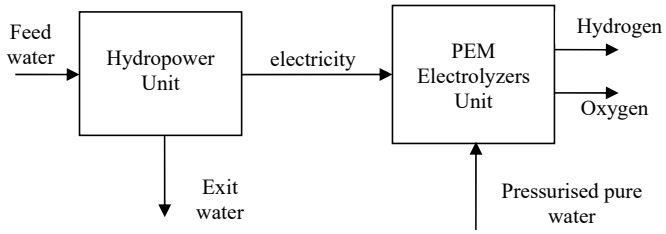


Fig. 2. Schematic illustration of the hydropower integrated hydrogen production system.

The following calculation procedure is followed for the parametric study: i) Determine the type of the hydropower plant; ii) Determine the main operating parameters such as gross head ranges, discharge ranges, slope angles, etc.; iii) Calculate the power generation from the plant; iv) Select hydrogen production device such as PEM electrolyser; v) Determine the number of PEM electrolyser; vi) Calculate the rate of hydrogen produced; vii) The energy requirement of the PEM electrolyser is calculated according to the amount of hydrogen, operation temperature and pressure; viii) The energy requirement of the high-pressure pump and circulating pump are calculated from requirements of PEM electrolyser; ix) Hydropower loads and Water flow rate determine depending of the energy requirement of the PEM electrolyser and pumps; x) Electric power calculated from gross head and water flow rate.

a) Local losses in the system is calculated as below,

$$\xi_l = \frac{k\, v^2}{2\, g} \tag{1}$$

b) Darcy-Weisbach friction factor (Barr equation) can be written as below [6],

$$\frac{1}{\sqrt{\lambda}} = -2log\left[\frac{k_s}{3.7D} + \frac{5.1286}{Re^{0.89}}\right] \tag{2}$$

c) Friction Loss in Penstock is calculated as below [5],

$$\xi_s = \frac{\lambda\, L\, v^2}{2\, g\, D} \tag{3}$$

d) Total losses in the system is shown as below,

$$\Sigma\xi = \Sigma\xi_l + \Sigma\xi_s \tag{4}$$

e) Calculation of Net Head can be written as below,

$$H_o = H_g - \Sigma\xi \tag{5}$$

f) Calculation of power generation [7]:

$$\dot{W} = 9.81\, \dot{Q}\, H_0\, \eta_t\, \eta_j\, \eta_{trs} \tag{6}$$

g) PEM Electrolyzer electricity consumption is shown as below [8]:

$$\begin{aligned}\dot{W}_{PEM} &= \dot{m}_{H_2}\left[T_{H_2}\left(s^o_{H_2} + c_{H_2}\ln\left(\frac{T_{H_2}}{298}\right) - Z_{H_2}R\ln\left(\frac{P_{H_2}}{1bar}\right)\right) - c_{H_2}\left(T_{H_2} - 298\right)\right]\\ &+\dot{m}_{O_2}\left[T_{O_2}\left(s^o_{O_2} + c_{O_2}\ln\left(\frac{T_{O_2}}{298}\right) - Z_{O_2}R\ln\left(\frac{P_{O_2}}{1bar}\right)\right) - c_{O_2}\left(T_{O_2} - 298\right)\right]\\ &-\dot{m}_{H_2O}\left[T_{H_2O}\left(s^o_{H_2O} + c_{H_2O}\ln\left(\frac{T_{H_2O}}{298}\right)\right) - \left(h^o_{H_2O} + c_{H_2O}\left(T_{H_2O} - 298\right)\right)\right]\\ &+\dot{m}_{H_2O}\left(-h^o_{H_2O} - c_{H_2O}\left(T_{H_2O} - 298\right)\right) + \dot{m}_{H_2}\left(c_{H_2}\left(T_{H_2} - 298\right)\right) + \dot{m}_{O_2}\left(0.5c_{O_2}\left(T_{O_2} - 298\right)\right)\end{aligned} \tag{7}$$

h) High-pressure water pump electricity consumption is calculated as below;

$$\dot{W}_{hpp} = \frac{\dot{m}_{pw} \times v_{pw}\left(P^{hpp}_{out} - P^{hpp}_{in}\right)}{\eta_{hpp}} \tag{8}$$

i) Required electricity for circulation pump can be written as below;

$$\dot{W}_{cp} = \frac{\dot{m}_{cw} \times v_{cw}\left(P^{cp}_{out} - P^{cp}_{in}\right)}{\eta_{cp}} \tag{9}$$

j) Required electricity for hydrogen production can be written as below;

$$\dot{W}_{H_2} = \dot{W}_{PEM} + \dot{W}_{hpp} + \dot{W}_{cp} \tag{10}$$

k) Mass flow rate of hydrogen can be written as below;

$$\dot{m}_{H_2} = \frac{\dot{W}_{hp}}{\dot{W}_{H_2}} \tag{11}$$

3. Result and Discussion

One of the main results of this study is presented in Fig. 3 representing the variations of hydrogen production rate as a function of gross head under the given operating conditions and efficiencies as in Figure. According to Fig. 3, Accordingly, minimum hydrogen production rate are calculated to be 1.324 kg/h at 50 m gross head and 0.2 m^3/s of discharge by utilizing 75.462 kW electricity from mini hydropower plant. Maximum hydrogen production rate are estimated to be 7.941 kg/h at 200 m gross head and 0.3 m^3/s of discharge by using 452.632 kW electricity from the plant. Detailed results and discussions have been presented in the full paper. All figures and other variations have been presented in the full paper.

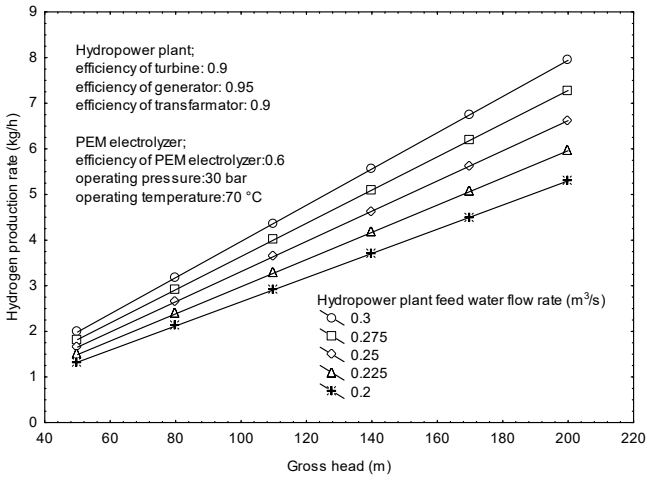


Fig. 3. Variation of hydrogen production rate as a function of gross head under the given operating conditions and efficiencies

4. Conclusion

This paper has introduced a parametric investigation of hydrogen production by using a run-of-river mini hydropower plant integrated PEM electrolyser group. The findings show that for the constant water flow rate of the hydropower plant, high hydrogen production rate requires high gross head. This increases the required electricity energy.

Nomenclature

k_v	Local friction factor in valve
k_h	Local friction factor outlet of forebay
P_∞	Reference environment pressure (bar)
T_∞	Reference environment temperature (Kelvin)
H_g	Gross head (m)
H_o	Net head (m)
$\dot{Q}$	Flow rate (m^3/s)
v	Velocity (m/s)
L	Length (m)
D	Diameter (m)
g	Gravity (m/s^2)
s	Entropy (J/gK)
h	enhtalpy (J/g)
c	Specific heat capacity (J/gK)
Z	Compressibility factor
R	Universal gas constant (J/kg K)
$\dot{m}$	Mass flow rate (kg/s)

Greek Letters

η	Efficiency
ξ	Losses
λ	friction factor

Acronyms

PEM	Proton exchange membrane
Re	Reynolds number

References

1. Cilogluları M, Erden M, Karakilcik M, Dincer I. Investigation of hydrogen production performance of a Photovoltaic and Thermal System. International Journal of Hydrogen Energy, 2016 xxx:1-6.

2. Nieminen J, Dincer I, Naterer G. Comparative performance analysis of PEM and solid oxide steam electrolysers. International Journal of Hydrogen Energy. 2010 35(20):10842–10850.
3. Ahmadi P, Dincer I, Rosen MA, Energy and exergy analyses of hydrogen production via solar-boosted ocean thermal energy conversion and PEM electrolysis. International Journal of Hydrogen Energy. 2013, 38(4):1795–1805.
4. Yah NY, Oumer AN, Idris MS. Small scale hydro-power as a source of renewable energy in Malaysia: A review. Renewable and Sustainable Energy Reviews. 2017, 72:228–239.
5. Özgür C. Pratik Hidrolik Problemleri, Teknik Kitaplar Yayınevi Altıncı Baskı, İstanbul, Ocak, 1957.
6. Featherstone RE and Nalluri C. Civil Engineering Hydraulics, 3rd Edition, Blackwell Science Ltd., Oxford, 399, 1995.
7. Kaçar O. Thermodynamic Modeling of Power Generation via A Run-Of-River-Type-Hydropower Plant (in Turkish). Master thesis, Niğde University, Graduate Scholl of Natural and Applied Sciences. 2009.
8. Inac S. Thermodynamic modelling and energy sustainability analysis of high pressure hydrogen Production System (in Turkish). Graduate School of Natural and Applied Science, MSc Thesis, Nigde University, Turkey; 2009.

ORAL PROCEEDINGS

POSTER PROCEEDINGS

Graphene Aerogel Supported Platinum Catalysts for Formic Acid Electrooxidation

M. Selim Çögenli, Ayşe Bayrakçeken Yurtcan
Department of Nanoscience and Nanoengineering, Atatürk University, Erzurum, Turkey
Department of Chemical Engineering, Atatürk University, Erzurum, Turkey
Email: selim.cogenli@atauni.edu.tr, ayse.bayrakceken@gmail.com

Abstract
In this study, GA and carbon were employed as hybrid supports for the dispersion of Platinum (Pt) nanoparticles to improve their electrocatalytic activities for the oxidation of formic acid. Chemical reduction method using microwave heating and hydrothermal were applied to the synthesis of Pt nanoparticles supported on the defect sites of hybrid support materials. They were called Pt/C MWI, Pt/GA MWI, Pt/C/GA MWI, Pt/C/GA Hydrothermal. The as-prepared catalysts was characterized by a variety of means such as SEM, XRD, BET. The SEM results showed that GA has a 3D macroporous structure. The results of electrochemical tests reveal that the Pt/C/GA Hydrothermal and Pt/GA MWI catalysts have a high tolerance against the poisoning effect of CO and direct pathway dominates the electrooxidation of formic acid.

Keywords: formic acid electrooxidation; graphene aerogel; catalyst

1. Introduction

Direct formic acid fuel cells (DFAFCs) have attracted significant attention because they are satisfactory power sources for portable devices [1]. A significant interest in the development of direct liquid fuel cell technology is the need for highly active catalysts for the formic acid oxidation reaction. The strategies to improve the durability and activity of catalyst can be in general categorized into two aspects: support materials and catalytic metals [2]. The support materials play a key role because of high specific surface area, which is necessary for improving the dispersion of catalytic metals, low combustive reactivity under both dry and humid air conditions at low temperatures, high conductivity [3].

Researchers have investigated the conductive carbon materials such as graphene, CNTs, and carbon nanofibers, which were used as support for electrocatalyst for improving the catalytic activity, stability and DFAFCs performance [1, 4-6]. Graphenes with various structures (e.g., networks, foams, aerogels, etc.) are now regarded as a desirable candidate for the catalyst support in fuel cells owing to their outstanding electronic conductivity, large surface area, ultrathin thickness, sufficient porosity, and thermal and chemical stability [7, 8]. Recently, better catalytic performance results were obtained for formic acid oxidation using graphene-carbon black [9] and graphene-carbon nanotubes [10] composite support materials. Three dimensional (3D) graphene aerogel (GA) has received enormous interest in catalysis and energy storage applications due to their rich macro porosity and multidimensional electron transport pathways [2, 11].

This paper includes the synthesis of graphene aerogel (GA), using GA and GA-carbon black (C) hybrid materials as supports for Pt nanoparticles in order to use for formic acid oxidation; a comparison of these results with carbon black supported catalyst was also provided. The Pt/GA-C catalysts were synthesized with both assistance of microwave irradiation and hydrothermal methods.

2. Experimental Study

2.1. Preparation of GO

Graphite oxide (GO) was prepared from graphite powder by modified Hummer's method [12]. For Hummers' method, concentrated H_2SO_4 (69 mL) was added to a mixture of 3.0 g graphite flakes and 1.5 g $NaNO_3$ and the mixture was cooled to 0 °C in ice bath. Then 9.0 g $KMnO_4$ was added slowly to keep the reaction temperature below 5 °C. The reaction was warmed to 35 °C and stirred for 120 min, at which time water (138 mL) was added slowly, producing a large exotherm to about 98 °C. Then the reaction was cooled using an ice bath for 10 min. Additional water (420 mL) and 30% H_2O_2 (3 mL) were added. The GO suspension exhibited a light brown color.

2.2. Preparation of graphene aerogel (GA)

In a typical experiment, 500 mg GO was dispersed in 100 mL distilled water under assistant of ultrasound. Subsequently, the stable suspension was transferred into a Teflon-lined autoclave with a stainless steel shell and hydrothermally treated at 180 ºC for 12 h. Then cooled down to room temperature. The hydrogel graphene was taken out from the autoclave, and it was dried by freeze drying for 12 hour to generate GA.

2.3. Synthesis of Pt/GA and Pt/GA/C by microwave irradiation technique

Graphene aerogel and carbon composite supported catalysts having 20 wt.% Pt were prepared by using microwave irradiation technique. Firstly, required amounts of GA, Vulcan XC72 carbon black (1:1) and 0.05M aqueous solution of H_2PtCl_6 added in 50 ml ethylene glycol and then stirred for 30 min. Then the resulting mixture was reduced for 60s in microwave oven. After microwave treatment, the mixture was cooled down with cold water, then filtered, washed with acetone and deionized water and finally dried at 100°C for 12 h.

2.4. Synthesis of Pt/GA/C by hydrothermal technique

In order to synthesize Pt/GA/C catalyst hydrothermally, firstly, Pt/C catalyst with Pt loading of 20 wt.% was synthesized by microwave irradiation technique. Briefly, 100 mg Vulcan XC-72 carbon black was dispersed in 50 ml ethylene glycol (EG) under magnetic stirring for 30 min. Then 0.05M H_2PtCl_6 solution was added into EG and then stirred by using ultrasonic treatment to form uniform ink. The suspension was placed in the center of a microwave oven for microwave heating for 60 s. After microwave treatment, the mixture was cooled down with cold water, then filtered, washed with acetone and deionized water and finally dried at 100°C for 12 h. Pt/C/GA catalyst was synthesized by hydrothermal assembly of GO and Pt/C, subsequently with freeze- drying. In a typical experiment, 50 mg homemade Pt/C catalyst was dispersed in 100 mL GO aqueous solution (5 mg/ml) under assistance of ultrasound. Subsequently, the stable suspension was transferred into a Teflon-lined autoclave with a stainless steel shell and hydrothermally treated at 180 °C for 12 h. Then it was dried by freeze drying for 12 hour.

2.5. Characterization of the catalysts

The morphology of as-synthesized catalysts were characterized by scanning electron microscope (SEM) (Model: FEI-Inspect s50). X-ray diffraction (XRD) analysis of as-prepared catalyst was carried out with Rigaku Miniflex X-ray diffractometer using a Cu X-ray source operating to get the XRD pattern. The Brunauer–Emmett–Teller (BET) method using nitrogen adsorption/desorption was performed to determine the specific surface area of the support material. The pore volume and pore size distributions were derived from the adsorption branches of isotherms by using the Barrett-Joyner-Halenda (BJH) model.

2.6. Electrochemical measurements of the catalysts

Electrochemical measurements including cyclic voltammetry (CV) and chronoamperometry (CA) were performed in a three-electrode system using glassy carbon (GC) electrode as counter electrode and Ag/AgCl as reference electrode. The catalyst ink was prepared by ultrasonically dispersing 13.5 mg of catalyst and 80 microliter of dilute aqueous Nafion solution (20 wt%) in 1 mL ethanol. The dispersion was then ultrasonicated for 20 min in order to be used in working electrode. The GC working electrode have 4 mm diameter and 0.1963 cm^2 apparent area. A quantity of 10 microliter of the dispersion was pipetted out on the top of the GC and then the electrode was dried at room temperature to eliminate the solvent. Electrochemical measurements were carried out in a conventional sealed three-electrode electrochemical cell at room temperature. CV and CA measurements were taken in electrolyte solution. The electrolyte solution (50ml 0.5 M H_2SO_4 and 50ml 0.5 M HCOOH) was purged with nitrogen gas for nearly 30 min before starting the experiment. The cyclic voltammograms (CVs) were recorded with VersaSTAT 3 Potentiostat-Galvanostat electrochemical analysis instrument.

3. Results and Discussion

XRD patterns of the Pt/C MWI, Pt/GA MWI, Pt/C/GA MWI, Pt/C/GA Hydrothermal catalysts are given in Fig. 1. The diffraction peak at around 25° was attributed to diffraction at the (002) plane of the hexagonal structure of Vulcan XC-72 carbon and GA. The diffraction peaks at around 39°, 46°, 68°, and 81° were due to the characteristic peaks of Pt (111), (200), (220), and (311) planes of Pt, respectively.

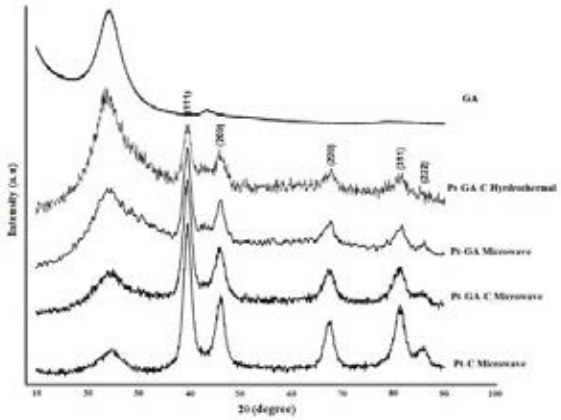


Fig. 1. XRD pattern of synthesized catalysts

In order to characterize the porous structure of GA, N_2 adsorption/desorption analysis is carried out and results are shown in Fig. 2. Based on Brunauer-Emmett-Teller (BET) method, the surface area of GA is 245 m^2/g. Besides the specific surface area analysis, the pore size distribution of GA was also derived from the adsorption branches of isotherm by using the Barrett-Joyner-Halenda (BJH) model. Porous GA showed a prominent pore size distribution in the range of 2–3 nm. The structure and morphology of the synthesized catalysts are investigated by SEM (Fig. 3).

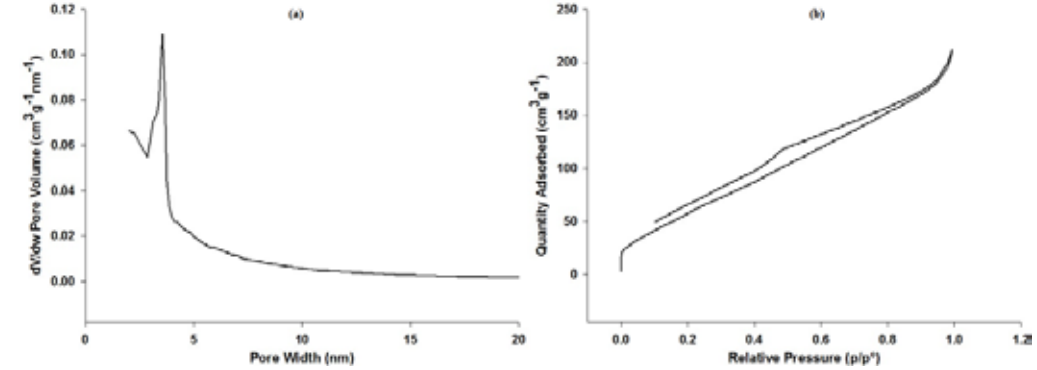


Fig. 2. (a) BJH pore size distribution and (b) Nitrogen adsorption and desorption isotherms of GA support

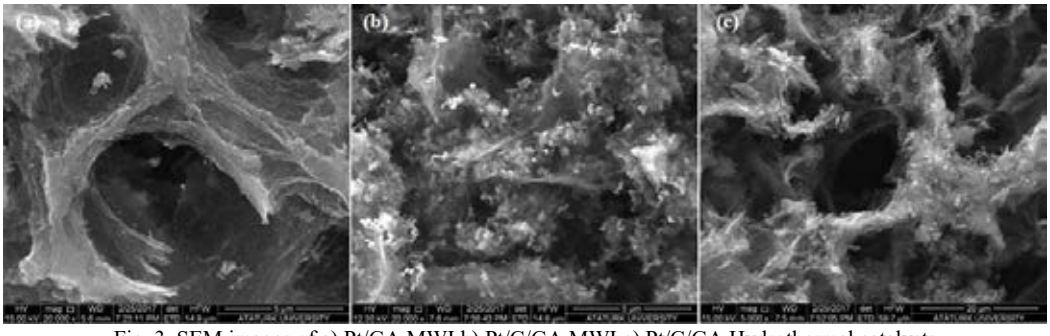


Fig. 3. SEM images of a) Pt/GA MWI b) Pt/C/GA MWI c) Pt/C/GA Hydrothermal catalysts

Formic acid oxidation peaks including anodic peaks of CO_2 (dehydrogenation), If_1, and CO (dehydration), If_2, can be seen nearly at 0.3 V and at 0.65 V, respectively. These two peaks were assigned to the oxidation of the intermediate CO generated by the dissociative (non-faradaic) adsorption step and to the direct oxidation of formic acid to CO_2 [13]. One cathodic peak occurs with the potential region of 0.4-0.5 V in the backward scan, I_b, resulting from the oxidation of CO generated from the dehydration reaction of HCOOH [14].

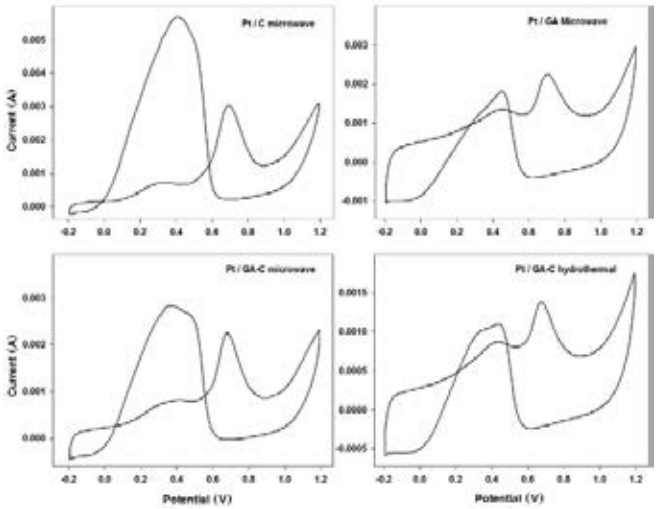


Fig. 4. Cyclic voltammograms of (20 wt. % Pt loading) Pt/C MWI, Pt/GA MWI, Pt/C/GA MWI, Pt/C/GA Hydrothermal catalysts in 0.5 M H_2SO_4 + 0.5M CHOOH at RT

The current at the If_1/If_2 ratio shows a sequence as Pt/GA MWI (0.59 mA) > Pt/C/GA Hydrothermal (0.51 mA) > Pt/C/GA MWI (0.34 mA) > Pt/C MWI (0.24 mA). These results prove that the direct pathway dominates the electrooxidation of formic acid. However, Pt/C MWI and Pt/C/GA MWI oxidizes the adsorbed carbonaceous intermediates (formed during the forward scan) at lower anodic potentials (nearly at 0.3 V) than Pt/C/GA Hydrothermal catalyst (nearly at 0.4 V) and Pt/GA MWI (nearly at 0.41 V). This indicate that Pt/C MWI and Pt/C/GA MWI catalysts have higher surface activities than Pt/C/GA Hydrothermal and Pt/GA MWI catalysts. Table 1 represents a collection of all data extracted from the experiments shown in Fig. 4.

Table 1. The If_1/If_2 ratios extracted from CV data

Samples	**I_{f1} (mA)**	**I_{f2} (mA)**	**I_b (mA)**	**I_{f1}/I_{f2}**
Pt/C MWI	0.71	3.01	5.63	0.24
Pt/GA MWI	1.33	2.25	1.80	0.59
Pt/GA/C MWI	0.77	2.25	2.84	0.34
Pt/GA/C Hydrothermal	0.72	1.40	1.10	0.51

Fig. 5. presents the CV curves of catalysts in 0.5 M solution of H_2SO_4. The first potential region from − 0.2 to 0.1 V presents adsorption/desorption of hydrogen. The capacitive currents were relatively high due to the high active surface area of GA itself. It was not clear, but peaks originating from oxidation and reduction were found around 0.4 V, which were caused by the electrochemical redox of the oxidized groups (-OH and -COOH) functionalized [15] on the surfaces of GA.

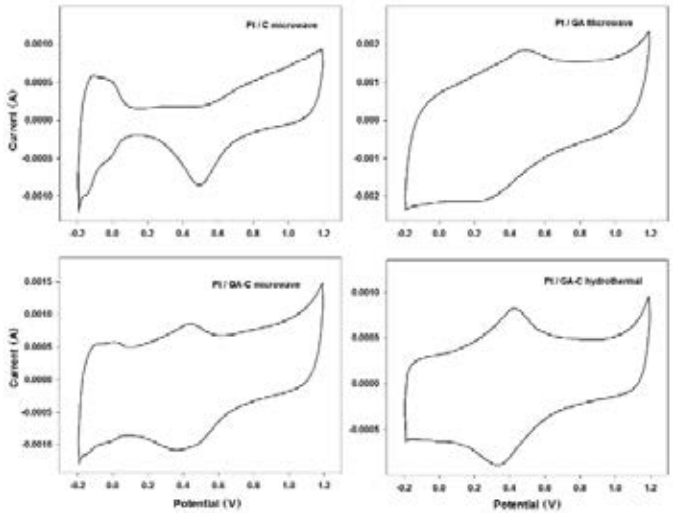


Fig. 5. Cyclic voltammograms of Pt/C MWI, Pt/GA MWI, Pt/C/GA MWI, Pt/C/GA Hydrothermal catalysts recorded by sweeping from −0.2 to +1.2 V linearly at 50 mV/s

The electrocatalytic stabilities of Pt/C and Pt/C/GA catalysts in a solution containing 0.5 M H_2SO_4 + 0.5M CHOOH was also compared by using chronoamperometry at a fixed potential of 0.3 V, as shown in Fig. 6. The stability of catalysts can be examined by the ratio of the final current, j_f, to the initial current, j_i, (i.e. j_f/j_i) obtained for each type of catalyst. It was seen that the current of Pt/C catalyst was higher than that of other catalysts during the whole testing time indicating that the electrocatalytic stability of Pt/C catalyst for formic acid oxidation was higher than that of other catalysts.

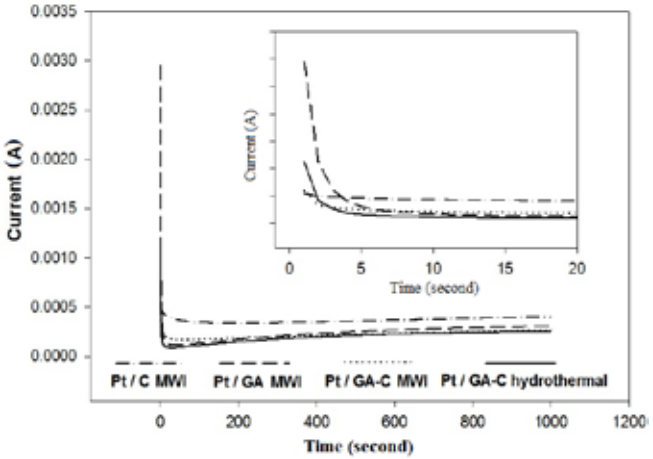


Fig. 6. Chronoamperometry measurements of (20 wt. % Pt loading) synthesized catalysts.

4. Conclusions

In this study, graphene hydrogels were first prepared from GO precursor solution via hydrothermal reaction and were subsequently freeze-dried to obtain the graphene aerogel (GA). Aerogel structured graphene was also reported for loading Pt nanoparticles as anode catalyst for oxidation of formic acid. GA, Vulcan XC72 (Carbon) and GA/C hybrid materials were successfully used as supports to disperse Pt nanoparticles by microwave irradiation technique. The current of Pt/GA MWI and Pt/C/GA hydrothermal towards formic acid oxidation for direct pathway (CO_2) is approximately 6 and 5 times greater than that of Pt/C. Although Pt nanoparticles on GA improved the catalytic

activity with respect to formic acid oxidation, the electrocatalytic stability of the Pt/C catalyst for formic acid oxidation was higher than that of other catalysts. The current at If_1/If_2 ratio shows a trend as Pt/C/GA Hydrothermal (0.51 mA) > Pt/C/GA MWI (0.34 mA). In summary, graphene aerogel and the combination of GA and carbon were lead to hybrid support materials with improved electrocatalytic activities for formic acid oxidation.

Acknowledgement
The authors are gratefully acknowledge the financial support of TUBİTAK through grant number 1649B031501611.

Nomenclature

I	Current (mA)
V	Voltage
M	Molarity (mol/L)
T	Temperature (°C or K)
wt.	Weight

Acronyms

DFAFC	Direct formic acid fuel cell
PGM	Platinum group metals
GA	Graphene aerogel
SEM	Scanning electron microscopy
BET	Brunauer Emmett Teller
XRD	X-ray diffractometer

References

1. Bong S, Uhm S, Kim YR, Lee J, Kim H. Graphene Supported Pd Electrocatalysts for Formic Acid Oxidation. Electrocatalysis. 2010;1:139-43.
2. Zhao L, Wang ZB, Li JL, Zhang JJ, Sui XL, Zhang LM. Hybrid of carbon-supported Pt nanoparticles and three dimensional graphene aerogel as high stable electrocatalyst for methanol electrooxidation. Electrochim Acta. 2016;189:175-83.
3. Shao YY, Liu J, Wang Y, Lin YH. Novel catalyst support materials for PEM fuel cells: current status and future prospects. J Mater Chem. 2009;19:46-59.
4. Yue RR, Wang CQ, Jiang FX, Wang HW, Du YK, Xu JK, et al. Electrocatalytic oxidation of formic acid on Pt-Pd decorated polyfluorenes with hydroxyl and carboxyl substitution. Int J Hydrogen Energ. 2013;38:12755-66.
5. Shao YY, Liu J, Wang Y, Lin YH. Novel catalyst support materials for PEM fuel cells: current status and future prospects. J Mater Chem. 2009;19:46-59.
6. Kumar MK, Jha NS, Mohan S, Jha SK. Reduced graphene oxide-supported nickel oxide catalyst with improved CO tolerance for formic acid electrooxidation. Int J Hydrogen Energ. 2014;39:12572-7.
7. Shi QR, Cha Y, Song Y, Lee JI, Zhu CZ, Li XY, et al. 3D graphene-based hybrid materials: synthesis and applications in energy storage and conversion. Nanoscale. 2016;8:15414-47.
8. Sun YQ, Wu QO, Shi GQ. Graphene based new energy materials. Energ Environ Sci. 2011;4:1113-32.
9. Qin YL, Wang JW, Wu YM, Wang LM. Improved hydrogen production from formic acid under ambient conditions using a PdAu catalyst on a graphene nanosheets-carbon black support. Rsc Adv. 2014;4:30068-73.
10. Bin Yousaf A, Imran M, Zeb A, Xie X, Liang K, Zhou X, et al. Synergistic effect of graphene and multi-walled carbon nanotubes composite supported Pd nanocubes on enhancing catalytic activity for electro-oxidation of formic acid. Catal Sci Technol. 2016;6:4794-801.
11. Si W, Wu X, Zhou J, Guo F, Zhuo S, Cui H, et al. Reduced graphene oxide aerogel with high-rate supercapacitive performance in aqueous electrolytes. Nanoscale Research Letters. 2013;8:247.
12. Marcano DC, Kosynkin DV, Berlin JM, Sinitskii A, Sun ZZ, Slesarev A, et al. Improved Synthesis of Graphene Oxide. Acs Nano. 2010;4:4806-14.
13. Vielstich W, Yokokawa H, Gasteiger HA. Handbook of fuel cells: fundamentals technology and applications: John Wiley & Sons; 2009.
14. Hsieh CT, Gu JL, Tzou DY, Chu YC, Chen YC. Microwave deposition of Pt catalysts on carbon nanotubes with different oxidation levels for formic acid oxidation. Int J Hydrogen Energ. 2013;38:10345-53.
15. Koo M, Bae JS, Kim HC, Nam DG, Ko CH, Yeum JH, et al. Electrochemical oxidation of some basic alcohols on multiwalled carbon nanotube-platinum composites. B Mater Sci. 2012;35:545-50.

Catalytic activity and stability of PtRu/C, PtPd/C and PtSn/C bimetalic catalysts towards methanol and formic acid oxidation reactions

M. Selim Çögenli, Ayşe Bayrakçeken Yurtcan
Department of Nanoscience and Nanoengineering, Atatürk University, Erzurum, Turkey
Department of Chemical Engineering, Atatürk University, Erzurum, Turkey
Email: selim.cogenli@atauni.edu.tr, ayse.bayrakceken@gmail.com

Abstract
Carbon supported Pt based catalysts were prepared by co-depositing PtRu, PtPd and PtSn with weight ratios of (2:1) on carbon black (Vulcan XC-72) via microwave heating of ethylene glycol (EG) solutions of $H_2PtCl_6.6H_2O$, $RuCl_3$, $PdCl_2$ and $SnCl_2.2H_2O$. These catalysts were systematically evaluated and compared with both commercial Pt black, PtRu black catalysts and with each other. The catalysts were characterized with TEM, XRD and ICP-MS. The electrocatalytic activities and stability of the catalysts were evaluated in sulfuric acid solution containing methanol and formic acid using electrochemical measurements. The results showed that PtSn/C catalyst showed a comparable activity and durability with Pt/C catalyst towards methanol oxidation. The PtPd/C catalyst gave activity better than both Pt black and Pt/C catalysts for formic acid oxidation. Electrochemical active surface areas (ECSA) obtained from supported binary catalysts were higher than that obtained on single Pt supported on Vulcan XC-72.

Keywords: Bimetallic catalyst; methanol oxidation; formic acid oxidation

1. Introduction

Liquid-feed fuel cells can use different types of liquid fuels contrary to use of direct hydrogen. Later the research focus was shifted to the oxidation of methanol in direct methanol fuel cells (DMFCs) [1]. In addition to alcohols, other organic compound such as acids (e.g., formic acid) may be used as liquid fuels for fuel cells [2]. DMFCs have been most studied due to low pollutant emission, low cost and high theoretical energy density. It has been considered as the most difficult fuel cell technology due to methanol crossover and catalytic inefficiency [3-5]. Direct formic acid fuel cell (DFAFC) has been widely studied as possible power sources for the portable electronic devices although it has been studied less than DMFC during the past 10 years. Although methanol has been the fuel most studied due to low pollutant emission, low cost and high theoretical energy density, formic acid has been proposed as an alternative to methanol because of not inflammable, safe storage and non-toxic [3, 4].

Platinum (Pt), Ruthenium (Ru) and Palladium (Pd) have very important role for methanol and formic acid oxidation because of utilization as anode catalysts in DMFC and DFAFC. Although Ru and Pd exhibit higher initial catalyst activity in contrast to Pt, they show less stability in long term measurement for methanol and formic acid oxidation, respectively [6]. The combination of Pt based intermetalic catalysts may increase both the catalytic activity and stability for methanol [7] and formic acid oxidation reactions [8]. There have been several studies including the use of catalysts such as PtM (M= Au, Ru, Pd, Bi, Pb, Co etc.) [6, 9-11]. These bimetalic catalysts showed better catalytic activity than pure noble metal like Pt, Ru or Pd for electro-oxidation of hydrogen-rich organic molecules such as formic acid and methanol.

In this study, carbon suppport Pt cataysts were modified by adding of Ru, Pd and Sn and synthesized by a microwave assisted catalyst preparation technique. This technique can be used as a general method to prepare supported metal particles from metal precursors. The catalysts were evaluated and tested for methanol and formic acid oxidation in acidic media by cyclic voltammetry and chronoamperometry. These catalysts were compared with both commercial Pt black, PtRu black catalysts and with each other.

2. Experimental Study

2.1. Preparation of catalysts

In this study, a simple microwave procedure for preparing Pt, PtRu, PtPd, PtSn bimetalic nanoparticles supported on carbon is reported. PtM (M=Ru, Pd, Sn)/Carbon nanocomposites containing 20 wt% of Pt and 10 wt% M were prepared by microwave irradiation technique. In a 100 mL beaker, 1.0 mL of an aqueous solution of 0.05 M $H_2PtCl_6.6H_2O$, $RuCl_3$, $PdCl_2$ and $SnCl_2$ (Aldrich, A.C.S. Reagent) separately was mixed with 50 mL of ethylene glycol (EG). 100 mg of carbon (Vulcan XC-72) were uniformly dispersed in the mixed solution by mechanical mixer. Carbon-supported PtM catalysts were prepared by co-depositing PtM with weight ratios of (2:1) on Vulcan XC-72 with microwave heating. The beaker was placed in the center of a microwave oven (Samsung, 850W) and heated for 120 s. The resulting suspension was washed with ethanol and deionized water then separated by using the centrifuge. The catalyst was finally dried in an oven at 100°C for 12 h.

2.2. Characterization of the catalysts

The catalysts were characterized with Rigaku Miniflex X-ray diffractometer using a Cu X-ray source operating to get XRD pattern. High resolution transmission electron microscopy (HRTEM) for the homemade catalysts were performed on a JEOL JEM 2100F field emission gun transmission electron microscope. The elemental composition was determined using an Inductively Coupled Plasma – Mass Spectrometer (Agilent 7800 ICP-MS).

2.3. Electrochemical measurements of the catalysts

Electrochemical measurements were carried out in a 100 mL three-electrode cell at room temperature (RT) with the use of an electrochemistry workstation. A Glassy carbon (GC) electrode, a Pt wire electrode, and a Ag/AgCl electrode were used as working, counter, and reference electrodes, respectively. The catalyst ink was prepared by ultrasonically dispersing 13.5 mg catalyst and 80 microliter of a dilute aqueous Nafion solution (20 wt%) in 1 mL ethanol. The dispersion was ultrasonicated for 20 min. A quantity of 10 microliter of the dispersion was pipetted out on the top of the GC (0.1963 cm^2) for working electrode. The cyclic voltammetry (CV) for H_2 adsorpsion/desorpsion region of the catalysts were measured in a potential range from −0.2 to –1.2 V and at a scan rate of 20 mV/s at RT in 0.5 M H_2SO_4. Methanol and formic acid oxidation activities of the catalyst were measured at the same potential and scan rate in 0.5 M H_2SO_4 (50 ml) + 0.5 M (50 ml) methanol or formic acid solutions. O_2 was removed from the solutions during the experiment with high-purity N_2 gas. The chronoamperometry curves that give us an information about catalyst durability were obtained by polarizing the electrode at 0.5 V for 500 s and 0.3V for 1000s in 50ml 0.5 M H_2SO_4 + 50 ml 0.5 M CH_3OH and CHOOH solutions, respectively.

3. Results and Discussion

XRD patterns of the carbon-supported Pt, PtPd, PtRu and PtSn catalysts are shown in Fig. 1. All patterns exhibit a diffraction peak at around 25° related to graphite-like structure of the Vulcan XC-72 carbon support. The diffraction pattern of Pt/C clearly shows the main characteristic peaks of the face-centered cubic (fcc) platinum crystalline structure. The diffraction peaks for PtRu/C, PtPd/C are slightly shifted to higher and PtSn/C catalyst shifted to lower 2θ values with respect to the corresponding peaks for pure Pt in Pt/C catalyst.

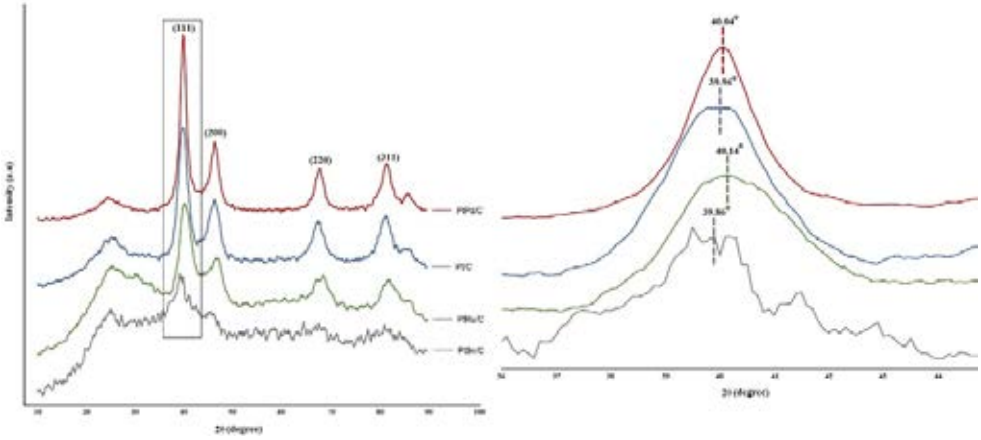


Fig. 1. XRD patterns of the synthesized catalysts

Inductively coupled plasma-mass spectrometry (ICP-MS) is applicable for the determination of metal loading in the catalysts. Pt, Pd, Ru, Sn metal loading (wt. %) values of the synthesized catalysts were given in Table 1. TEM images showed that binary PtSn, PtRu and PtPd nanoparticles are uniformly distributed on the carbon surface (Fig. 2a, 2b, 2c).

Table 1. ICP-MS results of the catalysts

	Weight (wt. %)			
	Pt	**Pd**	**Ru**	**Sn**
Pt/C	18.5	-	-	-
PtPd/C	19.6	11.9	-	-
PtRu/C	18.0	-	10.1	
PtSn/C	17.7	-	-	6.3

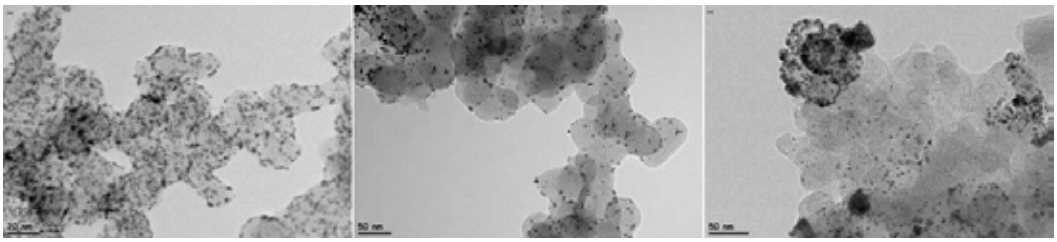


Fig. 2. TEM images of bimetalic a) PtSn/C b) PtRu/C c) PtPd/C catalysts

3.1. The electrochemically active surface area (ECSA) of the synthesized catalysts

The electrochemical behaviors of different catalysts are investigated by cyclic voltammetry (CV) measurement. The cyclic voltammograms of Pt/C, PtRu/C, PtPd/C and PtSn/C catalysts in 0.5 M H_2SO_4 are shown in Fig. 3. The first potential region from -0.2 to 0.1 V presents adsorption/desorption of hydrogen. This region is defined as electrochemical surface area (ECSA) that can be influenced by many factors such as different mole ratios for bimetallic catalysts and structure of the catalysts [12]. A relatively large ECSA was obtained from bimetallic catalysts by comparison with Pt/C.

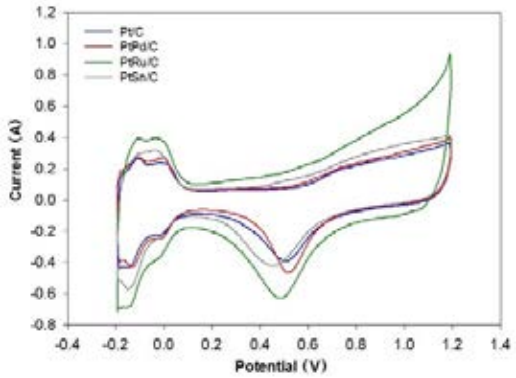


Fig. 3. CVs of the synthesized catalysts recorded by sweeping from -0.2 to +1.2 V at 20mV/s

3.2. Electrochemical evaluations of the synthesized and commercial catalysts for methanol oxidation

Figure 4 showed the CV curves of methanol electro-oxidation of different catalysts. CV curves of all catalysts showed two well-defined peaks at the forward and backward scans. The right peak, I_f, which was produced by the forward sweep and the left peak, I_b, which was produced by the backward sweep when the potentials are nearly 0.7V and 0.4V, respectively. A lower ratio (I_f/I_b) indicates a poorer catalytic performance. Among these catalysts, PtSn/C had the highest current ratio (2.09 mA), which implied the best electrocatalytic activity (Table 2). PtSn/C catalyst is about 1.5 times that of the commercial Pt black (about 1.37 mA) and higher than the synthesized Pt/C catalyst (about 1.03 mA). Methanol oxidation is enhanced by the addition of Pd and Sn. For Pt black, Pt/C, PtPd/C and PtSn/C, there is an enormous oxidation peak nearly at 0.4 V (vs. the Ag/AgCl reference electrode otherwise specially noted) in the cathodic scan which is commonly assigned to the oxidation of partially oxidized species that adsorbs onto the Pt surface after the anodic scan [13]. This peak totally disappeared for commercial PtRu black and synthesized PtRu/C, indicating that methanol can be fully oxidized during the anodic scan. The current of PtRu black and synthesized PtRu/C are 0.53 mA and 1.33 mA at 0.5V. Synthesized PtRu/C have higher activity, which is about 2.5 times that of the commercial PtRu black.

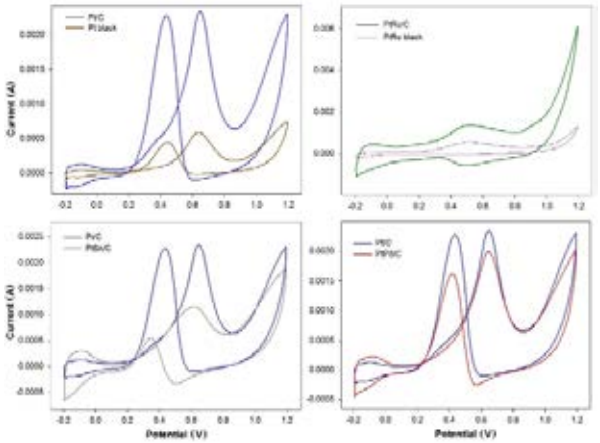


Fig. 4. Electrocatalytic activity for catalysts towards methanol oxidation is evaluated in a solution of 0.5 M H_2SO_4 containing 0.5 M CH_3OH at RT.

Table 2. I_f/I_b values calculated from the data extracted from Fig. 4.

Samples	I_f (mA)	I_b (mA)	I_f / I_b
Pt/C	2.35	2.28	1.03
Pt black	0.59	0.43	1.37
PtPd/C	2.00	1.62	1.23
PtSn/C	1.15	0.55	2.09

The electrocatalytic stabilities of the Pt/C and Pt/M catalysts in a solution containing 0.5 M CH_3OH and 0.5 M H_2SO_4 have also been compared by using chronoamperometry at a fixed potential of 0.50 V, as shown in Figure 5.

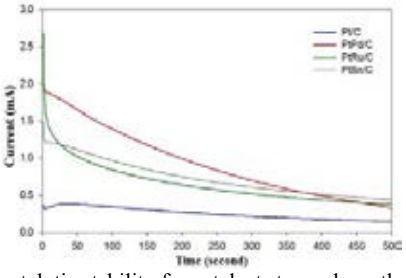


Fig. 5. Electrocatalytic stability for catalysts towards methanol oxidation

The ratios of the initial and final current for Pt/C, PtRu/C, PtPd/C and PtSn/C are 0.41, 0.14, 0.15 and 0.3, respectively. This ratio shows high performance in methanol oxidation by reducing the poisoning effect of generated CO species and demonstrating high stability for over than 500 s [14]. These results indicate that sample Pt/C shows the best stability with highest current rate of 0.41 as the catalyst for methanol oxidation compared with the other electrocatalysts for time periods.

3.3. Electrochemical evaluations of the synthesized and commercial catalysts for formic acid oxidation

The cyclic voltammograms were recorded in the potential range of -0.2 V to 1.2 V at 20 mV/s for synthesized Pt/C, PtRu/C, PtPd/C and PtSn/C catalysts (Fig. 6). Observation of a significant increase of the first peak, If_1, concurrently with a noticeable depression of the second oxidation peak, If_2. This indicates that the direct oxidation of formic acid becomes more favorable; while less poisoning intermediate (CO) is produced. The ratio of the two-oxidation peaks (If_1/ If_2) reflects the preferential oxidation pathway of formic acid at a particular electrode [15].

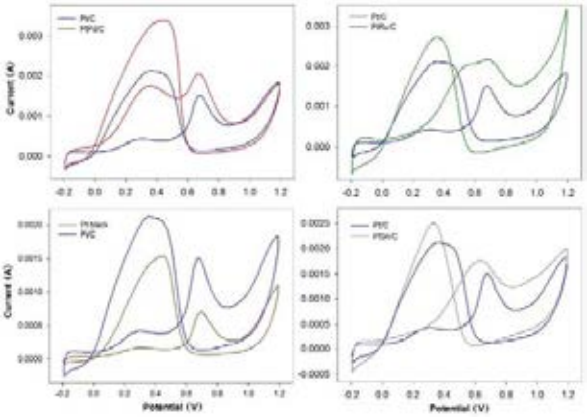


Fig. 6. Electrocatalytic activity of the catalysts towards formic acid oxidation in 0.5M H_2SO_4 +0.5M CHOOH at RT

The low activity of PtRu and PtSn bimetalic catalyst for formic acid oxidation is mainly a consequence of the relative inactivity of Ru and Sn atoms for formic acid oxidation in the potential region to nearly 0.3V. Results imply highest CO_2 form of the synthesized PtPd/C catalyst, and hence larger currents originating from the direct path in formic acid oxidation. Table 3 represents a collection of all data extracted by the experiment shown in Figure 6.

Table 3. I_{f1}/I_{f2} results calculated from the data extracted from Fig. 6.

Samples	I_{f1} (mA)	I_{f2} (mA)	I_b (mA)	I_{f1}/I_{f2}
Pt/C	0.43	1.50	2.10	0.29
Pt black	0.17	0.70	1.53	0.24
PtRu/C	N/A	2.14	2.70	N/A
PtPd/C	1.73	2.00	3.38	0.87
PtSn/C	N/A	1.72	2.50	N/A

The electrocatalytic stabilities of the Pt/C and binary catalysts in a solution containing 0.5 M CHOOH and 0.5 M H_2SO_4 have also been compared by using CA at a fixed potential of 0.3 V, as shown in Fig. 7. First, a sharp decrease in the current was observed corresponding to the formation of intermediate species (CO, OH, COOH and HCOOH) during formic acid oxidation reaction. This sharp decrease was followed by a slow decrease for longer time periods [16]. The initial and final current rate ratio of the PtSn/C was higher than that of other catalysts for formic acid oxidation.

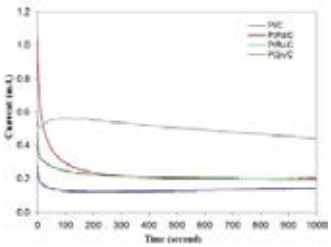


Figure 7. Electrocatalytic stability for catalysts towards formic acid oxidation

4. Conclusions

In conclusion, a microwave assisted simple, fast and rapid heating method has been successfully developed for the preparation of Pt/C, PtRu/C, PtPd/C and PtSn/C catalysts. The results from cyclic voltammetry measurements indicate that the PtSn/C bimetalic catalyst shows the best electrochemical catalytic activity for methanol oxidation. Although PtSn/C catalyst had more catalytic activity than the other synthesized binary catalysts except for PtRu/C, synthesized catalyst Pt/C have more stable than PtSn/C. Synthesized PtRu/C shows higher electrochemical catalytic activity compared with the commercial PtRu black catalysts for methanol oxidation. In contrast to methanol

oxidation, PtSn and PtRu are not suitable catalysts for formic acid oxidation. Although the catalytic activity of PtSn catalyst is low, it is the most stable catalyt for formic acid oxidation. The PtPd/C catalyst gave activity about 10 times better than Pt black and about 4 times better than Pt/C catalyst for formic acid oxidation.

Acknowledgement
The authors are gratefully acknowledge the financial support of TUBİTAK through grant number 1649B031501611 and Scientific Research projects Committee of Ataturk University with grant number of 2016/183.

Nomenclature

I Current (mA)
V Voltage
M Molarity (mol/L)
T Temperature (°C or K)
wt. Weight

Acronyms

DFAFC Direct formic acid fuel cell
DMFC Direct methanol fuel cell
ECSA Electrochemical active surface areas
TEM Transmission electron microscope
XRD X-ray diffractometer
ICP-MS Inductively Coupled Plasma – Mass Spectrometer

References

1. Zhang J, Liu H. Electrocatalysis of Direct Methanol Fuel Cells: From Fundamentals to Applications: Wiley; 2009.
2. Soloveichik GL. Liquid fuel cells. Beilstein Journal of Nanotechnology. 2014;5:1399-418.
3. Liu ZL, Zhang XH, Tay SW. Nanostructured PdRu/C catalysts for formic acid oxidation. J Solid State Electr. 2012;16:545-50.
4. Yovanovich M, Piasentin RM, Ayoub JMS, Nandenha J, Fontes EH, de Souza RFB, et al. PtBi/C Electrocatalysts for Formic Acid Electro-Oxidation in Acid and Alkaline Electrolyte. Int J Electrochem Sc. 2015;10:4801-11.
5. Wasmus S, Kuver A. Methanol oxidation and direct methanol fuel cells: a selective review. J Electroanal Chem. 1999;461:14-31.
6. Yu XW, Pickup PG. Carbon supported PtBi catalysts for direct formic acid fuel cells. Electrochim Acta. 2011;56:4037-43.
7. Choi JH, Jeong KJ, Dong Y, Han J, Lim TH, Lee JS, et al. Electro-oxidation of methanol and formic acid on PtRu and PtAu for direct liquid fuel cells. J Power Sources. 2006;163:71-5.
8. Feng LG, Si FZ, Yao SK, Cai WW, Xing W, Liu CP. Effect of deposition sequences on electrocatalytic properties of PtPd/C catalysts for formic acid electrooxidation. Catal Commun. 2011;12:772-5.
9. Croy JR, Mostafa S, Hickman L, Heinrich H, Cuenya BR. Bimetallic Pt-Metal catalysts for the decomposition of methanol: Effect of secondary metal on the oxidation state, activity, and selectivity of Pt. Appl Catal a-Gen. 2008;350:207-16.
10. Garrick TR, Diao W, Tengco JM, Monnier J, Weidner JW. The Effect of Bimetallic Surface Composition for Methanol Oxidation. Ecs Transactions. 2013;53:79-84.
11. Yu XW, Pickup PG. Screening of PdM and PtM catalysts in a multi-anode direct formic acid fuel cell. J Appl Electrochem. 2011;41:589-97.
12. Tan LY, Li LD, Peng Y, Guo L. Synthesis of Au@Pt bimetallic nanoparticles with concave Au nanocuboids as seeds and their enhanced electrocatalytic properties in the ethanol oxidation reaction. Nanotechnology. 2015;26.
13. Li YJ, Huang Y. Low-temperature, seed-mediated synthesis of monodispersed hyperbranched PtRu nanoparticles and their electrocatalytic activity in methanol oxidation. J Mater Chem. 2012;22:12461-4.
14. Sahin O, Kivrak H. A comparative study of electrochemical methods on Pt-Ru DMFC anode catalysts: The effect of Ru addition. Int J Hydrogen Energ. 2013;38:901-9.
15. El-Deab MS. Electrocatalysis by nanoparticles: Oxidation of formic acid at manganese oxide nanorods-modified Pt planar and nanohole-arrays. Journal of Advanced Research. 2010;1:87-93.
16. Sahin O, Duzenli D, Kivrak H. An ethanol electrooxidation study on carbon-supported Pt-Ru nanoparticles for direct ethanol fuel cells. Energy Sources, Part A: Recovery, Utilization, and Environmental Effects. 2016;38:628-34.

Electrocatalytic Hydrogen Production on GCE/RGO/Au Hybrid Electrode

Didem Balun Kayan, Merve İlhan, Derya Koçak
Chemistry Department, Faculty of Science and Arts, University of Aksaray, 68100, Aksaray, Turkey
Email: didembalun@aksaray.edu.tr

Abstract
We report on a electrocatalyst for hydrogen production based on a glassy carbon electrode (GCE) that was modified with a nanocomposite containing electrochemically reduced graphene oxide (RGO) and gold (Au) nanoparticles. The surface properties of the composite was characterized by field-emission scanning electron microscopy (FE-SEM) and the electrocatalytical performance evaluated as electrocatalyst toward hydrogen evolution reaction (HER) by linear sweep voltammetry (LSV), Tafel polarization curves and electrochemical impedance spectroscopy (EIS) analyses.

Keywords: Reduced graphene oxide; Au nanoparticles; hydrogen evolution reaction

1. Introduction

Designing clean, sustainable and environmentally-friendly energy sources is a very urgent research issue for the future of the world. Molecular hydrogen is widely considered as one of the most promising power vectors because of its high energy conversion efficiency and low pollutant emission which was powered by renewable energy sources such as water. Water electrolysis via hydrogen evolution reaction (HER) is the simplest way to produce hydrogen with high purity at the most economical price. The metals such as Platinum (Pt) and gold (Au) are regarded as the most appropriate metals for the electrocatalysis of HER. Unfortunately, their scarcity and high cost have hindered its commercial use in large scale [1-2]. In order to minimize the use of precious metals, one of the efficient strategies is the loading them on various carbon materials such as carbon black, carbon nanotubes, and graphene. Graphene has been considered as an ideal support due to its exceptional properties, including large surface area and high electrical conductivity which causes improvement on softness of the catalyst and increasing the dispersion of the active components [3]. Graphene, a single layer of sp^2-bonded carbon atoms, has attracted enormous attention owing to its unique structure and its exceptional electronic, mechanical, and thermal properties [4].

Thus, the aim of this study was to develop an efficient electrocatalyst for HER by decorating Au nanoparticles on graphene which achieved by the electrochemical reduced graphene oxide (RGO) on glassy carbon electrode. The graphene layer was achieved on the GCE by electroreducing graphene oxide dissolved in phosphate buffer solution at constant applied potential. After electrodeposition of Au nanoparticles on this RGO surface, the surface properties of the film-modified electrode were investigated by SEM images. The Au nanoparticles are uniformly dispersed on the graphene layer. Combining the advantages of graphene such as high surface area and conductivity, of Au nanoparticles with their excellent electrical conductivity, the hybrid film effectively enhanced the electron-transfer and promoted the hydrogen evolution reaction (HER). The hydrogen production performance of the GCE/RGO/Au hybrid material was tested by linear sweep voltammetry, Tafel polarization curves and electrochemical impedance spectroscopy techniques.

2. Experimental Study

Glassy carbon electrode (GCE), used here as the underlying substrate for reduced graphene oxide (RGO)/Au nanocomposite, was mechanically polished using a polishing microcloth with aqueous slurries of 0.3µm alumina powder and then held in ethanol and distilled water for 5 minutes in each solvent in ultrasonic bath prior to modification. The modified electrode was prepared by the drop-coating procedure; 7µl of 0.5mg/mL graphene oxide suspension was cast onto the cleaned GC surface and left to dry at 70°C for about 15 min. The dried GO layer reduced to RGO potentiostically at -0.9V for 1000s in 0.1M Na_2HPO_4 solution (pH=7). After that, GCE/RGO held in 1mM $HAuCl_4$/0.5M H_2SO_4 for 30 min and diffused Au ions on RGO layer reduced to Au nanoparticles at 0.5V for 900s. The as-prepared electrode rinsed with 0.5M H_2SO_4 solution and then used for electrochemical measurements. Ag/AgCl/Cl^- electrode and platinum wire was used as reference and counter electrodes, respectively, the applied potentials are given vs. normal hydrogen electrode (NHE). All measurements were carried out by using electrochemical analyzer (Gamry, Interface 1000). The schematic illustration of the experimental setup displayed in Fig.1.



Fig. 1. Schematic illustration of the experimental setup.

3. Results and Discussion

The surface analyses were realized before electrochemical characterizations. The SEM images of RGO and RGO/Au hybrid electrode are shown in Fig. 2. The wrinkled texture-like RGO sheets are coated on the surface of GCE, which would not only increase the surface area of the electrode, but also supply more active sites for the Au electrodeposition. Then the Au nanoparticles were electrodeposited onto the surface of RGO modified GCE. As shown in Fig. 2, the nucleation and growth process of Au particles with a diameter of average 35 nm on the surface of electrodes can be observed clearly. It can be seen that the Au particles with a high density are distributed in an almost homogeneous manner at the surface of the RGO/GCE.

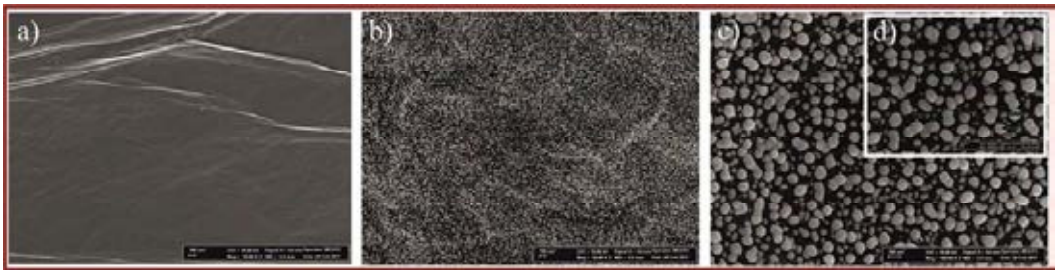


Fig. 2. FE-SEM images of a) RGO, b) RGO/Au nanoparticles c) and d) the higher magnification images of b

The linear sweep voltammetry applied to investigate the electrocatalytical performances of the bare and modified GCEs for HER shown in Fig. 3. The current response of GCE/RGO toward hydrogen evolution ($2H^+ + 2e^- \rightarrow H_2$) was larger than that of the bare GCE, suggesting that the electrochemical active sites of GCE increased by RGO surface modification, which results from the excellent conductivity, large surface area, and remaining oxygen-related defects of RGO film.

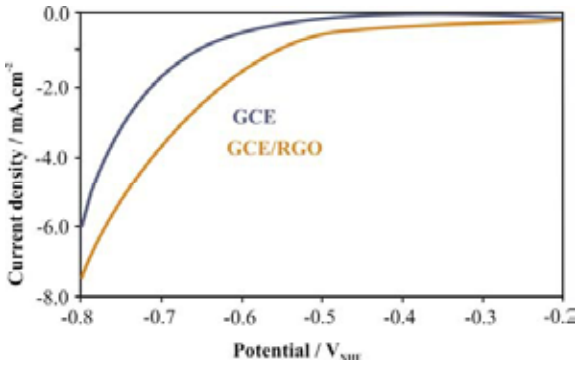


Fig. 3. Lineer sweep voltammograms of GCE and GCE/RGO recorded in 0.5M H_2SO_4 (ν=10mV s^{-1})

The LSV peak current on GCE/RGO/Au hybrid electrode is even stronger than those on GCE/RGO (Fig 4). There is an apparent difference between current density for GCE/RGO and GCE/RGO/Au hybrid electrode at the same voltage. As a result, we can say that the conductivity and surface area of the RGO–Au composite film significantly improved compared to the pure graphene film.

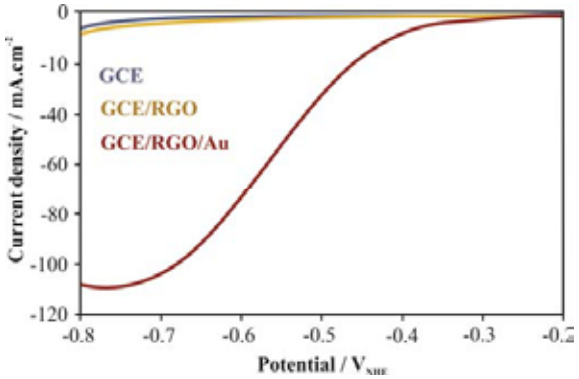


Fig. 4. Lineer sweep voltammograms of GCE, GCE/RGO and GCE/RGO/Au nanoparticles recorded in 0.5M H_2SO_4 (ν=10mV s^{-1})

Tafel curves also recorded in order to compare the electrocatalytic activity of the electrodes (Fig. 5). The Tafel slopes of the electrodes were then compared, which were obtained by fitting the linear portions of the polarization curves with the Tafel equation,

$\eta = b \log j + a$

where j is the current density and b is the Tafel slope. A lower Tafel slope corresponds to more favourable HER kinetics. The Tafel slope of bare GCE was 249 mV/dec, which was higher than GCE/RGO (178 mV/dec) indicating that the RGO layer enhance the hydrogen evolution. Figure 5 clearly shows that the GCE/RGO/Au hybrid electrode had better activity for the hydrogen evolution reaction; the Tafel slope was reduced to 136 mV/dec by the deposition of the Au nanoparticles on the RGO layer.

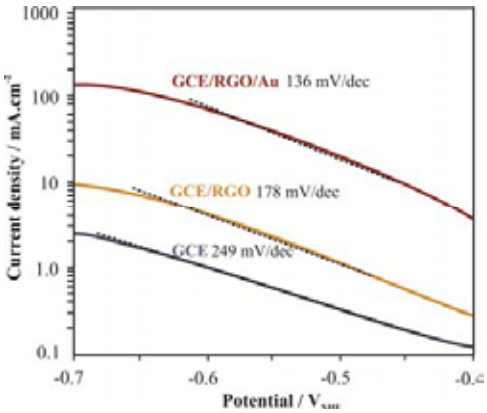


Fig. 5. Tafel polarization curves of GCE, GCE/RGO and GCE/RGO/Au nanoparticles recorded in 0.5M H_2SO_4 (v=1mV s^{-1}).

EIS analysis was used to further evaluate the HER performance of the electrodes. Figure 5 shows the typical EIS of bare GCE, GCE/RGO and GCE/RGO/Au hybrid electrodes acquired in 0.5 M H_2SO_4 electrolyte solution at constant applied potential (-0.55V).

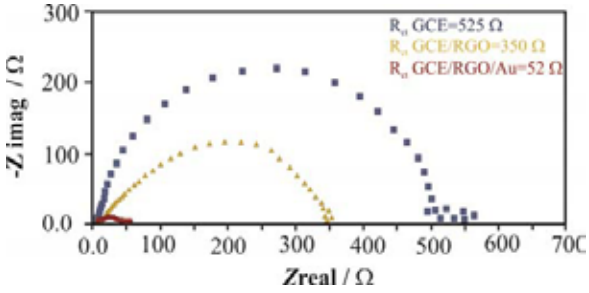


Fig. 6. The EIS measurements (Nyquist plots) of GCE, GCE/RGO and GCE/RGO/Au nanoparticles recorded in 0.5M H_2SO_4 at -0.55V, frequency range:0.1Hz-100kHz

RGO-Au modified electrode has higher electron conductivity than RGO modified and bare GCE, likely due to its smaller charge transfer (Rct) value. The smaller surface area and poor electron conductivity of the bare GCE lead to higher Rct value and higher resistance. Meanwhile, electron conductivity of RGO was found to be enhanced in presence than in the absence of Au nanoparticles. All these results clearly suggest that the conductivity of the Au nanoparticles and RGO may lead to faster electron transfer and faster hydrogen evolution at the electrode surface.

4. Conclusions

In this study we have investigated the electrocatalytic hydrogen production performance of glassy carbon electrode (GCE) modified by reduced graphene oxide (RGO) and Au nanoparticles, denoted as GCE/RGO/Au hybrid electrode. The hybrid electrode showed enhanced HER behaviour because of the high surface area and high conductivity of RGO/Au composite film.

Acknowledgements:
This research has been supported by Aksaray University Scientific Research Projects Coordination Unit (ASU-BAP, 2016-034).

References

1. Yang Y, Han C, Jiang B, Iocozzia J, He C, Shi D, Jiang T, Lin Z. Graphene-based materials with tailored nanostructures for energy conversion and storage. Mater Sci Eng R. 2016;102:1-72.

2. Gupta B, Melvin AA, Matthews T, Dash S, Tyagi AK. TiO_2 modification by gold (Au) for photocatalytic hydrogen (H_2) production. Renew Sust Energ Rev. 2016;58:1366-1375.
3. Ma J, Liu L, Chen Q, Yang M, Wang D, Tong Z, Chen Z. A facile approach to prepare crumpled CoTMPyP/electrochemically reduced graphene oxide nanohybrid as an efficient electrocatalyst for hydrogen evolution reaction. Appl Surf Sci. 2017;399:535-541
4. Lee C, Wei X, Kysar DJW, Hone J. Measurement of the elastic properties and intrinsic strength of monolayer graphene. Science, 2008; 321(5887):385–388.

Performance Analysis of a Conceptual Hydrogen Fueled Ramjet Engine: Exergetic Perspective

Yasin Söhret[1], Selcuk Ekici[2], T. Hikmet Karakoc[2]
[1]Suleyman Demirel University, Keciborlu Vocational School, Aircraft Technology Program, TR-32700, Isparta, Turkey
[2]Anadolu University, Faculty of Aeronautics and Astronautics, Department of Airframe and Powerplant Maintenance, TR-26470, Eskisehir, Turkey
Email: ysohret@gmail.com, selcukekici@gmail.com, hikmetkarakoc@gmail.com

Abstract
Ramjet engines are widely used devices in defense industry and military applications. A ramjet engine's working is thermodynamically based on Brayton cycle. It is known that exergy analysis is a beneficial tool to assess energy devices regarding operational conditions. In the current study, performance of a hydrogen fueled ramjet engine is evaluated by means of exergy. The introduced methodology to the best of authors' knowledge and the results obtained from the present study can be useful for anybody who is interested in thermal sciences and aero-propulsion technologies.

Keywords: Alternative fuel; cycle analysis; exergy; hydrogen; ramjet; thermodynamics.

1. Introduction

Depending on the increment of energy consumption in the world, fossil fuel reservoirs' depletion is a well-known fact. This situation forces humankind to utilize the current energy sources efficiently and to seek alternative energy sources. As a result of many researches that have been pursued for a long time, numerous alternative energy resources are revealed [1-5]. Hydrogen is one of the hottest prospect of energy resources for the future. Hydrogen can be provided from many organic compounds on the earth with the help of chemical methods in spite of its being unobtainable as a pure substance. Petroleum-derived fuels and organic wastes are the most commonly preferred reservoirs to produce hydrogen [6-8].

Recent studies on this field of science have presented evidences as to how hydrogen will fill the gap in providing energy demand in the future. The most promising progress until today has been achieved by taking benefit from hydrogen as a main fuel in combustion systems as well as in fuel cell technology using hydrogen. Being environment-friendly and clean combustion are prominent specifications of the hydrogen as a main fuel compared to conventional fuels such as gasoline, diesel, fuel-oil and so on [9]. The major problem arising out of fossil fuel combustion is the threat of facing environmental issues. From this perspective, hydrogen is considered as a certain solution to reduce especially carbon emissions in addition to unburned hydrocarbon formation. In this framework, various energy production system fueled with hydrogen has recently been investigated by many researchers [10-14]. Supplying energy to aerial vehicles and space crafts by hydrogen burning engines is particularly discussed. Few papers deal with peaks and falls of hydrogen utilization in aero engines. The storage and carriage of hydrogen as a fuel are the most prevalent problems with respect to safety flight conditions. The chemical behavior of the hydrogen to make compound displays an obstacle to overcome storage. However, a remarkable development of the liquefied hydrogen fuel storage has recently been succeeded [15, 16]. Xu et al. [15] discuss design and analysis of a liquid hydrogen fuel tank for a high-altitude long-endurance (HALE) type aircraft. In the study, the liquefied hydrogen fuel tank was asserted to be light weighted and well insulated to prevent heat losses. Thermal performance analysis and structural assessment of various material preferences are discussed in details. According to the results, liquefied hydrogen fuel storage is found to be feasible for aerospace applications. In another research [16], storage opportunity of the liquefied hydrogen fuel for long time space missions has been proven. At the end of the study it was found that conserving the liquefied hydrogen in the tank without evaporation during the space mission is possible. Ogrodnikov et al. [18] presents details of a hydrogen fueled scramjet in their studies.

Former studies have shown that utilizing hydrogen has been considered as a fuel for aerial vehicles and space crafts for a long time. The earliest accessible research in this field was carried out within the scope of a secret project of NASA in 1950s. However, technical limitations of liquefied hydrogen storage led to terminate the project [17]. Fortunately, state of the art enables us to consider liquefied hydrogen as a propellant fuel seriously. Liquefied hydrogen powered aerial vehicles have been studied more intensely as days pass. Ogorodnikov et al. [18] present conception and experiments of a hydrogen fueled scramjet in their studies. The study discusses design process of the scramjet in addition to results obtained from ground and preflight tests. Experimental knowledge including instrumentation and data processing is also given in details. Ref. [19] deals with the exergy analysis of a supersonic ramjet engine filled with conventional fuel. This parametric study presents the exergy value variation depending on

variable cross-section area and temperature of inlet flow. In Ref. [20], the researchers make use of exergetic approach to estimate specific impulse of a ramjet engine parametrically. Similar effort has been made for aircrafts as well as ramjets and space crafts [12]. In this framework, exergy-based sustainability and performance of a hydrogen fueled turbofan engine is discussed in Ref. [21].

Regarding former studies, liquefied hydrogen is a considerably feasible fuel for aerial vehicles. From this point of view, authors intend to introduce performance analysis of a conceptual designed and liquefied hydrogen fueled ramjet engine in terms of exergy. In the current study, exergy analysis of a hydrogen fueled ramjet engine is presented to the literature for the first time besides highlighting significance of the hydrogen as a propellant fuel.

2. Methods and Materials

2.1. Basics of Ramjet Engine

The ramjet engine is an aero-thermodynamic duct and contains no rotating component, either a compressor or a turbine. Any type of a ramjet engine, whether subsonic or supersonic, is comprised of an inlet, combustion zone and a nozzle. At this point, the inlet section is similar to a divergent duct and it implements subsonic compression of the air. The combustion zone of the ramjet engine where air and fuel react chemically is an advanced passage containing fuel spray nozzles. The nozzle component of the ramjet engine can be not only convergent type but also convergent-divergent type. While the air is passing through the inlet, it loses kinetic energy and pressure of the air increases as well as compression process at any type of a gas turbine engine. Then pressurized air reacts to the fuel exothermically within the combustion zone. As a result of the combustion process, energy carrying gas runs to the ambient through the nozzle. The aerodynamic structure of the nozzle leads to generate thrust. A schematic illustration of a supersonic ramjet engine is shown in Fig. 1. Fundamental design parameters of the conceptual ramjet engine are also given in Table 1. It is a known fact that performance of the ramjet engines is quite good under supersonic flight conditions in comparison with subsonic conditions [22-24]. Thus, flight Mach number of the ramjet engine was designated to be higher than 1.2.

Cycle analysis of the ramjet engine was conducted according to design parameters given in Table 1. Methodology used for cycle analysis can be found in Refs. [23, 24].

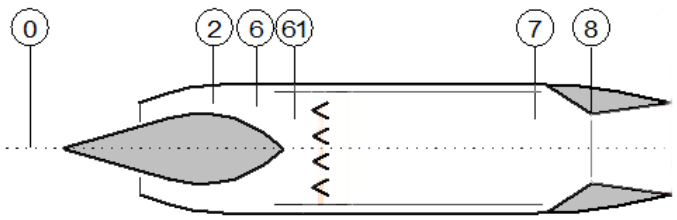


Fig. 1. Schematic demonstration of a supersonic ramjet engine

Table 1. Some major design parameters of the conceptual hydrogen fueled ramjet engine

Parameter	Value
Flight Mach number	2.32
Thrust	3.66 kN
Diffusor pressure ratio	0.97
Burner efficiency	0.98
Pressure loss	8.16%
Nozzle cooling air rate	4%

2.2. Exergetic Perspective

Exergy analysis of thermodynamics reveals achievable limitations of the system under operating conditions. In this framework, fundamental equations should be written to evaluate any system. Hence, mass and energy conservation statements for any steady-state system are expressed as follows [25-27]:

$$\sum \dot{m}_{in} = \sum \dot{m}_{out} \quad (1)$$

$$\dot{Q} - \dot{W} + \sum \dot{m}_{in}[h_{in} + (V_{in}^2/2) + gz_{in}] - \sum \dot{m}_{out}[h_{out} + (V_{out}^2/2) + gz_{out}] = 0 \quad (2)$$

Here, $\dot{m}$ is mass flow rate, whereas $\dot{Q}$, $\dot{W}$, h, $V^2/2$, and gz represent heat transfer rate, work rate, enthalpy, kinetic and potential energies. An exergy balance statement for a steady-state system may be arranged as following [28]:

$$\dot{E}_F - \dot{E}_P - \dot{E}_D - \dot{E}_L = 0 \tag{3}$$

where $\dot{E}_F$ and $\dot{E}_P$ denote exergy rates of fuel and product respectively, while $\dot{E}_D$ and $\dot{E}_L$ mean exergy destruction and exergy loss rates within the system. Exergy is also compiled of physical, chemical, kinetic and potential components, neglecting nuclear, magnetic, electrical and surface tension effects. Therefore, the components of exergy are physical, chemical, kinetic and potential [25-28]:

$$\dot{E} = \dot{m}(e^{PH} + e^{CH} + e^{KN} + e^{PT}) \tag{4}$$

Physical exergy is expressed as [27, 28]:

$$e^{PH} = c_p(T - T_0) - T_0\left[c_p \ln(T/T_0) - R \ln(P/P_0)\right] \tag{5}$$

The chemical exergy of a gas mixture and a liquid fuel are calculated by following expressions respectively [27, 28]:

$$\bar{e}^{CH}_{mix} = \sum x_k \bar{e}^{CH}_k + \bar{R}T_0 \sum x_k \ln x_k \tag{6}$$

$$e^{CH}_f = LHV\left[1.0401 + 0.1728\frac{h}{c} + 0.0432\frac{o}{c} + 0.2169\frac{s}{c}\left(1 - 2.0628\frac{h}{c}\right)\right] \tag{7}$$

Kinetic and potential exergies are equal to kinetic potential energies and they are stated as follows [25-28]:

$$e^{KN} = V^2/2 \tag{8}$$

$$e^{PT} = gz \tag{9}$$

In addition, the change of sun position during the experiments cannot be compensated since the setup is manually tracking the sun light. The accumulated charges during the hydrogen production experiment at 1.7 V are calculated to be 89.9 C and 108.1 C, respectively for concentrated light and non-concentrated light. Overall, under concentrated light, the hydrogen production rates increase considerably showing the effect of photocurrent contribution. Further studies for the tandem-semiconductors to increase the photo-absorption are under investigation.

In exergy analysis, some measures are used to evaluate performance of the system. These are exergy efficiency, improvement potential, relative irreversibility, fuel depletion rate and lack of productivity. Exergy efficiency, first of these measures, is defined as [29]:

$$\varepsilon = \frac{\dot{E}_P}{\dot{E}_F} \tag{10}$$

The potential of improvement of the system is the rate of exergy destruction minimization within the system [30]:

$$I\dot{P} = \dot{E}_D(1 - \varepsilon) \tag{11}$$

Relative irreversibility enables us to see the percentage of exergy destruction within the system component [31]:

$$\chi = \frac{\dot{E}_D}{\sum \dot{E}_D} \tag{12}$$

Fuel depletion ratio is an indicator of destruction rate of exergetic fuel within the system [31]:

$$\delta = \frac{\dot{E}_D}{\sum \dot{E}_F} \tag{13}$$

Lack of productivity, the last one of these measures, is stated as [31]:

$$\xi = \frac{\dot{E}_D}{\sum \dot{E}_P} \tag{14}$$

Equation set is used to perform exergy analysis of ramjet engine and its components are derived from explained methodology and summarized in Table 2 in accordance with following assumptions:

- Ramjet engine was operated under steady-state conditions.
- The air and combustion gases acted perfect gas behavior.
- The provided fuel to the ramjet engine was liquefied hydrogen.
- The combustion reaction was considered to be complete.
- Overall ramjet engine and its components were adiabatic.
- The composition of the combustion air was 75.67% nitrogen, 20.35% oxygen, 0.0345% carbon dioxide, 3.03% water vapor and 0.8255% other ingredients [25].

Table 2. Derived exergy balance statements for the ramjet engine and its components

Control volume	Exergy balance statement
Inlet	$\dot{E}_D = \dot{E}_6 - \dot{E}_1$
Combustion Zone	$\dot{E}_D = \dot{E}_{61} - (\dot{E}_7 - \dot{E}_6)$
Nozzle	$\dot{E}_D = \dot{E}_8 - \dot{E}_7$
Ramjet Engine	$\dot{E}_D = \dot{E}_{61} - (\dot{E}_8 - \dot{E}_1)$

3. Results and Discussion

In the current study, exergy which helps performance evaluation of a hydrogen fueled ramjet engine is presented. In Table 3, thermodynamic properties of working fluid at engine stations are given. Data given in Table 3 is obtained at the end of the cycle analysis.

Table 3. Thermodynamic measures at the ramjet engine stations

Station #	Mass flow rate (kg.s^{-1})	Pressure (kPa)	Temperature (K)
0	-	101.325	288.150
1	7.190	101.325	593.100
2	7.190	1159.538	593.100
6	6.902	1314.000	593.100
61	0.926	101.325	20.400
7	6.995	1032.951	1950.000
8	7.283	1032.951	1899.690

Performance evaluation of the engine is performed using first and second laws of thermodynamics on the basis of cycle data. Exergy analysis results are summarized in Table 4.

Table 4. Results obtained from exergy analysis of the ramjet engine

Component	$\dot{E}_{D,k}$ (MW)	ε_k (%)	$\dot{IP}_k$ (MW)	χ_k (%)	δ_k	ξ_k
Inlet	35.752	3.855	34.374	20.517	0.194	3.485
Combustion Zone	106.761	7.627	98.619	61.266	0.579	10.406
Nozzle	31.745	0.038	31.733	18.217	0.172	3.094
Ramjet Engine	105.340	8.856	96.011			

As shown in Fig. 2 in addition to Table 4, exergy efficiencies of inlet, combustion zone and nozzle are 3.88%, 7.62%, 0.03% and 8.85%, respectively. It is clearly understood from Table 4 and Fig. 3, highest exergy destruction occurs during the combustion process of the liquefied hydrogen with the compressed air. However the exergy destruction rates within the inlet and nozzle are approximately close. On the other hand, combustion zone of the ramjet engine is found to be origin of improvement compared to other components of the ramjet engine. As a result of this situation, the combustion zone has the highest relative irreversibility whereas the lowest relative

irreversibility is determined within the nozzle with the rate of 18.12%. Similar comment can be asserted for fuel depletion rates and lack of productivity of components. Fig. 4 is also plotted for a better understanding.

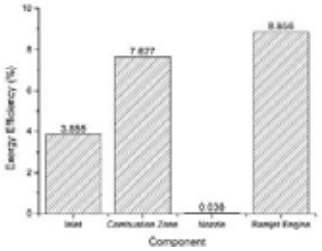


Fig. 2. Exergy efficiencies of the ramjet engine and its components

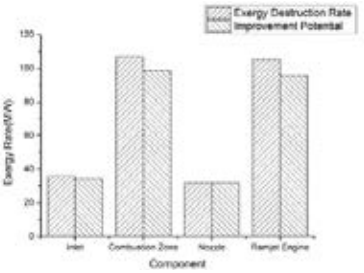


Fig. 3. Potential Exergy destruction and improvement rate distribution of the engine and its components

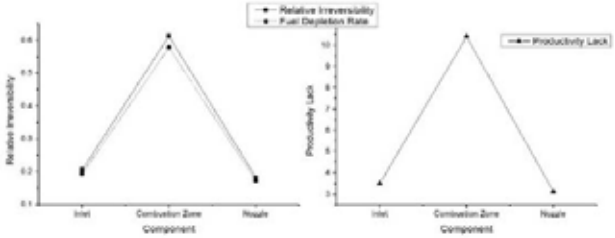


Fig. 4. Some exergy measures of ramjet engine components

4. Conclusions

The present study deals with exergy analysis of a ramjet engine. Being different from previous studies [19, 20], numerical data is used for this purpose. Additionally, a ramjet engine filled with hydrogen fuel is examined with the aid of exergy for the first time in the accessible literature. Therefore, this study and the introduced approach to the best of authors' knowledge may be beneficial for anybody who is interested in thermal science, alternative fuel and aero-propulsion technologies.

Acknowledgement

This study was carried out in the framework of a project financed by Anadolu University under contract number of 1404F237. Authors are thankful to Anadolu and Suleyman Demirel Universities of Turkey for their support.

References

1. K. Shivarama Krishna, K. Sathish Kumar, A review on hybrid renewable energy systems, Renewable and Sustainable Energy Reviews, 52, 2015, pp. 907-916, doi: 10.1016/j.rser.2015.07.187.
2. Richa Kothari, V.V. Tyagi, Ashish Pathak, Waste-to-energy: A way from renewable energy sources to sustainable development, Renewable and Sustainable Energy Reviews, 14 (9), pp. 3164-3170, doi: 10.1016/j.rser.2010.05.005.
3. S. Keleş, S. Bilgen, Renewable energy sources in Turkey for climate change mitigation and energy sustainability, Renewable and Sustainable Energy Reviews, 16 (7), 2012, pp. 5199-5206, doi: 10.1016/j.rser.2012.05.026.

4. N.L. Panwar, S.C. Kaushik, Surendra Kothari, Role of renewable energy sources in environmental protection: A review, Renewable and Sustainable Energy Reviews, 15 (3), 2011, pp. 1513-1524, doi: 10.1016/j.rser.2010.11.037.
5. Ibrahim Dincer, Renewable energy and sustainable development: a crucial review, Renewable and Sustainable Energy Reviews, 4 (2), 2000, pp. 157-175, doi: 10.1016/S1364-0321(99)00011-8.
6. Ibrahim Dincer, Canan Acar, Review and evaluation of hydrogen production methods for better sustainability, International Journal of Hydrogen Energy, 40 (34), 2015, pp. 11094-11111, doi: 10.1016/j.ijhydene.2014.12.035.
7. Suman Dutta, A review on production, storage of hydrogen and its utilization as an energy resource, Journal of Industrial and Engineering Chemistry, 20 (4), 2014, pp. 1148-1156, doi: 10.1016/j.jiec.2013.07.037.
8. Ibrahim Dincer, Green methods for hydrogen production, International Journal of Hydrogen Energy, 37 (2), 2012, pp. 1954-1971, doi: 10.1016/j.ijhydene.2011.03.173.
9. Sunita Sharma, Sib Krishna Ghoshal, Hydrogen the future transportation fuel: From production to applications, Renewable and Sustainable Energy Reviews, 43, 2015, pp. 1151-1158, doi: 10.1016/j.rser.2014.11.093.
10. H. Fayaz, R. Saidur, N. Razali, F.S. Anuar, A.R. Saleman, M.R. Islam, An overview of hydrogen as a vehicle fuel, Renewable and Sustainable Energy Reviews, 16, 8, 2012, pp. 5511-5528, doi: 10.1016/j.rser.2012.06.012.
11. S. Verhelst, Recent progress in the use of hydrogen as a fuel for internal combustion engines, International Journal of Hydrogen Energy, 39, 2, 2014, pp. 1071-1085, doi: 10.1016/j.ijhydene.2013.10.102.
12. Bhupendra Khandelwal, Adam Karakurt, Paulas R. Sekaran, Vishal Sethi, Riti Singh, Hydrogen powered aircraft: The future of air transport, Progress in Aerospace Sciences, 60, 2013, pp. 45-59, doi: 10.1016/j.paerosci.2012.12.002.
13. B.L. Salvi, K.A. Subramanian, N.L. Panwar, Alternative fuels for transportation vehicles: A technical review, Renewable and Sustainable Energy Reviews, 25, 2013, pp. 404-419, doi: 10.1016/j.rser.2013.04.017.
14. Pooya Azadi, Oliver R. Inderwildi, Ramin Farnood, David A. King, Liquid fuels, hydrogen and chemicals from lignin: A critical review, Renewable and Sustainable Energy Reviews, 21, 2013, pp. 506-523, doi: 10.1016/j.rser.2012.12.022.
15. Weiqiang Xu, Qianqian Li, Minjie Huang, Design and analysis of liquid hydrogen storage tank for high-altitude long-endurance remotely-operated aircraft, International Journal of Hydrogen Energy, 40, 46, 2015, pp. 16578-16586, doi: 10.1016/j.ijhydene.2015.09.028.
16. Xi-wan Sun, Zhen-yun Guo, Wei Huang, Passive zero-boil-off storage of liquid hydrogen for long-time space missions, International Journal of Hydrogen Energy, 40, 30, 2015, pp. 9347-9351, doi: 10.1016/j.ijhydene.2015.05.184.
17. http://history.nasa.gov/SP-4404/ch8-1.htm, Accessed on March 2, 2016.
18. Donat A. Ogorodnikov, Viacheslav A. Vinogradov, Yurii M. Shikhman, Vitaliy N. Strokin, Russian research on experimental hydrogen-fueled dual-mode scramjet: Conception and preflight tests, Journal of Propulsion and Power, 17 (5), 2001, 1041-1048, doi: 10.2514/2.5842.
19. A. F. Latypov, Exergy analysis of ramjet. Thermophysics and Aeromechanics, 16 (2), 2009, pp. 303-313, doi: 10.1134/s0869864309020152.
20. A. F. Latypov, Exergy method for estimating the ramjet specific impulse, Thermophysics and Aeromechanics, 20(5), 2013, pp. 539-552, doi:10.1134/s0869864313050023
21. Nevzet Kaya, Onder Turan, Adnan Midilli, and T. Hikmet Karakoc, Exergetic sustainability ımprovement potentials of a hydrogen fuelled turbofan engine uav by heating ıts fuel with exhaust gasses, International Journal of Hydrogen Energy, in press, doi: 10.1016/j.ijhydene.2015.08.089.
22. Donald S. Fry, A century of Ramjet Propulsion technology evolution, Journal of Propulsion and Power, 20 (1), 2004, pp. 27-58, doi: 10.2514/1.9178.
23. Ahmed F. El-Sayed, Aircraft Propulsion and Gas turbine engines, CRC Press: USA, 2008.
24. Jack D. Mattingly, Elements of propulsion: Gas turbines and rockets, AIAA Education Series, AIAA: USA.
25. Moran, M. J., Shapiro, H. N., Boettner, D. D., M. B. Bailey, Fundamentals of engineering thermodynamics. John Wiley & Sons, 2010.
26. Ibrahim Dincer, Marc A. Rosen, Exergy: Energy, Environment and Sustainable Development, Elsevier, 2012.
27. T. J. Kotas, the Exergy Method of Thermal Plant Analysis. Anchor Brendon Ltd, 1985.
28. A. Bejan, G. Tsatsaronis, M. Moran, Thermal design and optimization, John Wiley & Sons Inc, 1995.
29. G. Tsatsaronis, Recent developments in exergy analysis and exergoeconomics, International Journal of Exergy, 5(5-6), 2008, pp. 489-499, doi: 10.1504/ijex.2008.020822.
30. W. Van Gool, Exergy analysis of industrial processes, Energy, 17, 1992, pp. 791-803, doi: 10.1016/0360-5442(92)90123-h.

31. J.Y. Xiang, M. Cali, and M. Santarelli, Calculation for physical and chemical exergy of flows in systems elaborating mixed-phase flows and a case study in an IRSOFC plant, International Journal of Energy Research, 28, 2004, pp. 101-115, doi: 10.1002/er.953.

Hydrogen Storage Capacity of Palladium Doped Multi-Walled Carbon Nanotubes Prepared via Supercritical CO_2 Deposition Method

Ebru Erünal[1], Fatma Ulusal[2], Deniz Kaya[3], Mustafa Y. Aslan[3], Bilgehan Güzel[2], Deniz Üner[3]
[1]Chemical Engineering Department, Çukurova University, Adana, Turkey
[2]Chemistry Department, Çukurova University, Adana, Turkey
[3]Chemical Engineering Department, M.E.T.U., Ankara, Turkey
Email: eerunal@cu.edu.tr, fatma_ulusal@hotmail.com, deniz.kaya_01@metu.edu.tr, mustafay@metu.edu.tr, bilgehan@cu.edu.tr, uner@metu.edu.tr

Abstract
The crucial role of hydrogen storage in energy technologies has recently increased the interest in Carbon Nanotubes which are known to be promising materials with their hydrogen storing capacities with respect to their high surface-to-volume ratios, high stabilities, and light weights. However, their hydrogen storage capacities still should be improved for moderate pressure and ambient temperature applications. One of the most common strategies to enhance hydrogen storage capacity of carbon nanotubes is using them with transition metals. In this work, Pd doped Multi-Walled Carbon Nanotubes were prepared via supercritical carbondioxide deposition method in order to obtain a well dispersed nanoparticle material. Temperature programmed desorption (TPD) and reduction (TPR) experiments were conducted. TPR measurements revealed an initial Pd hydride decomposition. Moreover, adsorption and desorption hysteresis at ambient temperature were also measured. The cumulative adsorption was found as 737 μmole/ g sample while TPD measurements showed that 656 μmole hydrogen storage capacities were a result of Pd doping on these materials. This shows that Pd doping enhanced hydrogen capacity of carbon nanotubes. Moreover, Pd doping affects the desorption ability of multiwall carbon nanotubes.

Keywords: Hydrogen storage; multi-walled carbon nanotubes; temperature programmed reduction; temperature programmed desorption.

1. Introduction

Hydrogen Technologies, which enable the usage of hydrogen as one of the promising renewable and clean energy sources, are of great interest due to the decrease in fossil energy resources and also the environmental concerns related to fossil fuels [1,2]. In order to provide sustainability of Hydrogen Energy, efficient and safe storage conditions of Hydrogen are considered as one of the most important issues because of the high cost and risks of these technologies [3-7]. Currently, the disadvantages of conventional storage technologies increase the interest in nanomaterials which can be a good solution for hydrogen storage at ambient temperatures and moderate pressures rather than high cost high-pressure cryogenic systems. Carbon nanotubes (CNTies) are known as good candidates for this purpose with their low mass density, high surface area, narrow and nanometer pore size distribution [8-13]. However, when considering ambient temperatures and moderate pressures, it is necessary to improve their hydrogen adsorbing capacities. Doping certain transition metals on CNTies is one of the effective methods to improve these properties [14-17]. When compared to other transition metals, palladium (Pd) shows a strong hydrogen adsorption performance for hydrogen when dispersed on CNTies. It is attributed to the spillover process which is described in literature as the dissociation of dihydrogen on the metal, resulting in migration of hydrogen atoms through the metal particles and diffusion on the carbon nanotube supports [18-21]. Therefore, having uniformly dispersed Pd nanoparticles on Carbon Nanotube supports is very important to observe this phenomenon. Hence, the degree of dispersion and consequently particle size distribution on carbon nanotubes is directly dependent on preparation method of these materials [21]. So far different methods were used to synthesize similar methods [22,23]. Supercritical carbondioxide ($scCO_2$) deposition method is relatively new, environmentally friendly and powerful method to prepare well dispersed nanoparticles among these techniques [24,25]. It is basically the dissolution of a metal complex in a supercritical fluid, followed by adsorption or sorption of the metal complex onto the support, and finally, conversion of the adsorbed complex to metal species with either chemical or thermal reduction. In this study Pd doped Multi Wall Carbon Nanotubes (MW-CNTies) were prepared via $scCO_2$ deposition method in order to enhance hydrogen storage capacity of MW-CNTies at moderate pressure and ambient temperature applications. In order to see the hydrogen storage capacity adsorption/desorption tests of Pd/MW-CNTies at room temperature together with Temperature Programmed Reduction (TPR) and Desorption (TPD) tests were conducted.

2. Experimental Study

2.1 Materials

All materials were used without further purification. Multiwall Carbon Nanotube (MW-CNT) was purchased from Sigma-Aldrich with a purity of ≥95% (average dimensions: O.D.xL (6-9nm x5μm), diameter (mode, 5.5 nm; median, 6.6 nm). In order to synthesize the Pd precursor, Palladium chloride and 2,2'bipyridyl materials were purchased from ABCR GmbH (both with a purity of 99%). For adsorption experiments, ultrahigh pure grade (99.999%) of Hydrogen (H_2), Argon (Ar) and Helium (He) gases (purchased from Linde) were used.

2.2 SCF Deposition of 2,2'bipyridyldicholoropalladium(II) Precursors

The deposition of Pd precursors on MW-CNTies was carried out with 2,2'bipyridyldicholoropalladium(II) ($Pd(PyrCl_2)$) precursor which was synthesized from 0.312 g $PdCl_2$ in 0.5 ml HCl (%35) with vigorous stirring at 70°C. As 0.529 g of 2,2'bipyridyl was added to the solution a yellow precipitate formed. The precipitate was filtered, washed with ethanol solution and dried overnight to obtain $Pd(PyrCl_2)$. Chemical formula of the precursor is shown in Fig.1. The materials were analyzed via IR spectra (Perkin-Elmer RX-1) to verify the targeted structure was obtained.

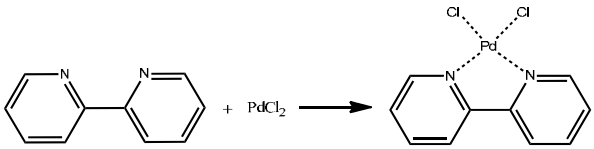


Fig.1. Synthesis reaction of $Pd(PyrCl_2)$ precursor from 2,2'bipyridyl and $PdCl_2$

The high pressure, stainless steel reactor with a 100 mL inner volume where the deposition reaction took place is shown in Fig.2. The obtained $Pd(PyrCl_2)$ precursor was dissolved in supercritical CO_2 according to the following procedure: 150 mg MW-CNT and 25 mg $Pd(PyrCl_2)$ were added to the reactor in order to obtain 5% of Pd/MW-CNT ratio. The system was incrementally heated up to 353 K by a circulating heater/cooler. 20.6 MPa (3000 psi) CO_2 gas was charged to the reactor with an Isco 260D syringe pump and kept at this condition for 1 h. Then the reactor pressure was decreased to 13.8 MPa. A 10 ml mixture of H_2 (1.03 MPa) and CO_2 gas was prepared in a high pressure vessel of 20.6 MPa capacity and sent to the reactor for chemical reduction of Pd/MW-CNT nanoparticles. The stirring rate was kept around 1100 rpm. After stirring for 5 hours, the temperature of the reactor was allowed to reach room temperature; and the supercritical solution was slowly released.

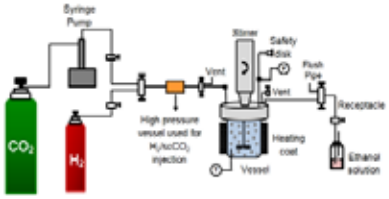


Fig.2. Supercritical CO_2 deposition reactor system

The prepared Pd/MWCNT particles were washed and dried. The synthesized nanoparticles were calcined at 300°C for 2 hours in order to eliminate the excess of the precursor. The quantitative analysis of palladium was done by ICP-OES (Perkin Elmer 2100 DV) while the surface morphology was analyzed with XRD (Rigaku Miniflex CuK_α, λ=0.154nm) and TEM (Jeol 2100F 200kV RTEM).

2.3 H_2 Adsorption-Desorption Experiments at Room Temperature

Hydrogen chemisorption experiments were performed in a home-built high-vacuum glass manifold equipped with a MKS Baratron Gauge (up to 100 Torr pressure), high vacuum Teflon valves (ACE Glass) and a vacuum pump (Pfeiffer vacuum pump up to 10^{-9} Torr). The general characteristics of the experimental set up and the measurements are described in detail elsewhere [26,27]. 0.10 g Pd doped MWCNT samples were kept under vacuum overnight in order to remove potential adsorbed impurities. Then, hydrogen adsorption isotherms for each

sample were obtained in 0.5–100 Torr pressure range. Each time the sample was exposed to 10 min H_2 in order to achieve thermal and chemical equilibrium in each pressure uptake.

2.4 Temperature Programmed Reduction and Desorption Tests

Temperature Programmed Reduction (TPR) and Temperature Programmed Desorption (TPD) analysis of Pd/MW-CNT were carried out on Micromeritics 2720 Instrument. H_2-TPR experiments of Pd/MW-CNT (ca. 20 mg) were performed in the presence of 25 ml/min, 10% H_2 balance Ar flow up to 880°C with a temperature ramp of 5°C/min. After H_2-TPR profiles were obtained, the samples were cooled down to room temperature with a flow of 10 % H_2 balance Ar. TPD experiments were performed immediately after cooling of the samples up to room temperature. TPD profiles of the samples were recorded in the presence of He flow up to 880°C with a temperature ramp of 5°C/min.

3. Results and Discussion

3.1 The characterization of Pd/MW-CNT Materials

The palladium load was determined around 3.75% with ICP-OES measurements. XRD results given in Fig.3 show three distinct peaks around 40.3°, Pd(111); 46.9°, Pd(200) and 68.4°, Pd (220), designating the metallic Pd formation in the material [28]. The MW-CNT peaks [29] around 26°; (002) and 43°; (100) are also detected. Moreover, the size of nanoparticles calculated via Sherrer equation according to Pd(111) peak suggests that nanoparticles size are around 10.5 nm.

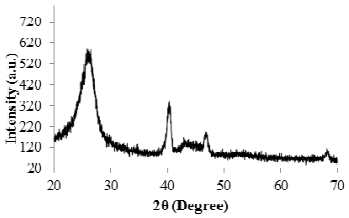


Fig.3. XRD measurements of synthesized Pd/MW-CNT

The homogeneous dispersion of nanoparticles with a broad size distribution was also verified with 100 nm TEM image of the material given in Fig.4. Material size distribution was determined between 10-20 nm range.

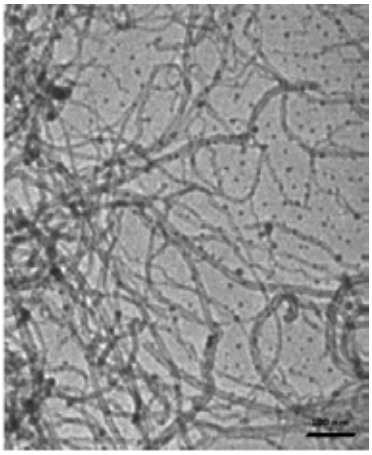


Fig.4. TEM image of synthesized Pd/MW-CNT at 100 nm

3.2 Hydrogen Uptake and Storage Capacity

Room temperature hydrogen adsorption and desorption of Pd/MW-CNTies experiment results are shown in Fig.5. According to adsorption experiments, cumulative hydrogen adsorption was calculated around 737 µmole/ g sample. This result already suggests enhancement of hydrogen adsorption capacity of undoped MW-CNTies from 44 µmole.

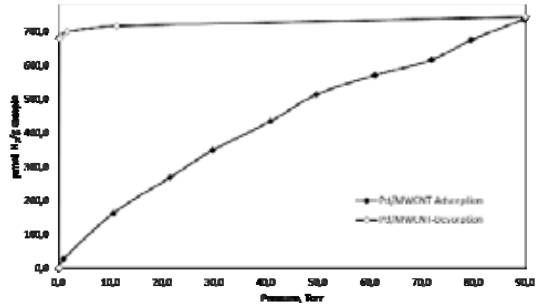


Fig.5. Hydrogen adsorption and desorption at room temperature on Pd/MW-CNT

Temperature programmed reduction data reveals a PdH decomposition around 50°C. According to this result the size of Pd nanoparticles is estimated between 10-20 nm which are consistent with XRD and TEM results. Moreover, hydrogen uptake of Pd is calculated around 577 μmole. According to the overall material, hydrogen uptake was calculated as 3 wt.%

4. Conclusions

Pd doped MW-CNTies were synthesized via supercritical deposition method and their hydrogen uptake and storage capacities were investigated. Both XRD analyses, TEM images and as well TPR results confirm that Pd nanoparticles are between 10-20 nm. Hydrogen uptake calculated from TPR experiments were around 577 μmole H/g material. The cumulative adsorption was found as 737 μmole/ g sample and 668 μmole of hydrogen storage capacity according to the desorption experiment at ambient temperature. As a conclusion, this study shows the enhanced storage capacity of Pd doped MW-CNTies which are found to be (undoped MW-CNTies) around 44 μmole/ g sample from ongoing investigations.

Acknowledgement

The authors acknowledge Prof. Dr. Ramazan Esen from Ç.U. Physics Department for XRD measurements. Financial support was provided by TUBITAK Project No.111T153 and BIDEB 2211-E.

Nomenclature

P	Pressure (Torr or MPa)
T	Temperature (°C or K)
wt.%	weight percent

Greek Letters

μ	Micro

Acronyms

CNT	Carbon Nanotube
IR	Infrared
MW-CNT	Multi-walled Carbon Nanotube
SCF	Supercritical Fluid
TEM	Transmission Emission Microscopy
XRD	X-Ray Diffraction

References

1. Schlapbach L, Züttel A. Hydrogen-storage materials for mobile applications. Nature 2001; 414:353-358.
2. Jena P. Materials for hydrogen storage: past, present, and future. J Phys Chem Lett. 2011; 2:206-211.
3. Corgnale C, Hardy BJ, Tamburello DA, Garrison SL, Anton DL. Acceptability envelope for metal hydride-based hydrogen storage systems. Int J Hydrogen Energy. 2012; 37:2812-2824.
4. Mpourmpakis G, Tylianakis E, Froudakis GE. Carbon nanoscrolls: a promising material for hydrogen storage. Nano Lett. 2007; 7:1893-1897.

5. Chen P, Zhu M. Recent progress in hydrogen storage. Mater Today 2008; 11:36-43.
6. Kumar A, Banerjee S, Pillai CGS, Bharadwaj SR. Hydrogen storage properties of $Ti_{2-x}CrVM_x$ (M: Fe, Co, Ni) alloys. Int J Hydrogen Energy 2013; 38:13335-13342.
7. Thomas KM. Hydrogen adsorption and storage on porous materials. Catal Today. 2007;120:389 -398.
8. Sakintuna B, Lamari-Darkrim F, Hirscher M. Metal hydride materials for solid hydrogen storage: a review. Int J Hydrogen Energy. 2007; 32:1121-1140.
9. Yürüm Y, Taralp A, Veziroglu TN. Storage of hydrogen in nanostructured carbon materials. Int J Hydrogen Energy. 2009; 34:3784-3798.
10. Lopez-Coral I, Irigoyen B, Juan A. Bonding in PdH_2 and Pd_2H_2 systems adsorbed on carbon nanotubes: Implications for hydrogen storage. Int J Hydrogen Energy. 2014; 39:8780-8790.
11. Lee SY, Park SJ. Effect of temperature on activated carbon nanotubes for hydrogen storage behaviors. Int J Hydrogen Energy. 2010; 35:6757-6762.
12. 12.Zhu H, Cao A, Li X, Xu C, Mao Z, Ruan D, Liang J, Wu D. Hydrogen adsorption in bundles of well-aligned carbon nanotubes at room temperature. Appl Surf Sci. 2001;178:50-55.
13. Ci L, Zhu H, Wei B, Xu C, Wu D. Annealing amorphous carbon nanotubes for their application in hydrogen storage. Appl Surf Sci. 2003;205:39-43.
14. Karousis N, Tsotsou GE, Evangelista F, Rudolf P, Ragoussis N, Tagmatarchis N. Carbon nanotubes decorated with palladium nanoparticles: synthesis, characterization, and catalytic activity. J Phys Chem C. 2008;112:13463-13469.
15. Kong J, Chapline MG, Dai H. Functionalized carbon nanotubes for molecular hydrogen sensors. Adv Mater. 2001;13:1384-1386.
16. Ang LM, Hor TSA, Xu GQ, Tung CH, Zhao SP, Wang JLS. Electroless plating of metals onto carbon nanotubes activated by a single-step activation method. Chem Mater. 1999;11:2115-2118.
17. Quinn BM, Dekker C, Lemay SG. Electrodeposition of noble metal nanoparticles on carbon nanotubes. J Am Chem Soc. 2005;127:6146-6147.
18. Yang RT, Wang Y. Catalyzed hydrogen spillover for hydrogen storage. J Am Chem Soc. 2009;131:4224-4226.
19. Lachawiec AJ, Qi GS, Yang RT. Hydrogen storage in nanostructured carbons by spillover: bridge-building enhancement. Langmuir. 2005;21:11418-11424.
20. Zacharia R, Kim KY, Fazle Kibria AKM, Nahm KS. Enhancement of hydrogen storage capacity of carbon nanotubes via spill-over from vanadium and palladium nanoparticles. Chem Phys Lett. 2005;412:369-375.
21. Banerjee S, Dasgupta K, Kumar A, Ruz P, Vishwanadh B, Joshi JB, Sudarsan V. Comparative evaluation of hydrogen storage behavior of Pd doped carbon nanotubes prepared by wet impregnation and polyol methods, Int journal of hydrogen energy. 2015; 40:3268-3276.
22. Liu S, Hao F, Liu P, Luo H. The influences of preparation methods on the structure and catalytic performance of single-wall carbon nanotubes supported palladium catalysts in nitrocyclohexane hydrogenation. RSC Adv. 2015;5: 22863–22868.
23. Nassr ABAA, Quetschke A, Koslowski E, Bron M, Electrocatalytic oxidation of formic acid on Pd/MWCNTs nanocatalysts prepared by the polyol method. Electrochim Acta. 2013;102:202– 211.
24. Zhang Y, Erkey C. Preparation of supported metallic nanoparticles using supercritical fluids: A review, J Supercrit Fluids. 2006;38:252-267.
25. Ulusal F, Darendeli B, Erunal E, Egitmen A, Guzel B. Supercritical Carbondioxide Deposition of -Alumina Supported Pd Nanocatalysts with New Precursors and Using on Suzuki-Miyaura Coupling Reactions. J of Supercrit Fluids. 2017; 127:111-120.
26. Uner D, Tapan NA, Ozen I, Uner. Oxygen adsorption on Pt/TiO_2 catalysts. Appl Catal A: Gen. 2003;251:225–234.
27. Üner D, Aslan MY. Using spilled over hydrogen in NH_3 synthesis over supported Ru catalysts. Catal Today.2016; 272:49-57.
28. Wang H, Liu CJ. Preparation and characterization of SBA-15 supported Pd catalyst for CO oxidation. Appl Catal B. 2011;106:672-680.
29. Cangül B, Zhang LC, Aindow M, Erkey C. Preparation of carbon black supported Pd, Pt and Pd–Pt nanoparticles using supercritical CO_2 deposition. J of Supercrit Fluids.2009; 50:82–90.

IHTEC 2017

2nd International Hydrogen Technologies Congress

March 15-18, 2017
Çukurova University,
Adana, Turkey

SPONSORS

ORGANIZATION SECRETARIAT

BROS
Congress, Incentive and Events

Cumhuriyet Mah. Tavukçu Fethi Sok. Köşe Palas Apt. No:28/3
Osmanbey - Şişli - İstanbul / TURKEY
Tel: + 90 212 296 66 70 - 119 / **Fax:** + 90 212 296 66 71
bilge.yuksel@brosgroup.net / www.brosgroup.net

ISBN: 978-605-66381-2-1

www.uhtek2017.org